

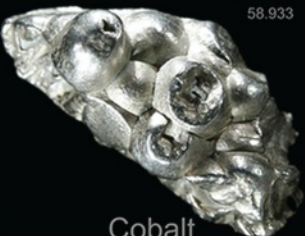





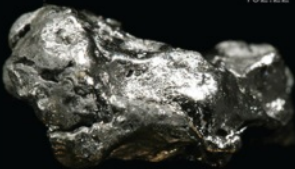
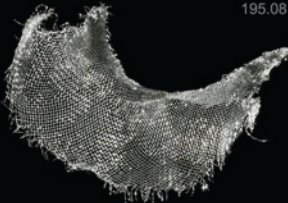

# Конденсированные среды и межфазные границы

РЕЦЕНЗИРУЕМЫЙ НАУЧНЫЙ ЖУРНАЛ

# Condensed Matter and Interphases

PEER-REVIEWED SCIENTIFIC JOURNAL

Том  
Vol. 24, No. 4  
2022

<p>Co 27 58.933</p>  <p>Cobalt</p>	<p>Ni 28 58.693</p>  <p>Nickel</p>	<p>Cu 29 63.546</p>  <p>Copper</p>
<p>Rh 45 102.91</p>  <p>Rhodium</p>	<p>Pd 46 106.42</p>  <p>Palladium</p>	<p>Ag 47 107.87</p>  <p>Silver</p>
<p>Ir 77 192.22</p>  <p>Iridium</p>	<p>Pt 78 195.08</p>  <p>Platinum</p>	<p>Au 79 196.97</p>  <p>Gold</p>

# Condensed Matter and Interphases

## Kondensirovannyye sredy i mezhfaznyye granitsy

Peer-reviewed scientific journal

Published since January 1999

Periodicity: Quarterly

Volume 24, No. 4, 2022

Full-text version is available in the Russian language on the website: <https://journals.vsu.ru/kcmf>

**Condensed Matter and Interphases** (Kondensirovannyye Sredy i Mezhfaznyye Granitsy) publishes articles in Russian and English dedicated to key issues of condensed matter and physicochemical processes at interfaces and in volumes.

**The mission of the journal** is to provide open access to the results of original research (theoretical and experimental) at the intersection of contemporary condensed matter physics and chemistry, material science and nanoindustry, solid state chemistry, inorganic chemistry, and physical chemistry, and to share scientific data in the **following sections**: atomic, electron, and cluster structure of solids, liquids, and interphase boundaries; phase equilibria and defect formation processes; structure and physical and chemical properties of interphases; laser thermochemistry and photostimulated processes on solid surfaces; physics and chemistry of surface, thin films and heterostructures; kinetics and mechanism of formation of film structures; electrophysical processes in interphase boundaries; chemistry of surface phenomena in sorbents; devices and new research methods.

**The journal accepts for publication**: reviews, original articles, short communications by leading Russian scientists, foreign researchers, lecturers, postgraduate and undergraduate students.

### FOUNDER AND PUBLISHER:

Voronezh State University

The journal is registered by the Russian Federal Service for Supervision of Communications, Information Technology and Mass Media, Certificate of Registration ПИ № ФЦ77-78771 date 20.07.2020

The journal is included in the List of peer reviewed scientific journals published by the Higher Attestation Commission in which major research results from the dissertations of Candidates of Sciences (PhD) and Doctor of Science (DSc) degrees are to be published. Scientific specialties of dissertations and their respective branches of science are as follows: 1.4.1. – Inorganic Chemistry (Chemical sciences); 1.4.4. – Physical Chemistry (Chemical sciences); 1.4.6. – Electrochemistry (Chemical sciences); 1.4.15. – Solid State Chemistry (Chemical sciences); 1.3.8. – Condensed Matter Physics (Physical sciences).

The journal is indexed and archived in: Russian Scientific Index Citations, Scopus, Chemical Abstract, EBSCO, DOAJ, CrossRef

Editorial Board and Publisher Office:  
1 Universitetskaya pl., Voronezh 394018  
Phone: +7 (432) 2208445  
<https://journals.vsu.ru/kcmf>  
E-mail: [kcmf@main.vsu.ru](mailto:kcmf@main.vsu.ru)

Price – not fixed

Subscription index  
in the Catalogue «Russian Post»  
is I1H134

When reprinting the materials, a reference to the Condensed Matter and Interphases must be cited

The journal's materials are available under the Creative Commons "Attribution" 4.0 Global License



© Voronezh State University, 2022

### EDITOR-IN-CHIEF:

**Victor N. Semenov**, Dr. Sci. (Chem.), Full Professor, Voronezh State University, (Voronezh, Russian Federation)

### VICE EDITORS-IN-CHIEF:

**Evelina P. Domashevskaya**, Dr. Sci. (Phys.–Math.), Full Professor, Voronezh State University, (Voronezh, Russian Federation)

**Polina M. Volovitch**, Ph.D. (Chem.), Associate Professor, Institut de Recherche de Chimie (Paris, France)

### EDITORIAL BOARD:

**Nikolay N. Afonin**, Dr. Sci. (Chem.), Voronezh State Pedagogical University (Voronezh, Russian Federation)

**Vera I. Vasil'eva**, DSc in Chemistry, Associate Professor, Voronezh State University, (Voronezh, Russian Federation)

**Aleksandr V. Vvedenskii**, Dr. Sci. (Chem.), Full Professor, Voronezh State University, (Voronezh, Russian Federation)

**Victor V. Gusarov**, Dr. Sci. (Chem.), Associate Member of the RAS, Ioffe Physical-Technical Institute RAS (St. Petersburg, Russian Federation)

**Vladimir E. Guterman**, Dr. Sci. (Chem.), Full Professor, Southern Federal University (Rostov-on-Don, Russian Federation)

**Boris M. Darinskii**, Dr. Sci. (Phys.–Math.), Full Professor, Voronezh State University, (Voronezh, Russian Federation)

**Vladimir P. Zlomanov**, Dr. Sci. (Chem.), Full Professor, Moscow State University, (Moscow, Russian Federation)

**Valentin M. Ievlev**, Dr. Sci. (Phys.–Math.), Full Member of the RAS, Moscow State University, (Moscow, Russian Federation)

**Aleksandr D. Izotov**, Dr. Sci. (Chem.), Associate Member of the RAS, Kurnakov Institute of General and Inorganic Chemistry RAS (Moscow, Russian Federation)

**Oleg A. Kozaderov**, Dr. Sci. (Chem.), Associate Professor, Voronezh State University, (Voronezh, Russian Federation)

**Andrey I. Marshakov**, Dr. Sci. (Chem.), Full Professor, Frumkin Institute of Physical Chemistry and Electrochemistry RAS (Moscow, Russian Federation)

**Irina Ya. Mittova**, Dr. Sci. (Chem.), Full Professor, Voronezh State University, (Voronezh, Russian Federation)

**Victor V. Nikonenko**, Dr. Sci. (Chem.), Full Professor, Kuban State University (Krasnodar, Russian Federation)

**Oleg V. Ovchinnikov**, Dr. Sci. (Phys.–Math.), Full Professor, Voronezh State University, (Voronezh, Russian Federation)

**Sergey N. Saltykov**, Dr. Sci. (Chem.), Associate Professor, Novolipetsk Steel (Lipetsk, Russian Federation)

**Vladimir F. Selemenev**, Dr. Sci. (Chem.), Full Professor, Voronezh State University, (Voronezh, Russian Federation)

**Vladimir A. Terekhov**, Dr. Sci. (Phys.–Math.), Full Professor, Voronezh State University, (Voronezh, Russian Federation)

**Evgeny A. Tutov**, Dr. Sci. (Chem.), Associate Professor, Voronezh State Technical University (Voronezh, Russian Federation)

**Pavel P. Fedorov**, Dr. Sci. (Chem.), Full Professor, Prokhorov General Physics Institute RAS (Moscow, Russian Federation)

**Vitaly A. Khonik**, Dr. Sci. (Phys.–Math.), Full Professor, Voronezh State Pedagogical University (Voronezh, Russian Federation)

**Vladimir A. Shaposhnik**, Dr. Sci. (Chem.), Full Professor, Voronezh State University (Voronezh, Russian Federation)

**Andrey B. Yaroslavtsev**, Dr. Sci. (Chem.), Full Member of the RAS, Kurnakov Institute of General and Inorganic Chemistry RAS (Moscow, Russian Federation)

### INTERNATIONAL MEMBERS OF THE EDITORIAL BOARD:

**Mahammad Babanly**, Dr. Sci. (Chem.), Associate Member of the ANAS, Institute of Catalysis and Inorganic Chemistry ANAS (Baku, Azerbaijan)

**Tiziano Bellezze**, Dr. Sci. (Chem.), Marche Polytechnic University (Ancona, Italy)

**Mane Rahul Maruti**, Ph.D. (Chem.), Shivaji University (Kolhapur, India)

**Nguyen Anh Tien**, Ph.D. (Chem.), Associate Professor, University of Pedagogy (Ho Chi Minh City, Vietnam)

**Vladimir V. Pankov**, Dr. Sci. (Chem.), Full Professor, Belarusian State University (Minsk, Belarus)

**Fritz Scholz**, Dr. Sci., Professor, Institut für Biochemie Analytische Chemie und Umweltchemie (Greifswald, Germany)

**Mathias S. Wickleder**, Dr. Sci., Professor, University of Cologne (Koln, Germany)

**Vladimir Sivakov**, Dr. rer. nat., Leibniz Institute of Photonic Technology (Jena, Germany)

### EXECUTIVE SECRETARY:

**Vera A. Logacheva**, Cand. Sci. (Chem.), Voronezh State University, (Voronezh, Russian Federation)

## CONTENTS

**Review***Kukushkin S. A., Osipov A. V.*

Thermodynamics, kinetics, and technology of synthesis of epitaxial layers of silicon carbide on silicon by coordinated substitution of atoms, and its unique properties. A review

407

**Original articles***Bordonskiy G. S.*

Influence of pore geometry on the state of bulk pore water in the pressure-temperature phase space

459

*Zelenaya A. E., Lutsyk V. I., Baldanov V. D.*

Computer model of Cu-Ni-Mn isobaric phase diagram: verification of crystallisation intervals and change of the three-phase reaction type

466

*Kul'kov V. G.*

Migration of an incommensurate intercrystalline boundary and boundary self-diffusion

475

*Lebedev K. A., Zabolotsky V. I., Vasil'eva V. I., Akberova E. M.*

Mathematical modelling of vortex structures in the channel of an electro dialysis cell with ion-exchange membranes of different surface morphology

483

*Lebedev L. A., Tenevich M. I., Popkov V. I.*

The effect of solution-combustion mode on the structure, morphology and size-sensitive photocatalytic performance of  $\text{MgFe}_2\text{O}_4$  nanopowders

496

*Niftaliev S. I., Kozaderova O. A., Kim K. B., Belousov P. E., Krupskaya V. V., Timkova A. V.*

The influence of acid activation of bentonite in the composition of a bipolar membrane on the characteristics of the electro dialysis conversion of sodium sulphate

504

*Ovchinnikov O. V., Smirnov M. S., Perepelitsa A. S., Aslanov S. V., Gureev A. P., Popov V. N., Tsybenko F. A., Hussein A. M. H.*

Photosensitisation of reactive oxygen species with titanium dioxide nanoparticles decorated with silver sulphide quantum dots

511

*Olshannikova S. S., Redko Yu. A., Lavlinskaya M. S., Sorokin A. V., Holyavka M. G., Yudin N. E., Artyukhov V. G.*

Study of the proteolytic activity of ficin associates with chitosan nanoparticles

523

*Samofalova T. V., Semenov V. N., Seregin P. V., Goloshchapov D. L., Buylov N. S.*

Deposition of zinc sulphide films from thiourea complexes and a study of their optical properties

529

*Fedorov P. P., Chernova E. V.*

The conditions for the solid state synthesis of solid solutions in zirconia and hafnia systems with the oxides of rare earth elements

537

*Tsibulnikova A. V., Khankaev A. A., Artamonov D. A., Samusev I. G., Slezhkin V. A., Lyatun I. I., Bryukhanov V. V.*

Modelling optical polarisation processes on laser modified titanium with a polyvinyl alcohol film

545

*Shein A. B., Kichigin V. I.*

Growth kinetics of anodic oxide layers on cobalt silicides in sulphuric acid solutions

559

*Yakovleva N. M., Shulga A. M., Lukianchuk I. V., Stepanova K. V., Kokatev A. N., Chubieva E. S.*

Anodic oxide coatings with a hierarchical micronanostructure on sintered titanium powders

572

90<sup>th</sup> anniversary of the Department of Physical Chemistry of Voronezh State University

584



## Review

Review article

<https://doi.org/10.17308/kcmf.2022.24/10549>

## Thermodynamics, kinetics, and technology of synthesis of epitaxial layers of silicon carbide on silicon by coordinated substitution of atoms, and its unique properties. A review

S. A. Kukushkin✉, A. V. Osipov

*Institute for Problems in Mechanical Engineering of the Russian Academy of Sciences,  
61 Bolshoi Prospekt V.O., St. Petersburg 199178, Russian Federation*

**Abstract**

The review analyses a new method for growing SiC epitaxial films on Si, which is based on the coordinated substitution of some silicon atoms in the Si crystal lattice with carbon atoms. The main idea and theory of the new method is presented. This method significantly differs from classical growth schemes of thin films. The developed method consists in replacing some Si atoms with C directly inside the silicon matrix and not in depositing atoms on the substrate surface. The method allows us to solve one of the main problems of heteroepitaxy, namely, to synthesise low-defect and unstrained epitaxial films with a large difference between the lattice parameters of the film and the substrate. For the first time in the world, a method of the coordinated substitution of atoms of one sort for atoms of another sort has been implemented right inside the original crystal without destruction of the crystal structure. The method resembles the “genetic synthesis” of protein structures in biology. The structural quality of layers obtained by this method significantly exceeds the quality of silicon carbide films grown on silicon substrates by the world’s leading companies. The method is cheap and technologically advanced. The new growth method is compared with classical thin-film growth methods. The thermodynamic and kinetic analysis of the process of substitution of atoms in the solid phase is presented. Using the example of SiC formation, the mechanisms of a wide class of heterogeneous chemical reactions between the gas phase and a solid are described. The review describes a new method for the synthesis of epitaxial SiC layers on single-crystal sapphire substrates, which is based on the method of coordinated substitution of atoms. It is shown that an interface layer with non-standard optical and electrophysical properties appears at the SiC/Si interface formed by this growth method. The unusual properties are caused by a collapse (shrinkage) of the material at which silicon carbide, as a new phase, separates from the silicon matrix. The silicon is subjected to abnormally strong compression. As a result of such shrinkage, every fifth SiC chemical bond is fully consistent with every fourth Si bond, while the remaining bonds are deformed. The latter leads to a change in the structure of the SiC surface zones adjacent to Si and to a transformation of SiC into a “magnetic semimetal”. The epitaxy of SiC films on Si due to the coordinated substitution of half of the Si atoms by C atoms results in absence of lattice misfit dislocations and thus ensures the high crystalline perfection of the SiC films. A description is given for two quantum effects observed in the SiC/Si structures at room temperature in weak magnetic fields: the Meissner–Ochsenfeld effect and the effect of the generation of the Aharonov–Bohm oscillations in the field dependences of the static magnetic susceptibility. A description is given for a discovered phenomenon of phase transition of charge carriers into a coherent state with the simultaneous appearance of a giant value of diamagnetism of the order of  $1/4\pi$  in weak magnetic fields, which has been associated with the appearance of a superconducting state.

**Keywords:** Silicon carbide on silicon, Solid-state reactions, Heterostructures, Epitaxial films, GaN, AlN, ZnO, Spintronics, Wide-bandgap semiconductors, Heat-resistant coatings, Superconductivity, Meissner–Ochsenfeld effect, Aharonov–Bohm effect, LEDs

**Funding:** The study was supported by the Ministry of Science and Higher Education within the framework of the state task for the Institute for Problems in Mechanical Engineering of the Russian Academy of Sciences (FFNF-2021-0001).

✉ Sergey A. Kukushkin, e-mail: [sergey.a.kukushkin@gmail.com](mailto:sergey.a.kukushkin@gmail.com)

© Kukushkin S. A., Osipov A. V., 2022



The content is available under Creative Commons Attribution 4.0 License.

**Acknowledgements:** This work was carried out using the equipment of the unique scientific facility “Physics, Chemistry and Mechanics of Crystals and Thin Films” of the Institute for Problems in Mechanical Engineering of the Russian Academy of Sciences (St.-Petersburg). The authors would like to express their profound gratitude to T. V. Lavrova for her help with manuscript preparation. The authors express special gratitude to R. S. Telyatnik for the great work on editing the English text of this paper. The authors are especially grateful to the editorial board of the journal “Condensed Matter and Interphases” for the invitation to write and publish this review in this journal.

**For citation:** Kukushkin S. A., Osipov A. V. Thermodynamics, kinetics, and technology of synthesis of epitaxial layers of silicon carbide on silicon by coordinated substitution of atoms, and its unique properties. Review. *Condensed Matter and Interphases*. 2022;24(4): 407–458. <https://doi.org/10.17308/kcmf.2022.24/10549>

**Для цитирования:** Кукушкин С. А, Осипов А. В. Термодинамика, кинетика и технология синтеза эпитаксиальных слоев карбида кремния на кремнии методом согласованного замещения атомов и его уникальные свойства. Обзор. *Конденсированные среды и межфазные границы*. 2022;24(4): 407–458. <https://doi.org/10.17308/kcmf.2022.24/10549>

### Table of contents

1.	Introduction .....	409
2.	The method of coordinated substitution of atoms: processes occurring in the solid Si phase during the growth of SiC epitaxial films on Si. A new mechanism of stress relaxation during the SiC nucleation on Si .....	412
2.1.	The growth of an epitaxial SiC layer on a Si(111) surface.....	412
2.1.1.	The stage of formation of dilatation dipoles as a necessary condition for the dislocation-free growth of SiC.....	412
2.1.2.	The stage of transformation of dilatation dipoles into epitaxial SiC.....	414
2.2.	The method of coordinated substitution of atoms as a first-order phase transition through an intermediate state .....	420
2.3.	Growth of the epitaxial SiC layer on the Si(100) surface .....	421
3.	Quantum-mechanical theory of epitaxial transformation of silicon into silicon carbide.....	424
3.1.	Energy profile, intermediate and transition states of the reaction of heterogeneous synthesis of SiC .....	426
3.2.	Transition of “pre-carbide” silicon into silicon carbide on the (100) surface .....	426
4.	Diffusion mechanism of CO and SiO molecules into Si with the simultaneous chemical transformation reaction of Si into SiC.....	428
5.	Vacancy growth of single-crystal silicon carbide — a new stage in the development of the method of coordinated substitution of atoms .....	430
6.	Coating method for smooth and profiled Si surfaces by ultrathin silicon carbide layers.....	433
7.	Formation of epitaxial SiC layers on the surface of other materials by the method of coordinated substitution of atoms .....	434
7.1.	Synthesis of epitaxial silicon carbide films on sapphire substrates ( $\alpha\text{-Al}_2\text{O}_3$ ) .....	434
7.1.1.	Current state and problems of growing of epitaxial SiC films on sapphire .....	434
7.1.2.	Growth of epitaxial Si films on sapphire with the Si (100) and (111) layer orientations .....	435
7.1.3.	Conversion of Si epitaxial films grown on sapphire into SiC epitaxial films by the method of coordinated substitution of atoms .....	437
7.1.4.	Structural and morphological features of the formation of SiC films on sapphire .....	438
7.2.	A new method of formation of protective SiC-C composite coatings on graphite.....	440
8.	Crystal structure, polytypism, optical, electrophysical, mechanical, and other properties of SiC synthesised on Si by the method of coordinated substitution of atoms .....	443
9.	Features and anomalies of optical, magnetic, and other properties of SiC films on Si grown by the method of coordinated substitution of atoms .....	445
9.1.	The physical nature of the emergence of features and anomalies in the properties of SiC films on Si grown by the method of coordinated substitution of atoms.....	445
9.2.	Structural features of the surface of SiC epitaxial films synthesised by the MCSA, determined using photoelectron spectroscopy .....	447
9.3.	Anomalies of magnetic properties of epitaxial SiC films synthesised by the MCSA.....	451
9.4.	Electronic phase transitions in SiC epitaxial layers synthesised by the MCSA.....	451
10.	Conclusions .....	453

## 1. Introduction

The purpose of our study was to summarise the latest data on the growth mechanisms, properties, and applications of silicon carbide films on silicon that are synthesised by a new method of the topochemical coordinated substitution of atoms. The reader may rightly ask the following question. Why do we need another review dedicated to a description of this method? Only in the last year and a half have the authors of this article published two reviews [1, 2] and a chapter in the book [3] on this topic, and three more review articles [4–6] were published several years earlier. This topic, however, turned out to be so deep and multifaceted, while silicon carbide synthesised by the method of coordinated substitution of atoms has shown such unusual properties — and findings in this field are updated literally daily — that we hope that the question of readers about the need for another review article will vanish in the process.

Before proceeding to a description of the growth of silicon carbide on silicon, let us try to answer the following questions. Why is silicon carbide needed at all, and then why silicon carbide on a silicon substrate is required? How is it superior to other materials? What useful properties does it have? By what parameters does it exceed silicon?

Silicon is one of the key basic materials for most modern electronic devices, computers, communications equipment, sensors, transmission and playback equipment. This material has both a number of advantages and some significant disadvantages. One of the important advantages of silicon is its availability: producing silicon wafers for chips and microcircuits, polishing the wafers, cleaning and cutting them are well developed all over the world. Therefore, electronic devices based on silicon wafers are relatively cheap. Despite this, the parameters of silicon-based electronic devices have a number of limitations. For example, with an increase in the ambient temperature, the semiconductor properties of silicon deteriorate significantly, and instability in the operation of devices and failures appear. Silicon cannot operate stably under conditions of increased radiation, for example, in space and in nuclear reactors. It also has a number of other unavoidable limitations. In

this regard, presently, it has become clear that, for some applications, other materials, which can at least partially, if not completely, replace silicon, should be used. Such semiconductor materials include wide-bandgap semiconductors [7]: silicon carbide (SiC), gallium nitride (GaN), aluminium nitride (AlN), gallium oxide ( $\text{Ga}_2\text{O}_3$ ), their solid solutions, and a number of other materials. These semiconductors possess excellent electrical characteristics and can ensure the operation of electronic and optoelectronic devices at elevated temperatures and under conditions of increased radiation. These semiconductor materials have high hardness and high elastic moduli. Silicon carbide, for example, approaches diamond in terms of hardness. Semiconductor materials such as SiC, AlN, GaN, and  $\text{Ga}_2\text{O}_3$  have a wide band gap. The width of the band gap of these materials varies from 2.4 eV for cubic SiC to 6.1 eV for AlN. Therefore, these materials are called wide-bandgap semiconductors. The main obstacle to realising the high potential of wide-bandgap semiconductors is a lack of technologies that allow producing epitaxial layers of these semiconductors to be affordable in terms of price and quality. It is also important to provide the possibility of integrating wide-bandgap semiconductors with traditional silicon electronics. This is necessary for the production of devices with wide-bandgap structures on silicon substrates, the production and the processing technologies of which have presently been brought to perfection. Currently, all industrialised countries and the largest electronic companies in the world are solving this problem.

Silicon carbide is the only binary compound of silicon and carbon that exists in the solid phase under normal conditions. Silicon carbide is a wide-bandgap semiconductor with a band gap between 2.32 eV and 3.24 eV, depending on the silicon carbide polytype. Single-crystal SiC has a high breakdown electric field strength, high drift velocity of electrons, and high thermal conductivity. Due to a dielectric strength of SiC that is an order of magnitude higher than that of silicon, the doping level of a SiC diode can be two orders of magnitude higher than that of silicon at the same breakdown voltage. Silicon carbide is a radiation-resistant material. The high thermal conductivity of SiC (at the level

of thermal conductivity of copper) significantly simplifies the problem of heat removal from devices. This property, combined with high allowable operating temperatures and high saturation velocities of charge carriers (high saturation currents of field-effect transistors), makes SiC devices very promising for use in power electronics. In addition, the high Debye temperature, which determines the temperature at which phonons arise, suggests a high thermal stability of SiC. Thus, in almost all important criteria, silicon carbide is superior to the classical semiconductor materials Si and GaAs. By the irony of history, the active use of silicon carbide in microelectronics began only recently, despite the fact that silicon carbide was one of the first materials used in solid-state electronics. Back in 1907, H. Round observed a luminescence when an electric current passed through a SiC crystal. Oleg Losev studied the electroluminescence of silicon carbide in more detail in 1923–1940. Losev also established the existence of a connection between rectification and electroluminescence in SiC. Thus, the two most important phenomena for semiconductor electronics — electroluminescence and rectification properties of *p-n* structures — were first discovered in SiC crystals.

The modern market requires the creation of a new type of light-emitting diodes, semiconductor lasers, high-electron-mobility transistors (HEMTs), sensors and gas transducers, microwave devices, and optical switches. Recently, there has been an urgent need for both LEDs emitting hard ultraviolet radiation and ultraviolet radiation sensors. It is possible to create such types of LEDs and sensors by using wide-bandgap semiconductors such as AlN and GaN. Currently, however, there are no cheap and high-quality native substrates of these materials. As a rule, these materials are grown on sapphire and silicon carbide substrates. Thus, silicon carbide is an indispensable material also as a substrate for creating heterostructures based on wide-bandgap semiconductors such as gallium and aluminium nitrides. It is heterostructures based on gallium nitride compounds grown on SiC substrates that make it possible to create transistors with high charge-carrier mobility, high-power LEDs, and blue lasers.

For many years, the use of single-crystal SiC in electronics has been constrained by the high cost of SiC and the difficulty of its production. Currently, this problem is gradually being solved. However, researchers are looking for other ways to produce SiC. One of these ways is the synthesis of SiC epitaxial layers on a silicon substrate. There is every reason to believe that in the future such structures will occupy their niche in micro- and optoelectronics, since they combine the properties of silicon as one of the main materials for electronics with the properties of such a wide-bandgap material as silicon carbide. These materials are much cheaper than SiC single crystals. Moreover, it is possible to grow SiC layers on Si substrates of a large diameter.

The complexity of obtaining SiC films of epitaxial quality is largely due to the fact that SiC crystallises in more than 250 different crystal structures (polytypes), and only one of these polytypes is cubic (3C-SiC). The remaining polytypes have hexagonal or rhombic symmetry. The cubic polytype has the narrowest band gap among all silicon carbide polytypes and slightly excels gallium phosphide (GaP) by maximum operating temperature. The width of the band gap of the 3C-SiC polytype is 2.32 eV. Although 3C-SiC has the width of the band gap and the dielectric strength lower than those of hexagonal polytypes of SiC, its electrical properties are much more isotropic than properties of the hexagonal and rhombic polytypes of SiC. In addition, the mobility of charge carriers in it is very high. Finally, and most important, the 3C-SiC polytype is the most suitable polytype for growth on cubic silicon, since the silicon crystal used as a substrate has cubic symmetry. At present, there are no commercial single crystals of the 3C-SiC polytype. Therefore, the only way to obtain the cubic SiC polytype is to grow 3C-SiC layers on a silicon substrate.

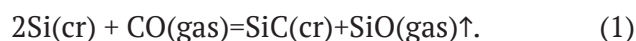
The first attempts to obtain SiC films on silicon substrates were made by S. Nishino [8]. He proposed to use the standard technique of chemical vapour deposition (CVD) for the formation of SiC films, which is widely used for the synthesis of semiconductor structures. Methyltrichlorosilane ( $\text{CH}_3\text{SiCl}_3$ ) and mixtures of  $\text{SiH}_4$  and  $\text{C}_3\text{H}_8$  were used as sources of carbon

and silicon [8]. Based on the grown films, several types of field-effect transistors were created. However, the parameters of these devices, as well as the quality of the films, were low. This was due to the fact that the lattice parameters of Si and SiC differ by approximately 19%. This is the first (and main) problem preventing the production of SiC epitaxial films on Si. Due to the difference in the lattice parameters of Si and SiC, a large number of misfit dislocations and other growth defects are formed at the interface between the film and the substrate; thick SiC films on Si, with a thickness of more than 1  $\mu\text{m}$ , contain cracks. The second but not less difficult problem is a large difference in thermal expansion coefficients between Si and 3C-SiC. According to the data provided in [9], the linear thermal expansion coefficient of 3C-SiC is  $3.9 \cdot 10^{-6} \text{ K}^{-1}$ , while the linear expansion coefficient of Si is  $2.6 \cdot 10^{-6} \text{ K}^{-1}$ . As a result, when a Si wafer with a SiC layer is cooled from the growth temperature to room temperature, a strong bending of the wafer and cracks occur. The review [10] presents a picture of the deflection of a Si wafer with an epitaxial SiC film. Finally, the third problem is associated with the low melting point of Si (Si melts at a temperature of 1412 °C). It is impossible to grow SiC films, synthesised on Si, at temperatures equal to or higher than 1500 °C. At temperatures above 1500 °C, the diffusion mobility of the components and the rate of the chemical reaction between the components from which SiC is grown are quite high. This allows implementing the oriented nucleation of two-dimensional SiC nuclei. Therefore, for the growth of SiC films at temperatures below 1412 °C, researchers have to apply various methods of preliminary modification of the Si surface. In the review [11], an analysis of a large set of experimental data on the growth of SiC films on Si was made. It turned out [10, 11] that, in order to obtain films of acceptable quality, the Si substrate must be carbonised before the growth. The SiC buffer layer grown as a result of carbonisation serves as a seed for further epitaxy of 3C-SiC layers and has a significant effect on their deformation. However, carbonisation failed to radically solve the

problem of obtaining 3C-SiC layers with a low defect content suitable for creating commercial semiconductor devices.

The main reason that did not allow researchers to obtain low-defect 3C-SiC layers by the carbonization method and thereby to form a highly oriented seed layer for further SiC growth will be described below.

In 2008, in the work [12], a new method for synthesising epitaxial SiC films on Si was theoretically predicted, experimentally confirmed, and patented [13]. The method [12] is based on the chemical transformation (conversion) of silicon surface layers into silicon carbide epitaxial layers due to the chemical interaction of gaseous carbon monoxide (CO) with the silicon substrate surface in the reaction



This method was called the method of coordinated substitution of atoms (MCSA) in later works [14]. The term “coordinated” means that new chemical bonds are formed simultaneously and in coordination with the destruction of old bonds, which leads to the preservation of the structure of chemical bonds. Later, in [4–12], a consistent theory that describes the entire spectrum of interconnected physicochemical processes occurring during the topochemical transformation of Si into SiC was developed.

A detailed description of processes of the SiC growth by the MCSA that were carried out from the beginning of the studies in 2004 and until 2014 can be found in the reviews [10–12]. These publications describe both theoretical and experimental studies and provide a detailed description of the installation for the growth of SiC. These studies also describe a number of technological methods necessary to obtain SiC layers of a high degree of crystalline perfection.

In this review, we will not discuss those. Here, we only briefly outline the basic technology of the SiC conversion from Si and then proceed to describe the new, obtained since 2014, theoretical and experimental data on the growth and structure of the SiC films.



## 2. The method of coordinated substitution of atoms: processes occurring in the solid Si phase during the growth of SiC epitaxial films on Si. A new mechanism of stress relaxation during the SiC nucleation on Si

### 2.1. The growth of an epitaxial SiC layer on a Si(111) surface

#### 2.1.1. The stage of formation of dilatation dipoles as a necessary condition for the dislocation-free growth of SiC

In this section, we briefly outline the main theoretical provisions of the MCSA. Previously, they have already been repeatedly described in one or another form in a number of our reviews [1–6]. For the convenience of the reader, we briefly repeat these results and then proceed to describe the new data.

The MCSA is based on the “assembly” of a new silicon carbide matrix based on the old silicon matrix by partial substitution of silicon atoms in the substrate crystalline matrix with carbon atoms. The “assembly” of the SiC matrix is carried out due to the chemical reaction (1). Reaction (1) proceeds in two stages [4–6, 15–20]. During the first stage, an intermediate state in silicon is formed (an analogue of the activated complex): “silicon vacancy – carbon atom – silicon matrix” ( $C-V_{Si}$ ). During this stage, carbon atoms are located in the interstitial positions of the silicon matrix. It can be said that a metastable superlattice is formed near the silicon surface. During the second stage of the reaction, it transforms into silicon carbide, and the released vacancies coalesce into pores that are being formed under the silicon carbide layer. In a crystal of cubic symmetry, these two dilatation centres (a carbon atom and a silicon vacancy) interact elastically with each other. If dilatation dipoles are located perpendicular to the plane (111) of silicon, then they are attracted to each other [15–20]. In this case, almost all of the dilatational elastic energy, arising due to the introduction of carbon atoms and the formation of vacancies, relaxes [15–20]. Since, during one of the stages of the transformation of Si into SiC, the formation of defects ( $C-V_{Si}$ ) occurs, and a mechanical elastic interaction arises between them, we had to face the need to derive a formula for the energy of their interaction. As a result, the theory of elastic

interaction of two point defects in crystals of cubic and hexagonal symmetry was developed [15, 16, 21], and the formula for the interaction energy of two point defects in these crystals was derived. For crystals of cubic symmetry, the interaction energy  $E_{int}(\cos\varphi(x, y, z))$  of two point defects is [15, 16, 21]

$$E_{int}(\cos\varphi(x, y, z)) = -\frac{E_0(\cos^4\varphi_x + \cos^4\varphi_y + \cos^4\varphi_z)}{r^3}, \quad (2)$$

where  $E_0 = 15K(3c_{11} - 4c_{44})\Omega^I\Omega^{II}\eta/8\pi(c_{12} + 2c_{44})$ ;  $K = (c_{11} + 2c_{12})/3$  is the compression modulus (for Si  $K^{Si} = 0.98 \cdot 10^{11} \text{ N}\cdot\text{m}^{-2}$ );  $c_{11}$ ,  $c_{12}$ , and  $c_{44}$  are elastic moduli of a cubic crystal; for Si,  $c_{11} = 1.66 \cdot 10^{11} \text{ N}\cdot\text{m}^{-2}$ ,  $c_{12} = 0.633 \cdot 10^{11} \text{ N}\cdot\text{m}^{-2}$ ,  $c_{44} = 0.796 \cdot 10^{11} \text{ N}\cdot\text{m}^{-2}$ ;  $\eta = (c_{11} - c_{12} - 2c_{44})/c_{44}$  is the crystal anisotropy parameter,  $\eta = -0.689$  for Si;  $\Omega^I$  and  $\Omega^{II}$  are associated with the difference between the volumes of the inclusion and the vacancy cavity;  $r$  is the distance between defects;  $\cos\varphi_i = x/r$  are the directional cosines between the  $x$ ,  $y$ ,  $z$  axes and the direction of the straight line connecting the centres of interacting defects. The value of  $(\cos^4\varphi_x + \cos^4\varphi_y + \cos^4\varphi_z - 3/5)$  has a maximum in the (100) direction equal to 0.4, a minimum in the  $\langle 111 \rangle$  direction equal to  $-0.27$ , and a saddle point of  $-0.1$  in the  $\langle 110 \rangle$  direction. Therefore, the greatest attraction between point defects occurs if these defects are in interstices located along the  $\langle 110 \rangle$  directions of silicon, i.e., if the carbon atom is located in the interstitial position under the (111) planes along the  $(\bar{1}10)$  plane, and the vacancy should be located along the  $\langle 111 \rangle$  direction with respect to this atom. In this case, the attraction between the silicon vacancy and the carbon atom will be at a maximum. The interaction energy is inversely proportional to the cube of the distance between defects. Such a system is a stable complex, which, by analogy with an electric dipole, was called a dilatation dipole [15, 16]. Formula (2) in this form was first obtained in [21]. It should be noted that the interaction of two point dipoles in crystals of cubic symmetry was first studied by Eshelby [22]. Subsequently, it turned out that the sign of the interaction energy obtained by him should be substituted by the opposite one. The sign of the interaction of point defects also turned out to be

incorrect when deriving the formula for the interaction energy from the anisotropic tensor Green's function obtained by Lifshits and Rozentsveig [23]. A detailed presentation of the interaction of point defects in anisotropic media can be found in [15, 16, 21–24].

The total elastic energy of a crystal during the formation of interacting defects in its volume has the form [16]:

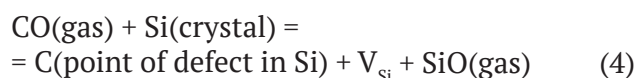
$$W(\cos\varphi(x, y, z)) = E_C + E_V + E_{\text{int}}(\cos\varphi(x, y, z)) \quad (3)$$

Here,  $E_V$  is the elastic energy arising in the Si crystal due to the deformation caused by the removal of the Si atom and the formation of the silicon vacancy;  $E_C$  is the elastic energy arising in the Si crystal due to the deformation caused by the introduction of carbon into the interstitial space of the Si lattice; the magnitudes of these energies  $E_V$  and  $E_C$  are determined from the expression  $E_{C,V} = \frac{2\mu^{\text{Si}} K^d}{2K^d + 4\mu^{\text{Si}}} \frac{(V^d + V^{\text{Si},m})^2}{3V^{\text{Si}}}$ ;  $V^d$  is

the volume occupied by a defect (a Si or C vacancy in an interstitial) in silicon;  $V^{\text{Si},m}$  is the volume of the interstitial position in silicon;  $\mu^{\text{Si}}$  – shear modulus of Si,  $\mu^{\text{Si}} = 5.2 \cdot 10^{10} \text{ N/m}^2$ ;  $K^d$  is the bulk modulus of a point defect (Si or C vacancies in the interstitial). Since the carbon atom and the vacancy are modelled as point incompressible dilatation centres, their bulk moduli can be set equal to  $K^d = \infty$ ;  $V^{\text{Si}}$  is volume per atom in silicon,  $V^{\text{Si}} = 2.0 \cdot 10^{-29} \text{ m}^3$ . Calculations of the values of elastic energy according to formulas (2) and (3) can be found in [15, 16]. The calculations have shown that the dilatational elastic energy can completely relax only due to dipoles. The lifetime of dilatation dipoles at temperatures 1100–1250 °C is approximately  $\sim 10^{-1} \div 1$  sec, therefore, elastic dipoles also play the role of ordering centres of epitaxy. If point defects are located along the  $\langle 100 \rangle$  direction, then, on the contrary, they will repel each other, dipoles will not be formed, and the resulting large elastic energy makes unfavourable the location of defects along the  $\langle 100 \rangle$  direction, which leads to misorientation of the layers.

Thus, during the first stage of the reaction, the CO molecule interacts with the surface of the silicon substrate and decomposes into a carbon atom and an oxygen atom. Oxygen atoms enter

into a chemical reaction with Si atoms, which results in the formation of SiO gas. The SiO gas is removed from the system, and a vacancy forms in the substrate in place of the silicon atom, converted into SiO gas. The excited carbon atom, which is released from the CO molecule by the chemical reaction, is shifted to an interstitial position in the silicon lattice [5, 14, 20]. This stage can be written as follows:



where  $V_{\text{Si}}$  is the silicon vacancy. It is at this stage the intermediate phase of the so-called “pre-carbide” silicon is formed. This phase is silicon saturated with defect pairs  $\text{C} + V_{\text{Si}}$ . As follows from (4), pairs of point dilatation defects C and  $V_{\text{Si}}$  always form and disappear in pairs. “Pre-carbide” silicon is actually silicon where every second Si atom is substituted with C atom via the reaction (4). Thus, one Si cell contains 4 pairs of dilatation defects  $\text{C} + V_{\text{Si}}$ , i.e., in “pre-carbide” silicon, everything is ready for the transformation of silicon into silicon carbide. This process occurs during the next stage of the reaction, which is described by the equation



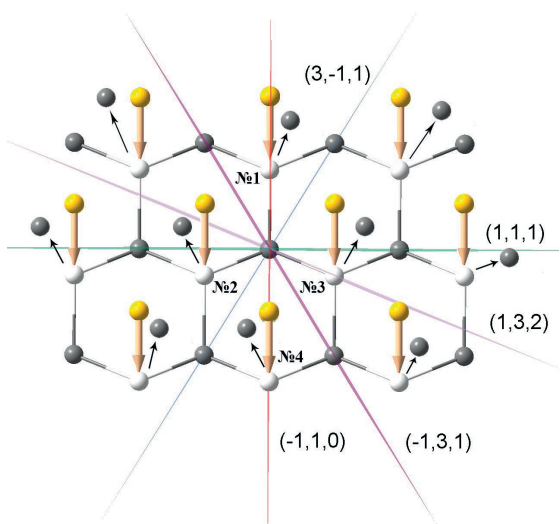
At this stage, the carbon atoms move in a coordinated manner towards the silicon vacancies, thus forming silicon carbide. The final topochemical reaction (1) is obtained by summing steps (4) and (5). It is the elastic interaction between pairs of point dilatation defects C and  $V_{\text{Si}}$  that determines the kinetics of reaction (1). It is important to emphasise that the first-order phase transition (5) proceeds in a coordinated manner, i.e., the breaking of old bonds between atoms and the formation of new bonds proceed simultaneously and in concert, which essentially ensures the high crystalline perfection of the silicon carbide film. Such a transformation is always accompanied by the formation of voids, since the volume of the Si cell is twice the volume of the SiC cell. The length of all bonds decreases by 20%, namely from 2.35 to 1.88 nm. The first-order phase transition (5) proceeds layer by layer, i.e., several layers of pre-carbide silicon are simultaneously converted into

SiC with the interface shifted perpendicularly to the substrate surface. The reaction rate constant of chemical reaction (5) is approximately two orders of magnitude higher than that of reaction (4), therefore step (5) proceeds noticeably later and much faster than step (4). This can explain the fact that the SiC film is formed with rather uniform thickness and without noticeable voids. All voids appear in silicon under the SiC film [1–6, 18–20].

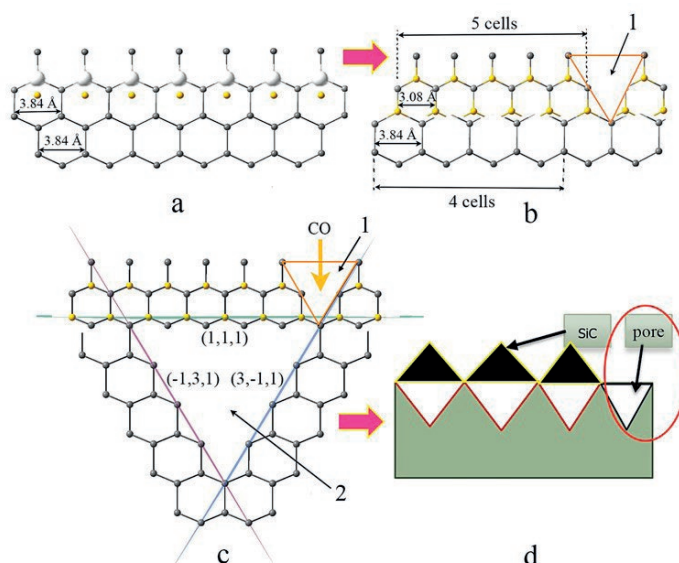
A surprising feature of reaction (1) is the fact that reaction ends with the formation of silicon carbide, and the reaction does not proceed further to the formation of carbon or even diamond. This is related to both step (4) and step (5). For reaction (4), it is necessary to have “free space” in a silicon cell to accommodate a carbon atom in it. Only one carbon atom can be located inside this cell. This is the reason why only four atoms in the silicon lattice can be substituted, and not all of its eight atoms. Otherwise, we would obtain a very strongly elastically stretched diamond lattice. This would require overcoming a very high activation energy. Such a reaction cannot proceed under these conditions. Even a simpler reaction of placing a carbon atom in each crystal cell of silicon cannot proceed. Carbon atoms can be inside the cell only if one silicon atom is removed from the silicon cell, i.e., the cell contains a silicon vacancy. Moreover, the point defects (carbon and vacancy) must be located strictly along the [111] crystallographic direction in Si. Only in this case, due to the elastic mechanical attraction of the dilatation defects, their total elastic energy is equal to zero. Otherwise, along other crystallographic directions in Si, reaction (4) does not occur. Thus, reaction (4) not only “selects” the required four Si atoms but also “selects” one single direction in the crystal space, along which the future SiC crystal lattice is formed. However, reaction (4) is not sufficient for the transition of Si into SiC. Reaction (5) completes the process of SiC synthesis. When reaction (5) proceeds, it is important that five SiC crystal cells formed as a result of this reaction almost exactly coincide with four Si cells [4, 10]. As a result, the reaction of displacement of atoms (5) occurs with minimal energy consumption. It is reaction (5) that completes the process of the “final docking” of crystal lattices.

### 2.1.2. The stage of transformation of dilatation dipoles into epitaxial SiC

The destruction of the dipole leads to an increase in the elastic energy of the silicon crystal and, accordingly, to an increase in its total free energy. When the dipole is destroyed, the carbon atom must take the place of the vacancy. This leads, on the one hand, to an increase in elastic energy, and, on the other hand, to a decrease in the total internal energy of the system, since the chemical bonds become saturated. If a break occurs only in the mechanical attraction between defects, then the estimate of the lifetime of the activation complex at a temperature of 1250 °C provides approximately the following value  $\tau_{lif} \sim 1$  sec. However, the transition of the intermediate substance into silicon carbide through breakage of the bond in a dipole and an increase in the elastic energy of the system are not acceptable for the growth of a single-crystal layer of silicon carbide. With such a transition, only a disordered defective carbide layer containing dislocations, cracks, etc. will grow, since the elastic energy at the beginning of such a transition will be high. There is another and the only possible way for the transition of the intermediate substance to silicon carbide without increasing the elastic energy in the system [5]. Let us turn our attention to Fig. 1. If carbon atoms move from interstitial positions to positions occupied by vacancies (numbers No. 1–No. 4), then a silicon carbide layer will be formed in the upper part of silicon. In silicon carbide, the lattice parameters are much smaller than in silicon. This means that part of the original volume occupied by the silicon lattice should be released. In this case, the relaxation of the elastic energy will occur. The placing sequence of the (111) planes of the silicon lattice in projection onto the  $(11\bar{2})$  plane is shown in Fig. 2, as well as in Fig. 1. Let the upper layer of silicon, which has already passed into the intermediate state (Fig. 2a), be transformed into a layer of silicon carbide (Fig. 2b). The interatomic distance between Si atoms along the  $(111)$  plane in the projection onto the plane  $(11\bar{2})$  equals 3.84 Å. We assume that the interatomic distance in the intermediate substance has not changed and corresponds to the distance between silicon atoms. The distance between C atoms lying along the  $(111)$  plane in



**Fig. 1.** Silicon lattice: the stacking sequence of (111) planes in the projection on (112) plane. ● – the silicon atoms, ● – the carbon atoms in interstitial positions, ○ – the silicon vacancies, ↓ – the directions of the interaction between defects in dilatation dipoles, № 1 – № 4 – the numbers of atoms to be removed for the formation of elastic dipoles



**Fig. 2.** Consecutive stages of transformation of the intermediate complex “carbon atom – silicon vacancy” into the silicon carbide (in the projection on  $(11\bar{2})$  plane). (a) Intermediate stage. (b) Stage of the “displacement” type phase transformation with the formation of the silicon carbide and the contraction pores. (c) Silicon carbide, etch pit and contraction pore admitting carbon monoxide into silicon bulk. (b) Stage of the “displacement” type phase transformation with the formation of the silicon carbide and the contraction pores. (c) Silicon carbide, etch pit and contraction pore admitting carbon monoxide into silicon bulk [5, 6]

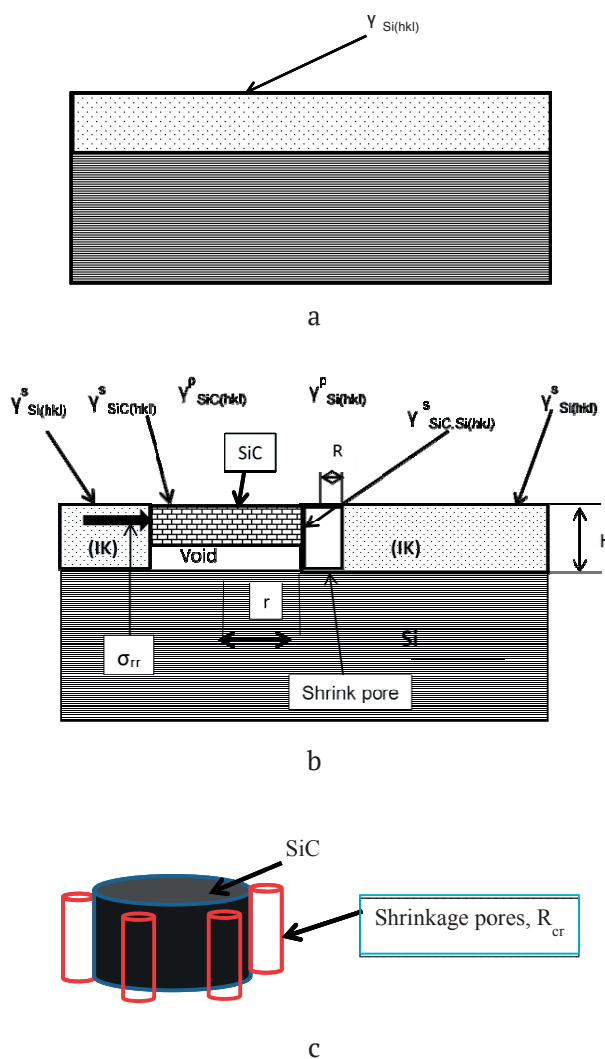
the projection on the  $(11\bar{2})$  plane in SiC is 3.08 Å. The distance between the planes of five SiC cells  $\approx 15.4$  Å, which, up to the first decimal place, coincides with the distance between the planes of four Si cells  $\approx 15.4$  Å. This means that not all bonds are broken during the transformation of the intermediate substance into silicon carbide but only the bonds that do not coincide with the bonds in Si (Fig. 2b). In this case, under the place where the bonds have been broken, namely under the Si layer, an empty space is formed. If we consider a higher number of layers instead of two layers of cells as in Fig. 2a, than it follows from solely geometric considerations that the etch pits will have a pyramidal shape. In the section by the  $(11\bar{2})$  plane, they will look like a triangle, bounded by the planes (111),  $(\bar{1}\bar{3}1)$  and  $(3\bar{1}1)$  (Fig. 2c). The shape of this figure will be similar to the shape of the etch pit formed during silicon etching [25]. Therefore, the voids under the silicon carbide layer will be called etch pits. Simultaneously with the etch pits, as can be seen

from Fig. 2b, due to the decrease in the volume of the material, stresses are formed and lead to the initiation of shrinkage pores located along the surface of the substrate. Shrinkage pores are formed in places that are multiples of five cell sizes of silicon carbide. The minimum shrinkage pore has a size comparable to the size of a silicon cell (Fig. 2b).

Thus, the SiC layer formed according to this mechanism consists of a SiC film layer covering triangular pores located under its surface and shrinkage pores located along the substrate surface (Fig. 2d). For the growth of the epitaxial layer of silicon carbide, it is necessary for the releasing part of the volume occupied by the intermediate substance transforming into a SiC film to be redistributed only between the film and etch pits. The formation of shrinkage pores is an undesirable process, since in this case, part of the film is broken. The transition of the intermediate complex into silicon carbide occurs when carbon atoms are displaced from interstitial positions in silicon to positions occupied by vacancies

(numbers No. 1–No. 4 (Fig. 1)). In this transition, the C atom combines with the Si atom and, since the C atom is smaller than the Si vacancy, a vacancy in Si is formed at the same time. It follows from formula (2) that, in this case, the attraction of defects will be changed to repulsion, since the sign of the defects changes in this case. As a result of this process, the total elastic energy of the system increases. To avoid it, a phase transition occurs in the system with the formation of a SiC nucleus and a pore [5]. This process minimises the total free energy of the system. During the phase transition, the initial volume of the intermediate complex changes dramatically. From the volume initially occupied by it, a layer of silicon carbide and pores are formed. The volume of the formed silicon carbide is much lower than the volume occupied by silicon. This means that the transition of the intermediate substance into silicon carbide with the formation of etch pits is a typical first-order phase transition. In [5], the minimum work of formation (free energy) of a SiC nucleus and an etch pit was calculated. The transition of an intermediate substance into silicon carbide is a first-order structural phase transition of the displacement type (carbon atoms are displaced from their original positions into the region of silicon vacancies). As the carbon atom shifts to position No. 1, and if the top silicon atom has not evaporated, the silicon carbide nucleus will have a pyramid shape, and the etch pits take the shape of a triangular depression. In order to simplify the calculations in [5], we assumed that the silicon carbide nuclei and etch pits have the shape of a flat disk of a certain size with radius  $r$  and height  $H/2$ , which is not true in general. The scheme of the transformation of the intermediate complex into the SiC nucleus and the etch pit is shown in Fig. 3. As can be seen, the silicon carbide layer is formed near the surface of the silicon substrate and emerges on its surface. This layer is only partially coherently, without mechanical deformation, bonded to the underlying silicon atoms. The pore is located under the rest of the surface of the nucleus. If the SiC nucleus was completely coherently bonded to the substrate, then the expression for the minimum work of the nucleus formation would contain a term describing the elastic energy of interaction between the nucleus

and the substrate. However, this is not the case, since simultaneously with the nucleus, an etch pit is also nucleated under its surface (Fig. 3c). This means that a part of the substrate material “turns into a void”, turning the energy of the elastic interaction of the film with the substrate to zero. At the same time, in contrast to conventional film growth, a SiC nucleus formed in this way is already epitaxially oriented. Its orientation is determined not by the surface of the substrate but by its internal structure where the intermediate



**Fig. 3.** Consecutive stages of transformation of the intermediate complex “carbon atom – silicon vacancy” into the silicon carbide (in the projection on  $(11\bar{2})$  plane). (a) Intermediate stage. (b) Stage of the “displacement” type phase transformation with the formation of the silicon carbide and the contraction pores. (c) Silicon carbide, etch pit and shrinkage pore admitting carbon monoxide into silicon bulk [5]

substance — silicon with elastic dipoles — have existed. This process can take place only with the simultaneous nucleation of the nucleus and an etch pit, which is ensured by the shift of carbon atoms, which leads to the simultaneous creation of vacancies and SiC molecules. If the nucleus is formed before the etch pit, then the free energy of the system would increase by an amount equal to the elastic energy of the coherent interaction of the nucleus and the substrate. Thus, a joint nucleus containing the etch pit and the silicon carbide nucleus is formed.

The formula for the thermodynamic work of formation of the joint nucleus etch pit – SiC nucleus was derived in [5]. Note that the concept of thermodynamic work is wider than the concept of free energy or the isobaric-isothermal Gibbs potential of the formation of a new phase nucleus. If the volume of the system is preserved during the phase transition, then the work of formation of the new phase is equal to the change in free energy, and, as is known, in the case of the phase transition of the first kind, the volume of the new phase is different from the volume of the old phase. Therefore, it is necessary to use free energy in thermodynamic calculations of phase transitions with a certain degree of caution. If the pressure in the system is constantly maintained during the phase transition, then the work of nucleation coincides with the isobaric-isothermal Gibbs potential. Therefore, in [5], a general expression was obtained specifically for the work of formation of a new phase, and not for specific cases. This expression looks like:

$$R_{\min}^{cr}(\cos\varphi(x, y, z)) = \frac{\Gamma_1\Gamma_2(4\pi\Gamma_2 - \Gamma_3\varepsilon)}{[\xi - \Lambda(\cos\varphi(x, y, z))]^2} + \frac{\pi\Gamma_2\Gamma_3^2}{\mu^{Si}\varepsilon[\xi - \Lambda(\cos\varphi(x, y, z))]} \quad (6)$$

In this formula,  $\Gamma_1 = (\gamma_{SiC_{hkl}}^S + \gamma_{SiC_{hkl}}^p - \gamma_{Si_{hkl}}^S + \gamma_{Si_{hkl}}^p)$  is the total surface energy of the formation of the SiC nucleus and etch pit;  $\Gamma_2 \cong (\gamma_{SiC, Si} + \gamma_{Si_{hkl}}^p)$  is the total surface energy of the nucleus and etch pit bordering the shrinkage pore;  $\Gamma_3 = (1/2)(\gamma_{SiC_{(hkl)}p}^p + \gamma_{Si_{(hkl)}i}^p - 2\gamma_{SiC, Si} / \pi)$  is the value describing the increase in surface energy in the system during the formation of the shrinkage pore;  $\gamma_{SiC_{hkl}}^S$  is the surface energy of the SiC nucle-

us for its facet with indices (hkl) appearing on the surface;  $\gamma_{Si_{(hkl)}}^S$  is the surface energy of the silicon substrate before substitution with the silicon carbide layer having the facet orientation (hkl);  $\gamma_{SiC_{hkl}}^p$  is the surface energy of the silicon carbide nucleus for the facet facing the etch pit;  $\gamma_{Si_{hkl}}^p$  is the surface energy of the (hkl) interface silicon–gaseous medium (vacuum) from the side of the pore; in the general case,  $\gamma_{Si_{hkl}}^p$  can be replaced by  $\gamma_{SiC_{hkl}}^p$  if the inner surface of the pore is covered with a layer of silicon carbide;  $\gamma_{SiC, Si}$  is the surface energy of the interface between the new SiC phase and the old Si phase (SiC–Si);  $\cos\varphi_{x,y,z}$  are the direction cosines between the crystallographic coordinate system (the  $x, y, z$  axes in the crystal) and the direction of the straight line connecting the centres of the interacting defects;  $\Lambda(\cos\varphi(x, y, z)) = W(\cos\varphi_{x,y,z})N_d + Y_{SiC}$ ;  $Y_{SiC} \approx \mu^{Si}\varepsilon^2/2$ ;  $N_d$  is the density of dilatation dipoles in the surface layer of the substrate;  $\mu^{Si}$  is the shear modulus of Si;  $\varepsilon$  is the strain in the layer of the substrate surface, which occurs due to the difference in the distance between the atoms in Si and in SiC along the (111) planes,  $\varepsilon \approx 0.2$ ;  $\xi = \chi(1/V^{Si} + 1/V^{SiC})$ ;  $\chi = k_B T \cdot \ln(P_{CO}K^{eq}/P_{SiO})$  is the chemical affinity;  $P_{CO}$  is the pressure of CO vapour;  $P_{SiO}$  is pressure of SiO vapour;  $K^{eq} = P_{CO}^{eq}/P_{SiO}^{eq}$  is the equilibrium constant of reaction (1),  $P_{CO}^{eq}$  and  $P_{SiO}^{eq}$  are the equilibrium pressures of CO and SiO gases. The temperature dependence of the constant  $K^{eq}$  is provided in [12].

A distinctive feature of formula (6) is the following. In contrast to the standard expressions for the work of formation of a new phase [26], formula (6) consists of two terms. The first term at  $\varepsilon = 0$  completely coincides with the standard expression for the formation of a cylindrical nucleus of a new phase [26], and the second term describes the effect of a shrinkage pore on the formation of a nucleus at  $\varepsilon \neq 0$ . Thus, the nucleation of silicon carbide stimulates the nucleation of a shrinkage pore, which, in turn, stimulates the formation of a SiC nucleus. In [5], we called the first, the main, phase transition the “master” one, and the transformation at which shrinkage pores are generated by the formation of the first phase was called the “slave” transition, since it is stimulated only by the formation of a new phase. In the process of nucleation of a new

phase, despite the existing connection, each of its components “fluctuates” independently. It is well known that at an increased concentration of one of the components of a chemical reaction, the precipitation of a pure phase of this component is possible [26, 27]. In our case, the situation is fundamentally different. Only one phase of SiC can be nucleated; shrinkage pores are nucleated only as a result of the formation of SiC nuclei. The SiC phase is the “master” phase, and the phase of the shrinkage pores is the “slave” phase. The formation of the SiC phase resembles a locomotive that pulls a train uphill. The composition itself can only reduce the speed of the transition over the hill, but it cannot speed up this process. The process of phase nucleation can be accelerated only by chemical affinity, which determines the rate of nucleation of SiC pulling the nucleation of shrinkage pores. In this case, the elastic field created by the SiC nuclei in the silicon substrate leads to a new phase transition, the formation of shrinkage pores. This process resembles the co-crystallization process that takes place in some solutions and melts. Thus, in some systems, one phase transition can cause another transformation, stimulated by excitation of some field. In our case, this field is an elastic field.

Nucleation rate of SiC with etch pits and shrinkage pores  $I(n_{cr}, \beta_{cr})$ , according to [5], has the form:

$$I(n_{cr}, \beta_{cr}) = \frac{2D_{cr}}{\sqrt{\pi}} (N_d + N^{Si}) \exp\left(-\frac{R_{min}^{cr}}{k_B T}\right) \quad (7)$$

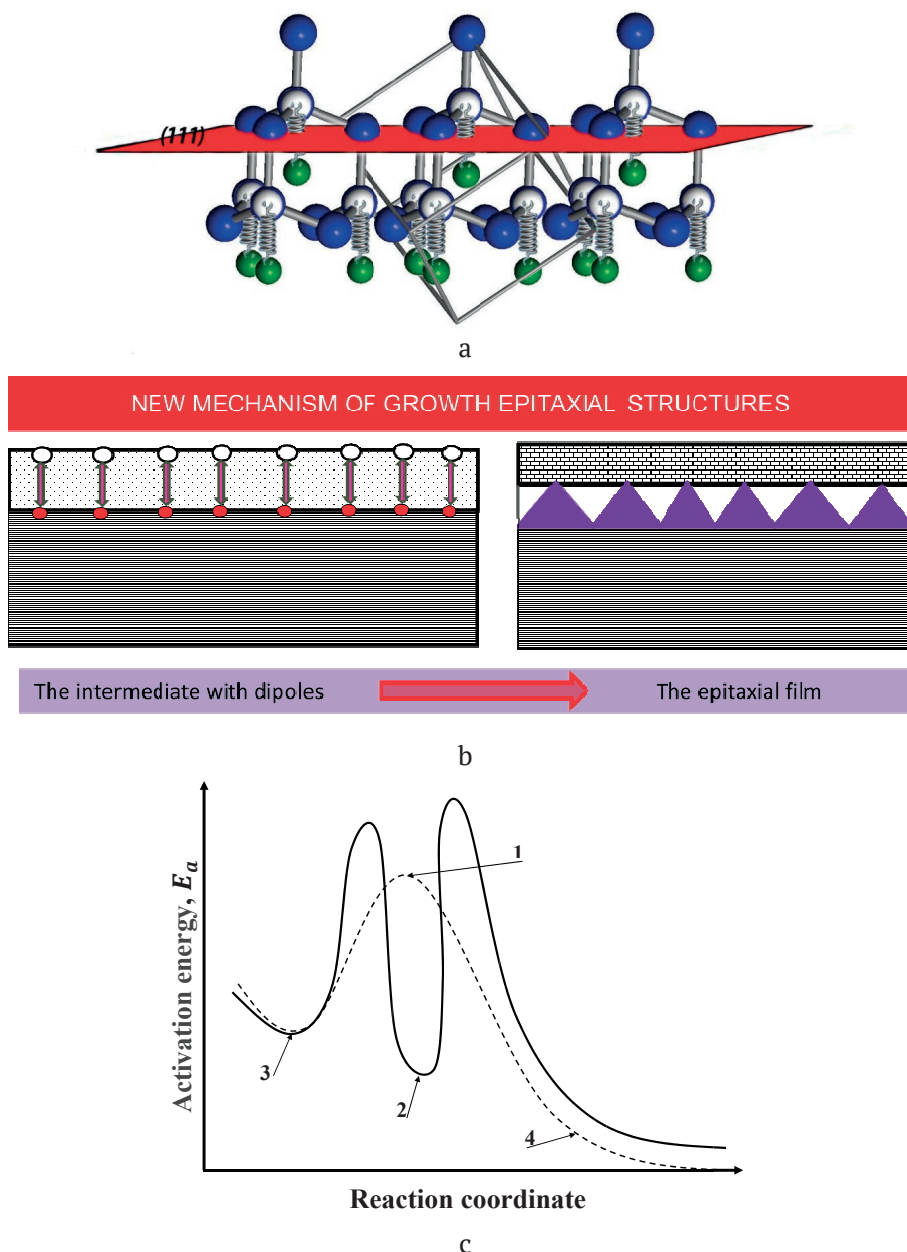
where the dipole density  $N_d \approx 1.2 \cdot 10^{28} \text{ m}^{-3}$ , the density of silicon atoms  $N^{Si} \approx 5 \cdot 10^{29} \text{ m}^{-3}$ ,  $D_{cr}$  is the diffusion coefficient in the “size space” — the kinetic coefficient that determines the rate of addition of atoms and vacancies to the SiC nucleus and pores. At a temperature of 1250 °C,  $\Gamma_{(111)} = 0.86 \text{ J} \cdot \text{m}^{-2}$  and  $\ln K/K^{eq} \sim 0.2$ , the diffusion coefficient in the size space is approximately equal to  $D_{cr} \approx 10^{-7} \text{ sec}^{-1}$  [5]. The density of dipoles and the density of atoms in silicon are approximately equal to the following values:  $N_d \approx 1.2 \cdot 10^{28} \text{ m}^{-3}$  and  $N^{Si} \approx 5 \cdot 10^{29} \text{ m}^{-3}$ . It follows that their ratio takes the following value:  $N^{Si}/N_d \approx 40$ . In this case, it follows from formula (7) that their nucleation rates will differ from each other by approximately the same number, i.e.,

$I(\beta_{cr})/I(n_{cr}) \sim 40$ . At a higher supersaturation, at which the critical radius of the SiC nucleus has a size of the order of several nanometres, the critical radius of the shrinkage pore will be of the order of atomic sizes. This means that the SiC nucleus will be surrounded by vacancy clusters, which can coalesce into thin cracks surrounding the nucleus grain (Fig. 3c). They will be located along the crystallographic directions. For the “healing” of shrinkage pores and cracks, we suggested to add silane ( $\text{SiH}_4$ ) into the reaction zone [1, 2, 5, 6, 28].  $\text{SiH}_4$  increases the total volume of silicon entering the surface of the substrate, and, thereby, reduces mechanical stresses in it. This leads to a decrease in the nucleation rate of shrinkage pores. Additional introduction of  $\text{SiH}_4$  into the system reduces the probability of formation of silicon vacancies in the near-surface layers of silicon, thereby reducing the driving force for the formation of shrinkage pores. Silane plays another important role, namely, it lowers the surface tension of the resulting silicon carbide and makes it possible to obtain not only C-terminated surfaces but also Si-terminated silicon carbide surfaces. This is due to the fact that the surface of silicon carbide, in this case, will interact not with vacuum (or CO gas) but with silicon carbide and adsorbed silicon and hydrogen atoms. The characteristic incubation time for the joint formation of SiC and shrinkage pores is of the order of  $\tau_{inc} \sim 10^{-4} \text{ sec}$  [5]. The critical thickness of the intermediate substance and, accordingly, the thickness of the film layer  $H_{film} = H_{cr}/2$  depend on the quantity  $\Gamma_1$ . The thickness of the SiC film layer can be changed by changing  $\Gamma_1$ . The value of  $\Gamma_1$  depends on the surface energies of silicon carbide and silicon. In [5], estimates of the surface energies and critical thicknesses of films formed at different temperatures of the synthesis and pressures of CO and  $\text{SH}_4$  mixture are given.

Thus, during the first stage of a chemical reaction, a metastable compound with composition and structure different from both Si and SiC is formed (Fig. 4a). It consists of layers of silicon and, divalent in this compound, carbon, which are separated by a layer of vacancies. Dipoles stabilise this structure by replacing broken chemical bonds with elastic interaction (Fig. 4a). Partial substitution of chemical bonds with mechanical interaction occurs. This allows

the reactants to pass to the final state of the reaction products with the lowest energy cost. Such a transition is often a first-order phase transition, the height of the energy barrier of which is close to  $k_b T$ . In this case, elastic dipoles located along the  $\langle 111 \rangle$  direction lead to the

anisotropy of the chemical reaction, lengthen the chemical bonds in silicon, and promote the formation of silicon carbide with the lowest energy consumption (Fig. 5b). The destruction of dipoles due to thermal fluctuations leads to the formation of dislocation-free SiC, and the



**Fig. 4.** Consecutive stages of the formation of the silicon carbide on the silicon substrate owing to reaction (1); (a) is the activated complex consisting of an ensemble of elastic dipoles in the silicon lattice; the plane (111) is perpendicular to dipole direction; springs indicate the elastic interaction between similar dilatation centers; (b) is the schematic representation of the new method of thin epitaxial film growth by the creation of dilatation dipoles ensemble; (c) is the path of the chemical transformation of Si into SiC by CO treatment (solid line) and a conventional path without dilatation dipoles formation (dashed line): 1 – activated complex of the standard chemical reactions, 2 – transition (intermediate) complex “silicon – dilatation dipoles”, 3 – reactants  $\text{CO}_{\text{gas}} + \text{Si}_{\text{solid}}$ , 4 – reaction products  $\text{SiC}_{\text{solid}} + \text{SiO}_{\text{gas}}$  [5, 6]



mobile silicon vacancies released in this case either move to the surface or gather together under the SiC film, thus forming pores in Si [13]. The majority of immobile carbon atoms that appear during the destruction of dipoles turn into SiC, but those that do not turn into SiC remain in SiC and may be present there as impurity. The phase transition from an intermediate complex to a final state is often accompanied by another first-order phase transition in the original matrix. This second transition is impossible without the formation of the final phase, i.e., without the first transition, therefore we can distinguish the “master” and “slave” phase transitions. As a result, the coordinate of the chemical reaction (1) in crystalline silicon along the  $\langle 111 \rangle$  direction looks like it is shown in Fig. 4c. If elastic dipoles were not formed, then the reaction would proceed along the curve depicted by the dashed line. Since dipoles are formed, the reaction proceeds along the curve depicted by the solid line. This line has a minimum associated with the formation of dipoles. This minimum distinguishes the intermediate substance formed in this case from the concept of activated or transition complex widely used in chemistry [43]. The activated

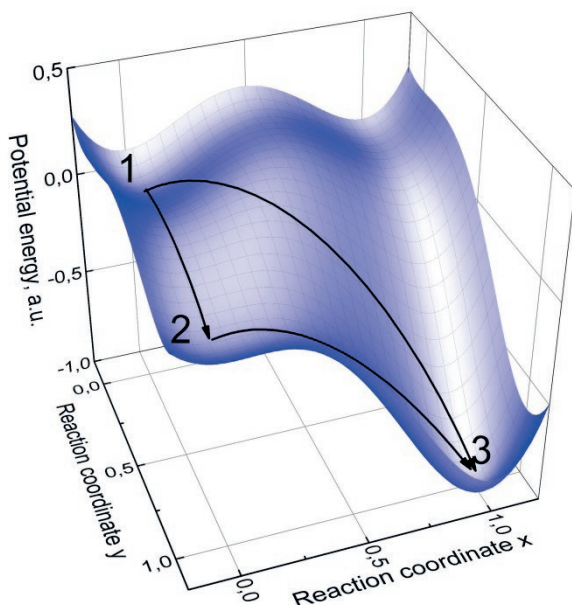
complex is formed at point 1 in Fig. 4c where the dashed line reaches its maximum, while the intermediate substance is located at point 2 in Fig. 4c where the solid line passes through the minimum.

For the transition to the equilibrium state, the system overcomes one more maximum. The nature of this maximum is related to the need for the system to overcome the energy of formation of new surfaces (of silicon carbide and pores) and the elastic energy at the moment of carbon atom bonding with silicon vacancies. For example, during phase transitions in solids, the “master” transition can lead to the appearance of elastic stresses between the original and new phases. The elastic stresses arising in this case will lead to another, “slave”, phase transition in the initial phase. In this case, the master phase transition from Si to SiC leads to the formation of shrinkage pores in Si at the interface between SiC and Si. The slave phase transition is the nucleation of shrinkage pores.

It should be noted that it is also possible to obtain SiC as a result of the interaction of Si with  $\text{CO}_2$ . This will also lead to the formation of SiC. However, as a result of this reaction, solid amorphous  $\text{SiO}_2$  will be formed instead of the SiO gas. In this case, a SiC film containing a large number of SiC twins and other growth defects will grow.

## 2.2. The method of coordinated substitution of atoms as a first-order phase transition through an intermediate state

We showed above that, before conversion into SiC, silicon interacting with CO first passes an intermediate state. This intermediate state is taken into account in formula (6) by the quantity included in its denominator:  $\Lambda(\cos \varphi(x, y, z)) = [W(\cos \varphi_{x,y,z})N_d + Y_{\text{SiC}}]$ . If dipoles were not formed in silicon, i.e., if the intermediate substance were not formed, then the value of  $W(\cos \varphi_{x,y,z})N_d$  would be equal to zero. In this case,  $\Lambda(\cos \varphi(x, y, z))$  would contain only the term  $Y_{\text{SiC}} \approx \mu^{\text{Si}} \varepsilon^2 / 2$ . This term takes into account the appearance of elastic energy in the substrate when a SiC nucleus appears. The term  $Y_{\text{SiC}}$  with a minus sign in the denominator of the work of formation of a new phase (6) could reduce the driving force of the phase transition to such an



**Fig. 5.** Potential energy surface in the reaction coordinate space: (1) initial state, (2) intermediate state, and (3) final state. Arrows show the direct phase transition at  $1 \rightarrow 3$  and the transition through the intermediate state  $1 \rightarrow 2 \rightarrow 3$  [29].

extent that a new phase could not be formed. This is due to the fact that it is subtracted from the value  $\zeta$  proportional to the chemical affinity  $\chi$ . However, nature behaves differently. The system minimises the free energy of the transition from solid Si and gas CO to solid SiC and gas SiO, thus forming the intermediate metastable state “elastic dipoles–silicon”. The formation of this transitional complex allows the system to bypass the high barrier of new phase nucleation along the “pass”. It should be noted that the work of formation of critical nuclei from the final phase from the transition state is much less than from the initial phase.

In [29], this approach was substantially developed. It was shown that the work of formation of a new phase in the presence of a transition state can even approach zero, providing a barrier-free transition through a single nucleus. In particular, during martensitic transformations, the transition through a pre-martensitic intermediate state occurs, and the melting of crystals proceeds through a pre-melting state. In the studied case, the transition from Si to SiC occurs through an intermediate “pre-carbide” state, which includes Si saturated with dilatation dipoles oriented along the [111] direction of silicon. It was proved in [29] that from the intermediate state the system enters the final state through the highest point of the lowest energy barrier in the coordinate space of the reaction or phase transition [29], i.e., the saddle point. Saddle points can only exist in systems with several independent reaction coordinates. It was established in [29] that the role of the order parameters in such systems belongs to the coordinates of chemical reactions. In the case of SiC growing from Si, two reaction coordinates, one responsible for the formation of SiC, and the other responsible for the formation of SiO, are the reaction coordinates. The reaction with the formation of gas is faster and ends earlier, since the reaction with the formation of the SiC crystal requires the restructuring of the entire crystal structure and the formation of shrinkage pores due to the fact that the volume of one cell decreases twice. The transition scheme is shown in Fig. 5. In [29], analytical formulas describing the phase transition through an intermediate state were

obtained, and the instant formation of the new phase upon transition from an intermediate state from one island was shown, i.e., the intermediate state transforms into a new phase simultaneously throughout the entire volume. In this case, the entire matrix of the initial phase determines the crystalline orientation of the new phase, which is a great advantage of this thin film growth mechanism. This approach opens up completely new prospects for the synthesis of high-quality epitaxial films and other materials. It becomes possible to grow film structures entirely from one nucleus. There is no need to deal with grain boundary defects that arise when nuclei merge with each other.

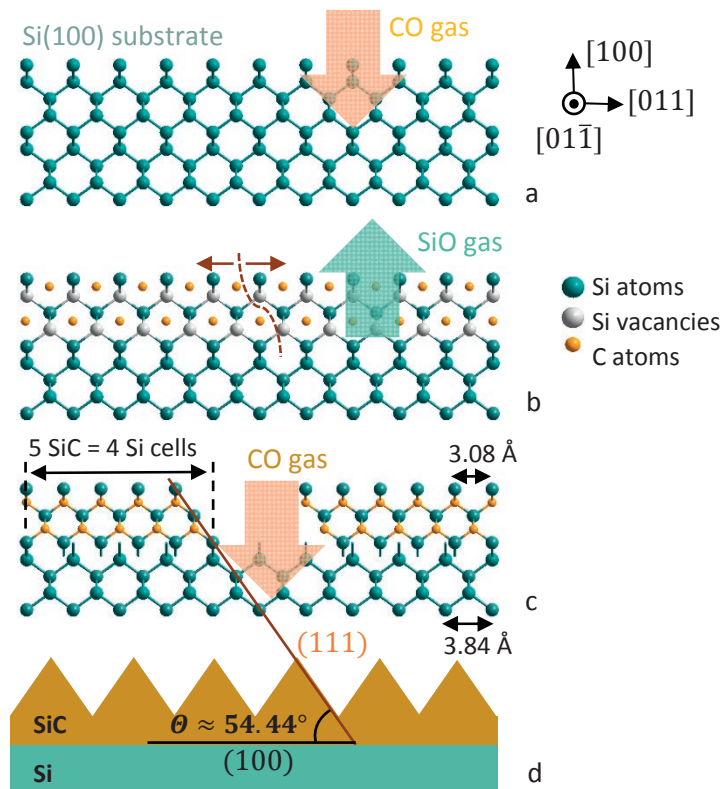
### *2.3. Growth of the epitaxial SiC layer on the Si(100) surface*

Thus, a distinctive feature of the MCSA is the formation of the (111) plane regardless of the initial Si crystallographic plane, on which SiC was synthesised. This effect is due to the fact that carbon-vacancy structures (these are dilatation dipoles at the initial stage) are always located along the  $\langle 111 \rangle$  direction and located in the  $(-110)$  plane perpendicular to the (111) plane. Further, after the formation of elastic dipoles, SiC is formed according to reaction (5). In this case, shrinkage with the separation of the SiC nucleus from the Si matrix occurs with the simultaneous formation of shrinkage pores. In [5, 30], a theory of the formation of shrinkage pores was developed based on the model of the nucleation of cavities from an ensemble of vacancies that appear under the action of a tensile load [31]. Delamination of one material from another is also possible as a result of the formation of partial dislocations in slip planes and the initiation of vacancy dislocation loops [32]. It is known [33], that the slip planes in crystals with a diamond lattice at temperatures exceeding 0.5 of the melting point of the crystal (in our case, for the synthesis of SiC, this condition is certainly met for Si) are the family of (111) planes, while the slip itself occurs along the  $\langle 110 \rangle$  directions. Therefore, on a smooth (100) silicon surface, SiC with the (100) orientation cannot be nucleated. However, nature does otherwise. The (100) Si facet upon conversion transforms into a SiC facet consisting of many facets resembling sawtooth

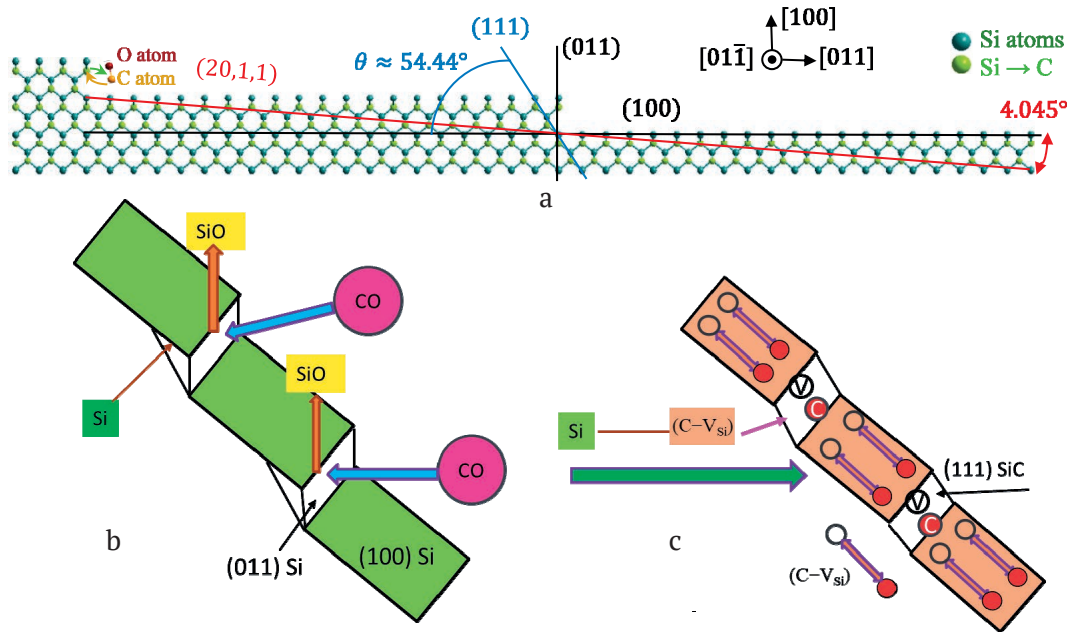
structures, the side facets of which are covered with the (111), (110), and (210) planes, as shown in Fig. 6 [30]. The angle between the direction of the (100) facet and the (111) facets is  $54^\circ 44'$ . Any arbitrarily small deviation of the (100) facet from this direction makes it vicinal, which leads to the instantaneous formation of a very thin (several atomic layers) film.

A different picture will be observed if SiC is grown by the MCSA on the (100) surface misoriented by  $2\text{--}7^\circ$  in the  $\langle 011 \rangle$  direction. If this surface is heated to a temperature exceeding  $600^\circ\text{C}$ , then the (100) plane of silicon will be covered with steps. The terraces of this structure will be the (100) planes, and the steps will be limited by the (011) planes. There are “channels” along the  $\langle 011 \rangle$  directions in the silicon lattice, which is associated with the features of the crystallographic structure of the Si lattice.

Therefore, along this direction, CO molecules move perpendicular to the steps deep into Si. The Si surface is saturated with CO, and, as described above, the interaction of Si with CO occurs, resulting in the formation of an intermediate state, which is further converted into SiC. During this transformation, part of the Si from the (011) step evaporates, and the (111) SiC step is formed [30]. This process is schematically shown in Fig. 7. This transformation removes the “degeneracy” inherent to the non-deflected (100) facet and leads to the formation of facets consisting of the (111) SiC facets, but located already on the former (011) steps, and not randomly located as on the (100) facet. Naturally, these facets also make an angle of  $\sim 55^\circ$  with the (100) facet and  $\sim 35^\circ$  with the (011) facet. Since the attraction between a silicon vacancy and a carbon atom in the silicon matrix is maximal along the  $\langle 111 \rangle$  direction, a



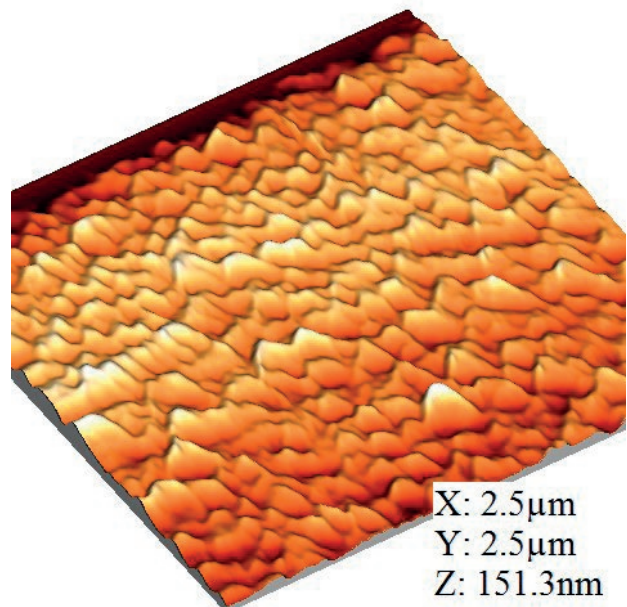
**Fig. 6.** Schematic representation of the successive stages of transformation of the singular Si(100) surface into SiC covered with facets during the exposure of the Si surface to the CO gas in accordance with reaction (1): (a) bringing the Si(100) surface in contact with the CO gas; (b) the first stage of the reaction, namely, the removal of Si using the SiO gas and the formation of dilatation dipoles ( $\text{C}-\text{V}_{\text{Si}}$ ); (c) the phase transition from the intermediate state of silicon into a SiC layer; and (d) the formation of a sawtooth surface of the SiC film covered with (111) facets;  $\theta = 54^\circ 44'$  is the angle between the SiC(111) facet and the Si(100) surface [30]



**Fig. 7.** Schematic representation of the mechanism of successive stages of the occurrence of reaction (1) on the vicinal Si(100) surface covered with (011) steps: (a) the vicinal Si(100) surface deviated by  $4^\circ$  in the [011] direction with (011) steps toward the plane; (b) the initial Si(100) surface covered with (011) steps; and (c) the intermediate state formed during the transformation of the intermediate state into the SiC(111) plane, which lies at an angle of  $\theta = 54^\circ 44'$  to the (100) face [30]

part of the (011) Si step can turn into the (112) SiC kink. It is known, that the angle between the (112) and (100) planes in a cubic crystal with the diamond lattice is  $\sim 35^\circ$ . As a result, a longitudinal wedge-shaped protrusion of silicon carbide is formed with the top protruding above the step platform and an inclined edge reaching the platform of the underlying step, with the formation of a slope. These SiC facets resemble “fish scales” or “knight’s chainmail,” the wafers of which closely fit with each other [30]. The experimental AFM image of a SiC layer coated with the (111) facets grown on a (100) Si vicinal surface deviated from the  $\langle 100 \rangle$  direction by  $4^\circ$  towards  $\langle 011 \rangle$  is shown in Fig. 8. Thus, the Si(100) surface is covered with an array of wedge-shaped parallel steps, which are triangular prisms (side facets of pyramids).

Since the symmetry of such prisms is characteristic of both cubic and hexagonal crystals, the symmetry is not degenerate. This means that both crystals with cubic and hexagonal symmetry can grow on these



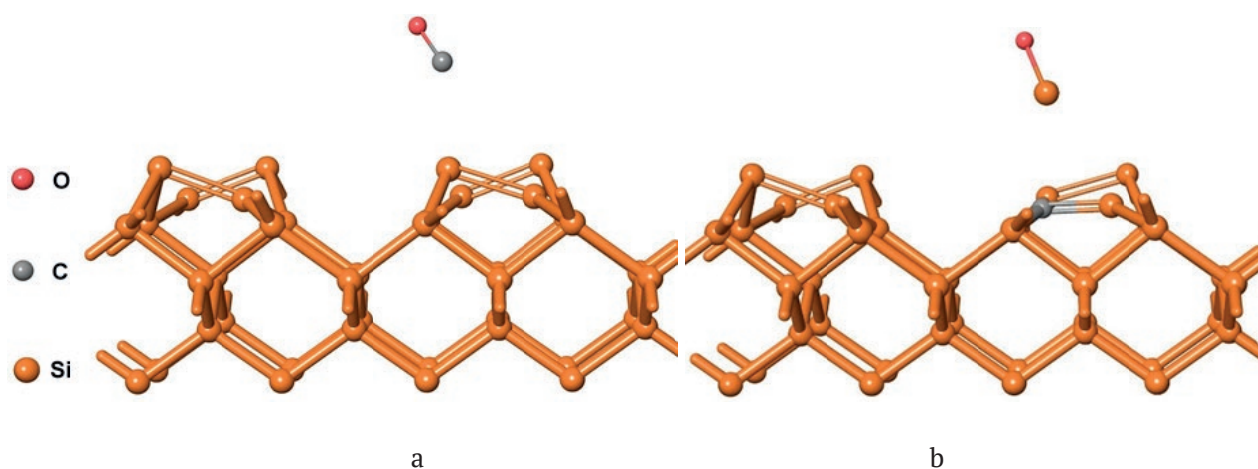
**Fig. 8.** AFM image of the SiC layer covered with the (111) facets grown on the vicinal (100) Si surface p-type conductivity deviated from the  $\langle 100 \rangle$  direction by  $4^\circ$  toward  $\langle 011 \rangle$  [30]

surfaces. Most importantly, this will depend not on the orientation of the substrate but only on the thermodynamic conditions, i.e., on the temperature and densities of the incident fluxes of the components from which the layer grows. If the hexagonal modification is stable under the given conditions, then the hexagonal modification will grow; if the cubic structure is stable, then the cubic modification will grow. This opens up completely new perspectives for growing hexagonal semi-polar crystals.

In [30], a fundamentally new mechanism was also discovered for the process of substitution of atoms on the vicinal Si facets of *n*- and *p*-type of conductivity that are deviated from the singular facet (100). The following findings were revealed. 1) On the vicinal Si surface of *p*-type of conductivity, deviated by 4° or more from the singular facet (100), an ordered SiC phase is formed in the process of SiC synthesis. The surface morphology of this phase has the form of facets (flakes) consisting of layers of both cubic and hexagonal phases. 2) On the vicinal Si surface of *n*-type of conductivity, deviated by 4° or more from the singular facet (100), only the ordered 3C-SiC cubic phase is formed in the process of SiC synthesis. The reasons for this difference are due to the different mechanism and different rates of formation of dilatation dipoles and carbon-vacancy structures on the (100) facet in Si doped with donor and acceptor impurities [30].

### 3. Quantum-mechanical theory of epitaxial transformation of silicon into silicon carbide

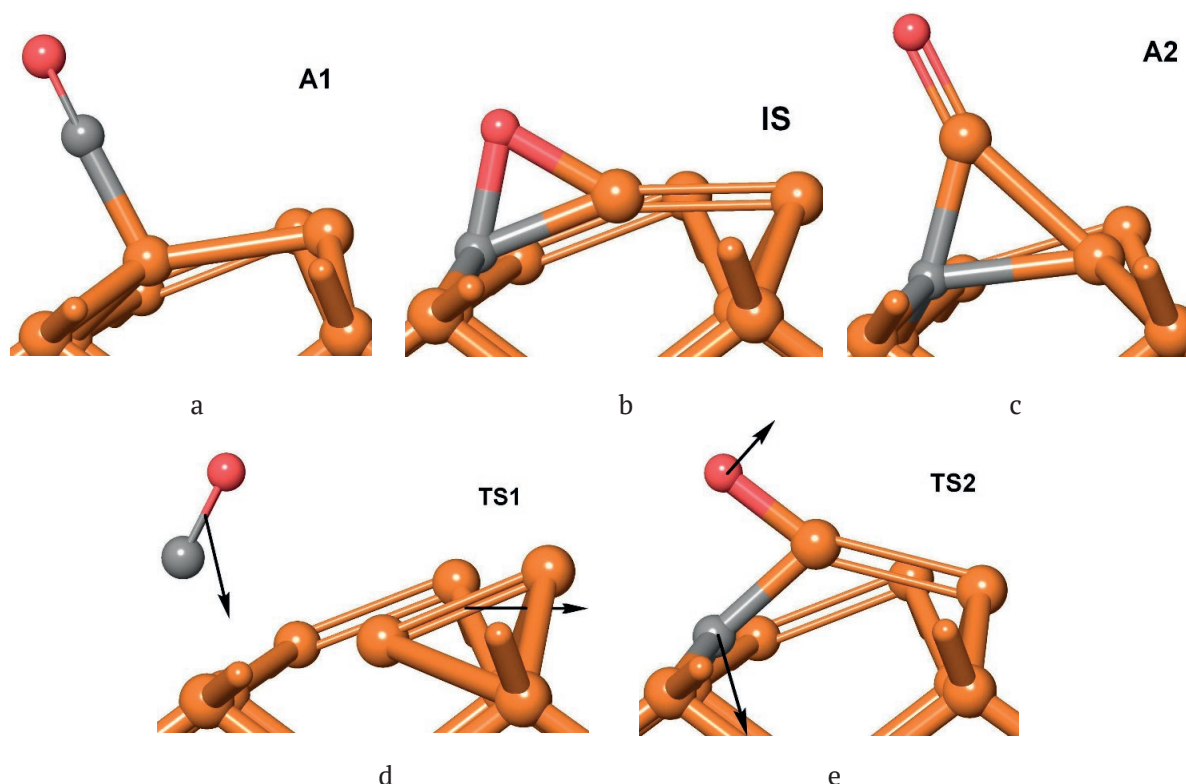
Thus, we found out that during the first stage (4) of SiC synthesis, pairs of defects of C and  $V_{Si}$  are formed and saturate the silicon crystal. The C atom is attracted to the silicon vacancy; therefore, the C atom actually replaces the Si atom in the Si crystal. When every second atom in the Si crystal is substituted by a C atom, the crystal will be saturated with pairs of  $C+V_{Si}$  defects, and the stage (4) is completed. Such a Si crystal can be called “pre-carbide” silicon, since everything in it is ready for the transition into SiC. In the second stage (5), large areas of pre-carbide silicon “collapse” with the formation of SiC. Since the volume at stage (5) decreases (the volume of one SiC cell is two times smaller than the volume of one Si cell), this is a first-order phase transition. In [14, 34], the study of the main elementary processes that occur during the transformation of a silicon crystal into a silicon carbide crystal due to a chemical substitution reaction with CO gas was continued. As a result, a quantum-mechanical theory of the coordinated transformation of Si into SiC was proposed. In this case, the density-functional theory (DFT) in the generalised gradient approximation (GGA) was used. The energy profile of this reaction for the Si(100) surface was calculated using the nudged elastic band method (NEB) in the PBE functional approximation using pseudopotentials



**Fig. 9.** Initial reactants (a) and final reaction products (b) of stage (4) with the reconstruction  $p(2 \times 2)$  of the Si(100) surface. At the bottom the broken silicon bonds are saturated with hydrogen, which is not shown for simplicity. On all three axes, there are periodic boundary conditions. [14, 34]

and the plane-wave basis with the reconstruction of  $p(2 \times 2)$  (Fig. 9). It has been established that this reaction (4) is feasible only since it proceeds through the intermediate state IS (Fig. 10b), in which all atoms are chemically bonded to each other. In fact, this intermediate state breaks the reaction into two independent steps. During the first stage, the entire CO molecule is absorbed by the Si surface, and then, after a slight rearrangement (Fig. 10e), the SiO molecule is pushed out by the surface. Due to this, the system reduces the activation barrier of this reaction to 2.6 eV. In [14, 34], the geometry of all intermediate and transition states was calculated (Fig. 10 a-e), and the frequency spectrum of the transition states TS1 and TS2 was found. The only imaginary frequencies of these states are  $|\omega_{TS1}| = 160 \text{ cm}^{-1}$  and  $|\omega_{TS2}| = 430 \text{ cm}^{-1}$ . The eigenvectors corresponding to the given eigenvalues show the minimum energy path (MEP) at these points (Figs. 10d and 10e). It was shown that the main transition state TS1 is reactant-like, and the auxiliary intermediate state TS2 is product-like. On the (100) surface, the

geometry of pre-carbide silicon corresponding to the local energy minimum and the geometry of silicon carbide corresponding to the global minimum were calculated. It was shown that the C-Si bonds in pre-carbide silicon on (100) are stretched on average by 11%. The energy of the first-order phase transition from pre-carbide silicon into silicon carbide was calculated for a region of size  $L \times L(4)$ . It was shown that such a transition is possible only if the size of the transition region  $L$  is higher than a certain minimum size  $L_{\min} = 30 \text{ nm}$ . Such an unusual character of the simultaneous transformation of silicon into silicon carbide with the preservation of the entire structure of chemical bonds explains the absence of lattice misfit dislocations in these SiC/Si films. This fundamentally distinguishes this method of SiC/Si growth from the standard one (for example, CVD), where islands grow atom by atom, which inevitably leads to the appearance of misfit dislocations. The estimates made in [16, 21] using the methods of classical mechanics are in qualitative agreement with the results of this study.

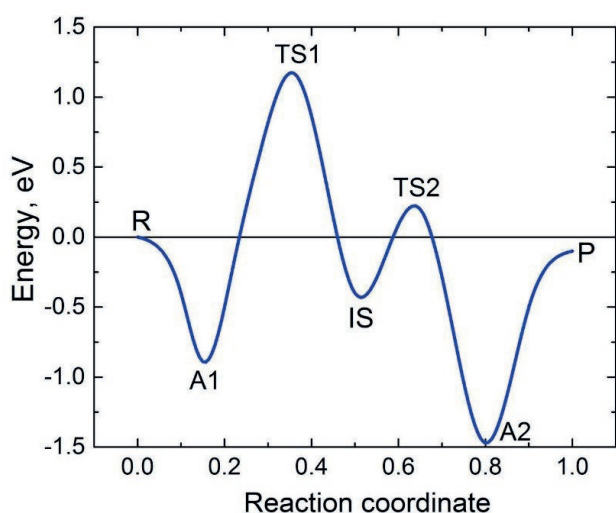


**Fig. 10.** Geometry of three intermediate states (a), (b), (c) and two transition states (d) and (e) of the reaction (4) [14, 34]

### 3.1. Energy profile, intermediate and transition states of the reaction of heterogeneous synthesis of SiC

It should be noted that, in addition to the predictable intermediate states A1 and A2 corresponding to CO and SiO molecules adsorbed on the crystal surface (such states always occur in the presence of a surface), the system has a key intermediate state IS (Fig. 10b), in which all atoms are in a chemically bound state. The decisive role of this intermediate state in the course of reaction (4) is that it changes the reaction path by lowering the height of the activation barrier. If it were not for the IS state, then the intermediate state would be different, and the height of the activation barrier would be approximately 4.0 eV. This means that at temperatures of 1200–1300 °C the rate of reactions (1) and (4) would be almost equal to zero. The intermediate IS state (Fig. 10b) splits the reaction from state A1 to state A2 into two elementary reactions and lowers the height of the activation barrier to 2.6 eV (Fig. 11). This means that the A1 state with an adsorbed CO molecule exists approximately  $10^{-5}$  sec at  $T = 1250$  °C. The found barrier provides the experimentally observed rate of reactions (1) and (4) [35].

The CO molecule moves vertically as a whole, ensuring that the C atom enters the right place



**Fig. 11.** Cross section of the surface of the potential energy of the reaction (2) along the reaction pathway. The geometry of the system of atoms corresponding to three intermediate states A1, IS, A2 and 2 transition states TS1, TS2 is shown in Fig.10; R is the reactants; P is the final products [14, 34]

(Fig. 10b). At the same time, the Si-Si dimer makes room for this (Fig. 11b), also moving as a whole in the horizontal direction. At the saddle point, the C atom is located at approximately the same distance  $\sim 2.65$  Å from the three nearest Si atoms without forming a chemical bond with them. This explains such a low value of the frequency modulus  $\omega_{TS1}$ . The positive frequencies of the TS1 spectrum are closer to the frequencies of the A1 spectrum than to the frequencies of the IS spectrum, therefore the TS1 transition state can be characterised as reactant-like.

In the TS2 transition state (Fig. 10e), atoms, not molecules, are moving. The carbon atom moves almost vertically down and reaches its final position (Fig. 11c). The oxygen atom moves almost parallel to the Si-C bond. Since both the O atom and the C atom are chemically bonded to Si atoms, the frequency  $|\omega_{TS2}|$  is noticeably higher than the frequency  $|\omega_{TS1}|$ . The positive frequencies of the TS2 spectrum are closer to the frequencies of the A2 spectrum than to the frequencies of the IS spectrum, therefore the TS2 transition state can be characterised as a product-like one.

### 3.2. Transition of “pre-carbide” silicon into silicon carbide on the (100) surface

Thus, stage (4) ensures the substitution of every second Si atom by a C atom according to the mechanism described above. In this case, it is very important to emphasise that the breaking of Si-Si bonds in silicon and the formation of new C-Si bonds occur in a coordinated manner through the intermediate IS state and almost simultaneously (the IS state lives approximately  $10^{-10}$  sec). If the Si→C substitution occurs in the volume of the Si crystal, then the C atom takes the place of the Si atom. This fact is related to the fact that the C atom and the silicon vacancy  $V_{Si}$  are attracted to each other, forming a bound state called a dilatation dipole by analogy with an electric dipole, as mentioned above. In the framework of classical solid body mechanics, for the calculation of the elastic energy of the dilatation dipole [16, 21, 36, 37], a number of strong assumptions had to be made, in particular, point defects were considered as having no dimensions. Using the apparatus of quantum mechanics, not only an estimation but a very accurate calculation of the interaction energy of C and  $V_{Si}$  is possible, which

was done by the methods of quantum mechanics in [14, 34].

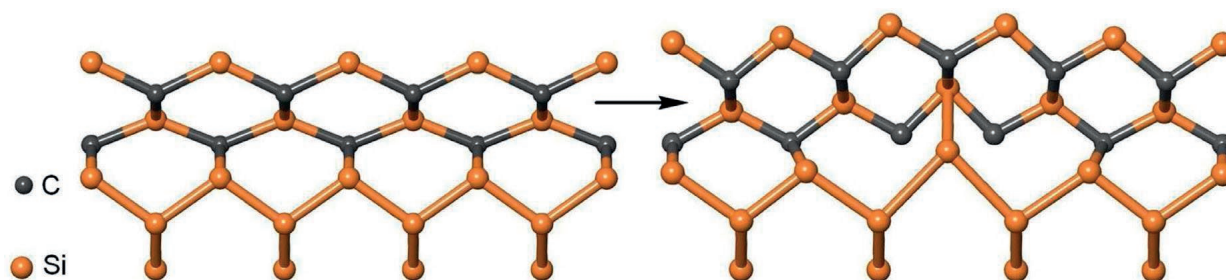
Let us now consider the (100) surface of a silicon substrate where every second Si atom of the upper atomic monolayer with a thickness of 3.84 Å was substituted by a C atom according to the mechanism described above, after which the geometry of the system was optimised from this initial position (Fig. 12, left side). In order not to involve surface reconstruction in the considered processes, all broken bonds are saturated with hydrogen (for simplicity, hydrogen atoms are not shown in Fig. 12). The optimization of the geometry leads to the fact that the atoms of the film are slightly pressed against the substrate, reducing the bond length. The average C-Si bond length after optimization on the (100) surface is 2.09 Å. After substitution of every second Si atom with a C atom and optimising the geometry according to the terminology of [1, 2, 4–6], this silicon is “pre-carbide” silicon where everything is ready for transformation into silicon carbide. This silicon is obtained after the completion of the stage (2). Since the optimal C-Si bond length in silicon carbide is 1.88 Å, the bonds in pre-carbide silicon on the (100) surface are stretched by an average of 11%, which leads to additional elastic energy. This is the driving force of the transformation of pre-carbide silicon into silicon carbide (5).

Too many atoms are involved in the transition from pre-carbide silicon into silicon carbide (3) (the minimum required number of atoms is  $\sim 10^5$ ), therefore it is not possible to construct an exact quantum-mechanical theory for this transition. Nevertheless, using relatively simple quantum-mechanical calculations, it is possible to determine all the main characteristics of the phase transition (5) and provide a qualitative

description for it. In [14], this was done for the (100) surface.

The state of pre-carbide silicon, which corresponds to a local energy minimum in a simple two-dimensional model on the Si(100) surface, is shown in Fig. 12 (see the left side of Fig. 12). The two-dimensionality of the model means that the thickness of the considered layer perpendicular to the plane of the figure is equal to the size of the primitive Si cell, i.e., 3.84 Å. In this dimension (i.e., perpendicular to the plane of the figure), atoms cannot move, and periodic boundary conditions apply. The relaxation of atoms can occur only in two other dimensions, i.e., in the plane of the figure. The stretching of bonds by 11% leads to the fact that the energy of the system has a global minimum, located below the local minimum. The calculations by the density-functional theory method showed that, within the framework of the above-mentioned DFT approximations and two-dimensional model, the global minimum corresponds to the “collapse” of pre-carbide silicon into silicon carbide with the optimal C-Si bond length. In this case, 5 primitive SiC cells fit 4 primitive Si cells (their total length is equal to 15.36 Å) (see the right side of Fig. 12). It turned out that one of the upper Si atoms (i.e., every fourth one) actually enters the material of the SiC film and play an important ordering role, since it forms a bond with two Si atoms from the SiC film. The length of this bond is 2.59 Å, i.e., it is stretched by 10%.

Quantum-mechanical calculations within the above approximations show that the SiC state is more favourable than the state of pre-carbide silicon by the value  $\Delta E_1 = 0.25$  eV per primitive SiC cell. However, for the formation of such state from pre-carbide silicon (Fig. 12), it is necessary to break two C-Si bonds in pre-carbide



**Fig. 12.** Transition from precarbide silicon to silicon carbide on Si(100) (reaction (3)). Hydrogen saturating dangling bonds is not shown for simplicity [14]



silicon with the total energy  $\Delta E_2 = 10.0$  eV. These bonds are stretched by 11%, therefore they are weakened, therefore the energy  $\Delta E_2$  is so low.

So, a square of the pre-carbide silicon monolayer located on the (100) surface and having the size ( $L \times L$ ) enclosing ( $L/a^2$ ) primitive cells ( $a = 3.84$  Å is the size of the primitive cell of silicon) requires the following energy to collapse into SiC:

$$\Delta E = -\Delta E_1 \left( \frac{L}{a} \right)^2 + 2 \frac{L}{a} \Delta E_2 \quad (8)$$

since the bonds break up along half the perimeter. From the condition  $\Delta E = 0$ , it is possible to determine the minimum size of a cluster of pre-carbide silicon, for which the transformation into silicon carbide is beneficial:

$$L_{\min} = 2 \frac{\Delta E_2}{\Delta E_1} a \quad (9)$$

As it follows from (8), the larger the cluster size, the more favourable the phase transition. However, the larger  $L$ , the larger activation barrier proportional to  $L$  must be overcome. The size of the barrier is influenced by many factors. First, during the collapse, the outermost atoms make a path equal to  $0.2\sqrt{2}L$ . In an ideal situation, when the substrate potential is exactly equal to the sine, the energy of cluster movement along the substrate is 0, since such movement is described by the soliton solution of the sine-Gordon equation. However, in practice, the potential of the silicon substrate differs from the sine, so energy has to be spent on moving. In addition, when the cluster moves, the length of the C-Si bonds changes, i.e., the cluster does not move as a whole, which also requires energy. Second, the “collapse” opens up part of the Si substrate surface, and some Si atoms can move upward, lowering the total energy. In addition, these atoms can react with CO and provide the appearance of SiC in the gap between SiC clusters. In practice, a certain amount of silane  $\text{SiH}_4$  is added to CO gas exactly to “heal” the voids between SiC clusters [5]. This process facilitates the collapse of pre-carbide silicon clusters and reduces the corresponding activation barrier.

An estimate of the SiC cluster size made in [14] showed that the average size of a pre-carbide

silicon cluster undergoing the first-order phase transition is of the following order of magnitude:

$$L \sim 2L_{\min} = 4 \frac{\Delta E_2}{\Delta E_1} a = 160a \approx 60 \text{ nm}. \quad (10)$$

#### 4. Diffusion mechanism of CO and SiO molecules into Si with the simultaneous chemical transformation reaction of Si into SiC

In [38], a new mechanism of film growth during the topochemical transformation reaction of Si into SiC under the action of CO was theoretically proposed and experimentally confirmed. The main idea of [38] is as follows. The drift of CO molecules during a chemical reaction with Si occurs first through the channels of the Si crystal saturated with dilatation dipoles  $\text{C} + \text{V}_{\text{Si}}$  and then through the SiC channels due to the difference in CO pressures outside and inside the crystal. Film growth in this model stops when the reaction product SiO “block up” the crystal channels, reducing their hydraulic diameter. This is the fundamental difference between this model and the diffusion model, where the increase in film thickness continues indefinitely as  $\sqrt{t}$ . In this study, for the first time, experiments were performed to measure the dependence of the maximum film thickness on pressure for films on Si(111) and Si(100), and it was shown that there is a pressure corresponding to the maximum film thickness. With a further increase in pressure, the film thickness decreases, whereas it should be vice versa for ordinary diffusion growth, since diffusion only increases. In [38], a general formula describing the dependence of the thickness of a SiC film formed during the topochemical growth was derived. For small time values  $t$ , this dependence is diffusional:

$$L(t) = \sqrt{Dt} \quad (11)$$

and for bigger time values it is presented as:

$$L(t) = L_m \left[ 1 - \exp\left(-\frac{Dt}{2L_m^2}\right) \right] \quad (12)$$

$$L_m(P_{\text{CO}}) = L_* \frac{4P_{\text{CO}}/p_*}{\left[1 + (P_{\text{CO}}/p_*)^n\right]^2} \quad (13)$$

where  $p_*$  and  $L_*$  are parameters which have the dimensions of pressure and lengths, respectively;

$n$  is the inverse polytropic index,

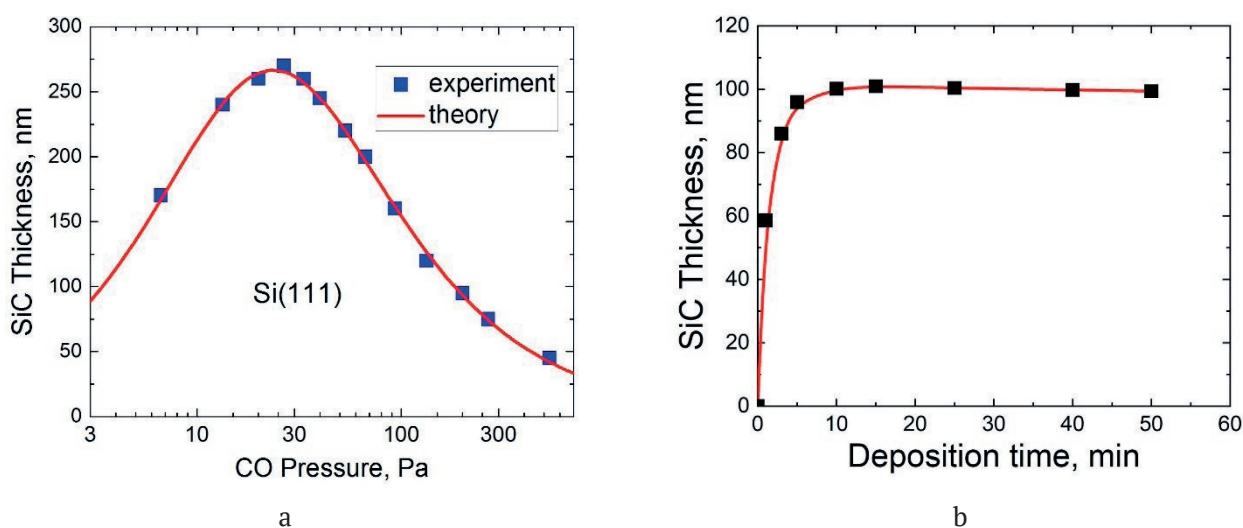
$$n = \frac{C - C_v}{C - C_p} = \frac{C - 2.5R}{C - 3.5R}; p_* = \left(\frac{p_0}{va}\right)^{\frac{1}{n}}; L_* = \frac{\pi(d_0/2)^2 p_*}{8\eta j_e};$$

$j_e$  is the volumetric equilibrium flow rate of CO gas per unit area of the channel;  $d_0$  is the hydraulic diameter of the channel;  $\eta$  is the dynamic viscosity. The dependence of the thickness of the SiC layer growing on the Si (111) facet on the CO pressure is shown in Fig. 13a; the time dependence of the thickness of the SiC layer growing on the Si(111) facet is shown in Fig. 13b. Similar curves for the growth of SiC on the Si (100) facet can be found in [38]. It can be seen from these data that, starting from a certain value of the CO pressure, the growth of the layer thickness slows down, in contrast to the thickness of the layer growing due to diffusion. The growth of the layer thickness also stops with time (at a fixed pressure). After the layer reaches a certain thickness, it no longer grows [38, 39].

The study of the processes of diffusion of CO and SiO gases was started in [38] and continued in [40, 41]. The key role of vacancies  $V_{Si}$  and  $V_C$  in the kinetics of reaction (1) was shown in [40, 41] using quantum chemistry methods. The transport of the reagent CO gas into the reaction zone and of the reaction product SiO gas from the reaction zone occurs only in the  $\langle 110 \rangle$  direction and equivalent directions, i.e., in the direction of the SiC channels. The migration of CO and SiO molecules is equivalent to the migration of

the O atom and vacancies  $V_{Si}$  and  $V_C$ , since it is not necessary for the Si and C atoms to migrate, because the O atom easily forms a chemical bond with any atom of the SiC crystal. The energy barrier to migration of vacancies is more than 2 times lower than the barrier to the migration of atoms and, in an ideal crystal, is equal to 3.6 eV for  $V_{Si}$  and 3.9 eV for  $V_C$ . Therefore, at low temperatures, the synthesis of SiC is limited by migration of  $V_C$ . In a 3C-SiC crystal containing twin boundaries, the migration barriers can be 10–20% lower. Starting from a temperature of 1100–1200°C, a significant part of silicon vacancies will transform into carbon vacancies plus immobile carbon structures (the activation energy of this process is 3.1 eV). Therefore, due to the lack of silicon vacancies, they can limit the synthesis of SiC. In this case, SiC synthesised by the MCSA will contain both carbon clusters and traces of microexplosions caused by the accumulation of a large amount of SiO inside the SiC layer.

The processes of diffusion and evolution of a porous layer were also studied in [42]. In that study, the temporal evolution of the average thickness of the porous layer when the sample was kept in a CO atmosphere was studied experimentally and theoretically. The result of the study showed that the thickness at the initial stages is proportional to the cube root of time. A model that describes the process of formation of the porous layer both at the initial stages, when the layer represents isolated pores, and at the



**Fig. 13.** Dependences of the final thickness of a SiC film on Si(111) on (a) the CO pressure (squares) and (b) growth time (squares). The solid lines stand for theoretical dependences calculated by formulas (11) and (12) [38]

later stages, when the pores coalesce and move deep inside as a single flat front, was proposed. It was theoretically shown that in the latter case the thickness of the porous layer is proportional to the square root of time.

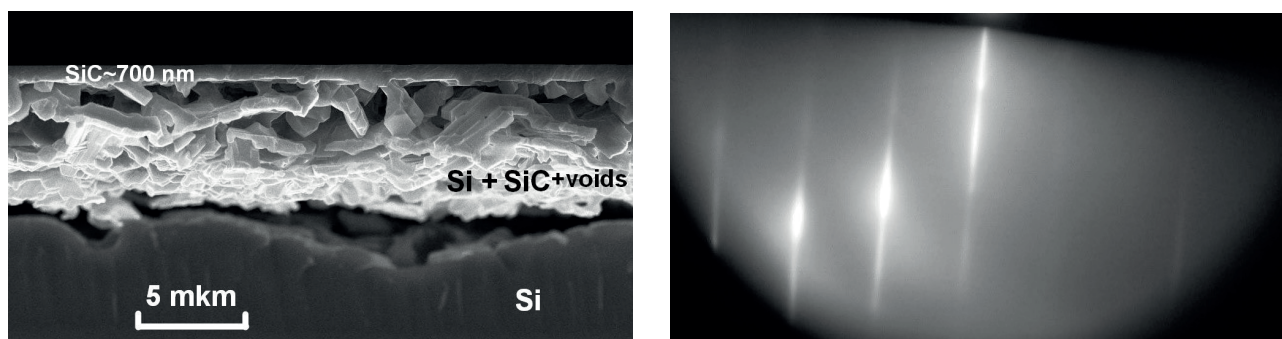
### 5. Vacancy growth of single-crystal silicon carbide – a new stage in the development of the method of coordinated substitution of atoms

A surprising feature of the method of substitution of atoms is that the dependence of the thickness of the grown SiC layer on the pressure of carbon monoxide CO has a dome-like shape [38], i.e., at first it increases to a certain maximum value, then decreases almost to zero (Fig. 13).

The drift model of epitaxy, developed in [38], allowed to explain the similar behaviour of the layer thickness on the CO pressure. It turned out that the gaseous reaction product SiO interferes with the flow of the gaseous reagent CO through the channels of the crystal lattice, thus reducing their hydraulic diameter. Naturally, the thickness of the SiC films in this case is not high. In particular, at a growth temperature of 1300 °C, the highest-quality films on Si(111) have a thickness of 20–100 nm and are obtained at the CO pressures  $P_{CO} \approx 200 - 500$  Pa. The process of forming the SiC coating proceeds through a number of intermediate stages. During the first stage of the reaction, the CO molecule interacts with Si and decomposes into a carbon atom and an oxygen atom. The oxygen atom enters into a chemical reaction with the Si atom, which results in the formation of SiO gas. The SiO gas diffuses

through the crystal lattice to the surface and is removed from the system by a vacuum pump. A vacancy is formed in place of the removed silicon atom. Vacancies of this type, formed as a result of the interaction of CO with Si, will be referred to below as vacancies of a chemical nature or just “chemical” vacancies. An excited carbon atom released from the CO molecule as a result of the chemical reaction does not immediately take the place vacated after the removal of the Si atom via SiO but occupies an intermediate interstitial position, thus forming the so-called dilatation dipole, i.e., the complex “interstitial C – ‘chemical’ Si vacancy”. During the final stage, interstitial carbon atoms “collapse” into “chemical” silicon vacancies due to the relaxation of elastic energy, thus forming a SiC coating.

The main disadvantage of this method is the physically limited thickness of the resulting SiC coating. It is impossible to grow the SiC coating with a thickness of more than 200–250 nm by this method. This is due to the peculiarities of the course of the chemical reaction: CO gas – crystalline silicon. As the structure of the surface layers of silicon is transformed into silicon carbide, the access of the reactant gas to the reaction front in the volume of silicon becomes more difficult, and when the critical thickness is reached, the reaction stops. This is explained by the fact that during the transformation of Si into SiC, the distance between atoms in the crystal cell of the formed SiC is smaller than in the initial Si. Accordingly, the diameter of channels, through which CO gas penetrates and SiO gas is removed, is also smaller in SiC. Therefore, as SiC



**Fig. 14.** Microscopic image of the cross-section of SiC-3C/Si(111) (a) and RHEED pattern obtained at an electron energy of 50 keV from its surface (b) samples grown by modified atomic substitution method at a temperature  $T = 1350$  °C and CO pressure  $p_{CO} = 80$  Pa for 10 min with preliminary saturation of Si by vacancies. Under a high quality SiC-3C layer with thickness of  $\sim 700$  nm there is a layer of lower quality SiC with voids and unreacted silicon. The diffraction pattern corresponds to the epitaxial structure; polycrystalline phase is absent [43]

is formed, the rate of movement of gases slows down. As a result, CO gas cannot penetrate to a great depth, while SiO gas ceases to be removed from the system, so the chemical equilibrium is established – the reaction stops. If the required thickness of the SiC layer exceeds 250 nm, it is necessary to repeat the procedure of depositing precursor layers (with the thickness up to 250 nm) on the already formed two-layer SiC coatings with their subsequent modification in a vacuum furnace in the presence of CO until the required thickness of the layered coating is reached. This significantly complicates the technology. In addition, repeated deposition of thin layers of silicon (the precursor layer) on an already formed SiC surface in order to increase the thickness leads to a deterioration in the crystalline perfection of the final layer, since during heterogeneous nucleation of Si on SiC, defects and dislocations are formed due to differences in the lattice parameters, and significant elastic stresses occur as well.

However, for some applications it is necessary to obtain high-quality single-crystal SiC films of noticeably higher thickness, for example, 200–1000 nm. In [43], a method that allows to increase the thickness of the silicon carbide layer by about an order of magnitude was proposed and implemented. The method is based on the theoretical conclusions of [5] and consists in the saturation of the surface of the silicon substrate with vacancies by pre-annealing in vacuum at  $T=1350$  °C during  $\sim 1-30$  min annealing time is determined by the need to obtain films of a given thickness). Thus, at the beginning of synthesis, silicon vacancies are specially created in the silicon substrate before the growth of SiC. This allows to create new pathways for CO diffusion and SiO removal in the substrate. Silicon vacancies penetrate from silicon into silicon carbide and provide a high rate of removal of the reaction product SiO outside of the reaction zone. Therefore, SiO much less hinders the growth of SiC, moreover, using vacancies, CO also penetrates deep into SiC more efficiently, which ultimately leads to much thicker SiC layers. This leads to the fact that when silicon atoms are substituted by carbon atoms, the interstitial-driven mass transfer mechanism switches to the vacancy-driven one. As a result, the SiC layer thickness

not only increases, but, when it becomes higher than 400 nm, the layer delaminates from the Si substrate. The SEM micrograph of a thick SiC layer grown by the method [43] is shown in Fig. 14a.

During vacancy-driven growth, a silicon substrate is placed in a vacuum furnace and subjected to preliminary annealing at a temperature of 1250–1400 °C for 1–60 min under vacuum conditions (at a pressure of about 20 Pa or less). Due to preliminary annealing under vacuum conditions, the near-surface region of silicon is saturated with point defects in the silicon lattice – “thermal” vacancies (in contrast to the “chemical” vacancies that arise during the reaction of CO and Si and are mentioned earlier in the description of the prototype method). It is known that two types of “thermal” vacancies are formed in silicon crystals. Some “thermal” vacancies are Schottky vacancies, and others are Frenkel “thermal” vacancies. Schottky vacancies are formed near the surface of a silicon crystal as a result of the emergence of a silicon atom on the Si surface. Frenkel vacancies are formed as a result of the efflux of an atom from a crystal lattice site into the interstitial space. The higher the temperature, the higher the concentration of both “thermal” Frenkel vacancies and “thermal” Schottky vacancies.

After annealing in vacuum, a silicon carbide two-layer structure is formed by supplying CO gas at a pressure of 20–600 Pa into a vacuum furnace, and the substrate is kept in a CO atmosphere at a temperature of 1250–1390 °C. During this stage, chemical reaction (1) proceeds in the near-surface region of the substrate. However, unlike the described above method, in which vacancies are formed simultaneously with the occurrence of chemical reaction (1), in this case, at the stage of formation of “chemical” vacancies during the interaction of CO and Si, the system already contains a large number of “thermal” (nonequilibrium) vacancies. This makes it an open, non-equilibrium system. In the diffusion zone region, i.e., in the zone where the concentration of “thermal” (nonequilibrium) vacancies is increased, the chemical bonds within silicon are significantly weakened. The silicon lattice is in an unstable state. Gases easily penetrate inside silicon. The process

resembles the absorption of moisture by originally compressed porous sponge. Due to the creation of a high vacuum at the beginning of the process, silicon evaporates all the time from the surface of the silicon substrate, it does not deposit on the substrate and does not “block up” the formed vacancy channels. Hollow vertically oriented chains consisting of vacancies are formed inside silicon. When silicon evaporates, especially in a vacuum state, the presence of a vacancy leads to elastic compression of the silicon surface layer, since some of the silicon atoms have evaporated. It should be noted that since vacancies change the volume of the crystal, it is “more advantageous” for them to form in a coordinated manner, by forming lines or chains consisting of vacancies along the crystal surface. Such a process is impossible without the constant pumping-out of silicon vapours.

In the second step, as soon as CO gas is introduced into the system, it quickly saturates the elastically stressed layer, like a compressed sponge absorbs moisture. The elastic stresses relax, but the silicon structure prepared by such annealing already contains the gas that has penetrated into it, and a chemical reaction starts. In contrast to the method described in paragraph 2, in this case, the chemical reaction starts at a great depth and it starts evenly over the entire initially compressed silicon layer. The Si layer of thickness (0.5–5  $\mu\text{m}$ ) is converted into a layer of silicon carbide with the formation of a decompressed contact at the interface due to the formation of flattened gaps, the size of which exceeds the size of the pores by 2–3 times. The thickness of the SiC layer will depend on the rate of evaporation of silicon, which is determined by the temperature, the degree of vacuum created by the pump, and the reaction time. At temperatures below 1250 °C, the flow of evaporating silicon will not be large; therefore, the thickness of the SiC layer also will not be large. If the evaporating silicon is not pumped out, then it will quickly diffuse back from the surface, and the vacancies will “heal”. The system will then reach a state of equilibrium, i.e., the process will follow the path outlined in paragraph 2. In this case, reaction (1) occurs much easier and, accordingly, faster. The diffusion layer is transformed into a two-layer silicon carbide structure, the upper layer of which

is formed from silicon carbide and has a single-crystal structure, and the underlying transition layer has a nanoporous structure and is formed by silicon carbide and unreacted silicon residues. In addition, an increased concentration of “thermal” (nonequilibrium) vacancies allows the process of withdrawal of reaction products (SiO) to be significantly accelerated, which accelerates the process of chemical transformation of Si into SiC.

Thus, a two-layer structure, the upper layer of which is a continuous layer of SiC, and the lower layer is decompressed, is formed due to the following processes. Schottky vacancies consistently form lines or chains near the surface of the substrate. If atoms evaporating from the surface of the crystal are pumped out, then “thermal” Schottky vacancies will all the time diffuse deep into the crystal from the surface. They will diffuse in a consistent manner. The chains of vacancies formed on the surface will “move” deep into the substrate. This will lead to the formation of hollow vertically oriented channels (chains of vacancies). CO gas penetrates into the substrate through these channels. The higher the silicon pre-annealing temperature and the longer the annealing time, the thicker the silicon layer saturated with vacancies becomes and the higher the vacancy density in this silicon layer becomes. The presence of vacancies leads to a decrease in the volume of the upper Si diffusion layer. As a result, this layer becomes compressed. It should be noted, that if atoms are not removed from the surface by a pump, then, on the contrary, the crystal will swell, and its volume will increase. This is the fundamental difference between the nonequilibrium and equilibrium processes of the formation of Schottky vacancies. Diffusion of Schottky vacancies will occur up to the depth of the silicon layer at which the formation of Frenkel defects begins to predominate. Frenkel vacancies are formed as a result of the exit of an atom from the lattice into the interstitial space; therefore, they practically do not lead to a change in the volume of the crystal. The following processes will occur on the interface of these regions. Since any system tends to equilibrium, the interstitial atom of the Frenkel defect will move to the upper zone into a vacancy formed by the Schottky mechanism and will move to the surface under the action of an elastic stress gradient until it evaporates under

the action of the pump. The compressed layer of silicon will push it out, and the vacancy will again move in the opposite direction and again capture the next lower atom. This process will continue until the rate of evaporation of atoms, which is determined by the degree of pumping-out of gases, is equal to the rate of migration of atoms in the field of the elastic stress gradient. At a certain thickness of the elastic layer, they are balanced, and the process stops. As we noted above, this process depends on the degree and speed of pumping of gases and on the annealing temperature. When the diffusion zone, i.e., the ensemble of chains, in the process of diffusion, reaches the zone in which Frenkel defects are formed, the interstitial atoms will start to “jump” into these vacancy formations. It is obvious that the jumps of these atoms will also be performed in a coordinated manner, since in this case the total elastic energy decreases more than in the case when atoms move one by one. As soon as they enter vacancies, they start to move towards the surface. This movement resembles the movement of an elevator. When CO gas is supplied, it penetrates deep into the upper layer along “thermal” vacancies, thus converting the surrounding silicon into SiC. However, in this case, according to reaction (1), one Si atom is removed together with the SiO gas. In place of this atom, a “chemical” vacancy is formed. These vacancies will no longer form along the chains of “thermal” vacancies in the compressed layer (there are no silicon atoms in these directions, they have already evaporated), but in the directions specified by the emerging SiC crystalline layer. However, as soon as the gas reaches the layer in which “thermal” Frenkel vacancies are formed, the gas begins to “pull out” interstitial silicon atoms. In this case, additional randomly arranged vacancy “channels” are formed. The elastic deformation in this part of the crystal completely relaxes, and in the upper ordered part a strong compression (shrinkage) of the entire upper layer occurs, and it separates from the layer where vacancies are generated according to the Frenkel mechanism. The upper crystalline layer is formed as the result of compression. Most of the vacancies located in this layer disappear, some of them are displaced deep into the silicon, additionally forming a system of randomly oriented vacancy channels,

which are transformed under the action of CO gas into a nanoporous layer containing lacunae. The degree of single-crystallinity of the layer depends on the initial concentration of vacancies in the upper layer of silicon and the degree of its “loosening”. At temperatures below 1250°C, there are not enough vacancies for its formation, and at a temperature slightly below 1400°C (at a higher temperature silicon melts), the density of vacancies is very high, and the formed Si is “loose”, consisting of many exfoliating crystalline patches (flakes). A typical electron diffraction pattern of the surface of a SiC/Si sample grown using the method of coordinated vacancy-driven substitution of atoms is shown in Fig.14b and unambiguously indicates the high crystalline perfection of the surface of this layer.

## 6. Coating method for smooth and profiled Si surfaces by ultrathin silicon carbide layers

In [44], a method was developed for coating Si surfaces with ultrathin layers of SiC, completely preserving their original morphology and structure. For the solution of a number of problems in electronics, it is often necessary to artificially create a certain type of profile of the nanometre scale on the surface. For example, the method that allows to artificially create the required nanoscale profile on the Si(100) surface was developed in [45]. The profile created in [45] was a nanoscale ridge-like structure, called by the authors of [45] nano-patterned silicon (NPSi(100), triangular in shape, oriented along the  $\langle 011 \rangle$  direction with an average period  $\lambda \approx 70$  nm and a height  $h \approx 70 \div 90$  nm). A raster image of

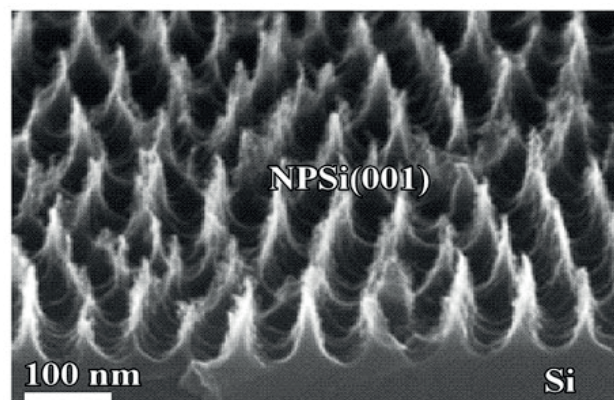


Fig. 15. SEM image of the end section and surface of the NPSi(100) structure [44]

the cleavage cross-section of this structure is shown in Fig. 15. Such structures are created for the formation of electron emitters. It seems important and natural to cover the surface of such silicon “pointed needle-shaped figures” with mechanically stronger chemically resistant material less prone to evaporation during field emission than silicon. Such a material, in particular, is silicon carbide. The MCSA described above in paragraphs 1–4 was used for covering of NPSi(100) structure. The main goal of the study was to determine the parameters of SiC synthesis, namely, the synthesis temperature, the pressure of synthesis gases (a mixture of carbon monoxide (CO) and monosilane ( $\text{SiH}_4$ )) is used in the substitution method [8]), at which the profiled Si surface is transformed into a profiled SiC surface without changing its geometry and morphology. As a result of studies carried out in [44], it was found that the optimal synthesis temperature for creating such coatings is a temperature equal to 1050 °C. During the synthesis of a SiC film at this temperature, a continuous single-crystal coating of SiC with a thickness of about 3–5 nm is formed without nanopores and nanocracks. This film did not dissolve and remained unchanged when it was in the etching solution for more than 120 s. The SEM images of the cleavage cross-section of a SiC film synthesised at a temperature of 1050 °C (Fig. 16a) and then kept in a selective etchant for 120 sec is shown in Fig. 16 (Fig. 16b). As can be seen from Fig. 16, the original NPSi(100) profile remained unchanged during etching. Only the silicon layer of the Si substrate was etched. The

SiC layer covers the Si like a “lid”. This layer is a replica of the original NPSi(100) structure completely converted into SiC.

At lower temperatures, the layer corresponding to the chemical composition of SiC is not formed. It can be said that at a temperature of 1000 °C and lower temperatures, “carbonization” of silicon rather than the formation of such a chemical compound as SiC occurs. At temperatures exceeding 1050 °C, the initial profile formed on silicon is not preserved.

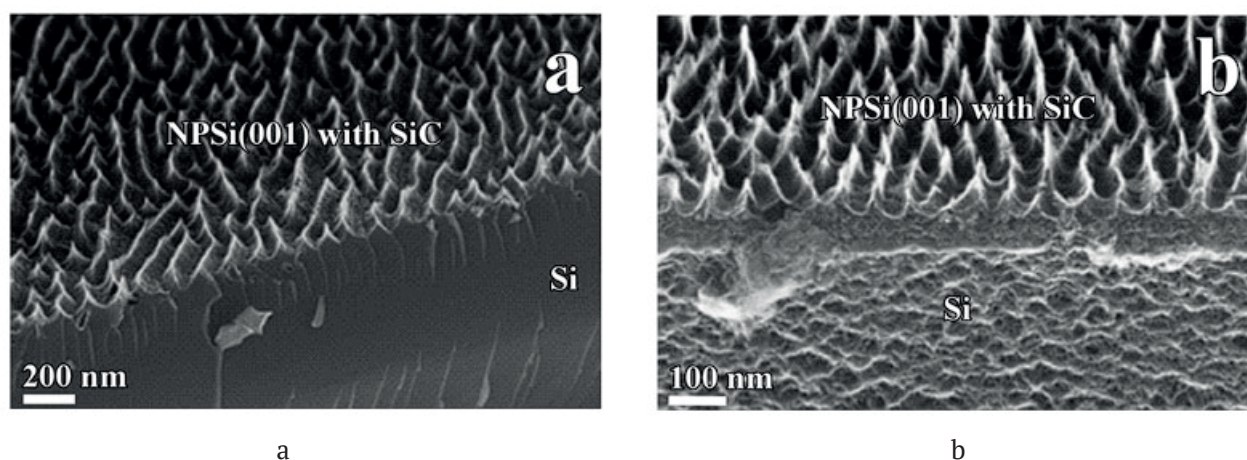
Thus, the method of substitution of atoms can be used to transform (convert) pre-profiled Si surfaces with the desired geometric pattern or smooth Si surfaces into chemically stable SiC surfaces of the same geometry without any noticeable distortions.

## 7. Formation of epitaxial SiC layers on the surface of other materials by the method of coordinated substitution of atoms

### 7.1. Synthesis of epitaxial silicon carbide films on sapphire substrates ( $\alpha\text{-Al}_2\text{O}_3$ )

#### 7.1.1. Current state and problems of growing of epitaxial SiC films on sapphire

Researchers have been engaged in the growth of epitaxial SiC on sapphire for a long time. For example, in [46],  $\beta$ -SiC films were mechanically transferred to sapphire substrates for the creation of an optical waveguide. For the better conjugation of the sapphire and silicon carbide lattices, usually an AlN layer is applied as a buffer layer between sapphire and silicon carbide. The authors of [47]



**Fig. 16.** SEM images of end sections of SiC/Si nanostructure synthesized at 1050 °C. (a) Surface of the NPSi(100) structure with SiC layer after synthesis at 1050 °C. (b) The surface of the SiC/Si nanostructure after etching in a mixture of acids HF and HNO<sub>3</sub> for 120 s [44]

showed that preliminary deposition of an AlN buffer layer on a sapphire substrate significantly improves the quality of the SiC layer and leads to the formation of an epitaxial 6H-SiC layer on sapphire. In [48], polycrystalline SiC layers were deposited on the “c” plane of sapphire by CVD in ultra-high vacuum in order to further obtain graphene layers on their basis on an insulating substrate, such as a sapphire substrate. In [49], polycrystalline SiC films were grown on sapphire by low-pressure CVD (LPCVD) for the obtaining optical temperature sensors based on the Fabry–Perot interferometric method. The authors of [50] used the MBE method to grow epitaxial films of the 4H-SiC polytype on a sapphire substrate with a preliminarily deposited AlN layer using fullerenes  $C_{60}$ . Rocking curves had the full width at half maximum  $FWHM_{\omega_0} \approx 0.24^\circ$ , which is a very good result. However, this method uses a complex MBE technology and also requires an additional layer of AlN to be applied to the sapphire. Later in [51], the authors, using an AlN layer as a buffer layer and pretreatment of the sapphire substrate or that with the AlN layer in a hydrogen flow and then in a propane flow ( $C_3H_8$ ), were able to grow the 2H-SiC polytype by MCVD. According to the TEM images presented in this article, the quality of the 2H-SiC layer is very high in some places of the film, and the conjugation between the 2H-SiC and AlN layers is good. However, based on the data obtained from the rocking curves (Fig. 1 from [51]), the best samples had the value  $FWHM_{\omega_0} = 40$  arcmin. On average, the best films had  $FWHM_{\omega_0} \approx 80$  arcmin, i.e., they were closer to texture than to epitaxy. Therefore, in our opinion, the data presented in [51] are very contradictory. The authors of the study [52] grew 3C-SiC layers on the (0001) plane of sapphire using the MOCVD method. The grown 3C-SiC films had thicknesses of 5–7  $\mu\text{m}$ . Unfortunately, nothing definite can be concluded about the quality of the grown layers, since the authors did not present the results of studies on the widths of the rocking curves, i.e., the values of  $FWHM_{\omega_0}$ . Based on the shown XRD plots, the XRD peaks corresponding to the 3C-SiC layer were quite broad, which indicates that the films were probably polycrystalline. Moreover, SEM images of cleavage cross-sections of the 3C-SiC films clearly show multiple dislocations (or twin grains). This is natural, since there is a

large difference of about 12% between the lattice parameter of 3C-SiC and the lattice parameters on the (0001) plane of sapphire. Note that there is a patent dated May 12, 2012 [53], that describes a method for growing an epitaxial SiC layer on sapphire by the MCVD method in ultra-high vacuum (about  $10^{-6}$  Torr.). The SiC films had thicknesses of about 90 nm. The study describes studies on the growth of 3C-SiC on sapphire from a melt [54].

Thus, at present, interest in the growth of SiC epitaxial films on sapphire is constantly increasing. Indeed, high hardness, inertness to chemically active media, and excellent insulating properties can ensure good use of sapphire substrates with a layer of such a wide-bandgap semiconductor as SiC in microelectronics, as well as in the manufacture of various types of sensors. In addition, based on SiC, it is possible to obtain graphene layers on an insulating sapphire substrate.

For growing a SiC layer on sapphire by the atom substitution method, it was proposed [55, 56] to first deposit a layer of epitaxial Si on the surface of a sapphire substrate and then convert it into SiC by reaction (1). It should be noted that the proposed approach of applying silicon carbide coatings to high-temperature materials can be used not only in semiconductor technology but also for creating a new class of composite, heat-resistant, and other hard coatings.

The growth of an epitaxial layer of silicon carbide on sapphire ( $Al_2O_3$ ) by substitution of atoms is carried out in two stages. During the first stage, it is necessary to grow an epitaxial silicon layer, and during the second stage, it is necessary to convert the epitaxial Si into an epitaxial SiC layer by the MCSA method. This scheme was implemented in [55, 56].

#### *7.1.2. Growth of epitaxial Si films on sapphire with the Si (100) and (111) layer orientations*

The silicon on sapphire (SOS) structure is a thin layer of single-crystal silicon formed by heteroepitaxy on a dielectric substrate of synthetic sapphire (leucosapphire,  $\alpha-Al_2O_3$ ). The physicochemical interaction between silicon and sapphire at the stage of formation of the transition layer creates a strong bond at the interface between the layer and the



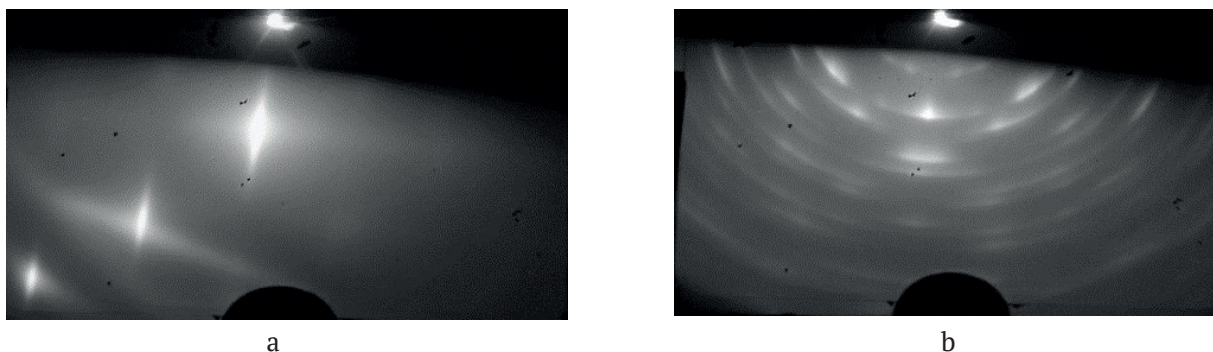
substrate, which ensures sufficient mechanical strength of the heteroepitaxial structure. High hardness, inertness to chemically active media, excellent insulating properties, sufficient thermal conductivity and transparency in the ultraviolet range of the sapphire substrate make it promising to use SOS structures in microelectronics (radiation-resistant integrated circuits (IC), combinational logic circuits, high-voltage fast recovery rectifiers), in the manufacture of transducers and sensors (photodetectors and resistive integrated circuits), as well as in the manufacture of microelectromechanical systems (MEMS) and nanoelectromechanical systems (NEMS) [57–61].

Barriers to the widespread use of SOS structures are the high density of structural defects in the SOS layer and the complexity of optimising the process of epitaxial growth. For SOS heteroepitaxial structures, the mismatch between the lattice parameters of silicon and sapphire in the lateral direction can reach 12.5% in case of formation of an epitaxial Si(111) layer on the c-plane (0001) of a sapphire substrate and about 6% when a Si(100) layer grows on the r-plane (1 $\bar{1}$ 20) of sapphire. The lattice mismatch and the difference in the values of the thermal expansion coefficients of silicon and sapphire lead to the formation of mechanical stresses in the epitaxial silicon layers and, as a consequence, to the formation of misfit dislocations. The vicinal surface of sapphire may contain a large number of centres for the formation of structural disturbances (disorientation centres), from which packing defects and twin lamellae (microtwins) occur during the initial stages of growth [57, 60, 61]. The growth of Si on sapphire occurs according

to the Stranski–Krastanov mechanism, i.e., three-dimensional islands are formed at the initial stage of film growth. The deposited silicon can chemically interact with the sapphire surface, thereby contaminating the growth islands and thus increasing their mutual misorientation and the defectiveness of the forming layer. The optimal conditions for the epitaxial growth process determine the structural characteristics of the SOS, which, in turn, are the key parameter for most applications.

In [56], epitaxial silicon layers with the thickness of 300–600 nm were grown on sapphire substrates with c-plane and r-plane orientations. The structures were obtained using an industrial vertical epitaxial reactor PE2061S (LPE, Italy). The operating pressure of about 1 atm was maintained in the reactor chamber, dried H<sub>2</sub> with a water vapour content < 5 ppb was used as the carrier gas. During growth, silicon layers were deposited on sapphire from a vapour–gas SiH<sub>4</sub> and H<sub>2</sub> mixture at a volume ratio of SiH<sub>4</sub>:H<sub>2</sub> about 0.01:1. Si layers of the (100) orientation grew on the r-plane (1 $\bar{1}$ 20) of sapphire. The grown Si(100)/Al<sub>2</sub>O<sub>3</sub> (1 $\bar{1}$ 20) layers had a high structural quality of epitaxial Si with the full width of the rocking curve at half maximum FWHM ≤ 0.3°. The mean square roughness of the working surface did not exceed 1±0.5 nm.

For the growth of Si on the c-plane (0001) of Al<sub>2</sub>O<sub>3</sub> sapphire from the same manufacturer was used [56]. Si of the (111) orientation grew on this substrate. The crystal structure of the Si(111)/Al<sub>2</sub>O<sub>3</sub>(0001) layers was a textured crystal with an ordered distribution of Si crystallites of the (111) orientation. The mean square roughness of these structures did not exceed 5 ± 0.5 nm.



**Fig. 17.** RHEED pattern of fast electron diffraction from Si samples grown on Al<sub>2</sub>O<sub>3</sub>; (a) – Si(100)/Al<sub>2</sub>O<sub>3</sub> layer on r-plane (1 $\bar{1}$ 20); (b) – Si(111)/Al<sub>2</sub>O<sub>3</sub> layer on c-plane (0001) Al<sub>2</sub>O<sub>3</sub> [56]

Fig. 17 shows reflection high-energy electron diffraction (RHEED) images of a Si sample grown on the r-plane ( $1\bar{1}20$ ) of sapphire (Fig. 17(a)) and a Si sample grown on the c-plane (0001) of sapphire (Fig. 17(b)). It is clearly seen from these data that the Si(100) film grown on the r-plane of sapphire is epitaxial, well oriented, as evidenced from the nature of the reflections, and approaches the quality of a single crystal, since Kikuchi lines are present on its RHEED pattern indicating the high crystalline perfection of this layer (Fig. 17(a)). A Si(111) film grown on the c-plane sapphire is a texture (Fig. 17c).

Fig. 18 shows typical SEM micrographs of a cross section of a Si (100) sample grown on the r-plane ( $1\bar{1}20$ ) of sapphire (Fig. 18 (a)), and a cross section of a Si (111) sample grown on the c-plane (0001) of sapphire (Fig. 18 (b)). Fig. 18 clearly shows that the structure of the Si(111) film grown on the c-plane of  $\text{Al}_2\text{O}_3$  is less dense and looser than the structure of the Si(100) film grown on the r-plane of  $\text{Al}_2\text{O}_3$ . The Si(111)/ $\text{Al}_2\text{O}_3$ (0001) interface contains dislocations and other defects.

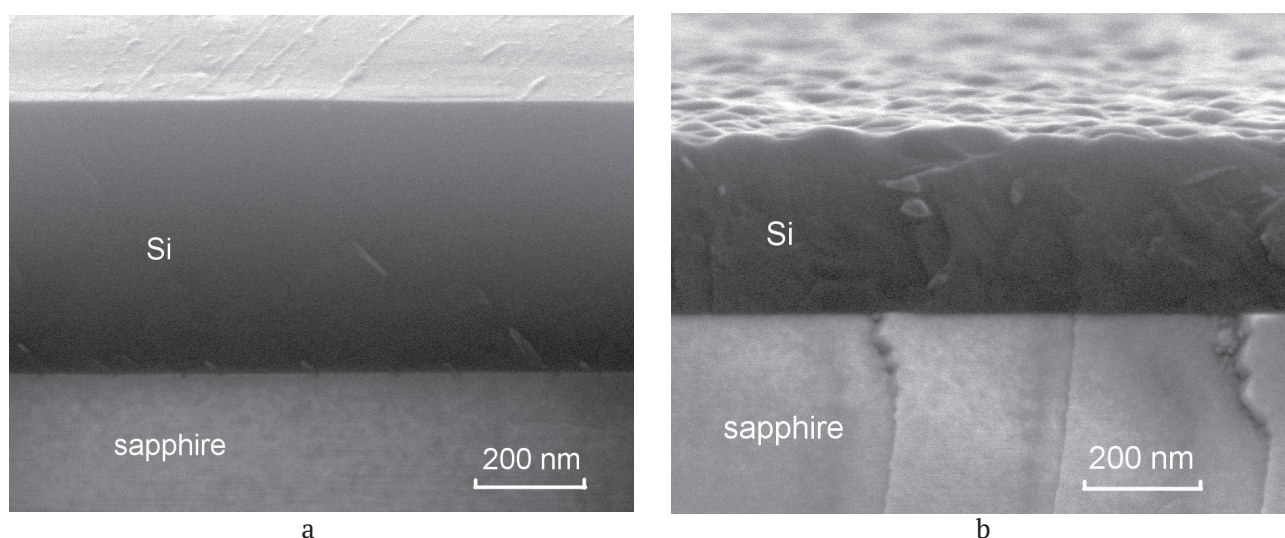
In [56], there were obtained also X-ray diffraction patterns (XRD), which showed that the Si(100)/ $\text{Al}_2\text{O}_3$  ( $1\bar{1}20$ ) structure is strained; therefore, for the Si(100) layer, the Si(200) forbidden reflection was observed. The XRD pattern of a sample of the Si(111)/ $\text{Al}_2\text{O}_3$ (0001) structure was measured in symmetrical geometry  $\theta/2\theta$ . The diffraction pattern showed that the

silicon film is textured. The main orientations of silicon crystals present in the layers correspond to the [220] and [111] peaks.

Thus, Si films with the (100) orientation can be grown epitaxially, and for this, it is necessary to use the r-plane ( $1\bar{1}20$ ) of sapphire substrates, and Si(111) films cannot be obtained epitaxially on the c-plane of  $\text{Al}_2\text{O}_3$  substrates. Supposedly, other sapphire facets should be used for epitaxial growth of Si.

### 7.1.3. Conversion of Si epitaxial films grown on sapphire into SiC epitaxial films by the method of coordinated substitution of atoms

After growing Si films on sapphire, in order to transform them into SiC layers, the resulting SOS structures must be chemically treated with CO gas according to reaction (1). Before this procedure, it is necessary to be clearly aware about the degree of the structural perfection of SiC layers which can be grown on Si(100)/ $\text{Al}_2\text{O}_3$  and Si(111)/ $\text{Al}_2\text{O}_3$  substrates. From the previous analysis it can be concluded that a SiC layer of the epitaxial quality but with a small admixture of SiC twins of the (110) orientation can be obtained on the Si(100)/ $\text{Al}_2\text{O}_3$  substrates. On the Si(111)/ $\text{Al}_2\text{O}_3$  substrates with a textured Si layer, it is only possible to obtain SiC as a textured layer. In the first case, this is due to the fact that, as shown in Section 2.3.1, SiC (111) facets will form on the Si (100) surface during the transformation of Si into SiC. Their



**Fig. 18.** Typical SEM images of the cross-section and the surface of Si (100) and Si (111) films grown on  $\text{Al}_2\text{O}_3$ ; (a) cross-section and surface of the Si (100)/r-plane  $\text{Al}_2\text{O}_3$  structure; (b) cross-section and surface of the Si (111)/c-plane  $\text{Al}_2\text{O}_3$  structure [56]

formation leads to the formation of epitaxial SiC with a small admixture of SiC facets of other orientations, in particular (110). In the second case, it is impossible to obtain a single-crystal SiC (111) layer until it will not be possible to grow a single-crystal (epitaxial) Si layer on sapphire. In principle, both of these tasks are solvable. In the first case, as was shown in paragraph 2.3.1, the growth of a vicinal Si surface, deviated by 4–6 degrees from the base plane (100), is required. Such a structure can be very attractive for the growth of semipolar AlN and GaN layers [62]. We expect to obtain it in the future. For SiC of epitaxial quality on Si(111)/Al<sub>2</sub>O<sub>3</sub>, it is necessary to obtain epitaxial Si(111) on Al<sub>2</sub>O<sub>3</sub>. As soon as such a silicon is obtained, epitaxial SiC will also be obtained.

Before the growth of SiC, as in the case of growth on silicon substrates, it is necessary to remove the silicon oxide layer, which can be formed during the interaction of Si with atmospheric oxygen from the surface. Otherwise, the chemical reaction between CO and Si, on the surface of which SiO<sub>2</sub> is located, will proceed differently compared to reaction (1). Dilatation dipoles will not form in this case, and the polycrystalline SiC film will grow. Thus, for obtaining an epitaxial SiC layer, before carrying out the reaction (1), it is necessary to prepare the Si surface for SiC growth, by obtaining a smooth (flat) surface at the atomic level and remove even silicon dioxide nanolayers from the surface of the silicon wafer. In addition, it is necessary to passivate the surface of the Si layer with hydrogen from its possible rapid oxidation during storage and transportation. The method of preparing and passivating the Si surface was developed for the growth of SiC in [63] and described in detail in [64].

In [56], the growth of SiC films was carried out according to the MCSA, which was described in detail above. To compare the growth of SiC films on Si/Al<sub>2</sub>O<sub>3</sub> with the growth of SiC films on silicon single-crystal substrates under standard conditions selected by many years of research [1–6, 12], samples were synthesised under conditions when SiC films on single-crystal Si were obtained as highly oriented single-crystal structures. For example, Si(100) films on sapphire were converted into SiC layers at a temperature of  $T = 1290$  °C.

The total pressure of the gas mixture (CO+SiH<sub>4</sub>) was 133 Pa. The CO gas flow was 12 sccm. The SiH<sub>4</sub> gas flow was 3.5 sccm. The synthesis was performed for 15 min. The growth of SiC films from Si(111) on sapphire was also carried out in a mixture of CO and SiH<sub>4</sub> gases. The growth temperature, growth time, and gas flow rate were the same as for the growth of SiC films from Si(100). Only the total pressure of the (CO+SiH<sub>4</sub>) gas mixture was different. In this case, we grew films with a total gas mixture pressure of 67 Pa.

After the SiC formation process, the samples were examined by scanning electron microscopy, confocal Raman microscopy, ellipsometry, X-ray diffraction analysis, and reflection high-energy electron diffraction (REED).

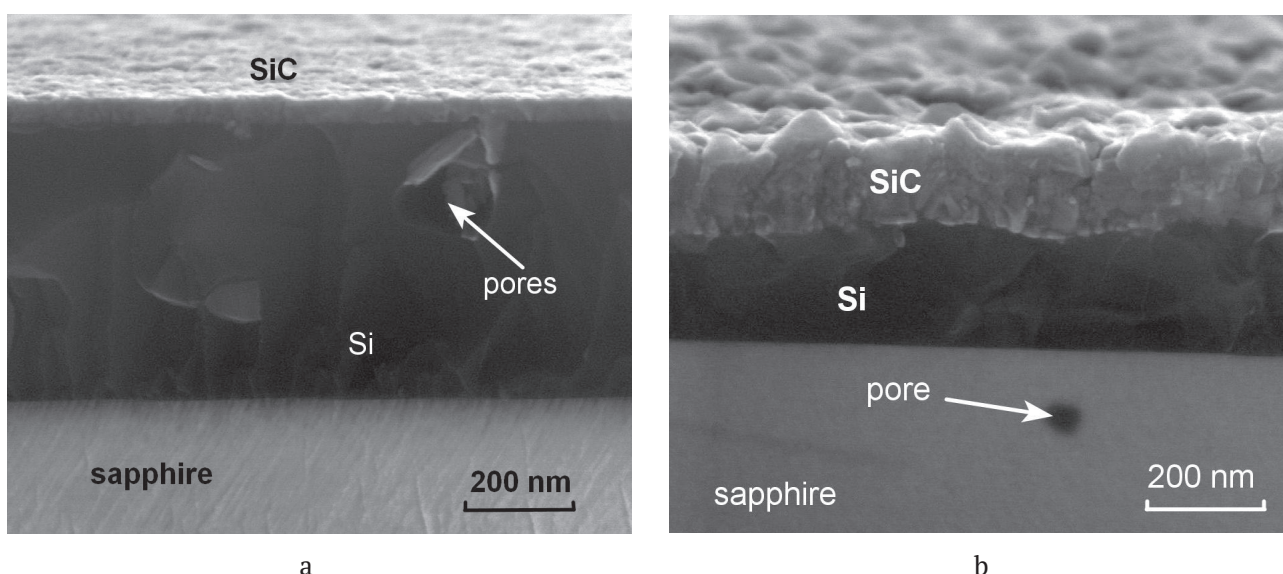
#### 7.1.4. Structural and morphological features of the formation of SiC films on sapphire

SEM images of cross sections from different parts of SiC/Si(100) and SiC/Si(111) samples on Al<sub>2</sub>O<sub>3</sub> are shown in Fig. 19. Fig. 19a shows a cross section with a region almost free of pores in the SiC/Si(100)/r-plane (1120) Al<sub>2</sub>O<sub>3</sub> structure, Fig. 19b shows a cross section of the SiC/Si(111)/c-plane Al<sub>2</sub>O<sub>3</sub> structure with an area practically free from pores.

The analysis of a large number of SEM micrographs taken in [56] from different parts of the surface of these samples showed that in the SiC/Si(100)/r-plane (1120) Al<sub>2</sub>O<sub>3</sub> there are places with a large number of pores. However, in general, the density of pores in the SiC/Si(100)/r-plane (1120) Al<sub>2</sub>O<sub>3</sub> sample was significantly lower than the density of pores in the SiC/Si(111)/c-plane Al<sub>2</sub>O<sub>3</sub> sample. It is interesting to note that if structure of the initial silicon on sapphire more “loose”, less crystalline, and closer to texture, then CO gas penetrate deeper into the Si layer. As it can be seen from Fig. 20, the c-plane, i.e., the (0001) sapphire plane, begins to be etched during the SiC synthesis (a pore in sapphire is clearly visible in Fig. 19b; other micrographs confirming this process are also presented in [56]. In our opinion, the etching can be associated with a chemical reaction of the type:



which, as shown in [56], can occur at temperatures of the order of  $T \sim 1280$  °C. CO<sub>2</sub> gas released during the reaction will react with Si at the Si/



**Fig. 19.** SEM images of the cross-sections of different areas of the SiC/Si (100) and SiC/Si (111) samples grown on  $\text{Al}_2\text{O}_3$ ; (a) cross-section of a region containing pores, coated with a SiC layer in the SiC/Si (100)/r-plane ( $1\bar{1}20$ )  $\text{Al}_2\text{O}_3$  structure; (b) cross-section of an area practically free from pores on the SiC/Si(111)/c-plane  $\text{Al}_2\text{O}_3$  structure [56]

$\text{Al}_2\text{O}_3$  interface and will again form SiC but with an admixture of quartz (crystalline  $\text{SiO}_2$ ) in accordance with reaction (5):

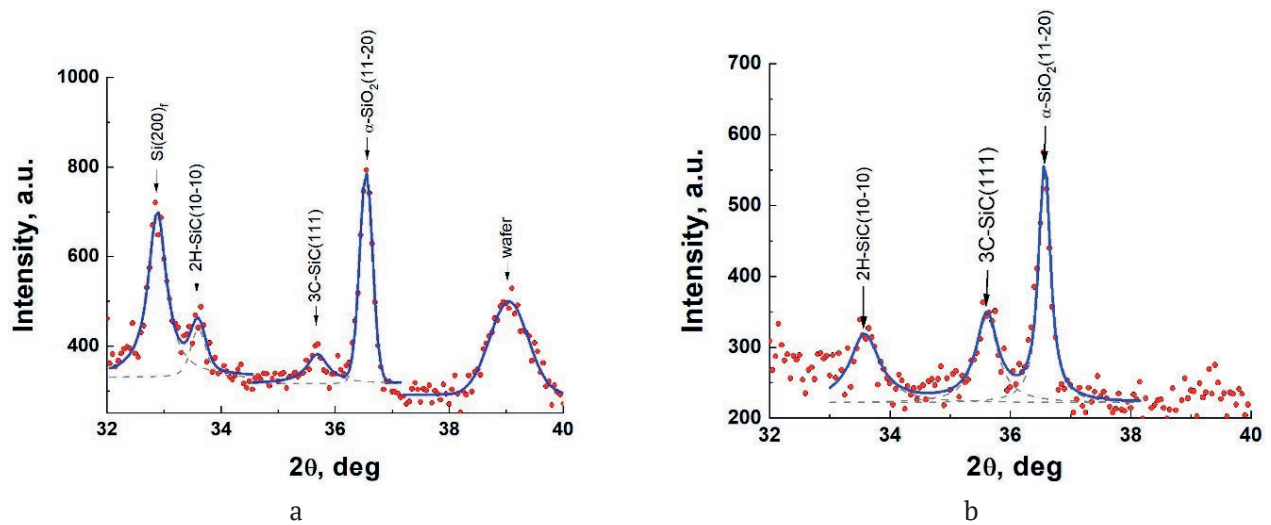


Moreover, in the presence of CO and  $\text{CO}_2$  a number of other reactions are also possible, which we do not consider here. Obviously, at the temperature at which SiC is synthesised, silicon oxide can be formed both in the form of quartz glass and in the form of crystalline quartz. It is quite possible that, during the formation inside the ordered phases (Si, SiC,  $\text{Al}_2\text{O}_3$ ), more probably  $\text{SiO}_2$  in the crystalline form will be formed, which we actually detected [56] in SiC/ $\text{Al}_2\text{O}_3$  layers in the study of X-ray spectra of SiC samples grown on Si(100)/ $\text{Al}_2\text{O}_3$  and Si(111)/ $\text{Al}_2\text{O}_3$  and shown in Fig. 20. X-ray diffraction patterns (XRD) obtained from samples grown on Si(100)/ $\text{Al}_2\text{O}_3$ (r-plane) and Si(111)/ $\text{Al}_2\text{O}_3$ (c-plane) are shown in Fig. 20. On a SiC sample grown on Si(100)/r-plane  $\text{Al}_2\text{O}_3$ , XRD peaks were observed. The positions of these peaks corresponded to SiC of both the 2H-SiC and 3C-SiC modifications. There are peaks from the 2H-SiC and 3C-SiC phases on XRD taken from a SiC sample grown by the conversion of Si(111) on the c-plane of sapphire. A peak, the position of which corresponds to the  $\alpha$ -quartz phase, can be distinguished for all samples. It should be noted that in this case, we cannot state with complete

certainty that the 2H-SiC phase is formed on sapphire in the process of Si/ $\text{Al}_2\text{O}_3$  conversion into SiC/ $\text{Al}_2\text{O}_3$ . This XRD peak is “blurred”. It is known that XRD peaks of other hexagonal polytypes are also located in this region of the XRD scan (2 $\theta$ ). It was noted in reviews [1–6, 12] that SiC layers of various polytypes can form during the growth of SiC by the method of substitution of atoms. Therefore, the formation of 2H-SiC layers should not be surprising, since the physicochemical nature of the method of substitution does not prohibit the formation of this phase.

As it can be seen from the data in Fig. 20, along with SiC,  $\alpha$ -quartz is also formed. We attribute its appearance to the occurrence of reactions (14) and (15), which take place during the growth of SiC on sapphire. During the growth of SiC by the method of substitution of atoms on pure Si, the formation of  $\alpha$ -quartz under the given synthesis conditions was not observed.

In [56], RHEED, Raman, and ellipsometric spectra of SiC samples grown on a Si (100)/ $\text{Al}_2\text{O}_3$  r-plane and on a Si(111)/ $\text{Al}_2\text{O}_3$  c plane were shown. We do not present them in this review, but refer the reader to the original study [56]. Here it should be noted once again that the SiC layer grown on single-crystal Si is much more oriented than the layer grown on sapphire. However, as follows from our study of SiC growth on Si(100)/r-plane  $\text{Al}_2\text{O}_3$  and Si(111)/ $\text{Al}_2\text{O}_3$  c-plane, it is enough to deposit a



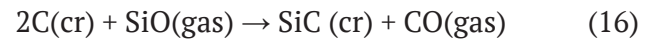
**Fig. 20.** X-ray diffractograms from SiC samples grown Si(100)/Al<sub>2</sub>O<sub>3</sub> r-plane and Si(111)/Al<sub>2</sub>O<sub>3</sub> c-plane ; (a) SiC on Si(100) r-plane (1-20) Al<sub>2</sub>O<sub>3</sub>; (b) SiC на Si(111) на c-plane Al<sub>2</sub>O<sub>3</sub> [56]

high-quality Si layer on sapphire, and as a result, the SiC layer will also be epitaxial. Moreover, the higher the degree of single-crystallinity of the Si layer, the higher the degree of single-crystallinity of the SiC layer.

### 7.2. A new method of formation of protective SiC-C composite coatings on graphite

Graphite products are widely used in various areas of technology and industry — from parts of high-temperature furnaces to nuclear reactors — and during use, these products are subjected to various loads: mechanical, chemical, and thermal. For the protection of graphite from such impacts, various protective coatings are often applied to it, ranging from niobium, oxides, nitrides, and ending with various composite layers. In particular, one of the promising coatings is silicon carbide, which has chemical resistance, high hardness and thermal conductivity. In [65, 66], a method for depositing silicon carbide coatings on graphite by annealing a graphite sample in contact with a Si melt in a carbon monoxide (CO) atmosphere was developed. The method is based on the interaction of CO and silicon with the formation of SiC and is similar in many respects to the MCSA but differs from it by relying not only on one reaction (1) but two chemical reactions occurring simultaneously inside the graphite. One of the reactions is the chemical interaction of Si melt, located on the surface of graphite, with CO at a temperature exceeding the melting point of

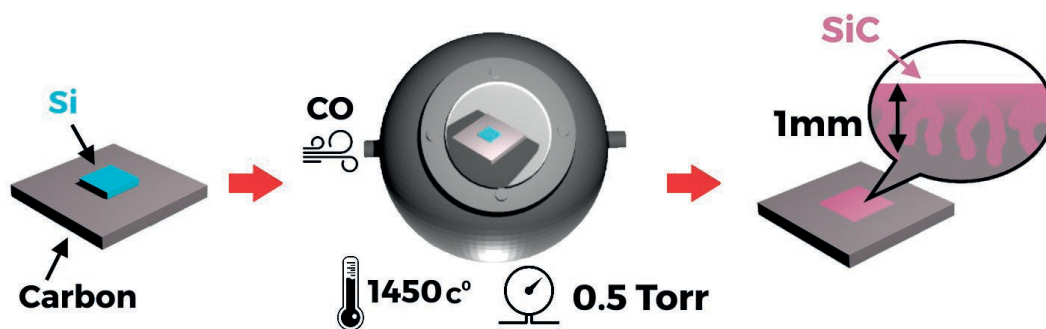
silicon (1412 °C), which results in transformation of Si into SiC. This is the reaction (1). The second reaction, proceeding simultaneously with the first one, is the interaction of the product of the first reaction – gaseous silicon monoxide (SiO) – with graphite, which results in transformation of the latter into SiC. This reaction is as follows:



Thus, during the synthesis of a SiC coating on graphite, at the initial moment of time, as a result of reaction (1), SiC and gaseous SiO are formed. Then the gaseous SiO, which is removed from the system during the growth of SiC by the MCSA, reacts with graphite at the interface. In this case, SiC is formed, but already from the graphite side. At the same time, CO is released, it reacts from the interface side with Si and finally converts the residual silicon into silicon carbide. A schematic representation of the method of formation of this coating is shown in Fig. 21.

The coating formed as a result of these processes has high mechanical strength and hardness. In the process of composite synthesis by this method, a coating with a thickness exceeding 1 mm is formed. Samples of composite coatings were studied using scanning electron microscopy, energy-dispersive spectroscopy, Raman spectroscopy, and also by nanoindentation [65, 66].

Studies have shown that the composite material obtained by this method consists of a



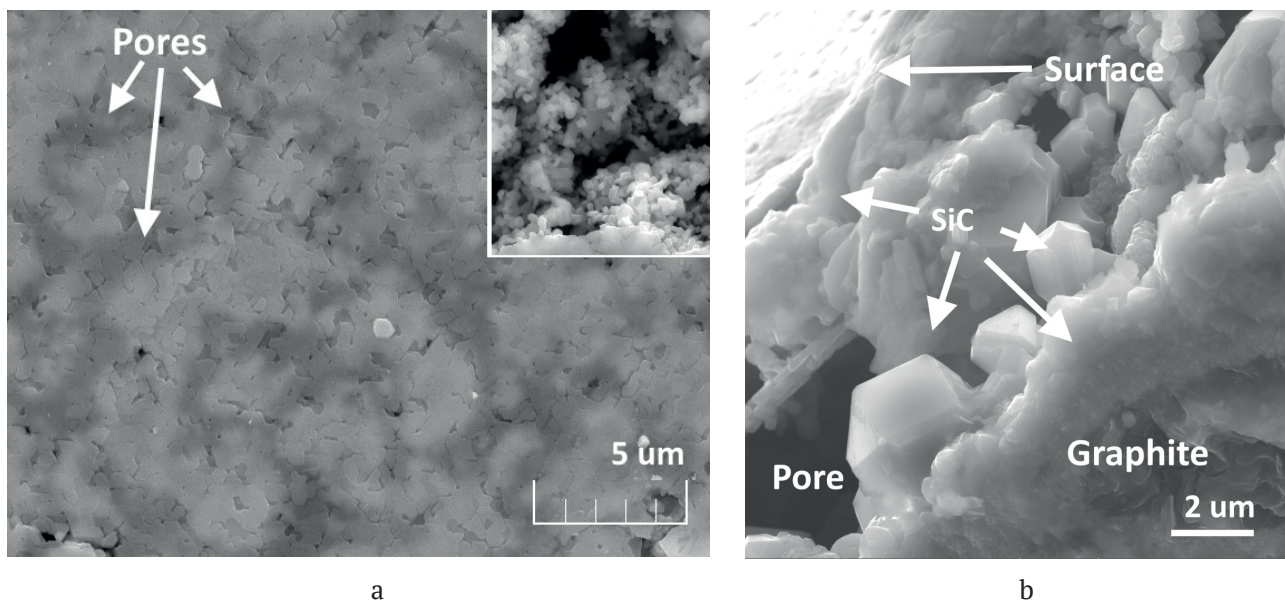
**Fig. 21.** Schematic representation of the method of forming the SiC-graphite composite on the surface of the graphite product [65]

continuous silicon carbide film on the surface and has a branched structure consisting of dendritic SiC crystals extending deep into the product, interspersed with large (up to 20 μm) single-crystal grains of predominantly cubic polytype with a small fraction of hexagonal polytypes. The deposition of the coating leads to a significant hardening of the material: the composite coating has a hardness of 28 GPa, which is ~254 times higher than the hardness of the original graphite surface.

For the experiments, MPG-7 graphite sample was used, on the top of which a silicon wafer with the thickness of 300 μm and an area of about 1 cm<sup>2</sup> was placed. The structure was annealed in a vacuum furnace in a CO atmosphere with the

addition of silane at a temperature of 1450 °C and a total pressure of 0.5 Torr for 20 minutes. After the synthesis, the resulting samples of SiC coatings were studied by scanning electron microscopy using Tescan Mira 3 microscope. The mechanical properties of the surface were studied using a Nanotest 600 installation for nanoindentation.

SEM images of the sample surface and sample cleavage are shown in Figs. 22a and 22b, respectively. As can be seen from Fig. 22b, the coating is a continuous crystalline layer, on which there are areas with different contrasts. A detailed study of the surface after mechanical separation of the SiC film allowed to conclude that voids were observed under the dark regions

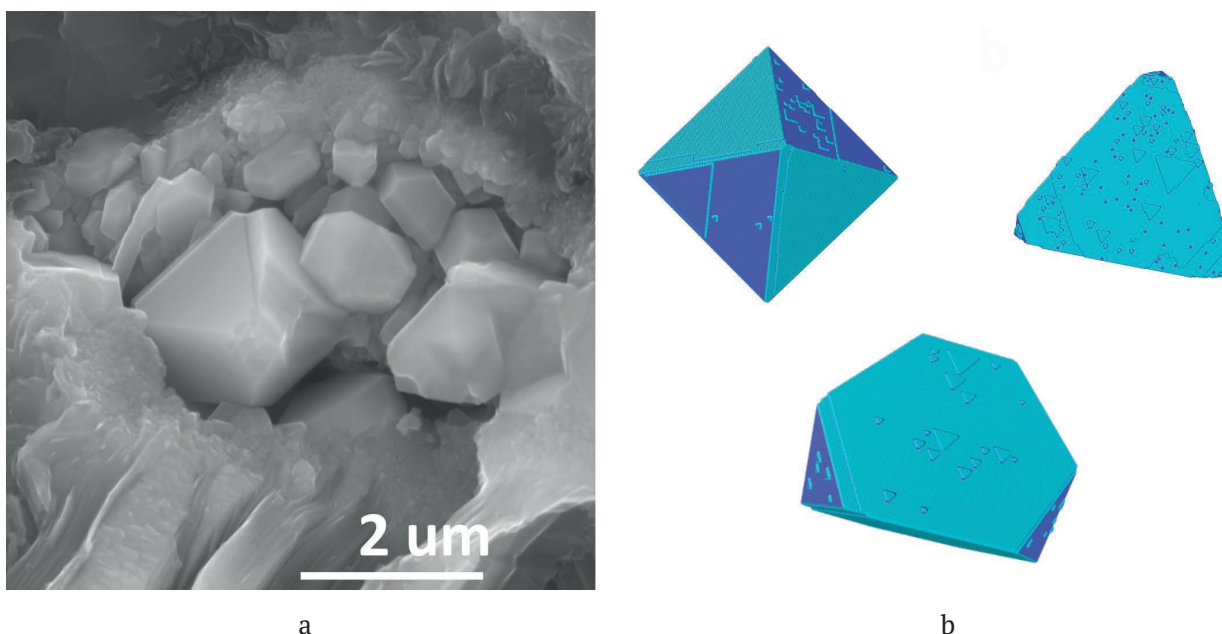


**Fig. 22.** SEM-image of the surface (a) and chip (b) of the sample of SiC composite coating on the graphite surface. The dark areas in figure (a) correspond to the pores under the SiC film surface. The inset to figure (a) shows the inner surface of the pore after removal of the SiC film [65]

(see the inset to Fig. 22b). The pores are also visible on the cleavage of the sample (Fig. 22b, right side). As can be seen on Fig. 22b, the immediate surface SiC layer is continuous and has a thickness of the order of several micrometres. At great depths from the surface, a mixed structure of pores, crystals, and druses of silicon carbide with graphite inclusions starts, and at depths of the order of several hundred micrometres, the volume fraction of SiC gradually approaches zero. The penetration of silicon carbide to such depths is due to the rather large porosity of the initial graphite matrix and the fact that the silicon melt that has flowed into the pores was converted into SiC as a result of the reaction with CO. SiC has a volume of the unit cell two times smaller than that of silicon [1–6,12]. As a result, during the formation of SiC, new voids appear, and the channels in the graphite are not “blocked”, but remain open for further penetration of the silicon melt into the depths. As a result, “roots” of SiC, firmly binding the upper single-crystal SiC film with the graphite matrix are formed in the volume of graphite. Different shapes of the resulting SiC microcrystals, which correspond to the cubic polytype of silicon carbide can be seen on SEM images of regions of the crystal (see Fig. 23a) at a depth of about 150  $\mu\text{m}$ . It should be noted that the Monte Carlo simulation of growth

of SiC crystals of the cubic polytype using Crystal Grower package [67], performed in this study for various ratios of the Si and C components, provides a spectrum of crystal shapes actually observed in the experiment (Fig. 23b). Thus, regular octahedral crystals were observed during the formation of a crystal from a mixture of stoichiometric composition, while with an excess of carbon in the system, crystalline forms with “bevelled” facets were observed.

The microhardness of the coating was measured using a nanoindenter at a maximum indentation force of 1 mN. The indenter was loaded and unloaded at a rate of 0.5 and 1 mN/s, respectively. It should be noted that due to the presence of porous regions under the surface of a thin single-crystal SiC layer (see Fig. 22), in some cases, an increase in the indentation force led to the appearance of significant deformation jumps in the nanoindentation curves up to several hundreds of nanometres (see the dotted curve in Fig. 25a). Such jumps, caused by the presence of pores, significantly distort the result of the analysis of experimental data. It should be noted that deformation jumps were also recorded at nanoindentation up to 1 mN, but this happened much less frequently. For the determination of the hardness of the modified and original graphite, nanoindentation curves were selected exclusively



**Fig. 23.** SEM - image of SiC crystals observed in the pores in the carbon matrix, and growth shapes of cubic SiC obtained by Monte Carlo simulation in the Crystal Grower package [67] at different ratios of Si and C components during growth [65, 66]

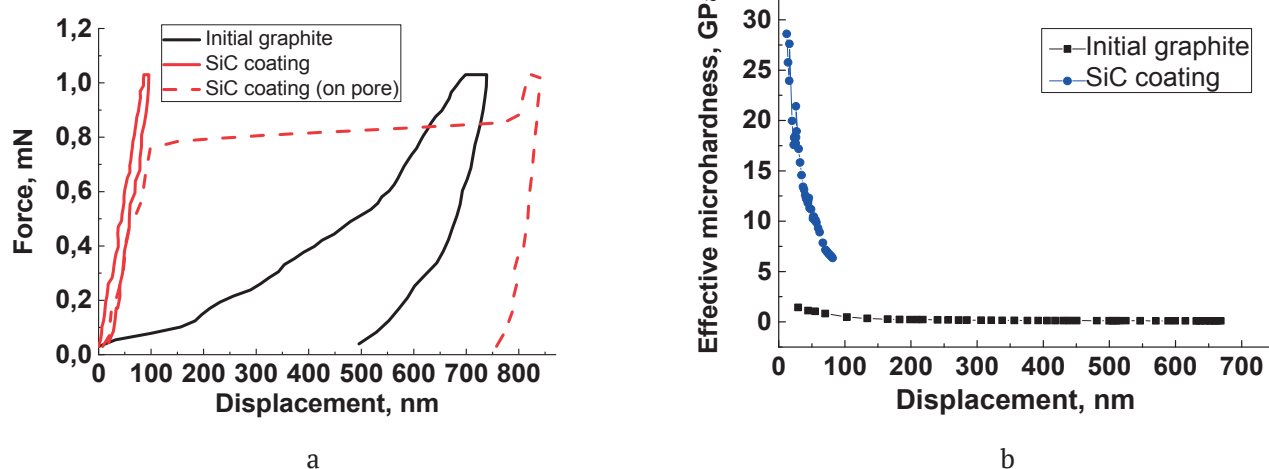
without strain jumps. Typical dependences of the indentation force on the depth of penetration of the indenter into the studied material for the modified and original graphite regions are shown by solid curves in Fig. 24a. The dependences of microhardness on depth, calculated using the standard method [68], are shown in Figs. 24b. It can be seen that the SiC coating significantly increased the surface hardness to 25–28 GPa, while the hardness of the original graphite was 100–130 MPa.

Thus, it was shown in [65, 66] that the annealing of graphite in contact with a silicon melt in a CO atmosphere allow to form a protective coating of silicon carbide, which is a continuous film on the surface and a branched system of crystals and crystalline druses extending to a large depth. The coating significantly increases the hardness and mechanical resistance of the material, and has antioxidant properties, thus protecting the surface of the graphite product from various influences.

### 8. Crystal structure, polytypism, optical, electrophysical, mechanical, and other properties of SiC synthesised on Si by the method of coordinated substitution of atoms

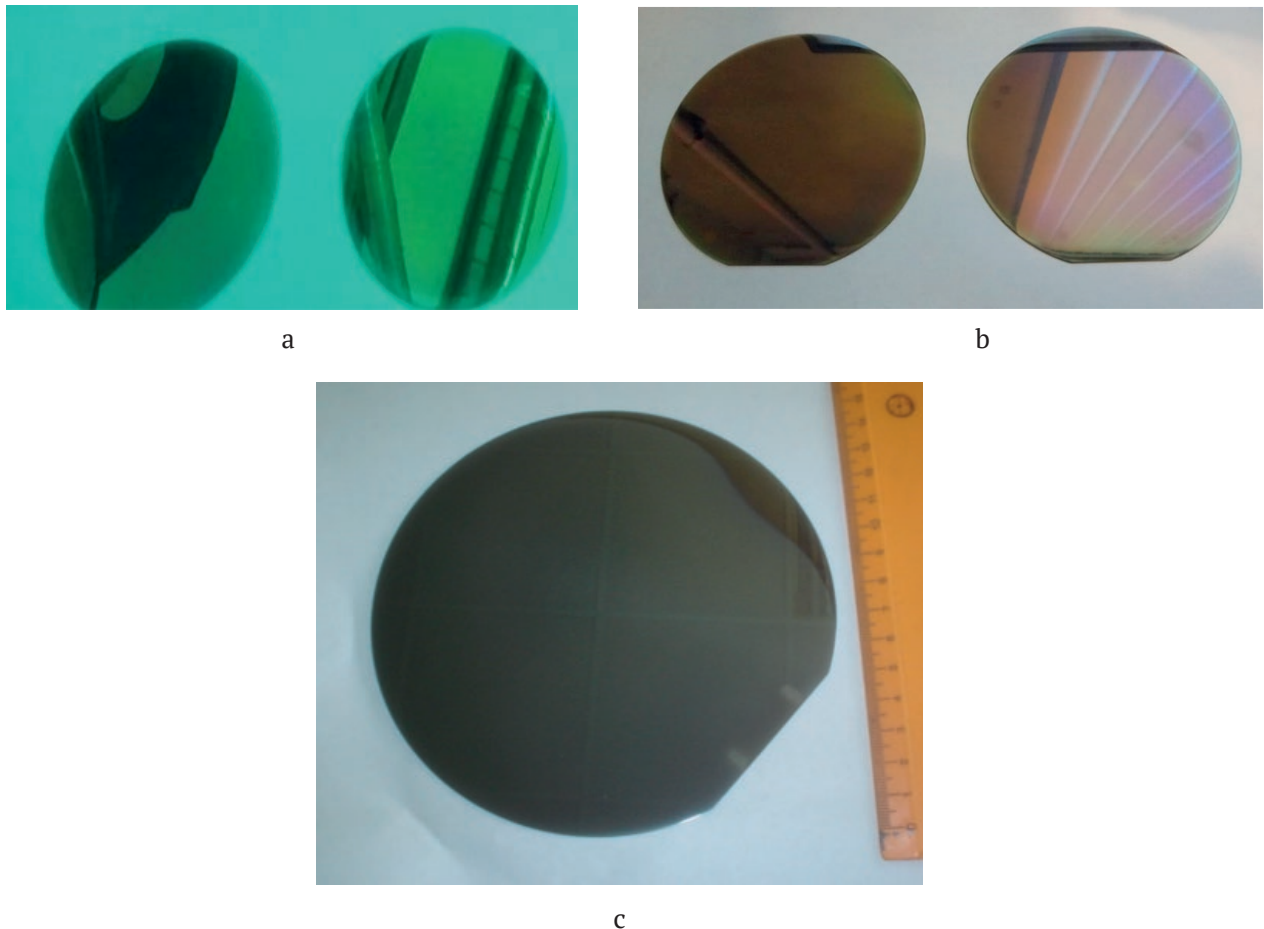
The semi-industrial technology [28, 69], which allows to grow epitaxial SiC layers with a diameter of 50.8 mm (2 inches); 76.2 mm (3 inches); 100 mm (4 inches) and 150 mm (6 inches)

was developed based on the described above MCSA. Photographs of SiC/Si wafers of various diameters are shown in Fig. 25. The SiC layers were grown in a vacuum furnace VHT 8/18(22)-GR 1800 manufactured by Nabertherm GmbH. Heating of the graphite chamber with a volume of 8 litres was carried out using graphite heaters. Preliminary evacuation was carried out with a turbomolecular pump up to a pressure of  $10^{-2}$  Pa. The heating and cooling rates in the temperature range 1000–1390 °C were 30 and 15 K/min, respectively. The chamber was supplied with carbon monoxide at a flow rate of 50–100 sccm ( $\text{cm}^3/\text{min}$ ). For the stabilization of the partial pressure of silicon, silane ( $\text{SiH}_4$ ) with a flow rate of 10–20 sccm was supplied into the chamber. The temperature during the growth of SiC layers was 1000–1390 °C and the operating pressure was 70–700 Pa. The wafers were subjected to the maximum temperature for 5–30 min. The total time of the technological process (from loading to unloading) was 5–7 hours. Up to 20 SiC layers on silicon wafers with a diameter of 100 mm and 6 layers of SiC on silicon wafers with a diameter of 150 mm can be simultaneously grown in a single process. As substrates for silicon carbide epitaxy, we used silicon wafers of various grades, usually, (111), (110), (100) orientations; however, SiC growth was also carried out on Si wafers of other orientations. Before growing the SiC layer, the Si wafers were passivated with hydrogen according to the procedure [63, 64]. A detailed description



**Fig. 24.** Load-discharge curves of the original graphite (black solid line) as well as of the formed coating in two areas: lying directly on the graphite (blue solid line) and “hanging” over the pore (blue dashed line) (a). Dependence of the effective hardness of the materials on the depth (b) [65, 66]





**Fig. 25.** Photographs of silicon carbide samples on silicon substrates 50.8 mm (2 in) in diameter (Fig. 25a); 76.2 mm (3 in) (Fig. 25b); and 150 mm (6 in) (Fig. 25c) grown by matched atom replacement on a small-scale industrial scale

of the procedure for synthesising SiC layers on wafers of a given diameter can be found in [69]. The SiC films grown on Si wafers were studied using spectral ellipsometry, SEM microscopy, X-ray diffraction, and Raman scattering. Studies have shown that the SiC layers were epitaxial over the entire surface of the 150 mm wafer. The plates were not stressed, even, without bends. The half-width of the x-ray rocking curve ( $\text{FWHM}_{\omega_0}$ ) of the wafers varied from  $0.35^\circ$  to  $0.55^\circ$  at a layer thickness of 80–100 nm. Wafers are suitable for use as templates for growth of thick SiC, AlN, GaN, ZnO, films on their surface and other wide band semiconductors using standard CVD, HVPE, and MBE methods. The wafers were even and without bends, as can be seen from Fig. 25. RMS roughness, measured at scanning fields of  $5 \times 5 \mu\text{m}$  and  $20 \times 20 \mu\text{m}$ , was 1–5 nm and was constant over the entire diameter of the wafers. The crystal perfection of the SiC layer was determined using the widths of

the X-ray rocking curves ( $\text{FWHM}_{\omega_0}$ ) measured at various points of the wafer surface in the  $\omega$ - $\theta$  mode, ellipsometry data, RHEED, Romanov spectroscopy, Rutherford backscattering, and a number of other methods. The films were studied using the following methods: spectral ellipsometry using a J. A. Woollam M2000-RCE ellipsometer in the range of 0.7–6.5 eV, Raman spectroscopy using a Witec Alpha 300R confocal Raman microscope, RHEED at an electron energy of 50 keV, X-ray diffraction (taken as diffraction patterns in the  $\omega$ - $2\theta$  mode, and rocking curves in the  $\omega$ - $\theta$  mode). The surface of the films was studied using atomic force microscopy (AFM method) and using a New View 6000 profilometer (Zygo). The surface of the SiC/Si layers and the surface of the end cleavages were studied by scanning electron microscopy (SEM) equipped with an X-ray spectrometer (EDS), which allowed determining the chemical composition of the

layers. The interface and defects in the layers were studied using high resolution tunnel electron microscopy (TEM). Many samples were studied using the Rutherford backscattering spectroscopy (RBS) method using helium and hydrogen ion beams [70], as well as by IR spectroscopy using a Bruker IFS-113v infrared Fourier spectrometer and an NicoletIS-50 IR spectrometer (Thermo Scientific, USA) [71-73]. SiC/Si samples were also studied by X-ray reflectometry [72, 73]. Photoemission studies of the samples were carried using the BESSY II synchrotron at Helmholtz Zentrum in Berlin (Germany) using synchrotron radiation with a photon energy in the range of 80–450 eV [74–78].

Thus, a comprehensive analysis of the structural, crystallographic, physicochemical, electrophysical, optical, and spectroscopic studies of SiC films on Si was carried out. These studies and results were described in a number of articles and summarised in reviews [1-6], therefore we do not provide a detailed description of them here. We only note the following. We have studied more than ten thousand film samples, as a result of which reliable information was obtained on the structure and properties of SiC films on Si. The result of the experimental studies was the following. 1) The main theoretical idea about the implementation of epitaxial growth of films via the formation of an ensemble of dilatation dipoles was proved. 2) It has been shown that as a result of the transformation of the intermediate into silicon carbide, a SiC film is formed, which is “hanging” over the cavities like a bridge over a river or a house built on piles. Further formation of SiC will occur inside the cavities. SiC crystals are deposited on the reverse, inner side of the film, i.e., on the side of the cavities. Such sediments resemble “stalactites” and “stalagmites” growing in a cave. The quality of the top layer of the film is high, since there are practically no elastic stresses and growth defects on the film surface. The reverse side of the film contains numerous disordered “stalactite-like” structures. The structure of the upper SiC layer obtained using the MCSA is epitaxial with a high degree of crystallinity.

The main polytype formed during the growth of SiC by the MCSA, is the cubic polytype 3C-SiC. During topochemical transformation,

the 4H-SiC and 6H-SiC polytypes [1–6] and even rather rare 2H-SiC and 8H-SiC polytypes can be formed. In [79], we determined the polytype composition of SiC films obtained on Si by the MCSA at  $T = 1250$  °C,  $P = 2$  Torr, and growth time of 15 min using a Woollam VUV-VASE JA ultraviolet ellipsometer with a rotating analyser in the range of 1.3–9.3 eV. It has been shown that, under these conditions, the cubic polytype 3C was mainly formed on Si(111), the hexagonal 4H polytype with a small admixture of 3C was mainly formed on (110), and a mixture of 3C, 6H, and 4H polytypes was formed on (100). It turned out that during the growth of SiC using the MCSA, under a number of synthesis conditions, the formation of new, previously unknown trigonal (rhombohedral) SiC phase is possible [81,82].

In the next section, we will describe only the most interesting and, from our point of view, unique properties of SiC/Si layers, which this heterostructure possesses due to the formation of silicon carbide by the coordinated substitution of atoms.

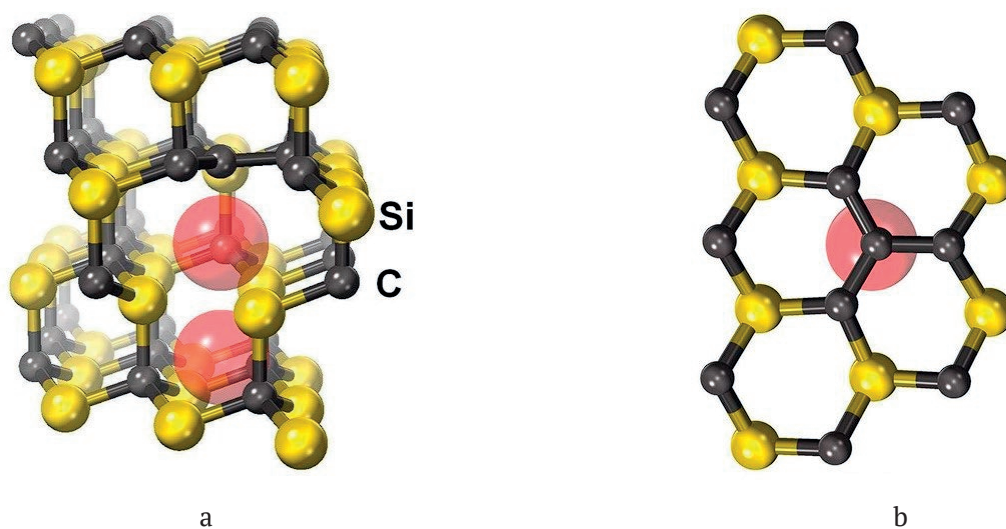
## **9. Features and anomalies of optical, magnetic, and other properties of SiC films on Si grown by the method of coordinated substitution of atoms**

### *9.1. The physical nature of the emergence of features and anomalies in the properties of SiC films on Si grown by the method of coordinated substitution of atoms*

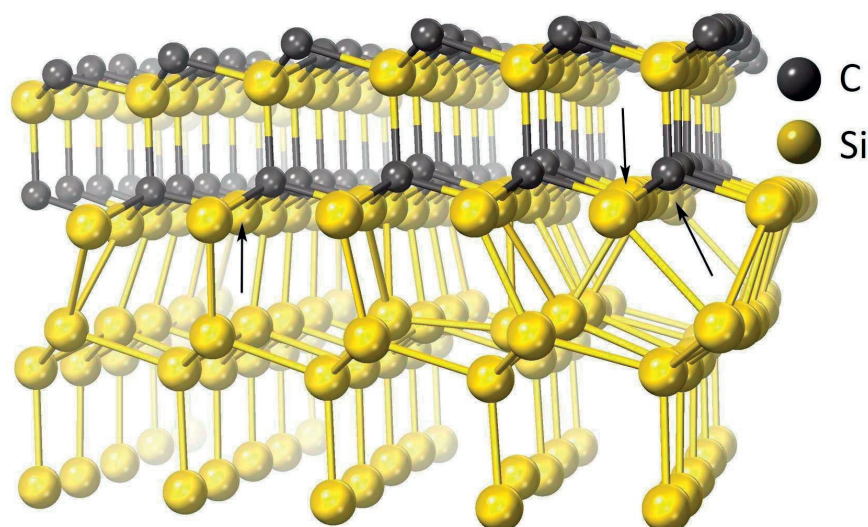
The main feature of SiC grown on Si using the MCSA, is the presence of carbon-vacancy structures formed in the process of shrinkage or “collapse” of the material in it. It turned out, that the “collapse” leads not only to the formation of an ensemble of point defects. When separating from the silicon matrix, silicon is subjected to abnormally strong compression from silicon carbide. The “collapse” corresponds to a phase transition from a metastable state with stretched bonds, in which 4 SiC cells are consistent with 4 Si cells, into a stable SiC phase, in which already 5 SiC cells are consistent with 4 Si cells, and the Si-C bonds are much less distorted ( about 0.2%). The pressure exerted by stretched Si-C bonds on the nearest silicon layer can reach 100 GPa. As a result of such shrinkage, every

fifth SiC chemical bond is fully consistent with every fourth Si bond, the remaining bonds either break (hence the appearance of vacancies and pores) or undergo compression. The latter obviously leads to a change in the structure of the surface zones of SiC adjacent to Si and its “metallization” or transformation into a “semimetal”. When silicon carbide is doped with boron atoms, the latter enter the voids of carbon-vacancy structures (see Fig. 26) [1] and greatly change their properties. The “collapse” of one layer with the initial lattice into the SiC lattice and a model of the carbon-vacancy dipole formed in SiC [82, 83] schematically shown in Fig. 27. The investigation [82, 83] of SiC/Si samples grown on the (111), (110), and (100) Si facets by ellipsometry using a Woollam VUV-WASE JA ultraviolet ellipsometer with rotating analyser in the range 0.5–9.3 eV has revealed the following. At the 3C-SiC(111)/Si(111) interface, an interface layer with completely new optical and electrical properties was formed. The optical properties of this interface cannot be described in terms of the Effective Media Approximation (EMA) [82, 83]. For their theoretical description, a model with oscillators not related to either SiC or Si should be used. The best agreement with experiment was shown using the Tauc–Lorentz (TL) model, according to which the SiC/Si interface is a

material with a zero band gap [82, 83]. Thus, in studies [82, 83] it was found that thin layers with semimetallic properties are formed at the 3C-SiC(111) and Si(111) interface. These layers are fundamentally different from the properties of both SiC and Si, and cannot be obtained using the EMA approach. This is due to the complex nature of the interaction of two surfaces when the SiC layer attracts individual Si atoms from the substrate, and the absence of misfit dislocations. As a result, an interface structure is formed (Fig. 27), where 88% of the Si atoms at the interface form a chemical bond with the substrate atoms, and 12% of the Si atoms at the SiC(111) interface do not form bonds, since they are located too far from the Si atoms of the substrate. Such a structure was described in detail within the framework of the density functional theory [82, 83] (Fig. 27) using quantum chemistry methods. It was shown, that *p*-electrons of 12% of Si atoms at the SiC(111) interface with dangling bonds provide a sharp peak in the density of electronic states just in the Fermi energy region (Fig. 28). In this case, the conduction band either touches or even goes deep into the valence band by a value on the order of several hundredths of eV, which approximately corresponds to the calculation error or is less than it. It was shown that this theoretical representation is in full



**Fig. 26.** Carbon–vacancy structure in SiC grown by the MCSA method: (a) a nearly planar cluster of four C atoms formed owing to the displacement of the C atom in the  $\langle 111 \rangle$  direction (from bottom to top) to the site of the silicon vacancy and two voids (shown in red) above and below the initial position of the C atom (vertical axis corresponds to the  $\langle 111 \rangle$  direction) and (b) the top view of the same structure [1]



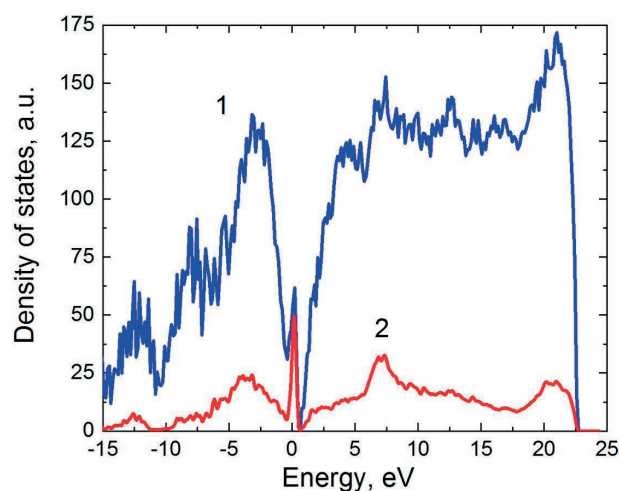
**Fig. 27.** Configuration of atoms at the dislocation-free 3C-SiC (111)/Si (111) interface corresponding to the minimum energy. The arrows indicate 3 out of 25 Si atoms that do not form bonds with atoms of the substrate. It is their p electrons that make the decisive contribution to the narrow peak of the density of electronic states in the vicinity of the Fermi energy (Fig. 28) [82, 83]

agreement with the experimental results on ellipsometry, according to which the optical properties of the layer at the 3C-SiC(111)/Si(111) interface correspond to the Tauc-Lorentz (TL) parameterization with a band width close to zero. The measured ellipsometric spectra show that the conductivity of the interface approximately corresponds to such a metal as lead at electric field frequencies of more than 700 THz. At lower frequencies, the conductivity deteriorated.

The experiment showed that in the samples of SiC films grown on the Si (100) surface, the formation of such a layer with the properties of a “semimetal” is not observed, and its optical properties are described with high accuracy by the simplest ellipsometric EMA model.

Samples of SiC films grown on the Si (110) surface had properties intermediate in the comparison with (111) and (110) interfaces. In this case, on this surface, we observed the formation of an interface with a very small (<0.5 eV) band gap, not equal to zero.

All SiC samples grown on Si by the standard CVD method (we studied samples produced by “Advanced EpiCo”), regardless of the orientation of the substrate (111), (110), and (100), are described with high accuracy by the simplest ellipsometric EMA model. There were no traces of the presence of “semimetal” in them.



**Fig. 28.** Dependence of the density of electronic states of the studied system on energy (curve 1). The Fermi energy corresponds to 0. Curve 2 is the contribution of the p electrons of the Si atoms at the SiC boundary that do not form bonds with the Si atoms of the substrate [82, 83]

## 9.2. Structural features of the surface of SiC epitaxial films synthesised by theMCSA, determined using photoelectron spectroscopy

Photoelectron spectroscopy (PES) is a powerful tool for studying the electronic properties of materials and the most important experimental method for obtaining the most complete information about the band structure of occupied electronic states, which are highly

sensitive to chemical interactions. Photoemission studies were carried out by us using a BESSY II synchrotron (Berlin, Germany) by the PES method at photon energies in the range of 130–450 eV. The experiments were carried out in ultra-high vacuum  $\sim 5 \cdot 10^{-10}$  Torr at room temperature. Photoelectrons were recorded along the normal to the surface, and the excitation beam was incident on the sample surface at an angle of  $45^\circ$ . The total energy resolution was 50 meV.

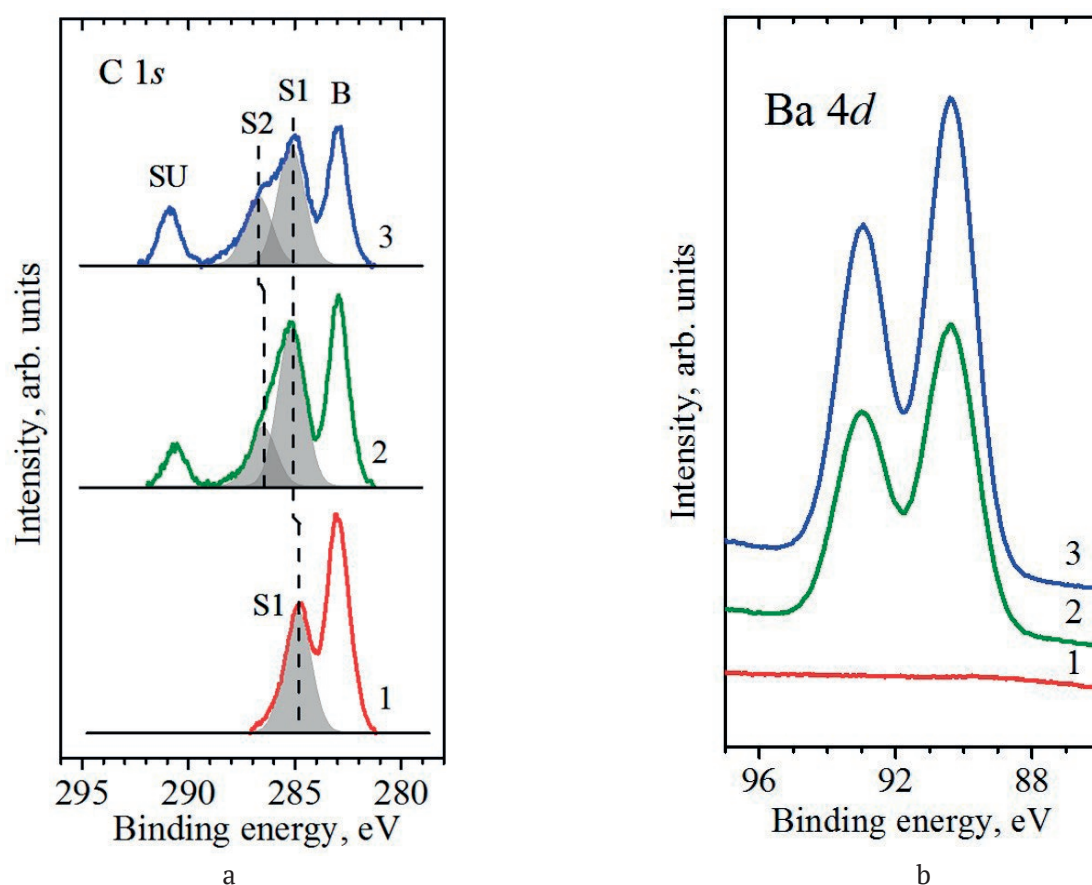
It was found in [74, 75] that the adsorption of alkaline earth metals on the singular surface of SiC films synthesised by the MCSA results in a chemical shift of the electron density from silicon to carbon. This result fundamentally differs from similar data obtained both on hexagonal SiC crystals [84] grown by the standard method and on SiC crystals of the cubic polytype ( $\text{Si}_x\text{C}_{1-x}$ ) grown by CVD [85]. On the surface of these materials, the electron density shifts not only for Si, but also for carbon, towards higher energies. Moreover, these shifts are less distinct than the shifts in the SiC samples obtained by the MCSA. This means that in the electron density shift in SiC crystals and films grown by standard methods, as well as in hexagonal crystals, the reconstruction of their surface leads to the formation of chemical bonds between Si and C that are different from those in SiC synthesised by the MCSA. In the case of SiC grown by the MCSA, some of the bonds are simply broken on its surface. In this case, the carbon atom “pulls” the electron density from silicon. The adsorption of Ba atoms partially restores the equilibrium state of the electron density, returning the perturbed states to a state close to the state of Si and C atoms in the bulk of the SiC film. It is interesting to note that the (0001) surface of the 6H-SiC polytype has a more or less similar spectrum [86]. When this surface reconstructs to  $\sqrt{3} \times \sqrt{3}$  the electron density shift of carbon coincides in direction with the electron density shift in the case of SiC grown by the MCSA. However, in this case, the electron density in silicon shifts in the opposite direction.

In [76–78], the electronic and photoemission properties of epitaxial SiC layers grown by the MCSA on vicinal silicon Si(111) surfaces deviated from the (111) plane by  $4^\circ$  and  $8^\circ$  were studied. The studies have shown that the electronic properties of SiC grown on vicinal Si facets are

fundamentally different from the analogous properties of the same SiC grown on singular Si facets. The main differences were as follows. First, a feature of SiC grown by the MCSA is the excess content of carbon atoms compared to Si atoms and the presence of silicon vacancies, which, as we mentioned above, was also confirmed by other analytical methods. Second, the spectral lines of both carbon and silicon were shifted near the surface toward higher binding energies. This means that a chemical shift of the electron density occurs on the vicinal surface both at the Si atoms and at some of the C atoms. Thirdly, the adsorption of Ba atoms only enhances this process, leads to the formation of bonds between carbon atoms and the enhancement of the ionic component between C atoms and Ba atoms.

Fig. 29 shows the spectra of the core level C1s obtained for the pure SiC surface (curve 1 (Fig. 29a)) and for the Ba/SiC interface (Fig. 29b) with different Ba coatings (curves 2, 3). It was found that the C1s spectrum for the pure surface, SiC consists of two modes. The fundamental mode B corresponds to C atoms in the bulk of the sample. The S1 mode at a higher binding energy corresponds to carbon atoms that are located on terraces in the surface layer above Si atoms and, upon interaction, form a C–Si double layer. Sufficiently similar spectra can be observed for the 3C-SiC(111) surface [87]. The position of the S1 mode at high binding energies indicates that for a clean carbon-enriched surface in the C-Si layer, the degree of bond ionicity for C atoms increases. An extremely unusual C1s spectrum was observed for Ba/SiC(111)- $8^\circ$  interface formation (Fig. 29(a/b), curves 2, 3). It was found that two new modes S2 (energy shift by 3.8 eV) and SU (energy shift 7.0 eV). The S1 mode shifts towards higher binding energies by  $\sim 0.3$  eV. Spectrum C 1s with such a rich set of intense modes in combination with the spectral width was observed for the first time during the adsorption of metal atoms on SiC. This points to the structural features of the vicinal surface of the SiC(111)- $8^\circ$  nanolayer<sup>o</sup> with terraces and steps, as well as unusual electronic and morphological features of surface C atoms forming C-Si bonds and hybridised  $sp^2$  and  $sp^3$  bonds in a carbon-rich C-C layer on the surface.

It should also be noted that the SU peak is a “shake-up” satellite. In this case, the binding

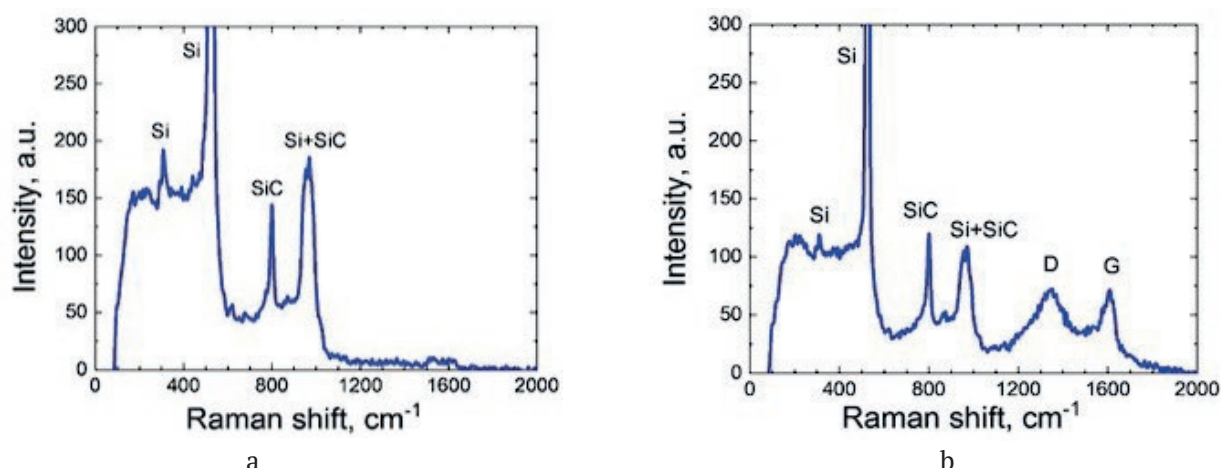


**Fig. 29.** Photoemission spectra of the core level C 1s (a) and the core level of Ba 4d (b) for the pure surface of SiC(111)-8° (1) and for the interface Ba/SiC(111)-8° when coated with Ba 0.5 (2) and 1.2 ML (3). Excitation energy  $h\nu = 450$  eV (a) and  $h\nu = 130$  eV (b) [76-78]

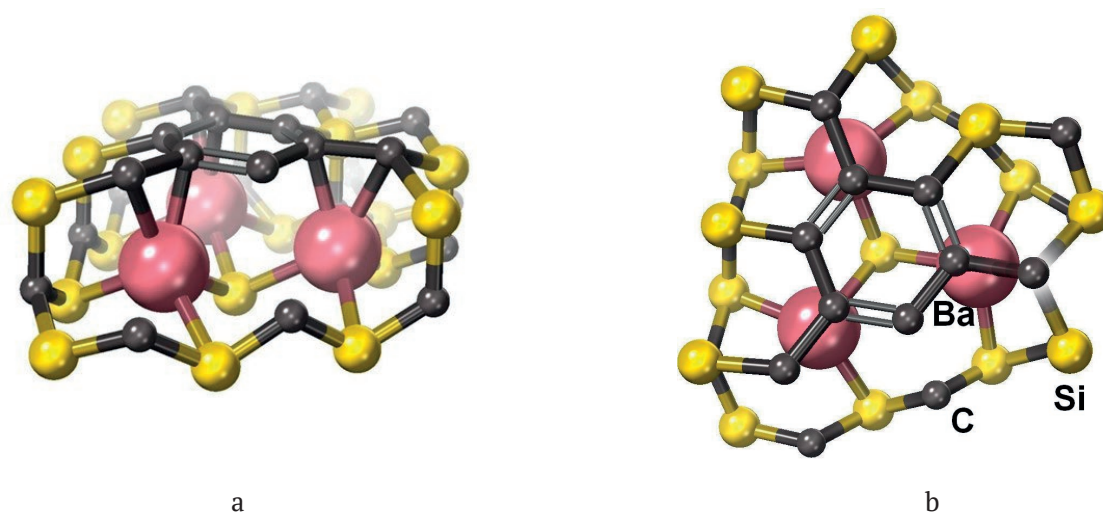
energy of the SU state coincides with the known value of the binding energy for the “shake-up” satellite in graphene on the 4H-SiC(0001) surface [88]. The SU shake-up satellite was also observed in the C 1s spectra in other organic compounds. The Raman spectrum of the SiC/Si(111)-8° sample in the initial state and the Raman spectrum of the Ba/SiC/Si(111)-8° interface with an adsorbed Ba monolayer were studied (see Fig. 30) for obtaining additional information about the state of the carbon layer on the vicinal surface after the adsorption of Ba and the nature of the unusual form of the C 1s spectrum. It was established that new features appeared for the interface in the spectral region 1200–1800  $\text{cm}^{-1}$  that were not observed in this region for the same SiC layer, but without Ba. In the presence of Ba atoms, two D and G bands characteristic of aromatic compounds appeared. In the general case, the presence of G and D bands indicated the presence of  $sp^2$  hexagonal carbon rings with a  $sp^2$ -type of hybridization. Thus, Raman spectroscopy also

confirmed the conclusions about the formation of a new, previously unknown aromatic-like carbon compound during the adsorption of Ba on vicinal SiC samples grown by the atom substitution method.

Fig. 31 shows a diagram of a possible modification of the atomic structure of the SiC surface and the formation of new carbon bonds during the adsorption of Ba. The effect of the formation of aromatic-like rings on the surface of SiC samples is new and is stably observed only on the vicinal SiC-4° and SiC-8° surfaces during the adsorption of Ba and Cs metals. However, the presence of the shake-up satellite SU peak in Fig. 29 with a binding energy in the region of 292 eV, according to the data of [89–91], unambiguously indicates that the loss of energy by photoelectrons is used for the excitation of transitions between  $\pi$  bonding and  $\pi^*$  antibonding ( $\pi \rightarrow \pi^*$ ) molecular orbitals (MO) in aromatic rings of organic compounds. Shake-up satellites were formed due to the relaxation



**Fig. 30.** Raman spectra of SiC/Si(111)-8° samples; (a) without a Ba monolayer; (b) of the same sample, but covered with an adsorbed Ba monolayer [76-78]



**Fig. 31.** Schematic representation of the carbon-based 2D structure stabilized by Ba atoms on the vicinal surface of the SiC nanolayer. The 2D cluster structure consists of carbon rings, in which the chemical bonding is close in character to the bonding in aromatic-like compounds. (a) is the Side view; (b) is the Top view [76-78]

of the electron subsystem of the core hole after its photoionization. After photoionization, the shielding of formed core hole occurs (relaxation of the electron system), as a result of which the relaxation energy is released. This energy is added to the energy of the electron leaving the atom. The appearance of the core hole potential can cause the rearrangement of the electron subsystem up to the excitation of valence electrons to higher free energy levels. In this case, the energy used for electronic excitations reduces the energy of the emitted photoelectron. As a result, the kinetic energy of the photoelectron recorded by the analyser decreases by the value of the excitation energy.

Thus, special 2D carbon structures were formed on the surface of inorganic SiC nanoscale samples grown on vicinal Si surfaces due to the special structure of SiC layers and in the presence of adsorbed Ba atoms. These 2D structures (see Fig. 31) consist of carbon rings, in which the chemical bond between carbon atoms, in our opinion, is close in nature to the bond realised in organic aromatic compounds. The formation of shake-up satellites is characteristic of many organic substances and, in particular, various kinds of organic alcohols, polymethyl methacrylate, as was recently shown in [91]. Similar spectra were also observed in complex, so-called organometallic complexes synthesised on

the basis of metals  $d$  elements such as Au, Cu, Ag [92]. The described effects were not observed both for the formation of graphene structures obtained on the surface of hexagonal 6H-SiC(0001) crystals [93] and on the surface of 4H-SiC crystals with facet orientation  $(1\bar{1}02)$ .

### 9.3. Anomalies of magnetic properties of epitaxial SiC films synthesised by the MCSA

In [94], a series of experimental studies of the magnetic properties, namely, the field and temperature dependences of the static magnetic susceptibility were performed for samples of thin films with a thickness of about 80–100 nm of single-crystal SiC grown on the (100), (110), and (111) surfaces of a single-crystal Si by the MCSA due to the chemical reaction of silicon with carbon monoxide gas CO. As a result of studies in SiC structures grown on Si (110) and Si (111), two quantum effects at room temperature were found to occur in weak magnetic fields. These effects were: firstly, the formation of a hysteresis of the static magnetic susceptibility [94], and secondly, the appearance of the Aharonov-Bohm oscillations in the field dependences of the static magnetic susceptibility [94]. The formation of the first effect we associated with the Meissner-Oxensfeld effect, and the second effect was due to the presence of microdefects in the form of nanotubes and micropores in these structures under the SiC layer. These microdefects were formed during the synthesis of these structures, and silicon in the state of “magnetic semimetal”, as we mentioned above. In SiC structures grown on Si(100), these effects were not found [94], which was due to the different mechanism of SiC formation on the (100) Si surface, discussed above. Thus, as a result of experimental studies, the following nontrivial quantum effects at room temperature were discovered for the first time: the appearance of the magnetic moment quantization effect in SiC structures grown by the MCSA for Si (110) and Si (111); the formation of a hysteresis of the static magnetic susceptibility at room temperature in weak magnetic fields, which was interpreted by us as a manifestation of the Meissner – Oxensfeld effect [94].

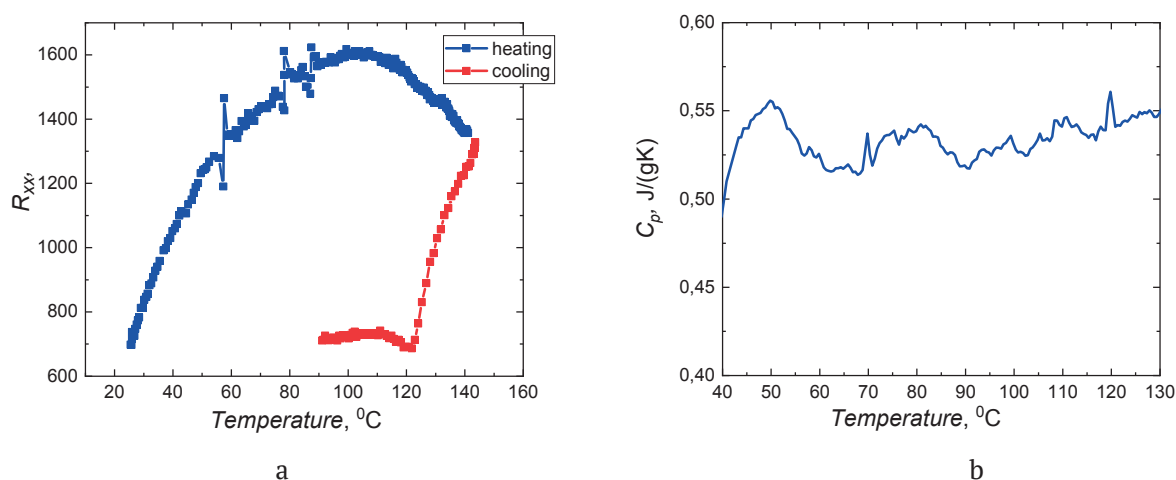
The simultaneous occurrence of the hysteresis of the static magnetic susceptibility and the

Meissner – Oxensfeld effect was explained in [94] by the suppression of the electron–electron interaction by electric fields. These electric fields arise due to the presence of microdefects in the SiC/Si structures, which consist of dipole centres with a negative correlation energy. In turn, dipole centres are formed from carbon-vacancy structures at the SiC(111)/Si(111) interface, where silicon is in a state close to that of a magnetic semimetal. In SiC structures grown on Si(100), in which carbon-vacancy structures are practically absent and silicon in the semimetallic state is not formed at the SiC-Si interface, these effects were not observed [94].

### 9.4. Electronic phase transitions in SiC epitaxial layers synthesised by the MCSA

In [95], at temperatures equal to 56, 76, 122, and 130 °C, unusual features of the temperature dependences of the longitudinal resistance and heat capacity of epitaxial SiC films grown on Si by the MCSA were detected. The observed features of the heat capacity and longitudinal resistance, taking into account the previously discovered Meissner-Oxensfeld effect [94] and the emergence of gigantic diamagnetism in weak magnetic fields of the order  $(1/4\pi)$  were interpreted in [95] as electronic phase transitions in ensembles of charge carriers into a coherent (possibly superconducting, if diamagnetism is taken into account) state. Fig. 32 shows the temperature dependences of longitudinal resistance  $R_{xx}$  and heat capacity  $C_p$  obtained by differential scanning calorimetry (DSC) for epitaxial SiC/Si structures grown by MCSA [95]. It follows from these data that the temperature dependences of the heat capacity are characterised by synchronously arising features at temperatures 56, 76, 122, and 130 °C (which were recorded as the temperature decreased from high to low values). It should be noted that a similar behaviour was also observed in the temperature dependences of the static magnetic susceptibility [94]. Sharp peaks are clearly visible on the graphs of dependencies and longitudinal resistance and heat capacity  $C_p$ . First of all, it is a sharply distinguished peak in the region of 56 °C. Next comes the system of peaks up to 130 °C. In this region, peaks are distinguished in the region of 76–130 °C and a peak in the region





**Fig. 32.** Temperature dependences of the longitudinal resistance  $R_{xx}$  and the heat capacity  $C_p$  obtained by the differential scanning calorimetry (DSC) of epitaxial SiC/Si structures grown by the method of the coordinated substitution of atoms. Dependence of the (a) longitudinal resistance and (b) heat capacity  $C_p$  obtained by heating the SiC/Si sample in the range from 30 to 200 °C at a rate of 6 °C per minute in air after subtracting the heat capacity  $C_p$  of the initial silicon measured under the same conditions [95]

of 122 °C. Peculiarities above 130°C (Fig. 32b) were not considered in [94], since, as it is known, various transitions can be observed in this region, associated exclusively with silicon, which are not related to this problem. The observed features of peaks in heat capacity and longitudinal resistance can be interpreted as a consequence of phase transitions of charge carriers into a coherent (superconducting, if diamagnetism is taken into account) state. It should also be taken into account that the value of the critical temperature is interconnected with the size of the energy gap (in the framework of the BCS theory), and, accordingly, with the frequency (wavelength) of terahertz radiation, if the pixel length is represented as a characteristic of the Josephson transition. In [94], a pixel is understood as a microdefect limited by a different number of centres with a negative correlation energy and containing pairs of charge carriers. Pixels can form chains consisting of several pixels. Communication between pixels depends on temperature. If the temperature is higher than a certain critical temperature, then there is a destruction of coherence in a chain consisting of pixels containing pairs of charge carriers. In [94], a table containing data on the widths of the energy gaps, the sizes of microdefects, and the values of critical temperatures, i.e., temperatures at which features in the behaviour of the longitudinal

resistance and heat capacity appear, is presented.

It should be noted that the data presented in a number of recently published papers [96–98] show that obtaining record high values of the critical temperatures of the transition to the superconducting state is associated with the use of high sample compression pressures. These pressures are of the order of 100–270 GPa when the samples are compressed. Thus, it was found in [96] that in lanthanum and yttrium hydrides compounds at temperatures of 245–260 K and pressures of the order of 1 million atmospheres;  $\text{LaH}_{10\pm x}$  becomes a superconductor upon cooling to 250 K at a pressure of 188 GPa. In  $\text{YH}_6$  compounds, a superconducting transition was observed at a temperature of 227 K and a pressure of 237 GPa. It was found in [96, 97] that upon compression of  $\text{LaH}_{10}$  compound up to 170 GPa, the critical transition temperature was  $T_c = -13$  °C. In 2020, a new record for carbon-doped sulphur hydride was published in Nature [98]. At a pressure of 267 GPa, the critical transition temperature of this compound was raised to 15°C.

In this regard, we note once again that SiC films grown by the MCSA, by the nature of their formation [1, 2, 4–6], are substances in which phase transitions of charge carriers into a coherent state can be observed. With standard methods of growth of SiC films on Si, in which the SiC layer grows due to the supply of matter

to the Si surface, the SiC layer is not compressed. The SiC layer on the contrary is subjected to tensile strains from the side of silicon. In the synthesis of SiC on Si by the MCSA, in contrast to the classical growth of SiC, the SiC layer shrinks, during which great compression pressures appear for a short time at the SiC-Si interface. It should be noted that the SiC synthesis method based on the substitution of atoms and proposed in [12] opens up new possibilities for creating high pressures in materials using “chemical” transformations in the process of substitution of some of their atoms.

## 10. Conclusions

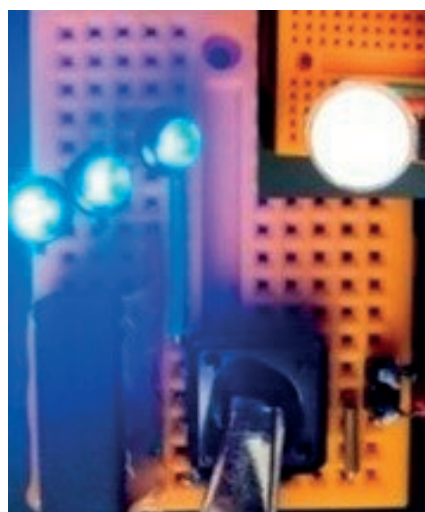
The review reflects the main results of the theory, mechanisms, and technology of growing SiC on Si by the method of coordinated substitution of atoms (MCSA). New unique physicochemical properties of the SiC/Si structures have been described in detail. The possibilities of the MCSA for growing epitaxial SiC films not only on Si single crystals but also on other materials, in particular, sapphire, have been described. A new method for creating heat-resistant and antioxidant carbide-carbon coatings, which is based on the new fundamental principles of the MCSA, is described. In this review, we have completely ignored our studies on the practical application of SiC/Si and our studies on the growth of a whole class of semiconductor compounds on the SiC/Si substrates, such as  $A^3B^5$  compounds (AlN, GaN, AlGaIn, and  $Ga_2O_3$ ) and  $A^2B^6$  semiconductor compounds, almost the entire series of which was grown by us on the SiC/Si substrates. An overview of these studies can be found in our previous review articles [1–6,62]. Also, for the first time, we have developed a semi-industrial technology for the production of chips for micro-LEDs on silicon, and a working prototype of a white LED on silicon was created, a photograph of which is shown in Fig. 33.

### Author contributions

All authors made an equivalent contribution to the preparation of the publication.

### Conflict of interests

The authors declare that they have no known competing financial interests or personal



**Fig. 33.** Packaged Micro-LED: three Micro-LEDs without phosphor coating and an LED with a polymer lens containing a phosphor [99]

relationships that could have influenced the work reported in this paper.

## References

1. Kukushkin S. A., and Osipov A. V. Nanoscale single-crystal silicon carbide on silicon and unique properties of this material. *Inorganic Materials*. 2021;57(13): 1319–1329. <https://doi.org/10.1134/S0020168521130021>
2. Kukushkin S. A., Osipov A. V. Epitaxial silicon carbide on silicon. Method of coordinated substitution of atoms (A Review). *Russian Journal of General Chemistry*. 2022;92: 584–610. <https://doi.org/10.1134/S1070363222040028>
3. Kukushkin S., Osipov A., Redkov A. SiC/Si as a new platform for growth of wide-bandgap semiconductors. In: *Mechanics and Control of Solids and Structures. Advanced Structured Materials*. V. A. Polyanskiy, A. K. Belyaev (eds.). Vol. 164. Springer; 2022. pp. 335–367. <https://doi.org/10.1007/978-3-030-93076-9>
4. Kukushkin S. A., Osipov A. V., Feoktistov N. A. Chemical self-assembly of a single-crystal SiC film on a silicon substrate: a new method of directed nucleation. *Rossiiskii khimicheskii zhurnal*. 2013;57(6): 36–47. (In Russ., abstract in Eng.). Available at: <https://www.elibrary.ru/item.asp?id=24069701>
5. Kukushkin S. A., Osipov A. V. Topical review. Theory and practice of SiC growth on Si and its applications to wide-gap semiconductor films. *Journal of Physics D: Applied Physics*. 2014;47: 313001–313001–41. <https://doi.org/10.1088/0022-3727/47/31/313001>
6. Kukushkin S. A., Osipov A. V., Feoktistov N. A. Synthesis of epitaxial silicon carbide films through the substitution of atoms in the silicon crystal lattice: A

- review. *Physics of the Solid State*. 2014;56: 1507–1535. <https://doi.org/10.1134/S1063783414080137>
7. Takahashi K., Yoshikawa A., Sandhu A. (eds.). *Wide bandgap semiconductors*. Springer-Verlag Berlin and Heidelberg GmbH & Co. K; 2007. 470 p. <https://doi.org/10.1007/978-3-540-47235-3>
8. Nishino S., Powell J.A., Will H.A. Production of large-area single-crystal wafers of cubic SiC for semiconductor devices. *Applied Physics Letters*. 1983;42(5): 460–462. <https://doi.org/10.1063/1.93970>
9. Kukushkin S. A., Osipov A. V., Bessolov V. N., Medvedev B. K., Nevolin V. K., Tcarik K. A. Substrates for epitaxy of gallium nitride: new materials and techniques. *Reviews on Advanced Materials Science*. 2008;17: 1–32. Available at: [https://www.ipme.ru/e-journals/RAMS/no\\_11708/kukushkin.pdf](https://www.ipme.ru/e-journals/RAMS/no_11708/kukushkin.pdf)
10. Severino A., Locke C., Anzalone R., Camarda M., Piluso N., La Magna A., Sadow S., Abbondanza G., D'Arrigo G., La Via F. 3C-SiC film growth on Si substrates. *ECS Transactions*. 2011;35(6): 99–116. <https://doi.org/10.1149/1.3570851>
11. Ferro G. 3C-SiC heteroepitaxial growth on silicon: The quest for holy grail. *Critical Reviews in Solid State and Materials Sciences*. 2015;40(1): 56–76. <https://doi.org/10.1080/10408436.2014.940440>
12. Kukushkin S. A., Osipov A. V. New method for growing silicon carbide on silicon by solid-phase epitaxy: Model and experiment. *Physics of the Solid State*. 2008;50: 1238–1245. <https://doi.org/10.1134/S1063783408070081>
13. Kukushkin S. A., Osipov A. V., Feoktistov N. A. A method of manufacturing an article containing a silicon substrate with a silicon carbide film on its surface\*. Patent RF, No. 2363067. Publ. 27.07.2009; bul. No. 21. (In Russ.)
14. Kukushkin S. A., Osipov A. V. Quantum mechanical theory of epitaxial transformation of silicon to silicon carbide. *Journal of Physics D: Applied Physics*. 2017;50 (46): 464006 (7pp). <https://doi.org/10.1088/1361-6463/AA8F69>
15. Kukushkin S. A., Osipov A. V. Thin-film heteroepitaxy by the formation of the dilatation dipole ensemble. *Doklady Physics*. 2012;57: 217–220. <https://doi.org/10.1134/S1028335812050072>
16. Kukushkin S. A., Osipov A. V. A new mechanism of elastic energy relaxation in heteroepitaxy of monocrystalline films: Interaction of point defects and dilatation dipoles. *Mechanics of Solids*. 2013;48: 216–227. <https://doi.org/10.3103/S0025654413020143>
17. Kukushkin S. A. and Osipov A. V. A new method for the synthesis of epitaxial layers of silicon carbide on silicon owing to formation of dilatation dipoles. *Journal of Applied Physics*. 2013;113(2): 4909-1-4909-7. <https://doi.org/10.1063/1.4773343>
18. Kukushkin S. A., Osipov A. V. Anisotropy of the solid-state epitaxy of silicon carbide in silicon. *Semiconductors*. 2013;47: 1551–1555. <https://doi.org/10.1134/S1063782613120129>
19. Kukushkin S. A., Osipov A. V. First-order phase transition through an intermediate state *Physics of the Solid State*. 2014;56: 792–800. <https://doi.org/10.1134/S1063783414040143>
20. Kukushkin S. A., Osipov A. V. Mechanism of formation of carbon-vacancy structures in silicon carbide during its growth by atomic substitution. *Physics of the Solid State*. 2018;60: 1891–1896. <https://doi.org/10.1134/S1063783418090184>
21. Kukushkin S. A., Osipov A. V., Telyatnik R. S. Elastic interaction of point defects in cubic and hexagonal crystals. *Physics of the Solid State*. 2016;58: 971–980. <https://doi.org/10.1134/S1063783416050140>
22. Eshelby J. D. *The continuum theory of dislocations in crystals*. New York: Academic Press; 1956. pp. 79–144.
23. Lifshits I. M., Rozentsveig L. N. On the construction of the Green tensor for the basic equation of the theory of elasticity in the case of an unbounded elastically anisotropic medium\*. *Journal of Experimental and Theoretical Physics*. 1947;17(9): 783–791. (In Russ.)
24. Kuz'michev S. V., Kukushkin S. A., Osipov A. V. Elastic interaction of point defects in crystals with cubic symmetry. *Mechanics of Solids*. 2013;48: 431–438. <https://doi.org/10.3103/S0025654413040110>
25. Sangwal K. *Etching of crystals: Theory, experiment and application*. North-Holland: 1987. 497.
26. Kukushkin S. A., Osipov A. V. Thin-film condensation processes\*. *Physics - Uspekhi* (1998),41(10): 983–1014. <https://doi.org/10.1070/PU1998v041n10ABEH000461>
27. Kukushkin S. A., Slezov V. V. Disperse systems on the surface of solids (evolutionary approach): mechanisms of thin film formation. St. Petersburg: Nauka Publ.; 1996. 304. (In Russ.)
28. Zhukov S. G., Kukushkin S. A., Lukyanov A. V., Osipov A. V., Feoktistov N. A. *Method of manufacturing products containing a silicon substrate with a silicon carbide film on its surface\**. Patent RF: No. 2522812. Publ. 20.07.2014, bul. No. 20. (In Russ.)
29. Kukushkin S. A., Osipov A. V. First-order phase transition through an intermediate state. *Physics of the Solid State*. 2014;56: 792–800. <https://doi.org/10.1134/S1063783414040143>
30. Kukushkin S. A., Osipov A. V., Soshnikov I.P. Growth of Epitaxial SiC Layer on Si (100) Surface of n- and p-type of Conductivity by the Atoms Substitution Method. *Reviews on Advanced Materials Science*. 2017;52: 29-42. Available at: [http://www.ipme.ru/e-journals/RAMS/no\\_15217/05\\_15217\\_kukushkin.pdf](http://www.ipme.ru/e-journals/RAMS/no_15217/05_15217_kukushkin.pdf)
31. Kukushkin S. A. Nucleation of pores in brittle solids under load. *Journal of Applied Physics*. 2005;98: 033503-1-033503-12. <https://doi.org/10.1063/1.1957131>

32. Geguzin Ya. E. *Diffusion zone*. Moscow: Science Publ.; 1979. 34 p. (In Russ.)
33. Kelly A., Groves G. W. *Crystallography and crystal defects*. London: Longman; 1970. 428 p.
34. Kukushkin S. A., Osipov A. V. A quantum-mechanical model of dilatation dipoles in topochemical synthesis of silicon carbide from silicon. *Physics of the Solid State*. 2017;59: 1238–1241. <https://doi.org/10.1134/S1063783417060130>
35. Kukushkin S. A., Osipov A. V. Phase equilibrium in the formation of silicon carbide by topochemical conversion of silicon. *Physics of the Solid State*. 2016;58: 747–751. <https://doi.org/10.1134/S1063783416040120>
36. Kukushkin S. A., Osipov A. V. The equilibrium state in the Si-O-C ternary system during SiC growth by chemical substitution of atoms. *Technical Physics Letters*. 2015;41: 259–262. <https://doi.org/10.1134/S1063783416040120>
37. Grudinkin S. A., Golubev V. G., Osipov A. V., Feoktistov N. A., Kukushkin S. A. Infrared spectroscopy of silicon carbide layers synthesized by the substitution of atoms on the surface of single-crystal silicon. *Physics of the Solid State*. 2015;57: 2543–2549. <https://doi.org/10.1134/S1063783415120136>
38. Kukushkin S. A., Osipov A. V. Drift mechanism of mass transfer on heterogeneous reaction in crystalline silicon substrate. *Physica B: Condensed Matter*. 2017;512(1): 26–31. <https://doi.org/10.1016/j.physb.2017.02.018>
39. Kidalov V. V., Kukushkin S. A., Osipov A. V., Redkov A. V., Grashchenko A. S., Soshnikov I. P., Boiko M. E., Sharkov M. D., Dyadenchuk A. F. Properties of SiC films obtained by the method of substitution of atoms on porous silicon. *ECS Journal of Solid State Science and Technology*. 2018. 7(4): P158–P160. <https://doi.org/10.1149/2.0061804jss>
40. Kukushkin S. A., Osipov A. V., Osipova E. V. Mechanism of molecule migration of carbon and silicon monoxides in silicon carbide crystal. *Materials Physics and Mechanics*. 2019;42: 178–182. [https://doi.org/10.18720/MPM.4222019\\_3](https://doi.org/10.18720/MPM.4222019_3)
41. Kukushkin S. A., Osipov A. V. Mechanism of diffusion of carbon and silicon monoxides in a cubic silicon carbide crystal. *Phys. Solid State*. 2019;61: 2338–2341. <https://doi.org/10.1134/S1063783419120242>
42. Редьков А. В., Гращенко А. С., Кукушкин С. А., Осипов А. В., Котляр К. П., Лихачев А. И., Нашекин А. В., Сошников И. П. Эволюция ансамбля микропор в структуре SiC/Si в процессе роста методом замещения атомов. *ФТТ*. 2019; 61(3): 2334–2337. DOI: 10.1134/S1063783419030272.
43. Grashchenko A. S., Kukushkin S. A., Osipov A. V., Redkov A. V. Vacancy growth of monocrystalline SiC from Si by the method of self-consistent substitution of atoms. *Catalysis Today*. 2022;397–399: 375–378. <https://doi.org/10.1016/J.CATTOD.2021.08.012>
44. Grashchenko A. S., Kukushkin S. A., Osipov A. V. Coating of a nanostructured profiled Si surface with a SiC layer. *Technical Physics Letters*. 2020;46: 1012–1015. <https://doi.org/10.1134/S1063785020100235>
45. Smirnov V. K., Kibalov D. S., Orlov O. M., Graboshnikov V. V. Technology for nanoperiodic doping of a metal-oxide-semiconductor field-effect transistor channel using a self-forming wave-ordered structure. *Nanotechnology*. 2003;14: 709–715. <https://doi.org/10.1088/0957-4484/14/7/304>
46. Tang X., Wongchotigul K., Spencer M. G. Optical waveguide formed by cubic silicon carbide on sapphire substrates. *Applied Physics Letters*. 1991;58: 917. <https://doi.org/10.1063/1.104476>
47. Sywe B. S., Yu Z. J., Burckhard S., Edgar J. H., Chaudhuri J. Epitaxial growth of SiC on sapphire substrates with an AlN buffer layer. *Journal of The Electrochemical Society*. 1994;141: 510. <https://doi.org/10.1149/1.2054756>
48. McArdle T. J., Chu J. O., Zhu Y., Liu Z., Krishnan M., Breslin C. M., Dimitrakopoulos C., Wisnieff R., Grill A. Multilayer epitaxial graphene formed by pyrolysis of polycrystalline silicon-carbide grown on c-plane sapphire substrates. *Applied Physics Letters*. 2011;98: 132108. <https://doi.org/10.1063/1.3575202>
49. Cheng L., Steckl A. J., Scofield J. SiC thin-film Fabry-Perot interferometer for fiber-optic temperature sensor. *IEEE Transactions on Electron Devices*. 2003;50: 2159. <https://doi.org/10.1109/TED.2003.816106>
50. Li J. C., Batoni P., Tsu R. Synthesis and characterization of 4H-SiC on C-plane sapphire by C<sub>60</sub> and Si molecular beam epitaxy. *Thin Solid Films*. 2010;518(6): 1658. <https://doi.org/10.1016/j.tsf.2009.11.088>
51. Luong T. T., Tran B. T., Ho Y. T., Wei T. W., Wu Y. H., Yen T. Ch., Wei L. L., Maa J. Sh., Chang E. Yi. 2H-silicon carbide epitaxial growth on c-plane sapphire substrate using an AlN buffer layer and effects of surface pre-treatments. *Electronic Materials Letters*. 2015;11: 352–359. <https://doi.org/10.1007/s13391-015-4208-9>
52. Beisenov R., Ebrahim R., Mansurov Z. A., Tokmoldin S. Zh, Mansurov B. Z., Ignatiev A. Growth of 3C-SiC films on Si (111) and sapphire (0001) substrates by MOCVD. *Eurasian Chemico-Technological Journal*. 2013;15(1): 25. <https://doi.org/10.18321/ectj136>
53. Chu J. O., Dimitrakopoulos C. D., Grill A., McArdle T. J., Saenger K. L., Wisnieff R. L., Zhu. Yu. *Epitaxial growth of silicon carbide on sapphire*. Patent US: No. US 2012/0112198 A1. Pub. Date: May 10, 2012. Available at: URL:<https://patentimages.storage.googleapis.com/91/9f/23/96f2953b645053/US20120112198A1.pdf>

54. Shibata K., Harada Sh., Ujihara T. 3C-SiC crystal on sapphire by solution growth method. *Materials Science Forum*. 2015;821–823: 185. <https://doi.org/10.4028/www.scientific.net/MSF.821-823.185>
55. Kukushkin S. A., Osipov A. V. Mechanisms of epitaxial growth of SiC films by the method of atom substitution on the surfaces (100) and (111) of Si single crystals and on surfaces of Si films grown on single crystals  $Al_2O_3$ . *IOP Conference Series: Materials Science and Engineering*. 2018;387: 012044-1-5. <https://doi.org/10.1088/1757-899X/387/1/012044>
56. Kukushkin S. A., Osipov A. V., Redkov A. V., Grashchenko A. S., Feoktistov N. A., Fedotov S. D., Statsenko V. N., Sokolov E. M., Timoshenkov S. P. A new method for synthesis of epitaxial films of silicon carbide on sapphire substrates ( $\alpha-Al_2O_3$ ). *Reviews on Advanced Materials Science*. 2018;57(1): 82-96. <https://doi.org/10.1515/rams-2018-0050>
57. Cristoloveanu S., Li Sh. S. Electrical characterization of silicon-on-insulator materials and devices. In: *Springer Science and Business Media*. 1995;305: 381. <https://doi.org/10.1007/978-1-4615-2245-4>
58. Munteanu D., Cristoloveanu S., Rozeau O., Jomaah J., Boussey J., Wetzell M., Houssaye P. de la, Lagnado L. Characterization of silicon-on-sapphire material and devices for radio frequency applications. *Journal of The Electrochemical Society*. 2001;148(4): 218. <https://doi.org/10.1149/1.1355693>
59. Colinge J. P. SOI CMOS for high-temperature applications. In: *Perspectives, Science and Technologies for Novel Silicon on Insulator Devices*. Hemment P. L. F., Lysenko V. S., Nazarov A. N. (eds.). NATO Science Series. Vol. 73. Dordrecht: Springer; 2000. pp. 249–256. [https://doi.org/10.1007/978-94-011-4261-8\\_24](https://doi.org/10.1007/978-94-011-4261-8_24)
60. Celler G. K., Cristoloveanu S. Frontiers of silicon-on-insulator. *Journal of Applied Physics*. 2003;93(9): 4955–4978. <https://doi.org/10.1063/1.1558223>
61. Sokolov E. M., Fedotov S. D., Statsenko V. N., Timoshenkov S. P., Emelyanov A. V. Study of the structural properties of silicon-on-sapphire layers in hydride-chloride vapor-phase epitaxy. *Semiconductors*. 2017;51(13): 1692–1697. <https://doi.org/10.1134/S1063782617130127>
62. Bessolov V. N., Konenkova E. V., Kukushkin S. A., Osipov A. V., Rodin S. N. Semipolar gallium nitride on silicon: technology and properties. *Reviews on Advanced Materials Science*. 2014;38(1): 75–93. [https://www.ipme.ru/e-journals/RAMS/no\\_13814/08\\_13814\\_kukushkin.pdf](https://www.ipme.ru/e-journals/RAMS/no_13814/08_13814_kukushkin.pdf)
63. Kalinkin I. P., Kukushkin S. A., Osipov A. V. *Method for processing the surface of a single-crystal silicon wafer\**. Patent RF: No. 2323503. Publ. 04/27/2008, bul. No. 12.
64. Kalinkin I. P., Kukushkin S. A., Osipov A. V. Effect of chemical treatment of a silicon surface on the quality and structure of silicon-carbide epitaxial films synthesized by atom substitution. *Semiconductors*. 2018;52: 802–808. <https://doi.org/10.1134/S1063782618060118>
65. Grashchenko A. S., Kukushkin S. A., Osipov A. V., Redkov A. V. Formation of composite SiC-C coatings on graphite via annealing Si-melt in CO. *Surface & Coatings Technology*. 2021;423(15): 127610. <https://doi.org/10.1016/j.surfcoat.2021.127610>
66. Grashchenko A. S., Kukushkin S. A., Osipov A. V., Redkov A. V. The mechanical properties of a SiC composite coating on graphite produced by the atom-substitution method. *Technical Physics Letters*. 2022;48, 62–65. <https://doi.org/10.1134/S1063785022030038>
67. Perdew J. P., Burke K., Ernzerhof M. Generalized gradient approximation made simple. *Physical Review Letters*. 1996;77(18): 3865–3868. <https://doi.org/10.1103/PhysRevLett.77.3865>
68. Fischer-Cripps A. C. *Nanoindentation*. (Third Edition) Springer; 2004. 279 p. <https://doi.org/10.1115/1.1704625>
69. Kukushkin S. A., Lukyanov A. V., Osipov A. V., Feoktistov N. A. Epitaxial silicon carbide on a 6" silicon wafer. *Technical Physics Letters*. 2014;40: 36–39. <https://doi.org/10.1134/S1063785014010088>
70. Egorov V. K., Egorov E. V., Kukushkin S. A., Osipov A. V. Structural heteroepitaxy during topochemical transformation of silicon to silicon carbide. *Physics of the Solid State*. 2017;59: 773–779. <https://doi.org/10.1134/S1063783417040072>
71. Grudinkin S. A., Kukushkin S. A., Osipov A. V., Feoktistov N. A. IR spectra of carbon-vacancy clusters in the topochemical transformation of silicon into silicon carbide. *Physics of the Solid State*. 2017;59: 2430–2435. <https://doi.org/10.1134/S1063783417120186>
72. Kukushkin S. A., Nussupov K. K., Osipov A. V., Beisenkhanov N. B., Bakranova D. I. X-ray reflectometry and simulation of the parameters of SiC epitaxial films on Si(111), grown by the atomic substitution method. *Physics of the Solid State*. 2017;59: 1014–1026. <https://doi.org/10.1134/S1063783417050195>
73. Kukushkin S. A., Nussupov K. Kh., Osipov A. V., Beisenkhanov N. B., Bakranova D. I. Structural properties and parameters of epitaxial silicon carbide films, grown by atomic substitution on the highresistance (111) oriented silicon. *Superlattices and Microstructures*. 2017;111: 899–911. <https://doi.org/10.1016/j.spmi.2017.07.050>
74. Benemanskaya G. V., Dementev P. A., Kukushkin S. A., Lapushkin M. N., Osipov A. V., Senkovskiy B., Timoshnev S. N. Photoemission study of nano SiC epitaxial layers synthesized by a new method of the

- atom substitution in Si crystal lattice. *Materials Physics and Mechanics*. 2015;22(2): 183–190. Available at: [https://ipme.ru/e-journals/MPM/no\\_22215/MPM22\\_09\\_kukushkin.pdf](https://ipme.ru/e-journals/MPM/no_22215/MPM22_09_kukushkin.pdf)
75. Kukushkin S. A., Benemanskaya G. V., Dementev P. A., Senkovskiy B., Timoshnev S. N. Synchrotron-radiation photoemission study of the ultrathin Ba/3C–SiC (111) interface. *Journal of Physics and Chemistry of Solids*. 2016;90: 40–44. <https://doi.org/10.1016/j.jpms.2015.10.018>
76. Benemanskaya G. V., Dementev P. A., Kukushkin S. A., Osipov A. V., Timoshnev S. N. Carbon-based aromatic-like nanostructures on the vicinal SiC surfaces induced by Ba adsorption. *ECS Journal of Solid State Science and Technology*. 2019;8(6): M53–M59. <https://doi.org/10.1149/2.0031906jss>
77. Benemanskaya G. V., Dement'ev P. A., Kukushkin S. A., Osipov A. V., Timoshnev S. N. A new type of carbon nanostructure on a vicinal SiC(111)-8° surface. *Technical Physics Letters*. 2019;45: 201–204. <https://doi.org/10.1134/S1063785019030039>
78. Benemanskaya G. V., Kukushkin S. A., Dementev P. A. Aromatic-like carbon nanostructures created on the vicinal SiC surfaces. *Physics of the Solid State*. 2019;61(12): 2455–2458. <https://doi.org/10.1134/S1063783419120059>
79. Kukushkin S. A., Osipov A. V. Anisotropy of the solid-state epitaxy of silicon carbide in silicon. *Semiconductors*. 2013;47: 1551–1555. <https://doi.org/10.1134/S1063782613120129>
80. Kitaev Y. E., Kukushkin S. A., Osipov A. V. Evolution of the symmetry of intermediate phases and their phonon spectra during the topochemical conversion of silicon into silicon carbide. *Physics of the Solid State*. 2017;59: 28–33. <https://doi.org/10.1134/S1063783417010164>
81. Kitaev Y. E., Kukushkin S. A., Osipov A. V., Redkov A. V. A new trigonal (rhombohedral) SiC phase: ab initio calculations, a symmetry analysis and the Raman spectra. *Physics of the Solid State*. 2018;60: 2066–2071. <https://doi.org/10.1134/S1063783418100116>
82. Kukushkin S. A., Osipov A. V. The optical properties, energy band structure, and interfacial conductance of a 3C–SiC(111)/Si(111) heterostructure grown by the method of atomic substitution. *Technical Physics Letters*. 2020;46: 1103–1106. <https://doi.org/10.1134/S1063785020110243>
83. Kukushkin S. A., Osipov A. V. Anomalous properties of the dislocation-free interface between Si (111) substrate and 3C–SiC (111) epitaxial layer. *Materials*. 2021;14(78): 1–12. <https://doi.org/10.3390/ma14010078>
84. Virojanadara C., Hetzel M., Johansson L. I., Choyke W. J., Starke U. Electronic and atomic structure of the 4H–SiC (1  $\bar{1}02$ ) – c(2 × 2) surface. *Surface Science*. 2008;602 (15): 525–533. <https://doi.org/10.1016/j.susc.2007.11.012>
85. Santoni A., Lancok J., Dhanak V. R., Loreti S., Miller G., Minarini C. A valence-band and core-level photoemission study of a-Si<sub>x</sub>C<sub>1-x</sub> thin films grown by low-temperature low-pressure chemical vapour deposition. *Applied Physics A*. 2005;81: 991–996. <https://doi.org/10.1007/s00339-004-2976-4>
86. Sieber N., Seyller Th., Ley L., James D., Riley J. D., Leckey R. C. G. Synchrotron x-ray photoelectron spectroscopy study of hydrogen-terminated 6H–SiC{0001} surfaces. *Physical Review B*. 2003;67(20): 205304-1-13. <https://doi.org/10.1103/PhysRevB.67.205304>
87. King S. W., Nemanich R. J., Davis R. F. Photoemission investigation of the Schottky barrier at the Sc/3C–SiC (111) interface. *Physica Status Solidi (b)*. 2015;252(2): 391–396. <https://doi.org/10.1002/pssb.201451340>
88. Watcharinyanon S., Johansson L. I., Xia C., Virojanadara C. Changes in structural and electronic properties of graphene grown on 6H–SiC(0001) induced by Na deposition. *Journal of Applied Physics*. 2012;111: 083711-1-6. <https://doi.org/10.1063/1.4704396>
89. Maiti J., Kakati N., Lee S. H., Yoon Y. S. Fluorination of multiwall carbon nano-tubes by a mild fluorinating reagent HPF<sub>6</sub>. *Journal of Fluorine Chemistry*. 2012;135: 362–366. <https://doi.org/10.1016/j.jfluchem.2011.10.004>
90. Flesch R., Serdaroglu E., Blobner F., Feulner P., Brykalova X. O., Pavlychev A. A., Kosugid N., Rühl E. Gas-to-solid shift of C 1s-excited benzene. *Physical Chemistry Chemical Physics*. 2012;14(26): 9397–9402. <https://doi.org/10.1039/C2CP23451C>
91. Kong M. J., Teplyakov A. V., Lyubovitsky J. G., Bent S. F. NEXAFS studies of adsorption of benzene on Si(100)-2 × 1. *Surface Science*. 1998;411(3): 286–293. [https://doi.org/10.1016/S0039-6028\(98\)00336-7](https://doi.org/10.1016/S0039-6028(98)00336-7)
92. Makarova A. A., Grachova E. V., Krupenya D. V., Vilkov O., Fedorov A., Usachov D., Generalov A., Koshevoy I. O., Tunik S. P., Rühl E., Laubschat C., Vyalikh D. V. Insight into the electronic structure of the supramolecular “rods-in-belt” Au<sup>I</sup>-Cu<sup>I</sup> and Au<sup>I</sup>-Ag<sup>I</sup> self-assembled complexes from X-ray photoelectron and absorption spectroscopy. *Journal of Electron Spectroscopy and Related Phenomena*. 2015;192: 26–34. <https://doi.org/10.1016/j.elspec.2014.01.004>
93. Kang C., Tang J., Li L., Pan H., Pengshou X., Wei S., Chen X., Xu X. In situ study on the electronic structure of graphene grown on 6H–SiC (000 $\bar{1}$ ) with synchrotron radiation photoelectron spectroscopy. *Applied Surface Science*. 2012; 258(6): 2187–2191. <https://doi.org/10.1016/j.apsusc.2011.02.068>
94. Bagraev N. T., Kukushkin S. A., Osipov A. V., Romanov V. V., Klyachkin L. E., Malyarenko A. M.,

Khromov V. S. Magnetic properties of thin epitaxial SiC layers grown by the atom-substitution method on single-crystal silicon surfaces. *Semiconductors*. 2021;55: 137–145. <https://doi.org/10.1134/S106378262102007X>

95. Bagraev N. T., Kukushkin S. A., Osipov A. V. et al. Phase transitions in silicon-carbide epitaxial layers grown on a silicon substrate by the method of the coordinated substitution of atoms. *Semiconductors*. 2022;56: 321–324. <https://doi.org/10.1134/S1063782622070016>

96. Somayazulu M., Ahart M., Mishra A. K., Geballe Z. M., Baldini M., Meng Y., Struzhkin V. V., Hemley R. J. Evidence for superconductivity above 260 K in lanthanum superhydride at megabar pressures. *Physical Review Letters*. 2019;122(2): 027001. <https://doi.org/10.1103/PhysRevLett.122.027001>

97. Thapa D. K., Islam S., Saha S. K., Mahapatra P. S., Bhattacharyya B., Sai T. P., Mahadevu R., Patil S., Ghosh A., Pandey A. Coexistence of diamagnetism and vanishingly small electrical resistance at ambient temperature and pressure in nanostructures. *Superconductivity (cond-mat.supr-con.)*. 2019; arXiv:1807.08572. <https://doi.org/10.48550/arXiv.1807.08572>

98. Snider E., Dasenbrock-Gammon N., McBride R., Debessai M., Vindana H., Vencatasamy K., Lawler K. V., Salamat A., Dias R. P. Room-temperature superconductivity in a carbonaceous sulfur hydride. *Nature*. 2020;586: 373–377. <https://doi.org/10.1038/s41586-020-2801-z>

99. Markov L. K., Kukushkin S. A., Smirnova I. P., Pavlyuchenko A. S., Grashchenko A. S, Osipov A. V., Svyatets G. V., Nikolaev A. E., Sakharov A. V., Lundin V. V., Tsatsulnikov A. F. A light-emitting diode based on AlInGaN heterostructures grown on SiC/Si substrates and its fabrication technology. *Technical Physics Letters*. 2022;48: 31–34. <https://doi.org/10.1134/S1063785022020043>

\*Translated by author of the article.

### Information about the authors

*Sergey A. Kukushkin*, Dr. Sci. (Phys.–Math.), Professor, Head of the Laboratory of Structural and Phase Transitions in Condensed Matter, Chief Researcher, Institute for Problems in Mechanical Engineering of the Russian Academy of Sciences (IPME RAS) (Saint-Petersburg, Russian Federation).

<https://orcid.org/0000-0002-2973-8645>  
[sergey.a.kukushkin@gmail.com](mailto:sergey.a.kukushkin@gmail.com)

*Andrey V. Osipov*, Dr. Sci. (Phys.–Math.), Chief Researcher of the Laboratory of Structural and Phase Transitions in Condensed Matter, Institute for Problems in Mechanical Engineering of the Russian Academy of Sciences (IPME RAS) (Saint-Petersburg, Russian Federation).

<https://orcid.org/0000-0002-2911-7806>  
[andrey.v.osipov@gmail.com](mailto:andrey.v.osipov@gmail.com)

*Received 07.10.2022; approved after reviewing 12.10.2022; accepted for publication 17.10.2022; published online 25.12.2022.*

*Translated by Valentina Mittova*

*Edited and proofread by Simon Cox*



# Condensed Matter and Interphases

Kondensirovannye Sredy i Mezhfaznye Granitsy  
<https://journals.vsu.ru/kcmf/>

## Original articles

Research article

<https://doi.org/10.17308/kcmf.2022.24/10550>

## Influence of pore geometry on the state of bulk pore water in the pressure-temperature phase space

G. S. Bordonskiy 

*Institute of Natural Resources, Ecology and Cryology of the Siberian Branch of Russian Academy of Sciences, 16a Nedorezova str., Chita 672002, Russian Federation*

### Abstract

In recent years, the existence of a second critical point of the liquid-liquid transition of water has been proven. In the pressure-temperature phase space, this point is located in the temperature range  $-50\text{ °C} \dots -100\text{ °C}$  and at pressure  $\sim 100\text{ MPa}$ . The exact position of this point is not yet known due to experimental difficulties in achieving the deep supercooling of bulk water. The Widom line, the locus of increased fluctuations in entropy and density, is associated with the second critical point. When approaching the Widom line, a sharp increase in a number of physical quantities was established: heat capacity at constant pressure, isothermal compressibility, volume expansion coefficient. However, the practical significance of these features is not clear, since for pressures close to atmospheric, the temperature on it is  $-45\text{ °C}$ . At the same time, it is known that at temperatures below  $-41\text{ °C}$  (homogeneous nucleation temperature), chemically pure supercooled bulk water is unstable due to the very rapid formation of ice crystal nuclei. Nevertheless, supercooling of bulk water to  $-70\text{ °C}$  in nanometre-sized pores is known.

In the present study, we investigated the possibility of reaching the state on the Widom line at negative pressures, for which, theoretically, the temperature of such a state becomes higher than  $-45\text{ °C}$  and can reach it positive values at a pressure of  $-100\text{ MPa}$ . Such a state, in this study, is assumed in the cylindrical hydrophilic pores with a diameter of several nanometres. For the investigation of this possibility and the achievable values of negative pressure (and high temperatures on the Widom line), we measured the low-frequency impedance of a cooled capacitive cell filled with a moistened MCM-41 nanoporous material. In addition, the thermal characteristics were measured in the form of a temperature response of the medium from a pulsed spot heater at a certain distance from it. The position of the Widom line, associated with the second critical point of water, was determined based on the anomalies of the measured physical values in the temperature range  $-50\text{ °C} \dots +10\text{ °C}$ . For MCM-41 with an average pore diameter of  $3.5\text{ nm}$ , dielectric and thermal extrema were found near  $-18\text{ °C}$ , which corresponds to a pressure of about  $-65\text{ MPa}$ .

Thus, the performed experiments have shown the possibility of reaching the state on the Widom line at temperatures characteristic of ordinary conditions. Consequently, a significant change in the physicochemical characteristics of dispersed moistened media in various natural and artificial objects is possible. The study of other sorbents with cylindrical pores in order to achieve positive temperatures on the Widom line is of interest.

**Keywords:** Supercooled water, Second critical point, Widom line, Negative pressure, Nanoporous media

**For citation:** Bordonskiy G. S. Influence of pore geometry on the state of bulk pore water in the pressure-temperature phase space. *Condensed Matter and Interphases*. 2022;24(4): 459–465. <https://doi.org/10.17308/kcmf.2022.24/10550>

**Для цитирования:** Бордонский Г. С. Влияние геометрии пор на состояние объемной поровой воды в фазовом пространстве давление-температура. *Конденсированные среды и межфазные границы*. 2022;24(4): 459–465. <https://doi.org/10.17308/kcmf.2022.24/10550>

✉ Georgy S. Bordonskiy, e-mail: [lgc255@mail.ru](mailto:lgc255@mail.ru)

© Bordonskiy G. S., 2022



The content is available under Creative Commons Attribution 4.0 License.



## 1. Introduction

Features of the physicochemical characteristics of supercooled bulk metastable water have attracted the attention of researchers in recent decades. Their study allowed a significantly advance in understanding the structure of water. For example, a second critical point of the liquid-liquid transition for water was discovered, which, according to various models, is located in the temperature range ( $T$ )  $-50$  °C...  $-100$  °C and at pressure ( $P$ )  $\sim 100$  MPa [1, 2]. It is associated with the existence of the Widom line, which is the locus of increased fluctuations in the entropy and density of the liquid. When approaching the Widom line, some thermodynamic quantities of water increase sharply, for example, the heat capacity at a constant pressure ( $C_p$ ), isothermal compressibility, and coefficient of volumetric expansion [1]. At  $P \sim 0.1$  MPa  $T$  on the Widom line is  $-45$  °C.

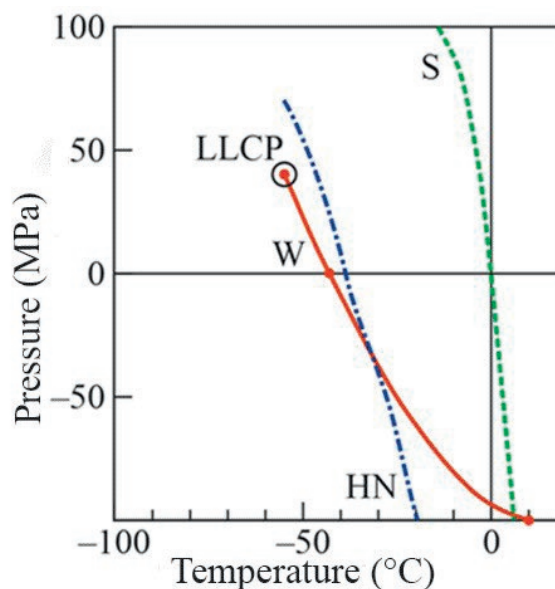
In recent studies, the behaviour of a number of physical quantities in the region of negative pressures near the Widom line was studied [3, 4]. It turned out that a simple extrapolation of the results, for example, for the speed of sound, obtained at positive  $P$ , leads to their strong differences from the experimental results. At the same time, there is a lack of studies dedicated to the clarification of certain models of bulk water.

The phase diagram of the bulk water in the region of positive and negative  $P$  according to the results of studies [1, 5, 6] is shown in Fig. 1. An interesting conclusion for research follows from the diagram. The Widom line can reach positive  $T$  near  $-100$  MPa. Consequently, anomalies in the physical characteristics of moistened porous media can be observed under normal conditions for media with a special pore geometry and a high degree of hydrophilicity. In this case, an important feature for practical applications can be, for example, the expected acceleration of physicochemical transformations involving water on the Widom line due to an increase in energy fluctuations [7].

The purpose of this study was the search for signs of the state of water located in porous media at temperatures of  $-25$  °C... $+10$  °C corresponding to the Widom line. The manifestation of this effect is assumed in hydrophilic media with cylindrical filamentous pores of nanometre diameter. In such

pores, when concave menisci are formed at both ends of the capillaries, the liquid is stretched, e.g., a negative pressure arises.

Let us estimate the magnitude of the negative pressure in the water of a cylindrical pore. For pores of small diameter, the concave meniscus has a radius ( $r$ ) close to the pore cross-sectional radius. We assumed that  $r$  is 1.75 nm. The pressure in water is calculated using Laplace's formula:  $P = 2\sigma/r$ , where  $\sigma$  is the coefficient of surface tension. At 0 °C  $\sigma = 0.075$  n/m and the calculation provides  $P \approx -110$  MPa. Thus, a significant negative pressure near 0 °C for positive  $T$  on the Widom line, in accordance with the graph in Fig. 1 it can theoretically be achieved in the pores of existing silicate sorbents (e.g. SBA-15; MCM-41) with cylindrical pores. However, the question about the tensile strength of water in capillaries arises, since it is known to decrease sharply in the temperature range from 5 to 0 °C, when a pressure of  $-10$  MPa is reached [8]. At the same time, the theoretical limit of the onset of cavitation phenomena is estimated at about  $-140$  MPa [9]. On the other hand, when small liquid fragments are formed in a cylindrical pore, the pressure in them must remain negative,



**Fig. 1.** Phase diagram of water in the region of the Widom line at positive and negative pressures. Adapted from [1, 5, 6]. LLCP (liquid-liquid critical point) is the second critical point, HN is the line of homogeneous nucleation, W is the Widom line, S is the boundary between stable and metastable water

since the concavity of the menisci in them remains even after crushing.

Obviously, the achieved negative pressure will depend on a number of pore characteristics: the degree of their hydrophilic properties, pore geometry, characteristics of water clusters, etc. The solution of this problem seems to be rather complicated [10]. Therefore, in order to determine actually achievable values of negative pressures, it seems appropriate to perform experimental studies of the characteristics of moistened sorbents, which should have special values near the Widom line. In this case, it is necessary to select sorbents, the water in the pores of which has characteristics close to characteristics of bulk water.

For this purpose, temperature measurements of the dielectric and thermal characteristics of the moistened silicate sorbent MCM-41 with cylindrical pores of nanometer diameter were performed.

## 2. Experimental

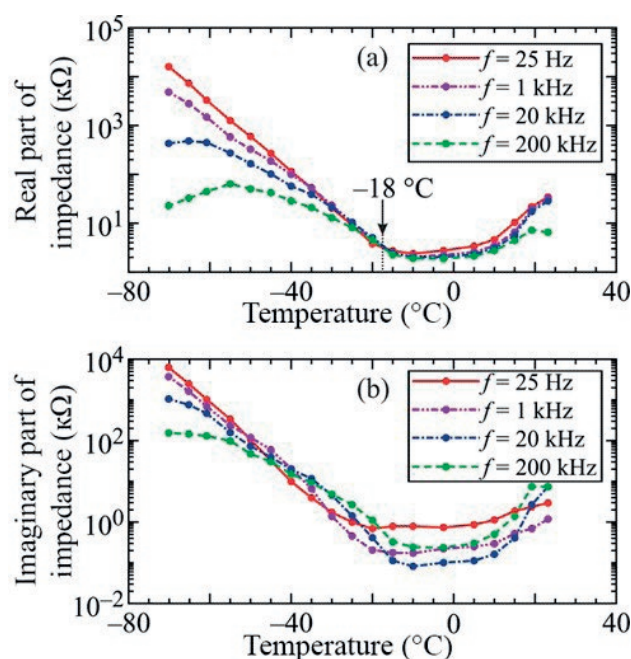
### 2.1. Dielectric measurements

The measurements were performed at frequencies from 25 Hz to 1 MHz. It was assumed that the state on the Widom line can be registered from a change in the electrical response to an alternating electric field, for example, from a change in the real ( $z'$ ) and imaginary ( $z''$ ) parts of the impedance of the cell with the test material. It is known that the relaxation frequency of water molecules is in the gigahertz range. For silicate materials, it corresponds to the optical frequency range. However, in porous moistened materials, low-frequency relaxation (Maxwell-Wagner) additionally occurs, which has a Debye character and relaxation frequencies much lower than for individual materials. It is important that the effective permittivity at low frequencies is proportional to the same value for the inclusion material [11]. This feature allows an investigation into the nature of the dependence of the dielectric constant of inclusions, e.g. water in pores, on temperature at low frequencies.

The low-frequency impedance of a capacitive cell filled with moistened MCM-41 with a weight humidity of 4–98% in the temperature range from 25 °C to –55 °C was determined. The used material had cylindrical pores with the diameter

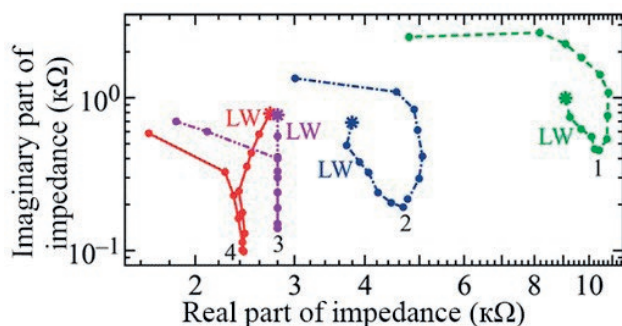
of 3.5 nm. For such a material, a decrease in the melting temperature of ice in pores ( $\Delta T_m$ ) when they are completely filled, is calculated using the modified Gibbs-Thomson formula:  $\Delta T_m = c/(r - t)$ , where  $c \approx 52$  (K nm),  $t \approx 0.38$  nm [12] and the value is approximately –38 °C. In this case, only the first two layers on the contact surface of two media differ in characteristics from bulk water [12, 13]. In the case of incomplete filling of the pores, as well as for the sample cooling mode, the shift of phase transition temperature can additionally increase by tens of degrees. This effect allows reaching the values of the phase transition temperature (liquid water)-ice: –50 °C... –70 °C, which is required to perform the experiment in the area of deep supercooling of water.

The measurements of  $z'$  and  $z''$  were performed using an RCL meter. The measuring cell was cooled with cold nitrogen vapour. The results of the determination of  $z'$ ,  $z''$  for a sample with a weight moisture content of 70% are shown in Fig. 2 a, b for some frequencies. On the graphs of dependences of the real and imaginary parts of the impedances, characteristic minima in the temperature range of –25 °C ... +20 °C were revealed. Another feature of the graphs shown in Fig. 2 is the absence of frequency dependence for  $z'$



**Fig. 2.** Dependences of  $z'$  (a) and  $z''$  (b) on temperature at four frequencies during sample cooling. The arrow marks a special temperature point (for  $z' = \text{const}$ )

at a temperature of  $-18\text{ }^{\circ}\text{C}$ , at which a coincidence of  $z'$  at frequencies from 25 Hz to 200 kHz was observed. These results were also presented as Argand diagrams (relationships between  $z'$  and  $z''$  at a fixed temperature depending on the frequency), which consisted of two branches - Fig. 3. For the convenience of comparison, the graphs are presented on a double logarithmic scale. One of the branches (LW) corresponded to liquid water, which was determined from temperature changes (this branch disappeared after freezing of water in pores below  $-40\text{ }^{\circ}\text{C}$ ). An analysis of the results showed that the equivalent circuit of the cell cannot be represented as a simple circuit of RC chains (where R is a resistor, C is a capacitor). It is known that Argand diagrams for  $z'$  and  $z''$  for the group of series-connected chains of parallel-connected R and C for their fixed values have a different form and represent linked fragments of circles [14]. However, in experiments, an unusual change in the nature of the diagrams was observed: the branch associated with water occupied a vertical position for an ambient temperature of  $-18\text{ }^{\circ}\text{C}$ , i.e.  $z'$  did not depend on the frequency.



**Fig. 3.** Argand diagrams of moistened MCM-41 for temperatures 1:  $-25\text{ }^{\circ}\text{C}$ , 2:  $-20\text{ }^{\circ}\text{C}$ , 3:  $-18\text{ }^{\circ}\text{C}$ , 4:  $-15\text{ }^{\circ}\text{C}$ . Points for a frequency of 25 Hz are marked with an asterisk, the other extreme points of the diagrams correspond to a measurement frequency of 500 kHz and 1 MHz. LW is the branch of the diagram corresponding to liquid water (it disappears when approaching  $-40\text{ }^{\circ}\text{C}$ )

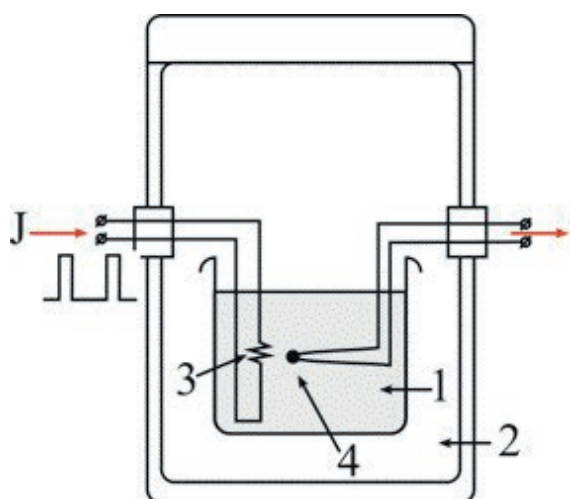
## 2.2. Thermal measurements

It is known that the heat capacity  $C_p$  increases significantly for water on the Widom line, which takes place at  $-45\text{ }^{\circ}\text{C}$  at near atmospheric pressure (0.1 MPa). Anomalous behaviour, according to theoretical estimates, should also be observed for the heat capacity at constant volume. In the case

of a significant change in pressure, some increase in the volume of the liquid is possible, therefore the thermal response of water in the pores will be a function of two heat capacities. However, in any case, measurements of thermal quantities near the temperature on the Widom line will apparently reveal non monotonic temperature dependences.

For the determination of this special temperature, the measurement of the characteristics of a single pulse of thermal energy propagating in a medium was used [15]. In this method, a short-term heating of the medium was created in a small volume of the sample, followed by recording the temperature at a certain distance from the source of thermal disturbance. It is known that for a flat heat flow front in a homogeneous medium, the thermal conductivity  $D = k/\rho C_p$ , where  $k$  is the coefficient of thermal conductivity,  $\rho$  is the density of the material,  $C_p$  is the specific effective heat capacity. Near the Widom line, in addition to the heat capacity anomaly, changes in the thermal conductivity coefficient also can be expected. In this case, for a point energy source and a spherical front of a propagating thermal pulse, a diffuse temperature pulse in time will be observed at the points of the medium. In general, the maximum temperature increment ( $\Delta T$ ) will increase with an increase in the coefficient  $D$  and decrease with an increase in  $C_p$ . Also  $\Delta T$  will depend in a complex way on the properties of the medium, the geometry of the sample, and the characteristics of the pulse source. However, the purpose of measurements was to determine the temperature range at which an anomaly in the response of the medium will be observed (these can be the temperatures of phase transitions, the critical point, and the area associated with it on the Widom line). For this purpose, it was sufficient to determine only the temperature of the medium for the maximum value of deviations of  $T$  caused by the propagation of a thermal pulse in the sample. The scheme of the installation for the measuring the thermal response to an impulse action is shown in Fig. 4.

During measurements, the moistened MCM-41 sorbent was placed in a cylindrical metal container (1), with the diameter of 16 mm and depth of 10 mm, where a filament heater (3) and a thermocouple (4) were located. The heater wire

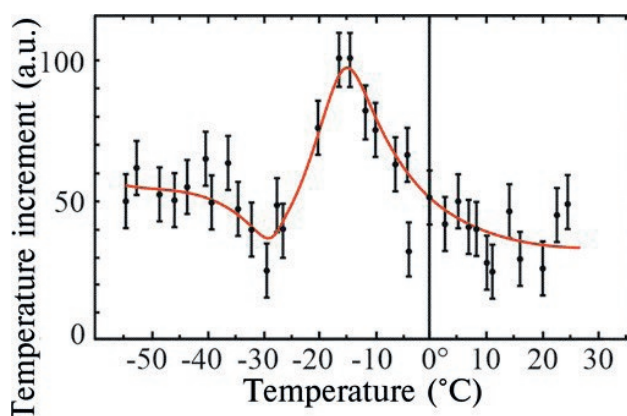


**Fig. 4.** Scheme of the installation for measuring the temperature increment in the medium caused by the propagation of a thermal pulse,  $J$  is current form through the heater, (designations are given in the text)

was placed in a volume of  $0.4 \text{ mm}^3$ , its electrical resistance was 3 Ohm, the distance from the heater to the thermocouple was  $\sim 7 \text{ mm}$ . Thermal waves were created by a sequence of short current pulses of 0.2–0.4 A with a cyclic change in the temperature of the climatic chamber (2) in the range from  $25^\circ\text{C}$  to  $-55^\circ\text{C}$ . The duration of the current pulse, the time between pulses, and the times of cooling and heating of the samples were experimentally chosen in order to obtain a noticeable temperature response during the passage of a thermal pulse with its subsequent relaxation.

The results of one of the measurements at a weight moisture content of 8% are shown in Fig. 5. The graph reveals an extremum of the measured value at temperatures of  $-14^\circ\text{C}$  ...  $-18^\circ\text{C}$ , indicating a special state of the medium in a certain temperature range and the centre with these values. A similar behaviour with slightly different extremes was also found in measurements with higher humidity MCM-41. Moreover, for a humidity of 98%, the extremum  $\Delta T$  for the supercooling region of water was not observed.

In addition, the thermometry of the samples was performed during their uniform heating from  $-55^\circ\text{C}$  to  $10^\circ\text{C}$  with a relative accuracy of  $0.1^\circ\text{C}$ . For example, for the medium with 70% humidity, a deviation of the time derivative of temperature



**Fig. 5.** The maximum value of the medium temperature increment in the thermal wave depending on the temperature of the moistened MCM-41 when the sample is heated from  $-55^\circ\text{C}$  (at arbitrary units)

from a linear dependence in the temperature range of  $-40^\circ\text{C}$  ...  $0^\circ\text{C}$  with a non-sharp deviation extremum (a decrease by 10% of the value) at  $-15^\circ\text{C}$  ...  $-20^\circ\text{C}$  was established. A decrease in the value of the derivative can be attributed to an increase in the heat capacity of water, which takes place near the Widom line [1].

### 3. Discussion

The performed experiments showed the coincidence of the anomalous behaviour of the dielectric and thermal characteristics of supercooled water located in the cylindrical pores of the MCM-41 silicate sorbent at a temperature significantly exceeding  $-45^\circ\text{C}$ . The behaviour of electrical and thermal characteristics revealed in new experiments suggests a special mechanism of susceptibility to external physical influences at certain temperatures. It was associated with the achievement of states of pore water on the Widom line at negative pressures. Anomalous behaviour was observed in the region with the centre near the temperature of  $-18^\circ\text{C}$  for experiments with MCM-41 (Fig. 2a), for which the pressure in the pores is approximately equal to  $-65 \text{ MPa}$  as follows from the plot of the Widom line in the pressure-temperature phase space (Fig. 1).

The effect was found for MCM-41 with a weight moisture content below 70% (which corresponded to less than 90% pore volume filling for its pore space parameters). For a medium with a weight moisture content of 98%, according to our measurements, there was no effect. This can

be explained by the fact that, for higher humidity, part of the water is located in the space between the granules, which eliminates the menisci and leads to the disappearance of the negative pressure in the pores.

In the case of hydrophobic pores, the pressure in the water should increase due to the convexity of the menisci and the Widom line, in accordance with the graph in Fig. 1 will appear at temperatures below  $-45\text{ }^{\circ}\text{C}$ . Similar pattern will be observed for completely filled spherical hydrophilic pores. In all cases, the effect will also depend on the features of the filling of the pore space with water, its geometry and defects in the pore structure, moisture values, and possible dissolution of the matrix substance.

As was noted in [1–4, 7], thermal and acoustic indicators change near the Widom line, and the acceleration of thermally activated physico-chemical transformations involving liquid water is possible. These features can manifest under natural conditions in various finely dispersed media of complex composition: in atmospheric aerosols, vegetation covers, soils, subsoils, in engineering structures and artificial environments in the case of significant specific volumes of filamentous pores of nanometre diameter.

#### 4. Conclusions

The experimental study of water in a silicate sorbent with filamentous pores revealed anomalous temperature dependences of the low-frequency impedance of the capacitive cell with the sample and the thermal response to pulsed heating of the medium. Extrema of these characteristics were found near  $-18\text{ }^{\circ}\text{C}$  for the moistened MCM-41 material with a pore diameter of 3.5 nm, which can be explained by the existence of a significant negative pressure in the pores, equal to  $-65\text{ MPa}$ . These parameters in the pressure-temperature phase space correspond to a point on the Widom line, where there is an increase in fluctuations in the entropy and density of bulk water, which generates anomalies in the physical characteristics of the fluid and its host medium. The study of other similar sorbents for investigation of the possibility of reaching pressures of  $\sim -100\text{ MPa}$  in pore water, which will correspond to positive temperatures on the Widom line is of interest.

#### Conflict of interests

The author declares that he has no known competing financial interests or personal relationships that could have appeared to influence the work reported in this paper.

#### References

1. Anisimov M. A. Cold and super-cooled water: a novel supercritical-fluid solvent. *Russian Journal of Physical Chemistry B*. 2012;6: 861–867. <https://doi.org/10.1134/S199079311208009X>
2. Shi R., Tanaka H. The anomalies and criticality of liquid water. *Proceeding of National Academy of Science (USA)*. 2020;117: 26591–26599. <https://doi.org/10.1073/pnas.2008426117>
3. Pallares G., Gonzalez M., Abascal I. L. F., Valeriani C., Caupin F. Equation of state for water and its line of density maxima down to  $-120\text{ MPa}$ . *Physical Chemistry Chemical Physics*. 2016;18: 5896–5900. <https://doi.org/10.1039/C5CP07580G>
4. Biddle J. W., Singh R. S., Sparano E. M., Ricci F., Gonzalez M. A., Valeriani C., Abascal J. L. F., Debenedetti P. G., Anisimov M. A., Caupin F. Two-structure thermodynamics for the TIP4P/2005 model of water covering supercooled and deeply stretched regions. *Journal of Chemical Physics*. 2017;146(3): 034502. <https://doi.org/10.1063/1.4973546>
5. Abascal I. L. F., Vega C. Widom line and the liquid-liquid critical point for the TIP4P/2005 water model. *Journal of Chemical Physics*. 2010;133: 234502–234510. <https://doi.org/10.1063/1.3506860>
6. Caupin F. Escaping the no man's land: recent experiments on metastable liquid water. *Journal of Non-Crystalline Solids*. 2015;407: 441–448. <https://doi.org/10.1016/j.jnoncrysol.2014.09.037>
7. Bordonskiy G. S., Gurulev A. A. Regarding physical and chemical transformation with the involvement of water near  $-45\text{ }^{\circ}\text{C}$ . *Condensed Matter and Interphases*. 2019;21(4): 478–489. (In Russ., abstract in Eng.). <https://doi.org/10.17308/kcmf.2019.21/2359>
8. Briggs L. G. Limiting negative pressure of water. *Journal of Applied Physics*. 1950;21: 721–722. <https://doi.org/10.1063/1.1699741>
9. Alvarenga A. D., Grimsditch M., Bondar R. J. Elastic properties of water under negative pressure. *Journal of Chemical Physics*. 1993;98(11): 8392–8396. <https://doi.org/10.1063/1.464497>
10. Shi K., Shen Y., Santiso E. E., Gibbins K. E. Microscopic pressure tensor in cylindrical geometry: pressure of water in a carbon nanotube. *Journal of Chemical Theory and Computation*. 2020;16: 5548–5561. <https://doi.org/10.1021/acs.jctc.0c00607>
11. Artyomenko L. V., Kozhevnicov N. O. Modelling the Maxwell-Wagner effect in frozen unconsolidated

rocks. *Earth's Cryosphere*. 1999;3(1): 60–68. (In Russ., abstract in Eng.). Available at: [http://earthcryosphere.ru/archive/1999\\_1/60-68.pdf](http://earthcryosphere.ru/archive/1999_1/60-68.pdf)

12. Cervený S., Mallamace F., Swenson J., Vogel M., Xu L. Confined water as model of supercooled water. *Chemical Reviews*. 2016;116(13): 7608–7625. <https://doi.org/10.1021/acs.chemrev.5b00609>

13. Menshikov L. I., Menshikov P. L., Fedichev P. O. Fenomenological model of hydrophobic and hydrophilic interaction. *Journal of Experimental and Theoretical Physics*. 2017;152(6): 1173–1188. <https://doi.org/10.1134/S1063776117120056>

14. Barsukov E., Macdonald J. R. (eds). *Impedance Spectroscopy. Theory, experiment and applications*. New Jersey: Wiley; 2005. 595 p.

15. Carballo-Sanchez A. F., Gurevich Y. G., Logvinov G. N., Drogobitskii Y. V., Titov O. Y. Propagation of a heat pulse in a bounded conducting medium: thermoelectric detection. *Physics of the Solid State*. 1999;41(4): 544–549. <https://doi.org/10.1134/1.1130821>

### Information about the authors

Georgy S. Bordonskiy, Dr. Sci. (Phys.–Math.), Professor, Chief Researcher of the Laboratory of Geophysics of Cryogenesis, Institute of Natural Resources, Ecology and Cryology of the Siberian Branch of the Russian Academy of Sciences (Chita, Russian Federation).

<https://orcid.org/0000-0002-0009-0822>  
lgc255@mail.ru

Received 18.05.2022; approved after reviewing 04.07.2022; accepted for publication 15.09.2022; published online 25.12.2022.

Translated by Valentina Mittova

Edited and proofread by Simon Cox



# Condensed Matter and Interphases

Kondensirovannyye Sredy i Mezhfaznye Granitsy  
<https://journals.vsu.ru/kcmf/>

## Original articles

Research article

<https://doi.org/10.17308/kcmf.2022.24/10551>

## Computer model of Cu-Ni-Mn isobaric phase diagram: verification of crystallisation intervals and change of the three-phase reaction type

A. E. Zelenaya✉, V. I. Lutsyk, V. D. Baldanov

*Institute of Physical Materials Science, Siberian Branch of the Russian Academy of Sciences,  
8 Sakhyanovoy str., Ulan-Ude 670047, Russian Federation*

### Abstract

The purpose of article was to show the possibilities of spatial computer models of phase diagrams in solving of the problems of digitalization of materials science. The study of the high-temperature part of the isobaric phase diagram for the Cu–Ni–Mn system was carried out taking into account two polymorphic modifications of manganese ( $\delta\text{Mn}$  and  $\gamma\text{Mn}$ ). For a better understanding of the phase diagram structure, at the first stage, its prototype was developed with increased temperature and concentration intervals between binary points with the preservation of topological structure, which is then modified into the model of phase diagram corresponding to the real system. The phase diagram of Cu–Mn–Ni system above 800°C was formed by three pairs of liquidus, solidus, and transus surfaces and three ruled surfaces with a horizontal arrangement of the forming segment.

Experimental part: the effect of changing the peritectic equilibrium ( $L + \delta\text{Mn} \rightarrow \gamma\text{Mn}$ ) to the metatectic one ( $\delta\text{Mn} \rightarrow L + \gamma\text{Mn}$ ) was revealed. The crystallisation features at the change of three-phase transformation type were considered, the surface of change of melt mass increment sign and the vertical mass balances for the three-phase region  $L + \delta\text{Mn} + \gamma\text{Mn}$  were constructed. The surface of two-phase reaction, on which the change of three-phase reaction type occurs, is a ruled surface and is determined, using the algorithm for calculating the change in sign of the mass increment of liquid phase. Three-phase region, taking into account the surface of type change of three-phase reaction, is divided into six concentration fields when projecting into the triangle of compositions. Four concentration fields differ in the crystallisation stages and the formed set of microstructures. Isothermal sections were calculated in the temperature range between two minimum points arranged in the Cu–Mn and Mn–Ni systems at zero crystallisation interval between the valleys of the liquidus and solidus surfaces and taking into account the crystallisation interval.

The spatial model of phase diagram greatly expands the possibilities of computer-aided design of materials. In particular, a solution for the problem of type changing of three-phase reaction was obtained, which cannot be realised either by thermodynamic calculations or by calculations from first principles.

**Keywords:** Phase diagram, Computer simulation, Cu–Ni–Mn system, Change of three-phase reaction type, Crystallisation interval, Microstructure

**Funding:** This work was been performed under the program of fundamental research IPMS SB RAS, project No. 0270-2021-0002.

**For citation:** Zelenaya A. E., Lutsyk V. I., Baldanov V. D. Computer model of Cu–Ni–Mn isobaric phase diagram: verification of crystallisation intervals and change of three-phase reaction type. *Condensed Matter and Interphases*. 2022;24(4): 466–474. <https://doi.org/10.17308/kcmf.2022.24/10551>

**Для цитирования:** Зеленая А. Э., Луцык В. И., Балданов В. Д. Компьютерная модель изобарной фазовой диаграммы Cu–Ni–Mn: верификация интервалов кристаллизации и смены типа трехфазной реакции. *Конденсированные среды и межфазные границы*. 2022;24(4): 466–474. <https://doi.org/10.17308/kcmf.2022.24/10551>

✉ Anna E. Zelenaya, e-mail: zel\_ann@mail.ru

© Zelenaya A. E., Lutsyk V. I., Baldanov V. D., 2022



The content is available under Creative Commons Attribution 4.0 License.

## 1. Introduction

Information about phase equilibria in the Cu–Mn–Ni system is of great importance for the creation of high-quality materials and solders with high physical and mechanical properties and corrosion resistance. In studies [1–2], the effect of addition of copper, nickel, and manganese for the creation of shape-memory alloys, as well as improvement of the physical properties of such alloys with the addition of manganese was studied. The study [3] investigated the thermoelectric properties of alloys based on the Cu–Ni–Mn system.

The high-temperature part of the phase diagrams of binary systems Cu–Mn, Mn–Ni and Cu–Ni is well studied. According to the generalised experimental data [4–5], a minimum is formed on the liquidus and solidus lines at 871 °C and 33.7 wt. % Mn in the Cu–Mn system. The system is also characterised by the occurrence of a metatectic reaction involving two high-temperature polymorphic modifications of manganese  $\delta\text{Mn}$  and  $\gamma\text{Mn}$  at 1099 °C:  $\delta\text{Mn} \rightarrow \text{L} + \gamma\text{Mn}$ . In [6–7], a detailed study in the high-temperature part of the diagram rich in manganese, aimed at establishing the boundaries of phase regions with  $\delta\text{Mn}$  and  $\gamma\text{Mn}$  was performed. Phase diagrams obtained using thermodynamic calculation methods [8–14] are in good agreement with experimental data.

The Mn–Ni system has a similar structure in the high-temperature part and also contains a minimum point on the liquidus and solidus lines at 1020 °C and 58.4 wt. % Mn, but unlike the Cu–Mn system, the transition from the polymorphic form  $\delta\text{Mn}$  to form  $\gamma\text{Mn}$  occurs according to the peritectic scheme at 1170 °C:  $\text{L} + \delta\text{Mn} \rightarrow \gamma\text{Mn}$  [6, 15–16]. The data of the experimental study were confirmed by the results of thermodynamic calculations [8, 17–18]. The Cu–Ni system has the simplest topological structure and is characterised by the formation of continuous range of the solid solutions without extrema on the liquidus and solidus lines [4–5, 8, 19–21].

For the Cu–Mn–Ni ternary system, in the earliest studies [22–25], isotherms were obtained for the liquidus and solidus surfaces in the temperature range of 1440–800 °C and six isopleths. A simplified version of the diagram with the formation of continuous range of the

solid solutions between all components and with the absence of a univariant line separating the fields of the onset of continuous crystallisation of solid solutions based on various polymorphic modifications of manganese was shown. At the same time, it was stated that if a line connecting the minimum points in the Cu–Mn and Mn–Ni binary systems is drawn, then the liquidus and solidus surfaces will adjoin along this line [24].

This assumption was also analysed graphically based on hypothetical phase diagrams with unlimited solubility of components and ternary points of minimum and maximum and corresponding extrema in all binary systems [26]. It was shown that the systems have contact lines between the liquidus and solidus surfaces in the direction from binary extrema to the ternary one. Isothermal sections with contact of liquidus and solidus isotherms along these lines were shown. At the same time, at the point of contact of the liquidus and solidus isotherms, both two fragments of the two-phase region L + S and two single-phase regions (L and S) adjoin. Such sections are typical for the section of saddle surfaces [27–28]. In [28], when discussing a similar diagram with maxima, the author described the contact between surfaces only at binary maximum points and at a ternary maximum point. On the section, only binary maximum points correspond to the contact of the liquidus and solidus isotherms.

In [29], using the example of the Cu–Mn–Ni system, the contact of the liquidus and solidus surfaces along the line connecting the points of binary minima was proved using the Gibbs phase rule. Based on the example of an isothermal section of a two-phase region without taking into account the contact of surfaces, it was shown that, assuming two degrees of freedom, two pairs of phases are in equilibrium, which contradicts the Gibbs phase rule. If the liquidus and solidus isotherms have a point of contact with a zero crystallisation interval, then, according to the authors, the violation of the phase rule does not occur. According to the calculations [30], it was shown that this line of contact of the liquidus and solidus between two minimum points is not straight. Experimental confirmation of the line corresponding to alloys with a zero crystallisation interval in the concentration range (35–44%



Mn, 0–15% Ni) was carried out in [31]. However, in later studies [32–33] the statement about the existence of a line of contact between the liquidus and solidus surfaces on the Cu–Mn–Ni diagram was proven to be false. According to the DTA data using the regression analysis method, the equations of the liquidus and solidus surfaces for the region of the Cu–Ni–Mn phase diagram from 0 to 20% Ni and from 30 to 50% Mn were calculated, the isotherms of the surfaces and the values of the crystallisation interval for the selected section of the diagram were shown. In this case, the temperature difference between the liquidus and solidus surfaces increases as the distance from the Cu–Mn binary system to the centre of the diagram increases.

The surface of the beginning of primary crystallisation based on the Cu(Ni) solid solution and isopleth drawn from Cu through the middle of the Mn–Ni system was obtained using the methods of thermodynamic calculation [34]. The authors [25] already calculated both liquidus surfaces corresponding to Mn and Cu(Ni) and six isopleths for the high-temperature part of the diagram. The sections were arranged in pairs parallel to the binary sides. On two sections located parallel to the binary systems Mn–Ni (at 20% Cu) and Cu–Mn (at 20% Ni), contact of the section lines of the liquidus and solidus surfaces was recorded, on two other similar sections there was no contact between the lines. It should be noted that when discussing systems Cu–Ti–Zr [35] and Ti–TiMn<sub>2</sub>–ZrMn<sub>2</sub>–Zr [36], containing binary systems with a minimum, points of contact of the section lines at the

boundary of the three-phase regions with the melt were revealed on the isopleths.

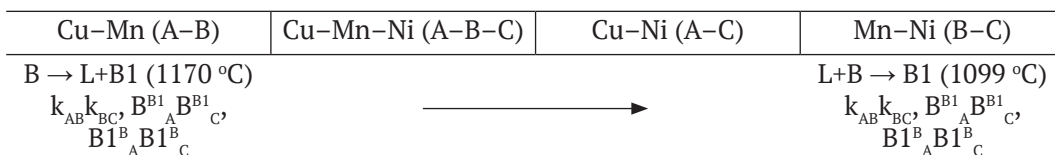
## 2. Computer model of the phase diagram of the Cu–Mn–Ni system, taking into account the zero crystallisation interval

A computer model of the high-temperature part of the phase diagram above 800 °C has been developed. When constructing a computer model of the Cu–Mn–Ni (A–B–C) system, the formation of two high-temperature polymorphic modifications of manganese ( $\delta\text{Mn} = \text{B}$ ,  $\gamma\text{Mn} = \text{B1}$ ) and minimum points in Cu–Mn binary systems ( $\text{min}_{\text{AB}}$ ) and Mn–Ni ( $\text{min}_{\text{BC}}$ ) was taken into account. We used data on the structure of binary systems according to the reference book [5] (Table 1) and the assumption that the liquidus and solidus surfaces come into contact along the line connecting the binary minima [22–24, 26, 29–31]. Invariant ternary points with the involvement of the melt in the system were not present in the system; therefore, the scheme of phase reactions has a simplified form (Scheme 1).

The model was developed based on the methodology of assembling it from phase regions and surfaces using the author’s software products [37–38].

The high-temperature part of the phase diagram of the Cu–Mn–Ni system above 800 °C was formed by three pairs of liquidus, solidus, and transus surfaces (upper «liquidus» surface  $t_{\text{B1}}^{\text{q}}$  and lower «solidus» surface  $t_{\text{B1}}^{\text{s}}$ ), and three ruled surfaces with a horizontal arrangement of the generating segment (Table 2). It includes two

**Scheme 1.** Scheme of phase reactions involving high-temperature manganese allotropes



**Table 1.** Coordinates of points on the contour of surfaces ( $z_i$  – weight fractions of components A, B, and C)

	$z_1$	$z_2$	$z_3$	$T$		$z_1$	$z_2$	$z_3$	$T$
A = Cu	1	0	0	1084.87	$k_{\text{AB}}$	0.27	0.73	0	1099
B = Mn	0	1	0	1246	$\text{B}_{\text{A}}^{\text{B1}}$	0.142	0.858	0	1099
C = Ni	0	0	1	1455	$\text{B1}_{\text{A}}^{\text{B}}$	0.132	0.868	0	1099
B1	0	1	0	1143	$k_{\text{BC}}$	0	0.902	0.098	1170
$\text{min}_{\text{AB}}$	0.663	0.337	0	871	$\text{B}_{\text{C}}^{\text{B1}}$	0	0.963	0.037	1170
$\text{min}_{\text{BC}}$	0	0.584	0.416	1020	$\text{B1}_{\text{C}}^{\text{B}}$	0	0.942	0.058	1170

**Table 2.** Surface contours

Symbol	Contour	СИМВОЛ	Symbol
Liquidus			
$q_B$	$Mn-k_{AB}-k_{BC}$	$q_{AC}$	$Cu-\min_{AB}-k_{AB}-k_{BC}-\min_{BC}-Ni$
Solidus			
$s_B$	$Mn-B_C^{B1}-B_A^{B1}$	$s_{AC}$	$Cu-\min_{AB}-B_A^B-B_C^B-\min_{BC}-Ni$
Transus			
$t_{B1}^q$	$B1-B_C^{B1}-B_A^{B1}$	$t_{B1}^s$	$B1-B_A^B-B_C^B$
Ruled surfaces			
$q_{AB}^r$	$k_{AB}-k_{BC}-B_C^B-B_A^B$	$s^r$	$B1_A^B-B1_C^B-B_C^{B1}-B_A^{B1}$
$q_{BA}^r$	$k_{AB}-k_{BC}-B_C^{B1}-B_A$		

**Table 3.** The structure of the phase regions

Phase regions	Surfaces	Phase regions	Surfaces
L + B(TP)	$q_B, s_B, q_{BA}^r$	B	$t_B^q, t_B^s$
L + B1(TP)	$q_{AC}, s_{AC}, q_{AB}^r$	B1	$s_{AC}, t_B^s$
L + B + B1	$q_{AB}^r, q_{BA}^r, s^r$	B + B1	$t_B^q, t_B^s, s^r$

one-phase (B, B1), three two-phase (L + B (SS), L + B1 (SS), B + B1) and one three-phase (L + B + B1) regions (Table 3) (SS – solid solution). Designations B and B1 correspond to two forms of high-temperature manganese allotropy. Since the points on the horizontal segments corresponding to the metatectic and peritectic reactions are located very close, the prototype of the phase diagram was initially developed, in which the points were separated by compositions and temperatures while maintaining the topological structure (Fig. 1a–b). Such a prototype provides the possibility of more visual representation of the phase diagram, understanding the structure of the phase regions and interpretation of the sections. When introducing the coordinates of real points into the prototype [5] (Table 1), the final model of the phase diagram of the Cu–Mn–Ni system (Fig. 1c–d) is obtained.

### 3. Results and discussion

#### 3.1. Change of three-phase reaction type

Based on a computer model in the three-phase region L+B+B1, a change of the peritectic transformation ( $L + B \rightarrow B1$ ) to metatectic ( $B \rightarrow L + B1$ ) was revealed. The three-phase region L + B + B1 is bounded by three ruled surfaces  $q_{AB}^r$ ,  $q_{BA}^r$  and  $s^r$  (Fig. 2a, c), while in the projection there is a crossing of their directing curves  $B_A^{B1}B_C^{B1}$  and  $B1_A^B B1_C^B$ . The surface of the two-phase reaction abc, on which a change of three-phase reaction

type occurs, is a ruled surface and it is determined using the algorithm for calculating the change of the mass increment sign of the phase L [39–40]. Three-phase region L + B + B1 with a surface of change of the three-phase reaction type abc for the phase diagram prototype (Fig. 2a–b) and the real Cu–Mn–Ni system (Fig. 2c–d) is shown in Fig. 2. This surface divides the L + B + B1 phase region into two parts, in its “upper” part, the peritectic reaction  $L + B \rightarrow B1$  occurs, in the “bottom” part metatectic reaction  $B \rightarrow L + B1$  takes place (Fig. 2b, d). This process is clearly demonstrated by the diagrams of vertical mass balance (Fig. 2e–f). For the prototype, the mass centre is designated as  $G_1$ , for a real system it is designated as  $G_2$ . For both mass centres in the three-phase region L + B + B1, the B1 phase portion first increases and the L and B phase portions decrease, which corresponds to the peritectic reaction  $L + B \rightarrow B1$ . At 501.6 °C (Fig. 2e) and 1130.71 °C (Fig. 2f), the change of mass increment sign of the L phase occurs, i.e., the decrease in the L phase portion stops and its growth begins, which already corresponds to the metatectic reaction  $B \rightarrow L+B1$ .

Concentration projection of the three-phase region L + B + B1, including the surface of the change of the three-phase reaction type abc, is divided into six fields, four of which differ in ongoing phase transformations and microstructure elements (Fig. 3, Table. 4). Fields 2, 3, and 6 are characterised by the

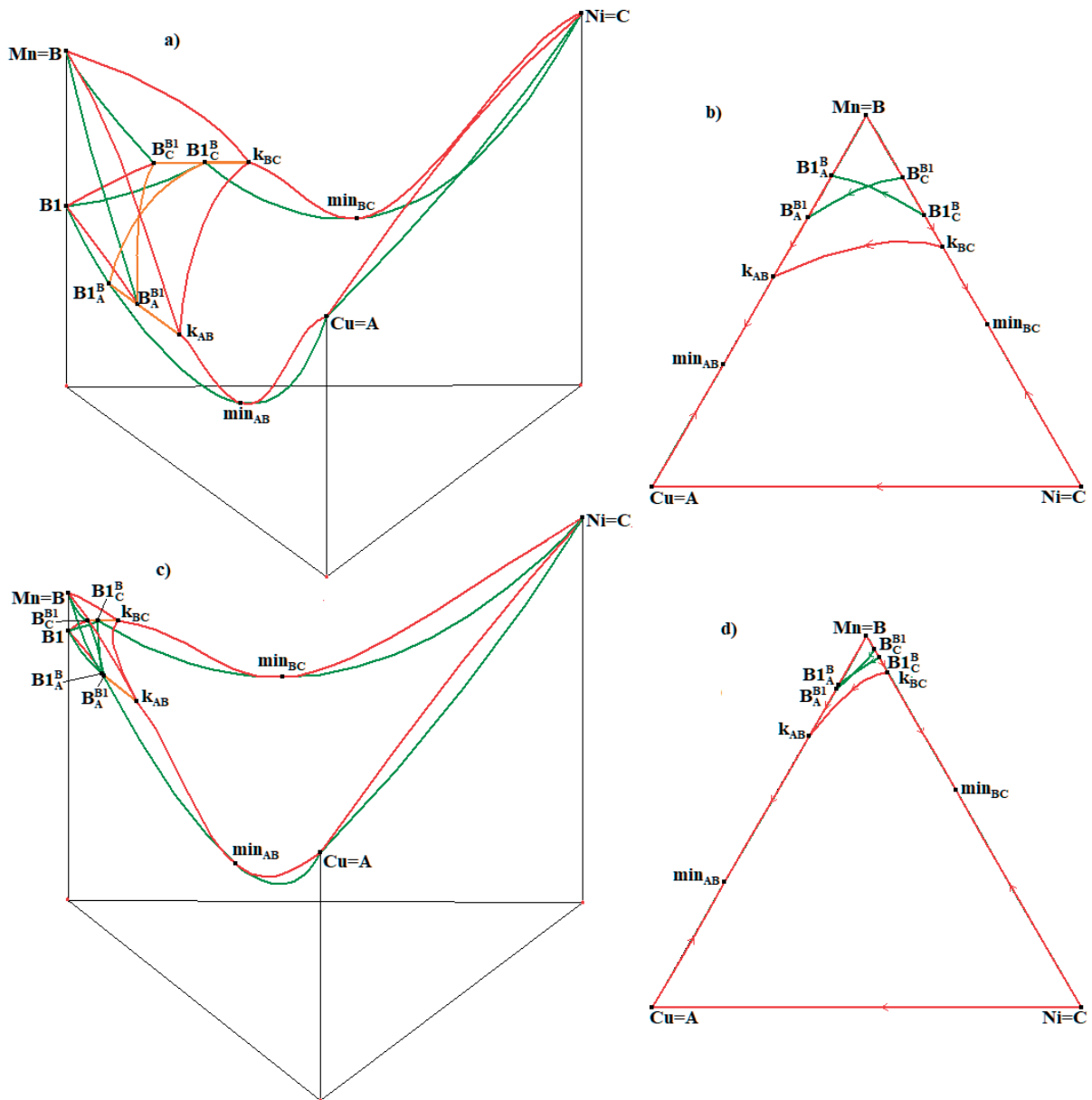
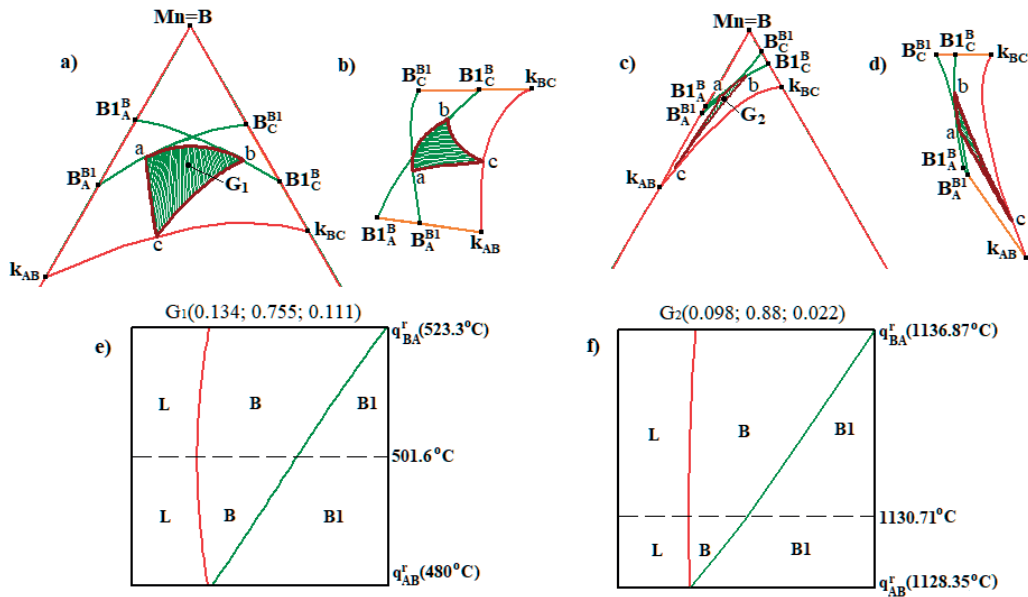


Fig. 1. 3D model and XY projection of the prototype (a–b) and the real Cu–Mn–Ni diagram (c–d)

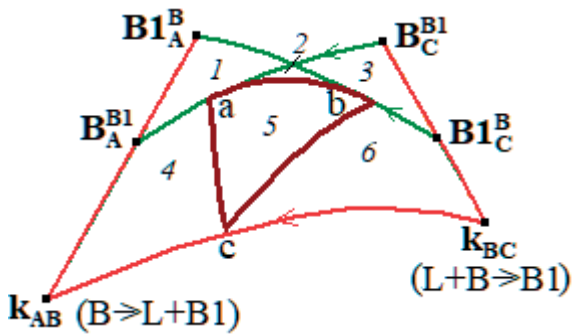
Table 4 Microstructure formed in the three-phase region L + B + B1\*

Field	Phase regions	Scheme of phase reactions	Microstructure
1	L + B(TP)	$L^1 \rightarrow B^1$ ,	$B^1$ ,
	B		
	B + B1	$B^1 \rightarrow B1^{1p}$ ,	$B1^{1p}$ ,
2, 3, 6	L + B(TP)	$L^1 \rightarrow B^1$ ,	$B^1$ ,
	L + B + B1	$L^p + B \rightarrow B1^p$	$B1^p$
	L + B + B1	$B^m \rightarrow L^m + B1^m$	$B1^m$
4	L + B(TP)	$L^1 \rightarrow B^1$ ,	$B^1$ ,
	L + B + B1	$B^m \rightarrow L^m + B1^m$	$B1^m$
	L + B(TP)	$L^1 \rightarrow B^1$ ,	$B^1$ ,
5	L + B + B1	$L^p + B \rightarrow B1^p$	$B1^p$ ,
	L + B + B1	$B^m \rightarrow L^m + B1^m$	$B1^m$

\* 1 – primary crystallisation, <sup>1p</sup> – primary postperitectic crystallisation, <sup>p</sup> – peritectic reaction, <sup>m</sup> – metatectic reaction



**Fig. 2.** XY projection and 3D model of the change surface of three-phase transformation type in the phase region L + B + B1 for the prototype (a–b) and the real system (c–d); calculation of the diagrams of vertical mass balances for mass centres G1(e) and G2(f)



**Fig. 3.** Projection of three-phase region L + B + B1 with division into concentration fields

formation of primary crystals  $B^1$  and crystals  $B1^p$ , resulting from the peritectic reaction. Fields 1 and 4 contain primary crystals  $B^1$  and crystals  $B1^m$  released as a result of a metatectic reaction. However, since these two fields differ in crystallisation stages, field 1 additionally includes primary crystals  $B1^{1p}$ . Field 5 besides  $B^1$ , includes microstructures such as  $B1^p$ , and  $B1^m$ , since it is the surface on which the change of the three-phase reaction type takes place.

### 3.2. Calculation of isothermal sections

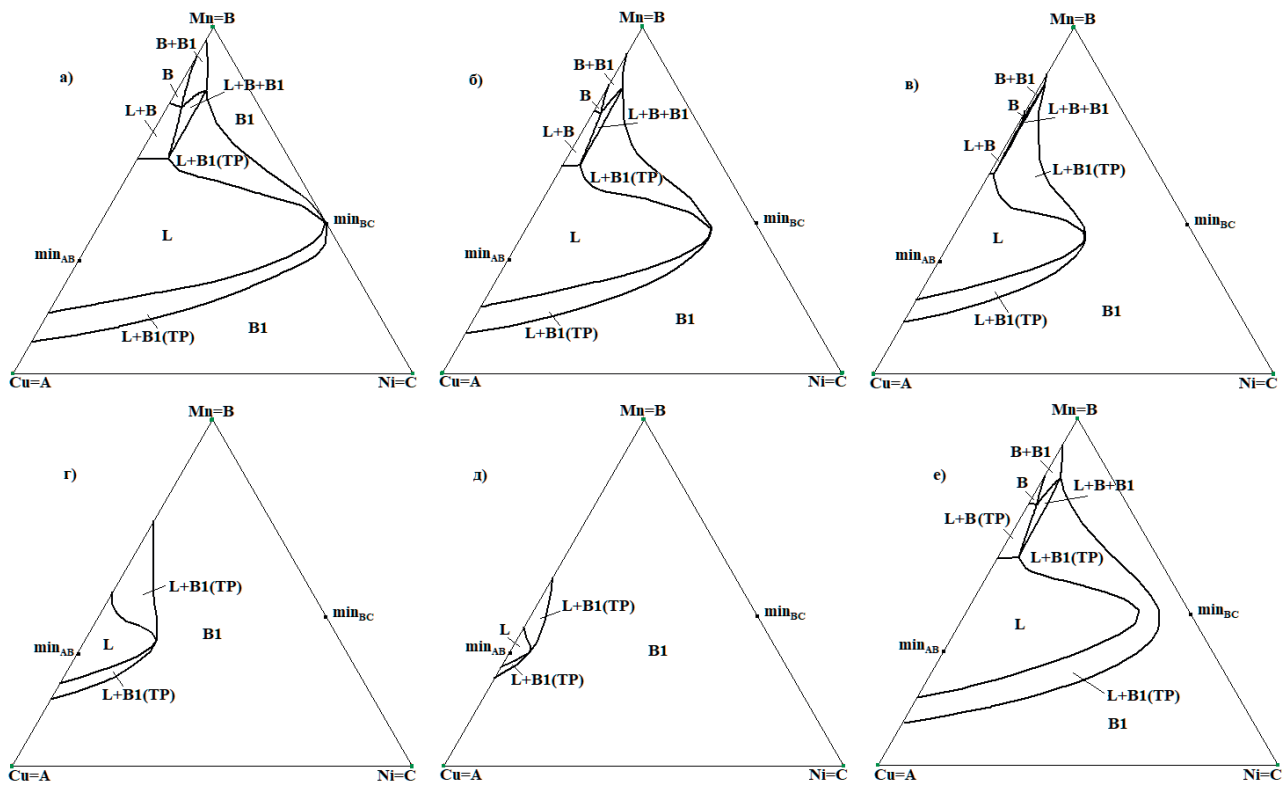
Calculation of isothermal sections based on the prototype in the temperature range between two minimum points  $min_{AB}$  and  $min_{BC}$  is shown in Fig. 4. On the section coinciding with the temperature of the minimum point  $min_{BC}$  (Fig. 4a),

the liquidus and solidus isotherms adjoin at this point. As the temperature decreases, the liquidus and solidus isotherms gradually approach the minimum  $min_{AB}$ . Since the model was constructed taking into account the zero crystallisation interval, there is contact between isotherms along the  $min_{AB}min_{BC}$  line (Fig. 4b–e). The point of contact of the liquidus and solidus isotherms is a common boundary between the one-phase regions L and B1 and two fragments of the two-phase region L + B1(SS). At minimum temperature  $min_{AB}$  the isotherms merge into a point, and only one phase B1 remains in the section.

Since the question of the crystallisation interval along the line connecting the minimum points remains controversial, an additional model of the phase diagram of the Cu–Mn–Ni system was developed with a non-zero value of the crystallisation interval along the  $min_{AB}min_{BC}$  line. An isothermal section for such a variant of the diagram is shown in Fig. 4e. In this case, the one-phase regions corresponding to the melt L and the solid phase B1 are separated by a two-phase region L+B1(SS).

## 4. Conclusions

A computer model of the phase diagram of the Cu–Mn–Ni system above 800 °C has been developed. The high-temperature part of



**Fig. 4.** Isothermal sections for the phase diagram prototype with zero crystallisation interval along the line  $\min_{AB}\min_{BC}$  at  $T_{\min_{BC}} = 450$  °C (a), 414 °C (b), 376 °C (c), 338 °C (d), 310 °C (e); isothermal section at 414 °C in the presence of crystallisation interval (f)

the diagram includes 9 surfaces and 6 phase regions. It was revealed that in the three-phase region  $L+B+B1$  there is a change from peritectic equilibrium to monotectic equilibrium, which was confirmed by the calculation of material balance diagrams. Three-phase region, taking into account the surface of type change of three-phase reaction, is divided into six concentration fields when projecting into the composition triangle. Four concentration fields differ in the crystallisation stages and the formed set of microstructures. Based on the prototype of the phase diagram, the calculation of isothermal sections in the temperature range between two minimum points in the Cu–Mn and Mn–Ni binary systems was carried out. Taking into account the crystallisation interval in the sections, the two-phase region  $L+B1(SS)$  separates the one-phase regions  $L$  and  $B1$ . At a zero crystallisation interval along the line connecting the minimum points, a point of contact of the liquidus and solidus isotherms appears on the sections. At this point, the one-phase regions  $L$  and  $B1$  and two parts of the two-phase region  $L+B1(SS)$  are in contact.

The spatial computer model allowed us to obtain a solution to the problem, which cannot be achieved using thermodynamic calculations and calculations based on first principles. The presented methodology can also be applied to other systems with Mn, where the effect of a change of the type of phase reaction in the three-phase region with two high-temperature modifications of Mn can be revealed [41–44].

#### Author contributions

All authors made an equivalent contribution to the preparation of the publication.

#### Conflict of interests

The authors declare that they have no known competing financial interests or personal relationships that could have influenced the work reported in this paper.

#### References

1. Akash K., Mani Prabu S. S., Gustmann T., Jayachandran S., Pauly S., Palani I. A. Enhancing the life cycle behaviour of Cu–Al–Ni shape memory alloy bimorph by Mn addition. *Materials Letters*. 2018;226: 55–58. <https://doi.org/10.1016/j.matlet.2018.05.008>

2. Gera D., Santos J., Kiminami C. S., Gargarella P. Comparison of Cu–Al–Ni–Mn–Zr shape memory alloy prepared by selective laser melting and conventional powder metallurgy. *Transactions of Nonferrous Metals Society of China*. 2020;30(12): 3322–3332. [https://doi.org/10.1016/S1003-6326\(20\)65464-4](https://doi.org/10.1016/S1003-6326(20)65464-4)
3. Kang H., Yang Z., Yang X., Li J., He W., Chen Z., Guo E., Zhao L.-D., Wang T. Preparing bulk Cu–Ni–Mn based thermoelectric alloys and synergistically improving their thermoelectric and mechanical properties using nanotwins and nanoprecipitates. *Materials Today Physics*. 2021;17: 100332. <https://doi.org/10.1016/j.mtphys.2020.100332>
4. *Binary alloy phase diagrams*. Vol. 1. Massalski T. B. (ed.). Ohio: American Society for Metals, Metals Park; 1986. 1100 p.
5. *State diagrams of binary metal systems\**. Vol. 2. Ljakishev N. P. (ed.). Moscow: Mashinostroenie Publ.; 1997. 1024 p. (In Russ.)
6. Hellawell A., Hume-Rothery W. The construction of alloys of iron and manganese with transition elements of the first long period. *Philosophical Transactions of the Royal Society of London. Series A, Mathematical and Physical Sciences*. 1957;249: 417–459. <http://doi.org/10.1098/rsta.1957.0004>
7. Wachtel E., Terzieff P., Bahle J. Aufbau und magnetische Eigenschaften manganreicher Cu–Mn– und Mn–Sn–Legierungen. *Monatshefte für Chemie*. 1986;117(12): 1349–1366. <http://doi.org/10.1007/bf00810745>
8. Kaufman L. Coupled phase diagrams and thermochemical data for transition metal binary systems-VI. *Calphad*. 1979;3(1): 45–76. [https://doi.org/10.1016/0364-5916\(79\)90020-8](https://doi.org/10.1016/0364-5916(79)90020-8)
9. Lewin K., Sichen D., Seetharaman S. Thermodynamic study of the Cu–Mn system. *Scandinavian Journal of Metallurgy*. 1993;22(6): 310–316. Available at: [https://www.researchgate.net/publication/262068679\\_Thermodynamic\\_study\\_of\\_the\\_Cu-Mn\\_system](https://www.researchgate.net/publication/262068679_Thermodynamic_study_of_the_Cu-Mn_system)
10. Miettinen J. Thermodynamic description of the Cu–Mn–Zn system in the copper-rich corner. *Calphad*. 2004;28(3): 313–320. <https://doi.org/10.1016/j.calphad.2004.09.003>
11. Turchanin M. A., Agraval P. G., Abdulov A. R. Phase equilibria and thermodynamics of binary copper systems with 3d-metals. IV. Copper – Manganese system. *Powder Metallurgy and Metal Ceramics*. 2006;45(11–12): 569–581. <https://doi.org/10.1007/s11106-006-0121-y>
12. Wang C. P., Liu X. J., Ohnuma I., Kainuma R., Ishida K. Thermodynamic assessments of the Cu–Mn–X (X: Fe, Co) systems. *Journal of Alloys and Compounds*. 2007;438(1–2): 129–141. <https://doi.org/10.1016/j.jallcom.2006.08.018>
13. He C., Du Y., Chen H.-L., Liu S., Xu H., Ouyang Y., Liu Z.-K. Thermodynamic modeling of the Cu–Mn system supported by key experiments. *Journal of Alloys and Compounds*. 2008;457(1–2): 233–238. <https://doi.org/10.1016/j.jallcom.2007.03.041>
14. Cui S., Jung I.-H. Thermodynamic modeling of the Cu–Fe–Cr and Cu–Fe–Mn systems. *Calphad*. 2017;56: 241–259. <https://doi.org/10.1016/j.calphad.2017.01.004>
15. *Binary alloy phase diagrams*. Vol. 2. Massalski T. B. (ed.). Ohio: American Society for Metals, Metals Park; 1986. 2224 p.
16. Gokcen N. A. The Mn–Ni (manganese-nickel) system. *Journal of Phase Equilibria*. 1991;12(3): 313–321. <https://doi.org/10.1007/BF02649919>
17. Miettinen J. Thermodynamic solution phase data for binary Mn–based systems. *Calphad*. 2001;25(1): 43–58. [https://doi.org/10.1016/S0364-5916\(01\)00029-3](https://doi.org/10.1016/S0364-5916(01)00029-3)
18. Guo C., Du Z. Thermodynamic optimization of the Mn–Ni system. *Intermetallics*. 2005;13(5): 525–534. <https://doi.org/10.1016/j.intermet.2004.09.002>
19. an Mey S. Thermodynamic re-evaluation of the Cu–Ni system. *Calphad*. 1992;16(3): 255–260. [https://doi.org/10.1016/0364-5916\(92\)90022-P](https://doi.org/10.1016/0364-5916(92)90022-P)
20. Turchanin M. A., Agraval P. G., Abdulov A. R. Phase equilibria and thermodynamics of binary copper systems with 3d-metals. VI. Copper-nickel system. *Powder Metallurgy and Metal Ceramics*. 2007;46: 467–477. <https://doi.org/10.1007/s11106-007-0073-x>
21. Tesfaye F., Vaajamo I., Hamuyuni J., Lindberg D., Taskinen P., Hupa L. Experimental investigation and thermodynamic re-assessment of the ternary copper-nickel-lead system. *Calphad*. 2018;61: 148–156. <https://doi.org/10.1016/j.calphad.2018.03.006>
22. Parravano N. Alloys of nickel, manganese, and copper. *Gazzetta Chimica Italiana*. 1913;42: 385–394.
23. Parravano N. Ternary alloys of iron-nickel-manganese, nickel-manganese-copper, and iron-manganese-copper. *Intern. Z. Metallog.* 1913;4: 171–202.
24. Anosov V. Ja., Pogodin S. A. *Fundamentals of physical and chemical analysis*. Moscow: Nauka Publ.; 1976. 504 p. (In Russ.)
25. Sun W., Xu H., Du Y., Liu S., Chen H., Zhang L., Huang B.-Y. Experimental investigation and thermodynamic modeling of the Cu–Mn–Ni system. *Calphad*. 2009;33(4): 642–649. <https://doi.org/10.1016/j.calphad.2009.07.003>
26. Pikunov M. V., Sidorov E. V. Phase diagrams of three-component systems corresponding to unbounded solid solutions with a temperature extremum. *Steel in Translation*. 2008;38(1): 1–4. <https://doi.org/10.3103/S0967091208010014>
27. Palatnik L. S., Landau A. I. *Phase Equilibria in Multicomponent Phase Diagrams*. New York: Holt Rinehart and Winston, Inc.; 1964. 454 p.
28. Petrov D. A. *Binary and ternary systems*. Moscow: Metallurgija Publ.; 1986. 256 p. (In Russ.)
29. Pikunov M. V., Sidorov E. V. Structure of the phase diagram of the Cu–Ni–Mn system. *Steel in*

*Translation*. 2008;38(5): 351–354. <https://doi.org/10.3103/S096709120805001X>

30. Bazhenov V. E., Pikunov M. V. Temperature-minimum line in the Cu–Ni–Mn phase diagram. *Steel in Translation*. 2010;40(3): 225–228. <https://doi.org/10.3103/S0967091210030071>

31. Pashkov A. I. *Research and development of technology for obtaining alloys of the Cu–Mn–Ni system by mechanical alloying for high-temperature soldering\**. Cand. tech. sci. diss. Abstr. Moscow: 2009. 28 p. (In Russ.). Available at: <https://www.dissercat.com/content/issledovanie-i-razrabotka-tekhnologii-polucheniya-splavov-sistemy-cu-mn-ni-metodom-mekhanich>

32. Bazhenov V. E. *The study of crystallization processes of ternary alloys in order to assess their tendency to non-equilibrium crystallization\**. Cand. tech. sci. diss. Abstr. Moscow: 2013. 25 p. (In Russ.). Available at: <https://www.dissercat.com/content/izuchenie-kristallizatsionnykh-protsesov-troinykh-splavov-tselyu-otsenki-ikh-sklonnosti-k>

33. Bazhenov E. V. On the Cu–Ni–Mn system state diagram. *Izvestiya Vuzov. Tsvetnaya Metallurgiya = Izvestiya. Non-Ferrous Metallurgy*. 2013;(1): 49–55. (In Russ., abstract in Eng.). <https://doi.org/10.17073/0021-3438-2013-1-49-55>

34. Miettinen J. Thermodynamic description of the Cu–Mn–Ni system at the Cu–Ni side. *Calphad*. 2003;27(2): 147–152. <https://doi.org/10.1016/j.calphad.2003.08.003>

35. Turchanin M. A., Velikanova T. Y., Agraval P. G., Abdulov A. R., Dreval' L. A. Thermodynamic assessment of the Cu–Ti–Zr system. III. Cu–Ti–Zr system. *Powder Metallurgy and Metal Ceramics*. 2008;47: 586–606. <https://doi.org/10.1007/s11106-008-9062-y>

36. Ivanchenko V. G., Pryadko T. V., Gavrylenko I. S., Pogorelaya V. V. Phase equilibria in the Ti–TiMn<sub>2</sub>–ZrMn<sub>2</sub>–Zr partial system. *Chemistry of Metals and Alloys*. 2008;1: 67–72. <https://doi.org/10.30970/cma1.0004>

37. Lutsyk V. I., Zelenaya A. E., Zyryanov A. M. Multicomponent systems simulation by the software of “Diagrams Designer”. *Journal of International Scientific Publications: Materials, Methods & Technologies*. 2008;2: 176–184. Available at: <https://www.scientific-publications.net/download/materials-methods-and-technologies-2008.pdf>

38. Vorob'eva V. P., Zelenaya A. E., Lutsyk V. I., Lamueva M. V. A 3D computer model of the CaO–MgO–Al<sub>2</sub>O<sub>3</sub> T-x-y diagram at temperatures above 1300 °C. *Condensed Matter and Interphases*. 2021;23(3): 380–386. <https://doi.org/10.17308/kcmf.2021.23/3529>

39. Lutsyk V. I., Vorob'eva V. P. Investigation of the conditions for changing the type of three-phase transformation in the Ti–Ir–Ru system. *Perspektivnye materialy = Perspective materials*. 2011;(S13): 191–198. (In Russ., abstract in Eng.). Available at: <https://elibrary.ru/item.asp?id=17635587>

40. Lutsyk V. I., Zelenaya A. E., Zyryanov A. M. Specific features of the crystallization of melts in systems with a transition from syntectic equilibrium to monotectic equilibrium. *Crystallography Reports*. 2009;54(7): 1300–1307. <https://doi.org/10.1134/S1063774509070281>

41. Kainzbauer P., Richter K. W., Effenberger H. S., Giester G., Ipseret H. The ternary Bi–Mn–Sb phase diagram and the crystal structure of the ternary\* phase Bi<sub>0.8</sub>MnSb<sub>0.2</sub>. *Journal of Phase Equilibria and Diffusion*. 2019;40: 462–481. <https://doi.org/10.1007/s11669-019-00719-x>

42. Florian G., Gabor A. R., Nicolae C. A.... Rotaru P. Thermomechanical, calorimetric and magnetic properties of a Ni–Ti shape-memory alloy wire. *Journal of Thermal Analysis and Calorimetry*. 2020;140(2): 147–527. <https://doi.org/10.1007/s10973-019-08869-3>

43. Li H., Ruan J., Ueshima N., Oikawa K. Experimental investigations of fcc/bcc phase equilibria in the Cr–Mn–Ni ternary system. *Intermetallics*. 2020;127: 106994. <https://doi.org/10.1016/j.intermet.2020.106994>

44. Ruan J., Ueshima N., Li H., Oikawa K. Phase equilibria, martensitic transformations and deformation behaviors of the subsystem of Cantor alloy-low-cost Fe–Mn–Cr alloys. *Materialia*. 2021;20: 101231. <https://doi.org/10.1016/j.mtla.2021.101231>

\* Translated by author of the article.

## Information about the authors

*Anna E. Zelenaya*, Cand. Sci. (Phys.–Math.), Senior Researcher of the Sector of Computer Materials Design, Institute of Physical Materials Science, Siberian Branch of the Russian Academy of Sciences (Ulan-Ude, Russian Federation).

<https://orcid.org/0000-0001-5232-8567>  
zel\_ann@mail.ru

*Vasily I. Lutsyk*, Dr. Sci. (Chem.), Head of the Sector of Computer Materials Design, Institute of Physical Materials Science, Siberian Branch of the Russian Academy of Sciences (Ulan-Ude, Russian Federation).

<https://orcid.org/0000-0002-6175-0329>  
vluts@ipms.bsnet.ru

*Viktor D. Baldanov*, post-graduate student of the Sector of Computer Materials Design, Institute of Physical Materials Science, Siberian Branch of the Russian Academy of Sciences (Ulan-Ude, Russian Federation).

<https://orcid.org/0000-0002-3946-9565>  
victor\_baldanov@mail.ru

Received 08.06.2022; approved after reviewing 12.07.2022; accepted for publication 15.09.2022; published online 25.12.2022.

Translated by Valentina Mittova

Edited and proofread by Simon Cox



# Condensed Matter and Interphases

Kondensirovannye Sredy i Mezhfaznye Granitsy  
<https://journals.vsu.ru/kcmf/>

## Original articles

Research article

<https://doi.org/10.17308/kcmf.2022.24/10552>

## Migration of an incommensurate intercrystalline boundary and boundary self-diffusion

V. G. Kul'kov✉

*Volzhs Branch of Moscow Power Engineering Institute,  
69 Lenina prospect, Volzhsky 404101, Russian Federation*

### Abstract

Most grain boundaries found in polycrystalline metals are not special. The angle of their mutual disorientation is an arbitrary value, and the axis of rotation is arbitrarily oriented to the plane of the boundary. Periodic atomic structures such as lattices of coincident nodes, alternating polyhedra, and others do not arise within such boundaries. They are called boundaries of a general type, non-special, arbitrary, or incommensurate. The general theory of relaxation processes at such boundaries has not yet been sufficiently developed. The aim of the study was the development of the model of migration of an incommensurate intercrystalline boundary at the atomic level and the description of the process of self-diffusion along it.

A circle called the main region is described around each boundary lattice node of one of the crystallites. If there is an atom in the node, then an atom of another crystallite is excluded from entering it. In the case of a vacant node in the main region, such an atom can be located. An atom in a planar picture means an atomic series in the three-dimensional case. The distribution of vacant nodes of the growing crystallite is uniform over the flat reduced main region. The migration mechanism involves the implementation of the following main processes: local rearrangement of atomic configurations and self-diffusion of atoms in the transverse direction of the slope axis.

The characteristic times of these processes and the expression for the migration rate were found. The migrating boundary contains a large number of delocalised vacancies. This leads to the high diffusion mobility of atoms. Most vacancies in the boundary are not of thermal origin, but are determined only by the geometric atomic structure of the boundary. In this case, the expression for the boundary self-diffusion coefficient does not contain a multiplier depending on the activation energy of vacancy formation. This leads to the fact that the coefficient of self-diffusion along the migrating boundary is significantly higher than in the stationary boundary. The model of an incommensurate boundary allows us to describe its migration and calculate the self-diffusion coefficient.

**Keywords:** Incommensurate intercrystalline boundaries, Delocalised vacancies, Boundary self-diffusion, Migration mobility

**For citation:** Kul'kov V. G. Migration of an incommensurate intercrystalline boundary and boundary self-diffusion. *Condensed Matter and Interphases*. 2022;24(4): 475–482. <https://doi.org/10.17308/kcmf.2022.24/10552>

**Для цитирования:** Кульков В. Г. Миграция несоизмерной межкристаллитной границы и граничная самодиффузия. *Конденсированные среды и межфазные границы*. 2022;24(4): 475–482. <https://doi.org/10.17308/kcmf.2022.24/10552>

✉ Viktor G. Kul'kov, e-mail: [vikulkov@yandex.ru](mailto:vikulkov@yandex.ru)

© Kul'kov V. G., 2022



The content is available under Creative Commons Attribution 4.0 License.



## 1. Introduction

A large number of various models have been proposed to describe the atomic structure of intercrystalline boundaries in metals and relaxation processes involving them. Among them there is a special class of boundaries. They separate two crystallites mutually rotated for angle at which a lattice of coinciding nodes, common to them, is formed. The atomic structure of such boundaries has a semblance of a crystal structure and is characterised by periodicity. Small deviations from the special misorientation of crystallites are provided by the introduction of grain boundary dislocations. The theory of special boundaries is well developed. However, among the boundaries actually existing in polycrystalline materials, their number is low and, according to various estimates, is approximately one tenth. A significant proportion of boundaries do not correspond to special misorientations. Their atomic structure is formed by conjugation of two surfaces with rational Miller indices whose translation periods in one or two directions are incommensurable, such as, for example,  $\sqrt{2}$  and 1. This means that the lengths of such segments cannot be expressed as rational numbers when measured with a ruler with a one scale bar. The imposition of such surfaces excludes the possibility of the appearance of periodic structures in the boundary. Similar structures also appear when noncrystallographic planes of adjacent lattices with Miller indices, some of which are irrational numbers, are conjugated. Grain boundaries of this type are called arbitrary, ordinary, non-special, or incommensurate.

The model of the atomic structure of an incommensurate intercrystalline boundary was successfully used to describe structural rearrangements in the process of intergranular slippage [1]. According to this model, rearrangements of atomic configurations in the near-boundary region occur in the effective potential field that exists in this region and is created by the totality of all near-boundary atoms. The characteristic of the position of each atom is a scalar or vector value, called the mismatch parameter (distance), which uniquely determines its geometric and energy state. It determines the position of each atom of one of the two connecting crystallites with respect to the coordinate system of the other. A somewhat different parameter was introduced to describe the

change in the atomic structure of grain boundaries in aluminium and is called the order parameter [2]. For atoms with certain regions of variation of the mismatch parameters, double-well energy configurations with different pit depths are formed in the boundary. The elementary act of sliding is the jump of an atom from one pit to an adjacent deeper pit. The dimensions of such regions depend on the structure of the boundary and the magnitude of the stresses acting in it. The resulting rate of the process is determined by the size of the regions, the value of the activation barrier, and the density of states. Accounting for these factors for boundaries with different types of incommensurability leads to different types of functional relationship between the slip rate and the magnitude of the applied stresses [3]. The development of ideas about incommensurate structures allowed possible to describe not only their energy [4], but also many grain-boundary processes, such as the formation of point defects, heat capacity, the role of boundaries as sources of vacancies, and internal friction [5, 6]. Incommensurate boundaries were studied by high resolution electron microscopy [7–11] and computer simulation [12, 13]. Boundaries of this type are also widespread in nanocrystalline materials [10, 14]. There is evidence [15] that the presence of incommensurability at the interface between the sample and the film deposited on its surface significantly affects its antioxidant properties. The ideas about relationship between the tribological properties of samples and the structure of surface layers have become widespread. The relationship between microstructure and friction allows not only to estimate the lowest possible coefficient of friction between pure metals and alloys, but also suggests the possibility of creating materials with a low coefficient of friction using grain boundary technology. The connection between the mechanisms of interfacial deformation and friction modes can also be interpreted in an atomistic sense using the concept of commensurate and incommensurable interfaces [16].

An attempt to describe the mechanism of boundary migration was proposed in [17]. Under conditions of boundary displacement along its normal, the introduction of the third component of the discrepancy parameter vector is required. In the general case, it is defined as the radius vector of an atom of one grain in the coordinate system associated with the unit cell of the potential relief

of another grain. The presence of an effective thermodynamic migration force means an increased free energy of the atoms of one of the grains compared to the atoms of the neighbouring grain. Relaxation in such a system leads to a shift of the interface towards an energetically favourable position, and the growth of one grain at the expense of another. The model predicts a functional dependence of the migration rate on the effective thermodynamic force of a power form with exponents varying from 1 to 3. Such an effect was repeatedly observed in the experiment [18, 19]. There is currently no general microscopic theory of such a relaxation process as boundary migration. The purpose of this study was the development of the ideas of [17] and development of the model for the migration of an incommensurate intercrystalline slope boundary at the atomic level and a description of self-diffusion processes.

## 2. Migration model of slope boundary

Let us determine the atomic structure of the unrelaxed slope boundary. For this, consider the geometric picture of the imposition of two identical simple cubic lattices, mutually deployed at a non-special angle. The result of the overlay is shown in Fig. 1. The light and dark nodes denote the projections of the atomic rows of the lattices. For plotting a straight line, which is a trace of the boundary plane, it is necessary to leave nodes of only one colour on different sides. Around each such node located near the boundary, a sphere of radius equal to the interatomic distance is drawn as from the centre. Circles which are sections of these spheres by the plane of the figure are shown in Fig. 1. Any other atom cannot enter them according to the hard sphere model. The boundary atom located in the centre, can move to the darkened area

of the circle, where there are no restrictions from neighbouring circles, if there are vacant positions in this part. By analogy with [17], the interior of the darkened part of the circle is the main region. The coordinate axes  $x$  and  $y$ , slope axis  $z$  normal to them and to the plane of the figure are shown in Fig. a. The slope axis has the symbol  $[001]$  in all lattices. The slope boundary separates two crystallites with different lattice orientations, mutually rotated to the arbitrary angle relative to the axis  $z$ . Nodes of crystallite 2 are shown as black dots. It is believed that they are all filled with atoms, with the exception of nodes in the main regions. The nodes within each main regions are empty and serve as possible places to be filled with atoms. In this case, the lattice of the second crystallite is completed at the expense of the atoms of the first one, and the entire boundary shifts upwards in Fig. 1.

The presence of an effective migration driving force means that each atom of the first crystallite has an excess of energy  $W$  compared to the atoms of the second crystallite. The incorporation of the atom in an empty node in the main region leads to the dissipation of excess of energy. As can be seen from Fig. 1, the presence of empty nodes in the main region in the amount of 0, 1, and 2, indicated by the corresponding numbers, is possible. The size of the main region does not allow placing more nodes in it. If all the main regions are transferred along the boundary and combined with one of the boundaries, then we reach the concept of a reduced region [3, 17]. In the reduced region the position of each empty node can be marked and the density of their distribution can be considered. Incommensurate structures are characterised by uniform geometric distribution of nodes in the reduced main region [1]. Each empty node in the main region can be filled with

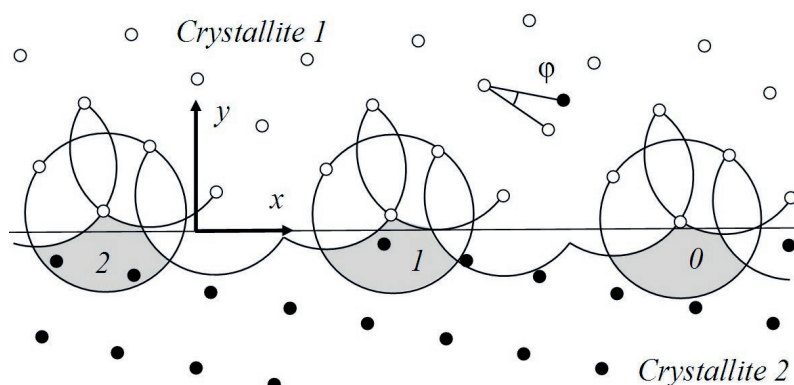


Fig. 1. The picture of the overlapping nodes of the two lattices and the main regions

only one atomic row, its position is unique and serves as the label for this row. Its coordinates are completely similar to the discrepancy parameter introduced earlier for incommensurate structures. The real arrangement of atomic rows due to the relaxation of the structure will differ somewhat from the position of the nodes. However, these nodes determine the most important characteristics of atomic series, such as the activation energy of the transition and the energy in the final arrangement. The thick line in Fig. 2 shows the reduced main region corresponding to the boundary shown in Fig. 1. If one of the nodes of the lattice of the second crystallite falls into the *A* zone, then another node falls into the *A'* zone. The boundaries of the zones are connected by the translation operation for the lattice period of the second crystallite. Only one node can be located in *B* zone. If there are no nodes in the main region, then one of the lattice nodes must necessarily fall into the *C* zone adjacent to the main region. The plotting of the *C* zone is of an auxiliary nature, since its nodes cannot be filled during the migration process. Thus, if the lattice node of the second crystallite falls into one of the zones *A*, *B*, or *C*, then the main region contains 2, 1, or 0 nodes, respectively. Areas of the *A*, *A'*, and *C* zones equal to each other  $S_0 = S_2$ . The areas of the *A*, *B*, and *C* zones are designated as  $S_2$ ,  $S_1$ , and  $S_0$  with an index indicating the number of nodes. The probabilities of the location of nodes in them is  $w_i = S_i/S$ , where  $S = S_0 + S_1 + S_2 = 2S_0 + S_1$  is the total area of the reduced main region.

If the main region contains only one site, then the filling of the vacant row occurs by a thermally activated transition of the atomic row of the first crystallite located at the top of the region, overcoming a barrier equal on average to  $W_1$ . The presence of a barrier is determined by the need to break the bonds of atoms with their immediate neighbours from their crystallite. The transition

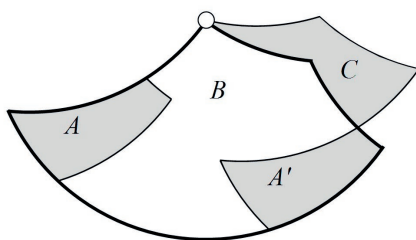


Fig. 2. The reduced main region of the slope boundary

of the atomic series is a conservative process. It is carried out according to a mechanism similar to a dislocation slip through the formation and propagation of double inflections. The transition time [20] is  $\tau_1 = (c_k v_k)^{-1}$ , where  $c_k = 2a^{-1} \exp(-W_k/kT)$  is the concentration of inflections,  $v_k$  is their lateral propagation velocity. This value can be found using the Einstein relation  $v_k = D_k F_k / kT$ , if we take into account that the force affects the inflection  $F_k = Wh/a^2$ , and their diffusion coefficient is  $D_k = v_0 a^2 \exp(-W_{mk}/kT)$ . Here  $W_k$  and  $W_{mk}$  are the energy of formation and migration of the inflection,  $h$  is its width, equal to the row shift distance,  $v_0$  is the Debye frequency of vibrations of the atom,  $k$  is the Boltzmann constant;  $T$  is the thermodynamic temperature,  $W$  is the energy difference between atoms in crystallites 1 and 2. From here it follows that:

$$\tau_1 = \frac{akT}{2v_0Wh} \exp\left(\frac{W_k + W_{mk}}{kT}\right). \quad (1)$$

The inflection energy can be determined [20] from the expression  $W_k = 2a\sqrt{2U_p U_0}/\pi$ , where  $U_p = W_1/a$  is the Peierls energy for a unit length of an atomic series,  $W_1$  is the activation energy of an atom jump to a new position, previously introduced as the barrier value,  $U_0$  is the energy of the unit length of the series. This value can be found by considering the row in the inflection region to be stretched by  $(l_k^2 + h^2)^{1/2} - l_k$ . Then  $W_k = h^2 \sqrt{\lambda W_1} / \pi l_k$ . Here  $l_k$  is the length of the inflection,  $\lambda$  is the stiffness coefficient of the interatomic bond.

In the same way, one of the two nodes that fell into the main region is built up. The second of them is built up by the atoms of the first crystallite from another main region with missing vacant node. This requires the diffusion movement of atoms over a distance between the main regions containing 2 and 0 nodes.

Here we consider the case of sufficiently large values of the migration driving forces. In this case, the process involves all boundary atoms located on one side of the boundary in a layer with a thickness of the order of the lattice period  $a$ . We call such atomic rows “active”. Their number per unit length of the boundary is  $N_1 = a^{-1}$ . The distribution density of nodes in the reduced area per unit length of the boundary is then equal to  $\rho = a^{-3}$ . The number of active atomic

rows with two vacant sites in the main region is  $N_2 = \rho w_2 S$ . There is the same number of active atomic rows with main regions without nodes. The atoms of the first crystallite from the regions of the last type pass into the main regions with two vacant sites and complete one of them. In the two-dimensional problem, the nodes in the main domain correspond to their rows in the real boundary along  $z$ . The average distance passed by such atoms along the boundary is:

$$l = \frac{1}{2N_2} = \frac{a^3}{2w_2 S}. \quad (2)$$

The transition of atoms occurs by diffusion. Transition time:

$$\tau_2 = l / uF, \quad (3)$$

where  $u = D/kT$  is the mobility of atoms,  $D$  is the coefficient of grain boundary diffusion,  $F$  is the force required to move atoms from the source to the drain along the boundary. For the driving force of diffusion, we can take the expression  $F = W/l$ . From formulas (2) and (3), we obtain the transition time:

$$\tau_2 = \left( \frac{a^3}{2w_2 S} \right)^2 \frac{kT}{DW}. \quad (4)$$

Estimates show that  $\tau_2 \gg \tau_1$ , therefore the boundary migration rate is limited by diffusion processes in the boundary.

The migrating boundary absorbs vacancies, some of which are redistributed in it and participate in diffusion processes, and some leave the boundary, remaining in a new crystallite. Taking into account that the main regions are densely located at the boundary, it can be assumed that all vacancies are absorbed by only the three types of the described main regions. A vacancy absorbed by an atom that is the centre of the main region of the  $A$  type, creates three vacant nodes in it. One of them refers to the absorbed atom of the first crystallite, the other two are located at the sites of the second crystallite. It should be noted that before the vacancy was absorbed, there were no vacancies in this region. A vacancy in the boundary is the lattice node in which an atom can be located without the occurrence of a high-energy configuration associated with the displacement of other atoms from their positions. The nodes that were originally available in the main region do

not satisfy this condition and therefore are not vacancies. Such a concept of a grain boundary vacancy should be distinguished from an excess volume due to a lattice mismatch in the boundary region. Relaxation in the boundary region leads to the concept of a delocalised vacancy. In the described situation, two vacancies appear in a growing crystallite, since the maximum number of atoms that can be located in it is two. Both of them can fill two nodes of the second crystallite. Filling the vacant position of the first crystallite is associated with energy consumption  $W$  and restores the atom to its original position, reversing the migration process in the opposite direction, in addition, another atom can no longer be located in this main region. Therefore, we exclude such a process from consideration and take the number of vacancies in this area is equal to two. Using molecular dynamics methods, it was found that the binding energy of vacancies into clusters at the boundary is very low [21], therefore they easily dissociate. This can also be attributed to the two considered vacancies, located in such a way that they form a divacancy in the boundary. One of them can pass into the volume of the second crystallite to replenish their equilibrium concentration in it. The second must be replaced by an atom according to the described scheme. This vacancy leaves its original position and increases the total number of vacancies in the grain boundary system by one.

The absorption of a vacancy of the first crystallite in the main regions with the number of nodes in them equal 1 or 0, by analogy, creates one vacancy or does not create any vacancies. In this case, the appeared vacancy is able to pass into a growing crystallite. Due to the absorption of a vacancy by an atom from the main region of the third described type with a zero number of nodes, the need for its diffusion transition to a vacancy located in the region of the previously considered type with two vacant nodes disappears. The whole described process is equivalent to a simple transition of the atom of the first crystallite from the centre of the main region to one of the sites present in it. Thus, the absorption and emission of vacancies by the boundary does not change the essence of the processes in the main regions and clarifies only the mechanism of transfer of vacancies from one crystallite to another through the boundary.

The total number of vacancies in the boundary participating in diffusion processes is equal to the sum of their equilibrium number in the stationary boundary  $C_0$ , vacancies from the main type  $A$  region and absorbed vacancies in the region without nodes. When the boundary is shifted by a distance  $a$  it absorbs  $C_1/a$  vacancies per unit length, where  $C_1$  is their concentration (atomic fraction) in the first crystallite. They are distributed among the three types of main regions described. Therefore, a region without nodes generates  $C_1 w_0/a$  vacancies. Regardless of the absorption of lattice vacancies, each region of the  $A$  type creates  $w_2/a$  vacancies. Therefore, their total concentration in the boundary, taking into account the fact that  $w_2 = w_0$ , is equal to  $C_b = C_0 + w_2(1 + C_1)$ . Neglecting the concentrations in the equilibrium boundary and in the bulk of the crystallite in comparison with  $w_0$ , we can assume that  $\ll \text{kul\_e029.eps} \gg$ .

Based on general principles, we obtain the following expression for the boundary coefficient of self-diffusion:

$$D = \theta a^2 w_2 v_0 \exp\left(-\frac{W_m}{kT}\right). \quad (5)$$

Here  $\theta$  is a geometric factor of the order of unity,  $W_m$  is the activation energy of migration of vacancies in the boundary.

### 3. Discussion

Above, we considered the process of shifting the boundary by a distance  $a$ . The migration rate is determined by the expression  $v = a\tau^{-1}$ . Neglecting the time  $\tau_1$  migratory boundary mobility is  $I = v/\sigma$ , where  $\sigma = Wa^{-3}$  is the value of the effective driving force of migration for a unit area. Using (4), the expression for mobility can be reduced to the form:

$$I = \frac{4Dw_2^2 S^2}{a^2 kT}. \quad (6)$$

When considering the processes of the emergence of vacancies in a migrating boundary, the result, according to which the concentration of vacancies in the boundary is equal to  $C_b = w_2$  was obtained. This is a very large value. It can explain the high diffusion mobility of atoms in the migrating boundary [22, 23]. It should be noted that the majority of vacancies in the boundary are not of thermal origin, but are determined only by

the geometric atomic structure of the migrating boundary. The expression for the boundary diffusion coefficient now does not contain a factor that depends on the activation energy of vacancy formation. Using such an approach, it is easy to understand the observed increase in the boundary self-diffusion coefficient in migrating boundaries [24–26]. The structural state of grain boundaries during their migration is essentially nonequilibrium [24]. It can be compared with stationary nonequilibrium grain boundaries in freshly prepared ultra-fine-grained materials. As it is known, they contain a significant excess free volume in the form of delocalised vacancies [27]. The diffusion activation energy in such boundaries can be two times lower than in boundaries with an equilibrium structure [28]. The nonequilibrium of migrating boundaries is associated by many authors with an increase in the free volume in the boundary, which is either the result of the absorption of excess vacancies in the volume of the disappearing grain, or the capture of dislocations with their subsequent dissociation [27, 29]. In the present study, the mechanism of generation of vacancies inside the boundary is described without taking into account all these processes. Here, the degree of nonequilibrium of the boundary is determined only by local atomic rearrangements. The effects listed above can have an additional influence, leading to an increase in the degree of nonequilibrium. An increase in the excess volume in the boundary inevitably leads to its broadening.

Let us estimate the ratio of the boundary self-diffusion coefficients in the migrating and stationary boundaries. We accept for the latter the expression  $D_e = \lambda a^2 v_0 \exp(-(W_f + W_m)/kT)$ , where  $W_f$  and  $W_m$  are the energies of formation and migration of grain boundary vacancies,  $\lambda$  is the coefficient. Taking into account (5), this ratio is  $n = D/D_e = w_2 \exp(W_f/kT)$ . Here  $\theta \approx \lambda$  is accepted. Taking  $w_2 \approx 0.1$ ;  $W_f \approx 0.4W_b$ , where  $W_b = W_f + W_m$  is the activation energy of grain boundary self-diffusion;  $W_b/kT_m = 9$  [27];  $T_m/T = 0.5$ ,  $T_m$  is melting temperature; we obtain  $n \approx 1.3 \cdot 10^2$ , which agrees with the experimental data for the migrating boundary  $n \sim 10^2$  [24]. In [30], the experimentally measured value of the diffusion coefficient of Ca into calcite at a temperature of 900 °C at the migrating boundary exceeded its value for the stationary boundary by five orders of magnitude. It should be noted that there is a fundamental

difference between the nonequilibrium structures in the considered cases of a moving boundary during its migration and a solid boundary in nanostructured systems. When the boundary stops, the nonequilibrium concentration of vacancies in it, after a certain relaxation time, reaches the value characteristic for the stationary boundary. This nonequilibrium is dynamic in nature, when vacancies are continuously generated in the moving boundary and disappear. The non-simultaneity of these processes leads to an excess of vacancies in the boundary. Stationary grain boundaries can be called nonequilibrium if they have an excess free volume, increased energy, or are sources of dislocations [31–34]. The disequilibrium of the boundaries is often associated with the presence of long-range stress fields, while in the migrating boundary, according to the described model, they are absent.

#### 4. Conclusions

Based on the concept of the atomic structure of an incommensurate intercrystalline slope boundary, a model of its migration has been developed. It was shown that the rearrangement of atomic configurations in the boundary region has both local and non-local nature with the involvement of diffusion processes. The relaxation of the atomic structure leads to the fact that the concentration of vacancies in the migrating boundary exceeds that in the stationary boundary. This causes an increase in the self-diffusion coefficient along such a boundary.

#### Author contributions

V. G. Kul'kov – idea, model development, article writing.

#### Conflict of interests

The author declares that he has no known competing financial interests or personal relationships that could have appeared to influence the work reported in this paper.

#### References

1. Darinskii B. M., Saiko D. S., Fedorov Yu. A. Sliding along the boundary forming an incommensurable structure\*. *Izvestiya vysshikh uchebnykh zavedenii. Fizika = Russian Physics Journal*. 1987;30(9): 53–57. <https://www.elibrary.ru/item.asp?id=36961888> (In Russ.)
2. Żydek A., Wermiński M. and Trybula M. Description of grain boundary structure and topology in nanocrystalline aluminum using Voronoi analysis

and order parameter. *Computational Materials Science*. 2021;197: 110660. <https://doi.org/10.1016/j.commatsci.2021.110660>

3. Darinskii B. M., Kul'kov V. G. Intercrystalline sliding along the boundaries formed by densely packed planes\*. *Poverkhnost'. Fizika, khimiya, mekhanika = Physics, Chemistry and Mechanics of Surfaces*. 1993;75(5): 153–156. <https://www.elibrary.ru/item.asp?id=36705071> (In Russ.)

4. Shtremel M. A., Markovich A. L. Energy of incommensurate grain boundaries. *The Physics of Metals and Metallography*. 1991;71(6): 21–29. <https://www.elibrary.ru/item.asp?id=31078891>

5. Darinskii B. M., Kalinin Yu. E., Mushtenko S. V., Saiko D. S. Structure of grain boundaries of a general type and mechanism of grain boundary internal friction peak. *Solid State Phenomena*. 2003;89: 203–232. <https://doi.org/10.4028/www.scientific.net/SSP.89.203>

6. Darinskii B. M., Kalinin Y. E., Sajko D. S. Atomic structure of the intercrystalline general type boundaries. Mechanisms of the grain boundary peak of internal friction. Premelting. *Solid State Phenomena*. 2006;115: 73–86. <https://doi.org/10.4028/www.scientific.net/SSP.115.73>

7. Gautam A., Radetic T., Lancon F., Dahmen U. Quantitative study of an incommensurate grain boundary using aberration corrected microscopy. *Microscopy and Microanalysis*. 2011;17(S2): 1338–1339. <https://doi.org/10.1017/S1431927611007562>

8. Gautam A., Ophus C., Lancon F., Radmilovic V., Dahmen U. Atomic structure characterization of an incommensurate grain boundary. *Acta Materialia*. 2013;61(13): 5078–5086. <https://doi.org/10.1016/j.actamat.2013.04.028>

9. Deymier P. A., Shamsuzzoha M., Weinberg J. D. Experimental evidence for a structural unit model of quasiperiodic grain boundaries in aluminum. *Journal of Materials Research*. 1991;6(7): 1461–1468. DOI: <https://doi.org/10.1557/JMR.1991.1461>

10. Lancon F., Ye J., Caliste D., Radetic T., Minor A. M., Dahmen U. Superglide at an internal incommensurate boundary. *Nano Letters*. 2010;10(2): 695–700. <https://doi.org/10.1021/nl903885p>

11. Wang Sh., Yu Yue, Zhang Sh., Zhang Sh., Xu H., Zou X., Zhang J., Atomic-scale studies of overlapping grain boundaries between parallel and quasi-parallel grains in low-symmetry monolayer ReS<sub>2</sub>. *Matter*. 2020;3(6): 2108–2123. <https://doi.org/10.1016/j.matt.2020.09.015>

12. Rouviere J., Lancon F., Rousseau K., Caliste D., Jouneau P., Fourne F. Structure of an incommensurate 90° Si grain boundary resolved with the help of a Cs-corrector for illumination. *Journal of Physics: Conference Series*. 2010;209: 012041. <https://doi.org/10.1088/1742-6596/209/1/012041>

13. Sutton A. P. An analytic model for grain-boundary expansions and cleavage energies. *Philosophical Magazine A*. 1991;63(4): 793–818. <https://doi.org/10.1080/01621859108839411>

doi.org/10.1080/01418619108213914

14. Farkas D., Froseth A., Swygenhoven H. Grain boundary migration during room temperature deformation of nanocrystalline Ni. *Scripta Materialia*. 2006;55(8): 695–698. <https://doi.org/10.1016/j.scriptamat.2006.06.032>

15. Wang L., Qi J., Zhang S., Ding M., Wei W., Wang J., Zhang Zh., Qiao R., Zhang Zh., Li Z., Liu K., Fu Yu., Hong H., Liu C., Wu M., Wang W., He Yu., Cu Yi., Li Q., Bai X., Liu K. Abnormal anti-oxidation behavior of hexagonal boron nitride grown on copper. *Nano Research*. 2022. <https://doi.org/10.1007/s12274-022-4388-1>

16. Chandross M., Argibay N. Friction of metals: A review of microstructural evolution and nanoscale phenomena in shearing contacts. *Tribology Letters*. 2021;69:119. <https://doi.org/10.1007/s11249-021-01477-z>

17. Kul'kov V. G., Polyakov A. S. Migration of an incommensurate high angle grain boundary. *Russian Metallurgy (Metally)*. 2012;(4): 263–268. <https://doi.org/10.1134/S0036029512040064>

18. Gupta B. K., Madhuri M. K., Gupta S. P. Diffusion induced grain boundary migration in the Cu–Cd system. *Acta Materialia*. 2003;51(17): 4991–5000. [https://doi.org/10.1016/S1359-6454\(03\)00325-2](https://doi.org/10.1016/S1359-6454(03)00325-2)

19. Viswanathan R., Bauer C. L. Kinetics of grain boundary migration in copper bicrystals with [001] rotation axes. *Acta Metallurgica*. 1973;21(8): 1099–1109. [https://doi.org/10.1016/0001-6160\(73\)90026-6](https://doi.org/10.1016/0001-6160(73)90026-6)

20. Hirth J., Lothe J. *Theory of Dislocations*. John Wiley and Sons; 1982. 857 p.

21. Li X., Liu W., Xu Y., Liu C. S., Fang Q. F., Pan B. C., Wang Zh. Energetic and kinetic behaviors of small vacancy clusters near a symmetric  $\Sigma 5(310)/[001]$  tilt grain boundary in bcc Fe. *Journal of Nuclear Materials*. 2013;440(1–3): 250–256. <https://doi.org/10.1016/j.jnucmat.2013.05.021>

22. Smidoda K., Gottschalk W., Gleiter H. Diffusion in migrating interfaces. *Acta Metallurgica*. 1978;26(12): 1833–1836. [https://doi.org/10.1016/0001-6160\(78\)90095-0](https://doi.org/10.1016/0001-6160(78)90095-0)

23. Krasil'nikov, V. V., Savotchenko, S. E. Grain boundary diffusion patterns under nonequilibrium and migration of grain boundaries in nanostructure materials. *Bulletin of the Russian Academy of Sciences: Physics*. 2009;73(9): 1277–1283. <https://doi.org/10.3103/S1062873809090214>

24. Gorelik S. S., Dobatkin S. V., Kaputkina L. M. *Recrystallization of metals and alloys*. M.: MISIS Publ.; 2005, 432 p. (In Russ.)

25. Prokoshkina D., Klinger L., Moros A., Wilde G., Rabkin E., Divinski S.V. Effect of recrystallization on diffusion in ultrafine-grained Ni. *Acta Materialia*. 2014;69: 314–325. <https://doi.org/10.1016/j.actamat.2014.02.002>

26. Chuvil'deev V. N., Nokhrin A. V., Pirozhnikova O. E., Gryaznov M. Y., Lopatin Y. G., Kopylov V. I.,

Myshlyaev M. M. Changes in the diffusion properties of nonequilibrium grain boundaries upon recrystallization and superplastic deformation of submicrocrystalline metals and alloys. *Physics of the Solid State*. 2017;59(8): 1584–1593. <https://doi.org/10.1134/S1063783417080066>

27. Chuvil'deev V. N. *Nonequilibrium grain boundaries in metals. Theory and applications*. M.: Fizmatlit Publ., 2004. 304 p. (In Russ.)

28. Kim H. K. Activation energies for the grain growth of an AZ31 Mg alloy after equal channel angular pressing. *Journal of Materials Science*. 2004;39(23): 7107–7109. <https://doi.org/10.1023/B:JMSSC.0000047560.93940.45>

29. *Physical Metallurgy*. Edited by R. W. Cahn, P. Haasen, North-Holland Physics Publishing, 1983, 1973 p.

30. McCaig A., Covey-Crump S. J., Ben Ismail W., Lloyd G. Fast diffusion along mobile grain boundaries in calcite. *Contributions to Mineralogy and Petrology*. 2007;153: 159–175. <https://doi.org/10.1007/s00410-006-0138-8>

31. Tucker G. J., McDowell D. L. Non-equilibrium grain boundary structure and inelastic deformation using atomistic simulations. *International Journal of Plasticity*. 2011;27(6): 841–857. <https://doi.org/10.1016/j.ijplas.2010.09.011>

32. Nazarov A. A., Murzaev R. T. Nonequilibrium grain boundaries and their relaxation under oscillating stresses in columnar nickel nanocrystals studied by molecular dynamics. *Computational Materials Science*. 2018;151: 204–213. <https://doi.org/10.1016/j.commatsci.2018.05.015>

33. Wang Yu., Fu R., Jing L., Sang D., Li Yi. Tensile behaviors of pure copper with different fraction of nonequilibrium grain boundaries. *Materials Science and Engineering: A*. 2018;724: 164–170. <https://doi.org/10.1016/j.msea.2018.03.086>

34. Chuvil'deev V. N., Kopylov V. I., Zeiger W. A theory of non-equilibrium grain boundaries and its applications to nano- and micro-crystalline materials processed by ECAP. *Annales de Chimie Science des Materiaux*. 2002;27(3): 55–64. [https://doi.org/10.1016/S0151-9107\(02\)80007-1](https://doi.org/10.1016/S0151-9107(02)80007-1)

\*Translated by author of the article.

## Information about the author

Viktor G. Kul'kov, Dr. Sci. (Phys.–Math.), Associate Professor, Professor at the Volzhsky Branch of National Research University «Moscow Power Engineering Institute» (Volzhsky, Russian Federation).

<https://orcid.org/0000-0001-8449-026X>

vikulkov@yandex.ru

Received 13.06.2022; approved after reviewing 18.07.2022; accepted for publication 15.09.2022; published online 25.12.2022.

Translated by Valentina Mittova

Edited and proofread by Simon Cox



## Original articles

Research article

<https://doi.org/10.17308/kcmf.2022.24/10553>

## Mathematical modelling of vortex structures in the channel of an electro dialysis cell with ion-exchange membranes of different surface morphology

K. A. Lebedev<sup>1✉</sup>, V. I. Zabolotsky<sup>1</sup>, V. I. Vasil'eva<sup>2</sup>, E. M. Akberova<sup>2</sup><sup>1</sup>Kuban State University,  
149 Stavropolskaya ul., Krasnodar 350040, Russian Federation<sup>2</sup>Voronezh State University,  
1 Universitetskaya pl., Voronezh 394018, Russian Federation**Abstract**

One of the ways to obtain membranes with electroconvection as the dominant mechanism of ion transport is to optimise the surface of known brands of commercial heterogeneous membranes by changing their manufacturing technology. For example, the degree of dispersion of the ion-exchanger or the volume ratio of the ion-exchanger to inert binder can be changed. The aim of this study was to determine and theoretically analyse the fundamental correlations between the intensity of electroconvection and the surface morphology of ion-exchange membranes with different ion-exchanger particle content.

The article presents a mathematical model of ion transport across the ion-exchange membrane/solution interface in the channel of an electro dialysis cell. The phenomenon of electroconvection in electromembrane systems (EMS) was modelled by solving two-dimensional Navier-Stokes equations for an incompressible liquid with no-slip boundary conditions and a set distribution of the electric body force. The body force distribution was set taking into account the real size of ion-exchanger particles and the distance between them that determine the electrical heterogeneity of the surface of experimental ion-exchange membranes with different mass fractions of ion-exchange resin.

It was determined that in the numerical modelling, the most important parameters were the size of the sections of electrical heterogeneity of the membrane surface, the current density, and the length of the space charge region (SCR). Numerical calculations were presented to determine the vortex size depending on the current density and the degree of electrical heterogeneity of the membrane surface.

It was shown that an increase in the mass fraction of ion-exchange resin in the production of heterogeneous sulphocation-exchange membranes resulted in a decrease in the step of electrical surface heterogeneity and promoted the formation of electroconvective vortices interacting with each other. Within the boundary conditions and approximations of the mathematical model, the vortex sizes reach their maximum value in the middle of the heterogeneity section  $L_0$ .

**Keywords:** Mathematical modelling, Electroconvection, Vortex structures, Heterogeneous ion-exchange membrane, Surface morphology, Electrical heterogeneity of surface

**Funding:** The study was supported by a grant from the Russian Science Foundation No. 21-19-00397, <https://rscf.ru/en/project/21-19-00397/>

**For citation:** Lebedev K. A., Zabolotsky V. I., Vasil'eva V. I., Akberova E. M. Mathematical modelling of vortex structures in the channel of an electro dialysis cell with ion-exchange membranes of different surface morphology. *Condensed Matter and Interphases*. 2022;24(4): 483–495. <https://doi.org/10.17308/kcmf.2022.24/10553>

**Для цитирования:** Лебедев К. А., Заболотский В. И., Васильева В. И., Акберова Э. М. Математическое моделирование вихревых структур в канале электро диализной ячейки с ионообменными мембранами разной морфологии поверхности. *Конденсированные среды и межфазные границы*. 2022;24(4): 483–495. <https://doi.org/10.17308/kcmf.2022.24/10553>

✉ Konstantin A. Lebedev, e-mail: [klebedev.ya@yandex.ru](mailto:klebedev.ya@yandex.ru)

© Lebedev K. A., Zabolotsky V. I., Vasil'eva V. I., Akberova E. M., 2022



The content is available under Creative Commons Attribution 4.0 License.



## 1. Introduction

One of the current goals of membrane electrochemistry and electromembrane technology is to enhance the mass transfer of electrolyte ions through ion exchange membranes. In EMS with a conventional electrodiffusion ion transport mechanism, the velocity of the process is limited by the value of the limiting electrodiffusion current. Hydrodynamic techniques are widely used to increase the value, such as increasing the flow velocity of the solution, using turbulent inserts and/or a mixed layer of ion exchangers, and profiling the membrane surface.

Another approach to the intensification of electromembrane processes is based on the use of new mechanisms of ion delivery to the membrane surface. Under intensive current modes, electroconvection is the dominant mechanism [1–6]. In such cases, the velocity of the process involving heterogeneous membranes with an electrically heterogeneous surface may exceed the velocity of transfer across homogeneous membranes. This aspect is important because foreign-made homogeneous membranes are several times more expensive than heterogeneous membranes. Key factors in the development of electroconvection are the chemical nature of the functional groups and polymer matrix and the morphology of the membrane surface. The surface morphology depends on the distribution of conductive sections of the ion-exchanger and inert sections of the polyethylene binder, as well as their size.

The basic principles of electroconvection are described in works by Dukhin and Mishchuk [3, 4], Rubinstein et al. [4–7]. Studies [8–10] describe the possibility of enhancing mass transfer in EMS by improving the surface morphology of ion-exchange membranes. The use of membranes with optimised surface morphology in electro dialysis for desalting and deionisation of natural waters and technological solutions provides the prerequisites for a significant increase in efficiency of these processes in overlimiting current modes. The transport characteristics of ion-exchange membranes depend on the degree of electrical (alternation of conductive and non-conductive surface sections) and geometrical (microrelief) heterogeneity of their surface [1, 2]. The results of mathematical modelling showed that alternating

conductive and non-conductive sections on the surface of heterogeneous membranes can ensure the occurrence of electroconvective flows at significantly smaller jumps of electric potential in comparison to homogeneous membranes.

The aim of this study was to determine and theoretically analyse the fundamental correlations between the intensity of electroconvection and the surface morphology of ion-exchange membranes with different ion-exchanger particle content.

## 2. Theoretical analysis

### 2.1. Theory of electroconvection in electromembrane systems

A characteristic feature of electro dialysis in overlimiting current modes is that the electric field induces a body force, which stimulates the movement of both ions and the volume of the solution. This phenomenon is called electroconvection. It manifests as microscopic hydrodynamic phenomena (even at the Reynolds number  $Re = 0$ ), which have the properties of regular turbulence at high values of  $Re$ . The influence of any non-hydrodynamic processes on the solution flow is carried out through the body force in the Navier–Stokes equation [11, 12]. Electroconvection is caused by the vortex nature of the body force ( $rot \vec{f} \neq 0$ ). In the case of EMS, the volumetric force is the electric force acting on the space charge:  $\vec{f} = \rho \vec{E}$  where  $\rho$  is the charge distribution density and  $E$  is the electric field intensity. Electroconvection in EMS with homogeneous ion-exchange membranes is determined by a counterion concentration gradient, which is caused by uneven desalting of the solution along the length of the channel of the electro dialysis unit [13]. Due to the difference in charge numbers and diffusion coefficients of cations and anions, values of  $\vec{f}$  near the anion-exchange and cation-exchange membranes are different. Consequently, the solution flow in the channel is asymmetrical. This mechanism of electroconvection has been theoretically studied by Rubinstein et al. [5–7]. Electroconvection has a threshold character and appears when a certain critical value of electric potential drop is reached.

In EMS with heterogeneous membranes, the electroconvection mechanism is different. Heterogeneous membranes are produced by hot

pressing or rolling dispersed ion-exchange resins with a particle size of 10 to 100  $\mu\text{m}$  and an inert polyethylene binder. The structure and surface of heterogeneous membranes are inhomogeneous. On the membrane surface, there is an alternation of the active conductive sections (ion exchanger particles) and inert non-conductive sections of polyethylene. The proportion of active surface depends on the membrane production technology. At overlimiting current densities, an electric vortex force arises in the system, resulting in the occurrence of electroconvective vortices. In [3, 4], it was shown that this mechanism has no threshold value of potential drop. It occurs at significantly lower values of electric current density than in the homogeneous membrane systems. Enhanced ion transport may depend on the surface morphology of ion-selective membranes as well as the heterogeneity of their electrochemical properties.

In contrast to conventional turbulence, which has been extensively studied theoretically and experimentally for many decades, the phenomenon of electroconvective turbulence has just undergone the initial basic numerical experiments. The current aim is to provide the resultant mathematical statements that adequately describe the experimental data.

## 2.2. Mathematical modelling of electroconvective vortex structures in the channel of an electro dialysis unit for membranes with two conductive sections

Studies [1, 6] set the goal to theoretically investigate the regularities of electroconvection in a smooth rectangular desalting channel of an electro dialysis unit with heterogeneous ion-exchange membranes. The two-dimensional mathematical model describing the processes during operation of the electro dialysis cell in overlimiting current modes is based on the Navier-Stokes equations written in terms of the continuity condition for a steady-state mode [6]:

$$(u \cdot \nabla)u = \nabla \cdot \left( -\frac{1}{\rho} p + \nu(\nabla \cdot u) \right) + \frac{1}{\rho} \bar{f}(x, y), \quad (1)$$

$$(\nabla \cdot u) = 0, \quad (2)$$

where  $u$  is the velocity vector,  $\bar{f}(x, y)$  is the body force acting in the space charge region (SCR) ( $\text{N/m}^3$ ),  $\rho$  is the solution density ( $1000 \text{ kg/m}^3$ ),

$\nu = 10^{-6} \text{ m}^2/\text{s}$  is the dynamic viscosity,  $\text{Re}_y = \frac{V_{\max} H}{\nu}$

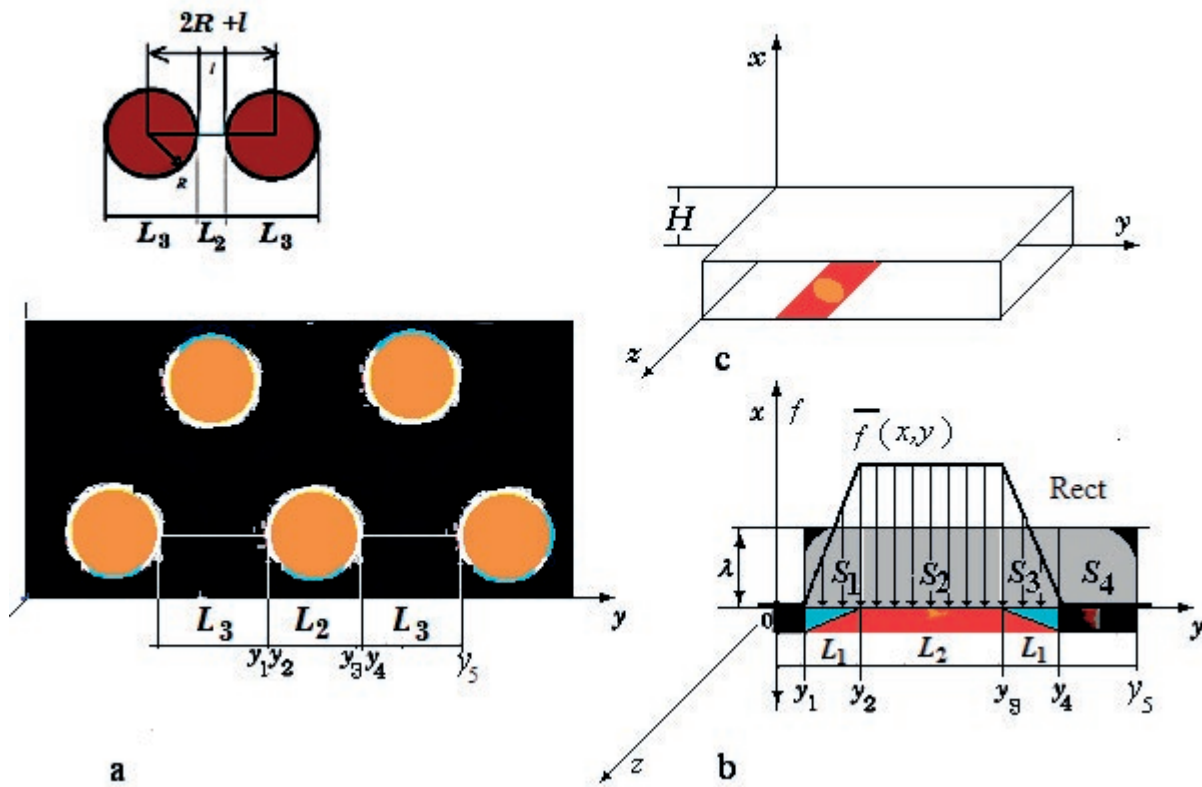
is the Reynolds number,  $V_{\max}$  is the longitudinal maximum velocity of solution flow in the electro dialysis cell,  $p$  is the pressure; and  $H$  is the intermembrane distance.

When formulating the boundary conditions, it was assumed that the velocity profile at the inlet of the membrane channel was parabolic (laminar flow). No-slip conditions were applied to the membrane surface. At the outlet of the channel, the hydrostatic pressure was zero:

$$\begin{aligned} y = 0, u = u_{\max} x \left( 1 - \frac{x}{h} \right); \quad x = 0, u = 0; \\ y = L, p = 0; \quad x = H, u = 0. \end{aligned} \quad (3)$$

To solve equations (1) – (3), it is necessary to know the distribution of the body force  $\bar{f}(x, y)$ , arising under the effect of the electric field on the volumetric space charge near the interfaces in the channel. Figure 1 shows a schematic of the membrane surface (Fig. 1a), the distribution profile of the electric force acting over the membrane sections with different values of electrical conductivity (Fig. 1b), and the position of the membrane in the electro dialysis channel (Fig. 1c). We identified conductive and non-conductive sections on the surface of heterogeneous membranes, as well as a transition section of about  $0.1 \mu\text{m}$ . Consequently, the body force  $\bar{f}$  was specified in the regions of the electroneutrality violation zone  $S_2$ , adjacent to the boundaries of  $x = 0$ ,  $x = H = 2 \text{ mm}$  (Fig. 1c). According to Rubinstein's theory [5], the space charge extent  $\lambda$  at its limit can approach the thickness of the diffusion layer. In paper [1], it was assumed to be  $\lambda = 2 \mu\text{m}$ . In this study, the value of  $\lambda$  was assumed to depend on the current density  $\lambda = \left( 1 - \frac{i_{\text{lim}}}{i} \right) \delta$ , where  $\delta$  is the thickness

of the diffusion layer. Under the condition of  $i = i_{\text{lim}}^0$ , the value of space charge region (SCR) is zero. As the current increases, the value of  $\lambda$  approaches the value of the diffusion layer thickness. If we build models using atomic force microscopy data [13], the thickness of the SCR can be in the range of 200–1200 nm [14] or even less than 50–100 nm. The size of the SCR is quite



**Fig. 1.** Schematic representation of the model membrane surface in the electro dialysis cell (a): the circles are conductive sections of the ion exchanger  $L_2$ , the dark field is the non-conductive sections of the polyethylene  $L_3$ , and the boundary is the transition sections  $L_1$ . Electric force distribution profile (b) acting on  $S_1, S_2, S_3, S_4$ :  $S_1 = \{(x, y) : y_1 \leq y \leq y_2, 0 \leq x \leq \lambda\}$ ,  $S_2 = \{(x, y) : y_3 \leq y \leq y_4, 0 \leq x \leq \lambda\}$ ,  $S_3 = \{(x, y) : y_2 \leq y \leq y_3, 0 \leq x \leq \lambda\}$ ,  $S_4 = \{(x, y) : y_4 \leq y \leq y_5, 0 \leq x \leq \lambda\}$  with characteristic size values of  $L_1, L_2, L_3$ , respectively;  $\lambda$  is the thickness of the SCR. Rect indicates the rectangle corresponding to the conductive sections of the membrane, consisting of the combined rectangles  $S_1, S_2, S_3$  with a height of  $\lambda$  and a width of  $2L_3 + L_2$

difficult to determine, it requires many factors to be taken into account.

In this study, we first coordinated the data in Rubinstein’s model and in the works of other authors [15], who considered the space charge to be the main driving force of electroconvection [16–20]. The height of the trapezoid  $f_{max}$  (Fig. 1b) is the maximum of the space charge distribution function, which corresponds to its value at the membrane surface. It is calculated by formula (5). The electric body force  $\vec{f}_x = \rho_e E_x$  (N/m<sup>3</sup>) is determined by the electric charge density  $\rho_e$  and the electric field strength  $E$ . A force vector field arises as a result of the electric field in a SCR with a thickness of  $\lambda$ . The  $y$ -axis component of the force is zero  $\vec{f}_y(x, y) = 0$ . Similarly to studies [1, 10], we assumed that  $\vec{f}$  varies piecewise-linearly along the longitudinal axis  $y$ : in section  $S_1$ , the force changes from 0 to  $|f_{max}|$ , and in  $S_2$

it decreases from  $|f_{max}|$  to 0. In section  $S_3$ , the force is constant and equal to  $f = f_{max}$ . In the non-conductive section  $S_4$ , the electric force is zero. Therefore,

$$f(x, y) = \begin{cases} \frac{y - y_1}{y_2 - y_1} f_{max}; (x, y) \in S_1 \\ f_{max}; (x, y) \in S_2 \\ \frac{y - y_4}{y_3 - y_4} f_{max}; (x, y) \in S_3 \\ 0; (x, y) \in S_4, \end{cases} \quad (4)$$

In [1], the relationship between the body force and the current density was determined:

$$f_{max} = Fc_1 E = \frac{RT}{D_1 F} i = k_f i, \quad (5)$$

where  $k_f = 2.5 \cdot 10^7$  has the dimension of N/(m·A), if the current density is expressed in [A/m<sup>2</sup>]. This

force acts at each point of the SCR, which is formed in a rectangle with a length of  $L_2$  and a width of  $\lambda$ , where  $\lambda = \left(1 - \frac{i_{lim}^0}{i}\right) \delta$  is the thickness

of the SCR and  $\delta$  is the thickness of the diffusion layer. The electric force is directed along the normal to the membrane (coaxial to the spatial coordinate  $x$ ). The coordinates of the electro dialysis cell (c) are:  $y$  – length,  $0 \leq y \leq L$ ;  $x$  – height,  $0 \leq x \leq H$ ;  $H$  – intermembrane distance,  $z$  – width of the electro dialysis cell.

In [10], two cases of the surface morphology of ion-exchange membranes with a geometric heterogeneity step of  $2R+l$  were considered: 1)  $2R+l=2\cdot30+70=130\ \mu\text{m}$ ,  $2R/l=60/70=0.875$ ; 2)  $2R+l=2\cdot50+30=130\ \mu\text{m}$ ,  $2R/l=100/30=3.34$ , for the channel length  $L=130$  and its width of  $400\ \mu\text{m}$ . In our study, we used the surface characteristics of the experimental sulphocation-exchange membranes with different ion-exchange resin contents (Table 1) and, correspondingly, with different surface parameters: 1)  $2R+l=9.3\ \mu\text{m}$ ,  $2R/l=0.89$ ; 2)  $2R+l=8.2\ \mu\text{m}$ ,  $2R/l=1.05$  at the channel length  $L=6.2$ ; 3)  $2R+l=7.1\ \mu\text{m}$ ,  $2R/l=1.84$  at the channel length  $L=7.1$  and its width of  $2000\ \mu\text{m}$ . Since we used the same grinding of the ion exchange resin for the experimental membrane samples, all the samples had approximately the same radius of ion exchange particles  $R$ .

### 2.3. Mathematical description of the membrane/solution interface, considering the microrelief

In theoretical works describing the regularities of the transmembrane electrodiffusion ion transport, the model of a homogeneous membrane with a flat boundary is usually used. However, direct experiments on the surface profile of the membrane by AFM (Fig. 2) showed that the

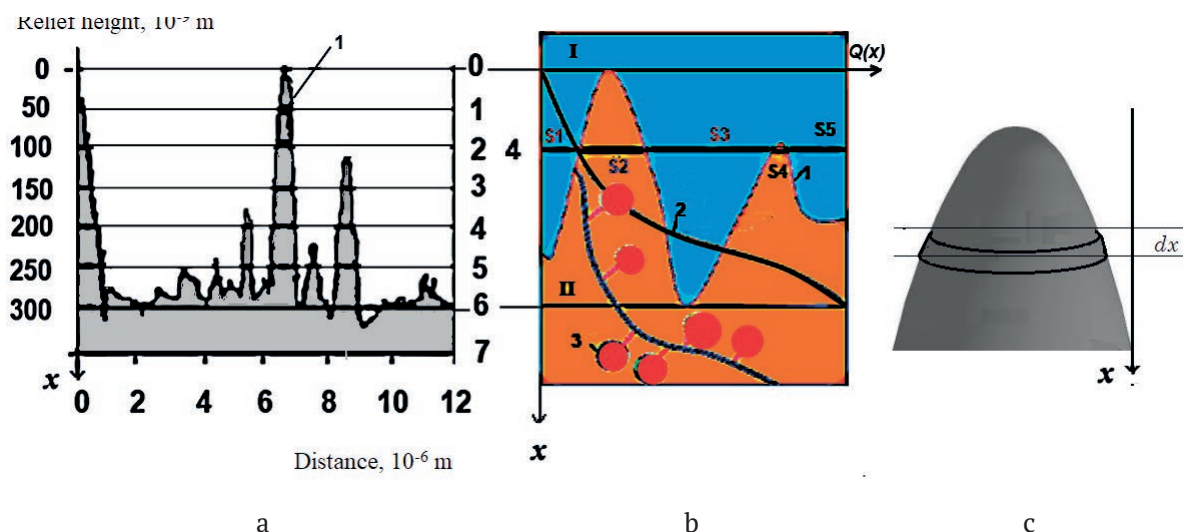
transition boundary from the solution phase to the solid phase of the membrane cannot be modelled correctly by an ideal plane. The electrical properties of the boundary with a microprofile depend on the distribution of the local exchange capacity  $Q(x)$  of the membrane within the specified spatial limits. The approximation of the distribution of the averaged exchange capacity along the normal to the membrane surface  $Q(x) = q(x)Q_0$  was one of the problems in the mathematical description of the ion transport along a rough surface. Figure 2 shows an example of obtaining  $q(x)$ . Digital techniques of atomic force microscopy were applied to obtain the cross-sectional area of the solid phase  $S(x)$ , the microprofile was partitioned by height at different distances. We assumed that the solid phase fraction is  $q(x) = S(x)/S_0$ , where  $S_0$  is the area of the experimentally studied membrane section. The cross-sections of the sulphocation-exchange membrane microprofile were numbered from 0 to 7. For each cross-section, the solid phase fraction is calculated as the ratio of the total area of the blackened areas  $S$  along the cross-section of the membrane microprofile (projected on the membrane surface) to the total area of the experimentally studied membrane sample  $S_0$ . The calculated area has a size of  $S_0 = 12 \times 12 \times 10^{-12}\ \text{m}^2$ . The horizontal scale in Fig. 2 is 1000 times larger than the vertical scale. The proportion of the ion exchanger in cross-section 4 is defined as  $\frac{Q}{Q_0} \approx q(x) = \frac{S}{S_0} = \frac{S2+S4}{S1+S2+S3+S4+S5}$ . As

the cross-section number increases, the solid phase fraction  $q(x) = Q/Q_0$  increases. This results in dependence of the exchange capacity  $Q(x)$  on  $x$ -coordinate (Table 2). The continuous distribution of the solid phase volume fraction

**Table 1.** Surface characteristics of experimental samples of swollen heterogeneous sulphocation-exchange membranes

Ion exchanger fraction, wt%	$S, \%$	$\bar{r}, \mu\text{m}$	$P, \%$	$\bar{r}, \mu\text{m}$	$\bar{l}, \mu\text{m}$	$2R+l, \mu\text{m}$	$2R/l$
45	21±1	2.2±0.1	1.9±0.1	1.9±0.1	4.9±0.4	9.3	0.89
55	25±2	2.1±0.1	2.2±0.3	1.9±0.2	4.0±0.3	8.2	1.05
70	38±2	2.30±0.04	3.2±0.4	1.9±0.1	2.5±0.1	7.1	1.84

$S, \%$  is the ion exchanger fraction;  $\bar{r}, \mu\text{m}$  is the weighted average radius of ion exchange sections;  $P, \%$  is the macropore fraction;  $\bar{r}, \mu\text{m}$  is the weighted average pore radius; and  $\bar{l}, \mu\text{m}$  is the weighted average distance between the conductive regions



**Fig. 2.** Microprofile of the sulphocation-exchange membrane surface (a), the cross-sections in which the volume fraction of the solid phase was calculated (b), and a single microrelief section with a defined volume element of characteristic length  $dx$  (c). I – solution phase; II – membrane phase; 1 – surface microprofile; 2 – exchange capacity; 3 – ionogenic groups; and 4 – the cross-section used to determine the ionite content

**Table 2.** Volume fraction of the ion exchanger depending on the number of the layer cross-section

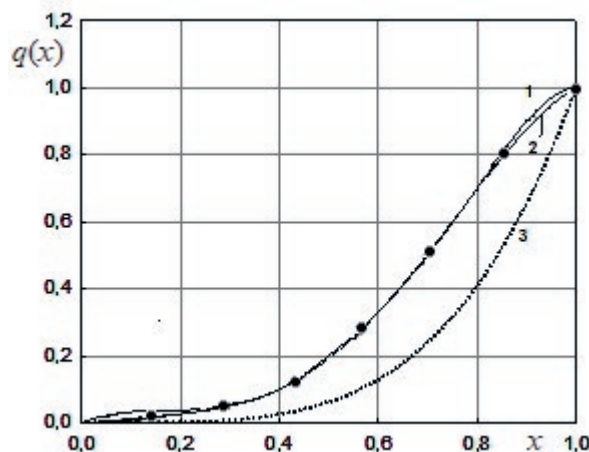
Cross-section	0	1	2	3	4	5	6	7
Volume fraction of the solid phase $q = Q/Q_0$	0	0.025	0.050	0.067	0.167	0.583	0.980	1.000

along the layer coordinate in the solution was obtained by interpolating using 3rd degree splines and 4th degree polynomials (Fig. 3).

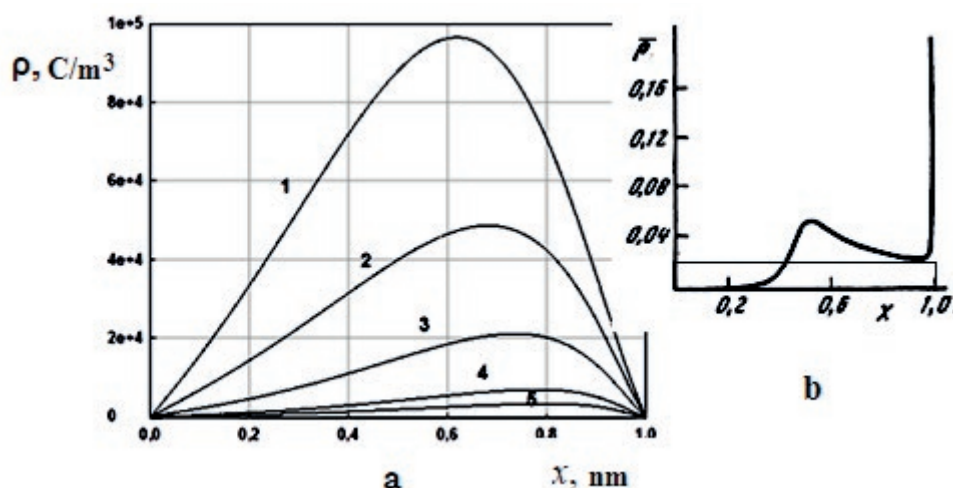
We chose such a volume element so that it exceeded the size of the individual phases of the system. At the same time, it should be small enough to consider the dependence of the average volume concentration of ionogenic groups  $q(x)$  and ionized groups on the side surface of the selected element as a function of the  $x$ -coordinate. The  $q(x)$  dependence also takes into account, on average, the growth of the lateral area of the  $dx$  element, where the ionised groups involved in the splitting of water molecules are concentrated. In order not to complicate the theory with secondary dependencies, we assumed  $q(x)$  to be the only primary characteristic that depends on the  $x$ -coordinate. The ion concentration  $c_i$  at a certain coordinate of  $x$  represents the average concentration of ions in the solid phase and in the solution phase. At  $x = 0$ , all ions are in the solution, and at  $x = \delta$  they are in the solid phase.

Numerical calculations were carried out for micro-layer thickness between 1 and 300 nm. The exchange capacity distribution as a function

of the dimensionless coordinate was assumed to be the same for all cases. Fig. 4 shows the change in the shape of the space charge and its integral value. The distribution of the space charge  $\rho$  over the layer thickness is determined



**Fig. 3.** Dependence of the solid phase volume fraction  $q$  on dimensionless layer thickness in the solution. 1 – interpolation of the data in Table 2 using splines; 2 – the polynomial approximation  $q(x) = -4.45x^4 + 8.28x^5 - 3.397x^2 + 0.569x$ ; and 3 – the function of  $q(x) = x^4$



**Fig. 4.** Distribution of volumetric space charge  $\rho$  (C/m<sup>3</sup>) over the dimensionless coordinate of the layer at a thickness of: 1 – 10; 2 – 50; 3 – 100; 4 – 200; and 5 – 300 nm (a) and distribution of dimensionless charge density on dimensionless thickness of diffusion layer in the Rubinstein model [22, p. 325] (b)

by the boundary conditions of the problem set in study [21]. At the left and right boundaries of the layer, the electroneutrality condition is met. Therefore, the charge is zero at the boundary points  $X = 0$  and  $X = 1$ . As the layer thickness increases, the maximum space charge decreases monotonically (Fig. 4a). The change of surface charge distribution over thickness of diffusion boundary layer according to the widely known Rubinstein model [22, p. 325] is shown in Fig. 4b. The mathematical models differ both by the approach to their description and by the studied objects. However, when the results were compared, we found that both models make it possible to estimate the space charge at the membrane surface and the size of the area of its localisation. It helped to better understand the mechanism of electroconvection in EMS.

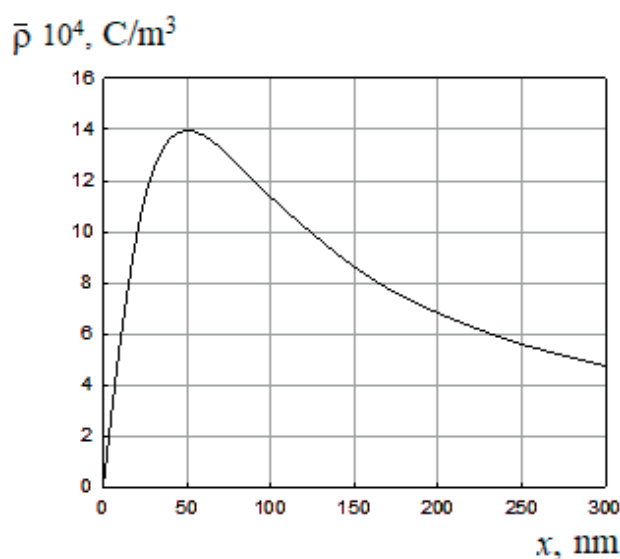
The integral value of the dimensionless charge was approximately estimated as the area under the curve using the mean integral value (rectangle in Figure 4b). The conversion to a dimensional value provided the value:

$$\bar{\rho} = Fc_0\delta \int_0^L \rho \approx 0.002 \text{ C/m}^2, \text{ where } F=10^5 \text{ C/mol};$$

$$c_0 = 1 \text{ mol/m}^3; \text{ and } \delta = 10^{-6} \text{ m}.$$

The change in the integral value of the surface charge was not monotonic (Fig. 5). In the framework of the boundary value problem with electroneutrality conditions at the boundaries, the surface charge approaches zero as the layer thickness increases. The charge distribution

over the layer thickness in the considered model corresponds to a thin boundary layer forming near the membrane in the Rubinstein model. We compared this value with the corresponding value at  $x = 50$  nm (Fig. 5) and observed the same order of values ( $\sim 0.0014 \text{ C/m}^2$ ). The difference is that in the Rubinstein model the charge is distributed in a diffusion layer with a thickness of  $(1-100) \cdot 10^{-6} \text{ m}$ , while in the presented model it is distributed at the interface in an area with a thickness of  $(10-300) \cdot 10^{-9} \text{ m}$ . The thickness ratio is in the range of 10–1000.



**Fig. 5.** Dependence of the dimensional integral surface charge density  $\bar{\rho} = \int_0^L \rho dx$  on the layer thickness

It should be noted that both considered mathematical models do not provide entirely real values of size of the space charge distribution region. Spatial charge can be described more thoroughly, if the boundary value problem domain is extended beyond the height of the microprofile both towards the diffusion layer and towards the membrane phase region.

### 3. Results and discussion

Numerical calculations were performed under the condition of trapezoidal distribution of the body force (Fig. 1b) by formula (4) in accordance with characteristic structural parameters of the surface of real experimental ion-exchange membranes (Table 1). Fig. 6a shows the distribution of ion concentration near the surface of the cation-exchange membrane and the scheme of formation of two differently directed electroconvective vortices ( $d$  is the vortex diameter,  $\delta$  is the diffusion layer thickness,  $\lambda$  is the SCR thickness,  $C'_{Na}$  and  $C'_{Cl}$  are the concentrations of counterions and coions in the solution, respectively,  $\rho_{av} = \int_0^\lambda \rho(x) dx / \lambda$  is the mean integral charge density, and  $C_{Na}$  is the concentration of counterions in the SCR). Fig. 6b shows the results

of numerical calculation of fluid flow lines in the section of membrane channel with heterogeneous membrane, where  $y$  is the horizontal coordinate,  $x$  is the vertical coordinate,  $L_3$  and  $L_2$  are the lengths of conductive (ion exchanger) and non-conductive (polyethylene) sections, respectively, and  $L_1$  is the length of the transition sections.

We carried out two sequences of numerical calculations to determine the dependence of the size of electroconvective vortices on the current density for experimental membranes with different dimensions of conductive and non-conductive sections (Table 1). Taking into account the notations, the total length of conductive and non-conductive sections was ( $L_0 = 2L_3 + L_2 + 4L_1$ ) 13.7  $\mu\text{m}$  and 11.7  $\mu\text{m}$  for membranes with mass fraction of ion exchange resin of 45 % and 70 %, respectively. Fig. 7 shows the distribution of fluid flow lines in the case when electroconvection occurs near both membranes, which form the desalting channel in the electro dialysis cell. When developing a two-dimensional mathematical model, we considered ion exchange membranes with only two conductive areas on the surface. The conductive sections are located in the middle part of the channel in order to avoid the influence of inlet and outlet boundary conditions of the

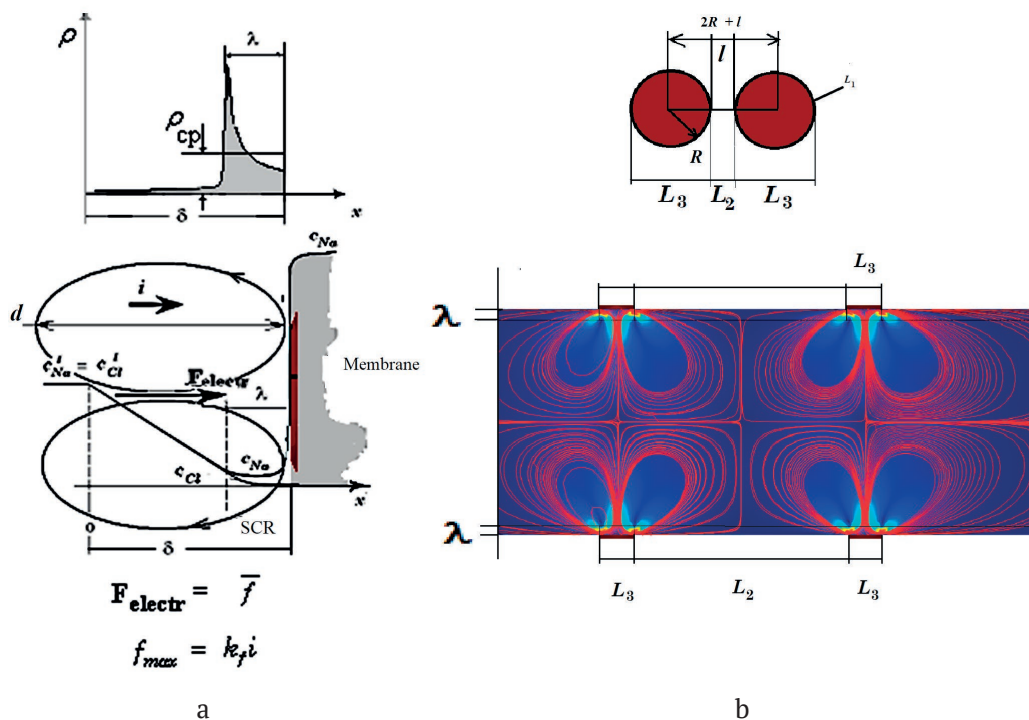
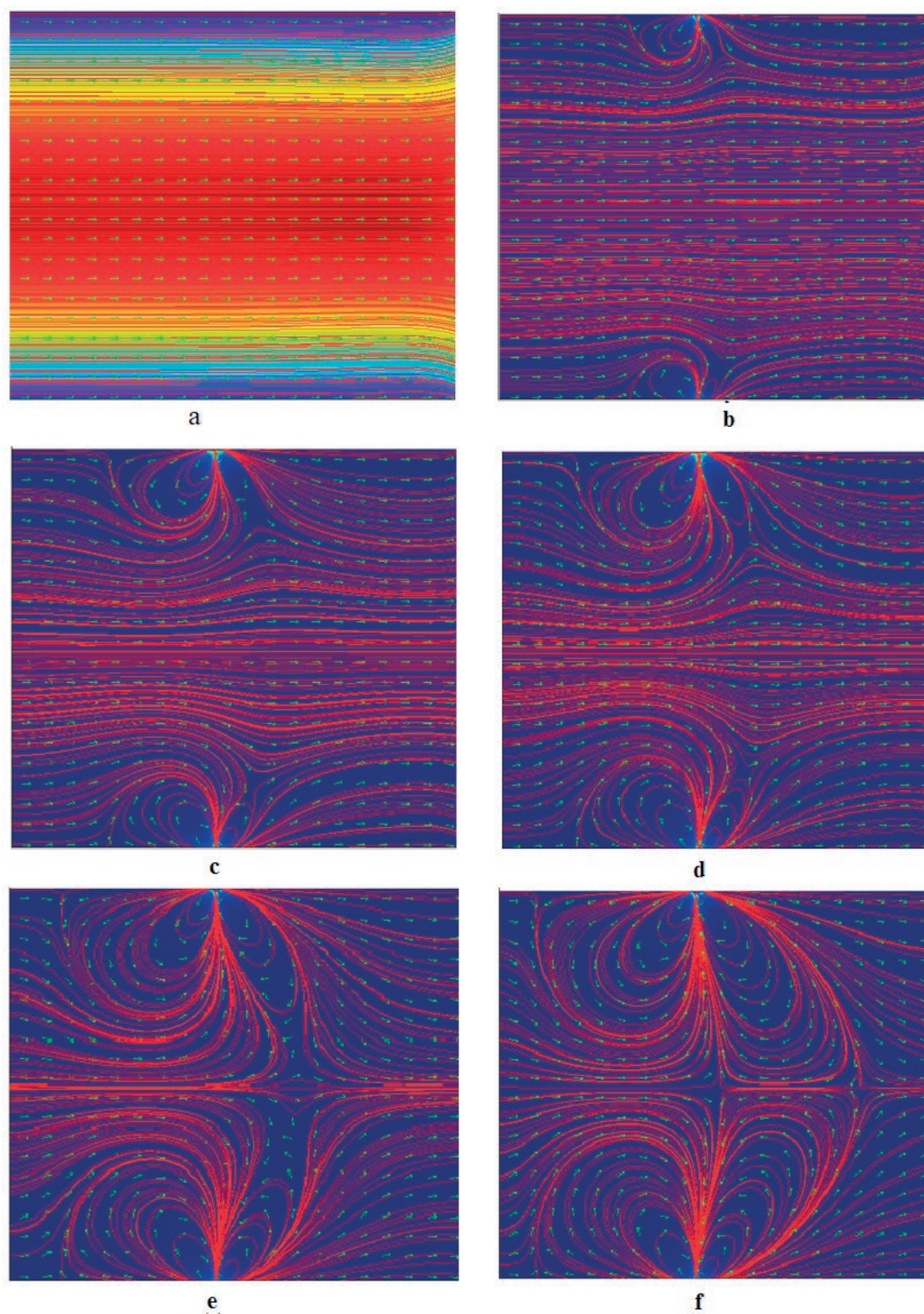


Fig. 6. The ion concentration distribution in the solution (a) and the pattern of the occurrence of electroconvective vortices (b) near the surface of heterogeneous cation-exchange membrane



**Fig. 7.** Current lines and fluid flow velocity vectors in a membrane channel with two conductive sections on each of the membranes at different values exceeding the limiting current density  $i/i_{lim}$ : a – 1; b – 4; c – 8; d – 16, e – 32; and f – 64



channel. The rest of the membrane surface is inert (polyethylene). Numerical experiments with a sodium chloride solution showed that two vortices are formed near each membrane due to the heterogeneity of their surface (Fig. 7). The vortices are formed in front of the conductive section. In the case of the cation-exchange membrane, they rotate clockwise, and in the case of the anion-exchange membrane, the rotation is counterclockwise. At high current, the diameter of the vortices is commensurate with the channel width. It was determined that vortex structures arise with the onset of the limiting state, when, according to Rubinstein’s theory, a space charge begins to form. The formation of four vortices was confirmed for membranes with large dimensions of surface inhomogeneity [10]. The total dimensions of the conductive and non-conductive sections of the studied membranes were, on average, an order of magnitude smaller. Therefore, the two internal vortices were almost invisible and had no effect on the external vortices. As the current density increases, the vortex sizes change nonlinearly and reach a value equal to half of the membrane channel thickness. Their further growth is limited by the size of the channel and the interaction of vortices on opposite membranes. The vortex diameter is considered to be the largest distance  $d$  between the points belonging to the area embraced by the closed current lines.

We assumed that the diameter  $d$  of the vortex at the membrane element (Fig. 1) depends on the magnitude of the electric force acting on the volume of the solution  $F_{\max} = k_F (i - i_{\lim}) \delta$  according to nonlinear law [20]:

$$d(i) = \gamma_2 [F_{\max}(i)]^\alpha + \gamma_1 F_{0\max}(i) + \gamma_0, \tag{6}$$

where  $\gamma_i$ ,  $\alpha$  are the a priori numerical coefficients:  $\gamma_2$ ,  $\alpha$  are the coefficients taking into account the interaction of vortices;  $\gamma_1$  is the coefficient of linear effect of electroconvection; and  $\gamma_0$  is the coefficient considering other forces influencing the occurrence of vortices, besides the electric force. For current density not too much exceeding its limit value, there is no interaction of vortices. Therefore, formula (6) is simplified to  $d(i) = \gamma_1 F_{\max} + \gamma_0$ . In the dimensionless form, the formula is:

$$\frac{d}{H} = \bar{\gamma}_2 [I - 1]^\alpha + \bar{\gamma}_1 (I - 1) + \bar{\gamma}_0, \tag{7}$$

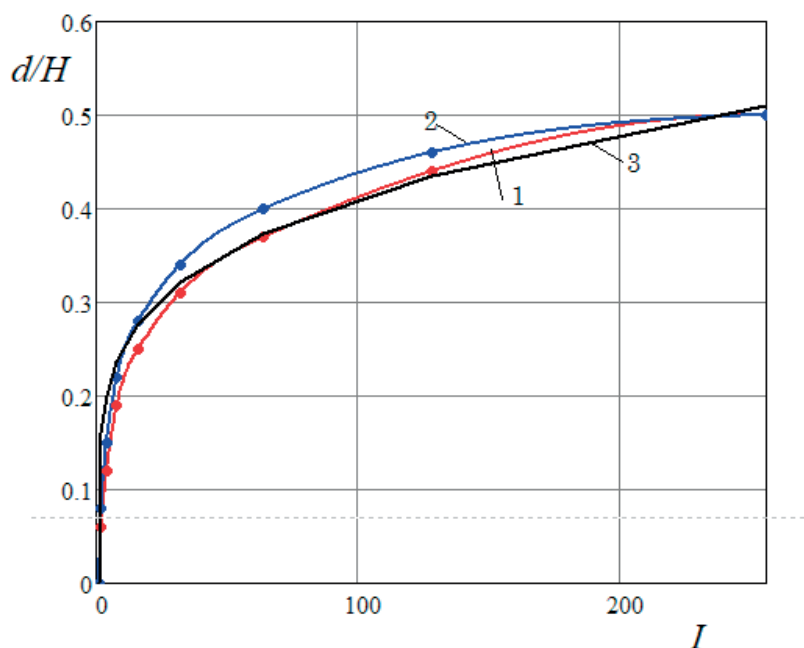
where  $\bar{\gamma}_2$ ,  $\bar{\gamma}_1$ ,  $\bar{\gamma}_0$  are the dimensionless parameters:

$$\bar{\gamma}_2 = \frac{\gamma_2 k_F \delta^\alpha i_{\lim}^0}{H}, \quad \bar{\gamma}_1 = \frac{\gamma_1 k_F \delta^\alpha i_{\lim}^0}{H}, \quad \bar{\gamma}_0 = \frac{\gamma_0}{H}.$$

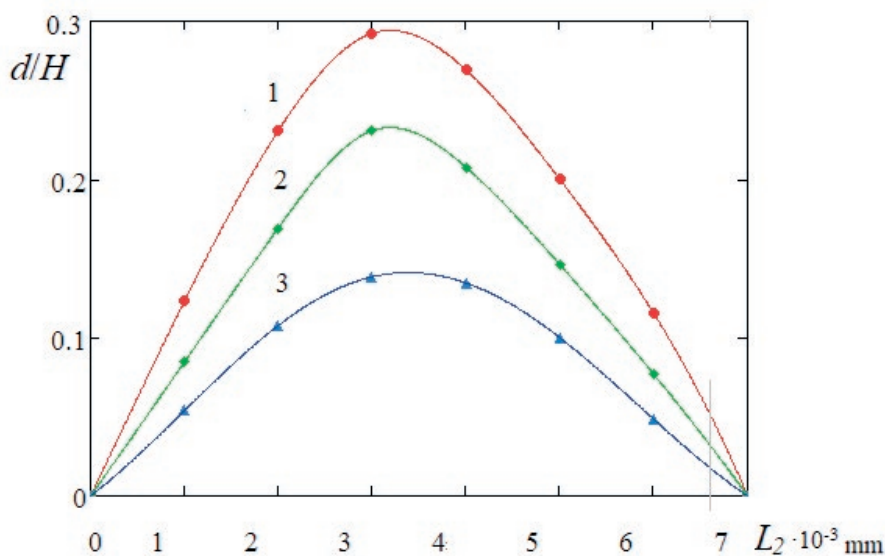
Formula (7) reveals the role of the dimensionless current parameter  $I = \frac{i}{i_{\lim}}$  in the formation of

vortex structures [17]. However, the size of the SCR is a more significant factor. In reality, alternating conductive and non-conductive sections are located along the entire length of the channel. The electric force acts on the space charge localised near the solution/membrane interface. If in this case  $rot(f) = 0$ , i.e. the vector field is potential (vortexless), the pressure changes evenly and no vortex motion occurs in the solution. On the other hand, the  $rot(f)$  value decreases as the proportion of conductive sections decreases. So, no vortex motion of the fluid can be observed in the case of a completely non-conductive surface. In both cases, the vortex diameter approaches zero. In intermediate cases, for the value of  $rot(f) \neq 0$ , there will be an extremum in the dependence of the size of electroconvective vortices on the ratio of surface inhomogeneities. The body force of electroconvection causes an uneven overpressure, which pushes the solution towards the membrane surface, but meets the resistance of the underlying fluid layers and the surface itself. This causes a change in the flow direction up to a complete reversal of the direction of fluid movement from the membrane surface to the depth of the solution. Oppositely directed currents form vortices, which partially destroy the diffusion layer and reduce the thickness of the charged layer. In turn, this leads to a decrease in the body force and, consequently, to a decrease in the vortex diameter.

We carried out numerical calculations of the dependence of the vortex diameters on current density for experimental heterogeneous sulphocation-exchange membranes with different ratios of conductive ( $L_3$ ) and non-conductive ( $L_2$ ) sections (Fig. 8). We also calculated the dependence of the vortex diameters on the length of non-conductive sections  $L_2$  at different values of the body force, determining the



**Fig. 8.** Vortex diameter dependence on current at sulphocation-exchange membrane surface with the total size of conductive and non-conductive sections of  $2L_3+L_2 = 13.7 \mu\text{m}$  (1) and  $11.7 \mu\text{m}$  (2) in the channel of an electro dialysis cell with a thickness of  $H = 2 \text{ mm}$  at the Reynolds number  $Re = 2$ . 1, 2 – numerical calculation, 3 – calculated by formula (9) at  $\bar{\gamma}_2 = 0,16$ ;  $\bar{\gamma}_1 = 10^{-4}$ ;  $\bar{\gamma}_0 = 0$ ;  $\alpha = 0.2$



**Fig. 9.** Dimensionless dependence of vortex diameters on the channel width, as a function of the non-conductive section length  $L_2$  at different values of the body force generating the rotor,  $10^9 \text{ N/m}^3$ : 1 – 4; 2 – 2; and 3 – 0.6

force rotor (Fig. 9). For this purpose, at a given total length of the section  $L_0$ , we changed the length of the conductive surface section  $L_3$ . The length of the non-conductive section  $L_2$  was expressed by  $L_0$  and  $L_3$ . We obtained the expression  $L_2 = (L_0 - 2L_3 - 4L_1) / 2$ , where  $L_1$  is the length of the transition region at the

boundary between the conductive and non-conductive sections. The initial values of  $\bar{L}_3 = 0.0046 \text{ mm}$ ,  $\bar{L}_2 = 0.0025 \text{ mm}$ ,  $\bar{L}_1 = 0.0001 \text{ mm}$ , and  $L_0 = 0.0075 \text{ mm}$  were the experimentally found dimensions of the surface sections of the experimental membranes (Table 1). The minimum possible value of  $L_{2\text{min}} = (L_0 - 4L_1) / 2$  corresponds to

the case of  $L_3 = 0$ , where there are no conductive sections on the surface. When modelling another marginal case with a decrease in  $L_2$ , the rotor of the body force decreased linearly according to the formula:

$$F = F_0 \cdot E_1(L_3), \quad (8)$$

$$\text{where } E_1(L_3) = \begin{cases} \frac{L_3}{\bar{L}_3}, & \text{if } L_3 \leq \bar{L}_3 \\ 1, & \text{if } L_3 \geq \bar{L}_3 \end{cases}.$$

It was determined that under the conditions and approximations of the mathematical model, the vortex sizes reach their maximum value in the middle of the total length of the section  $L_0$ .

#### 4. Conclusions

It was shown that the application of Rubinstein's theory of spatial charge together with the numerical modelling of ion transport phenomena using the Navier-Stokes hydrodynamic equations made it possible to conduct theoretical studies of convectively unstable structures in EMS. It was found that in the numerical modelling, the most important parameters are the size of the electrical heterogeneity sections of the membrane surface, the current density, and the length of the space charge region. The use of mathematical approaches allowed us to study the occurrence of electroconvective vortices at the membrane surface, including the study of the mutual influence of the vortices on each other.

We determined the fundamental correlations between the membrane surface morphology, electroconvection strength, and overlimiting mass transfer in electromembrane systems with different ion-exchange resin particle content. It was shown that an increase in the proportion of ion-exchange resin in the production of heterogeneous strongly acidic membranes promoted the formation and development of electroconvection in the membrane channel due to a decrease in the electrical inhomogeneity step of the surface.

The developed mathematical model of electroconvection in membrane channels with heterogeneous ion-exchange membranes may be a theoretical basis for targeted modification of their surface in order to develop new generation membranes. For these membranes, electroconvection will be the main mechanism of

electrolyte ion transfer under intensive current modes.

#### Author contributions

All authors made an equivalent contribution to the preparation of the publication.

#### Conflict of interests

The authors declare that they have no known competing financial interests or personal relationships that could have influenced the work reported in this paper.

#### References

- Zabolotskii V. I., Nikonenko V. V., Urtenov M. K., Lebedev K. A., Bugakov V. V. Electroconvection in systems with heterogeneous ion-exchange membranes. *Russian Journal of Electrochemistry*. 2012;48(7): 692–703. <https://doi.org/10.1134/S102319351206016X>
- Zabolotsky V. I., Novak L., Kovalenko A. V., Nikonenko V. V., Urtenov M. Kh., Lebedev K. A., But A. Yu. Electroconvection in systems with heterogeneous ion-exchange membranes. *Petroleum Chemistry*. 2017;57(9): 779–789. <https://doi.org/10.1134/S0965544117090109>
- Dukhin S. S., Mishchuk N. A. Intensification of electro dialysis based on electroosmosis of the second kind. *Journal of Membrane Science*. 1993;79(2-3): 199–210. [https://doi.org/10.1016/0376-7388\(93\)85116-E](https://doi.org/10.1016/0376-7388(93)85116-E)
- Mishchuk N. A. Electro-osmosis of the second kind near the heterogeneous ion-exchange membrane. *Colloids and Surfaces A: Physicochemical and Engineering Aspects*. 1998;140(1-3): 75–89. [https://doi.org/10.1016/S0927-7757\(98\)00216-7](https://doi.org/10.1016/S0927-7757(98)00216-7)
- Rubinshtein I., Shtilman L. Voltage against current curves of cation-exchange membranes. *Journal of the Chemical Society, Faraday Transactions 2: Molecular and Chemical Physics*. 1979;75: 231–246. <https://doi.org/10.1039/F29797500231>
- Rubinstein I., Zaltzman B., Kedem O. Electric fields in and around ion-exchange membranes. *Journal of Membrane Science*. 1997;125(1): 17–21. [https://doi.org/10.1016/S0376-7388\(96\)00194-9](https://doi.org/10.1016/S0376-7388(96)00194-9)
- Rubinshtein I., Zaltsman B., Pretz I., Linder C. Experimental Verification of the electroosmotic mechanism of overlimiting conductance through a cation exchange electro dialysis membrane. *Russian Journal of Electrochemistry*. 2002;38: 853–863. <https://doi.org/10.1023/A:1016861711744>
- Zabolotskii V. I., Loza S. A., Sharafan M. V. Physicochemical properties of profiled heterogeneous ion-exchange membranes. *Russian Journal of Electrochemistry*. 2005;41(10): 1053–1060. <https://doi.org/10.1007/s11175-005-0180-2>
- Pis'menskaya N. D., Nikonenko V. V., Mel'Nik N. A., Pourcelli G., Larchet G. Effect of the

ion-exchange-membrane/solution interfacial characteristics on the mass transfer at severe current regimes. *Russian Journal of Electrochemistry*. 2012;48(6): 610–628. <https://doi.org/10.1134/S1023193512060092>

10. Zabolotsky V. I., Lebedev K. A., Vasilenko P. A., Kuzyakina M. V. Mathematical modeling of vortex structures during electroconvection in the channel of an electro dialyzer cell on model membranes with two conductive sections. *Ecological Bulletin of Scientific Centers of the Black Sea Economic Cooperation*. 2019;16(1): 73–82. (In Russ.) <https://doi:10.31429/vestnik-16-1-73-82>

11. Newman J. S. *Electrochemical systems*. New Jersey: Prentice-Hall, Inc., Englewood Cliffs; 1973. 432 p.

12. Roache P. J. *Computational fluid dynamics*. Hermosa Publishers; 1976. 446 p.

13. Vasil'eva V. I., Bityutskaya L. A., Zaichenko N. A., Grechkina M. V., Botova T. S., Agapov B. L. Microscopic analysis of the surface morphology of ion-exchange membranes\*. *Sorbtsionnye i Khromatograficheskie Protsessy*. 2008;8(2): 260–271. (In Russ.) <http://www.chem.vsu.ru/sorbcr/images/pdf/20080210.pdf>

14. Nikonenko V. V., Kovalenko A. V., Urtenov M. K., Pismenskaya N. D., Han J. Sistat P., Pourcelly G. Desalination at overlimiting currents: State-of-the-art and perspectives. *Desalination*. 2014;342: 85–106. <https://doi.org/10.1016/j.desal.2014.01.008>

15. Zabolotskii V. I., Lebedev K. A., Lovtsov E. G. Mathematical model for the overlimiting state of an ion-exchange membrane system. *Russian Journal of Electrochemistry*. 2006;48(2):836–846. <https://doi.org/10.1134/S1023193506080052>

16. Nikonenko V. V., Mareev S. A., Pis'menskaya N. D., Uzdanova A. M., Kovalenko A. V., Urtenov M. Kh., Pourcelly G. Effect of electroconvection and its use in intensifying the mass transfer in electro dialysis (Review). *Russian Journal of Electrochemistry*. 2017;53: 1122–1144. <https://doi.org/10.1134/S1023193517090099>

17. Rubinstein S. M., Manukyan G., Staicu A., Rubinstei I., Zaltzman B., Lammertink R. G. H., Mugele F., Wessling M. Direct observation of a nonequilibrium electro-osmotic instability. *Physical Review Letters*. 2008;101: 236101. <https://doi.org/10.1103/PhysRevLett.101.236101>

18. Urtenov M. Kh. *Boundary value problems for systems of nernst-planck-poisson equations (factorization, decomposition, models, numerical analysis)\**. Krasnodar: KubGU Publ.; 1998. 126 p. (In Russ.)

19. Babeshko V. A., Zabolotskii V. I., Korzhenko N. M., Seidov R. R., Urtenov M. Kh. Stationary transport theory of binary electrolytes in the one-dimensional case: numerical analysis. *Doklady Physical Chemistry*. 1997;42(8): 836–846. Available at: <https://www.elibrary.ru/item.asp?id=13268324>

20. Zabolotskii V. I., Lebedev K. A., Urtenov M. K., Nikonenko V. V., Vasilenko P. A., Shaposhnik V. A., Vasil'eva V. I. A mathematical model describing voltammograms and transport numbers under intensive electro dialysis modes. *Russian Journal of Electrochemistry*. 2013;49( 4). 369–380. <https://doi.org/10.1134/S1023193513040149>

21. Kasparov M. A., Lebedev K. A. Mathematical model of ion transport through the interface 'ion-exchange membrane / strong electrolyte'. *Ecological Bulletin of Scientific Centers of the Black Sea Economic Cooperation*. 2017;14(4-1): 40–49. (In Russ., abstract in Eng.). Available at: <https://vestnik.kubsu.ru/article/view/756>

22. Zabolotsky V. I., Nikonenko V. V. *Ion transport in membranes\**. Moscow: Nauka Publ.; 1996. 392 p. (In Russ.)

23. Zabolotskiy V. I., But A. Yu., Vasil'eva V. I., Akberova E. M., Melnikov S. S. Ion transport and electrochemical stability of strongly basic anion-exchange membranes under high current electro dialysis conditions. *Journal of Membrane Science*. 2017;526: 60–72. <https://doi.org/10.1016/j.memsci.2016.12.028>  
\*Translated by author of the article.

## Information about the authors

*Konstantin A. Lebedev*, Dr. Sci. (Phys.–Math.), Professor of the Department of Intellectual Information Systems, Kuban State University (Krasnodar, Russian Federation).

<https://orcid.org/0000-0003-0950-9770>  
[klebedev.ya@yandex.ru](mailto:klebedev.ya@yandex.ru)

*Viktor I. Zabolotsky*, Dr. Sci. (Chem.), Head of the Department of Physical Chemistry, Kuban State University (Krasnodar, Russian Federation).

<https://orcid.org/0000-0002-9414-7307>  
[vizab@chem.kubsu.ru](mailto:vizab@chem.kubsu.ru)

*Vera I. Vasil'eva*, Dr. Sci. (Chem.), Professor of the Department of Analytical Chemistry, Voronezh State University (Voronezh, Russian Federation).

<https://orcid.org/0000-0003-2739-302X>  
[viv155@mail.ru](mailto:viv155@mail.ru)

*Elmara M. Akberova*, Cand. Sci. (Chem.), Leading Engineer of the Department of Analytical Chemistry, Voronezh State University (Voronezh, Russian Federation).

<https://orcid.org/0000-0003-3461-7335>  
[elmara\\_09@inbox.ru](mailto:elmara_09@inbox.ru)

Received 11.10.2021; approved after reviewing 07.11.2022; accepted for publication 15.11.2022; published online 25.12.2022.

Translated by Anastasiia Ananeva  
Edited and proofread by Simon Cox



## Original articles

Research article

<https://doi.org/10.17308/kcmf.2022.24/10645>

## The effect of solution-combustion mode on the structure, morphology and size-sensitive photocatalytic performance of $\text{MgFe}_2\text{O}_4$ nanopowders

L. A. Lebedev , M. I. Tenevich, V. I. Popkov

Ioffe Institute,  
26 Politekhnikeskaya str., Saint Petersburg 194021, Russian Federation

### Abstract

Ferrites play a significant role in a number of applications from magnetic ceramic to multifunctional catalytic and antimicrobial material. As a catalytic material, it is crucial to have not only high activity but also be made from abundant elements via energy-efficient techniques, to make it valuable for industrial application. Magnesioferrite nanocrystalline powder series were prepared via solution-combustion route while varying fuel/oxidizer ratio. They were investigated by XRD, BET, SEM, DRS, and Fenton-like photocatalytic activity. Temperature-time profiles were measured for the combustion reaction of all mixtures. Results show a strong correlation between fuel content and temperature, structure, and morphology. But despite average surface area and crystallite size, the sample synthesized with excess fuel showed high dye adsorption capacity and catalytic activity.

**Keywords:** Photocatalyst, Ferrites, Spinel, Solution-combustion synthesis, Fenton-like process

**Acknowledgments:** The XRD and SEM studies were performed on the equipment of the Engineering Center of Saint Petersburg State Institute of Technology.

**For citation:** Lebedev L. A., Tenevich M. I., Popkov V. I. The Effect of solution-combustion mode on the structure, morphology and size-sensitive photocatalytic performance of  $\text{MgFe}_2\text{O}_4$  nanopowders. *Condensed Matter and Interphases*. 2022;24(4): 496–503. <https://doi.org/10.17308/kcmf.2022.24/10645>

**Для цитирования:** Лебедев Л. А., Теневич М. И., Попков В. И. Влияние режима растворного горения на структуру, морфологию и размерно-чувствительные фотокаталитические свойства нанопорошков  $\text{MgFe}_2\text{O}_4$  Конденсированные среды и межфазные границы. 2022;24(4): 496–503. <https://doi.org/10.17308/kcmf.2022.24/10645>

 Lev A. Lebedev, e-mail: 1595lion@gmail.com

© Lebedev L. A., Tenevich M. I., Popkov V. I., 2022



The content is available under Creative Commons Attribution 4.0 License.

## 1. Introduction

In recent years, photocatalytic materials draw significant attention due to their ability to promote a number of chemical processes using a renewable energy source – sunlight. For instance, this type of catalysts can be utilized for several so-called “green processes”, from wastewater processing [1–3] and carbon oxide capturing [1–4], to hydrogen production [7] and antibacterial treatment [8, 9]. There are a wide variety of materials that can be used for this purpose, but for commercial applications, materials made from abundant elements are more favourable.

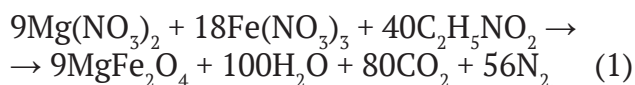
In this research work, magnesium ferrite spinel was the material of choice due to the inexpensiveness of its precursor elements and the known high photocatalytic activity of ferrite spinels [10]. Ferrites are not only catalytically active but also exhibit magnetic properties [11–17], which makes them multifunctional and suitable for facile separation from reaction mass when needed.

Surface properties play a significant role in any heterocatalytic reaction [18]. Therefore, the control over the surface area, its morphology, chemical composition, and some other characteristics, determines the resulting performance of any catalytic material. For the synthetic approach, the solution-combustion technique was selected, because of its short reaction times and energy efficiency [10, 12 19–23].

## 2. Experimental

### 2.1. Synthesis

For sample preparation glycine ( $C_2H_5NO_2$ ) was used as fuel and added to an aqueous solution of magnesium ( $Mg(NO_3)_2 \cdot 6H_2O$ ) and ferric ( $Fe(NO_3)_3 \cdot 9H_2O$ ) nitrate in a quartz beaker and heated until water boils off and further to start combustion process (ignition starts at 250–270 °C). All chemicals were used as purchased without further purification. Synthetic ratios were calculated based on equation 1:



The stoichiometric factor  $\Phi$  was proportional to the equation and was equal to 1 for glycine to nitrate ion ratio 5/9, and changed accordingly by

multiplication of glycine amount for the same weight of nitrates.

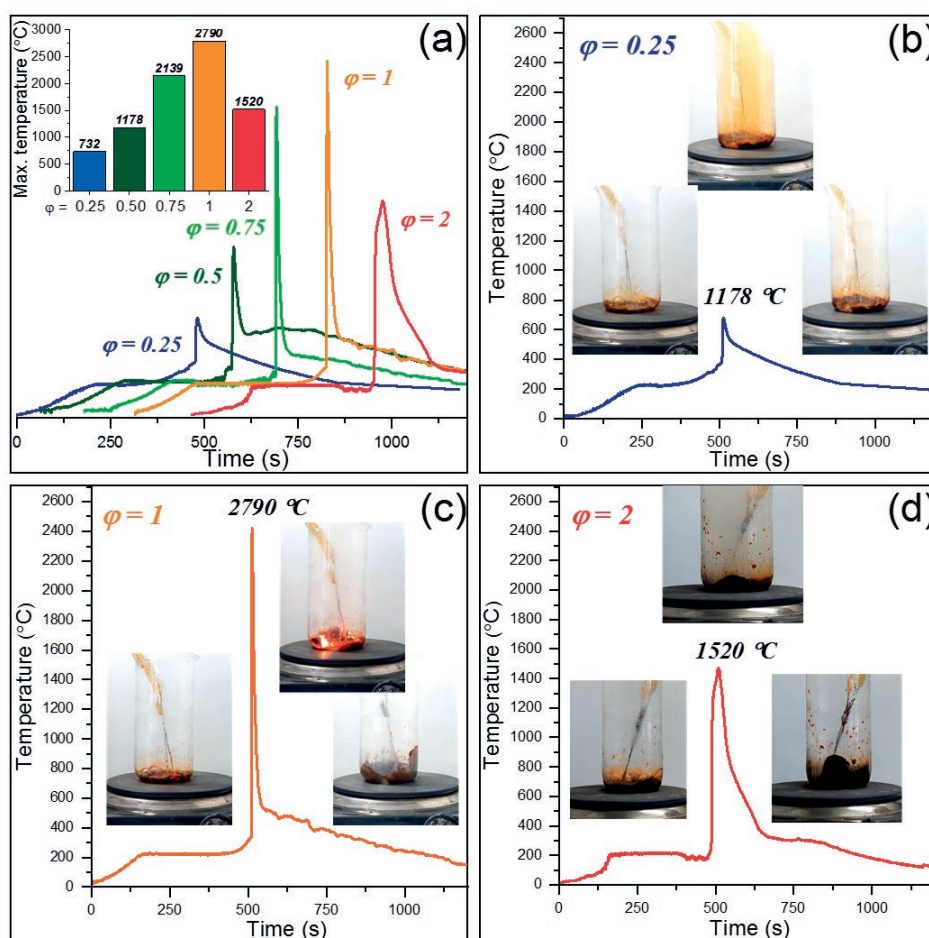
### 2.2. Characterization

Temperature measurements were conducted using a quartz beaker with inserted K-type thermocouple assembly 0.4 mm in diameter sealed in a glass capillary tube 0.5 mm in diameter attached to ADC-module E20-10 (Lcard) with a sampling rate of 1KSample/s. The miniature size of the thermocouple provides low thermal inertia as well as glass cover prevents short circuits and dissolution by reaction mixture. X-ray diffraction patterns were measured with Rigaku SmartLab3 ( $Cu-K_\alpha$  radiation, at  $I = 50$  mA and  $U = 40$  kV). The diffraction patterns of samples were recorded in the Bragg–Brentano focusing geometry with a step of  $0.01^\circ$  and speed of  $1^\circ/\text{min}$  in the angle range  $10\text{--}90^\circ$ . The specific surface area was measured with Sorbi-M automatic BET sorbometer. Scanning electron microscopy images were taken with VEGA3 TESCAN scanning electron microscope. Diffusion reflectance and absorption spectra of samples were measured on an Avaspec-ULS2048 compact spectrometer equipped with an AvaSphere-30-Refl integrating sphere for DRS spectra and a 3D-printed cuvette holder for absorption measurements. Catalytic activity was measured via methylene blue discoloration under two 35W Xe-arc lamp irradiation, with 30-minute intervals for two hours total.

## 3. Results and discussion

### 3.1. Temperature-time analysis of solution combustion

Temperature-time profiles are shown in Fig. 1a accompanied by a bar graph of the maximum combustion temperature for each sample. It can be noticed that samples with fuel deficiency as well as proficiency have lower reaction temperature compared to the stoichiometric ratio, but the profiles are different. In Fig. 1b, c and d photos of reaction mixtures during each stage of the process are shown, and there is a significant change in the combustion stage. For samples with fuel deficiency combustion followed by the evolution of large amounts of nitrogen oxides that can be observed by the brown coloration of the beaker, it indicates that thermal decomposition



**Fig. 1.** Time-temperature profiles of solution-combustion synthesis of  $\text{MgFe}_2\text{O}_4$ : (a) – comparison of time-temperature profiles of samples with different stoichiometric ratios, insert bar graph shows maximum peak temperature of reaction; (b), (c) and (d) – thermal profiles curves with photos of reaction beaker at different stages of reaction for 0.25, 1 and 2 stoichiometric ratios respectively

of nitrates prevailed for this  $\Phi$ . That type of combustion mode can be called thermolysis due to prevailing of thermal de-composition over combustion process.

For  $\Phi = 1$ , combustion proceeds vigorously, with a high amount of energy, seen by a bright glow of reaction products and the absence of fumes, due to most of the products being hot water vapour along with nitrogen and carbon dioxide gases. From the temperature-time profile and visual observation, this combustion mode can be classified as volume type. The maximum temperature was measured as high as 2790 °C while it was in a short period.

Mixture with doubled fuel content ( $\Phi = 2$ ) showed partly similar behavior as fuel deficient mixture, during combustion, large amounts of gases come out along with foaming of products.

Thereby, the reaction mixture forms a thermal insulating cocoon, widening the thermal profile peak. The formation of active char foam also prolongs reaction time due to the smoldering process on ambient air. Thus reaction mode can be marked as a smoldering type (24–27).

### 3.2. X-ray powder diffraction

The structural analysis shown in Fig. 2 confirmed that all prepared samples were magnesioferrite spinels. There is an expected correlation between  $\Phi$  value and crystallinity, that goes along with maximum temperature change. Higher combustion temperatures provide better crystallinity and bigger crystallite size, where a sample with  $\Phi = 0.25$  is al-most amorphous to  $\Phi = 1$  with the biggest crystal size and low amorphous phase content.

### 3.3. The $N_2$ Adsorption/Desorption Isotherms (BET)

The surface area with SEM photos is presented in Fig. 3. A high correlation of surface area with reaction temperature can be observed, where  $\Phi = 0.25$  sample has the highest area, with the lowest reaction temperature, and  $\Phi = 1$  sample has the lowest, with the highest combustion temperature, for  $\Phi = 0.5$  and 2 area values as well as temperature values are close to each other. From SEM images, fuel deficient sample exhibit a sponge-like structure with big, thin-walled pores that resemble bubbles, stoichiometric sample looks similar to previously mentioned, but most of the “bubbles” are popped and only skeletal borders are left, which could mean that most of the surface gone due to high reaction temperature and melting of thin pore walls. Sample with excess fuel has denser foam-like, compared to previous samples, structure with much smaller pores, but regarding that specific area is not as high as could be expected in comparison with sample  $\Phi = 0.25$ , which means that some pores are sealed and thus unavailable.

### 3.4. Diffusion reflectance spectroscopy

Optical band gap values were calculated from diffuse reflective spectra shown in Fig. 4. Fuel ratio-dependent changes in band gap can be observed as a gradual decrease from 2.24 to 2.10 eV with an increase of  $\Phi$  value, but this change occurs within the 10% region. Nevertheless, this can be utilized to fine-tune material bandgap or make it more susceptible to lower energy irradiation.

### 3.5. Fenton-like properties

To study the photocatalytic activity of obtained samples, Fenton-like decolorization of methylene blue (MB) dye was used. Absorbance spectra and results of their processing are shown in Fig. 4c-f. From adsorption capacity and photodecomposition rate constant data, one can see that sample with double fuel excess has the most remarkable parameters among some prepared samples, despite the fact of its average specific surface value. Such a significant activity can be attributed to specific surface morphology as well as the number and accessibility of active

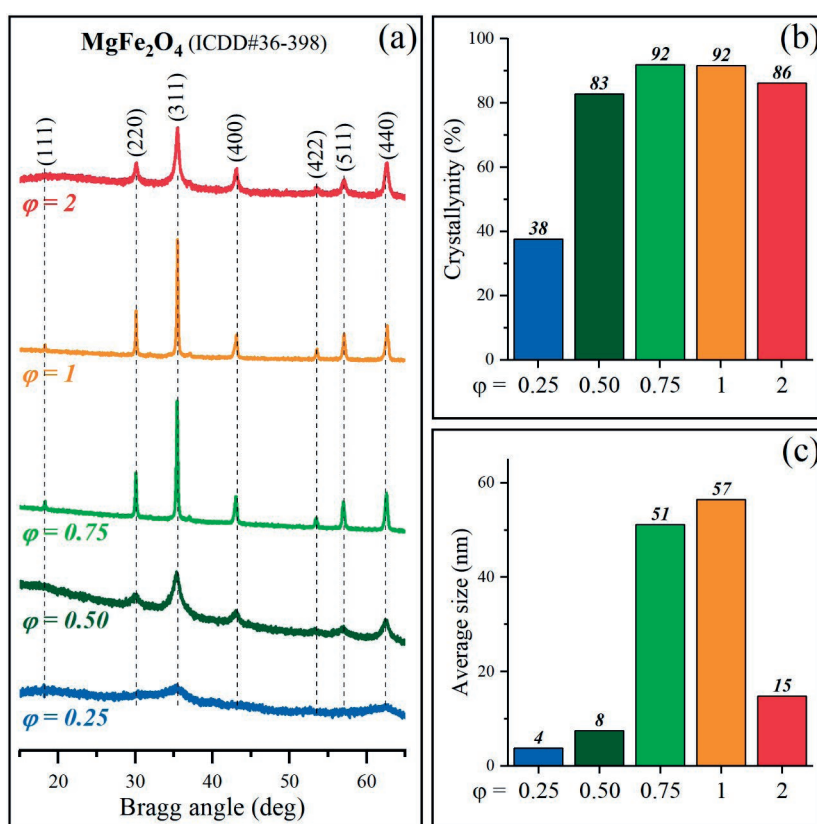
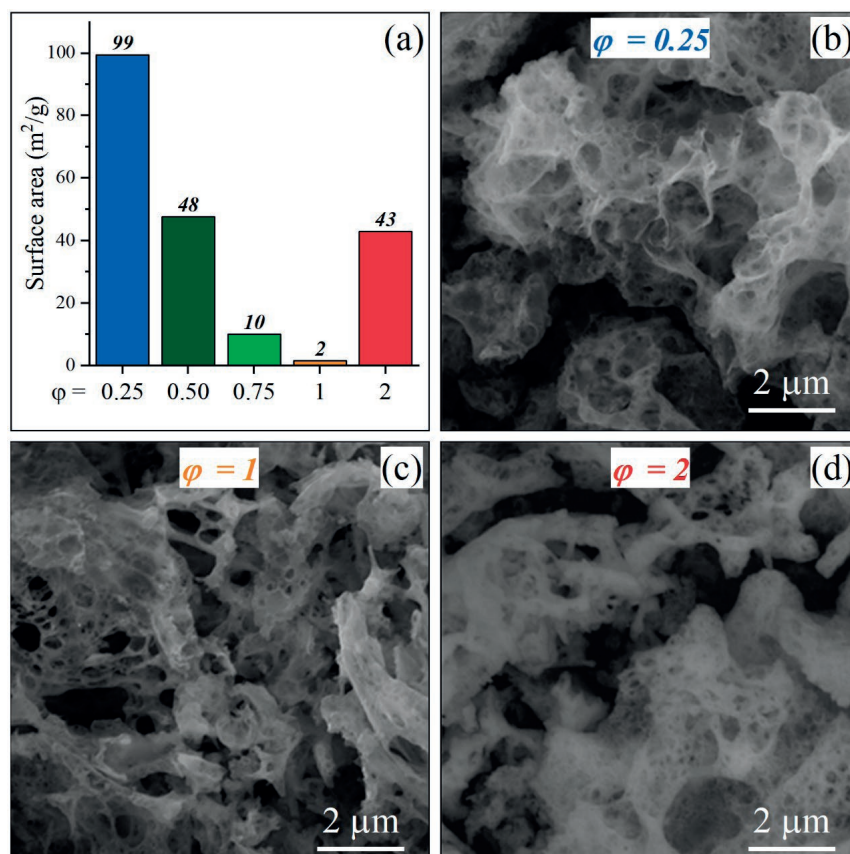


Fig. 2. (a) – XRD patterns of  $MgFe_2O_4$  samples; (b) – crystallinity; (c) – average crystal size





**Fig. 3.** (a) – BET surface area of spinel samples; (b), (c) and (d) are SEM images of MgFe<sub>2</sub>O<sub>4</sub> spinels prepared at  $\Phi = 0.25, 1$  and  $2$  respectively

centres. In contrast to samples with  $\Phi$  in a range from 0.25 to 1, where the main surface species can be oxide or hydroxide groups, because of full combustion and carbon depletion, sample with higher content of the fuel, has a chance to form not only carbon-based structures but also carboxylic, carbonate and other species on the mixed oxide surface, determined by fuel composition and reaction conditions.

#### 4. Conclusions

A highly photo-Fenton-like active MgFe<sub>2</sub>O<sub>4</sub> spinel sample was synthesized by solution-combustion approach, with variable fuel content  $\Phi$ . In this research work, it was shown that change in  $\Phi$  value not only affects combustion temperature but also the combustion mode itself, changing the shape of the temperature-time profile that can result in a combination of morphological, structural, and surface properties. Such a behavior can be observed for half and twice excess of fuel, temperatures are similar and

the same for crystallinity and surface area, but due to other types of combustion (smoldering) and thus wider temperature peak, the sample with  $\Phi = 2$  has a larger crystallite size, smaller pores, and significantly higher adsorption and catalytic properties. Further investigation of this phenomenon can provide data to additionally enhance the photocatalytic activity of these materials by tuning their properties with reaction conditions such as fuel type and ratio.

#### Contribution of the authors

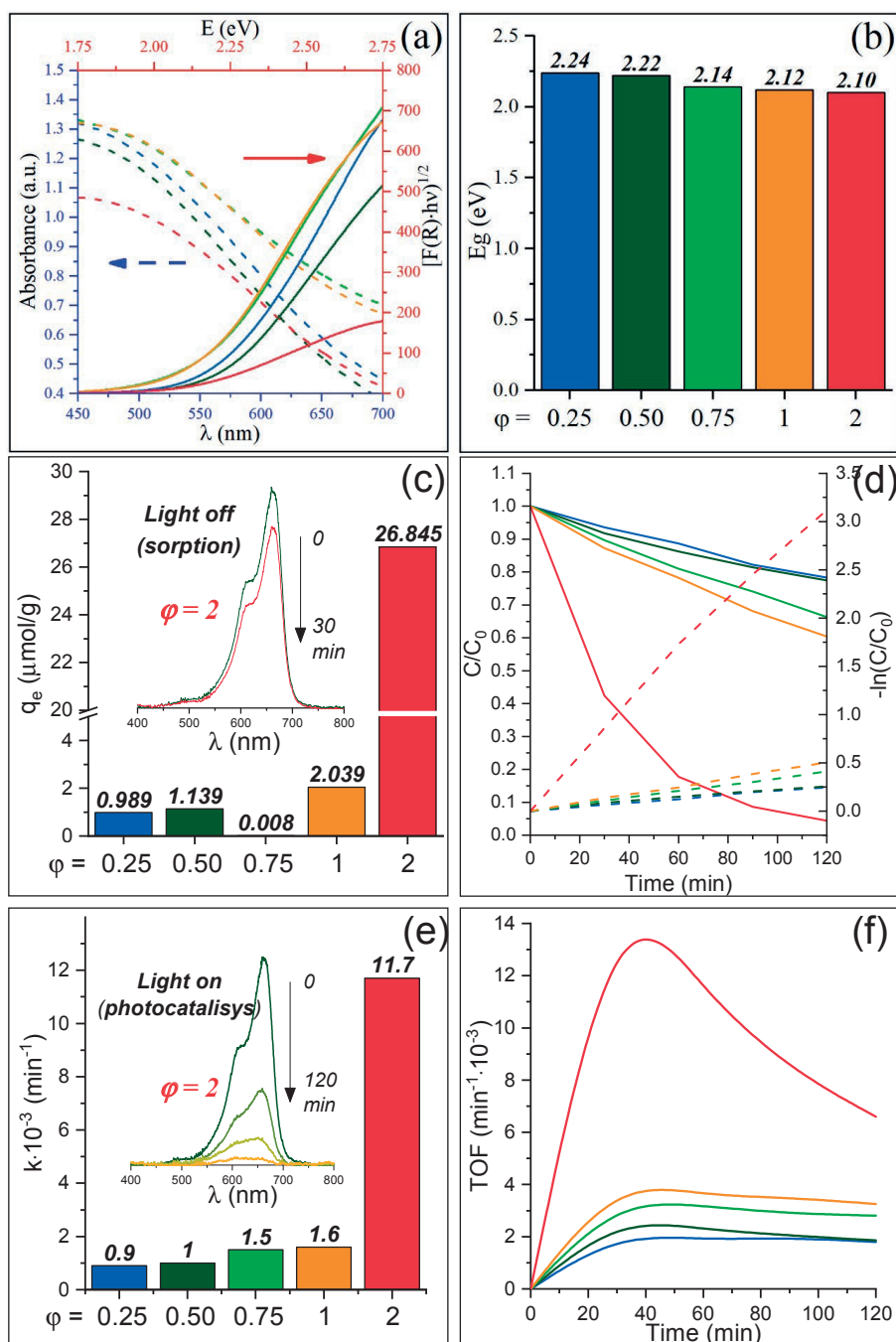
The authors contributed equally to this article.

#### Conflict of interests

The authors declare that they have no known competing financial interests or personal relationships that could have influenced the work reported in this paper.

#### References

1. Oliveira T. P., Rodrigues S. F., Marques G. N., ... Oliveira, M. M.. CuFe<sub>2</sub>O<sub>4</sub> for the degradation of dyes



**Fig. 4.** (a) – dash lines – DRS spectra of samples, solid line – Tauc plots; (b) - optical bandgaps of MgFe<sub>2</sub>O<sub>4</sub> prepared at different  $\Phi$  values; (c) – adsorption capacity; insert – absorption spectra of MB solution initial and after 30 minutes of sorption on sample with  $\Phi = 2$ ; (d) - solid line –  $C/C_0$  plot, dash line –  $-\ln(C/C_0)$ ; (e) – photodecomposition rate constant; insert – absorption spectra of MB solution undergoing degradation on sample with  $\Phi = 2$  and (f) – turnover frequency of synthesized spinel samples

under visible light. *Catalysts*. 2022;12(6): 623. <https://doi.org/10.3390/catal12060623>

2. Ali M. A., Idris M. R., Quayum M. E.. Fabrication of ZnO nanoparticles by solution-combustion method for the photocatalytic degradation of organic dye. *Journal of Nanostructure in Chemistry*. 2013;3(1): 2–7. <https://doi.org/10.1186/2193-8865-3-36>

3. Kefeni K. K., Mamba B. B. Photocatalytic application of spinel ferrite nanoparticles and nanocomposites in wastewater treatment: Review. *Sustainable Materials and Technologies*. 2020;23: e00140. <https://doi.org/10.1016/j.susmat.2019.e00140>

4. Bowker M. Photocatalytic hydrogen production and oxygenate photoreforming. *Catalysis Letters*.

- 2012;142(8): 923–929. <https://doi.org/10.1007/s10562-012-0875-4>
5. Lyulyukin M. N., Kurenkova A. Y., Bukhtiyarov A. V., Kozlova E. A. Carbon dioxide reduction under visible light: a comparison of cadmium sulfide and titania photocatalysts. *Mendeleev Communications*. 2020;30(2): 192–194. <https://doi.org/10.1016/j.mencom.2020.03.021>
  6. Muhammad N. A., Wang Y., Muhammad F. E., He T. Photoreduction of carbon dioxide using strontium zirconate nanoparticles. *Science China Materials*. 2015;58(8): 634–639. <https://doi.org/10.1007/s40843-015-0077-7>
  7. Chandrasekaran S., Bowen C., Zhang P., Li Z., Yuan Q., Ren X. Spinel photocatalysts for environmental remediation, hydrogen generation, CO<sub>2</sub> reduction and photoelectrochemical water splitting. *Journal of Materials Chemistry A*. 2018;6(24): 11078–11104. <https://doi.org/10.1039/c8ta03669a>
  8. Martinson K. D., Beliaeva A. D., Sakhno D. D., ... Popkov V. I. Synthesis, structure, and antimicrobial performance of Ni<sub>x</sub>Zn<sub>1-x</sub>Fe<sub>2</sub>O<sub>4</sub> (x = 0, 0.3, 0.7, 1.0) magnetic powders toward *E. coli*, *B. cereus*, *S. citreus*, and *C. tropicalis*. *Water*. 2022;14(3): 454. <https://doi.org/10.3390/w14030454>
  9. Maksoud M. I. A. A., El-Sayyad G. S., Ashour A. H., ... El-Okr M. M. Antibacterial, antibiofilm, and photocatalytic activities of metals-substituted spinel cobalt ferrite nanoparticles. *Microbial Pathogenesis*. 2019;127: 144–158. <https://doi.org/10.1016/j.micpath.2018.11.045>
  10. Martinson K. D., Belyak V. E., Sakhno D. D., Kiryanov N. V., Chebanenko M. I., Popkov V. I. Effect of fuel type on solution combustion synthesis and photocatalytic activity of NiFe<sub>2</sub>O<sub>4</sub> nanopowders. *Nano-systems: Physics, Chemistry, Mathematics*. 2021;12(6): 792–798. <https://doi.org/10.17586/2220-8054-2021-12-6-792-798>
  11. Lomanova N. A., Panchuk V. V., Semenov V. G., Pleshakov I. V., Volkov M. P., Gusarov V. V. Bismuth orthoferrite nanocrystals: magnetic characteristics and size effects. *Ferroelectrics*. 2020;569(1): 240–250. <https://doi.org/10.1080/00150193.2020.1822683>
  12. Lomanova N. A., Tomkovich M. V., Osipov A. V., ... Gusarov V. V. Formation of Bi<sub>1-x</sub>Ca<sub>x</sub>FeO<sub>3-δ</sub> nanocrystals via glycine-nitrate combustion. *Russian Journal of General Chemistry*. 2019;89(9): 1843–1850. <https://doi.org/10.1134/s1070363219090196>
  13. Popkov V. I., Almjasheva O. V., Gusarov V. V. Formation mechanism of nanocrystalline yttrium orthoferrite under heat treatment of the coprecipitated hydroxides. *Russian Journal of General Chemistry*. 2015;85(6): 1370–1375. <https://doi.org/10.1134/s107036321506002x>
  14. Kopeychenko E. I., Mittova I. Y., Perov N. S., Nguyen A. T., Mittova V. O., Alekhina Y. A., Salmanov I. V. Nanocrystalline heterogeneous multiferroics based on yttrium ferrite (core) with calcium zirconate (titanate) shell. *Russian Journal of General Chemistry*. 2020;90(6): 1030–1035. <https://doi.org/10.1134/s1070363220060158>
  15. Tomina E. V., Kurkin N. A., Korol' A. K., ... Bui V. X. Spray pyrolysis synthesis, electrical and magnetic properties of Ho<sub>x</sub>Bi<sub>1-x</sub>FeO<sub>3</sub> nanocrystals. *Journal of Materials Science: Materials in Electronics*. 2022;33(32): 24594–24605. <https://doi.org/10.1007/s10854-022-09170-0>
  16. Vo Q. M., Mittova V. O., Nguyen V. H., Mittova I. Y., Nguyen A. T. Strontium doping as a means of influencing the characteristics of neodymium orthoferrite nanocrystals synthesized by co-precipitation method. *Journal of Materials Science: Materials in Electronics*. 2021;32(22): 26944–26954. <https://doi.org/10.1007/s10854-021-07068-x>
  17. Kopeychenko E. I., Mittova I. Y., Perov N. S., ... Pham V. Synthesis, composition, and magnetic properties of cadmium-doped lanthanum ferrite nanopowders. *Inorganic Materials*. 2021;57(4): 367–371. <https://doi.org/10.1134/s0020168521040075>
  18. Tikhanova S. M., Lebedev L. A., Martinson K. D., ... Popkov V. I. The synthesis of novel heterojunction h-YbFeO<sub>3</sub>/o-YbFeO<sub>3</sub> photocatalyst with enhanced Fenton-like activity under visible-light. *New Journal of Chemistry*. 2021;45(3): 1541–1550. <https://doi.org/10.1039/d0nj04895j>
  19. Abbas R., Martinson K. D., Kiseleva T. Y., Markov G. P., Tyapkin P. Y., Popkov V. I. Effect of fuel type on the solution combustion synthesis, structure, and magnetic properties of YIG nanocrystals. *Materials Today Communications*. 2022;32: 103866. <https://doi.org/10.1016/j.mtcomm.2022.103866>
  20. Martinson K. D., Belyak V. E., Sakhno D. D., Chebanenko M. I., Panteleev I. B. Mn–Zn ferrite nanoparticles by calcining amorphous products of solution combustion synthesis: preparation and magnetic behavior. *International Journal of Self-Propagating High-Temperature Synthesis*. 2022;31(1): 17–23. <https://doi.org/10.3103/s106138622201006x>
  21. Martinson K. D., Belyak V. E., Sakhno D. D., ... Popkov V. I. Solution combustion assisted synthesis of ultra-magnetically soft LiZnTiMn ferrite ceramics. *Journal of Alloys and Compounds*. 2022;894: 162554. <https://doi.org/10.1016/j.jallcom.2021.162554>
  22. Martinson K. D., Sakhno D. D., Belyak V. E., Kondrashkova I. S. Ni<sub>0.4</sub>Zn<sub>0.6</sub>Fe<sub>2</sub>O<sub>4</sub> nanopowders by solution-combustion synthesis: Influence of red/ox ratio on their morphology, structure, and magnetic properties. *International Journal of Self-Propagating High-Temperature Synthesis*. 2020;29(4): 202–207. <https://doi.org/10.3103/s106138622004007x>
  23. Ivanets A. I., Roshchina M. Yu., Prozorovich V. G. Ibuprofen oxidative degradation in the presence of Fenton-catalyst based on MgFe<sub>2</sub>O<sub>4</sub> nanoparticles.

*Proceedings of the National Academy of Sciences of Belarus, Chemical Series*. 2019;55(3): 345–351. <https://doi.org/10.29235/1561-8331-2019-55-3-345-351>

24. Varma A., Mukasyan A. S., Rogachev A. S., Manukyan K. V. Solution combustion synthesis of nanoscale materials. *Chemical Reviews*. 2016;116(23): 14493–14586. <https://doi.org/10.1021/acs.chemrev.6b00279>

25. Wang X., Qin M., Fang F., Jia B., Wu H., Qu X., Volinsky A. A. Solution combustion synthesis of nanostructured iron oxides with controllable morphology, composition and electrochemical performance. *Ceramics International*. 2018;44(4): 4237–4247. <https://doi.org/10.1016/j.ceramint.2017.12.004>

26. Siddique F., Gonzalez-Cortes S., Mirzaei A., Xiao T., Rafiq M. A., Zhang X. Solution combustion synthesis: the relevant metrics for producing advanced and nanostructured photocatalysts. *Nanoscale*. 2022;14: 11806–11868. <https://doi.org/10.1039/d2nr02714c>

27. Ghosh S. K., Prakash A., Datta S., Roy S. K., Basu D. Effect of fuel characteristics on synthesis of calcium hydroxyapatite by solution combustion route. *Bulletin of Materials Science*. 2010;33(1): 7–16. <https://doi.org/10.1007/s12034-010-0010-3>

### Information about the authors

*Lev A. Lebedev*, Specialist, Junior Research Fellow, Hydrogen Energy Lab, Ioffe Institute, (Saint Petersburg, Russian Federation).

<https://orcid.org/0000-0001-9449-9487>  
1595lion@gmail.com

*Maxim I. Tenevich*, PhD student, Junior Research Fellow, Hydrogen Energy Lab, Ioffe Institute, (Saint Petersburg, Russian Federation).

<https://orcid.org/0000-0003-2003-0672>

*Vadim I. Popkov*, Cand. Sci. (Chem.), Lab Head, Hydrogen Energy Lab, Ioffe Institute, (Saint Petersburg, Russian Federation).

<https://orcid.org/0000-0002-8450-4278>  
vadim.i.popkov@mail.ioffe.ru

*Received 01.07.2022; approved after reviewing 18.07.2022; accepted for publication 15.09.2022; published online 25.12.2022.*

*Translated by the authors*



## Original articles

Research article

<https://doi.org/10.17308/kcmf.2022.24/10554>

## The influence of acid activation of bentonite in the composition of a bipolar membrane on the characteristics of the electro dialysis conversion of sodium sulphate

S. I. Niftaliev<sup>1</sup>, O. A. Kozaderova<sup>1</sup>, K. B. Kim<sup>1✉</sup>, P. E. Belousov<sup>2</sup>, V. V. Krupskaya<sup>2</sup>, A. V. Timkova<sup>1</sup>

<sup>1</sup>Voronezh State University of Engineering Technologies,  
19 Revolutsii pr., Voronezh 394036, Russian Federation

<sup>2</sup>Institute of Geology of Ore Deposits, Petrography, Mineralogy, and Geochemistry of the Russian Academy of Sciences,  
35 Staromonetny per., Moscow 119017, Russian Federation

### Abstract

The effect on the characteristics of the electro dialysis process of the acid activation of bentonite included in the cation-exchange layer of an experimental bipolar membrane obtained by applying a liquid LF-4SK cation-exchange layer containing bentonite particles onto an anion-exchange membrane-substrate MA-41 was studied.

Acid activation of bentonite was carried out with nitric acid ( $C = 1$  and  $4 \text{ mol/dm}^3$ ) for 6 hours at temperatures of 20 and 90 °C. The conversion of sodium sulphate ( $C = 0.5 \text{ mol/dm}^3$ ) was carried out in a six-section electro dialysis apparatus with experimental bipolar membranes containing bentonite in its original form and after acid activation. It has been shown that the addition of bentonite treated with nitric acid ( $C = 4 \text{ mol/dm}^3$ ,  $t = 90 \text{ °C}$ ,  $\tau = 6 \text{ h}$ ) to the cation-exchange layer of a bipolar membrane leads to an increase in productivity, current efficiency and a decrease in energy costs compared to a membrane containing bentonite in its original form.

Experimental bipolar membranes made on the basis of MA-41 and a liquid sulphonic cation exchanger containing acid-activated bentonite clays make it possible to obtain an acid and alkali performance comparable to that of the MB-3 bipolar membrane.

**Keywords:** Electro dialysis, Bipolar membrane, Acid activation, Bentonite, Sodium sulphate, Acid, Alkali

**Funding:** The work was carried out within the framework of the grant of the President of the Russian Federation for state support of young Russian scientists - candidates of science (MK-685.2021.1.3).

**For citation:** Niftaliev S. I., Kozaderova O. A., Kim K. B., Belousov P. E., Krupskaya V. V., Timkova A. V. The influence of acid activation of bentonite in the composition of a bipolar membrane on the characteristics of the electro dialysis conversion of sodium sulphate. *Condensed Matter and Interphases*. 2022;24(4): 504–510. <https://doi.org/10.17308/kcmf.2022.24/10554>

**Для цитирования:** Нифталиев С. И., Козадерова О. А., Ким К. Б., Белоусов П. Е., Крупская В. В., Тимкова А. В. Влияние кислотной активации бентонита в составе биполярной мембраны на характеристики электро диализной конверсии сульфата натрия. *Конденсированные среды и межфазные границы*. 2022;24(4): 504–510. <https://doi.org/10.17308/kcmf.2022.24/10554>

✉ Ksenia B. Kim, e-mail: [kmkseniya@yandex.ru](mailto:kmkseniya@yandex.ru)

© Niftaliev S. I., Kozaderova O. A., Kim K. B., Belousov P. E., Krupskaya V. V., Timkova A. V., 2022



The content is available under Creative Commons Attribution 4.0 License.

## 1. Introduction

Electrodialysis with bipolar membranes is a technology for the production of acids and bases without the formation of secondary by-products and the use of additional chemicals [1–4]. The efficiency of the electrodialysis process is largely determined by the electrochemical characteristics of the used bipolar membranes [5–7]. Catalytic additives of various nature are introduced into the bipolar region of the membrane, which affect the dissociation of water molecules for the improvement of their properties [8–16]. There are data that silicate and hydroxyl groups are effective catalysts for water dissociation in the bipolar region [17–18]. The addition of particles of clay material to a bipolar ion-exchange membrane allows obtaining a nanocomposite with improved characteristics [19–21], due to the peculiarity of the structure and composition of clay, as well as the presence of such properties as hydrophilicity and the ability to ion exchange. The chemical activation of clay is carried out for the improvement of the properties, for example, treatment with sodium or calcium salts [22], as well as thermal activation [23]. Among various methods, acid treatment is the most effective way to activate the surface and increase its specific area, which occurs as a result of the modification of the components of bentonite clays, primarily montmorillonite and other clay minerals [24–26].

The aim of this study was the investigation of the effect of acid activation of bentonite in the composition of an experimental bipolar membrane on the characteristics of the electrodialysis conversion of sodium sulphate.

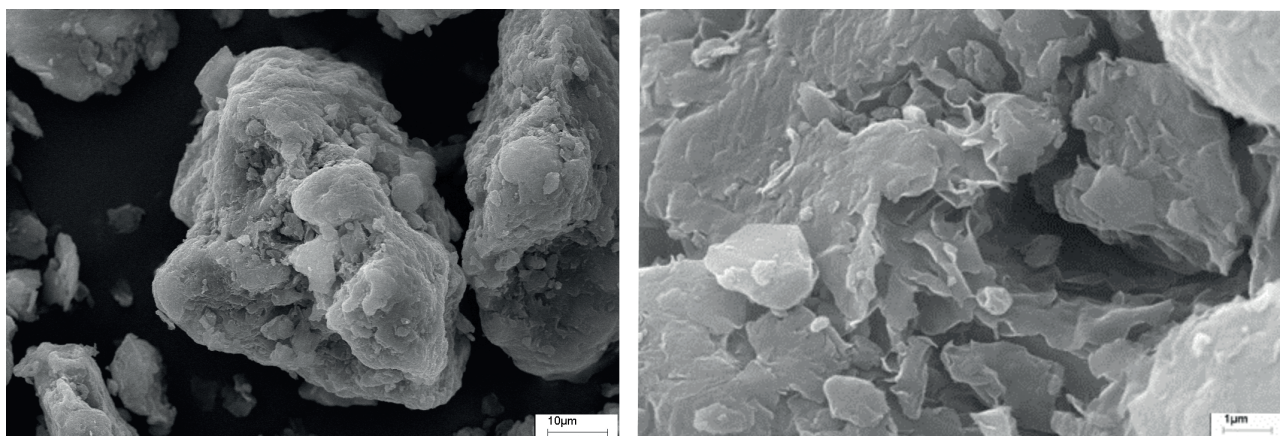
## 2. Experimental

An experimental ion-exchange bipolar membrane was obtained by applying a liquid sulphopolymer LF-4SK layer containing bentonite particles onto an MA-41 anion-exchange membrane according to a well-known method [27]. In this study, bentonite from the Trebia deposit (Morocco) was added to the cation-exchange layer of the membrane (Fig. 1). The sample of natural bentonite consists of 76% smectite and the following impurities: 5% illite, 5% quartz, 21% feldspar, 2% calcite [26]. Smectite is represented by alkaline montmorillonite with a predominance of sodium cations in the interlayer, the main charge is localized in the octahedral layer.

For acid treatment of bentonite, nitric acid of various concentrations was used (1 and 4 mol/dm<sup>3</sup>), the process was carried out with constant stirring at temperatures of 20 and 90 °C. Next, the solid phase was washed with distilled water to a neutral pH value and dried at 60 °C to constant weight.

The study considers four types of experimental bipolar membranes, in the cation-exchange layer of which bentonite (3% by mass) is added:

- MB<sub>MAR. ORIG</sub> – original bentonite;
- MB<sub>MAR1</sub> – bentonite processed under the following conditions:  $C(\text{HNO}_3) = 1 \text{ mol/dm}^3$ ,  $t = 20^\circ\text{C}$ ,  $\tau = 6 \text{ h}$ ;
- MB<sub>MAR2</sub> –  $C(\text{HNO}_3) = 1 \text{ mol/dm}^3$ ,  $t = 90^\circ\text{C}$ ,  $\tau = 6 \text{ h}$ ;
- MB<sub>MAR2</sub> –  $C(\text{HNO}_3) = 4 \text{ mol/dm}^3$ ,  $t = 90^\circ\text{C}$ ,  $\tau = 6 \text{ h}$ .



**Fig. 1.** Images of the surface of an air-dry sample of bentonite (Trebia deposit, Morocco), obtained by scanning electron microscopy (LEO 1450VPCarlZeiss) at different magnifications

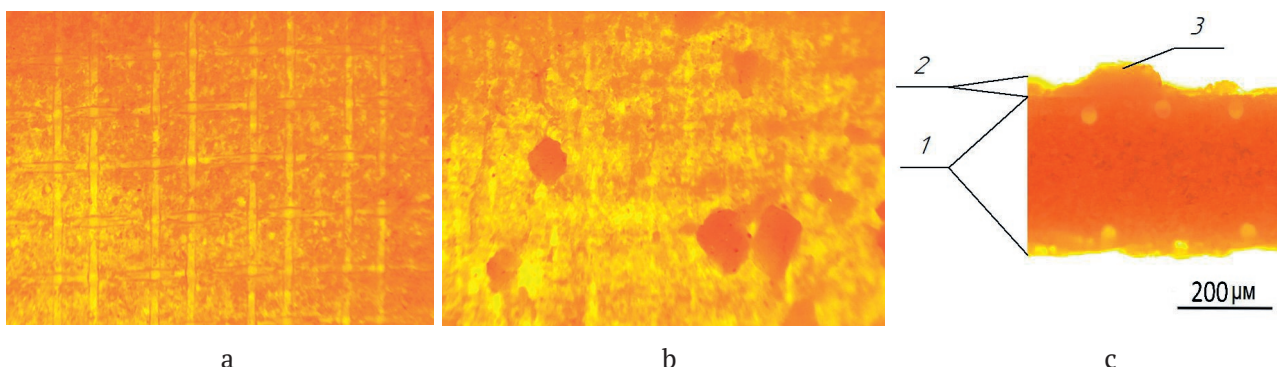
Images of the surface and section of the experimental bipolar membrane with bentonite particles were obtained using a Levenhuk 625 optical microscope (Fig. 2).

The properties of experimental ion-exchange membranes were studied during the electro dialysis of sodium sulphate solution (0.5 mol/dm<sup>3</sup>) and compared with the best domestic bipolar membrane MB-3 (UCC Shchekinoazot), with the lowest electrical resistance during operation [28].

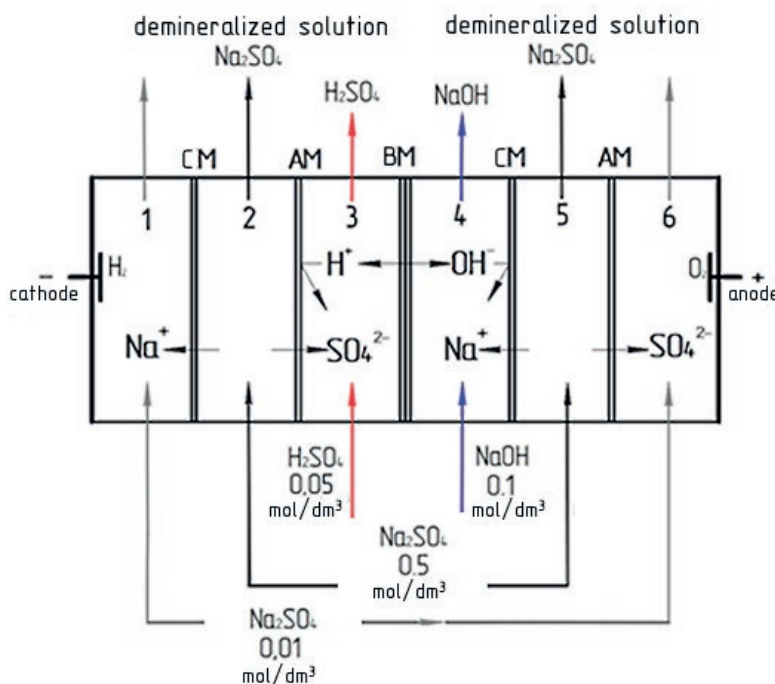
The studies were carried out in a six-section

flow type electro dialysis cell (Fig. 3) consisting of the studied bipolar membrane, heterogeneous cation- (RalexCMH-PP) and anion-exchange (Ralex AMH-PP) membranes manufactured by MEGA (Czech Republic) [29].

The concentration of acid and alkali obtained during the conversion of sodium sulphate was determined by acid-base titration. The efficiency of the electro dialysis process (fluxes of hydrogen and hydroxyl ions generated inside the bipolar membrane,  $J$ , mol/(cm<sup>2</sup>·s); current efficiency  $\eta$ , %; specific energy consumption for the production



**Fig. 2.** Photographs of membranes (optical microscope Levenhuk 625): a – surface of the anionic membrane of the MA-41 substrate; b – surface of the cation-exchange layer with bentonite particles; c – experimental bipolar membrane (1 – membrane-substrate, 2 – cation-exchange layer, 3 – particle of bentonite clay on the surface of the cation-exchange layer)



**Fig. 3.** Scheme of the flow of ions in the chambers of the electro dialysis cell during the conversion of sodium sulphate ( $C = 0.5 \text{ mol/dm}^3$ ): CM – a cation exchange membrane, AM – an anion exchange membrane, BM – a bipolar membrane

of the target product  $W$ , kWh/kg) was calculated using the following formulas:

$$J_i = \frac{(C_0 - C_i) \cdot V}{\tau \cdot S}, \quad (1)$$

$$\eta = \frac{(C_0 - C_i) \cdot V \cdot F}{\tau \cdot I} \cdot 100, \quad (2)$$

$$W = \frac{I \cdot U \cdot \tau}{m}, \quad (3)$$

where  $C_0$  is initial concentration of the solution, mol/dm<sup>3</sup>;  $C_i$  is concentration of ions in the studied section, mol/dm<sup>3</sup>;  $V$  is solution volume, dm<sup>3</sup>;  $F$  is Faraday number A·s/mol;  $\tau$  is time, s;  $I$  is current, A;  $U$  is voltage, V;  $m$  is the mass of the product, kg.

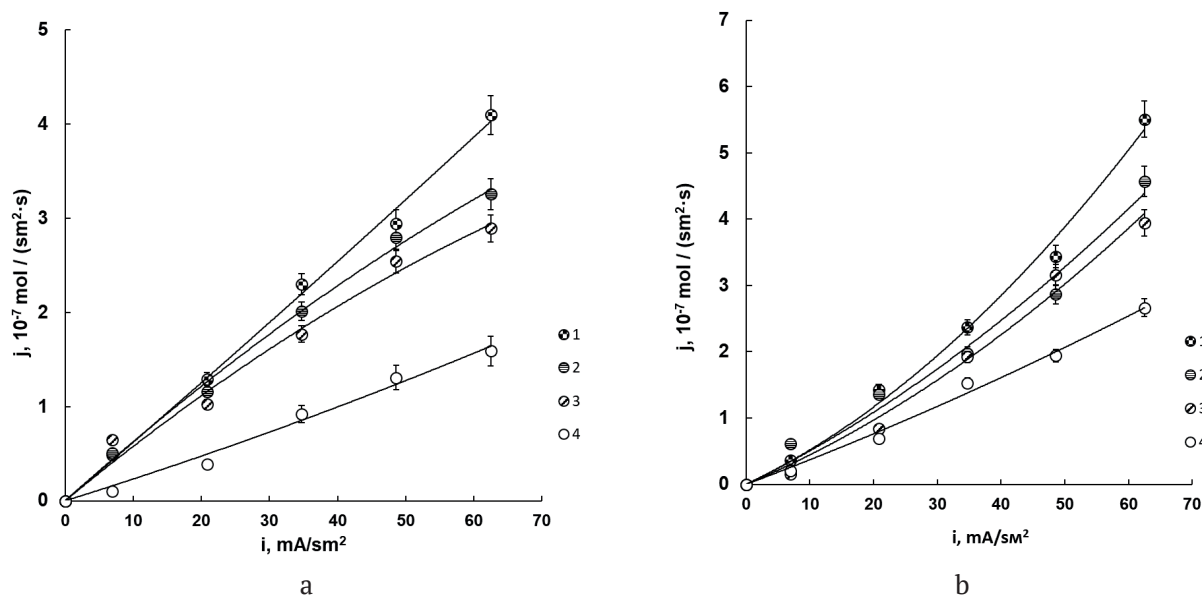
### 3. Results and discussion

The obtained experimental results (Fig. 4) allow us to conclude that the acid activation of bentonite introduced into the bipolar membrane led to an increase in the flux of H<sup>+</sup> ions by 2.5 times, and the flux of OH<sup>-</sup> ions increased by 2.1 times.

The addition of acid-treated bentonite to the cation-exchange layer of the bipolar membrane also led to a reduction in energy costs (Fig. 5).

Bipolar ion exchange membranes containing acid-activated bentonite (MB<sub>MAR3</sub>), in terms of performance and current efficiency are not inferior to industrial MB-3 samples [3] (Table 1).

The obtained results can be explained by the significant changes in the composition and structure of montmorillonite which occur

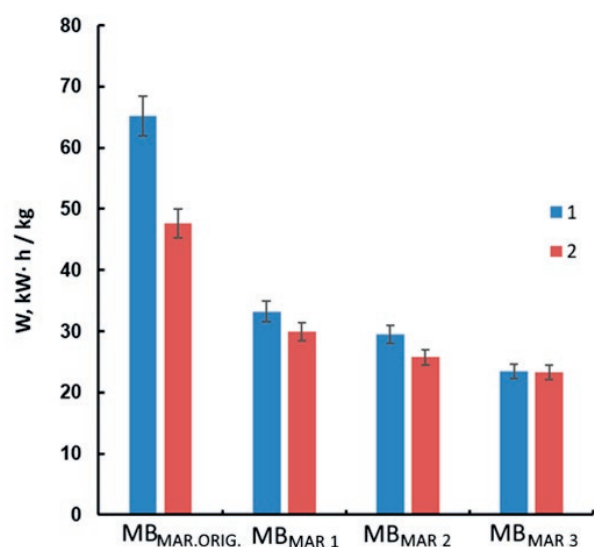


**Fig. 4.** Dependence of the fluxes of H<sup>+</sup> (a) and OH<sup>-</sup> (b) ions generated in a bipolar membrane on the current density for experimental samples: 1 – MB<sub>MAR3</sub>, 2 – MB<sub>MAR2</sub>, 3 – MB<sub>MAR1</sub>, 4 – MB<sub>MAR.Orig</sub>

**Table 1.** Characteristics of the process of sodium sulfate conversion during electro dialysis with MB-3 and experimental membranes (at current density  $i = 60$  mA/cm<sup>2</sup>)

	H <sub>2</sub> SO <sub>4</sub>		NaOH	
	$P$ , mol /m <sup>2</sup> ·h	$\eta$ , %	$P$ , mol /m <sup>2</sup> ·h	$\eta$ , %
MB <sub>MAR.Orig</sub>	2.91±0.29	25.01	9.58±0.96	41.11
MB <sub>MAR1</sub>	5.24±0.52	44.70	16.46±1.65	60.89
MB <sub>MAR2</sub>	5.90±0.59	50.30	14.19±1.42	70.58
MB <sub>MAR3</sub>	7.43±0.74	63.10	19.82±1.98	85.02
MB-3[3]	6.93±0.69	59.21	18.10±1.81	77.10





**Fig. 5.** Energy costs for obtaining the target product (at current density  $i = 60 \text{ mA/cm}^2$ ): 1 –  $\text{H}_2\text{SO}_4$ , 2 –  $\text{NaOH}$

during acid activation. The content of alumina in the sample decreased from 23.3 to 7.6%, the content of magnesium oxide decreased from 2.4 to 0.5%, and the content of silica increased from 59.5 to 80.22% [26]. This was due to the replacement of interlayer cations by oxonium ions, leaching of octahedral cations, and partial resolution of layer 2:1 and, as a consequence, the formation of amorphous silica [26]. Also, after acid treatment, the average size of aggregates of clay particles decreased from 270 to 150 nm [26]. The specific surface area increased from 26 to 78  $\text{m}^2/\text{g}$ , on the one hand, due to an increase in the proportion of amorphous silica, on the other hand, due to surface modification and an increase in microporosity (the total pore volume increased from 0.431 to 4.397  $\text{cm}^3/\text{d}$ ) [30]. Thus, the improvement in the characteristics of electro dialysis using bipolar membranes containing acid-activated bentonite is associated with an increase in bentonite catalytically active with respect to the water dissociation reaction of silicon groups and, possibly, an improvement in the dispersion of bentonite clay particles in a liquid sulphopolymer.

#### 4. Conclusions

The conducted studies have shown that the addition of acid-activated bentonite to the cation-exchange layer of a bipolar membrane increases the dissociation of water molecules. Activation

with nitric acid ( $C = 4 \text{ mol/dm}^3$ ,  $t = 90 \text{ }^\circ\text{C}$ ,  $t = 6 \text{ h}$ ) of bentonite, which is the part of the experimental bipolar membrane, improves the characteristics of the electro dialysis conversion of sodium sulphate compared to the membrane containing bentonite in its original form (for  $\text{H}^+$  productivity and current efficiency increase by 2.5 times, energy costs for obtaining the target product decrease by 2.7 times; for  $\text{OH}^-$  productivity and current efficiency increase by 2.1 times, energy costs for obtaining the target product decrease by 2 times). This is due to the fact that acid activation increases the content of silicon groups in bentonite, which accelerates the dissociation of water molecules, and hence the rate of generation of  $\text{H}^+$  and  $\text{OH}^-$  in the bipolar region of the membrane increases significantly. Also, when bentonite is treated with nitric acid, a decrease in the particle size and an increase in the specific surface area and microporosity were observed, which probably improves the dispersion of bentonite particles in the liquid polymer LF-4SK.

The use of a bipolar membrane with acid-activated bentonite allows obtaining fluxes of  $\text{H}^+/\text{OH}^-$ -ions during the conversion of sodium sulphate, comparable to the fluxes of these ions obtained using bipolar membrane MB-3 (the best domestic sample).

#### Author contributions

All authors made an equivalent contribution to the preparation of the publication.

#### Conflict of interests

The authors declare that they have no known competing financial interests or personal relationships that could have influenced the work reported in this paper.

#### References

1. Melnikov S. S., Mugtamov O. A., Zabolotsky V. I. Study of electro dialysis concentration process of inorganic acids and salts for the two-stage conversion of salts into acids utilizing bipolar electro dialysis. *Separation and Purification Technology*. 2020;235: 116198–116208. <https://doi.org/10.1016/j.seppur.2019.116198>
2. Wiśniewski J., Wiśniewska G., Winnicki T. Application of bipolar electro dialysis to the recovery of acids and bases from water solutions. *Desalination*. 2004;169(1): 11–20. <https://doi.org/10.1016/j.desal.2004.08.003>

3. Kozaderova O. A., Niftaliyev S. I., Kim K. B. Application of bipolar membranes MB-2 modified by chromium (III) hydroxide for sodium sulfate conversion process. *ChemChemTech*. 2019;62 (3): 30–36. (In Russ., abstract in Eng.). <https://doi.org/10.6060/ivkkt201962fp.5811>
4. Öner M. R., Kanca A., Ata O. N., Yapıcı S., Yaylalı N. A. Bipolar membrane electrodialysis for mixed salt water treatment: Evaluation of parameters on process performance. *Journal of Environmental Chemical Engineering*. 2021;9(4): 105750–105763. <https://doi.org/10.1016/j.jece.2021.105750>
5. Niftaliev S., Kozaderova O., Kim K. Application of bipolar electrodialysis with modified membranes for the purification of chromic wastewater from galvanic production. *Ecology and Industry of Russia*. 2021;25(10): 4–9. (In Russ., abstract in Eng.) <https://doi.org/10.18412/1816-0395-2021-10-4-9>
6. Purcelli J. Electrodialysis with bipolar membranes: principles, optimization, and application. *Russian Journal of Electrochemistry*. 2002;38: 919–926. <https://doi.org/10.1023/A:1016882216287>
7. Zabolotskii V. I., Utin S. V., Lebedev K. A., Vasilenko P. A., Shel'deshov N. V. Study of pH correction process of chloride-bicarbonate dilute solutions by electrodialysis with bipolar membranes. *Russian Journal of Electrochemistry*. 2012;48(7): 767–772. <https://doi.org/10.1134/S1023193512070130>
8. Kovalev N. V., Karpenko T. V., Sheldeshov N. V., Zabolotsky V. I. Preparation and electrochemical properties of heterogeneous bipolar membranes with a catalyst for the water dissociation reaction. *Membranes and Membrane Technologies*. 2021;3: 231–244. <https://doi.org/10.1134/S251775162104003X>
9. Mel'nikov S. S., Shapovalova O. V., Shel'deshov N. V., Zabolotsky V. I. Effect of d-metal hydroxides on water dissociation in bipolar membranes. *Petroleum Chemistry*. 2011;51: 577–584. <https://doi.org/10.1134/S0965544111070097>
10. Xue Y.-H., Fu R.-Q., Fu Yan-xun, Xu T.-W. Fundamental studies on the intermediate layer of a bipolar membrane. V. Effect of silver halide and its dope in gelatin on water dissociation at the interface of a bipolar membrane. *Journal of Colloid and Interface Science*. 2006;298: 313–320. <https://doi.org/10.1016/j.jcis.2005.11.049>
11. Liu Y., Chen J., Chen R., Zhou T., Ke C., Chen X. Effects of multi-walled carbon nanotubes on bipolar membrane properties. *Mater. Chem. Phys*. 2018;203: 259–265. <https://doi.org/10.1016/j.matchemphys.2017.09.068>
12. Manohar M., Das A. K., Shahi V. K. Efficient bipolar membrane with functionalized graphene oxide interfacial layer for water splitting and converting salt into acid/base by electrodialysis. *Industrial and Engineering Chemistry Research*. 2018;57: 1129–1136. <https://doi.org/10.1021/acs.iecr.7b03885>
13. Martínez R. J., Farrell J. Water splitting activity of oxygen-containing groups in graphene oxide catalyst in bipolar membranes. *Computational and Theoretical Chemistry*. 2019;1164: 112556. <https://doi.org/10.1016/j.comptc.2019.112556>
14. Simons R. Water splitting in ion exchange membranes. *Electrochimica Acta*. 1985;30(3): 275–282. [https://doi.org/10.1016/0013-4686\(85\)80184-5](https://doi.org/10.1016/0013-4686(85)80184-5)
15. Kozaderova O. A. Electrochemical characterization of an MB-2 bipolar membrane modified by nanosized chromium(III) hydroxide. *Nanotechnologies in Russia*. 2018;13(9-10): 508–515. <https://doi.org/10.1134/S1995078018050075>
16. Cheng G., Zhao Y., Li W., Zhang J., Wang X., Dong C. Performance enhancement of bipolar membranes modified by Fe complex catalyst. *Journal of Membrane Science*. 2019;589: 117243. <https://doi.org/10.1016/j.memsci.2019.117243>
17. Kang M.-S., Choi Y.-J., Lee H.-J., Moon S.-H. Effects of inorganic substances on water splitting in ion-exchange membranes; I. Electrochemical characteristics of ion-exchange membranes coated with iron hydroxide/oxide and silica sol. *Journal Colloid and Interface Science*. 2003;273 (2): 523–532. <https://doi.org/10.1016/j.jcis.2004.01.050>
18. Kang M.-S., Choi Y.-J., Lee H.-J., Moon S.-H. Effects of inorganic substances on water splitting in ion-exchange membranes. II. Optimal contents of inorganic substances in preparing bipolar membranes. *Journal of Colloid and Interface Science*. 2004;273: 533–539. <https://doi.org/10.1016/j.jcis.2004.01.051>
19. Eswaraswamy B., Suhag A., Goel P., Mandal P., Chattopadhyay S. Potential of montmorillonite nanoclay as water dissociation catalyst at the interface of bipolar membrane. *Separation and Purification Technology*. 2022;295: 121257–121268. <https://doi.org/10.1016/j.seppur.2022.121257>
20. Kozaderova O. A., Kim K. B., Belousov P. E., Timkova A. V., Niftaliev S. I. Electrodialysis of a sodium sulphate solution with experimental bentonite-modified bipolar membranes. *Condensed Matter and Interphases*. 2021;23(4): 518–528. <https://doi.org/10.17308/kcmf.2021.23/3670>
21. Peng F., Peng S., Huang C., Xu T. Modifying bipolar membranes with palygorskite and FeCl<sub>3</sub>. *Journal of Membrane Science*. 2008;322: 122–127. <https://doi.org/10.1016/j.memsci.2008.05.027>
22. Lin J., Jiang B., Zhan Y. Effect of pre-treatment of bentonite with sodium and calcium ions on phosphate adsorption onto zirconium-modified bentonite. *Journal of Environmental Management*. 2018;217: 183–195. <https://doi.org/10.1016/j.jenvman.2018.03.079>

23. Masindi V., Ramakokovhu M. M. The performance of thermally activated and vibratory ball milled South African bentonite clay for the removal of chromium ions from aqueous solution. *Materials Today: Proceedings*. 2021;38 (2): 964–974. <https://doi.org/10.1016/j.matpr.2020.05.490>

24. Komadel P. Acid activated clays: Materials in continuous demand. *Applied Clay Science*. 2016;131: 84–99. <https://doi.org/10.1016/j.clay.2016.05.001>

25. Atamanova O. V., Tikhomirova E. I., Kasymbekov Zh. K., Podoksenov A. A. Improving the sorption ability of modified bentonite during wastewater treatment by means of its activation. *Water and ecology: problems and solutions. Water and Ecology: Problems and Solutions*. 2020;1(81): 3–12. (In Russ., abstract in Eng.). <https://doi.org/10.23968/2305-3488.2020.25.1.3-12>

26. Krupskaya V., Novikova L., Tyupina E., Belousov P., Dorzhieva O., Zakusin S., Kim K., Roessner F., Badetti E., Brunelli A., Belchinskaya L. The influence of acid modification on the structure of montmorillonites and surface properties of bentonites. *Applied Clay Science*. 2019;172: 1–10. <https://doi.org/10.1016/j.clay.2019.02.001>

27. Niftaliev S. I., Kozaderova O. A., Kim K. B., Belousov P. E., Timkova A. V., Golovkov I. A. Obtaining bentonite-modified bipolar ion-exchange membranes and study of their electrochemical characteristics. *Proceedings of the Voronezh State University of Engineering Technologies*. 2021;83(3): 216–225. (In Russ., abstract in Eng.). <https://doi.org/10.20914/2310-1202-2021-3-216-225>

28. Zabolotsky V. I., Berezina N. P., Nikonenko V. V., Shudrenko A. A. The evolution of membranous technologies on the base of electrodialysis method in Russia. *Science of Kuban*. 2010;3: 4–10. (In Russ., abstract in Eng.). Available at: <https://www.elibrary.ru/item.asp?id=23764497>

29. *Membrane properties*. Available at: <http://www.ralex.eu/Membrany/Uvod.aspx>

30. Timofeeva M. N., Panchenko V. N., Gil A., Vicente M. A. Effect of nitric acid modification of montmorillonite clay on synthesis of solketal from glycerol and acetone. *Catalysis Communications*. 2017;90: 65–69. <https://doi.org/10.1016/j.catcom.2016.11.020>

## Information about the authors

*Sabukhi I. Niftaliev*, Dr. Sci. (Chem.), Professor, Head of Department of Inorganic Chemistry and Chemical Technology, Voronezh State University of Engineering Technologies (Voronezh, Russian Federation).

<https://orcid.org/0000-0001-7887-3061>  
sabukhi@gmail.com

*Olga A. Kozaderova*, Dr. Sci. (Chem.), Professor at the Department of Inorganic Chemistry and Chemical Technology, Voronezh State University of Engineering Technologies (Voronezh, Russian Federation).

<https://orcid.org/0000-0002-8135-5801>  
kozaderova-olga@mail.ru

*Ksenia B. Kim*, Cand. Sci. (Chem.), Associate Professor at the Department of Inorganic Chemistry and Chemical Technology, Voronezh State University of Engineering Technologies (Voronezh, Russian Federation).

<https://orcid.org/0000-0001-5564-8267>  
kmkseniya@yandex.ru

*Petr E. Belousov*, Cand. Sci. (Geology and Mineralogy), Senior Researcher, Institute of Geology of Ore Deposits, Petrography, Mineralogy, and Geochemistry of the Russian Academy of Sciences (Moscow, Russian Federation).

<https://orcid.org/0000-0002-2657-5828>  
pitbl@mail.ru

*Victoria V. Krupskaya*, Cand. Sci. (Geology and Mineralogy), Senior Researcher, Institute of Geology of Ore Deposits, Petrography, Mineralogy, and Geochemistry of the Russian Academy of Sciences (Moscow, Russian Federation).

<https://orcid.org/0000-0002-6127-748X>  
krupskaya@ruclay.com

*Anna V. Timkova*, postgraduate student, Department of Inorganic Chemistry and Chemical Technology, Voronezh State University of Engineering Technologies (Voronezh, Russian Federation).

<https://orcid.org/0000-0003-0630-2993>  
timkova.anna@mail.ru

*Received 15.07.2022; approved after reviewing 15.09.2022; accepted for publication 15.10.2022; published online 25.12.2022.*

*Translated by Valentina Mittova*

*Edited and proofread by Simon Cox*



# Condensed Matter and Interphases

Kondensirovannye Sredy i Mezhfaznye Granitsy  
<https://journals.vsu.ru/kcmf/>

## Original articles

Research article

<https://doi.org/10.17308/kcmf.2022.24/10555>

## Photosensitisation of reactive oxygen species with titanium dioxide nanoparticles decorated with silver sulphide quantum dots

O. V. Ovchinnikov, M. S. Smirnov, A. S. Perepelitsa✉, S. V. Aslanov✉, A. P. Gureev, V. N. Popov, F. A. Tsybenko, A. M. H. Hussein

Voronezh State University,  
1 Universitetskaya pl., Voronezh, 394018, Russian Federation

### Abstract

At present, the development of methods for sensitisation to the visible and IR spectral regions of systems for the photocatalytic production of reactive oxygen species based on titanium dioxide nanoparticles is of great interest. The purpose of this work was to establish the regularities of the photogeneration of reactive oxygen species during the formation of TiO<sub>2</sub> nanoparticle – Ag<sub>2</sub>S quantum dots nanoheterosystems under the action of radiation in visible and near-infrared spectral regions.

The paper analyses the photocatalytic properties of anatase nanoparticles 10–15 nm in size decorated with colloidal Ag<sub>2</sub>S quantum dots with an average size of 2.5 nm passivated with thioglycolic and 2-mercaptopropionic acids. Selective sensor dyes were used to estimate the effectiveness of sensitisation of various reactive oxygen species with the studied photocatalysts under excitation in the UV and visible region. It was shown that decorating TiO<sub>2</sub> nanoparticles with quantum dots leads to an increased efficiency of the production by the system of hydroxyl radical, superoxide anion, and hydrogen peroxide under photoexcitation in the TiO<sub>2</sub> absorption region (UV range). Sensitisation of the production of reactive oxygen species by nanosystems was detected during excitation by radiation in the visible spectral region (outside the intrinsic TiO<sub>2</sub> absorption band). It was also found that there is an increase in the efficiency of the production of reactive oxygen species (up to 1.5 times) when thioglycolic acid is replaced with 2-mercaptopropionic acid as a passivator of Ag<sub>2</sub>S quantum dots. The obtained data were used to develop a schematic diagram of photoprocesses in the system.

**Keywords:** Reactive oxygen species, Photocatalysis, Nanoparticles, Titanium dioxide, Quantum dots, Silver sulphide, Photosensitisation

**Funding:** This work was supported by the Russian Foundation for Basic Research grant No. 20-32-90167 “Postgraduate students”.

**Acknowledgements:** The studies of structural properties conducted by the methods of transmission electron microscopy and X-ray diffractometry were carried out using the equipment of the VSU Centre for Collective Use of Scientific Equipment.

**For citation:** Ovchinnikov O. V., Smirnov M. S., Perepelitsa A. S., Aslanov S. V., Gureev A. P., Popov V. N., Tsybenko F. A., Hussein A. M. H. Photosensitisation of reactive oxygen species with titanium dioxide nanoparticles decorated with silver sulphide quantum dots. *Condensed Matter and Interphases*. 2022;24(4): 511–522. <https://doi.org/10.17308/kcmf.2022.24/10555>

**Для цитирования:** Овчинников О. В., Смирнов М. С., Перепелица А. С., Асланов С. В., Гуреев А. П., Попов В. Н., Цыбенко Ф. А., Хуссейн А. М. Х. Фотосенсибилизация активных форм кислорода наночастицами диоксида титана, декорированными квантовыми точками сульфида серебра. *Конденсированные среды и межфазные границы*. 2022;24(4): 511–522. <https://doi.org/10.17308/kcmf.2022.24/10555>

✉ Alexei S. Perepelitsa, e-mail: a-perepelitsa@yandex.ru

✉ Sergei V. Aslanov, e-mail: windmaster7@yandex.ru

© Ovchinnikov O. V., Smirnov M. S., Perepelitsa A. S., Aslanov S. V., Gureev A. P., Popov V. N., Tsybenko F. A., Hussein A. M. H. 2022



The content is available under Creative Commons Attribution 4.0 License.

## 1. Introduction

Currently, scientists are actively developing hybrid nanosystems for photovoltaics and photocatalysis applications [1–4]. They are also studying the possibility of using them in clean-up systems [5–7], hydrogen production systems [8–10], for the creation of photobactericidal coatings and systems used to produce reactive oxygen species [11, 12]. Titanium dioxide ( $\text{TiO}_2$ ) has been recognised as being the most suitable for such applications [13, 14]. However, the edge of photosensitivity for titanium dioxide (anatase and rutile) is about 3.1–3.2 eV [15, 16]. Therefore, there is a practically important problem of photosensitising  $\text{TiO}_2$  to visible and IR radiation. Such photosensitisers can be organic dyes [1, 2, 4], plasmonic nanoparticles [17, 18], metal ions [19, 20], and semiconductor quantum dots (QDs) [23, 24].

$\text{Ag}_2\text{S}$  QDs are appropriate for sensitising  $\text{TiO}_2$  to the visible region. Silver sulphide is non-toxic, insoluble in water, chemically stable, and has the band gap of a massive crystal equal to 1.0 eV [25].  $\text{Ag}_2\text{S}$  QDs have size-dependent luminescent and absorption properties [26] and can excite  $\text{TiO}_2$  throughout the visible and near-infra-red region.

Silver sulphide is mainly considered for use as a sensitizer for heterosystems based on  $\text{Ag}_2\text{S}$  epitaxial nanoparticles which are grown or deposited on the surface of  $\text{TiO}_2$  nanoparticles (NPs). As a rule, large  $\text{Ag}_2\text{S}$  nanoparticles are used, of about 5 nm in size and over that hardly have any size effect [27–33]. There are practically no publications devoted to the consideration of the photocatalytic properties of nanosystems based on  $\text{TiO}_2$  nanoparticles (NPs) decorated with colloidal silver sulphide QDs 1–4 nm in size. In addition, the influence of QD passivators on the photocatalytic properties of the  $\text{TiO}_2$  NP –  $\text{Ag}_2\text{S}$  QDs nanosystems still has not been established. Due to the significant nonstoichiometry,  $\text{Ag}_2\text{S}$  QDs are characterised by the presence of a large concentration of defects whose levels can participate in photocatalytic reactions [34] and manifest themselves in the recombination luminescence of the QDs [26, 35, 36]. Thus, it is important to obtain  $\text{Ag}_2\text{S}$  QDs with an interface structure that provides adsorption on the  $\text{TiO}_2$  surface and effective photosensitisation of the production of reactive oxygen species.

The purpose of this work was to establish the patterns of photosensitisation of reactive oxygen species (ROS) during the formation of the  $\text{TiO}_2$  NP –  $\text{Ag}_2\text{S}$  QDs nanoheterosystems when the latter are passivated with thioglycolic and 2-mercaptopropionic acids.

## 2. Experimental

### 2.1. Methods for sample synthesis

Used reagents: silver nitrate ( $\text{AgNO}_3$ ), thioglycolic acid (TGA), 2-mercaptopropionic acid (2MPA), sodium sulphide ( $\text{Na}_2\text{S}$ ), titanium tetrachloride ( $\text{TiCl}_4$ ), absolute ethanol, ammonium hydroxide ( $\text{NH}_4\text{OH}$ ), sodium hydroxide (NaOH), 5-amino-2,3-dihydro-1,4-phthalazinedione (luminol), 2H-1-benzopyranone-2 (coumarin), imidazole, 4-nitroso-N,N-dimethylaniline (RNO) were purchased from Sigma-Aldrich and were used without further purification. Amplex UltraRed and horseradish peroxidase were purchased from Thermofisher Scientific.

Colloidal  $\text{Ag}_2\text{S}$  QDs passivated with thioglycolic (hereinafter  $\text{Ag}_2\text{S}/\text{TGA}$ ) and 2-mercaptopropionic (hereinafter  $\text{Ag}_2\text{S}/2\text{MPA}$ ) acids were synthesised in water using  $\text{Na}_2\text{S}$  as a source of sulphur with the mixture pH of 10 [36]. During the last stage, 50 ml of 1  $\mu\text{M}$  aqueous  $\text{Na}_2\text{S}$  solution was added to the reaction mixture to achieve QDs with an average size of about 2.5 nm. The QDs were then purified from the reaction products by centrifugation and subsequent dissolution in water.

$\text{TiO}_2$  NPs were synthesised using the sol-gel method by means of titanium tetrachloride hydrolysis. As part of a typical approach, 3.5 ml of  $\text{TiCl}_4$  was dissolved in 35 ml of absolute ethanol in an ice bath at 0 °C. The gel was kept for 5 days in a refrigerator and dried at 80 °C. The collected white  $\text{TiO}_2$  crystals were washed several times in distilled water and centrifuged to remove residual reaction products. They were then annealed in air for 2 hours at 400 °C to form a crystalline anatase structure and remove organic impurities. The collected fine crystalline powder was sonicated at 60 kHz for an hour to separate stuck nanoparticles.

To obtain the  $\text{TiO}_2$ – $\text{Ag}_2\text{S}$  nanoheterosystems (hereinafter referred to as NSs), the  $\text{TiO}_2$  NP powder was dissolved in water and sonicated for half an hour until a uniform suspension was obtained. After that, the solution of  $\text{TiO}_2$  NPs

was mixed with the solution of QDs at the rate of 10 Ag<sub>2</sub>S QDs per 1 TiO<sub>2</sub> NP and dried at the temperature of 65 °C with constant stirring. The resulting powder was ground in a mortar, sonicated for an hour, and washed with distilled water.

## 2.2. Equipment and experimental techniques

The OceanOptics USB2000+XR1 fiber spectrometer (Ocean Optics, USA) equipped with a USB-DT light source and an IS80 integrating sphere was used to measure optical absorption spectra and diffuse reflection spectra in the range of 200–900 nm. Barium sulphate powder (P.A.) was used as a white standard. The measured diffuse reflection spectra were rearranged as the  $F(\hbar\omega)$  function known as the Kubelka–Munk function [37]:

$$F(R) = \frac{k}{s} = \frac{1 - R^2}{2R},$$

where  $R$  is the diffuse reflection,  $k$  is the absorption coefficient, and  $s$  is the scattering coefficient. The position of the band gap was estimated by plotting the  $\alpha^{1/2}(\hbar\omega) = F(\hbar\omega) \cdot \hbar\omega$  dependencies where  $F(\hbar\omega)$  is the Kubelka–Munk function of the diffuse reflection spectrum. The linear part of the function was approximated by a straight line to the intersection with the x-axis [38].

A computer-aided spectrometric system based on a MDR-4 diffraction monochromator (Lomo, Russia) with a PDF10/C semiconductor low-noise photodiode (ThorLabs, USA) as a detector was used to measure luminescence spectra in the range of 700–1200 nm. A NDB7675 laser diode (Nichia, Japan) with the wavelength of 462 nm was used as a source of luminescence excitation. A Nichia NCSU276C LED module (Nichia, Japan) with the wavelength of 365 nm, TDS-P001L4G05 LED module (TDS Lighling Co., China) with the wavelength of 520 nm, and a LS-Xe-150 xenon lamp (OKB Spektr, Russia), equipped with interference filters were used to stimulate the production of reactive oxygen species of TiO<sub>2</sub> NPs.

Luminescence quantum yield was measured using a standard method of comparing with a reference [39]. A solution of indocyanine green in dimethyl sulfoxide with a luminescence quantum yield of 13% was used as a reference [40].

The production of superoxide anion (O<sub>2</sub><sup>-</sup>) was measured by the chemiluminescent method using luminol [41]. The integral intensity of chemiluminescence was recorded using an R928P photoelectron multiplier (Hamamatsu, Japan) operating in photon counting mode.

Hydrogen peroxide (H<sub>2</sub>O<sub>2</sub>) was detected with an Amplex UltraRed selective sensor [42]. The luminescence intensity was recorded at the wavelength of 596 nm.

The concentration of hydroxyl radical (·OH) was determined by the luminescence of 7-hydroxycoumarin (7HC) in the 470 nm region [43].

The concentration of singlet oxygen (<sup>1</sup>O<sub>2</sub>) was measured by the absorption method using an imidazole solution with the addition of 4-nitroso-N,N-dimethylaniline (RNO) dye [44] in a ratio of 160:1. The measurement was made by decreasing the optical density of RNO absorption band in the 445 nm region.

The structural properties of the samples were examined by transmission electron microscopy (TEM) using a LIBRA 120 transmission electron microscope (CarlZeiss, Germany) and by X-ray diffractometry (XRD) using a THERMO ARL X'TRA X-ray diffractometer (Thermofisher Scientific, Switzerland).

## 3. Results and Discussion

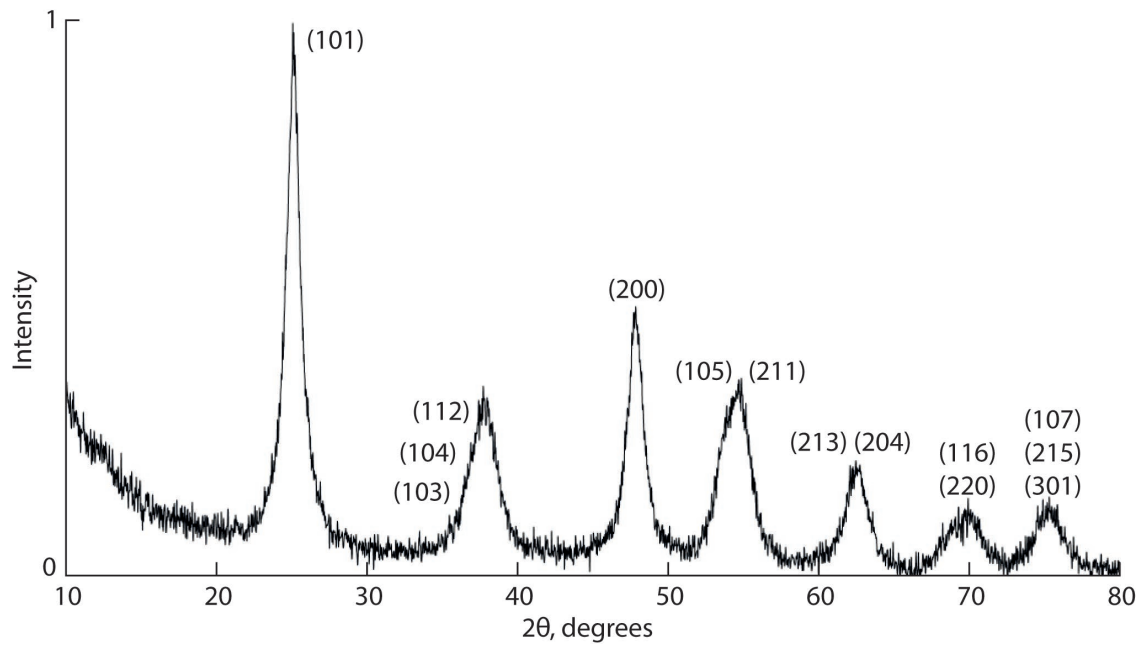
### 3.1. Structural properties of the studied samples

The structure of the synthesised TiO<sub>2</sub> NPs was examined by X-ray diffraction. Figure 1 shows the X-ray diffraction pattern obtained for the  $K_{\alpha_1}$  emission of copper (1.054 Å).

The analysis of diffraction patterns showed the presence of reflexes corresponding to the anatase crystal lattice broadened due to the small size of nanoparticles [45]. Size estimation by the Scherrer formula:

$$d = \frac{0.9\lambda}{\beta \cos\theta},$$

where  $\beta$  is the half-width of the reflection,  $\lambda$  is the wavelength of radiation ( $K_{\alpha_1}$  Cu, 1.054 Å),  $\theta$  is the diffraction angle, showed the presence of crystallites with an average size of about 12 nm. This is consistent with the TEM data for the images shown in Figure 2.

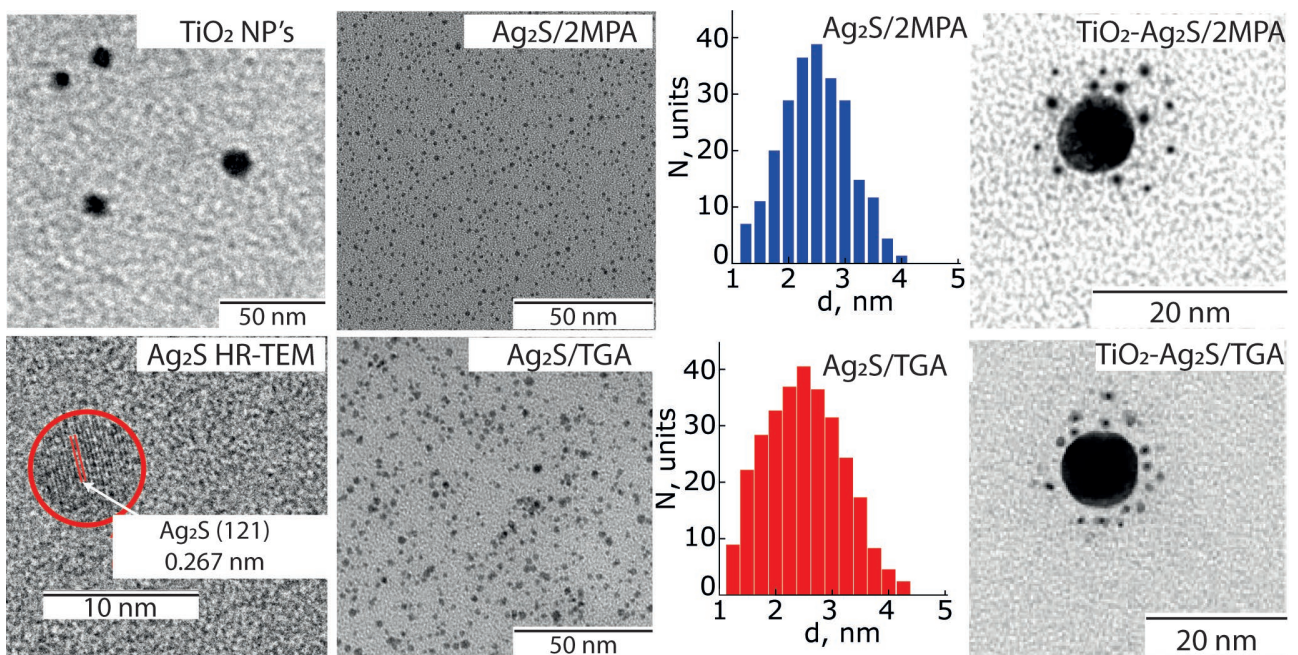


**Fig. 1.** X-ray diffraction pattern of  $\text{TiO}_2$  NPs

The analysis of TEM images showed that the  $\text{TiO}_2$  NPs had a shape close to spherical and had an average size of about 11 nm with a dispersion of ~27%.

The samples of  $\text{Ag}_2\text{S}$  QDs had an average size of 2.5 nm with a dispersion in size of 35 and 40% for  $\text{Ag}_2\text{S}/2\text{MPA}$  and  $\text{Ag}_2\text{S}/\text{TGA}$ , respectively. The

study of high-resolution TEM images showed the presence of diffraction of the crystallographic plane (121) of the monoclinic crystal modification of  $\text{Ag}_2\text{S}$  (space group  $P2_1/c$  with an interplanar distance of ~0.27 nm). In the TEM images of the  $\text{TiO}_2$ - $\text{Ag}_2\text{S}/2\text{MPA}$  and  $\text{TiO}_2$ - $\text{Ag}_2\text{S}/\text{TGA}$  NSs, there were QD clusters near the surface of the  $\text{TiO}_2$



**Fig. 2.** TEM images of  $\text{TiO}_2$  NPs,  $\text{Ag}_2\text{S}$  QDs,  $\text{TiO}_2$ - $\text{Ag}_2\text{S}$  NSs, histograms of  $\text{Ag}_2\text{S}$  QD size distribution, and a high resolution TEM image of  $\text{Ag}_2\text{S}$  nanocrystal

nanoparticles. Thus, a conclusion can be made about the adsorption of  $\text{Ag}_2\text{S}$  QDs on the surface of the  $\text{TiO}_2$  NPs.

### 3.2. Absorption and luminescence properties of the studied samples

Optical absorption spectra were broad bands with the absorption edge shifted towards the short-wave region relative to the absorption edge of massive  $\text{Ag}_2\text{S}$  (1.0 eV). In the 700 nm region (Fig. 3a), there were features associated with excitonic absorption. Using the data on the position of the exciton transition, the size of QDs was estimated using the effective mass approximation [46]:

$$E_g^{\text{eff}} = E_g^{\text{bulk}} + \frac{\hbar^2 \pi^2}{2\mu R^2} + \frac{1.8e^2}{\epsilon R} - 0.248E_{Ry}^*,$$

where  $E_g^{\text{eff}}$  is the peak exciton absorption,  $E_g^{\text{bulk}}$  is the width of the band gap of the bulk crystal,

$\mu = \frac{m_e^* m_{h+}^*}{m_e^* + m_{h+}^*}$  is the reduced effective mass of

exciton,  $e$  is the charge of the electron,  $\epsilon$  is the

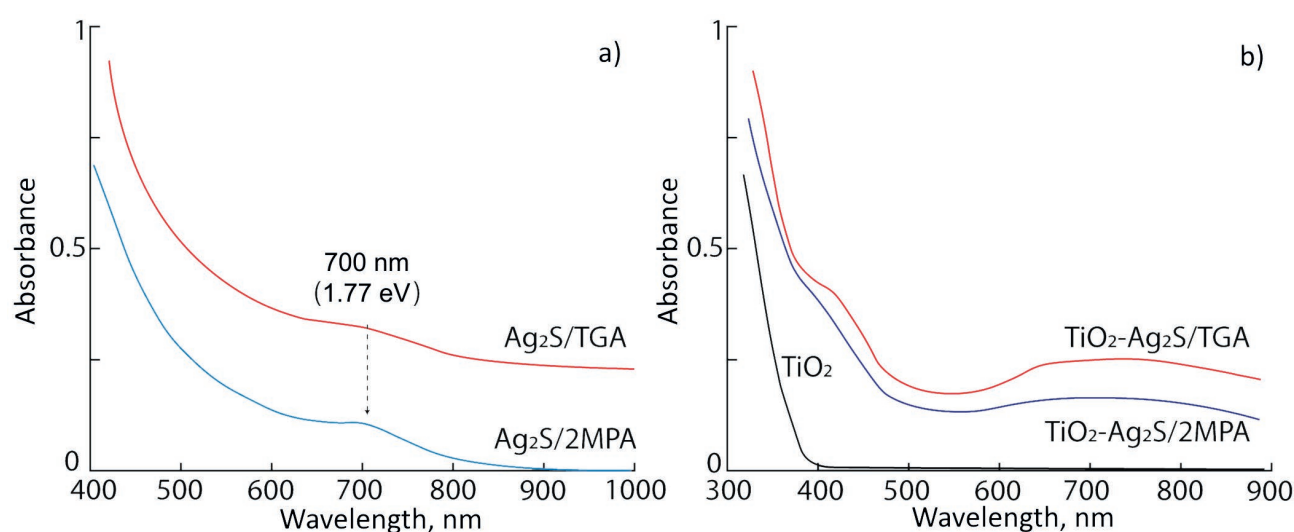
dielectric permeability,  $E_{Ry}^* = \frac{e^4}{2\epsilon^2 \hbar^2 (\frac{1}{m_e^*} + \frac{1}{m_{h+}^*})}$  is

Rydberg's effective energy. The average size for the  $\text{Ag}_2\text{S}/\text{TGA}$  QDs and  $\text{Ag}_2\text{S}/\text{2MPA}$  QDs was about 2.4 nm, which is close to the TEM data.

The edge of the absorption spectra obtained from diffuse reflection (Fig. 3b) for  $\text{TiO}_2$  NPs was located in the region of 3.21 eV, which coincides with the data on the width of the band gap of anatase (3.2 eV) [14, 38]. The absorption spectra of  $\text{TiO}_2-\text{Ag}_2\text{S}/\text{2MPA}$  and  $\text{TiO}_2-\text{Ag}_2\text{S}/\text{TGA}$  NSs (Fig. 3b) had complex structure and were not a simple superposition of the absorption spectra of  $\text{Ag}_2\text{S}$  QDs and  $\text{TiO}_2$  NPs. Such spectral behaviour can be a result of the formation of agglomerates of  $\text{Ag}_2\text{S}$  QDs during their adsorption on the surface of  $\text{TiO}_2$  NPs. It can indicate the emergence of charge carrier transitions between the components of the  $\text{TiO}_2$  NP– $\text{Ag}_2\text{S}$  QDs hybrid system.

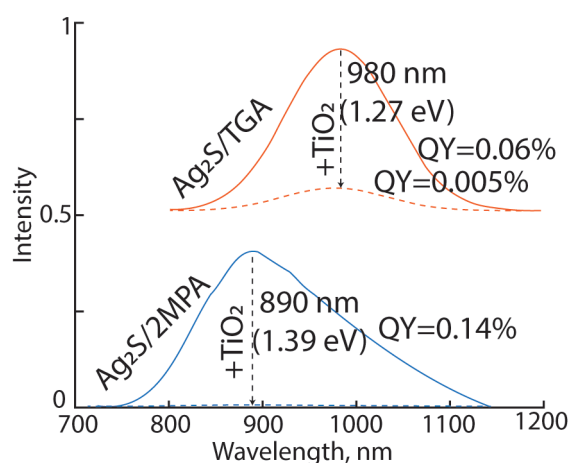
In the luminescence spectra of the  $\text{Ag}_2\text{S}/\text{2MPA}$  and  $\text{Ag}_2\text{S}/\text{TGA}$  QD samples (Figure 4), luminescence bands were observed with their maxima at 890 nm (1.39 eV) and 980 nm (1.27 eV) and quantum yields of 0.14 and 0.06%, respectively. The value of the Stokes shift of the luminescence peak (0.4–0.5 eV) and the half-width of the emission band of  $\sim 0.3$  eV indicate the trap state nature of luminescence [26]. It is worth noting the fact that when the average size of QDs in the samples was the same, the luminescence peaks were shifted by 90 nm relative to each other, which indicates the influence of the surface environment on the energy of the luminescence centre [26, 35, 36, 47].

For  $\text{Ag}_2\text{S}/\text{2MPA}$  QDs, a 70-fold decrease in the luminescence quantum yield of  $\text{Ag}_2\text{S}$  QDs



**Fig. 3.** (a) Optical absorption spectra of  $\text{Ag}_2\text{S}$  QDs. (b) Optical absorption spectra obtained using the method of diffuse reflection and the Kubelka–Munk equation for  $\text{TiO}_2$  NPs,  $\text{TiO}_2-\text{Ag}_2\text{S}/\text{2MPA}$  NSs, and  $\text{TiO}_2-\text{Ag}_2\text{S}/\text{TGA}$  NSs





**Fig. 4.** Luminescence spectra of  $\text{Ag}_2\text{S}$  QDs and  $\text{TiO}_2$ - $\text{Ag}_2\text{S}$  NSs

was observed when they were used to decorate  $\text{TiO}_2$  NPs. For  $\text{Ag}_2\text{S}/\text{TGA}$  QDs, there was a 12-fold decrease. A significant luminescence quenching indicates the formation of charge transfer channels in the nanoheterosystem. Thus, during the formation of  $\text{TiO}_2$ - $\text{Ag}_2\text{S}/2\text{MPA}$  and  $\text{TiO}_2$ - $\text{Ag}_2\text{S}/\text{TGA}$  NSs, there was a transformation of the structure of the optical absorption spectra of the NS components and luminescence quenching of  $\text{Ag}_2\text{S}$  QDs.

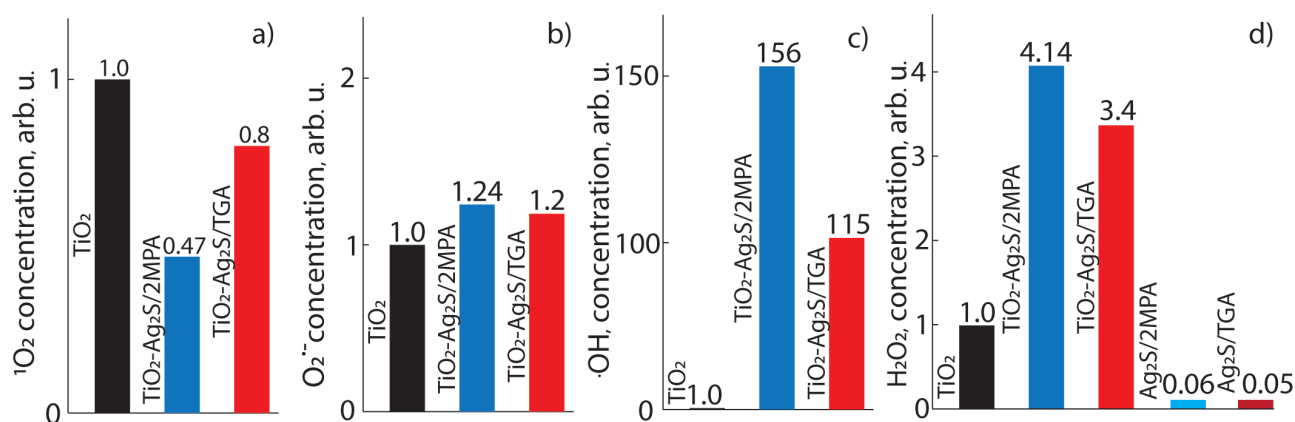
### 3.3. ROS Sensitisation with the studied samples of the $\text{TiO}_2$ - $\text{Ag}_2\text{S}$ nanoheterosystems

Figure 5 shows the results of measurements of ROS generation by nanoheterosystems during excitation in the absorption region of  $\text{TiO}_2$  NPs.  $\text{TiO}_2$  NPs in water exposed to radiation with the wavelength of 365 nm produced superoxide

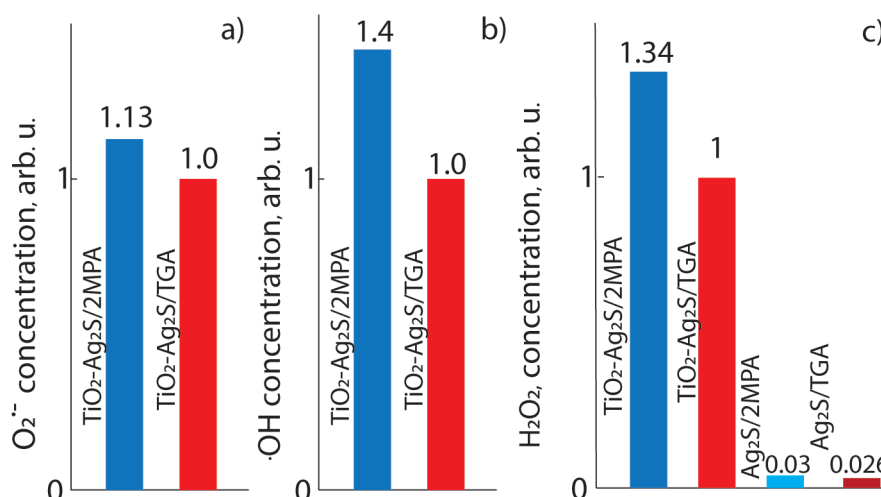
anion ( $\text{O}_2^{\cdot-}$ ), singlet oxygen ( $^1\text{O}_2$ ), hydroxyl radical ( $\cdot\text{OH}$ ), and hydrogen peroxide ( $\text{H}_2\text{O}_2$ ), which is consistent with the data [13]. In the colloidal solutions of  $\text{Ag}_2\text{S}/2\text{MPA}$  and  $\text{Ag}_2\text{S}/\text{TGA}$  QDs, only the production of hydrogen peroxide was recorded (Fig. 5d), which had not been previously recorded for  $\text{Ag}_2\text{S}$  QDs in the literature. The formation of nanosystems led to a change in the efficiency of production of all types of ROS. When  $\text{TiO}_2$ - $\text{Ag}_2\text{S}/2\text{MPA}$  NSs and  $\text{TiO}_2$ - $\text{Ag}_2\text{S}/\text{TGA}$  NSs were excited in the absorption region of titanium dioxide, the production of superoxide anion accelerated by 1.24 and 1.2 times, the production of hydroxyl radical accelerated by 156 and 115 times, and the production of hydrogen peroxide accelerated by 4.14 and 3.4 times, respectively, relative to  $\text{TiO}_2$  NPs. At the same time, there was a decrease in the efficiency of production of singlet oxygen by 2.1 and 1.25 times, respectively, for  $\text{TiO}_2$ - $\text{Ag}_2\text{S}/2\text{MPA}$  NSs and  $\text{TiO}_2$ - $\text{Ag}_2\text{S}/\text{TGA}$  NSs as compared to  $\text{TiO}_2$  NPs.

When  $\text{Ag}_2\text{S}$  QDs and  $\text{TiO}_2$ - $\text{Ag}_2\text{S}$  NSs were illuminated with the wavelength of 520 nm, the radiation which is only absorbed by  $\text{Ag}_2\text{S}$  QDs, certain types of ROS were generated (Fig. 6). Both types of  $\text{Ag}_2\text{S}$  QDs only produced hydrogen peroxide with nearly the same efficiency. Non-decorated  $\text{TiO}_2$  NPs did not produce ROS under photoexcitation with the wavelength of 520 nm.

The formation of  $\text{TiO}_2$ - $\text{Ag}_2\text{S}/2\text{MPA}$  NSs and  $\text{TiO}_2$ - $\text{Ag}_2\text{S}/\text{TGA}$  NSs led to an increase in hydrogen peroxide generation by 44 and 38.5 for visible radiation (520 nm) as compared to the original  $\text{Ag}_2\text{S}/2\text{MPA}$  QDs and  $\text{Ag}_2\text{S}/\text{TGA}$  QDs. In addition,



**Fig. 5.** Histograms of relative concentrations of ROS produced by  $\text{Ag}_2\text{S}$  QDs and  $\text{TiO}_2$ - $\text{Ag}_2\text{S}$  NSs under excitation at  $\lambda = 365$  nm: singlet oxygen (a), superoxide anion (b), hydroxyl radical (c), hydrogen peroxide (g). Histograms are normalised relative to  $\text{TiO}_2$ .



**Fig. 6.** Histograms of relative concentrations of ROS produced by Ag<sub>2</sub>S QDs and TiO<sub>2</sub>-Ag<sub>2</sub>S NSs under excitation at  $\lambda = 520$  nm: superoxide-anion (a), hydroxyl radical (b), hydrogen peroxide (c). Histograms are normalised relative to TiO<sub>2</sub>-Ag<sub>2</sub>S/TGA NSs

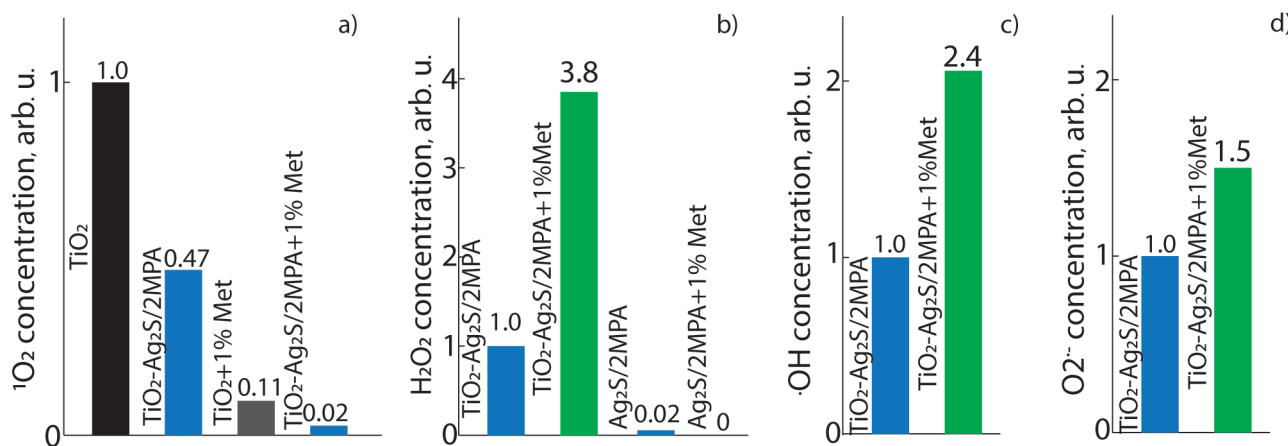
after decoration, anion superoxide and hydroxyl radical were formed, and the effectiveness of TiO<sub>2</sub>-Ag<sub>2</sub>S/2MPA NSs was respectively 1.13 and 1.4 times higher than of TiO<sub>2</sub>-Ag<sub>2</sub>S/TGA NSs. None of the samples produced singlet oxygen under the excitation with the wavelength of 520 nm.

#### 3.4. ROS generation mechanisms in the studied nanoheterosystems

The analysis of data [48–54] allowed determining possible mechanisms of ROS production. Nanoheterosystems produce singlet oxygen only when excited in the UV region. What is more, the association with Ag<sub>2</sub>S QDs results in reduced efficiency. This indicates a hole transfer from

TiO<sub>2</sub> to Ag<sub>2</sub>S and that the generation of <sup>1</sup>O<sub>2</sub> in the system occurs due to the interaction of superoxide anion molecules with holes generated in TiO<sub>2</sub> under the action of excitation radiation, following the  $O_2^- + h^+ \rightarrow {}^1O_2$  mechanism [53]. The absence of <sup>1</sup>O<sub>2</sub> production when illuminated with visible radiation is determined by the absence of holes in TiO<sub>2</sub>. To confirm this hypothesis, the generation of ROS in NSs was measured in the presence of a colloidal solution of a hole acceptor, 1% methanol (Fig. 7a). The introduction of 1% methanol resulted in a ninefold decrease in the efficiency of singlet oxygen generation for TiO<sub>2</sub>, whereas for TiO<sub>2</sub>-Ag<sub>2</sub>S NSs there was a 20-fold decrease.

H<sub>2</sub>O<sub>2</sub> production in Ag<sub>2</sub>S/2MPA QDs and Ag<sub>2</sub>S/TGA QDs was performed according to the



**Fig. 7.** ROS production by the samples of TiO<sub>2</sub> NPs and TiO<sub>2</sub>-Ag<sub>2</sub>S/2MPA NSs in the presence of a hole acceptor (methanol): singlet oxygen ( $\lambda_{exc} = 365$  nm) (a), hydrogen peroxide ( $\lambda_{exc} = 520$  nm) (b), hydroxyl radical ( $\lambda_{exc} = 520$  nm) (c), anionic superoxide ( $\lambda_{exc} = 520$  nm) (d)

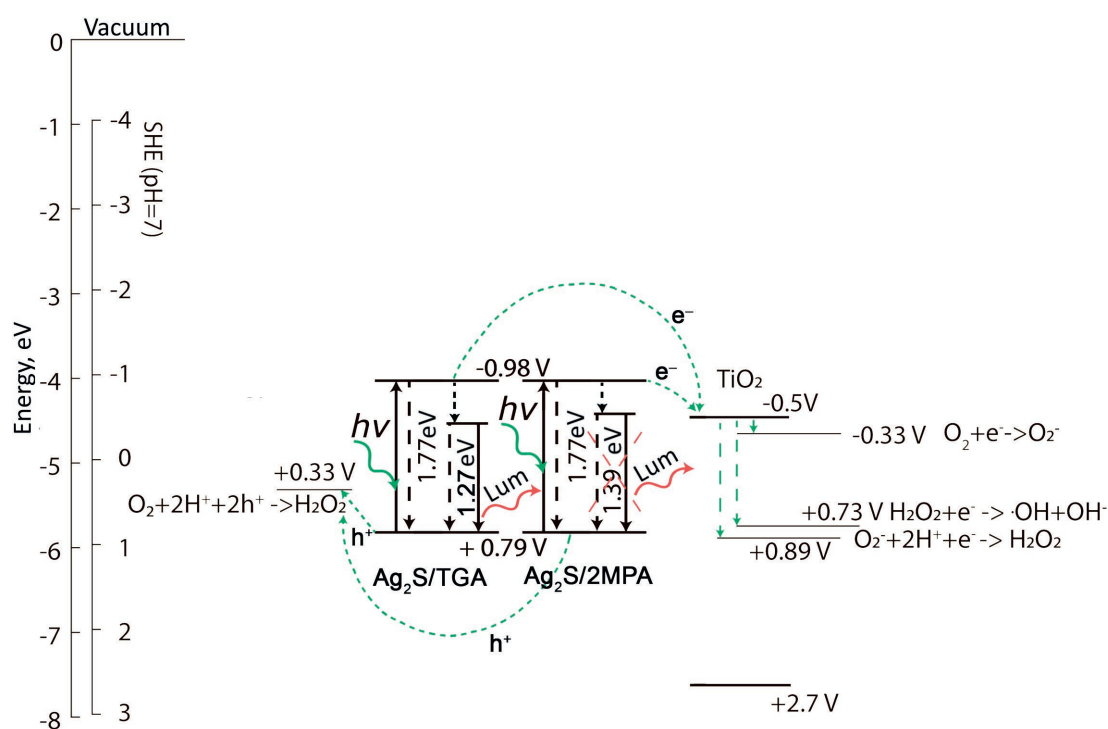
reaction:  $O_2 + 2H^+ + 2h^+ \rightarrow H_2O_2$  [53]. The fact that the reaction terminated when a hole acceptor was added speaks in favour of this theory (Fig. 7b). At the same time, it is likely that in NSs the process of  $H_2O_2$  production took place on the surface of  $TiO_2$  NPs during photoexcitation due to the reaction of  $O_2^- + 2H^+ + e^- \rightarrow H_2O_2$  [53]. The 3.8-fold increase in the efficiency of production of  $H_2O_2$  by  $TiO_2$ - $Ag_2S$  NSs when a hole acceptor was added was probably due to the acceleration of hole recombination, and hence the increase in the number of electrons transferred to  $TiO_2$ .

The production of  $\cdot OH$  radicals occurred on the surface of  $TiO_2$  by decomposition of hydrogen peroxide according to the reaction:  $H_2O_2 + e^- \rightarrow \cdot OH + OH^-$  [53]. When 1% methanol was added, the production of  $\cdot OH$  radicals increased by 2.4 times, which was due to an increase in the concentration of peroxide in the solution.

Superoxide anion was generated by NSs on the surface of  $TiO_2$  according to the reaction  $O_2 + e^- \rightarrow O_2^-$  [53, 54] similar to the case of pure  $TiO_2$  NPs. This is supported by the fact that  $O_2^-$

was not generated by pure  $Ag_2S$  QDs. An increased production of  $O_2^-$  under the action of UV radiation was due to a more efficient electron transfer from  $Ag_2S$  QDs to  $TiO_2$  NPs, which was indirectly confirmed by quenching QD luminescence during the assembly of NSs.

The proposed reactions were used to build a schematic diagram of photoprocesses in the  $TiO_2$ - $Ag_2S$  NSs during excitation by radiation in the visible spectral region (Fig. 8). Photogenerated electrons pass from size quantization levels of  $Ag_2S$  QDs to the conduction band of  $TiO_2$  NPs, where they localise in the near-surface layer and interact with the molecules of  $H_2O$  and  $O_2$  dissolved in water, which is accompanied by the release of superoxide anion, hydroxyl radical, and hydrogen peroxide. The holes at the levels of size quantization of  $Ag_2S$  QDs interact with hydrogen ions and oxygen molecules, which results in the production of hydrogen peroxide. NSs are reduced due to the absorption from the environment ( $H_2O$ ) of free charge carriers which are formed during the decomposition of short-lived ROS.



**Fig. 8.** Schematic diagram of photoprocesses and photocatalytic reactions in the studied samples of  $TiO_2$ - $Ag_2S/2MPA$  NSs and  $TiO_2$ - $Ag_2S/TGA$  NSs during excitation at  $\lambda = 520\text{ nm}$ . The data on redox potential and the location of bands were taken from [1, 2, 10, 25, 46, 48–54]

#### 4. Conclusion

The study established new regularities of photosensitisation processes for reactive oxygen species of TiO<sub>2</sub> NPs (anatase) decorated with Ag<sub>2</sub>S/2MPA and Ag<sub>2</sub>S/TGA QDs. It was found that there is a decrease in the luminescence quantum yield of Ag<sub>2</sub>S QDs (a 70-fold decrease for Ag<sub>2</sub>S/2MPA QDs and a 12-fold decrease for Ag<sub>2</sub>S/TGA QDs) when TiO<sub>2</sub> NPs are decorated, which indicates the separation of charge carriers between the nanosystem components. The photoexcitation of Ag<sub>2</sub>S QDs is accompanied by the production of hydrogen peroxide. It was shown that the formation of TiO<sub>2</sub>-Ag<sub>2</sub>S NSs (when excited in the absorption region of TiO<sub>2</sub>) leads to an increase in the efficiency of the production of superoxide anion by 1.2–1.4 times, hydrogen peroxide by 4–6 times, and hydroxyl radical by 100–150 times and reduces the efficiency of the production of singlet oxygen by up to two times. It was found that the excitation of the NSs in the visible region is accompanied by the photosensitisation of superoxide anions, hydroxyl radicals, and hydrogen peroxide, which does not happen in the case of TiO<sub>2</sub> NPs. It was noted that the type of surface environment of QDs affects the efficiency of the production of individual ROS: when the system is excited by radiation in the visible spectral region, NSs based on Ag<sub>2</sub>S/2MPA QDs produce ROS 1.1–1.4 times more actively than NSs based on Ag<sub>2</sub>S/TGA QDs. As a result of the study, we developed a schematic diagram of photoprocesses that determine ROS generation.

#### Author contributions

O. V. Ovchinnikov, head of scientific research, scientific editing of the text, discussion of the results of the study. M. S. Smirnov, scientific editing of the text, conducting experiments, discussion of the results of the study. S. V. Aslanov, conducting scientific research, writing the article. A. S. Perepelitsa, conducting scientific research, scientific editing of the text. A. P. Gureev, conducting experiments to measure the production of H<sub>2</sub>O<sub>2</sub>. V. N. Popov, discussion of the results, scientific editing of the text. F. A. Tsybenko, conducting scientific research. A. M. H. Hussein, conducting scientific research.

#### Conflicts of interest

The authors declare that they have no known competing financial interests or personal relationships that could have influenced the work reported in this paper.

#### References

1. *Nanomaterials for solar cell applications*. S. Thomas, E. H. M. Sakho, N. Kalarikkal, S. O. Oluwafemi, J. Wu (eds.). Amsterdam: Elsevier; 2019. <https://doi.org/10.1016/C2016-0-03432-0>
2. Yang D. *Titanium dioxide – material for a sustainable environment*. London: IntechOpen; 2018. 518 p. <https://doi.org/10.5772/intechopen.70290>
3. Roose B., Pathak S., Steiner U. Doping of TiO<sub>2</sub> for sensitized solar cells. *Chemical Society Reviews*. 2015;44: 8326–8349. <https://doi.org/10.1039/C5CS00352K>
4. Hou X., Aitola K., Lund P. D. TiO<sub>2</sub> nanotubes for dye-sensitized solar cells – A review. *Energy Science & Engineering*. 2021;9(7): 921–937. <https://doi.org/10.1002/ese3.831>
5. He F., Jeon W., Choi W. Photocatalytic air purification mimicking the self-cleaning process of the atmosphere. *Nature Communications*. 2021;12: 2528. <https://doi.org/10.1038/s41467-021-22839-0>
6. Ochiai T., Hoshi T., Silmen H., Nakata K., Murakami T., Tatejima H., Koide Y., Houas A., Horie T., Morito Y., Fujishima A. Fabrication of a TiO<sub>2</sub> nanoparticles impregnated titanium mesh filter and its application for environmental purification. *Catalysis Science & Technology*. 2011;1: 1324–1327. <https://doi.org/10.1039/C1CY00185J>
7. Stefanov B. *Photocatalytic TiO<sub>2</sub> thin films for air cleaning: Effect of facet orientation, chemical functionalization, and reaction conditions. Effect of facet orientation, chemical functionalization, and reaction conditions*. Doctor's thesis of philosopher. Digital Comprehensive Summaries of Uppsala Dissertations from the Faculty of Science and Technology. Uppsala: Acta Universitatis Upsaliensis; 1307. 2015. 148 pp.
8. Chiarello G. L., Dozzi M. V., Selli E. TiO<sub>2</sub>-based materials for photocatalytic hydrogen production. *Journal of Energy Chemistry*. 2017;26(2): 250–258. <https://doi.org/10.1016/j.jechem.2017.02.005>
9. Kumaravel V., Mathew S., Bartlett J., Pillai S. C. Photocatalytic hydrogen production using metal doped TiO<sub>2</sub>: A review of recent advances. *Applied Catalysis B: Environmental*. 2019;244(5): 1021–1064. <https://doi.org/10.1016/j.apcatb.2018.11.080>
10. Yu J., Qi L., Jaroniec M. Hydrogen production by photocatalytic water splitting over Pt/TiO<sub>2</sub> nanosheets with exposed (001) facets. *Journal of Phys-*

- ical Chemistry C*. 2010;114(30): 13118–13125. <https://doi.org/10.1021/jp104488b>
11. Binas V., Venieri D., Kotzias D., Kiriakidis G. Modified TiO<sub>2</sub> based photocatalysts for improved air and health quality. *Journal of Materiomics*. 2017;3(1): 3–16. <https://doi.org/10.1016/j.jmat.2016.11.002>
  12. Magalhães P., Andrade L., Nunes O. C., Mendes A. Titanium dioxide photocatalysis: fundamentals and application on photoinactivation. *Reviews on Advanced Materials Science*. 2017;51(2): 91–129. Available at: [https://ipme.ru/e-journals/RAMS/no\\_25117/01\\_25117\\_magalhaes.pdf](https://ipme.ru/e-journals/RAMS/no_25117/01_25117_magalhaes.pdf)
  13. Nakata K., Fujishima A. TiO<sub>2</sub> photocatalysis: Design and applications. *Journal of Photochemistry and Photobiology C: Photochemistry Reviews*. 2012;13(3): 169–189. <https://doi.org/10.1016/j.jphotochemrev.2012.06.001>
  14. Kapilashrami M., Zhang Y., Liu Y.-S., Hagfeldt A., Guo J. Probing the optical property and electronic structure of TiO<sub>2</sub> nanomaterials for renewable energy applications. *Chemical Review*. 2014;114: 9662–9707. <https://doi.org/10.1021/cr5000893>
  15. Reddy K., Manorama S. V., Ramachandra Reddy A. Bandgap studies on anatase titanium dioxide nanoparticles. *Materials Chemistry and Physics*. 2003;78(1): 239–245. [https://doi.org/10.1016/S0254-0584\(02\)00343-7](https://doi.org/10.1016/S0254-0584(02)00343-7)
  16. Zhu T., Gao S.-P. The stability, electronic structure, and optical property of TiO<sub>2</sub> Polymorphs. *Journal of Physical Chemistry C*. 2014;118(21): 11385–11396. <https://doi.org/10.1021/jp412462m>
  17. Qin L., Wang G., Tan Y. Plasmonic Pt nanoparticles – TiO<sub>2</sub> hierarchical nano-architecture as a visible light photocatalyst for water splitting. *Scientific Reports*. 2018;8: 16198. <https://doi.org/10.1038/s41598-018-33795-z>
  18. Yoo S. M., Rawala J. S. B., Lee J. E., Kim J., Ryu H.-Y., Park D.-W., Lee W. I. Size-dependence of plasmonic Au nanoparticles in photocatalytic behavior of Au/TiO<sub>2</sub> and Au@SiO<sub>2</sub>/TiO<sub>2</sub>. *Applied Catalysis A: General*. 2015;499: 47–54. <https://doi.org/10.1016/j.apcata.2015.04.003>
  19. Khlyustova A., Sirotkin N., Kusova T. Doped TiO<sub>2</sub>: the effect of doping elements on photocatalytic activity. *Materials Advances*. 2020;1: 1193–1201. <https://doi.org/10.1039/D0MA00171F>
  20. Ansari S. A., Khan M. M., Ansari M. O., Cho M. H. Nitrogen-doped titanium dioxide (N-doped TiO<sub>2</sub>) for visible light photocatalysis. *New Journal of Chemistry*. 2016;40: 3000–3009. <https://doi.org/10.1039/C5NJ03478G>
  21. He J., Du Y., Bai Y., An J., Cai X., Chen Y., Wang P., Yang X., Feng Q. Facile formation of anatase/rutile TiO<sub>2</sub> nanocomposites with enhanced photocatalytic activity. *Molecules*. 2019;24: 2996. <https://doi.org/10.3390/molecules24162996>
  22. Padayachee D., Mahomed A. S., Singh S., Friedrich H. B. Effect of the TiO<sub>2</sub> anatase/rutile ratio and interface for the oxidative activation of n-octane. *ACS Catalysis*. 2020;10(3): 2211–2220. <https://doi.org/10.1021/acscatal.9b04004>
  23. Wageh S., Al-Ghamdi A. A., Soylu M., Al-Turki Y., Al-Senany N., Yakuphanoglu F. CdS quantum dots and dye co-sensitized nanorods TiO<sub>2</sub> solar. *Journal of Nanoelectronics and Optoelectronics*. 2014;9(5): 662–665. <http://dx.doi.org/10.1166/jno.2014.1651>
  24. Zumeta-Dubé I., Ruiz-Ruiz V.-F., Díaz D., Rodil-Posadas S., Zeinert A. TiO<sub>2</sub> sensitization with Bi<sub>2</sub>S<sub>3</sub> quantum dots: The inconvenience of sodium ions in the deposition procedure. *Journal of Physical Chemistry C*. 2014;118(22): 11495–11504. <https://doi.org/10.1021/jp411516a>
  25. Guo Y., Lei H., Li B., Chen Z., Wen J., Yang G., Fang G. Improved performance in Ag<sub>2</sub>S/P3HT hybrid solar cells with a solution processed SnO<sub>2</sub> electron transport layer. *RSC Advances*. 2016;6: 77701–77708. <https://doi.org/10.1039/C6RA19590C>
  26. Ovchinnikov O. V., Smirnov M. S. IR luminescence mechanism in colloidal Ag<sub>2</sub>S quantum dots. *Journal of Luminescence*. 2020;227: 117526. <https://doi.org/10.1016/j.jlumin.2020.117526>
  27. Zhu L., Meng Z., Thisha G., Oh W.-C. Hydrothermal synthesis of porous Ag<sub>2</sub>S sensitized TiO<sub>2</sub> catalysts and their photocatalytic activities in the visible light range. *Chinese Journal of Catalysis*. 2012;33(2–3): 254–260. [https://doi.org/10.1016/S1872-2067\(10\)60296-3](https://doi.org/10.1016/S1872-2067(10)60296-3)
  28. Yadav S., Jeevanandam P. Synthesis of Ag<sub>2</sub>S-TiO<sub>2</sub> Nanocomposites and their catalytic activity towards rhodamine B photodegradation. *Journal of Alloys and Compounds*. 2015;649: 483–490. <https://doi.org/10.1016/j.jallcom.2015.07.184>
  29. Ghafoor S., Ata S., Manmood N., Arshad S. B. Photosensitization of TiO<sub>2</sub> nanofibers by Ag<sub>2</sub>S with the synergistic effect of excess surface Ti<sup>3+</sup> states for enhanced photocatalytic activity under simulated sunlight. *Scientific Reports*. 2017;7: 255. <https://doi.org/10.1038/s41598-017-00366-7>
  30. Li Z., Xiong S., Wang G., Xie Z., Zhang Z. Role of Ag<sub>2</sub>S coupling on enhancing the visible-light-induced catalytic property of TiO<sub>2</sub> nanorod arrays. *Scientific Reports*. 2016;6: 19754. <https://doi.org/10.1038/srep19754>
  31. Dong M., Li Q.-H., Li R., Cui Y.-Q., Wang X.-X., Yu J.-Q., Long Y.-Z. Efficient under visible catalysts from electrospun flexible Ag<sub>2</sub>S/TiO<sub>2</sub> composite fiber membrane. *Journal of Materials Science*. 2021;56: 7966–7981. <https://doi.org/10.1007/s10853-021-05796-3>
  32. Zhu L., Meng Z.-D., Oh W.-C. MWCNT-Based Ag<sub>2</sub>S-TiO<sub>2</sub> nanocomposites photocatalyst: ultrasound-assisted synthesis, characterization, and en-

- hanced catalytic efficiency. *Journal of Nanomaterials*. 2012;586520. <https://doi.org/10.1155/2012/586526>
33. Yang M., Shi X. Biosynthesis of Ag<sub>2</sub>S/TiO<sub>2</sub> nanotubes nanocomposites by *Shewanella oneidensis* MR-1 for the catalytic degradation of 4-nitrophenol. *Environmental Science and Pollution Research*. 2019;26(12): 12237–12246. <https://doi.org/10.1007/s11356-019-04462-1>
34. Tachan Z., Hod I., Shalom M., Grinis L., Zaban A. The importance of the TiO<sub>2</sub>/quantum dots interface in the recombination processes of quantum dot sensitized solar cells. *Physical Chemistry Chemical Physics*. 2013;15(11): 3841. <https://doi.org/10.1039/C3CP44719G>
35. Ovchinnikov O. V., Aslanov S. V., Smirnov M. S., Grevtseva I. G., Perepelitsa A. S. Photostimulated control of luminescence quantum yield for colloidal Ag<sub>2</sub>S/2-MPA quantum dots. *RSC Advances*. 2019;9: 37312–37320. <https://doi.org/10.1039/C9RA07047H>
36. Ovchinnikov O. V., Grevtseva I. G., Smirnov M. S., Kondratenko T. S., Perepelitsa A. S., Aslanov S. V., Khokhlov V. U., Tatyana E. P., Matsukovich A. S. Effect of thioglycolic acid molecules on luminescence properties of Ag<sub>2</sub>S quantum dots. *Optical and Quantum Electronics*. 2020;52: 198. <https://doi.org/10.1007/s11082-020-02314-8>
37. Kubelka P., Munk F. An article on optics of paint layers. *Fuer Tekn. Physik*. 1931;12: 593–609.
38. Murphy A. B. Band-gap determination from diffuse reflectance measurements of semiconductor films, and application to photoelectrochemical water-splitting. *Solar Energy Materials & Solar Cells*. 2007;91: 1326–1337. <https://doi.org/10.1016/j.solmat.2007.05.005>
39. Lakowitz R. *Principles of Fluorescent Spectroscopy* 3-ed. Springer; 2006. 954 pp.
40. Reindl S., Penzkofer A., Gong S.-H., Landthaler M., Szeimies R. M., Abels C., Bäuml W. Quantum yield of triplet formation for indocyanine green. *Journal of Photochemistry and Photobiology A: Chemistry*. 1997;105(1): 65–68. [https://doi.org/10.1016/S1010-6030\(96\)04584-4](https://doi.org/10.1016/S1010-6030(96)04584-4)
41. Bedouhene S., Moulti-Mati F., Hurtado-Nedelec M., Dang P. M.-C., El-Benna J. Luminol-amplified chemiluminescence detects mainly superoxide anion produced by human neutrophils. *American Journal of Blood Research*. 2017;7(4): 41–48. Available at: <https://www.ncbi.nlm.nih.gov/pmc/articles/PMC5545213/>
42. Mohanty J. G., Jaffe J. S., Schulman E. S., Raible D. G. A highly sensitive fluorescent micro-assay of H<sub>2</sub>O<sub>2</sub> release from activated human leukocytes using a dihydroxyphenoxazine derivative. *Journal of Immunological Methods*. 1997;202(2): 133–141. [https://doi.org/10.1016/S0022-1759\(96\)00244-X](https://doi.org/10.1016/S0022-1759(96)00244-X)
43. Wafi A., Szabó-Bárdos E., Horváth O., Makó E., Jakab M., Zsirka B. Coumarin-based quantification of hydroxyl radicals and other reactive species generated on excited nitrogen-doped TiO<sub>2</sub>. *Journal of Photochemistry and Photobiology A: Chemistry*. 2021;404: 112913. <https://doi.org/10.1016/j.jphotochem.2020.112913>
44. Herman J., Neal S. L. Efficiency comparison of the imidazole plus RNO method for singlet oxygen detection in biorelevant solvents. *Analytical and Bioanalytical Chemistry*. 2019;411(20): 5287–5296. <https://doi.org/10.1007/s00216-019-01910-2>
45. Ijadpanah-Saravi H., Safari M., Khodadadi-Darban A., Rezaei A. Synthesis of titanium dioxide nanoparticles for photocatalytic degradation of cyanide in wastewater. *Analytical Letters*. 2014;47(10): 1772–1782. <https://doi.org/10.1080/00032719.2014.880170>
46. Kayanuma Y. Quantum-size effects of interacting electrons and holes in semiconductor microcrystals with spherical shape. *Physical Review B*. 1988;38(14): 9797–9805. <https://doi.org/10.1103/PhysRevB.38.9797>
47. Ovchinnikov O. V., Smirnov M. S., Aslanov S. V. Luminescence quantum yield and recombination constants in colloidal core/shell Ag<sub>2</sub>S/ZnS and Ag<sub>2</sub>S/SiO<sub>2</sub> quantum dots. *Optics and Spectroscopy*. 2020;128: 2028–2035. <https://doi.org/10.1134/S0030400X2012098X>
48. Athanasekou C. P., Likodimos V., Falaras P. Recent developments of TiO<sub>2</sub> photocatalysis involving advanced oxidation and reduction reactions in water. *Journal of Environmental Chemical Engineering*. 2018;6(6): 7386–7394. <https://doi.org/10.1016/j.jece.2018.07.026>
49. Turrens J. F. Mitochondrial formation of reactive oxygen species. *The Journal of Physiology*. 2003;552(2): 335–44. <https://doi.org/10.1113/jphysiol.2003.049478>
50. Fujishima A., Zhang X., Tryk D. A. TiO<sub>2</sub> photocatalysis and related surface phenomena. *Surface Science Reports*. 2008;63(12): 515–582. <https://doi.org/10.1016/j.surfrep.2008.10.001>
51. Kohtani S., Yoshioka E., Miyabe H. Photocatalytic hydrogenation on semiconductor particles. In: *Hydrogenation* (ed. I. Karame). *IntechOpen*. 2012. 340 pp. <https://doi.org/10.5772/45732>
52. Bard A. J., Parsons R., Jordan J. *Standart potentials in aqueous solutions*. Routledge, 1985. 848 pp. <https://doi.org/10.1201/9780203738764>
53. Nosaka Y., Nosaka A. Y. Generation and detection of reactive oxygen species in photocatalysis. *Chemical Reviews*. 2017;117: 11302–11336. <https://doi.org/10.1021/acs.chemrev.7b00161>
54. Belovolova L. V. Reactive oxygen species in aqueous media (A Review). *Optics and Spectroscopy*. 2020;128: 932–951. <https://doi.org/10.1134/S0030400X20070036>

**Information about the authors**

*Oleg V. Ovchinnikov*, Dr. Sci. (Phys.–Math.), Professor, Dean of the Faculty of Physics, Voronezh State University (Voronezh, Russian Federation).

<https://orcid.org/0000-0001-6032-9295>  
ovchinnikov\_o\_v@rambler.ru

*Mikhail S. Smirnov*, Dr. Sci. (Phys.–Math.), Associate Professor, Associate Professor of the Department of Optics and Spectroscopy, Voronezh State University (Voronezh, Russian Federation).

<https://orcid.org/0000-0001-8765-0986>  
smirnov\_m\_s@mail.ru

*Aleksey S. Perepelitsa*, Cand. Sci. (Phys.–Math.), Senior Lecturer of the Department of Optics and Spectroscopy, Voronezh State University (Voronezh, Russian Federation).

<https://orcid.org/0000-0002-1264-0107>  
a-perepelitsa@yandex.ru

*Sergey V. Aslanov*, graduate student of the Department of Optics and Spectroscopy, Voronezh State University (Voronezh, Russian Federation).

<https://orcid.org/0000-0002-3961-2480>  
windmaster7@yandex.ru

*Vasily N. Popov*, Dr. Sci. (Biol.), Professor, Head of the Department of Genetics, Cytology and Bioengineering, Voronezh State University (Voronezh, Russian Federation).

<https://orcid.org/0000-0003-1294-8686>  
pvn@bio.vsu.ru

*Artem P. Gureev*, Cand. Sci. (Biol.), Senior Lecturer of the Department of Genetics, Cytology and Bioengineering, Voronezh State University (Voronezh, Russian Federation).

<https://orcid.org/0000-0003-3562-5329>  
gureev@bio.vsu.ru

*Fedor A. Tsybenko*, student of the Department of Optics and Spectroscopy, Voronezh State University (Voronezh, Russian Federation).

ozzy.642@yandex.ru

*Alaa M. H. Hussein*, graduate student of the Department of Optics and Spectroscopy, Voronezh State University (Voronezh, Russian Federation).

alaa.hussein@mail.ru

*Received 24.06.2022; approved 20.07.2022; accepted 15.08.2022; published online 25.12.2022.*

*Translated by Irina Charychanskaya  
Edited and proofread by Simon Cox*



## Original articles

Research article

<https://doi.org/10.17308/kcmf.2022.24/10556>

## Study of the proteolytic activity of ficin associates with chitosan nanoparticles

S. S. Olshannikova<sup>1</sup>, Yu. A. Redko<sup>1</sup>, M. S. Lavlinskaya<sup>1,2</sup>, A. V. Sorokin<sup>1,2</sup>, M. G. Holyavka<sup>1,2</sup>✉, N. E. Yudin<sup>1</sup>, V. G. Artyukhov<sup>1</sup>

<sup>1</sup>Voronezh State University,  
1 Universitetskaya pl., Voronezh 394018, Russian Federation

<sup>2</sup>Sevastopol State University,  
33 Universitetskaya ul., Sevastopol 299053, Russian Federation

### Abstract

The purpose of the research was to develop and study biocatalysts based on ficin associates with chitosan nanoparticles. We obtained medium and high molecular weight chitosan nanoparticles with the addition of ascorbic acid and without it. The zeta potential of all types of nanoparticles was 0 mV. The associates of ficin and chitosan nanoparticles formed with the addition of ascorbic acid exhibited higher proteolytic activity. While determining the stability of the associates of chitosan and ficin nanoparticles, we noticed a decrease in the proteolytic activity of the samples within seven days. Medium and high molecular weight chitosan nanoparticles obtained using ascorbic acid differed significantly in size from the nanoparticles produced without ascorbic acid. The proposed biocatalysts have high prospects for use in cosmetology, biomedicine, and pharmacy.

**Keywords:** Nanoparticles, Ficin, Chitosan, Association

**Funding:** The study was funded by the Priority-2030 programme of Sevastopol State University, strategic project No.3 (production of chitosan nanoparticles), and by the Ministry of Science and Higher Education of the Russian Federation in the framework of the government order to higher education institutions in the sphere of scientific research for years 2020-2022, project No. FZGU-2020-0044 (complexation of nanoparticles with enzymes).

**For citation:** Olshannikova S. S., Redko Yu. A., Lavlinskaya M. S., Sorokin A. V., Holyavka M. G., Yudin N. E., Artyukhov V. G. Study of the proteolytic activity of ficin associates with chitosan nanoparticles. *Condensed Matter and Interphases*. 2022;24(4): 523–528. <https://doi.org/10.17308/kcmf.2022.24/10556>

**Для цитирования:** Ольшанникова С. С., Редько Ю. А., Лавлинская М. С., Сорокин А. В., Холявка М. Г., Юдин Н. Е., Артюхов В. Г. Исследование протеолитической активности ассоциатов фицина с наночастицами хитозана. *Конденсированные среды и межфазные границы*. 2022;24(4): 523–528. <https://doi.org/10.17308/kcmf.2022.24/10556>

✉ Marina G. Holyavka, e-mail: [holyavka@rambler.ru](mailto:holyavka@rambler.ru)

© Olshannikova S. S., Redko Yu. A., Lavlinskaya M. S., Sorokin A. V., Holyavka M. G., Yudin N. E., Artyukhov V. G., 2022





## 1. Introduction

Recently, nanoparticles which are highly dispersed materials smaller than 100 nm, have gained great importance in modern medicine. Their applications range from contrast imaging agents to carriers for the delivery of genes and bioactive substances to target cells. These unique nanomaterials have a number of properties due to their size distinguishing them from macromaterials of similar composition. Among these properties are high reactivity, electromagnetic energy absorption, and high biological mobility [1–3].

Nanoparticles are also known as zero-dimensional nanomaterials. They are called so because the sum of their dimensions is at the nanoscale. This feature differs them from one- and two-dimensional nanomaterials (nanowires, nanotubes, and self-assembled monolayer films, etc.) having one or two dimensions outside the nanoscale [4].

As mentioned above, nanoparticles have numerous advantages for modern medicine. First, their structural stability and ability to protect the bioactive substance against degradation, deactivation, and clearance make it possible to maintain the required substance therapeutic concentration [5–7]. Moreover, it is possible to achieve the desired size and surface charge in the production of nanoparticles. The release kinetics of bioactive substances from the nanocomplexes is controllable. It occurs by diffusion, polymer swelling, or degradation, or a combination of these processes depending on the polymer type used to produce the carrier matrices [8]. Thus, nanoparticles are promising materials for the medical use. Chitosan is one of the promising polysaccharides for their production. It is a modified natural polyamino- $\beta$ -glycoside combining various mechanisms of medicine release. In addition to its biodegradability and the immune response absence, chitosan is marked by antibacterial activity due to the free primary amino group presences [9–10] and high mucoadhesive properties [11].

Proteases are the first enzymes used in food biotechnologies. Today, they proteases are applied in many industrial processes such as the tanning and pharmaceutical industry, as well as in biomedicine. Ficin occupies a special place among the frequently-used plant proteases.

Ficin (EC 3.4.22.3) is a proteolytic enzyme isolated from the genus *Ficus* plant latex. It is a monomeric protein consisting of a single polypeptide chain with a molecular weight of 25–26 kDa. Ficin is a representative of cysteine papain-like proteases and it is characterised by broad substrate specificity. The maximum catalytic activity is reached in the pH range of 6.5–9.5. [12–16]. Ficin exhibits antimicrobial activity against gram-positive and gram-negative bacteria. It is also known to have anti-inflammatory, anthelmintic, antithrombotic, fibrinolytic and anticancer properties, as well as immunomodulatory effect [17–19].

However, the use of native protease solutions is limited by their low stability and autolysis resulting in the loss of practically valuable enzyme properties. One way to save them is to obtain hybrid enzyme formulations using nanoparticle carriers [20].

Therefore, the aim of this research was to study the catalytic (proteolytic) activity of ficin associates with chitosan nanoparticles.

## 2. Experimental

Ficin was the object of the study, while azocasein was chosen as the substrate for hydrolysis (both produced by Sigma, USA). Nanoparticles were obtained from medium molecular weight (MMWC, 200 kDa) and high molecular weight (HMWC, 350 kDa) chitosan purchased by Bioprogress, Russia.

Chitosan nanoparticles with ascorbic acid and without it, and their associates with ficin were prepared using the method described in [20–22].

Protease activity of the immobilized ficin was measured by the common method described in [24]. The research was carried out using 0.5% azocasein solution in 50 mM Tris-HCl buffer with pH 7.5 for 2 h at 37 °C. The amount of ficin (in mg of protein) that hydrolysed 1  $\mu$ mol of substrate in 1 min was taken as a unit of catalytic activity.

Nano Zetasizer ZS (Malvern Instruments, USA) equipped with 4 mW He/Ne-laser with  $\lambda = 632.8$  nm and scattering angle 173 °C was used to measure the nanoparticle and ficin associates size and surface charge.

### 3. Results and discussion

In the first series of experiments, we determined the size and zeta potential of chitosan nanoparticles. The nanoparticle parameters are presented in Table 1. It was found that medium and high molecular weight chitosan nanoparticles obtained using ascorbic acid differed significantly in size from the ones produced without ascorbic acid. The median zeta potential of all nanoparticles was 0 mV.

When ficin was associated with medium and high molecular weight chitosan nanoparticles formed without ascorbic acid, the proteolytic activity of the associated enzyme was 84 and 88 % of native enzyme. When ficin was associated with nanoparticles obtained with ascorbic acid, its catalytic activity increased by 15 % for medium molecular weight chitosan and by 18 % for high-molecular-weight chitosan (Fig. 1). The better preserving enzyme activity in the complex with chitosan nanoparticles obtained with ascorbic

acid is probably due to the antioxidant effects of additive on the biocatalyst [25, 26].

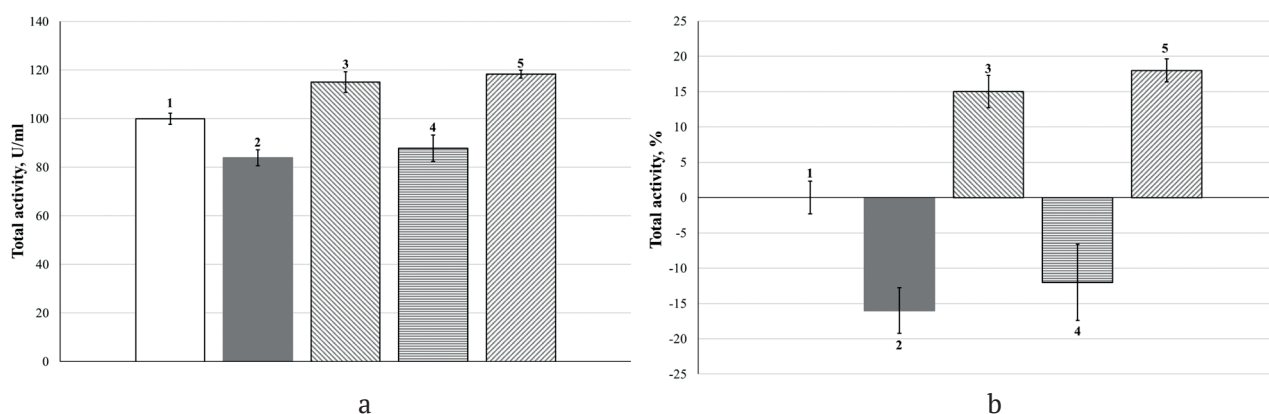
We carried out experiments to determine the residual proteolytic activity of native and associated ficin at 37 °C and pH 7.5 in 0.05 M Tris-HCl buffer. All samples showed a decrease in their activity within 7 days.

After incubation for 168 hours, native ficin retained 8 % of its initial catalytic activity. Its associates with medium and high molecular weight chitosan nanoparticles obtained without ascorbic acid retained 27 and 16 % of their activity, respectively. The ficin associates with medium and high molecular weight chitosan nanoparticles with ascorbic acid retained 39 and 18 % of their proteolytic activity, respectively (Fig. 2).

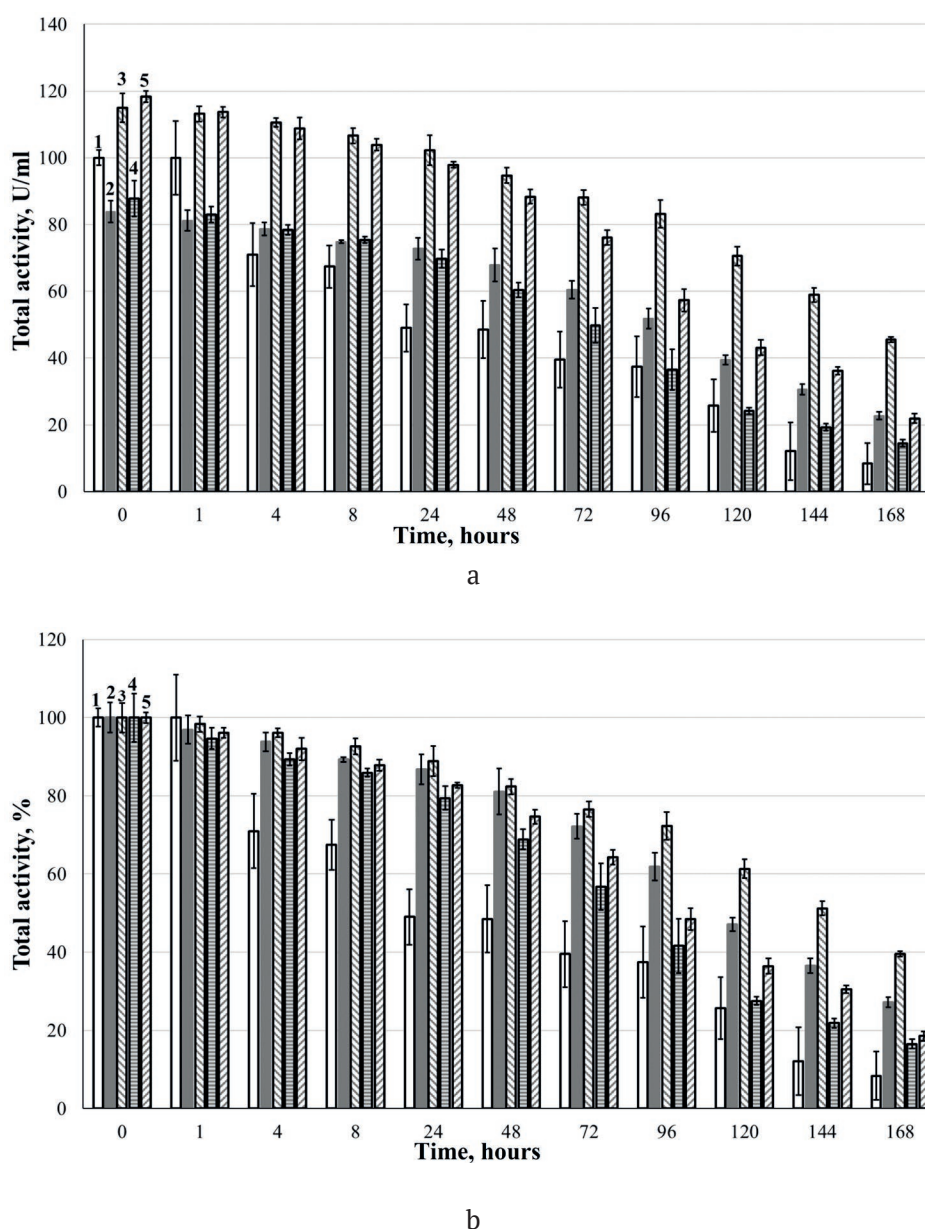
Starting from 4 hours of incubation at 37 °C in 0.05 M Tris-HCl buffer at pH 7.5, the ficin associates with nanoparticles were more stable than the free enzyme.

**Table 1.** Parameters of medium and high molecular weight chitosan nanoparticles

Chitosan nanoparticles	Average size, nm	Size range, nm	Median zeta-potential, mV	Zeta-potential range, mV
Medium molecular weight chitosan	12	7–21	0	0
Medium molecular weight chitosan with ascorbic acid	21	14–59	0	0
High molecular weight chitosan	33	18–79	0	0
High molecular weight chitosan with ascorbic acid	38	28–79	0	0



**Fig. 1.** Catalytic activity of ficin, units/ml (a) and its change, % (b): soluble ficin (1); ficin associated with medium molecular weight chitosan nanoparticles (2); ficin associated with medium molecular weight chitosan nanoparticles with ascorbic acid (3); ficin associated with high molecular weight chitosan nanoparticles (4); and ficin associated with high molecular weight chitosan nanoparticles with ascorbic acid (5). The activity of free ficin under optimum hydrolysis conditions was taken as 100 %.



**Fig. 2.** Residual catalytic activity of ficin after incubation of the samples at 37 °C (a: in units/ml of solution or suspension, b: % of the original value): 1 – soluble ficin; 2 – ficin associated with medium molecular weight chitosan nanoparticles; 3 – ficin associated with medium molecular weight chitosan nanoparticles with ascorbic acid; 4 – ficin associated with high molecular weight chitosan nanoparticles; and 5 – ficin associated with high molecular weight chitosan nanoparticles with ascorbic acid. The catalytic activity of the obtained samples under optimum hydrolysis conditions was taken as 100 %.

#### 4. Conclusions

Thus, we obtained medium and high molecular weight chitosan nanoparticles with or without ascorbic acid. The ficin associates and chitosan nanoparticles obtained with ascorbic acid exhibited higher proteolytic activity. While determining the stability of the ficin and chitosan nanoparticles, we noticed a decrease in the proteolytic activity of the samples within seven days.

#### Conflict of interests

The authors declare that they have no known competing financial interests or personal relationships that could have influenced the work reported in this paper.

#### Author contributions

All authors made an equivalent contribution to the preparation of the publication.

## References

- Murthy S. K. Nanoparticles in modern medicine: State of the art and future challenges. *International Journal of Nanomedicine*. 2007;2(2): 129–141. Режим доступа: <https://www.ncbi.nlm.nih.gov/pmc/articles/PMC2673971/>
- Parak W. J., Gerion D., Pellegrino T., Zanchet D., Micheel C., Williams C. S., Boudreau R., Le Gros M. A., Larabell C. A., Alivisatos A. P. Biological applications of colloidal nanocrystals. *Nanotechnology*. 2003;14: R15–R27. <https://doi.org/10.1088/0957-4484/14/7/201>
- Pankhurst Q. A., Connolly J., Jones S. K., Dobson J. Applications of magnetic nanoparticles in biomedicine. *Journal of Physics Series D: Applied Physics*. 2003;36: R167–R181. <https://doi.org/10.1088/0022-3727/36/13/201>
- Whitesides G. M. The ‘right’ size in Nanobiotechnology. *Nature Biotechnology*. 2003;21: 1161–1165. <https://doi.org/10.1038/nbt872>
- Xiong M.-H., Bao Y., Yang X.-Zh., Zhu Ya.-H., Wang J. Delivery of antibiotics with polymeric particles. *Advanced Drug Delivery Reviews*. 2014;78: 63–76. <https://doi.org/10.1016/j.addr.2014.02.002>
- Danhier F., Ansorenav E., Silva J. M., Coco R., Le Breton A., Préat V. PLGA-based nanoparticles: An overview of biomedical applications. *Journal of Controlled Release*. 2012;161(2): 505–522. <https://doi.org/10.1016/j.jconrel.2012.01.043>
- Egebro Birk S., Boisen A., Hagner Nielsen L. Polymeric nano- and microparticulate drug delivery systems for treatment of biofilms. *Advanced Drug Delivery Reviews*. 2021;174: 30–52. <https://doi.org/10.1016/j.addr.2021.04.005>
- Misra R., Acharya S., Dilnawaz F., Sahoo S. K. Sustained antibacterial activity of doxycycline-loaded poly(D,L-lactide-co-glycolide) and poly( $\epsilon$ -caprolactone) nanoparticles. *Nanomedicine*. 2009;4(5): 519–530. <https://doi.org/10.2217/nmm.09.28>
- Cheung R., Ng T., Wong J., Chan W. Chitosan: an update on potential biomedical and pharmaceutical applications. *Marine Drugs*. 2015;13: 5156–5186. <https://doi.org/10.3390/md13085156>
- Osman R., Kan P. L., Awad G., Mortada N., El-Shamy A. E., Alpar O. Spray dried inhalable ciprofloxacin powder with improved aerosolisation and antimicrobial activity. *International Journal of Pharmaceutics*. 2013;449: 44–58. <https://doi.org/10.1016/j.ijpharm.2013.04.009>
- Lehr C. M., Bouwstra J. A., Schacht E. H., Junginger H. E. In vitro evaluation of mucoadhesive properties of chitosan and some other natural polymers. *International Journal of Pharmaceutics*. 1992;78: 43–48. [https://doi.org/10.1016/0378-5173\(92\)90353-4](https://doi.org/10.1016/0378-5173(92)90353-4)
- Siar E.-H., Arana-Peña S., Barbosa O., Zidoune M. N., Fernandez-Lafuente R. Immobilization/stabilization of ficin extract on glutaraldehyde-activated agarose beads. Variables that control the final stability and activity in protein hydrolyses. *Catalysts*. 2018;8: 149. <https://doi.org/10.3390/catal8040149>
- Olshannikova S., Koroleva V., Holyavka M., Pashkov A., Artyukhov V. Covalent immobilization of thiol proteinases on chitosan. *Chemistry Proceedings*. 2020;2(1):7. <https://doi.org/10.3390/ECCS2020-07527>
- Silva-López R. E., Gonçalves R. N. Therapeutic proteases from plants: biopharmaceuticals with multiple applications. *Journal of Applied Biotechnology & Bioengineering*. 2019;6(2): 101–109. <https://doi.org/10.15406/jabb.2019.06.00180>
- Hu R., Chen G., Li Y. Production and characterization of antioxidative hydrolysates and peptides from corn gluten meal using papain, ficin, and bromelain. *Molecules*. 2020;25(18): 4091. <https://doi.org/10.3390/molecules25184091>
- Holyavka M., Pankova S., Koroleva V., Vyshkvorkina Yu., Lukin A., Kondratyev M., Artyukhov V. Influence of UV radiation on molecular structure and catalytic activity of free and immobilized bromelain, ficin and papain. *Journal of Photochemistry and Photobiology B: Biology*. 2019;201: 111681. <https://doi.org/10.1016/j.jphotobiol.2019.111681>
- Ribeiro J. S., Barboza A. d. S., Cuevas-Suárez C. E., Silva A. F., Piva E., Lund R. G. Novel in-office peroxide-free tooth-whitening gels: bleaching effectiveness, enamel surface alterations, and cell viability. *Scientific Reports*. 2020;10: 8. <https://doi.org/10.1038/s41598-020-66733-z>
- Aider M. Potential applications of ficin in the production of traditional cheeses and protein hydrolysates. *JDS Communications*. 2021;2(5): 233–237. <https://doi.org/10.3168/jdsc.2020-0073>
- Morellon-Sterling R., El-Siara H., Tavano O. L., Berenguer-Murcia A., Fernández-Lafuente R. Ficin: A protease extract with relevance in biotechnology and biocatalysis. *International Journal of Biological Macromolecules*. 2020;162: 394–404. <https://doi.org/10.1016/j.ijbiomac.2020.06.144>
- Szeto Y. S., Hu Z. *Method for preparing chitosan nano-particles*. Patent No US2008/0234471 A1. Publication Date: 25.09.2008.
- Ol’shannikova S. S., Red’ko Y. A., Lavlinskaya, M. S., Sorokin A. V., Holyavka M. G., Artyukhov V. G. Preparation of papain complexes with chitosan microparticles and evaluation of their stability using the enzyme activity level. *Pharmaceutical Chemistry Journal*. 2022;55: 1240–1244. <https://doi.org/10.1007/s11094-022-02564-8>
- Koroleva V. A., Holyavka M. G., Olshannikova S. S., Artyukhov V. G. Formation of ficin complexes with chitosan nanoparticles with a high level of proteolytic activity. *Russian Journal of Biopharmaceuticals*. 2018;10(4): 36–40. (In Russ.,

abstract in Eng.). Available at: <https://www.elibrary.ru/item.asp?id=36834674>

23. García-Carreño F. L. The digestive proteases of langostilla (pleuroncodes planipes, decapoda): their partial characterization, and the effect of feed on their composition. *Comparative Biochemistry and Physiology Part B: Comparative Biochemistry*. 1992;103: 575–578. [https://doi.org/10.1016/0305-0491\(92\)90373-Y](https://doi.org/10.1016/0305-0491(92)90373-Y)

24. Sabirova A. R., Rudakova N. L., Balaban N. P., Ilyinskaya O. N., Demidyuk I. V., Kostrov S. V., Rudenskaya G. N., Sharipova M. R. A novel secreted metzincin metalloproteinase from *Bacillus intermedius*. *FEBS Lett.* 2010;584 (21): 4419–4425. <https://doi.org/10.1016/j.febslet.2010.09.049>

25. Burri B., Jacob R. Human metabolism and the requirement for vitamin C. In: *Vitamin C in health and disease*. Packer L., Fuchs J. (eds.). New York: Marcel Dekker Inc., 1997; 25–58.

26. Arrigoni O., De Tullio M. C. Ascorbic acid: much more than just an antioxidant. *Biochimica et Biophysica Acta*. 2002;1569: 1–9. [https://doi.org/10.1016/s0304-4165\(01\)00235-5](https://doi.org/10.1016/s0304-4165(01)00235-5)

### Information about the authors

*Svetlana S. Olshannikova*, post-graduate student of the Biophysics and Biotechnology Department of Voronezh State University (Voronezh, Russian Federation).

<https://orcid.org/0000-0003-3381-2008>  
olshannikovas@gmail.com

*Yulia A. Redko*, bachelor of the Biophysics and Biotechnology Department of Voronezh State University (Voronezh, Russian Federation).

redkoju@yandex.ru

*Maria S. Lavlinskaya*, Cand. Sci. (Chem.), Senior Researcher of the Biophysics and Biotechnology Department of Voronezh State University (Voronezh, Russian Federation); Senior Researcher of the Bioresource Potential of the Seaside Territory Laboratory, Sevastopol State University (Sevastopol, Russian Federation).

<https://orcid.org/0000-0001-9058-027X>  
maria.lavlinskaya@gmail.com

*Andrey V. Sorokin*, post-graduate student of the Polymer Science and Colloid Chemistry Department, Junior Researcher of the Biophysics and Biotechnology Department of Voronezh State University (Voronezh, Russian Federation); Junior Researcher of the Bioresource Potential of the Seaside Territory Laboratory, Sevastopol State University (Sevastopol, Russian Federation).

<https://orcid.org/0000-0001-5268-9557>  
andrew.v.sorokin@gmail.com

*Marina G. Holyavka*, Dr. Sci. (Biology), Docent, Professor of the Biophysics and Biotechnology Department, Senior Researcher of the Biochemistry and Cell Physiology Department of Voronezh State University (Voronezh, Russian Federation); Professor of the Physics Department, Leading Researcher of the Molecular Substance Structure Research Core Center of Sevastopol State University (Sevastopol, Russian Federation).

<https://orcid.org/0000-0002-1390-4119>  
holyavka@rambler.ru

*Nikolay E. Yudin*, master student of Polymer Science and Colloid Chemistry Department of Voronezh State University (Voronezh, Russian Federation).

<https://orcid.org/0000-0001-5667-0319>  
koli4ka99@mail.ru

*Valery G. Artyukhov*, Dr. Sci. (Biology), Full Professor, Head of the Biophysics and Biotechnology Department, Senior Researcher of the Biochemistry and Cell Physiology of Voronezh State University (Voronezh, Russian Federation).

artyukhov@bio.vsu.ru

Received 06.05.2022; approved after reviewing 30.06.2022; accepted for publication 15.09.2022; published online 25.12.2022.

Translated by Anastasiia Ananeva  
Edited and proofread by Simon Cox



## Original articles

Research article

<https://doi.org/10.17308/kcmf.2022.24/10557>**Deposition of zinc sulphide films from thiourea complexes and a study of their optical properties**

T. V. Samofalova✉, V. N. Semenov, P. V. Seredin, D. L. Goloshchapov, N. S. Buylov

Voronezh State University,  
1 Universitetskaya pl., Voronezh 394018, Russian Federation**Abstract**

This work presents the results of a study of zinc sulphide films deposited by aerosol pyrolysis from aqueous solutions of thiourea complex compounds  $[\text{Zn}(\text{N}_2\text{H}_4\text{CS})_2\text{Cl}_2]$  and  $[\text{Zn}(\text{N}_2\text{H}_4\text{CS})_2\text{Br}_2]$  in the temperature range of 350–500 °C.

The IR and Raman spectra of zinc complexes were studied. It was determined that in the studied complexes, the thiourea molecule was coordinated to the metal cation through the sulphur atom. In the low-frequency Raman region ( $\nu < 400 \text{ cm}^{-1}$ ), we recorded the bands characterising the vibrations of the zinc-sulphur and zinc-chlorine (bromine) bonds of the studied complex compounds in the Raman scattering spectra. The optical properties of zinc sulphide films were studied using optical spectrophotometry. Based on the absorption spectra, the optical band gap of ZnS films was determined. It was 3.67–3.74 eV and 3.63–3.70 eV for the samples deposited from  $[\text{Zn}(\text{N}_2\text{H}_4\text{CS})_2\text{Cl}_2]$  and  $[\text{Zn}(\text{N}_2\text{H}_4\text{CS})_2\text{Br}_2]$  complexes, respectively. We recorded a decrease in the band gap of the synthesised layers upon an increase in the deposition temperature. It is due to changes in their defect structure.

One of the main types of defects in the ZnS films deposited from  $[\text{Zn}(\text{N}_2\text{H}_4\text{CS})_2\text{Cl}_2]$  and  $[\text{Zn}(\text{N}_2\text{H}_4\text{CS})_2\text{Br}_2]$  complexes is a halogen atom in the anion sublattice of the sulphide ( $\text{Cl}_s^-$ ,  $\text{Br}_s^-$ ). As the deposition temperature increases, the content of these defects in the films decreases due to the complete destruction of Zn–Cl and Zn–Br bonds and volatilisation of halogen during the thermolysis of the complexes. Oxygen ( $\text{O}_s^x$ ) occupies the vacated places of  $\text{Cl}_s^-$ ,  $\text{Br}_s^-$ . The films contained oxygen as they were synthesised in an oxidising atmosphere and due to partial hydrolysis of the initial zinc salt. An increase of oxygen content in the samples upon an increase of the deposition temperature results in a decrease of the optical band gap of the ZnS films.

**Keywords:** Thiourea complex compounds, Aerosol pyrolysis, Zinc sulphide, Films, Optical band gap

**Funding:** The study received financial support from the Ministry of Science and Higher Education of the Russian Federation within the framework of State Contract with universities regarding scientific research in 2022–2024, project No. FZGU-2022-0003

**For citation:** Samofalova T. V., Semenov V. N., Seredin P. V., Goloshchapov D. L., Buylov N. S. Deposition of zinc sulphide films from thiourea complexes and study of their optical properties. *Condensed Matter and Interphases*. 2022;24(4): 529–536. <https://doi.org/10.17308/kcmf.2022.24/10557>

**Для цитирования:** Самофалова Т. В., Семенов В. Н., Середин П. В., Голощачпов Д. Л., Буйлов Н. С. Осаждение пленок сульфида цинка из тиомочевинных комплексов и исследование их оптических свойств. *Конденсированные среды и межфазные границы*. 2022;24(4): 529–536. <https://doi.org/10.17308/kcmf.2022.24/10557>

✉ Tatyana V. Samofalova, e-mail: [TSamofalova@bk.ru](mailto:TSamofalova@bk.ru)

© Samofalova T. V., Semenov V. N., Seredin P. V., Goloshchapov D. L., Buylov N. S., 2022



The content is available under Creative Commons Attribution 4.0 License.

## 1. Introduction

Zinc sulphide films are of great interest because of their promising application in modern microelectronics. Various optoelectronic and recording devices, information display systems, electroluminescent light sources, etc., are based on zinc sulphide [1, 2]. Therefore, the synthesis of ZnS films with variable optical properties by a convenient and affordable method of aerosol pyrolysis of thiourea complex compounds (TCC) is a topical issue.

Aerosol pyrolysis makes it possible to synthesise targeted metal chalcogenide films with required semiconductor characteristics by producing complex compounds of different compositions and structures in a solution [3–5]. The sulphide phase is formed as a result of thermal destruction of the complex on a heated substrate. The crystal and defect structures of the sulphide films deposited by this method, as well as their properties, depend on the nature of the initial complex.

The aim of this study was to deposit zinc sulphide films from  $[\text{Zn}(\text{N}_2\text{H}_4\text{CS})_2\text{Cl}_2]$  and  $[\text{Zn}(\text{N}_2\text{H}_4\text{CS})_2\text{Br}_2]$  complex solutions at different temperatures and to study the optical properties of the deposited films.

## 2. Experimental

Zinc sulphide films were synthesised by aerosol pyrolysis using aqueous solutions of thiourea complex compounds formed by the interaction of zinc salt and thiourea. To prepare TCC in an aqueous solution, we used chemically pure  $\text{ZnCl}_2 \cdot 2.5\text{H}_2\text{O}$  and  $\text{ZnBr}_2$  salts, as well as extra pure  $\text{N}_2\text{H}_4\text{CS}$  thiourea. The concentration of the metal salt in the sprayed solution was 0.05 mol/l, the concentration of thiourea was 0.2 mol/l. Previous studies showed that at certain molar ratios of the used components, the formation of  $[\text{Zn}(\text{N}_2\text{H}_4\text{CS})_2\text{Cl}_2]$  and  $[\text{Zn}(\text{N}_2\text{H}_4\text{CS})_2\text{Br}_2]$  complex compounds occurred in the solution at room temperature [6].

The TCC solutions were sprayed onto a heated substrate by a pneumatic nozzle. As a result of the thermal destruction of the complexes, metal sulphides were obtained. The substrates were silica plates, which were prewashed in nitric acid and chromic mixture, then washed repeatedly in distilled water. The deposition temperature

was varied from 350 to 500 °C. Each sample was sprayed for 1 to 2 minutes.

To study the optical properties of the films, we recorded absorption spectra using a Shimadzu UV-2550 spectrophotometer in the range of 190–900 nm versus a pure substrate ( $\text{SiO}_2$  glass). The optical band gap  $E_g$  was determined based on the self-absorption edge from the spectral dependence  $D = f(h\nu)$  ( $D$  is the optical density), assuming direct allowed transitions [7]. The measurements were carried out at room temperature.

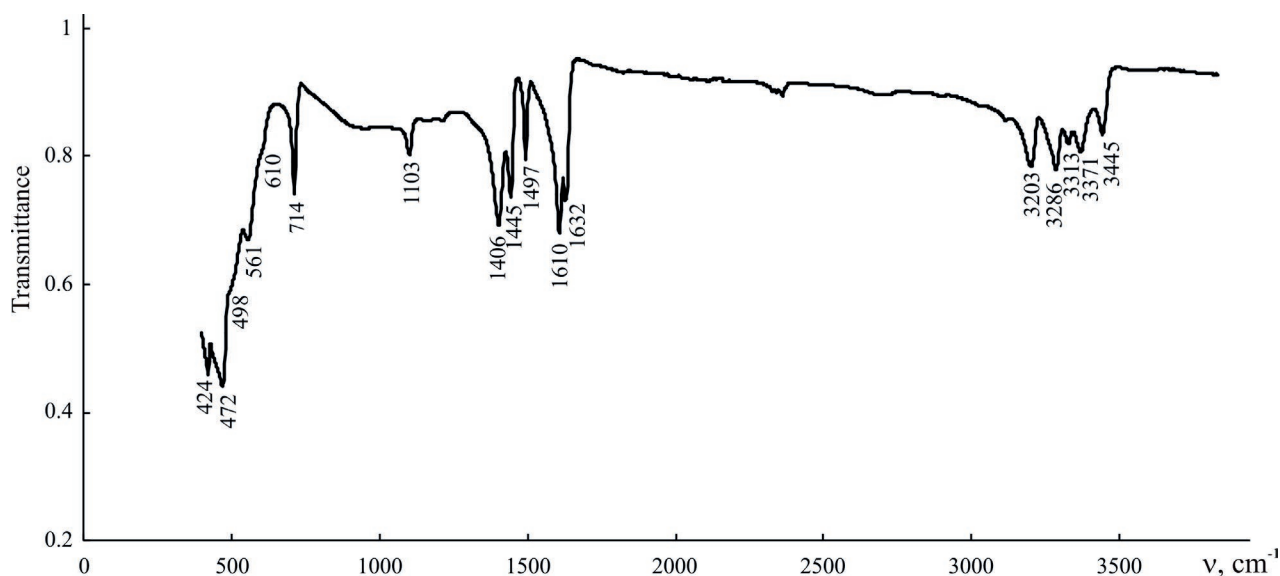
The infrared (IR) and Raman spectra of the complexes were recorded to understand the mechanism of interaction between zinc salt and thiourea. IR spectroscopy was carried out by the method of attenuated total reflectance. The transmission spectra were recorded using a Vertex 70 IR Fourier spectrometer in the range of 400–4000  $\text{cm}^{-1}$ . The zinc complexes were separated from the working solutions by the slow evaporation of the solvent. Initially, the samples were prepared in powder form.

The Raman spectra of the TCC were recorded using a RamMix M532 Raman microscope in the spectral range of 90–4000  $\text{cm}^{-1}$ . The study was conducted using a laser with a radiation wavelength of 532 nm, a radiation region of 4  $\mu\text{m}$ , and a spectral resolution of 2  $\text{cm}^{-1}$ .

## 3. Results and discussion

The IR spectroscopy of the complex compounds obtained from aqueous solutions of zinc salts and thiourea (Fig. 1, 2) showed a shift of the frequency of stretching vibrations  $\nu_{\text{NH}}$  and  $\nu_{\text{CN}}$  to the high frequency region compared with the vibration of free thiourea, and  $\nu_{\text{CS}}$  shifted to the low-frequency region of the spectrum (Tables 1, 2). It confirmed that the coordination of thiourea with zinc salt occurred through the sulphur atom  $\text{N}_2\text{H}_4\text{CS}$  [8]. This is attributed to the redistribution of electron density in the thiourea molecule upon S-coordination, which causes a decrease in the order of the C–S bond and an increase in the order of the C–N and N–H bonds [8, 9].

In the Raman spectra of the studied complex compounds, there were intense bands in the low-frequency region ( $\nu < 400 \text{ cm}^{-1}$ ) characterising the vibrations of the metal-ligand bonds (Fig. 3, 4). According to the results of studies [10–13], the bands with wave numbers of 250–280  $\text{cm}^{-1}$



**Fig. 1.** The IR spectrum of the complex compound obtained from an aqueous solution of zinc chloride and thiourea

**Table 1.** Maximum of absorption bands ( $\text{cm}^{-1}$ ) of IR spectra and Raman spectra of complex compounds, prepared from an aqueous solution of zinc chloride and thiourea

Assignment	$\text{N}_2\text{H}_4\text{CS}$ [8, 9]	$[\text{Zn}(\text{N}_2\text{H}_4\text{CS})_2\text{Cl}_2]$ (ИК, [8])	$\text{ZnCl}_2 + \text{N}_2\text{H}_4\text{CS}$ (IR, experiment)	$\text{ZnCl}_2 + \text{N}_2\text{H}_4\text{CS}$ (Raman, experiment)
$\nu(\text{NH})$			3445	3449
	3375	3370	3371	3379
	3273	3330	3313	3339
	3160	3210	3286	3297
			3203	3212
$\delta(\text{HNH})$		1630	1632	1630
$\delta(\text{HNC})$	1606	1612	1610	1612
$\nu(\text{CN})$	1464	1494	1497	1491
$\nu(\text{HNC})$	1408	1448	1445	1444
$\nu(\text{CS})$		1415	1406	1402
$\nu(\text{CN})$	1082	1106	1103	1107
$\nu(\text{CS})$	729	718	714	721
$\delta(\text{NCN})$	629	600	610	619
			561	
$\delta(\text{NCN})$	484	478	498	479
			472	
$\nu(\text{NCS})$	420	422	424	430
$\delta(\text{ZnCl})$				238
$\delta(\text{ZnS})$				275
				162

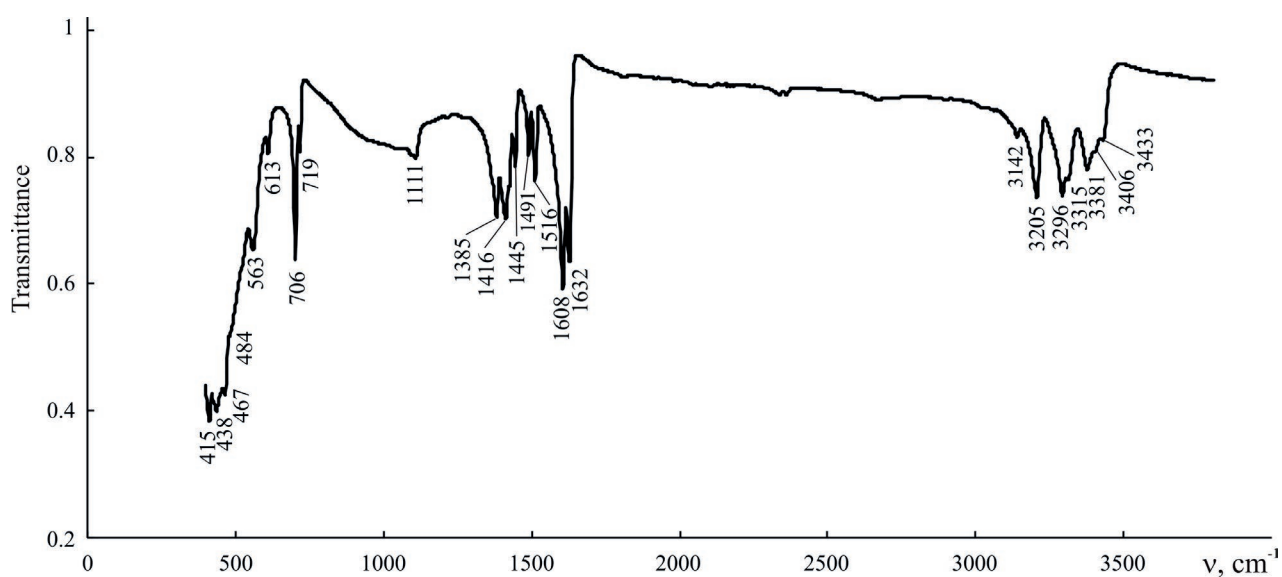
correspond to vibrations of the zinc-sulphur bond (Tables 1, 2). In the Raman spectrum of the  $[\text{Zn}(\text{N}_2\text{H}_4\text{CS})_2\text{Cl}_2]$  compound, we recorded a low intensity peak at  $162 \text{ cm}^{-1}$ , which can also be attributed to the vibrations of the Zn–S bond [14].

The band recorded in the Raman spectrum of the  $[\text{Zn}(\text{N}_2\text{H}_4\text{CS})_2\text{Cl}_2]$  compound at  $238 \text{ cm}^{-1}$  is

attributed to the vibrations of the Zn–Cl bond [15, 16]. For heavier elements, the vibration frequencies shifted to the low-frequency region. Thus, the Zn–Br bond vibration in the  $[\text{Zn}(\text{N}_2\text{H}_4\text{CS})_2\text{Br}_2]$  complex was observed at  $184 \text{ cm}^{-1}$  [17, 18].

In the Raman spectra of the studied complexes, there are two bands in the range of  $50\text{--}140 \text{ cm}^{-1}$ .





**Fig. 2.** The IR spectrum of the complex compound obtained from an aqueous solution of zinc bromide and thiourea

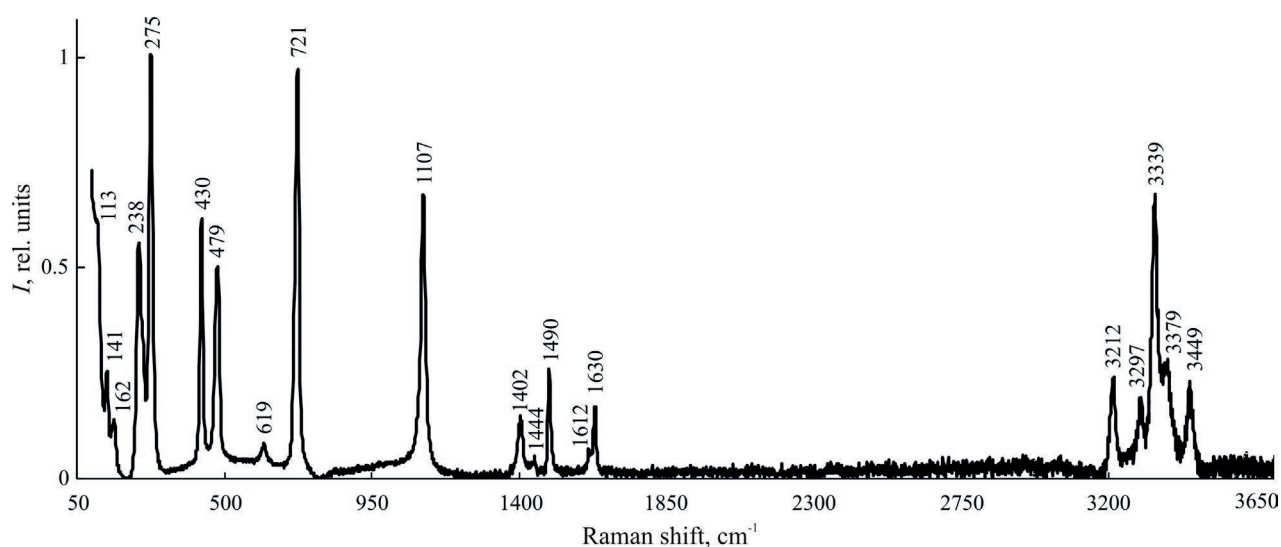
**Table 2.** Maximum of absorption bands ( $\text{cm}^{-1}$ ) of IR spectra and Raman spectra of complex compounds, prepared from an aqueous solution of zinc bromide and thiourea

Assignment	$\text{N}_2\text{H}_4\text{CS}$ [8, 9]	$\text{ZnBr}_2 + \text{N}_2\text{H}_4\text{CS}$ (IR, experiment)	$\text{ZnBr}_2 + \text{N}_2\text{H}_4\text{CS}$ (Raman, experiment)
$\nu(\text{NH})$		3433	3431
		3375	3398
		3273	3380
		3160	3327
			3217
			3205
			3142
$\delta(\text{HNH})$		1632	1631
$\delta(\text{HNC})$	1606	1608	1615
$\nu(\text{CN})$	1464	1516	1518
$\nu(\text{HNC})$		1491	1491
	1408	1445	1431
$\nu(\text{CS})$		1416	1385
$\nu(\text{CN})$		1385	
	1082	1111	1112
$\nu(\text{CS})$			1098
	729	719	721
$\delta(\text{NCN})$		706	705
	629	613	605
$\delta(\text{NCN})$		563	528
	484	484	
$\delta(\text{NCS})$		467	473
	420	438	430
$\nu(\text{ZnBr})$		409	
		415	
$\nu(\text{ZnS})$			184
			258

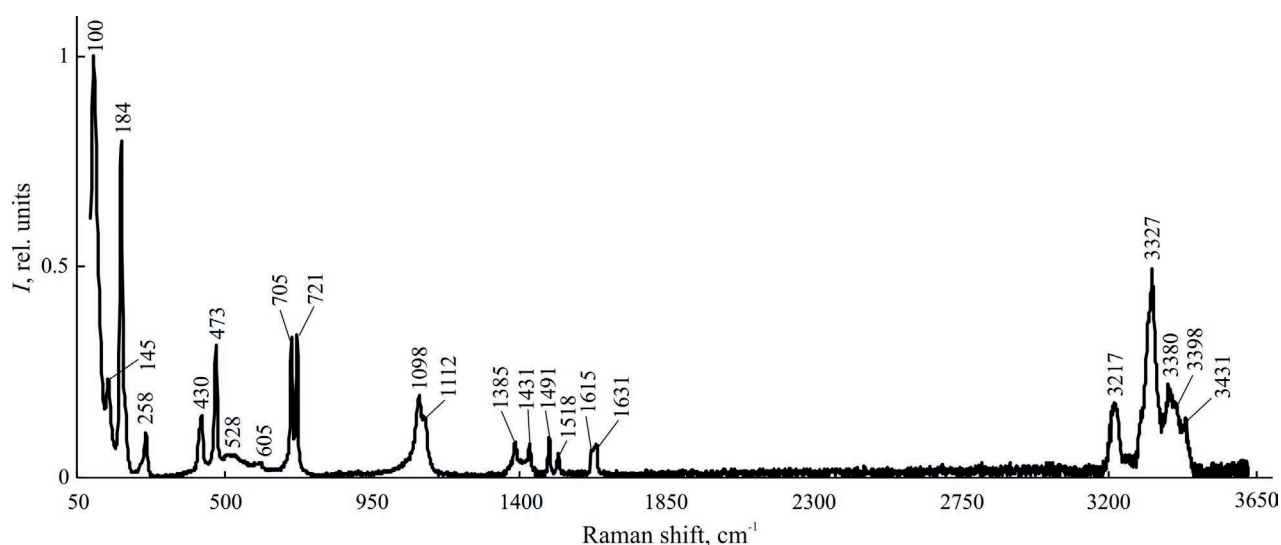
The more intense band is in the frequency range of 100–115  $\text{cm}^{-1}$ , and the less intense one is in the range of 140–145  $\text{cm}^{-1}$  (Fig. 3, 4). According to the authors of [12, 19], the bands observed in the above region characterise the translational and rotational motion of the thiourea molecule, which is part of the complex compound. Apparently, the first band recorded at 113  $\text{cm}^{-1}$  for the chloride complex and at 100  $\text{cm}^{-1}$  for the bromide TCC characterises the translational motion of the coordinated  $\text{N}_2\text{H}_4\text{CS}$  molecule. The low intensity band with maxima at 141 and 145  $\text{cm}^{-1}$  for the chloride and bromide complexes, respectively, characterises the rotational motion of the

thiourea molecule. The deformation vibrations  $\delta(\text{ClZnCl})$  and  $\delta(\text{BrZnBr})$  in zinc complexes, as a rule, appear in the lower frequency region, at 95–100  $\text{cm}^{-1}$  and 70–75  $\text{cm}^{-1}$ , respectively [20, 21].

Thus, the results of the IR and Raman spectroscopy prove the formation of metal-sulphur bonds in the inner sphere of the complex compound. The bonds are the fragments of the crystal structure of the prospective sulphide, which is formed during the thermolysis of the respective complex. The defect structure of the obtained sulphide depends on the immediate environment of the complexing substance in the first coordination sphere. Therefore, it is possible



**Fig. 3.** The Raman spectrum of the complex compound obtained from an aqueous solution of zinc chloride and thiourea



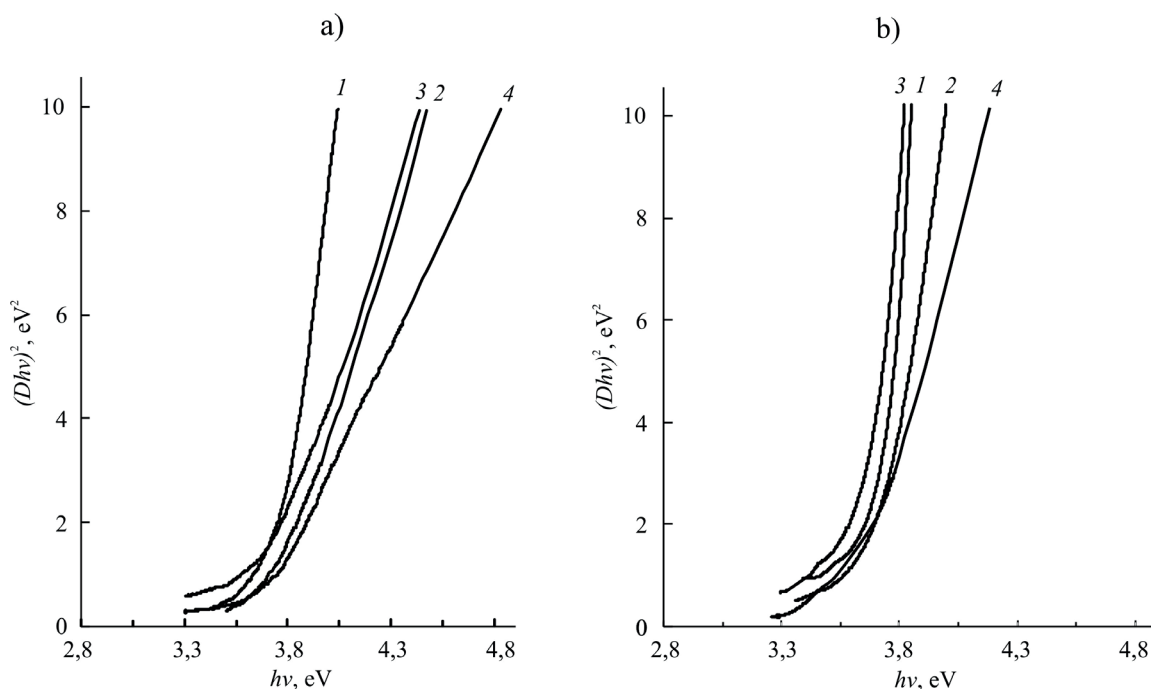
**Fig. 4.** The Raman spectrum of the complex compound obtained from an aqueous solution of zinc bromide and thiourea

to model the structure by introducing different acidic ligands [3–5]. The relationship between the composition and structure of the environment of the central ion in the TCC and the environment of the metal cation in the sulphide lattice is the basis for the directed synthesis of metal sulphide films with a particular set of semiconducting properties.

When studying the optical properties of the synthesized ZnS films, we obtained the absorption spectra in the region of the fundamental absorption edge. By extrapolating the linear section of the power dependence of the optical density on the photon energy  $(hvD)^2 = f(hv)$  (Fig. 5) to the abscissa axis, we determined the optical band gap of the zinc sulphide layers. The ZnS films deposited from the  $[\text{Zn}(\text{N}_2\text{H}_4\text{CS})_2\text{Cl}_2]$  complex solutions are characterised by the optical band gap of 3.67–3.74 eV. For the samples obtained using the  $[\text{Zn}(\text{N}_2\text{H}_4\text{CS})_2\text{Br}_2]$  TCC, the  $E_g$  values are 3.63–3.70 eV (Table 3). It is clear from the obtained data that the optical band gap of ZnS films generally decreases when the deposition temperature

increases from 350 to 500 °C. A similar trend was observed in studies of other authors [22, 23].

The specifics of the change in  $E_g$  depending on the spraying temperature of the samples can be associated with a change in the defect structure of the films. Thus, the samples deposited from the  $[\text{Zn}(\text{N}_2\text{H}_4\text{CS})_2\text{Cl}_2]$  and  $[\text{Zn}(\text{N}_2\text{H}_4\text{CS})_2\text{Br}_2]$  TCC contain chlorine (bromine) that replaces sulphur during the decomposition of the initial complexes. They also contain oxygen due to the synthesis in the air and partial hydrolysis of the initial zinc salt. With an increase in the deposition temperature, the Zn–Cl and Zn–Br bonds decompose more completely, and the content of halogen atoms in the films decreases. The reason is that they are removed as volatile products during the thermolysis of the  $[\text{Zn}(\text{N}_2\text{H}_4\text{CS})_2\text{Cl}_2]$  and  $[\text{Zn}(\text{N}_2\text{H}_4\text{CS})_2\text{Br}_2]$  compounds. In this case, there are less  $\text{Br}_s^{\cdot}$  and  $\text{Cl}_s^{\cdot}$  defects in ZnS films, and the vacated places of sulphur are occupied by oxygen, forming the  $\text{O}_s^x$  defects. In addition, due to the partial hydrolysis of the initial zinc



**Fig. 5.** The absorption spectra of the ZnS films obtained from the  $[\text{Zn}(\text{N}_2\text{H}_4\text{CS})_2\text{Cl}_2]$  (a) and  $[\text{Zn}(\text{N}_2\text{H}_4\text{CS})_2\text{Br}_2]$  (b) TCC solutions at different temperatures: 1 – 350 °C; 2 – 400 °C; 3 – 450 °C; 4 – 500 °C

**Table 3.** Optical band gap (eV) of ZnS films deposited at different temperatures

Complex compound	350 °C	400 °C	450 °C	500 °C
$[\text{Zn}(\text{N}_2\text{H}_4\text{CS})_2\text{Cl}_2]$	3.74	3.73	3.70	3.67
$[\text{Zn}(\text{N}_2\text{H}_4\text{CS})_2\text{Br}_2]$	3.70	3.70	3.65	3.63

salt in the samples synthesised by this method, ZnS may contain an impurity of ZnO oxide, which has a lower band gap than that of zinc sulphide. Its values are 3.35–3.43 eV [24]. Therefore, the presence of oxygen in the samples leads to a decrease in the optical band gap of ZnS with an increase in the deposition temperature.

It should be noted that pyrolytic deposition of zinc oxide films from an aqueous solution of zinc nitrate also showed a decrease in the optical band gap of the samples with an increase in the synthesis temperature [25]. Thus, for ZnO films obtained at 250 °C, the value of  $E_g$  was 3.45 eV, and when the deposition temperature reached 295 °C, the band gap decreased to 3.25 eV.

The zinc sulphide films obtained by the spraying of  $[\text{Zn}(\text{N}_2\text{H}_4\text{CS})_4](\text{NO}_3)_2$  and  $[\text{Zn}(\text{N}_2\text{H}_4\text{CS})_2(\text{CH}_3\text{COO})_2]$  complex solutions in the temperature range of 350–500 °C are characterised by the optical band gap of 3.39–3.41 eV and 3.38–3.50 eV, respectively. The lower  $E_g$  values of the ZnS layers obtained from the above compounds compared with those of the samples from the halide complexes are also due to the oxygen present in them.

#### 4. Conclusions

We synthesised zinc sulphide films from  $[\text{Zn}(\text{N}_2\text{H}_4\text{CS})_2\text{Cl}_2]$  and  $[\text{Zn}(\text{N}_2\text{H}_4\text{CS})_2\text{Br}_2]$  thiourea complex compounds by aerosol pyrolysis at temperatures from 350 to 500 °C. The coordination of thiourea to metal cation in the complex compound occurs through the sulphur atom. Using the absorption spectra of the ZnS films, we determined the values of their optical band gap (3.63–3.74 eV). The optical band gap of the ZnS films decreases as the deposition temperature increases from 350 to 500 °C. It is due to a change in the defect structure of the sulphide.

#### Author contributions

All authors made an equivalent contribution to the preparation of the publication.

#### Conflict of interests

The authors declare that they have no known competing financial interests or personal relationships that could have influenced the work reported in this paper.

#### References

1. Sychov M. M., Ogurtsov K. A., Bakhmetyev V. V., Kotomin A. A., Dushenok S. A., Kozlov A. S., Lebedev V. T., Kulvelis Y. V., Sokolov A. E., Trunov V. A., Török Gy. Effect of the Cu content and ZnS treatment on the characteristics of synthesized ZnS:(Cu, Cl) electroluminescent phosphors. *Semiconductors*. 2012; 46(5): 696–700. <https://doi.org/10.1134/S1063782612050223>
2. Bacherikov Yu. Yu., Kitsyuk N. V. Doped ZnS phosphors with a constant spectral density in the 500–750 nm range. *Technical Physics*. 2005;50(5): 658–659. <https://doi.org/10.1134/1.1927225>
3. Semenov V. N., Naumov A.V. Processes of directed synthesis of metal sulfide films from the thiocarbamide coordination compounds\*. *Vestnik Voronezhskogo gosudarstvennogo universiteta. Seriya: Himiya. Biologiya. Farmaciya*. 2000;2: 50–55. (In Russ.). Available at: <https://elibrary.ru/item.asp?id=21847224>
4. Naumov A. V., Samofalova T. V., Semenov V. N., Nechaev I. V. Thiourea complexes in synthesis of  $\text{Cd}_x\text{Zn}_{1-x}\text{S}$  solid solutions. *Russian Journal of Inorganic Chemistry*. 2011;56(4): 621–627. <https://doi.org/10.1134/S0036023611040218>
5. Samofalova T. V., Semenov V. N. Films based on a solid solution of CdS-ZnS system from thiourea coordination compounds and their properties. *Russian Journal of Applied Chemistry*. 2013;86(12): 1811–1818. <https://doi.org/10.1134/S1070427213120021>
6. Ugaj Ya. A., Semenov V. N. Interaction of thiourea with zinc salts in the preparation of ZnS films\*. *Russian Journal of General Chemistry*. 1989;59(10): 2177–2185. (In Russ.). Available at: <https://elibrary.ru/item.asp?id=28900634>
7. Ukhanov Yu. I. *Optical properties of semiconductors\**. Moscow: Nauka Publ.; 1977. 361 p. (In Russ.).
8. Kharitonov Yu. Ya., Brega V. D., Ablov A. V., Proskina N. N. IR absorption spectra and normal vibrations of metal complexes with thiourea\*. *Russian Journal of Inorganic Chemistry*. 1974;19(8): 2166–2177. (In Russ.).
9. Kharitonov Yu. Ya., Brega V. D., Ablov A. V. On normal vibrations of complex compounds of  $\text{Pd}^{\text{II}}$  and  $\text{Cd}^{\text{II}}$  with thiourea\*. *Russian Journal of Inorganic Chemistry*. 1971;16(2): 572–573. (In Russ.).
10. Serrano J. Cantarero A., Cardona M., Garro N., Lauck R., Tallman R. E., Ritter T. M., Weinstein B. A. Raman scattering in  $\beta$ -ZnS. *Physical Review B*. 2004;69: 1–11. <https://doi.org/10.1103/PHYSREVB.69.014301>
11. Kumari R. G., Ramakrishnana V., Carolinb M. L., Kumar J., Saruac A., Kuball M. Raman spectral investigation of thiourea complexes. *Spectrochimica Acta Part A: Molecular and Biomolecular Spectroscopy*. 2009;73(2): 263–267. <https://doi.org/10.1016/j.saa.2009.02.009>

12. Selvasekarapandian S., Vivekanandian K., Kolandaivel P., Gundurao T. K. Vibrational studies of bis(thiourea) cadmium chloride and tris(thiourea) zinc sulphate semiorganic non-linear optical crystals. *Crystal Research and Technology*. 1997;32(2): 299–309. [https://doi.org/10.1002/\(SICI\)1097-4555\(199710\)28:10<779::AID-JRS147>3.0.CO;2-5](https://doi.org/10.1002/(SICI)1097-4555(199710)28:10<779::AID-JRS147>3.0.CO;2-5)
13. Sidorov A. I., Tung N. D., Van Wu. N., Antropova T. V., Nashchekin A. V. Optical properties of nanocomposites on base of zinc and tin sulfides in nanoporous glass. *Optics and Spectroscopy*. 2019;127(5): 914–918. <https://doi.org/10.1134/S0030400X19110237>
14. RRUFF Database of Raman spectroscopy, X-ray diffraction and chemistry of minerals. Available at: <https://rruff.info/>
15. Irish D. E., Young T. F. Raman spectrum of molten zinc chloride. *The Journal of Chemical Physics*. 1965;43(5): 1765–1768. <https://doi.org/10.1063/1.1697005>
16. Alsayoud A. Q., Venkateswara M. R., Edwards A. N., Deymier P. A., Muralidharan K., Potter B. G., Runge Jr. K., Lucas P. Structure of ZnCl<sub>2</sub> Melt. Part I: Raman spectroscopy analysis driven by Ab Initio methods. *The Journal of Physical Chemistry B*. 2016;120(17): 4174–4181. <https://doi.org/10.1021/acs.jpcc.6b02452>
17. Heumen J. V., Ozeki T., Irish D. Raman spectral study of the equilibria of zinc bromide complexes in DMSO solutions. *Canadian Journal of Chemistry*. 1989;67: 2030–2036. <https://doi.org/10.1139/V89-314>
18. Kalman E., Serke I., Palinkas G. Complex formation in an aqueous ZnBr<sub>2</sub> solution based on electron diffraction, X-ray scattering and Raman spectra. *Zeitschrift fur Naturforschung*. 1983;38(2): 225–230. <https://doi.org/10.1515/zna-1983-0220>
19. Oussad M., Becker P., Kemiche M., Carabatos-Nedelec C. Low temperature phase transitions in zinc tris (thiourea) sulfate (ZTS) determined by Raman scattering. *Physica Status Solidi B*. 2000;222: 553–561. [https://doi.org/10.1002/\(SICI\)1521-3951\(199805\)207:1<103::AID-PSSB103>3.0.CO;2-L](https://doi.org/10.1002/(SICI)1521-3951(199805)207:1<103::AID-PSSB103>3.0.CO;2-L)
20. Hase Y., Airoidi C., Gushikem Y., Kawano Y. Raman spectra of Zn(CH<sub>3</sub>CN)<sub>2</sub>X<sub>2</sub> (X= Cl, Br and I). *Spectroscopy Letters*. 1976;9(2): 105–118. <https://doi.org/10.1080/00387017608067418>
21. Ishikawa D. N., Tellez S. C. A. Infrared and Raman spectra of Zn(NH<sub>3</sub>)<sub>2</sub>Br<sub>2</sub> with <sup>15</sup>N and <sup>2</sup>H isotopic substitution. *Vibrational Spectroscopy*. 1994;8: 87–95. [https://doi.org/10.1016/0924-2031\(94\)00014-8](https://doi.org/10.1016/0924-2031(94)00014-8)
22. Vishwakarma R. Effect of substrate temperature on ZnS films prepared by thermal evaporation technique. *Journal of Theoretical and Applied Physics*. 2015;9:185–192. <https://doi.org/10.1007/s40094-015-0177-5>
23. Offor P. O., Okorie B. A., Ezekoye B. A., Ezekoye V. A., Ezema J. I. Chemical spray pyrolysis synthesis of zinc sulphide (ZnS) thin films via double source precursors. *Journal of Ovonic Research*. 2015;11(2): 73–77. Режим доступа: [https://chalcogen.ro/73\\_Offor.pdf](https://chalcogen.ro/73_Offor.pdf)
24. *Physical Quantities: Handbook*. I. S. Grigor'ev, E. Z. Meilikhov (eds.). Moscow: Energoatomizdat Publ., 1991. 1232 p. (in Russ.)
25. Faraj M. G., Taboada P. Structural and optical properties of ZnO thin films prepared by spray pyrolysis on PI plastic substrates at various temperatures for integration in solar cell. *Journal of Materials Science: Materials in Electronics*. 2017;28: 16504–16508. <https://doi.org/10.1007/s10854-017-7562-6>

\* Translated by author of the article.

### Information about the author

*Tatyana V. Samofalova*, Cand. Sci. (Chem.), Associate Professor at the Department of General and Inorganic Chemistry, Voronezh State University (Voronezh, Russian Federation).

<https://orcid.org/0000-0002-4277-4536>

[TSamofalova@bk.ru](mailto:TSamofalova@bk.ru)

*Victor N. Semenov*, Dr. Sci. (Chem.), Full Professor, Head of the Department of General and Inorganic Chemistry, Voronezh State University (Voronezh, Russian Federation).

<https://orcid.org/0000-0002-4247-5667>

[office@chem.vsu.ru](mailto:office@chem.vsu.ru)

*Pavel V. Seredin*, Dr. Sci. (Phys.-Math.), Professor, Head of the Department of Solid State Physics and Nanostructures, Voronezh State University (Voronezh, Russian Federation).

<https://orcid.org/0000-0002-6724-0063>

[paul@phys.vsu.ru](mailto:paul@phys.vsu.ru)

*Dmitry L. Goloshchapov*, Cand. Sci. (Phys.-Math.), Associate Professor at the Department of Solid State Physics and Nanostructures, Voronezh State University (Voronezh, Russian Federation).

<https://orcid.org/0000-0002-1400-2870>

[goloshchapov@phys.vsu.ru](mailto:goloshchapov@phys.vsu.ru)

*Nikita S. Buylov*, Cand. Sci. (Phys.-Math.), Research Assistant, Laboratory of organic additives for the processes of chemical and electrochemical deposition of metals and alloys used in the electronics industry, Voronezh State University (Voronezh, Russian Federation).

<https://orcid.org/0000-0003-1793-4400>

[buylov@phys.vsu.ru](mailto:buylov@phys.vsu.ru)

Received 07.11.2022; approved after reviewing 18.11.2022; accepted for publication 15.12.2022; published online 25.12.2022.

Translated by Anastasiia Ananeva

Edited and proofread by Simon Cox



## Original articles

Research article

<https://doi.org/10.17308/kcmf.2022.24/10558>

## The conditions for the solid state synthesis of solid solutions in zirconia and hafnia systems with the oxides of rare earth elements

P. P. Fedorov✉, E. V. Chernova

Prokhorov General Physics Institute of the Russian Academy of Sciences,  
38 Vavilova str., Moscow 119991, Russian Federation

## Abstract

The goal of this work was to study the specific features of obtaining  $(\text{Zr,Hf})_{1-x}\text{R}_x\text{O}_{2-0.5x}$  solid solutions through solid-phase sintering and to analyse the correctness of the existing variants of phase diagrams for  $(\text{Zr, Hf})\text{O}_2\text{-R}_2\text{O}_3$  zirconia and hafnia systems with the oxides of rare earth elements.

We analysed the existing data on the duration of annealing used to study phase equilibria in zirconia and hafnia systems with the oxides of rare earth elements. The “annealing time logarithm – reciprocal temperature” dependences were constructed. It was shown that the effective diffusion coefficient upon annealing was at least 200 kJ/mol. The time of annealing required for the achievement of equilibrium at 1300 °C was no less than 6 months. The annealings for one year did not allow receiving reliable information on phase equilibria in these systems with temperatures lower than 1250 °C. All the data on phase diagrams presented in earlier studies for lower temperatures did not characterise the equilibrium state of systems. Apart from low-temperature phases of variable compositions presented in phase diagrams, among the characteristics of non-equilibrium states there were violations of the Hume-Rothery rule and observations of diffusionless processes of ordering of solid solutions, including those occurring upon “fluorite-pyrochlore” solid state transitions. Probable schemes of low temperature phase equilibria in the  $\text{ZrO}_2\text{-Er}_2\text{O}_3$  and  $\text{HfO}_2\text{-Eu}_2\text{O}_3$  systems were presented taking into account the third law of thermodynamics.

The obtained results are fundamental and will be useful for the assessment of the stability of thermal barrier coatings and fuel cells based on zirconium and hafnium oxides with the oxides of rare earth elements.

**Keywords:** Zirconia, Hafnia, Zirconium oxide, Hafnium oxide, Oxides of rare earth elements, Solid solutions, Ordering, Phase diagrams, Sintering

**Funding:** The study was supported by Russian Science Foundation grant No. 22-13-00167 <https://rscf.ru/project/22-13-00167/>

**For citation:** P. P. Fedorov, E.V. Chernova. The conditions for the solid state synthesis of solid solutions in zirconia and hafnia systems with the oxides of rare earth elements. *Condensed Matter and Interphases*. 2022;24(4): 537–544. <https://doi.org/10.17308/kcmf.2022.24/10558>

**Для цитирования:** Федоров П. П., Чернова Е. В. Условия твердофазного синтеза твердых растворов в системах из диоксидов циркония и гафния с оксидами редкоземельных элементов. *Конденсированные среды и межфазные границы*. 2022;24(4): 537–544. <https://doi.org/10.17308/kcmf.2022.24/10558>

✉ Pavel P. Fedorov, e-mail: [ppfedorov@yandex.ru](mailto:ppfedorov@yandex.ru)

© P. P. Fedorov, E.V. Chernova., 2022



The content is available under Creative Commons Attribution 4.0 License.

## 1. Introduction

Solid solutions of  $R_2O_3$  rare earth elements oxides in high-temperature cubic modifications of zirconium and hafnium dioxides with a general formula of  $(Zr,Hf)_{1-x}R_xO_{2-0.5x}$  are among the most refractory oxides with a melting temperature of over 2700 °C [1, 2]. The materials based on them are widely used as crystals for jewellery (fianites) [3, 4] as well as refractory and corrosion resistant ceramics [5–9]. The high anionic conductivity of these solid solutions is combined with low thermal conductivity [10]. These conditions allow using the corresponding materials in electrochemical devices (fuel cells and oxygen sensors) [11–13] and as thermal barrier coatings [14, 15]. In both areas the materials are used as films and require continuous work with increased temperatures (up to 30,000 hours at 800 °C and higher).

Cubic solid solutions of  $(Zr,Hf)_{1-x}R_xO_{2-0.5x}$  are obviously thermodynamically unstable at low temperatures. However, negligibly small coefficients of cation diffusion [16] prevent the decomposition of solid solutions, which makes the corresponding materials stable for an indefinitely long period of time at ambient temperatures. Still, what happens with an increase of temperature up to 800–1000 °C has been studied insufficiently [17].

To present the final scenario of the expected evolutions of the material based on zirconium and hafnium oxides stabilised by the oxides of rare earth elements upon a prolonged exposure to increased temperatures, it is advisable to know the phase T-x diagrams of the corresponding systems. Enormous efforts were needed to construct such phase diagrams (see, for instance, [18–35]), but the results of these studies cannot be considered satisfactory.

The main issues were associated with the achievement of equilibrium in the corresponding systems as the time required for the achievement of equilibrium increased exponentially with a decrease in temperature [36, 37]. The researchers from Tokyo Institute of Technology (M. Yashima, N. Ishizawa, M. Yoshimura, etc.) showed that in some works the annealing was insufficient [25, 33]. In particular, it turned out that the temperature of the eutectoid decomposition

of the solid solution based on the medium temperature tetragonal modification in the  $ZrO_2$ – $Er_2O_3$  system identified in [30] was understated by approximately 500 °C [25].

The systems  $ZrO_2$ – $R_2O_3$  were studied by different groups of researchers. The reports were presented in [18, 19]. The results obtained for various rare earth elements did not correspond well with one another. There is an array of data for the systems  $HfO_2$ – $R_2O_3$  which were obtained in the Materials Science Institute (Kyiv, L. M. Lopato, A. V. Shevchenko, E. R. Andrievskaya, etc.) in the course of studies conducted in accordance with one method, and the plotted phase diagrams showed natural changes for the motion along rare earth elements [18, 19].

The goal of this work was to study the specific features of obtaining  $(Zr,Hf)_{1-x}R_xO_{2-0.5x}$  solid solutions through solid-phase sintering and to analyse the correctness of the existing variants of phase diagrams for the  $(Zr, Hf)O_2$ – $R_2O_3$  systems.

## 2. Analysis methodology

As we showed before [36], there is a linear dependence of the annealing time logarithm ( $\tau$ ) on the reciprocal temperature upon the achievement of equilibrium during sintering. Indeed, Fick's diffusion equation shows that

$$X^2 \sim D\tau \quad (1)$$

where  $X$  is the thickness of the diffusion layer,  $D$  is the effective diffusion coefficient, and  $\tau$  is time. In its turn, the diffusion coefficient exponentially depends on temperature

$$D = D_0 \exp(-E/kT), \quad (2)$$

where  $E$  is the diffusion activation energy,  $T$  is the absolute temperature,  $k$  is the Boltzmann constant. Therefore, the following linear dependence is valid in case of the same dispersion of the sintered particles

$$1/\tau = A \exp(-E/kT), \quad (3)$$

where  $A$  is a constant, and from the tangent of the slope of the line in coordinates  $\lg \tau \sim 1/T$  it is possible to determine the activation energy of the limiting stage of the sintering process:

$$E = 206 \operatorname{tg} \alpha [\text{k}/\text{mol}] = 1.99 \operatorname{tg} \alpha [\text{eV}]. \quad (4)$$

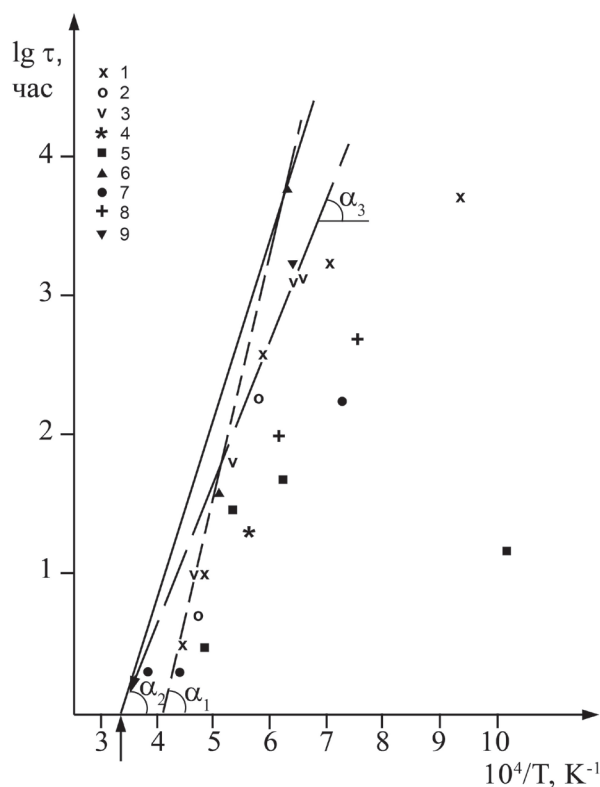
### 3. Results and discussion

Fig. 1 presents some previous data on the thermal processing modes used for the study of phase equilibria in zirconia and hafnia with the oxides of rare earth elements. It supplements the information that was earlier presented graphically in [36, 37]. The data on the systems with zirconia and hafnia are seldom studied together, which corresponds to the first stage of the analysis.

Fig. 1 shows that there is a great scatter of data. It is obvious that in many works the duration of synthesis was insufficient. The use of the following protocol seemed quite reasonable: 10 hours at 1900 °C, 30–60 hours at 1600 °C, 1200 hours at 1300 °C. Pascual and Duran [20] annealed the samples for 3 hours at 2000 °C, for 10 hours at 1800 °C, and for 385 hours at 1450 °C, which seems acceptable. However, the 8 months of annealing at 800 °C used in this work were definitely insufficient. Apparently Yashima et al. [25] achieved the most correct results. They annealed the samples in the  $ZrO_2-Er_2O_3$  system at 1690 °C for 48 hours and 8 months at 1315 °C. A linear dependence plotted in accordance with these data (angle  $\alpha_1$  on Fig.1) corresponded to the diffusion activation energy  $E = 360$  kJ/mol, which reasonably corresponded to the value of 391 kJ/mol obtained in [16] for bulk interdiffusion of cations within the range of 1584–2116 °C. Other variants of the approximation relationships presented such values as  $E = 260$  kJ/mol (angle  $\alpha_2$  on Fig. 1) and  $E = 200$  kJ/mol (angle  $\alpha_3$  on Fig.1). These values are closer to the values obtained by Glushkova and her colleagues [23, 38].

It can be seen that with a decrease in the temperature, the required duration of the experiments quickly exceeded laboratory capabilities and reached the time of about a year at 1250 °C. Since all real laboratory experiments described in previous works did not exceed the duration of 8 months, the results obtained for temperatures below 1300 °C cannot be considered as those associated with the state of equilibrium. It is also true for many published variants of phase diagrams. However, the inverse proposition is wrong: not all research results associated with high temperatures can be considered as equilibrium.

The violations of the third law of thermodynamics are among the indications of



**Fig. 1.** The duration of annealing for the synthesis of samples in systems  $(Zr, Hf)O_2-R_2O_3$  depending on the reciprocal synthesis temperature according to 1 – Pascual, Duran, 1983 [20]; 2 – Scott, 1978 [21]; 3 – Meister et al., 1991 [22]; 4 – Krzhizhanovskaya, 1990 [23]; 5 – Schedecker e.a., 1977 [24]; 6 – Yashima e.a., 1991 [25]; 7 – Ruh e.a., 1977 [26]; 8 – Thornber, e.a., 1970 [27]; 9 – Stubican e.a., 1984 [28]. The arrow shows the melting point of zirconium dioxide

thermodynamic incorrectness of the plotted phase diagrams. According to the consequence of this law, when the temperature tends to absolute zero, all phases of variable compositions in quasi-equilibrium processes disappear through decomposition or contraction of compositions to those stoichiometric [37]. The second important thermodynamic condition is the so-called Hume-Rothery rule, according to which the region of existence of a disordered phase sharply narrows when an ordered phase with a narrow region of homogeneity appears [39]. This rule is regularly violated when a solid phase ordering of heterovalent fluorite solid solution with phase separation of the pyrochlore structure is shown in the  $(Zr, Hf)O_2-R_2O_3$  systems [18, 19].

The use of the correction method for phase diagrams with extrapolation of phase equilibria to

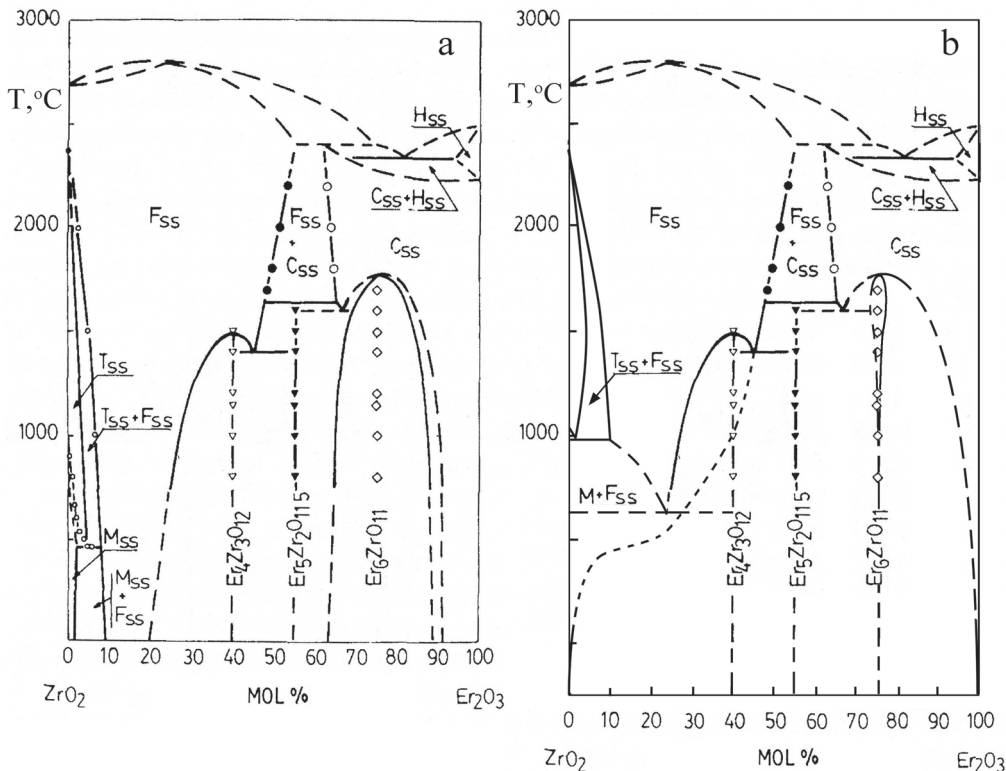


absolute zero seems promising for the  $(\text{Zr, Hf})\text{O}_2\text{-Er}_2\text{O}_3$  systems. This method has been successfully applied in a number of binary systems in our works [40–42].

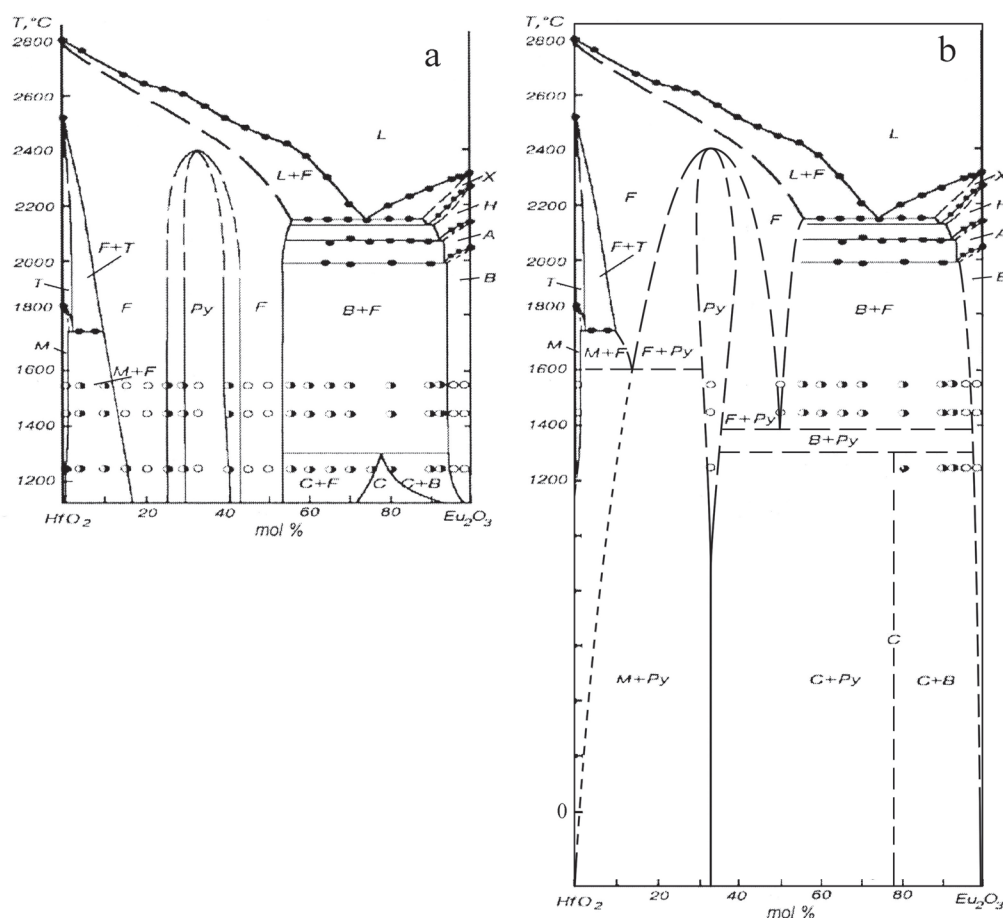
Fig. 2 shows corrections in the data on phase equilibria in the  $\text{ZrO}_2\text{-Er}_2\text{O}_3$  system while Fig. 3 shows corrections in the  $\text{HfO}_2\text{-Eu}_2\text{O}_3$  system [18]. The  $\text{ZrO}_2\text{-Er}_2\text{O}_3$  system is among the most well-studied systems of this group with the duration of annealing up to 8 months [25, 31]. The basis (Fig. 2a) was the diagram plotted in [31]. The region of low concentrations of erbium oxide was corrected according to the data from [25] (the temperature of the eutectoid decomposition of the tetragonal phase was increased by approximately 500 °C). Accordingly, the temperature of the eutectoid decomposition of the cubic solid solution, with account of the data from [25], was presumably targeted at  $600 \pm 100$  °C. The thin dashed line indicates a metastable extension of the curve of the maximum concentration of this solid solution (the solvus curve). This curve must pass through the origin of the coordinates and have a vertical tangent at this point. This condition can be fulfilled only if there is a point

of inflexion on the solvus curve (in this case, on the metastable part of this curve). Such inflexion points are typical for all heterovalent solid solutions based on compounds with the fluorite structure [43], which is associated with diffuse phase transitions in fluorite matrices [44]. In the region of high concentrations of erbium oxide, the correction has a significant effect on the decrease in the homogeneity region of the ordered phase, which must shrink to its ideal composition  $\text{Er}_6\text{ZrO}_{11}$  when the temperature decreases. It also affects the position of the decomposition curve of a solid solution based on the cubic modification of erbium oxide, which must come to the point of the pure component at  $T = 0$  K.

The correction of the phase diagram in the  $\text{HfO}_2\text{-Eu}_2\text{O}_3$  system (Fig. 3) in the region of ordering of the fluorite solid solution with the release of a pyrochlore-type phase was conducted in accordance with the third law of thermodynamics (the homogeneity region of the pyrochlore phase contracted to the stoichiometric composition, two-phase “fluorite + pyrochlore” regions expanded with a decrease in temperature, and two eutectoid equilibria limiting the region



**Fig. 2.** Phase diagram of the  $\text{ZrO}_2\text{-Er}_2\text{O}_3$  system according to [31] (a) and its correction with account of the requirements of the third law of thermodynamics (b)



**Fig. 3.** Phase diagram of the  $\text{HfO}_2\text{-Eu}_2\text{O}_3$  system according to [18] (a) and its correction with account of the requirements of the third law of thermodynamics (b)

of existence of the fluorite phase from below were implemented). It should also be noted that the region of phase equilibria near europium oxide was plotted in [18] assuming the existence of a low-temperature cubic modification of  $\text{Eu}_2\text{O}_3$ . This assumption, which is a part of the polymorphism and morphotropy scheme in a row of oxides of rare earth elements plotted in accordance with the data from [45], turned out to be incorrect due to the hydroxyl contamination. A low-temperature cubic phase identified in this system in the region of  $\sim 75$  mol%  $\text{Er}_2\text{O}_3$  is probably another ordered fluorite-like phase that requires further studying.

#### 4. Conclusions

Phase equilibria at low temperatures in systems with zirconia and hafnia are among the fundamental issues that still need solving. Since the time of achieving equilibrium, controlled by cationic diffusion, increases exponentially with decreasing temperature, the study of low-

temperature equilibria is a very difficult and often insoluble problem. Regions for which the time for establishing equilibrium by means of dry sintering is about 1 year can be considered as being low-temperature regions. For systems based on zirconium and hafnium oxides, this is no lower than  $1250^\circ\text{C}$ .

On numerous published  $(\text{Zr,Hf})\text{O}_2\text{-R}_2\text{O}_3$  “phase diagrams” at temperatures below  $1300^\circ\text{C}$ , frozen states are depicted instead of equilibrium phase regions. The actual behaviour of materials in these systems upon cooling is determined mainly not by equilibrium phase transformations, but by diffusionless phase transitions. Accordingly, in some cases two-phase regions on phase diagrams are reduced, and instead of them we see the martensitic phase transformation lines. This is also true for the processes of “fluorite-pyrochlore” ordering.

It should be noted that the ordering processes in the systems with zirconia and hafnia have

not been studied well, see, for example, [47]. Important discoveries can be made in this area.

Thermodynamic modelling is not always reliable. In particular, the temperature of the eutectoid decomposition of the cubic phase in the  $ZrO_2$ - $Y_2O_3$  system differed according to the data of different models by hundreds of degrees [48–50], while in [51] it was below absolute zero, which contradicted the third law of thermodynamics.

We need other methods to study low-temperature phase formation in the discussed systems in addition to simple sintering. It is reasonable to use the methods of synthesis involving a liquid phase. The use of hydrothermal synthesis for acceleration of achieving equilibrium allowed obtaining the most reliable data on  $ZrO_2$ - $R_2O_3$  ( $R = Er, Y, Sc$ ) and  $ZrO_2$ - $CeO_2$  systems [33, 52, 53]. It can be expected that the use of salt melts will allow making progress in this matter.

### Author contributions

All authors made an equivalent contribution to the preparation of the publication.

### Conflicts of interest

The authors declare that they have no known competing financial interests or personal relationships that could have influenced the work reported in this paper.

### References

1. Sabbarao E. C. Zirconia – an overview. In: *Proc. First Int. Conf.: Science and Technology of Zirconia*. Cleveland, Ohio; 1981. pp. 1–24.
2. Fedorov P. P., Yarotskaya, E. G. (). Zirconium dioxide. Review. *Condensed Matter and Interphases*. 2021;23(2): 169–187. <https://doi.org/10.17308/kcmf.2021.23/3427>
3. Kuz'minov Yu. S, Osiko V. V. *Fianites\**. Moscow: Nauka Publ.; 2001. 280 p. (In Russ.)
4. Osiko V. V., Borik M. A., Lomonova E. E. Synthesis of refractory materials by skull melting. In: Dhanaraj G., Byrappa K., Prasad V., Dudley, M. (eds.). In: *Springer Handbook of Crystal Growth*. N.Y.: Springer; 2010. p. 433–477. [https://doi.org/10.1007/978-3-540-74761-1\\_14](https://doi.org/10.1007/978-3-540-74761-1_14)
5. Zhigachev A. O., Golovin Yu. I., Umrikhin A. V., Korenkov V. V., Tyurin A. I., Rodaev V. V., D'yachek T. A. *Ceramic materials based on zirconium dioxide\** / Yu. I. Golovin (eds.). Moscow: Tekhnosfera Publ.; 2018. 357 p.
6. Stevens R. Engineering properties of zirconia. In: *Engineered Materials Handbook: Ceramics and Glasses*. ASM International. CRC Press; 1991;4: 775–786.
7. Bocanegra-Bernal M. H., de la Torre S. D. Phase transitions in zirconium dioxide and related materials for high performance engineering ceramics. *Journal of Materials Science*. 2002;37: 4947–4971. <https://doi.org/10.1023/A:1021099308957>
8. Kablov E. N. Strategical areas of developing materials and their processing technologies for the period up to 2030. *Aviation Materials and Technologies*. 2012;S: 7–17. (In Russ., abstract in Eng.). Available at: <https://www.elibrary.ru/item.asp?id=18084815>
9. Kelly J. R., Denry I. Stabilized zirconia as a structural ceramics: An overview. *Dental Materials*. 2008;24(3): 289–298. <https://doi.org/10.1016/j.dental.2007.05.005>
10. Fedorov P. P., Popov P. A. Principle of equivalency of the disorder sources and heat conductivity of solids. *Nanosystems: Physics, Chemistry, Mathematics*. 2013;4(1): 148–159. (In Russ., abstract in Eng.). Available at: <https://www.elibrary.ru/item.asp?id=18964066>
11. Goodenough J. B. Oxide-ion electrolytes. *Annual Review of Materials Research*. 2003;33(1): 91–128. <https://doi.org/10.1146/annurev.matsci.33.022802.091651>
12. Kendall K. Progress in solid oxide fuel cell materials. *International Materials Reviews*. 2005;50(5): 257–264. <https://doi.org/10.1179/174328005x41131>
13. Fergus J. F. Electrolytes for solid oxide fuel cells. *Journal of Power Sources*. 2006;162(1): 30–40. <https://doi.org/10.1016/j.jpowsour.2006.06.062>
14. Wu J., Wei X., Padture N. P., Klemens P. G., Gell M., García E., Miranzo P., Osendi M. I. Low-thermal-conductivity rare-earth zirconates for potential thermal-barrier-coating applications. *Journal of the American Ceramic Society*. 2002;85(12): 3031–3035. <https://doi.org/10.1111/j.1151-2916.2002.tb00574.x>
15. Schulz U., Leyens C., Fritscher K., Peters M., Saruhan-Brings B., Lavigne O., Dorvaux J.-M., Poulain M., Mévrel R., Caliez M. Some recent trends in research and technology of advanced thermal barrier coatings. *Aerospace Science and Technology*. 2003;7(1): 73–80. [https://doi.org/10.1016/s1270-9638\(02\)00003-2](https://doi.org/10.1016/s1270-9638(02)00003-2)
16. Sakka Y., Oishi Y., Ando K. Zr-Hf interdiffusion in polycrystalline  $Y_2O_3$ - $(Zr+Hf)O_2$ . *Journal of Materials Science*. 1982;17(11): 3101–3105. <https://doi.org/10.1007/bf01203471>
17. Haering C., Roosen A., Schichl H., Schnoller M. Degradation of the electrical conductivity in stabilized zirconia system. Part. II: Scandia-stabilized zirconia. *Solid State Ionics*. 2005;176(3–4): 261–268. <https://doi.org/10.1016/j.ssi.2004.07.039>
18. Andrievskaya E. R. Phase equilibria in the refractory oxide systems of zirconia, hafnia and yttria

with rare-earth oxides. *Journal of the European Ceramic Society*. 2008;28(12): 2363–2388. <https://doi.org/10.1016/j.jeurceramsoc.2008.01.009>

19. Andrievskaya E. R. *Phase equilibria in systems of hafnium, zirconium, yttrium oxides with oxides of rare earth elements\**. Kiev: Naukova dumka Publ.; 2010. (In Russ.)

20. Pascual C., Duran P. Subsolidus phase equilibria and ordering in the system  $ZrO_2$ - $Y_2O_3$ . *Journal of the American Ceramic Society*. 1983;66(1): 23–28. <https://doi.org/10.1111/j.1151-2916.1983.tb09961.x>

21. Scott H. G. On the continuous transition between two structure types in the zirconia-gadolinia system. *Journal of Materials Science*. 1978;13(7): 1592–1593. <https://doi.org/10.1007/bf00553219>

22. Maister I. M., Shevchenko A. V., Lopato L. M. Interaction in the system  $ZrO_2$ - $Y_2O_3$ - $Sc_2O_3$ \*. *Izvestiya Akademii nauk SSSR. Neorganicheskie materialy (Inorganic Materials)*. 1991;27(11):2337–2341. (In Russ.)

23. Krzhizhanovskaya V. A. *The mechanism of interaction of zirconium and hafnium dioxides with oxides of rare earth elements in solid phases\**. Cand. chem. sci. diss. Abstr. Leningrad: 1975. 18 p. (In Russ.)

24. Scheidecker R. W., Wilder R. W., Moeller H. The system  $HfO_2$ - $Eu_2O_3$ . *Journal of the American Ceramic Society*. 1977; 60(11-12): 501–504. <https://doi.org/10.1111/j.1151-2916.1977.tb14092.x>

25. Yashima M., Ishizawa N., Nama T., Yoshimura M. Stable and metastable phase relationships in the system  $ZrO_2$ - $ErO_{1.5}$ . *Journal of the American Ceramic Society*. 1991;74(3): 510–513. <https://doi.org/10.1111/j.1151-2916.1991.tb04052.x>

26. Ruh R., Garrett H. J., Domagala R. F., Patel V. A. The system zirconia-scandia. *Journal of the American Ceramic Society*. 1977;60(9-10): 399–403. <https://doi.org/10.1111/j.1151-2916.1977.tb15521.x>

27. Thornber M. R., Bevan D. J. M., Summerville E. Mixed oxides of the type  $MO_2$  fluorite- $M_2O_3$ . V. Phase studies in the systems  $ZrO_2$ - $M_2O_3$  ( $M = Sc, Yb, Er, Dy$ ). *Journal of Solid State Chemistry*. 1970;1(3-4): 545–553. [https://doi.org/10.1016/0022-4596\(70\)90140-4](https://doi.org/10.1016/0022-4596(70)90140-4)

28. Stubican V. S., Corman G. S., Hellmann J. R., Sent G. Phase relationships in some  $ZrO_2$  system. In: *Advanced in Ceramics. V.12. Science and Technology of Zirconia II*. N. Clausen, A. Ruhle, A. Heuer (eds.). Columbus, OH, American Ceramic Soc Inc; 1984. pp. 96–106.

29. Rouanet A. Contribution a l'etude des systems zircon-oxydes des lanthanides au voisinage de la fusion. *Revue Internationale Des Hautes Temperatures et Des Refractaires*. 1971;8: 161–180.

30. Duran P. The system erbia - zirconia. *Journal of the American Ceramic Society*. 1977;60(11-12): 510–513. <https://doi.org/10.1111/j.1151-2916.1977.tb14095.x>

31. Pascual C., Duran P. Phase equilibria and ordering in the erbia-zirconia system. *Journal of Materials Science*. 1981;16(11): 3067–3076. <https://doi.org/10.1007/bf00540314>

32. Noguchi T., Mizuno M., Yamada T. The liquifus curve of the  $ZrO_2$ - $Y_2O_3$  system as measured by a solar furnace. *Bulletin of the Chemical Society of Japan*. 1970;43(8): 2614–2616. <https://doi.org/10.1246/bcsj.43.2614>

33. Yashima M., Kakihana M., Yoshimura M. Metastable-stable phase diagrams in the zirconia-containing systems utilized in solid-oxide fuel cell application. *Solid State Ionics*. 1996;86-88: 1131–1149. [https://doi.org/10.1016/0167-2738\(96\)00386-4](https://doi.org/10.1016/0167-2738(96)00386-4)

34. Shevchenko A. V., Maister I. M., Lopato L. M. Interaction in  $HfO_2$ - $Sc_2O_3$  and  $ZrO_2$ - $Sc_2O_3$  systems at high temperatures\*. *Izvestiya Akademii nauk SSSR. Neorganicheskie materialy (Inorganic Materials)*. 1987;23: 1320–1324. (In Russ.)

35. Zyrin A. V., Red'ko V. P., Lopato L. M., Shevchenko A. V., Maister I. M., Zaitseva Z. A. Ordered phases in  $ZrO_2$ - $Sc_2O_3$  and  $HfO_2$ - $Sc_2O_3$  systems\*. *Izvestiya Akademii nauk SSSR. Neorganicheskie materialy (Inorganic Materials)*. 1987;23: 1325–1329. (In Russ.)

36. Fedorov P. P. Anneal times determined by studying phase transitions in solid binary systems. *Russian Journal of Inorganic Chemistry*. 1992;37: 973–975.

37. Fedorov P. P. Third law of thermodynamics as applied to phase diagrams. *Russian Journal of Inorganic Chemistry*. 2010;55: 1722–1739. <https://doi.org/10.1134/S0036023610110100>

38. Glushkova V. V. Study of the kinetics of solid-phase processes in systems with refractory oxides\*. In: *Thermodynamics and properties of condensed silicate and oxide systems*. Bratislava: VEDA; 1976. p. 122–127. (In Russ.)

39. Hume-Rothery W., Raynor G. V. *The structure of metals and alloys*. London: The institute of metals; 1956.

40. Fedorov P. P., Volkov S. N. Au–Cu phase diagram. *Russian Journal of Inorganic Chemistry*. 2016;61: 772–775. <https://doi.org/10.1134/S0036023616060061>

41. Fedorov P. P., Popov A. A., Shubin Yu. V., Chernova E. V. Nickel-platinum phase diagram\*. *Russian Journal of Inorganic Chemistry*. 2022;67(12): 1805–1809. (In Russ.). <https://doi.org/10.31857/S0044457X22600748>

42. Fedorov P. P., Shubin Yu. V., Chernova E. V. Copper–palladium phase diagram. *Russian Journal of Inorganic Chemistry*. 2021;66(6): 891–893. <https://doi.org/10.1134/s0036023621050053>

43. Fedorov P. P., Alexandrov A. A., Voronov V. V., Mayakova M. N., Baranchikov A. E., Ivanov V. K. Low-

temperature phase formation in the  $\text{SrF}_2$ - $\text{LaF}_3$  system. *Journal of the American Ceramic Society*. 2021;104(6): 2836–2848. <https://doi.org/10.1111/jace.17666>

44. Hutchings M. T., Clausen K., Dickens M. H., Hayes W., Kjems J. K., Schnabel P. G., Smith C. Investigation of thermally induced anion disorder in fluorites using neutron scattering techniques. *Journal of Physics C: Solid State Physics*. 1984;17(22): 3903–3940. <https://doi.org/10.1088/0022-3719/17/22/011>

45. Warshaw J., Roy R. Polymorphism of the rare earth sesquioxides. *Journal of Physical Chemistry*. 1961;65(11): 2048–2051. <https://doi.org/10.1021/j100828a030>

46. Fedorov P. P., Nazarkin M. V., Zakalyukin R. M. On polymorphism and morphotropism of rare earth sesquioxides. *Crystallography Reports*. 2002;47: 281–286. <https://doi.org/10.1134/1.1466504>

47. Withers R. L., Thompson J. G., Barlow P. J., Barry J. C. The “defect fluorite” phase in the  $\text{ZrO}_2$ - $\text{PrO}_{1.5}$  system and its relationship to the structure of pyrochlore. *Australian Journal of Chemistry*. 1992;45(9): 1375–1395. <https://doi.org/10.1071/ch9921375>

48. Degtyarev S. A., Voronin G. F. Calculation of the phase diagram in the  $\text{ZrO}_2$ - $\text{Y}_2\text{O}_3$  system\*. *Russian Journal of Physical Chemistry*. 1987;61(3): 617–622. (In Russ.)

49. Du Y., Jin Z., Huang P. Thermodynamic assessment of the  $\text{ZrO}_2$ - $\text{YO}_{1.5}$  system. *Journal of the American Ceramic Society*. 1991;74(7): 1569–1577. <https://doi.org/10.1111/j.1151-2916.1991.tb07142.x>

50. Jacobson N. S., Liu Z.-K., Kaufman L., Zhang F. Thermodynamic modeling of  $\text{YO}_{1.5}$ - $\text{ZrO}_2$  system. *Journal of the American Ceramic Society*. 2004;87(8): 1559–1566. <https://doi.org/10.1111/j.1551-2916.2004.01559.x>

51. Chen M., Hallstedt B., Gauckler L. J. Thermodynamic modeling of the  $\text{ZrO}_2$ - $\text{YO}_{1.5}$  system. *Solid State Ionics*. 2004;170(3-4): 255–274. <https://doi.org/10.1016/j.ssi.2004.02.017>

52. Tani E., Yoshimura M., Somiya S. Revised phase diagram of the system  $\text{ZrO}_2$ - $\text{CeO}_2$  below 1400 C. *American Ceramic Society*. 1983;66(7): 506–510. <https://doi.org/10.1111/j.1151-2916.1983.tb10591.x>

53. Thomson J. B., Armstrong A. R., Bruce P. G. An oxygen-rich pyrochlore with fluorite composition. *Journal of Solid State Chemistry*. 1999;144(1): 56–62. <https://doi.org/10.1006/jssc.1999.8347>

\*Translated by author of the article.

### Information about the authors

*Pavel P. Fedorov*, Dr. Sci. (Chem.), Full Professor, Chief Researcher, Prokhorov General Physics Institute of the Russian Academy of Sciences (Moscow, Russian Federation).

<https://orcid.org/0000-0002-2918-3926>

[ppfedorov@yandex.ru](mailto:ppfedorov@yandex.ru)

*Elena V. Chernova*, Junior Researcher, Prokhorov General Physics Institute of the Russian Academy of Science (Moscow, Russian Federation).

<https://orcid.org/0000-0001-7401-5019>

[e-chernova@yandex.ru](mailto:e-chernova@yandex.ru)

Received 08.06.2022; approved after reviewing 26.10.2022; accepted for publication 15.11.2022; published online 25.12.2022.

Translated by Marina Strepetova

Edited and proofread by Simon Cox



## Original articles

Research article

<https://doi.org/10.17308/kcmf.2022.24/10559>

## Modelling optical polarization processes on laser modified titanium with a polyvinyl alcohol film

A. V. Tsibulnikova<sup>1</sup>✉, A. A. Khankaev<sup>1</sup>, D. A. Artamonov<sup>1</sup>, I. G. Samusev<sup>1</sup>, V. A. Slezhkin<sup>2</sup>, I. I. Lyatun<sup>1</sup>, V. V. Bryukhanov<sup>1</sup>

<sup>1</sup>Immanuel Kant Baltic Federal University,  
14 A. Nevskogo ul., Kaliningrad 236016, Russian Federation

<sup>2</sup>Kaliningrad State Technical University,  
1 Sovetsky pr., Kaliningrad 236022, Russian Federation

### Abstract

The article presents the results of research of optical spectra of surface plasmon polaritons on laser modified titanium with a deposited micron polymer polyvinyl alcohol (PVA) film.

The metasurface of titanium was created by means of femtosecond laser treatment with  $\lambda = 1.035 \mu$  and the duration  $\tau = 280$  fs with linear and circular radiation polarization. Sets of laser pulses were applied pointwise to the surface with a step of  $100 \mu\text{m}$  with the interval  $t_i = 25\text{--}750$  ms. In the case of linear radiation polarization, tracks of ripple structures with a line density of up to  $N \sim 1,200 \text{ mm}^{-1}$  appeared on the scribed titanium surface. It was found that when titanium is exposed to circular polarization radiation, occasional ablation cavities with lobed circular ripple nano-microstructures appear along the line of beam pulse propagation.

Mathematical modelling of real  $\text{Re}(\epsilon)$  and imaginary  $\text{Im}(\epsilon)$  permittivity established that the spectral parameters in the reflectance spectra of polarized radiation almost fully matched. The analysis of the spectra also established that the maximum absorption was in the IR region due to the presence of a PVA film.

**Keywords:** Plasmon resonance, Laser structuring, Circular polarisation, Metasurface, PVA film

**Funding:** The study received financing within the framework of project No. FZWM-2020-0003 supported by the Ministry of Science and Higher Education.

**For citation:** Tsibulnikova A. V., Khankaev A. A., Artamonov D. A., Samusev I. G., Slezhkin V. A., Lyatun I. I., Bryukhanov V. V. Modelling optical polarization processes on laser modified titanium with a polyvinyl alcohol film. *Condensed Matter and Interphases*. 2022;24(4): 545–558. <https://doi.org/10.17308/kcmf.2022.24/10559>

**Для цитирования:** Цибульникова А. В., Ханкаев А. А., Артамонов Д. А., Самусев И. Г., Слезкин В. А., Лятун И. И., Брюханов В. В. Моделирование оптических поляризационных процессов на лазерно-модифицированном титане с пленкой поливинилового спирта. *Конденсированные среды и межфазные границы*. 2022;24(4): 545–558. <https://doi.org/10.17308/kcmf.2022.24/10559>

✉ Anna V. Tsibulnikova, e-mail: [anna.tsibulnikova@mail.ru](mailto:anna.tsibulnikova@mail.ru)

© Tsibulnikova A. V., Khankaev A. A., Artamonov D. A., Samusev I. G., Slezhkin V. A., Lyatun I. I., Bryukhanov V. V., 2022



## 1. Introduction

Currently, femtosecond laser structuring is one of the most promising ways to modify metal surfaces at the micro and nanoscale in order to provide them with special physical and optical properties [1–3]. The formation of laser induced periodic surface structures (LIPSS) is influenced not only by the parameters of laser radiation (duration, frequency, fluence), but also by the environment in which the radiation interacts with the material [4–6]. There is a great interest in such surfaces which is explained by their unique spectral [5–7], mechanical [5, 8–10], tribological [8, 10, 11], and other physicochemical properties [8, 10–12]. The peculiarities of the creation of LIPSS make it possible to use such metamaterials in various optosensor and biophysics applications [13–17] and also as plasmon transducers of electromagnetic radiation in visible and terahertz regions [18].

It is known that surface plasmons of different mode compositions are generated on micro- and nanostructured rough metal surfaces [18–21]. In addition to the morphological parameters of the structured surface, the generation efficiency of local plasmons on the elements of roughness is greatly influenced by the medium on the surface of the material, in which the electromagnetic wave propagates and exponentially decays in a direction perpendicular to its surface. It is known that the physical reason for the generation of surface plasmons on the metal surface is the presence of an interfacial nanometre film (for example, oxide) on the metal-dielectric interface where the transformation of electromagnetic energy takes place [22, 23]. Some authors also consider layered systems consisting of metal-dielectric compounds and conductive media [24–26]. The localization regions of surface plasmons for such media can be both within the optical range and within the range of infrared frequencies [18, 23, 27]. Thus, changes in the surface morphology by introduced metal-dielectric-metal nanoparticles or resonators leads to the formation of a resonance plasmon spectrum in the IR region [27]. These structural changes mean that many parameters need to be taken into account when modelling plasmon fields and designing plasmon emitters on metasurfaces, which makes this process challenging [28–31]

due to complex processes of radiation interaction and conversion on the surface of the modified material.

When metasurface is created by laser lithography, it is possible to use Pancharatnam–Berry phases of plasmon scattering [30] and create nano-optical elements and devices [32]. Thus, for example, when titanium is exposed to linear polarized femtosecond radiation, linear ablated structures of different geometric sizes shaped as strips consisting of grooves and bumps appear as a result of surface self-organisation [2, 4, 5, 16, 17]. When a metal metasurface is created by circular polarized femtosecond radiation [7, 32–34], there appears a vortex electromagnetic field leading to the formation of rotating ablated arched micro- and nanostructures which melt and solidify. Thus, nonlinear laser lithography allows creating on metal linear and “twisted” structures of different nanoroughness [35–37] with new optical elements.

The key physical problems of this work include: to use laser structuring to create ablated micro- and nanostructures on the surface of titanium by means of linear and circular radiation with a wavelength of 1  $\mu\text{m}$  at different energy levels of high intensity; to record surface plasmons appearing under the influence of radiation on the rough metasurface-dielectric (micron film of polyvinyl alcohol) interface; and to study the features of their optical polarized reflectance spectra.

It should be noted that this work continues a series of works dedicated to plasmon photoprocesses on laser-structured metal surfaces with the participation of dye molecules and biological objects.

## 2. Experimental

The femtosecond laser structuring of the surface of a rolled titanium strip (plate) with a thickness of  $d \sim 0.6$  mm was carried out using a TETA-25 laser system (Avesta, Russia). The laser emission parameters were as follows: the duration of a single pulse was 280 fs with a pulse repetition rate of 25 kHz. The laser operated in pulse decimation mode controlled by Lascos software. The sample (titanium plate) was shifted using a two-axis motorized positioner (Shtanda, Lithuania) controlled by

XILab software. The surface was structured by laser radiation with linear and circular polarization. Circular polarization was achieved by passing the laser beam through a CP1L1064 circular polarizer (Thorlabs, USA) placed on the laser's path between the focusing lens and the flat mirror. The laser output power was measured with an Ophir meter (Nova II, Israel).

### 2.1. Structuring the surface of the titanium plate

Pointwise structuring of the titanium surface was carried out as follows. The sample was placed on the motorised positioner and shifted relative to the position of the laser beam focused on the surface by a system of mirrors and lenses. When the sample was shifted, the angle between the polarization vector of the laser radiation and the direction of the sample movement was 45 degrees. The duration of the radiation exposure for a zone was between 25 and 750 ms. The distance between the centres of the zones was 100  $\mu\text{m}$ , which meant that there were no overlapping zones. The power of laser radiation incident on the sample was  $P = 40 \text{ mW}$ , which was sufficient to overcome the critical value necessary for titanium surface structuring [5].

This structuring method was implemented for two types of laser radiation polarization: linear and circular. Titanium linear structuring was performed at a scanning rate of 500  $\mu\text{m/s}$ .

Polymer PVA films were then coated to the structured titanium surfaces.

The morphology of the titanium surface was examined using a Zeiss Cross Beam-540 (FIB-SEM) electron microscope.

### 2.2. Applying PVA films on the laser-structured surface of titanium

An Ossila Spin Coater (Great Britain) was used to apply PVA films on the structured surfaces of titanium. The sample was spun to the rotation speed of 6,000 rpm, and then a drop of 9% aqueous PVA solution was applied at its centre. Under the action of centrifugal force, the solution evenly distributed over the surface of the sample. The thickness of the obtained film was 750 nm.

### 2.3. Spectral measurements

Permittivity spectra and reflectance spectra of polarized radiation were measured using a

spectral ellipsometer in the wavelength range of 450–1,000 nm (AUTO SE, Horiba-France).

## 3. Results and Discussion

Let us consider the effect of the type of laser radiation polarization on the LIPSS transformation under the changing duration of laser treatment.

### 3.1. Morphology of titanium structures obtained as a result of linear and circular polarization of laser radiation

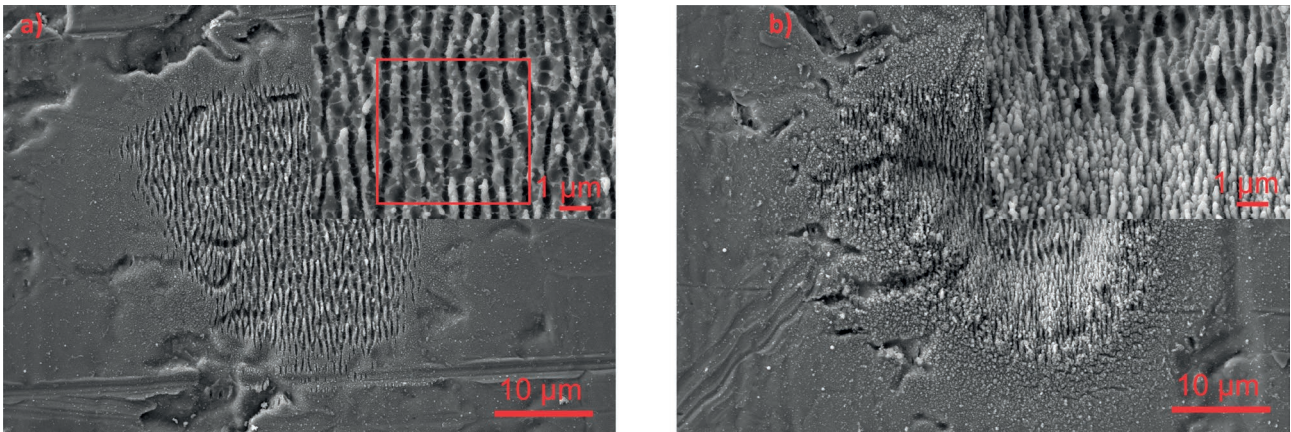
In the first series of experiments, SEM microscopy was used to study the morphological features of the titanium surface after it was exposed to a laser beam with linear and circular polarization of various durations.

Fig. 1 shows SEM scans of the surface after it had been exposed to a set of pulses with linear polarization with the total duration of laser treatment of 25 and 100 ms (Fig. (a) and (b)) and with circular polarization with the duration of laser treatment of 25s, 100, 250 ms, and 750 ms, respectively.

The general physical processes that result in the appearance of laser-modified structures on titanium metasurfaces presented in Fig. 1 have been described in detail in [5]. This work considers these processes in terms of optical wave processes of diffraction and interference that occur on the elements of the material roughness. It also takes into account thermodynamic processes of superfast melting which result in an instantaneous change in the phase of the material [38–41].

After 25 ms of laser treatment (number of pulses  $N_{\text{puls}} = 625$ ), ripple structures with connecting bridges began to form on the surface (Fig. 1a). The interval between such structures was  $\sim 1 \mu\text{m}$ . This corresponded to the wavelength of the laser radiation  $\lambda = 1,035 \text{ nm}$ . The width of such structures corresponded to half of the wavelength and was equal to  $\sim 500 \text{ nm}$ . As the laser beam penetrated deeper into the material (with an increase in the duration of treatment to 100 ms,  $N_{\text{puls}} = 2,500$ ), the initial large ripple structures with a size of 500 nm transformed into smaller/more frequent structures (Fig. 1b, insert) whose width was approximately 4 times smaller. It should be noted that in the case of linear polarization, the  $E$  vector in the incident





**Fig. 1.** SEM images of the titanium surface after femtosecond laser treatment with linear polarization of incident radiation with a total time of treatment of: a) 25 ms; b) 100 ms. Insert (a) shows a sample of ripple structures on the titanium metasurface which can serve as elements of a reflective diffraction grating

wave oscillated parallel to the plane of the sample surface. The formation of parallel ripple structures was also largely determined by the surface polarization (linearly oriented and perpendicular to the surface of the material).

At given values of the energy of laser treatment (with a total time of treatment of 25 ms), studied ripple structures on the titanium metasurface could be considered as elements of a reflective diffraction grating with the main diffraction maxima:  $d \cdot \sin \varphi = k \cdot \lambda$ , duration  $d = 770$  nm at an angle  $\varphi = 30^\circ$  and a line density  $N \sim 1,200$  mm<sup>-1</sup>, and a gloss wavelength of 750 nm. This means that the ripple structures on the titanium metasurface can become good optical elements of reflective diffraction gratings used in integrated nano-optics.

The formation of such titanium metasurface structures can be described as a three-step process under both types of polarisation of incident radiation. Due to the action of an electromagnetic wave with a duration of 280 fs and an energy density in the laser pulse ( $W = 0.17 \cdot 10^9$  W/m<sup>2</sup>) sufficient to melt and evaporate the material during one femto pulse, all the energy absorbed by the material was transmitted to the crystal lattice in several steps (heating of conduction electrons and transfer of heat from electrons to the lattice, electron-phonon interaction) [35, 42–44].

Superfast (less than the duration of 1 pulse) heating of electron gas in the metal accompanied by electron-phonon relaxation led to high-temperature heating of the metal which resulted in the formation of plasma and

instant (superfast) melting (less than 1 ns). The process of continuous melting of titanium lasted for 100 ms and was accompanied by a radial distribution of the material which resembled the effect of drilling followed by stretching of newly formed flat structures towards the centre. This was due to the forces of electromagnetic interaction between the charge density of molten metallic titanium. At the same time, it is known that heating titanium to 600–700 °C results in the formation of a TiO<sub>2</sub> oxide layer. The process of metal oxidation under the influence of laser radiation with a duration of about 1 ns and 1 fs has been well studied [34, 39]. Pulsed high-intensity laser treatment under the influence of radiation  $\lambda = 1.035$  μm, leads to a change in the morphology and phase composition of the oxide film on titanium. Thus, modern studies show [45, 46] that thermally oxidised films of titanium with a thickness of 120 nm are synthesised at a temperature of 600 to 1,000 °C. In this case, the structure of the film turns into rutile and takes the shape of a column and as temperature increases, the phase of the oxide film can change from amorphous to ordered (rutile, anatase). Experimental data show that long-term oxidation at temperatures of 1,000 °C leads to a transition from the parabolic to the linear law of growth of the oxide layer on the surface of titanium accompanied by the formation of pores and cracks in the formed oxide [47]. Also, it should be noted that the electronic processes in the film of titanium oxide in the UV region are caused by transitions in the band gap ( $\lambda \sim 3.6$  eV)

since it is a wide-gap semiconductor material [48]. Along with these slow thermal processes resulting in the formation of titanium oxide film, the material exposed to the femtosecond laser reaches melting and evaporation temperatures of up to 2,000 °C and then cools at a high rate [3], which is followed by the precipitation of the sprayed material. This results in the metasurface roughness and dispersion of nano- and micro-adsorbed titanium nanoparticles with the oxide film. Then, the material oxidizes over a time of about 1 ns and several tens of femtoseconds. This process has been well studied [34–43, 49].

Thus, when titanium was exposed to the femtosecond laser beam, a rough metasurface with precipitated titanium and titanium oxide nanoparticles was formed. Such a surface structure exhibited special spectral and plasmonic properties, which will be described later in this paper.

It should be noted that when the surface of titanium was exposed to laser radiation with circular polarization, the same thermal processes occurred on the surface of titanium and in the material as in the case of linear polarization. However, in the case of circular polarization, the  $E$  vector followed a spiral trajectory [32, 40, 49–51], which caused the induction of electrical dipoles on the lateral extensions of the cone. What is more, the vector of dipole moments parallel to the  $E$  vector was directed to the centre of the symmetry axis of the cone.

Let us consider the spatial distribution of the ablated material on the titanium metasurface under the circular polarisation of radiation (Fig. 2).

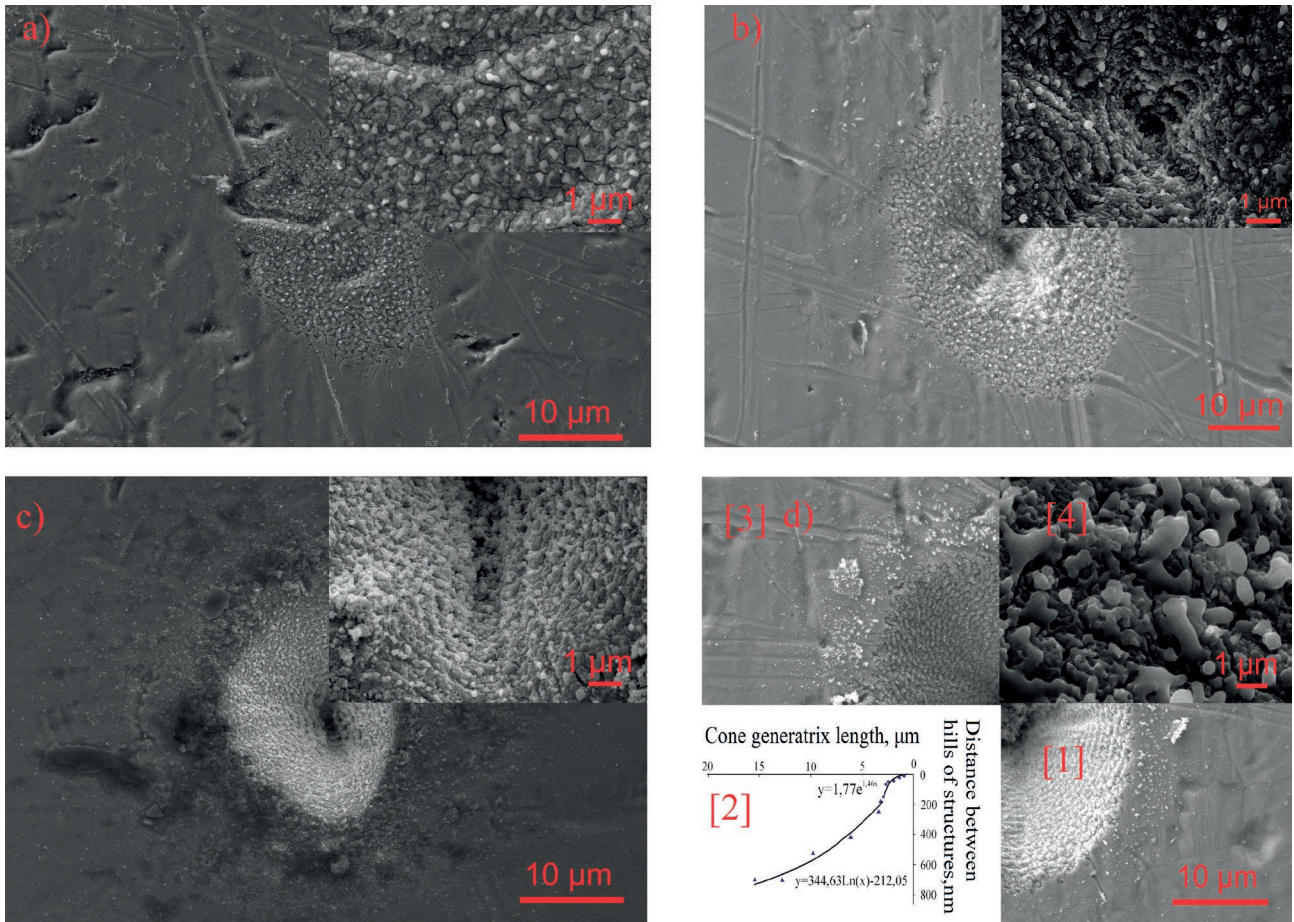
Exposure to laser radiation with a duration of 25 ms resulted in occasional ablation from the surface layer of titanium with a  $\text{TiO}_2$  oxide layer and local cracking of the material (Fig. 2a). It should be noted that the thickness of titanium oxide at ordinary temperature was approximately ~20 nm, which was determined by the ellipsometer resolution (AUTO SE, Horiba-France). It can be seen in the figure that islets of  $\text{TiO}_2$  film with an average size of < 1.0  $\mu\text{m}$  formed on the surface (Fig. 2a, insert). At the same time, there was almost uniform distribution of ablation cavities and metal splashes (light points) on the surface of titanium, which can be due to the uniform

distribution of the photonic field in the laser beam.

With an increase in the number of pulses to 2,500 (100 ms), the laser beam went deeper into the material and the ablated material (titanium and  $\text{TiO}_2$ ) distributed radially in the centre of the beam (insert, right corner of Fig. 2b). The centre of the beam formed deep cavities on the titanium surface and occasional ablated structures of different densities on the periphery. It was evident that with an increase in the energy, the fragmentation of the oxide film and cracking of the oxide layer continued.

Fig. 2d shows the region which was structured by the laser for 750 ms (~18,750 pulses) with circular polarization. As a result, a cone with a base equal to the diameter of the beam (~26  $\mu\text{m}$ ) was formed. From the base to the point of the cone, ablated material had distributed radially on the inner lateral surface of the cavity. An interesting effect was observed: the formation of lobed structures of metallic titanium coated with titanium oxides  $\text{TiO}_2$  (insert, Fig. 2d [4]), which were distributed along the circles, from the base to the centre, perpendicular to the lateral surface. Such structures are sometimes called surface debris.

As the energy density of the laser beam increased, the laser-ablated spot widened (Fig. 2d), however, the pattern remained almost the same. At the same time, in comparison with the ripple structures that appeared during linear laser polarization used to form ablated titanium metasurface, in the case of circular polarization of radiation, the ablated ripple structures (surface ripple of the shock wave) changed at an angle of  $\Delta\alpha \sim 15^\circ$ . The length of each nano-structure was determined by the pulse duration of the set of photons. The number of these structures on the disc of the ablated spot along the circumference and depth of the cavity was estimated (Fig. 2d – [2]). It appeared to be equal to approximately 90,000 units. This is significantly more than the number of laser pulses generated during 750 ms, which can be due to the additional vortex ablation of the material and hydrodynamic processes resulting in the formation of vortex ripple structures located along the radius of the ablation cavity, which was composed of two types of dependencies:



**Fig. 2.** SEM images of the modified titanium surface after femtosecond laser treatment with circular polarisation of incident IR radiation ( $\lambda = 1,036 \text{ nm}$ ) with a total time of treatment of: a) 25 ms; b) 100 ms; c) 250 ms; d) 750 ms. Figure 2d shows the SEM quadrants (1, 2, 3, 4) of an ablation cavity: (1) backlit; (2) graph of the function of the cavity profile; (3) surface; (4) (insertion) lobed ablated structures of  $1 \mu\text{m}$  (surface debris)

$$y = 344.6 \ln(x) - 212.05$$

and

$$y = 1.769e^{1.465x}$$

It can be assumed that the obtained logarithmic dependence reflects the combination of electron-phonon processes ( $t \sim 0.1 \text{ ps}$ ) and thermal processes of melting and evaporation of the material ( $t < 1 \text{ ns}$ ). According to the two-temperature model of titanium ablation used in our experiment, the exponential function can reflect material ablation with a high rate of material release from the cavity (“recast layer”) [35, 39, 41–44].

The obtained results of the study of metal titanium ablation with circular polarisation of radiation showed that the change in the type of polarisation of the incident beam significantly

changes the surface relief at the same power of treatment and with a different duration. Laser pulses with circular polarisation led to the formation of conical cavities with a radial distribution of the material along the lateral surface.

### 3.2. Deposition of a thin PVA film and calculation of its thickness

It was noted above that a nanometre oxide film appeared as a result of the exposure of the structured titanium metasurface to radiation. On the other hand, it is known [41] that all optical plasmon processes are generated in thin metal-dielectric structural films. It was interesting to apply a polymer film on the laser-structured titanium surface and to expose it to femtosecond laser radiation with circular polarisation. The thickness estimate is given below:

$$m_{PVA} = \omega \times m_p; V_{PVA} = \frac{m_{PVA}}{\rho}; \delta = \frac{V}{S}. \tag{1}$$

Where  $m_{PVA}$  is the mass of the PVA solution,  $\omega$  is the molar mass of the substance,  $m_p$  is the mass of the substance,  $V_{PVA}$  is the volume of PVA,  $\rho$  is the density of the substance,  $S$  is the area of the substrate surface, and  $\delta$  is the thickness of the film.

Thus, the thickness of the PVA film on the surface of the structured titanium was  $d \sim 750$  nm.

Optical density  $D$  of the PVA film on the glass is shown in Fig. 3. The ellipsometric method was used to determine the permittivity function of the film in the optical range from 450 to 1,000, which has constant values for functions  $Re(\epsilon) \approx 2.3$  and  $Im(\epsilon) \approx 0.1$ .

### 3.3. Optical properties of Ti LIPSS after the exposure of the PVA film to circularly polarized laser radiation and simulation of spectral functions

#### 3.3.1. Simulation of laser treatment with circular polarisation on the metasurface of titanium with PVA

Fig. 4 shows the optical spectra of the real  $Re(\epsilon)$  and imaginary  $Im(\epsilon)$  permittivity of titanium. The surfaces of titanium were modified in the form of cavities (Fig. 4) by means of laser structuring by sets of femto pulses (Fig. 4) with a duration of 100 ms and with circular polarization. PVA films ( $d \sim 750$  nm) were applied to the surface structured with laser pulses within a square area of  $2.25 \text{ mm}^2: 1.5 \times 1.5$  (Fig. 2b).

The curves in Fig. 4a correspond to the experimental and theoretical spectra of the permittivity function for the surface of structured titanium with PVA.

Let us consider the experimental curves of the permittivity function (solid curves). For example, in the spectrum of the imaginary component, maxima were observed at wavelengths of 500, 660, 780, and 815 nm. These wavelengths were characterised by the absorption of incident radiation by the surface. Let us determine the regions of plasmonic oscillations for a given surface taking into account the experimental permittivity spectrum obtained for a smooth unstructured titanium surface (Fig. 4b). It should be noted that the spectrum obtained for a smooth titanium plate corresponded to the literature

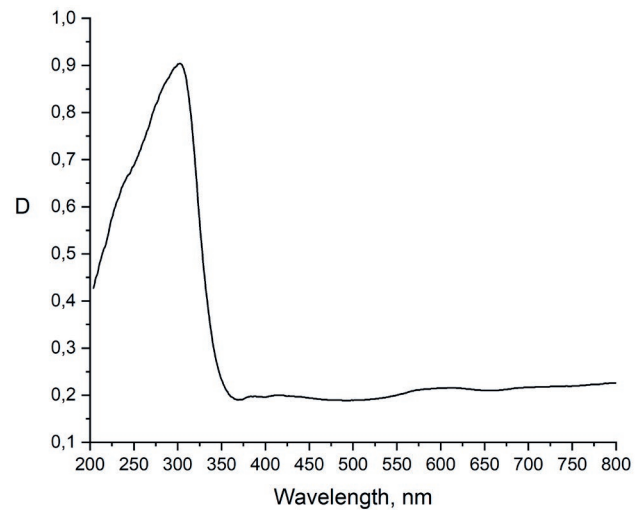


Fig. 3. Spectrum of optical density of a PVA film on silicate glass

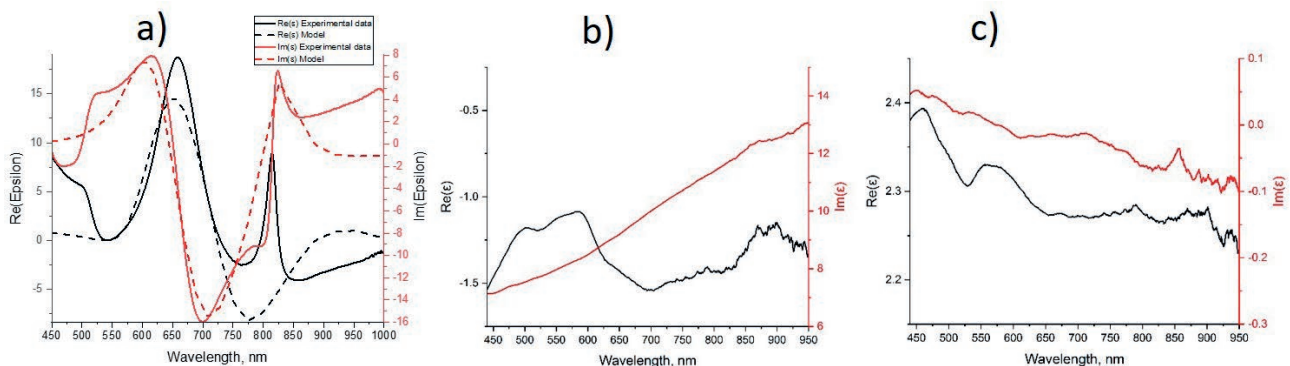


Fig. 4. Spectra of real  $Re(\epsilon)$  and imaginary  $Im(\epsilon)$  permittivity of titanium: (a) solid curve: experimental spectra and dotted curve: simulation for structured titanium with a PVA polymer film; (b) permittivity spectra for a smooth titanium plate; (c) permittivity spectra for a smooth titanium plate with a polymer PVA film

data presented in works [35, 47, 52] and the spectral distribution of functions confirmed to the classical Drude model for a free electron gas. For example, since maxima were present in the spectrum of negative  $\text{Re}(\epsilon)$  permittivity component within the range of 450–700 nm, the region of possible generation of surface plasmons could be located at wavelengths of 500 nm and 600 nm. However, the range of positive values for  $\text{Im}(\epsilon)$  (Fig. 4a) corresponded to 450–650 nm and 800–1,000 nm at these wavelengths  $\text{Re}(\epsilon) \sim 0$  (450–650 nm) and  $\text{Re}(\epsilon) < 0$  (800–1000 nm). Therefore, it can be argued that on the studied surface prepared by means of circular polarization of laser radiation, in the presence of a polymer film surface plasmons appear in the region of 500 and 600 nm. It should be noted that the unstructured titanium surface had no maxima of this kind in the presence of a polymer film and the functions of  $\epsilon$  remained almost constant over the entire wavelength range of 450–1,000 nm (Fig. 4c). This means plasmonic oscillations are generated and propagated over the rough surface (at 500 and 600 nm) on the structure of a metal-dielectric with a thin PVA polymer film [35, 41, 44–48, 50–53].

Let us consider the low-frequency range with the maximum of the imaginary component within the region of 800 nm (Fig. 4a). For example, resonance at this wavelength may be due to volume plasmon oscillations. Here it is necessary to add that this spectrum was quite narrow with a half-width of  $\Delta\lambda \sim 20$  nm, which may indicate high-volume and fast ( $\tau \sim 1\text{--}2$  fs) electronic processes in the metal. It should be noted that in the case of smooth titanium (Fig. 4b), there were no such maxima in the spectrum at this wavelength due to the complete screening of the incident radiation by free electrons.

To determine the contribution of various types of electrons (free and bonded) to the spectral composition of functions, curves  $\text{Re}(\epsilon)$  and  $\text{Im}(\epsilon)$

were simulated by means of ellipsometry. The Drude-Lorentz dispersion model was used to simulate the optical functions of the structured titanium surface with a thin-film polymer coating.

This dispersion model is a combination of the Lorentz and Drude models and it takes into account the contributions of both types of electrons [44–48, 50–54]:

$$\tilde{\epsilon}(\omega) = \epsilon_\infty + \frac{\omega_p^2}{-\omega^2 + i\Gamma_d\omega} + \frac{(\epsilon_s - \epsilon_\infty)c_i^2}{\omega_i^2 - \omega^2 + i\Gamma_0\omega} + \sum_{j=1}^2 \frac{f_j\omega_{0j}^2}{\omega_{0j}^2 - \omega^2 + i\gamma_j\omega}, \tag{1}$$

where  $\epsilon_\infty$  is high-frequency permittivity;  $\epsilon_s$  is the difference between  $\epsilon_s$  and  $\epsilon_\infty$  which determines the force of the Lorentz oscillator;  $\omega_i$  is the resonance frequency of the oscillator, whose energy corresponds to the absorption peak;  $\Gamma_0$  is the attenuation coefficient of the Drude oscillator ;  $f_j$  is the force of the oscillator;  $\omega_{0j}$  is resonance frequency; and  $\gamma_j$  is the spread-out parameter. Where  $\omega$  is plasma frequency corresponding to the position of the photon energy at  $\epsilon(\omega) = 0$ ; and  $\Gamma_d$  is the value of the resonance plasmon oscillator ( $0.4 < \Gamma_d < 4$ ).

The parameters of the dispersion model are given in Table 1.

The spectra simulation was carried out at 121 points on a structured titanium surface with an area of  $1.5 \times 1.5$  mm<sup>2</sup> in the presence of a polymer film. The average spectrum shown in Fig. 4a with dotted curves agrees well with the experimental spectra. Some differences between the value of the oscillator force  $f_1 = -4,308$  and the theoretical value of  $f_1^{\text{theor}} < 1.0$  in the Drude-Lorentz model can be due to the presence of a PVA polymer film whose dielectric properties can have a considerable influence in the blue region of the spectrum.

It should be noted that when the combined Drude-Lorentz model was used, the plasma

**Table 1.** Parameters of the dispersion model

$\epsilon_\infty$	$\epsilon_s$	$\omega_p$ , eV ( $\lambda$ , nm)	$\omega_p'$ , eV ( $\lambda$ , nm)	$\Gamma_0$	$\Gamma_d$	$f_1$	$\omega_{0,1}$ , eV ( $\lambda$ , nm)	$\gamma_1$	$f_2$	$\omega_{0,2}$ , eV ( $\lambda$ , nm)	$\gamma_2$
1.304	1.986	1.530 (784)	1.009 (1189)	0.224	7.995	-4.308	1.988 (603)	0.666	2.881	2.110 (569)	0.519

Note: Pearson correlation coefficient  $\chi^2$  for modelling is  $\chi^2 = 0.000073$  and indicates the possibility of using this model to calculate experimental functions.

frequency of oscillations in the region of 600 nm ( $\omega = 2.023$ ) manifested as the oscillator frequency with an oscillator force of 0.104 and an attenuation factor of 0.666. This model is of some interest and can be considered as an energy-efficient characteristic of the obtained surface with a given geometry of surface structures and a dielectric film of a certain thickness. The resonance frequency in the region of 580 nm also corresponded to plasmon oscillations, however, the attenuation factor decreased to 0.519.

At the same time, the simulation allowed us to determine the average value (calculated from the 121st measurement) of the thickness of the polymer coating and to use the experimental data to draw a conclusion about the continuity of the film applied to the structured titanium surface.

This research is essential for a variety of applications. For example, ellipsometry allowed establishing that the average thickness of the polymer coating was  $(710 \pm 20)$  nm, which almost coincided with the pre-calculated thickness of the PVA film (750 nm).

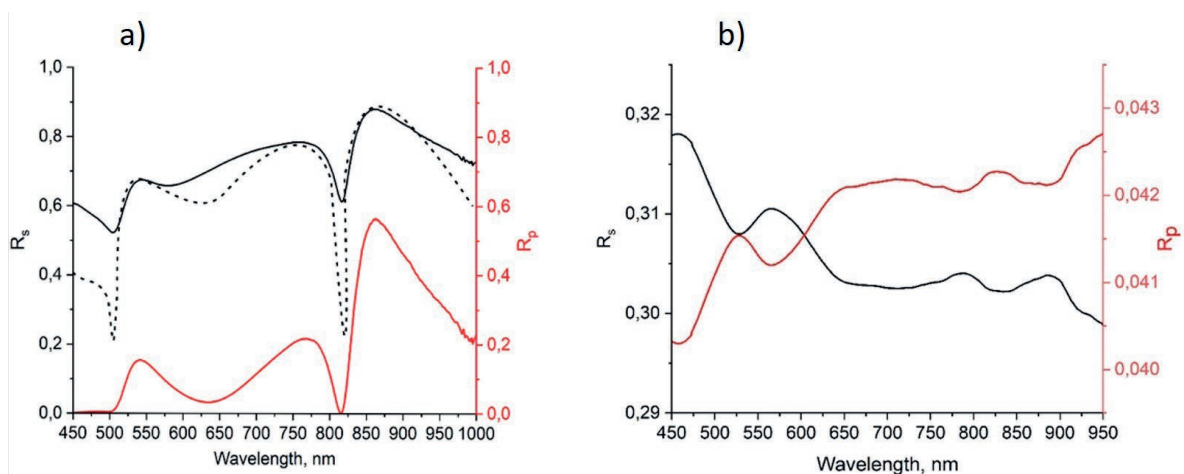
The results of the simulation are as follows: it was established that the spectra of surface and volume plasmons at  $\lambda = 600$  and 800 nm, respectively, can be described within the framework of the proposed model. It should be noted that the experimental spectrum  $\text{Re}(\epsilon)$  (Fig. 4a, red solid curve) had a narrow absorption maximum in the region of 815 nm due to the

absorption of the PVA film. It can be assumed that this maximum appeared as a result of dipole-dipole processes of energy absorption in the PVA film, which was also observed on the smooth surface of titanium with PVA (Fig. 4c, red solid curve). During simulation, this maximum shifted to the IR region and was a wide spectrum with a half-width of  $\sim 200$  nm. The obtained spectral difference can be explained by the fact that when modelling functions, it is difficult to take into account the physical and chemical parameters of the polymer coating (molecular structure, solubility of polymer globules). However, film thickness and optical density were taken into account.

### 3.3.2. Reflectance coefficients of *s*- and *p*-polarized light from the metasurface of titanium with PVA

It was of interest to study the optical reflectance spectra of linearly polarized laser radiation from the metasurface of titanium with a PVA film (Fig. 5) pre-treated with circularly polarized laser radiation within the range of 450–1,000 nm.

The reflectance coefficients of *s*- and *p*-polarized radiation of the structured titanium surface are shown in Fig. 5a. It was shown that these functions had their minima in the region of 450–500 nm and 815 nm. These wavelengths coincided with the regions shown in Fig. 4a, which



**Fig. 5.** (a) Reflectance coefficients of *s*- and *p*-polarised light from the structured surface with a PVA film (solid curves) and the reflectance spectrum of *s*-polarised light obtained by simulation according to formula (1), with a PVA film (black dotted curve). (b) Reflectance coefficients of *s*- and *p*-polarised light from unstructured surface with a PVA film (solid curves)

confirms the hypothesis about the generation of surface plasmons in this wavelength range. At the same time, it was  $p$ -polarized radiation that contributed more since it was absorbed more than  $s$ -component. This indicates that for  $p$ -polarized light, the difference between the values of the reflectance coefficients in their local minima is close to zero, and at these points the surface is almost mirror. What is more, for  $s$ -polarised radiation, the reflectance coefficients from the surface had rather large values of 0.52 and 0.58 for wavelengths of 500 and 815 nm, respectively. It should be noted that the spectral analysis shown in Fig. 4a and Fig. 5a revealed more significant differences in the position of the spectral maxima in the red region of the visible range at wavelengths of 650–850 nm. This may be due to the polarizing properties of the polymer film, which requires additional optical experiments to estimate the optical density of the PVA film based on its thickness.

In the case of reflection of  $s$ -polarized radiation, the simulation of the reflection processes of the titanium metasurface was performed according to the Fresnel equations [45, 48, 49]:

$$R_s^F = |r_s^F|^2, r_s^F = \frac{\left(\frac{\omega^2}{c^2}\varepsilon_1 - k_{\parallel}^2\right)^{1/2} - \left(\frac{\omega^2}{c^2}\varepsilon_2 - k_{\parallel}^2\right)^{1/2}}{\left(\frac{\omega^2}{c^2}\varepsilon_1 - k_{\parallel}^2\right)^{1/2} + \left(\frac{\omega^2}{c^2}\varepsilon_2 - k_{\parallel}^2\right)^{1/2}},$$

$$P_{SP} = k_{\parallel}^2 = \frac{\omega^2}{c^2} \frac{\varepsilon_1 \varepsilon_2}{\varepsilon_1 + \varepsilon_2}.$$

Where  $\varepsilon_1, \varepsilon_2$  is the permittivity of the metal and the plasmon propagation medium, respectively,  $\omega$  is the frequency of external radiation,  $c$  is the speed of light; and  $k_{\parallel}$  is the wave vector of plasmons.

The results of comparing experimental and modelling reflectance coefficients according to the above mentioned formulas are shown in Fig. 5a. It is obvious that experimental and theoretical data have extremes at the same wavelengths. However, it is worth noting that the values of the reflectance coefficients in their minimums do not coincide. Thus, it was shown that the minima model value of the reflectance coefficient of  $s$ -polarized light was  $\sim 0.2$  while

according to the experimental data the reflectance coefficient had a value of  $\sim 0.5$ .

It should be noted that the reflectance coefficients of  $s$ - and  $p$ -polarized radiation reflected from the unstructured titanium surface (smooth titanium, Fig. 5b) with a PVA film significantly differed in values in the wavelength range of 450–1,000 nm and were equal to  $R_s = 0.33$  and  $R_p = 0.04$ .

#### 4. Conclusions

Smooth titanium plates were structured by femtosecond laser treatment with linear and circular polarization with a wavelength of  $\lambda = 1.035 \mu\text{m}$  and a total time of treatment of:  $t_i = 25, 100, 250,$  and  $750$  ms and the duration of  $\tau = 280$  fs. This resulted in occasional ablation of the material and the formation of cavities  $< 1.0 \mu\text{m}$  in size and a repeated layer with surface ripples caused by the shock wave.

Spectral permittivity functions during plasmon generation were simulated for the titanium metasurface with a PVA film (750 nm thick).

When titanium plates were exposed to laser radiation with circular polarisation and different energy, ripple structures and cavities appeared following a completely different optical pattern. Thus, for example, exposure to a circular field resulted in the formation of cone-shaped loped cavities and circular ripple nano- and microstructures along the line of action of laser beam pulses.

The functions (logarithmic and exponential) of laser ablation of the material and their dependence on energy were studied along the lateral surface of cavities formed as a result of electron-phononic and thermal processes associated with laser treatment. When modelling plasmonic processes on the metasurface of titanium with PVA, it was established that spectral parameters almost fully matched with small offsets of spectra maxima of the real  $\text{Re}(\varepsilon)$  and imaginary  $\text{Im}(\varepsilon)$  permittivities. What is more, spectral shifts of less than  $< 20$  nm were mostly associated with the presence of a polymer PVA film on the titanium metasurface. Plasmonic processes of reflection of polarised light with  $R_s$  and  $R_p$  components from the titanium metasurface

after it was treated with circular radiation were modelled. It was found that the amplitude of the  $R_p$  polarized radiation was significantly smaller than that of the  $R_s$  component and at some points on the surface its spectral values were close to zero. It should be noted that the reflectance coefficients of  $R_s$  and  $R_p$  polarized radiation reflected from the unstructured titanium surface (smooth titanium) with a PVA film differed significantly in values within the wavelength range of 450–1,000 nm and were equal to  $R_s = 0.33$  and  $R_p = 0.04$ .

At the same time, it was established that linear-polarized radiation during a pointwise scanning of the titanium surface with a step of 100  $\mu\text{m}$  can be used to create ripple structures with a line density of  $N \sim 1,200 \text{ mm}^{-1}$  and a gloss wavelength of the reflected radiation of 750 nm, which can be of great practical importance in the field of creating diffractive elements in integrated optics.

#### Author contributions

Conceptualisation: V. Bryukhanov; methodology: V. Slezhkin; software: A. Khankaev; formal analysis: V. Slezhkin; research: A. Khankaev and D. Artamonov; writing the article, preparation of the initial project: V. Bryukhanov; review: A. Tsibulnikova; visualisation: I. Lyatun and A. Khankaev; management: V. Bryukhanov; administration and financing of the project: I. Samusev.

#### Conflict of interests

The authors declare that they have no known competing financial interests or personal relationships that could have influenced the work reported in this paper.

#### References

1. Yu X., Zhang Q., Qi D., Tang S., Dai S., Zhang P., Xu Y., Shen X. Femtosecond laser-induced large area of periodic structures on chalcogenide glass via twice laser direct-writing scanning process. *Optics & Laser Technology*. 2020;124: 105977. <https://doi.org/10.1016/j.optlastec.2019.105977>
2. Messaddeq S. H., Vallée R., Soucy P., Bernier M., El-Amraoui M., Messaddeq Y. Self-organized periodic structures on Ge-S based chalcogenide glass induced by femtosecond laser irradiation. *Optics Express*. 2012;20(28): 29882–29889. <https://doi.org/10.1364/OE.20.029882>
3. Lim H. U., Kang J., Guo C., Hwang T. Y. Femtosecond laser-induced dual periodic structures on Ni. *Frontiers in Optics*. 2017. Washington, D.C.: OSA; 2017. <https://doi.org/10.1364/FIO.2017.JTu3A.41>
4. Simões J. G. A. B., Riva R., Miyakawa W. High-speed laser-induced periodic surface structures (LIPSS) generation on stainless steel surface using a nanosecond pulsed laser. *Surface and Coatings Technology*. 2018;344: 423–32. <https://doi.org/10.1016/j.surfcoat.2018.03.052>
5. Bonse J, Kirner S V., Krüger J. Laser-induced periodic surface structures (LIPSS). In: *Handbook of laser micro- and nano-engineering*. Springer Nature; 2020. pp. 1–59. [https://doi.org/10.1007/978-3-319-69537-2\\_17-2](https://doi.org/10.1007/978-3-319-69537-2_17-2)
6. Lorenz P., Zagoranskiy I., Ehrhardt M., Zimmer K. P. Laser-induced large area sub- $\mu\text{m}$  and nanostructuring of dielectric surfaces and thin metal layer. In: *Proc. SPIE 10906, Laser-based Micro- and Nanoprocessing XIII, 109060T, 4 March 2019*. <https://doi.org/10.1117/12.2510206>
7. Silvennoinen M., Hasoň S., Silvennoinen R. Optical resonance on LIPSS sensed by polarized light. In: *Proc. SPIE 9066, Eleventh International Conference on Correlation Optics, 90660X, 17 December 2013*. <https://doi.org/10.1117/12.2047104>
8. Rathmann L., Beste L. H., Radel T. Laser based process chain to use LIPSS on forming tools. *Surface and Coatings Technology*. 2021;426: 127761. <https://doi.org/10.1016/j.surfcoat.2021.127761>
9. Romano J. M., Garcia-Girón A., Penchev P., Dimov S. S. Durability and wear resistance of LIPSS. In: *Proc. Volume 11674, Laser-based Micro- and Nanoprocessing XV; 116740N*. 2021. p. 19. <https://doi.org/10.1117/12.2584010>
10. Karkantonis T., Gaddam A., See T. L., Joshi S. S., Dimov S. Femtosecond laser-induced sub-micron and multi-scale topographies for durable lubricant impregnated surfaces for food packaging applications. *Surface and Coatings Technology* 2020;399: 126166. <https://doi.org/10.1016/j.surfcoat.2020.126166>
11. Gazizova M. Y., Smirnov N. A., Kudryashov S. I., ... Prokopenko N. A. Correlation of the tribological properties of LIPSS on TiN surface with 3D parameters of roughness. *IOP Conference Series: Materials Science and Engineering*. 2021;1014(1): 012014. <https://doi.org/10.1088/1757-899X/1014/1/012014>
12. Exir H., Weck A. Mechanism of superhydrophilic to superhydrophobic transition of femtosecond laser-induced periodic surface structures on titanium. *Surface and Coatings Technology* 2019;378: 124931. <https://doi.org/10.1016/j.surfcoat.2019.124931>
13. Orazi L., Pelaccia R., Mishchenko O., Reggiani B., Pogorielov M. Fast LIPSS based texturing process of dental implants with complex geometries.



*CIRP Annals*. 2020;69(1): 233–236. <https://doi.org/10.1016/j.cirp.2020.04.065>

14. Orazi L., Pogorielov M., Deineka V., ... Reggiani B. Osteoblast cell response to LIPSS-modified Ti-implants. *Key Engineering Materials*. 2019;813: 322–327. <https://doi.org/10.4028/www.scientific.net/KEM.813.322>

15. Khorkov K. S., Kochuev D. A., Dzus M. A., Prokoshchev V. G. Wettability surface control on stainless steel by LIPSS formation. *Journal of Physics: Conference Series*. 2021;1822(1): 012010. <https://doi.org/10.1088/1742-6596/1822/1/012010>

16. Zyubin A., Kon I., Tcibulnikova A., ... Demin M. Numerical FDTD-based simulations and Raman experiments of femtosecond LIPSS. *Optics Express*. 2021;29(3): 4547–4558. <https://doi.org/10.1364/oe.413460>

17. Vorobyev A. Y., Guo C. Femtosecond laser nanostructuring of metals. *Optics Express*. 2006;14(6): 2164. <https://doi.org/10.1364/OE.14.002164>

18. Zhang W., Cue N., Yoo K. M. Emission linewidth of laser action in random gain media. *Optics Letters*. 1995;20(9): 961. <https://doi.org/10.1364/OL.20.000961>

19. Drachev V. P., Chettiar U. K., Kildishev A. V., Yuan H.-K., Cai W., Shalaev V. M. The Ag dielectric function in plasmonic metamaterials. *Optics Express*. 2008;16: 1186–1195. <https://doi.org/10.1364/OE.16.001186>

20. De Sio L., Placido T., Comparelli R., ... Bunninge T. J. Next-generation thermo-plasmonic technologies and plasmonic nanoparticles in optoelectronics. *Progress in Quantum Electronics*. 2015;41: 23–70. <https://doi.org/10.1016/j.pquantelec.2015.03.001>

21. Chauhan M., Kumar Singh V. Review on recent experimental SPR/LSPR based fiber optic analyte sensors. *Optical Fiber Technology*. 2021;64. <https://doi.org/10.1016/j.yofte.2021.102580>

22. Misra S., Zhang D., Qi Z., ... Wang H. Morphology control of self-assembled three-phase Au-BaTiO<sub>3</sub>-ZnO hybrid metamaterial for tunable optical properties. *Crystal Growth and Design*. 2020;20(9): 6101–8. <https://doi.org/10.1021/acs.cgd.0c00801>

23. Jia X., Wang X. Optical fishnet metamaterial with negative, zero, positive refractive index and nearly perfect absorption behavior at different frequencies. *Optik*. 2019;182: 464–468. <https://doi.org/10.1016/j.ijleo.2019.01.066>

24. Kim J., Han K., Hahn J. W. Selective dual-band metamaterial perfect absorber for infrared stealth technology. *Scientific Reports*. 2017;7(1): 6740. <https://doi.org/10.1038/s41598-017-06749-0>

25. Pralle M. U., Moelders N., McNeal M. P., Puscasu I., Greenwald A. C., Daly J. T., Johnson E. A. Photonic crystal enhanced narrow-band infrared emitters. *Applied Physics Letters*. 2002;81(25): 4685–4687. <https://doi.org/10.1063/1.1526919>

26. Sikdar D., Pendry J. B., Kornyshev A. A. Nanoparticle meta-grid for enhanced light extraction from light-emitting devices. *Light: Science and Applications*. 2020;9(1): 1–11. <http://dx.doi.org/10.1038/s41377-020-00357-w>

27. Naik G. V., Kim J., Boltasseva A. Oxides and nitrides as alternative plasmonic materials in the optical range. *Optical Materials Express*. 2011;1(6): 1090. <https://doi.org/10.1364/OME.1.001090>

28. Sakurai A., Bo Z., Zhang Z. Prediction of the resonance condition of metamaterial emitters and absorbers using LC circuit model. In: *International Heat Transfer Conference 15, August, 10-15, 2014, Kyoto, Japan*. 2014. pp. 7067–7076. <https://doi.org/10.1615/IHTC15.rad.009012>

29. Wei D., Hu C., Chen M., ... Xie C. Optical modulator based on the coupling effect of different surface plasmon modes excited on the metasurface. *Optical Materials Express*. 2020;10(1): 105–118. <https://doi.org/10.1364/ome.382116>

30. Tao H., Bingham C. M., Strikwerda A. C., ... Averitt R. D. Highly flexible wide angle of incidence terahertz metamaterial absorber: Design, fabrication, and characterization. *Physical Review B – Condensed Matter and Materials Physics*. 2008;78: 241103. <https://doi.org/10.1103/PhysRevB.78.241103>

31. Alves F., Kearney B., Grbovic D., Karunasiri G. Narrowband terahertz emitters using metamaterial films. *Optics Express*. 2012;20(19): 21025–21032. <https://doi.org/10.1364/OE.20.021025>

32. Lazzini G., Romoli L., Tantussi F., Fuso F. Nanostructure patterns on stainless-steel upon ultrafast laser ablation with circular polarization. *Optics and Laser Technology*. 2018;107: 435–442. <https://doi.org/10.1016/j.optlastec.2018.06.023>

33. Khorasaninejad M., Chen W. T., Devlin R. C., Oh J., Zhu A. Y., Capasso F. Metalenses at visible wavelengths: Diffraction-limited focusing and sub-wavelength resolution imaging. *Science*. 2016;352(6290): 1190–1194. <https://doi.org/10.1126/science.aaf6644>

34. Öktem B., Pavlov I., Ilday S., Kalaycıoğlu H., Rybak A., Yavaş S., Erdoğan M., Ömer F. Nonlinear laser lithography for indefinitely large-area nanostructuring with femtosecond pulses. *Nature Photonics*. 2013;7(11): 897–901. <https://doi.org/10.1038/nphoton.2013.272>

35. Dostovalov A. V., Korolkov V. P., Babin S. A. Formation of thermochemical laser-induced periodic surface structures on Ti films by a femtosecond IR Gaussian beam: regimes, limiting factors, and optical properties. *Applied Physics B: Lasers and Optics*. 2017;123: 30. <https://doi.org/10.1007/s00340-016-6600-z>

36. Emmony D. C., Howson R. P., Willis L. J. Laser mirror damage in germanium at 10.6 μm. *Applied*

*Physics Letters*. 1973;23(11): 598–600. <https://doi.org/10.1063/1.1654761>

37. Sipe J. E., Young J. F., Preston J. S., van Driel H. M. Laser-induced periodic surface structure. I. Theory. *Physical Review B*. 1983;27(2): 1141–1154. <https://doi.org/10.1103/PhysRevB.27.1141>

38. Maier S. A. *Plasmonics: fundamentals and applications*. New York: Springer; 2007. <https://doi.org/10.1007/0-387-37825-1>

Klimov V. V. *Nanoplasmonics\**. Moscow: Physmathlit Publ.; 2009. 115 p. (In Russ.)

40. Inouye H., Tanaka K., Tanahashi I., Hirao K. Ultrafast dynamics of nonequilibrium electrons in a gold nanoparticle system. *Physical Review B*. 1998;57: 11334–11340. <https://doi.org/10.1103/PhysRevB.57.11334>

41. Grua P., Morreeuw P., Bercegol H., Jonusauskas G., Vallée F. Electron kinetics and emission for metal nanoparticles exposed to intense laser pulses. *Physical Review B – Condensed Matter and Materials Physics*. 2003;68(12): 035424. <https://doi.org/10.1103/PhysRevB.68.035424>

42. Agranovich V. M., Mills D. L. *Modern problems in condensed matter sciences*. Amsterdam: North-Holland Publishing Company; 1982. pp. 3–717. <https://doi.org/10.1016/B978-0-444-86165-8.50001-3>

43. Brodskii A. M., M. I. Urbakh. Optics of rough surfaces of metals. *Sov. Phys. JETP*. 1985;62(2): 391–399. Available at: [http://jetp.ras.ru/cgi-bin/dn/e\\_062\\_02\\_0391.pdf](http://jetp.ras.ru/cgi-bin/dn/e_062_02_0391.pdf)

44. Anisimov S. I., Luk'yanchuk B. S. Selected problems of laser ablation theory. *Physics-Uspekhi* 2002;45(3): 293–324. <https://doi.org/10.1070/PU2002v045n03ABEH000966>

45. Gerasimenko Yu. V., Logacheva V. A., Khoviv A. M. Synthesis and properties of titanium dioxide thin films. *Condensed Matter and Interphases*. 2010;12(2): 113–118. (In Russ., abstract in Eng.). Available at: <https://www.elibrary.ru/item.asp?id=15176043>

46. Hou Y. Q., Zhuang D. M., Zhang G., Zhao M., Wu M. S. Influence of annealing temperature on the properties of titanium oxide thin film. *Applied Surface Science*. 2003;218(1–4): 98–106. [https://doi.org/10.1016/S0169-4332\(03\)00569-5](https://doi.org/10.1016/S0169-4332(03)00569-5)

47. Makarov E. S., Kuznetsov M. L. The crystal structure and chemical character of lower oxides of titanium TiO<sub>0–0.48</sub>. *Journal of Structural Chemistry*. 1960;1: 156–162. <https://doi.org/10.1007/BF00738933>

48. Chibisov A. N., Bizyuk A. O. Electronic structure of titanium dioxide nanoparticles\*. *Vestnik Amurskogo gosudarstvennogo universiteta*. 2008;(43): 22–23. (In Russ.). Available at: <https://www.elibrary.ru/item.asp?id=19007690>

49. *Surface enhanced raman scattering*. R. Chang, T. Furtak (eds.). New York and London: Springer; 1982. <https://doi.org/10.1007/978-1-4615-9257-0>

50. Gräf S., Müller F. A. Polarisation-dependent generation of fs-laser induced periodic surface structures. *Applied Surface Science*. 2015;331: 150–155. <https://doi.org/10.1016/j.apsusc.2015.01.056>

51. Kang M., Chen J., Wang X. L., Wang H. T. Twisted vector field from an inhomogeneous and anisotropic metamaterial. *Journal of the Optical Society of America B*. 2012;29(4): 572–576. <https://doi.org/10.1364/JOSAB.29.000572>

52. Bäuerle D. *Laser processing and chemistry*. Berlin, Heidelberg: Springer Berlin Heidelberg; 1996. 279 p. <https://doi.org/10.1007/978-3-662-03253-4>

53. Ford G. W., Weber W. H. Electromagnetic interactions of molecules with metal surfaces. *Physics Reports*. 1984;113(4): 195–287. [https://doi.org/10.1016/0370-1573\(84\)90098-X](https://doi.org/10.1016/0370-1573(84)90098-X)

54. Rosenberg H. M. *The solid state : an introduction to the physics of solids for students of physics, materials science, and engineering*. Oxford University Press; 1992. 315 p.

### Информация об авторах

Anna V. Tsibulnikova, Cand. Sci. (Phys.–Math.), Senior Researcher of REC “Fundamental and applied photonics. Nanophotonics”, Immanuel Kant Baltic Federal University (Kaliningrad, Russian Federation).

<https://orcid.org/0000-0001-8578-0701>  
anna.tsibulnikova@mail.ru

Artemii A. Khankaev, postgraduate student, technician of REC “Fundamental and applied photonics. Nanophotonics”, Immanuel Kant Baltic Federal University (Kaliningrad, Russian Federation).

<https://orcid.org/0000-0003-0661-5228>  
akhankaev@gmail.com

Dmitry A. Artamonov, postgraduate student, technician of REC “Fundamental and applied photonics. Nanophotonics”, Immanuel Kant Baltic Federal University (Kaliningrad, Russian Federation).

euroset2016ig98@icloud.com

Ilya G. Samusev, Cand. Sci. (Phys.–Math.), Deputy Vice-Rector for Research, Head of R&D Department, Director of REC “Fundamental and applied photonics. Nanophotonics”, Immanuel Kant Baltic Federal University (Kaliningrad, Russian Federation).

<https://orcid.org/0000-0001-5026-7510>  
is.cranz@gmail.com

*Vasily A. Slezhkin*, Cand. Sci. (Chem.), Associate Professor, Kaliningrad State Technical University (Kaliningrad, Russian Federation).

<https://orcid.org/0000-0002-2801-7029>  
vasiliy.slezhkin@kltu.ru

*Ivan I. Lyatun*, Researcher, Laboratory of X-ray Coherent Optics, Immanuel Kant Baltic Federal University (Kaliningrad, Russian Federation).

<https://orcid.org/0000-0002-4988-8077>  
Ilyatun@kantiana.ru

*Valery V. Bryukhanov*, Dr. Sci. (Phys.–Math.), Leading Researcher, Research Center “Fundamental and Applied Photonics. Nanophotonics”, Immanuel Kant Baltic Federal University (Kaliningrad, Russian Federation).

<https://orcid.org/0000-0003-4689-7207>  
bryukhanov\_v.v@mail.ru

*Received 24.04.2022; approved after reviewing 17.08.2022; accepted for publication 15.09.2022; published online 25.12.2022.*

*Translated by Irina Charychanskaya  
Edited and proofread by Simon Cox*



## Original articles

Research article

<https://doi.org/10.17308/kcmf.2022.24/10560>

## Growth kinetics of anodic oxide layers on cobalt silicides in sulphuric acid solutions

A. B. Shein✉, V. I. Kichigin

Perm State National Research University,  
15 Bukireva ul., Perm 614990, Russian Federation

### Abstract

The aim of this research was to study the growth kinetics of anodic oxide films on cobalt silicides in sulphuric acid solutions under potentiostatic conditions with various pretreatment of the electrode surface. For the study, we used low and high silicon silicides ( $\text{Co}_2\text{Si}$  and  $\text{CoSi}_2$ ) in 0.05 and 0.5 M  $\text{H}_2\text{SO}_4$ .

We obtained the chronoamperograms in the time interval  $t = 0.3\text{--}3000$  s with the oxide formation potentials of  $E_f = 0.2, 0.5, \text{ and } 1.0$  V (SHE). It was determined that the kinetics of the growth of oxide layers on cobalt silicides in acidic solutions greatly depends on the method of the silicide surface pretreatment (mechanical polishing; cathodic pre-polarisation in a  $\text{H}_2\text{SO}_4$  solution; exposure to  $\text{H}_2\text{SO}_4$  solution at the open circuit potential; exposure in a 2 M KOH solution; and exposure to 2% HF solution). In most cases, at low  $t$  (up to 30–50 s), the oxide films grew due to the ion migration in the strong electric field generated in the film during anodic polarisation.

In some cases ( $\text{Co}_2\text{Si}$  silicide with higher cobalt content; pretreatment of  $\text{Co}_2\text{Si}$  in alkaline solution, further enriching the silicide surface with cobalt; and the region of high values of  $t$ ), the point defect model seemed to be executed.

**Keywords:** Cobalt silicide, Passivity, Oxide film, Growth kinetics, High field model, Point defect model

**Acknowledgements:** The research was supported by Perm Scientific and Educational Centre “Rational use of mineral resources”, 2022.

**For citation:** Shein A. B., Kichigin V. I. Growth kinetics of anodic oxide layers on cobalt silicides in sulphuric acid solutions. *Condensed Matter and Interphases*. 2022;24(4): 559–571. <https://doi.org/10.17308/kcmf.2022.24/10560>

**Для цитирования:** Шейн А.Б., Кичигин В.И. Кинетика роста анодных оксидных слоев на силицидах кобальта в растворах серной кислоты. *Конденсированные среды и межфазные границы*. 2022;24(4): 559–571. <https://doi.org/10.17308/kcmf.2022.24/10560>

✉ Anatoly B. Shein, e-mail: [ashein@psu.ru](mailto:ashein@psu.ru)

© Shein A. B., Kichigin V. I., 2022



## 1. Introduction

One of the most important characteristics of the corrosion and electrochemical behaviour of metals and alloys is the tendency for anodic passivation [1]. The passivity phenomenon is of great practical importance, because the formation of the passivating oxide films makes many materials highly resistant to corrosion in media where oxide layers are difficult to dissolve. In this regard, various aspects of anodic passivity are extensively studied, including the kinetics of the nucleation and growth of anodic oxide films (AOF).

The high corrosion resistance of transition metal silicides [2–10] is also attributed to the formation of dense passive films. The composition of oxide films on the transition metal silicides depends primarily on the silicide composition [5], the electrode potential [3], and pH of the solution [3]. When the silicon content in the silicide increases, the composition of the oxide film approaches that of  $\text{SiO}_2$  [3, 4, and 11]. According to [12], on Fe-Si alloys (at  $\geq 21$  at.% of Si), the outer part of the oxide film in a solution at pH 9 contains only Fe, and at pH 5 it contains about 50 at.% of Fe. In other words, the Fe content in the oxide layer decreases as the pH decreases. In strongly acidic solutions, almost pure protective  $\text{SiO}_2$  is formed and Fe is dissolved.

In research [13], the results of the study of anodic oxide layers on FeSi, CoSi, and NiSi monosilicides in a 0.5 M  $\text{H}_2\text{SO}_4$  solution were presented. Linear dependences of the layer thickness on the electrode potential  $E$  in the range of 0.5–1.1 V (SHE) were obtained. The calculated values of the specific electrical resistance of the oxide films demonstrated that the anodic oxide may contain small amounts of metal. Cyclic voltammetry showed that after the initiation of anodic polarisation, the metal atoms preferentially dissolved, i.e., silicon accumulated on the electrode surface. This is a precondition for the formation of oxide films with high barrier properties.

The growth patterns of the AOF on alloys are more complex than on pure metals [14–18]. This also applies to metal-silicon alloys. While some data on the composition of oxide films on transition metal silicides is available, the kinetics of the AOF growth on these materials has not been

studied. The purpose of this research was to study the kinetics of the formation of anodic oxides on  $\text{Co}_2\text{Si}$  and  $\text{CoSi}_2$  cobalt silicides in sulphuric acid solutions under potentiostatic conditions upon different pretreatment of the electrode surface.

## 2. Experimental

In this study, we used  $\text{Co}_2\text{Si}$  and  $\text{CoSi}_2$  cobalt silicides obtained by the Czochralski method. To study the AOF growth, the electrode surface must be unoxidised before the potential step is applied [19]. Therefore, we used various methods to ensure an active surface at the beginning of the experiment by removing the oxides formed due to the contact of the silicide with the air. When choosing these methods, we took into account possible chemical processes involving cobalt and silicon oxides, which may occur on the silicide surface. Differences in the state of the surface of the silicides resulting from different pretreatment methods are evident at the nucleation stage of the oxide phase, when the anode potential is applied. They affect the growth of the AOF and, consequently, the anodic current as a function of time.

The following electrode surface pretreatment methods were used:

1) Polishing with abrasive paper (finishing by P4000 paper), cleaning with ethyl alcohol, and rinsing in the working solution. Mechanical surface conditioning also preceded the other pretreatment methods.

2) Cathodic activation (1 mA/cm<sup>2</sup>, 20 min). Cathodic oxide reduction is often used (e.g., [14, 20]) to remove oxide films from the electrode surface. We also used this method. Though, in the case of cobalt silicides, cathodic activation may be ineffective, because anodic oxide films on  $\text{Co}_2\text{Si}$  are hard to reduce. On  $\text{CoSi}_2$ , cathodic reduction of anodic oxides barely takes place [21].

3) Exposure to 0.5 M  $\text{H}_2\text{SO}_4$  at an open circuit potential,  $E_{oc}$ , for 30 min. This treatment has almost no effect on the silica component of the oxide, but can affect cobalt oxides.

4) Exposure to 2% HF at  $E_{oc}$  for 5 min, rinsing in deionised water and in working solution. HF is known to dissolve  $\text{SiO}_2$  effectively [22], but it has almost no effect on silicon (it may dissolve one monolayer of silicon atoms) [23]. A 2% HF solution can also remove the cobalt component

of the oxide. This type of pretreatment probably provides the most oxide-free electrode surface.

As a variation of this pretreatment, we also used a 10 min exposure to 0.5 M H<sub>2</sub>SO<sub>4</sub> + 0.05 M HF at  $E_{oc}$ . It was assumed that HF would dissolve SiO<sub>2</sub> and the presence of sulphuric acid would lead to a faster dissolution of the cobalt oxides.

5) Exposure in 2 M KOH at  $E_{oc}$  for 40 min, rinsing (neutralisation) in the working solution, and transfer to the electrochemical cell with or without the electrode exposure at  $E_{oc}$ . In alkaline solutions, both silicon and silicon oxide dissolve [24], the silicide surface is enriched with a metallic component [2]. The exposure time was chosen in view of the results obtained in [25]. The study showed that the self-activation of Co<sub>2</sub>Si electrode in 2 M KOH occurs in about 2000 s (~33 min). The treatment in a KOH solution does not affect the cobalt oxides (if they are present

in the oxide film). The cobalt oxide may partially dissolve after transferring the electrode to a cell with a sulphuric acid solution.

The measurements were carried out at room temperature (22–25 °C) in non-deaerated solutions of 0.5 M H<sub>2</sub>SO<sub>4</sub> and 0.05 M H<sub>2</sub>SO<sub>4</sub> prepared from a chemically pure reagent and deionised water (Millipore). We used the following measurement procedure: the potential was changed from  $E_{oc}$  of the electrode, pretreated by one of the above methods, to a given value of  $E_f$  (in the range of 0.2–1.0 V, all potentials are provided for standard hydrogen electrode) for 50 minutes. The  $I, t$  curve ( $I$  is the current,  $t$  is the time) was recorded. The  $E_{oc}$  values for each of the silicides varied only slightly depending on the electrode pretreatment method (Tables 1, 2). Therefore, the value of  $E_f - E_{oc}$  at a given  $E_f$  was also approximately the same for different

**Table 1.** The values of  $d \lg i / d \lg t$  for Co<sub>2</sub>Si passivation in H<sub>2</sub>SO<sub>4</sub> solutions

Pretreatment of electrode surface	Concentration of H <sub>2</sub> SO <sub>4</sub> , M	$E_{oc}$ , V	$E_p$ , V	$d \lg i / d \lg t$	Time interval, s
Mechanical polishing	0.05	-0.266	0.5	-0.86	< 200
Mechanical polishing	0.05	-0.266	1.0	-0.80	< 200
Mechanical polishing	0.5	-0.232	0.5	-0.61 -0.92	1–10 50–2000
Mechanical polishing	0.5	-0.232	1.0	-0.70	< 10
30 min in 0.5 M H <sub>2</sub> SO <sub>4</sub> at $E_{oc}$	0.5	-0.225	1.0	-1.0 -0.84	5–30 100–3000
Cathodic polarization	0.5	-0.233	1.0	-0.71 -0.94	< 10 30–1000
Treatment in 2% HF	0.05	-0.270	1.0	-0.94 -0.86	1–10 500–1000
Treatment in 2% HF	0.5	-0.235	0.2	-0.76 -0.85	1–100 200–1000
Treatment in 2% HF	0.5	-0.235	0.5	-0.65 -1.2	1–30 500–3000
Treatment in 2% HF	0.5	-0.235	1.0	-0.78 -1.4	0.3–20 > 1250
Treatment in 0.5 M H <sub>2</sub> SO <sub>4</sub> + 0.05 M HF, 10 min	0.5	-0.233	0.5	-0.77	5–100
Treatment in 0.5 M H <sub>2</sub> SO <sub>4</sub> + 0.05 M HF, 10 min	0.5	-0.235	1.0	-0.87	1–220
Treatment in 2 M KOH	0.05	-0.278	1.0	-0.57 -0.91	3–15 30–1000
Treatment in 2 M KOH	0.5	-0.223	0.5	-0.66	1–10
Treatment in 2 M KOH	0.5	-0.223	1.0	-0.64 -0.84	< 2 30–1000
Treatment in 2 M KOH, 30 min in 0.5 M H <sub>2</sub> SO <sub>4</sub> at $E_{oc}$	0.5	-0.21	1.0	-0.77 -0.89	< 2 10–1000

**Table 2.** The values of  $d \lg i / d \lg t$  for  $\text{CoSi}_2$  passivation in  $\text{H}_2\text{SO}_4$  solutions

Pretreatment of electrode surface	Concentration of $\text{H}_2\text{SO}_4$ , M	$E_{oc}$ , V	$E_p$ , V	$d \lg i / d \lg t$	Time interval, s
Mechanical polishing	0.5	+0.12	1.0	-0.87	2–20
Treatment in 2 M KOH	0.5	-0.09	1.0	-0.67	< 10
				-0.78	10–100
				-0.84	100–1000
Treatment in 2 M KOH	0.5	-0.09	0.5	-0.64	1–10
				-0.86	100–1000
Treatment in 2% HF	0.5	-0.10	1.0	-0.83	< 10
Treatment in 2% HF	0.5	-0.10	0.5	-1.4	200–450
				-0.72	< 10
Treatment in 2% HF	0.5	-0.10	0.2	-0.98	200–500
				-0.50	10–50
Treatment in 2% HF	0.05	-0.145	1.0	-1.0	200–1000
				-0.88	1–5
				-0.71	60–200
				-1.1	300–1000

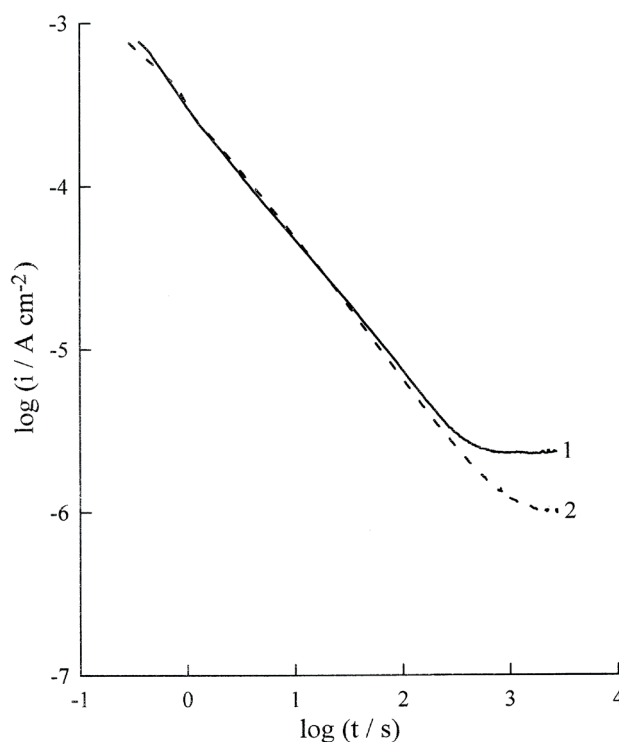
types of surface treatment. The measurements were taken with a Solartron 1287 potentiostat (Solartron Analytical). The data collection rate was 5 points per second.

### 3. Results and discussion

In some cases, the  $\lg i, \lg t$  dependences had a simple form of a single linear section (with a negative slope slightly less than 1) with the current density reaching a steady-state value at high  $t$  (Fig. 1). However, in most cases, chronoamperograms had a more complex shape with several linear sections, inflection points, etc. (Fig. 2). The values of the  $d \lg i / d \lg t$  slopes for the  $\text{Co}_2\text{Si}$  electrode are provided in Table 1.

Preliminary cathodic polarisation of the  $\text{Co}_2\text{Si}$  electrode in 0.5 M  $\text{H}_2\text{SO}_4$  had very little effect on the  $i, t$ -curves (Fig. 2). The current density slightly increased, while the shape of  $\lg i, \lg t$ -dependence did not change. Pre-exposure of the electrode in a 2 M KOH solution had a more prominent effect (Fig. 2). At short passivation time (up to  $t \sim 50$  s), the shapes of the  $\lg i, \lg t$ -curves depend on the pretreatment of the electrode surface. The lowest values of the current density were observed when the electrode was washed in deionised water and transferred to the measuring cell after exposure in a KOH solution. Higher current densities were observed when the electrode was washed in a 0.5 M  $\text{H}_2\text{SO}_4$  solution after exposure in a KOH solution (in this case, the alkaline solution remaining on the electrode was quickly neutralised) and then

transferred to the measuring cell. Even higher current densities were observed when, after exposure to a KOH solution and neutralisation in 0.5 M  $\text{H}_2\text{SO}_4$ , the electrode was kept for 30 min at the open circuit potential in a cell with a working solution of 0.5 M  $\text{H}_2\text{SO}_4$ . The increase in  $i$  at low  $t$  in the latter case was probably not



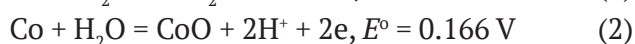
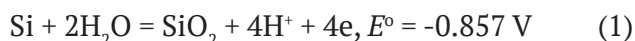
**Fig. 1.** Chronoamperograms of the  $\text{Co}_2\text{Si}$  electrode in 0.05 M  $\text{H}_2\text{SO}_4$ . 1 –  $E_f = 1.0$  V, 2 –  $E_f = 0.5$  V. Pretreated by mechanical polishing

due to an increase in the true surface area (since at large values of  $t$ , the current densities were approximately the same both with exposure at  $E_{oc}$  and without it), but to a more complete dissolution of cobalt oxides on the electrode surface due to its exposure at  $E_{oc}$ . Exposure of the  $Co_2Si$  electrode at the open circuit potential to the working solution without pretreatment in a KOH solution resulted in lower current densities.

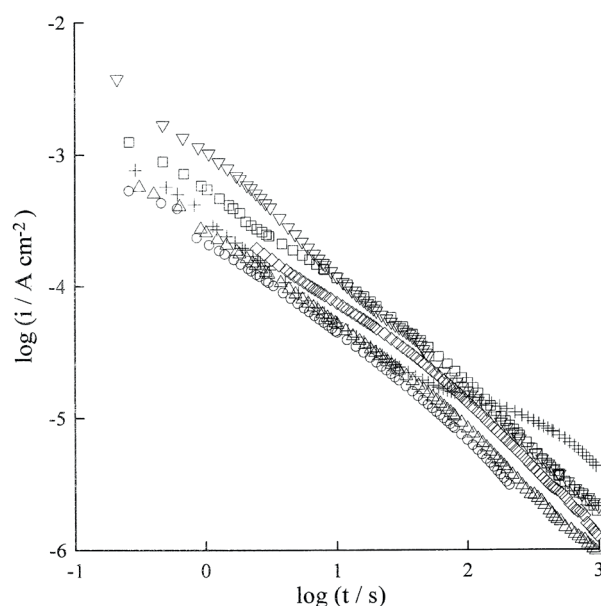
The chronoamperograms for the  $CoSi_2$  electrode in logarithmic scale were also similar to the linear dependences (Fig. 3). As in the case of  $Co_2Si$ , lower current densities were observed for the electrode with mechanically polished surface. The values of the  $d \lg i / d \lg t$  slopes for  $CoSi_2$  are provided in Table 2. At the same pretreatment of the electrode, the values of  $d \lg i / d \lg t$  for  $CoSi_2$  were slightly greater than for  $Co_2Si$  (at least at low  $t$ ).

A characteristic feature of the passivation of cobalt silicides is an inflection on the  $\lg i, \lg t$ -curve at  $t = 30\text{--}100$  s, when the surface was pretreated with 2% HF (Fig. 4, 5). The inflection was less prominent for the  $CoSi_2$  electrode than for the  $Co_2Si$  electrode. Upon the transition from  $Co_2Si$  to  $CoSi_2$ , the value of  $t_{ip}$  decreased noticeably, while  $i_{ip}$  changed less ( $t_{ip}$  and  $i_{ip}$  are the coordinates of the inflection point). The inflection section became longer with an increase in  $E_f$ . In the case of  $CoSi_2$ , the influence of  $E_f$  on the inflection point coordinates was more pronounced than in the case of  $Co_2Si$ . When the concentration of sulphuric acid decreased at the same  $E_f$ , the value of  $t_{ip}$  decreased slightly, and  $i_{ip}$  increased. The values of  $t_{ip}$  and  $i_{ip}$  are provided in Table 3. After the inflection, the  $d \lg i / d \lg t$  slope becomes steeper.

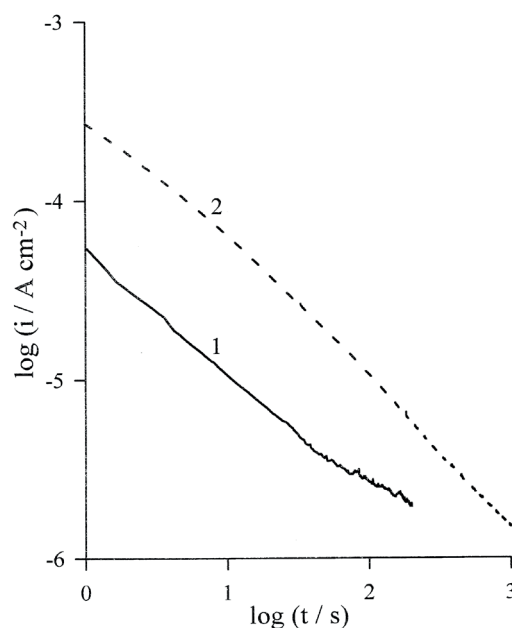
The formation of oxide films on cobalt silicides can be associated with the following overall reactions (in the studied potential range up to 1 V)



The standard potentials for the reactions were taken from [26]. Reactions (1) and (2) directly describe the oxidation of silicide components, while reaction (3) describes a possible transformation in cobalt oxide.

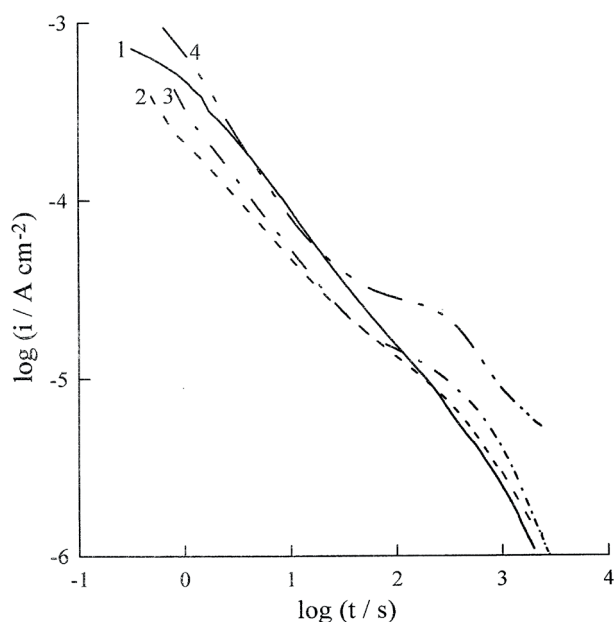


**Fig. 2.** Chronoamperograms of the  $Co_2Si$  electrode in 0.5 M  $H_2SO_4$  at  $E_f = 1.0$  V for different types of the electrode surface pretreatment: (○) – mechanical polishing; (△) – cathodic pre-polarisation of the electrode; (◇) – exposure of the electrode to 2 M KOH, washing in the deionised water; (□) – exposure of the electrode to 2 M KOH, washing (neutralisation) in 0.5 M  $H_2SO_4$ ; (▽) – exposure of the electrode to 2 M KOH, washing (neutralisation) in 0.5 M  $H_2SO_4$ , exposure to 0.5 M  $H_2SO_4$  for 30 min at  $E_{oc}$ ; and (+) – etching in 2% HF

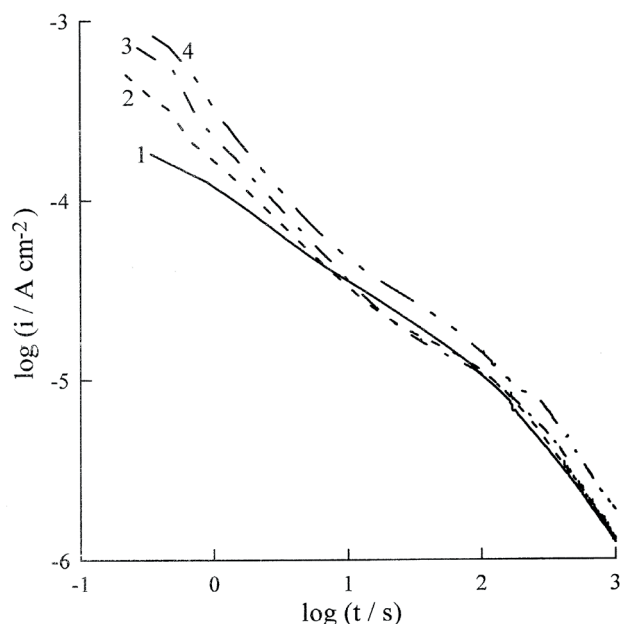


**Fig. 3.** Chronoamperograms of the  $CoSi_2$  electrode in 0.5 M  $H_2SO_4$  at  $E_f = 1.0$  V. 1 – mechanical polishing; 2 – exposure to 2 M KOH for 45 min





**Fig. 4.** Chronoamperograms of the  $\text{Co}_2\text{Si}$  electrode in  $0.5 \text{ M H}_2\text{SO}_4$  (1–3) or  $0.05 \text{ M H}_2\text{SO}_4$  (4). The surface was pretreated in 2% HF. Potential  $E_p$ , V: 1 – 0.2; 2 – 0.5; and 3, 4 – 1.0



**Fig. 5.** Chronoamperograms of the  $\text{CoSi}_2$  electrode in  $0.5 \text{ M H}_2\text{SO}_4$  (1–3) or  $0.05 \text{ M H}_2\text{SO}_4$  (4). The surface was pretreated in 2% HF. Potential  $E_p$ , V: 1 – 0.2; 2 – 0.5; 3, 4 – 1.0

**Table 3.** Inflection point coordinates (pretreatment with 2% HF)

Silicide	$C_{\text{H}_2\text{SO}_4}$ , M	$E_p$ , V	$\lg t_n$	$\lg i_n$
$\text{Co}_2\text{Si}$	0.05	1.0	1.95	-4.53
	0.5	0.2	1.93	-4.73
	0.5	0.5	1.94	-4.73
	0.5	1.0	2.03	-4.83
$\text{CoSi}_2$	0.05	1.0	1.39	-4.50
	0.5	0.2	1.34	-4.62
	0.5	0.5	1.63	-4.80
	0.5	1.0	1.74	-4.87

To describe the kinetics of anodic passivation, different models were proposed: the high electric field model [27, 28], point defect model [20, 29–31], generalised oxide growth model [32], and mass-charge balance model [33]. The brief review of the models is provided in [32, 34]. The high field model (HFM) and the point defect model (PDM) can be considered as the key models of the AOF growth, they have been tested on a large number of systems.

The high electric field model describes the movement of ions through interstitial positions in an oxide film by a thermally activated hopping mechanism. Due to this mechanism, a moving ion crosses a certain potential barrier that depends

on the electric field in the film. According to the HFM, the rate-determining stage of the oxide film growth is the migration of ions in the oxide or the injection of cations into the oxide at the metal/oxide interface. According to the model, the electric field strength during the oxide growth is very high ( $> 1 \text{ MV/cm}$ ). The film growth results in a decrease of the electric field strength in the film (under potentiostatic conditions), and hence in a decrease of the anodic current density. The HFM leads to the approximate fulfilment of the logarithmic growth law or the inverse logarithmic law [27].

According to the point defect model, the ion current in the AOF is carried by nonequilibrium anion and cation vacancies which are generated at the metal/oxide and oxide/electrolyte interfaces. The value of the electric field in the oxide film can be much lower than that in the HFM [28]. It is assumed that the electric field is independent (or little dependent) on the film thickness and electrode potential (this is the main difference between the PDM and HFM). The model takes into account the potential drops at the metal/film  $\phi_{m/f}$  and film/solution  $\phi_{f/s}$  interfaces, and  $\phi_{f/s}$  is the linear function of the applied potential and the pH of the solution. It also takes into account the chemical dissolution of the oxide. The PDM

provides a logarithmic law of the oxide layer growth.

To distinguish between the mechanisms determining the passivation kinetics of silicides, the diagnostic criteria proposed in [20] can be used. When the current densities  $i(t)$  are much higher than the steady-state current density, the dependence of  $F(i) = (-i')^{1/2}/i$  on  $\ln i$  is plotted, where  $i' = di/dt$  is the derivative of the current density with respect to time. If the value of  $(-i')^{1/2}/i$  is constant, the data are consistent with the point defect model. If  $(-i')^{1/2}/i$  increases linearly with  $\ln i$ , the high field model of film growth is applicable. When the current densities become comparable with the steady-state current density  $i_s$ , the dependence of  $[-i'/i(i - i_s)]^{1/2}$  on  $\ln i$  should be considered [20].

The theoretical expression for  $(-i')^{1/2}/i$  in the case of the high electric field model is presented as [20]:

$$\frac{\sqrt{-(di/dt)}}{i} = \frac{1}{zF} \sqrt{\frac{RTV_m}{aV}} (\ln i - \ln A) \quad (4)$$

where  $A = 2FaC_M v \exp(-W/RT)$ ,  $2a$  is the ion jump distance,  $C_M$  is the concentration of interstitial ions in the oxide film,  $v$  is the ion vibration frequency,  $W$  is the activation energy at zero field,  $z$  is the ion charge,  $V$  is the potential drop in the film, and  $V_m$  is the molar volume of the oxide.

The theoretical expression for  $(-i')^{1/2}/i$  in the case of the point defect model is presented as [20]:

$$\frac{\sqrt{-(di/dt)}}{i} = \sqrt{\frac{\alpha_2 \varepsilon V_m}{RT}} \quad (5)$$

where  $\alpha_2$  is the transfer coefficient for the oxygen vacancy generation reaction at the metal/oxide interface,  $\varepsilon = V/L$  is the electric field strength in the oxide film, and  $L$  is the film thickness.

Examples of the dependence of  $F(i) = (-i')^{1/2}/i$  on  $\ln i$  are shown in Fig. 6, 7. The derivative at the  $k^{\text{th}}$  point of the data set was calculated by the formula:  $-i'_k = (i_{k-1} - i_{k+1}) / (t_{k+1} - t_{k-1})$ . As can be seen, in many cases, linear dependence is executed. So, it can be assumed that in these cases, the anodic oxide film grows on the studied silicides in  $H_2SO_4$  solutions by the mechanism of ion migration in a high electric field. In general, linear dependences of  $(-i')^{1/2}/i$  on  $\ln i$  are well executed for low values of time and correspondingly lesser

thickness of the oxide films. This is in agreement with the general conclusion that the high field model should work better for very thin films [32], because in such films the electric field strength is the highest.

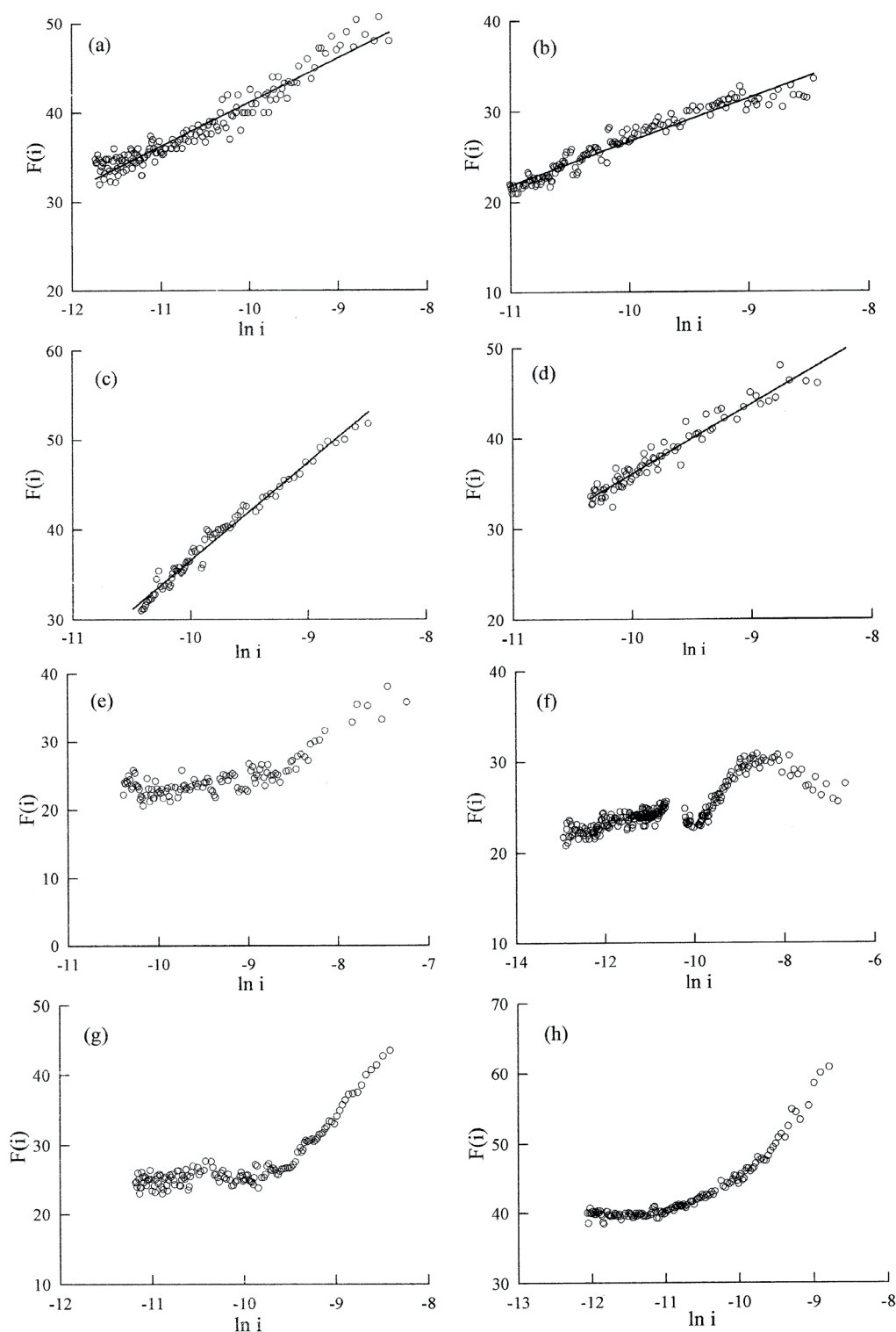
Within the HFM, the expression for the slope of the  $\lg i, \lg t$ -dependence was obtained [35]:

$$-\frac{d \ln i}{d \ln t} = -\frac{d \lg i}{d \lg t} = \frac{\ln(i/A)}{2 + \ln(i/A)} \quad (6)$$

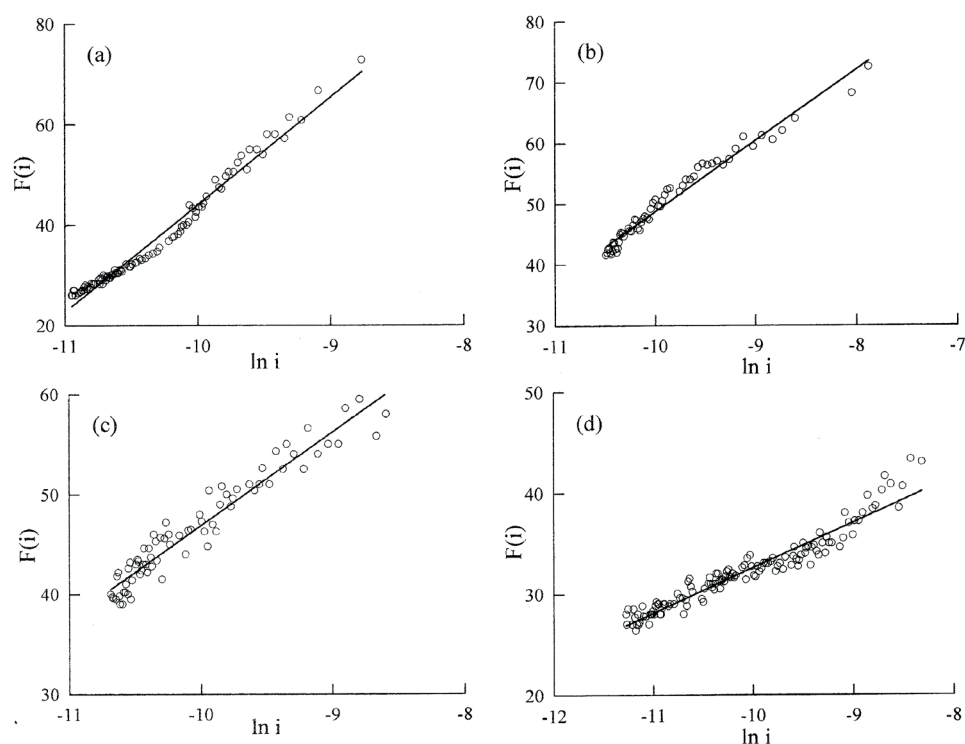
The implications of equation (6) are: 1) the slope of  $-d \lg i / d \lg t$  is always less than 1 and it can vary over a wide range; 2) the dependence of  $\lg i$  on  $\lg t$  is not strictly linear, but at significant values of  $\ln(i/A)$  and a relatively small time interval the curvature of the chronoamperogram is almost imperceptible. The experimental data (Fig. 1–5, Tables 1, 2) are consistent with (6), at least at low values of  $t$ .

The experimental values of the slopes of the dependences of  $(-i')^{1/2}/i$  on  $\ln i$  are provided in Tables 4, 5. According to (4), the theoretical slope of the dependence of  $(-i')^{1/2}/i$  on  $\ln i$  within the framework of the HFM is  $(1/zF)(RTV_m/aV)^{1/2}$ . The values of  $V_m$  and  $a$  for those oxides which can grow on silicides can only be estimated approximately because: a) the properties of very thin oxide films may differ from those of bulk oxides [19]; b) the exact composition of the oxide film growing on a silicide is not known. There is also an uncertainty regarding the value of  $V$ , as the set electrode potential  $E_p$  generally does not coincide with the potential drop on the oxide film.

For cobalt oxide  $CoO$ , we calculated  $V_m = 11.64 \text{ cm}^3/\text{mol}$  from the molecular weight and density. From the crystallographic data, we obtained the jump distance of the interstitial ions of 0.21 nm. Therefore, the theoretical slope of the dependence of  $(-i')^{1/2}/i$  on  $\ln i$  for  $CoO$  at  $V = 1 \text{ V}$  is  $8.6 (\text{C}/\text{cm}^2)^{-1/2}$ . For silica, the molar volume is  $27.27 \text{ cm}^3/\text{mol}$  [36]. The value of  $2a$  is close to the length of the  $Si-O$  bond [37], i.e., it is about 0.16 nm. So, the theoretical slope for  $SiO_2$  at  $V = 1 \text{ V}$  is  $7.53 (\text{C}/\text{cm}^2)^{-1/2}$  at  $z = 4$ . Therefore, the theoretical slopes for the considered oxides vary insignificantly, and at  $V = 1 \text{ V}$  they are in the range  $7.5-8.6 (\text{C}/\text{cm}^2)^{-1/2}$ . These values are in satisfactory agreement with the results in Tables 4, 5, although in some cases there are noticeable discrepancies. Some of them are



**Fig. 6.** Dependence of  $F(i)$  on  $\ln i$  for: a:  $\text{Co}_2\text{Si}/0.05 \text{ M H}_2\text{SO}_4$ ,  $E_f = 1.0 \text{ V}$ , the electrode pretreated by mechanical polishing; b:  $\text{Co}_2\text{Si}/0.5 \text{ M H}_2\text{SO}_4$ ,  $E_f = 0.2 \text{ V}$ , pretreatment in 2% HF; c:  $\text{Co}_2\text{Si}/0.5 \text{ M H}_2\text{SO}_4$ ,  $E_f = 0.5 \text{ V}$ , pretreatment in 2% HF; d:  $\text{Co}_2\text{Si}/0.5 \text{ M H}_2\text{SO}_4$ ,  $E_f = 1.0 \text{ V}$ , pretreatment in 2% HF; e:  $\text{Co}_2\text{Si}/0.5 \text{ M H}_2\text{SO}_4$ ,  $E_f = 1.0 \text{ V}$ ; pretreatment in 2 M KOH; f:  $\text{Co}_2\text{Si}/0.5 \text{ M H}_2\text{SO}_4$ ,  $E_f = 1.0 \text{ V}$ ; pretreatment in 2 M KOH followed by 30 min at the open circuit potential; g:  $\text{Co}_2\text{Si}/0.05 \text{ M H}_2\text{SO}_4$ ,  $E_f = 1 \text{ V}$ ; pretreatment in 2 M KOH; and h:  $\text{Co}_2\text{Si}/0.5 \text{ M H}_2\text{SO}_4$ ,  $E_f = 0.5 \text{ V}$ , pretreated by mechanical polishing. The density of the current  $i$  is expressed in  $\text{A}/\text{cm}^2$ , the value of  $F(i)$  is in  $(\text{C}/\text{cm}^2)^{-1/2}$



**Fig. 7.** Dependence of  $F(i)$  on  $\ln i$  for  $\text{CoSi}_2/0.5 \text{ M H}_2\text{SO}_4$ : a:  $E_f = 0.2 \text{ V}$ , pretreatment in 2% HF; b:  $E_f = 0.5 \text{ V}$ , pretreatment in 2% HF; c:  $E_f = 1.0 \text{ V}$ , pretreatment in 2% HF; and d:  $E_f = 1.0 \text{ V}$ , pretreatment in 2 M KOH. The density of the current  $i$  is expressed in  $\text{A}/\text{cm}^2$ , the value of  $F(i)$  is in  $(\text{C}/\text{cm}^2)^{-1/2}$

**Table 4.** The values of the slopes of the dependences of  $(-di/dt)^{1/2}/i$  on  $\ln i$  for the  $\text{Co}_2\text{Si}$  electrode

Pretreatment of electrode surface	Concentration of $\text{H}_2\text{SO}_4$ , $\text{mol L}^{-1}$	$E_p$ , V	Slope of $(-di/dt)^{1/2}/i$ vs. $\ln i$ plot, $(\text{C cm}^{-2})^{-1/2}$	Time interval, s
Mechanical polishing	0.05	1.0	5.0	1.5–90
Mechanical polishing	0.5	1.0	5.4	
Mechanical polishing	0.5	0.5	11.5	0.5–8
			~0	> 20
Cathodic polarization	0.5	1.0	6.4	
Treatment in 2% HF	0.5	0.2	6.2	10–100
Treatment in 2% HF	0.5	0.5	10.7	< 20
Treatment in 2% HF	0.5	1.0	6.9	1.2–20
Treatment in 2 M KOH	0.05	1.0	15.0	1.5–10
			~0	> 15
Treatment in 2 M KOH	0.5	1.0	Weak dependence	> 2
Treatment in 2 M KOH, 30 min in 0.5 M $\text{H}_2\text{SO}_4$ at $E_{oc}$	0.5	1.0	Complex weak dependence	

explained by the fact that  $V$  is different from 1 V.

The slope  $(1/zF)(RTV_m/aV)^{1/2}$  should increase as the potential drop in the oxide film decreases (upon the same electrode pretreatment). This was well achieved for the  $\text{CoSi}_2$  electrode in 0.5 M  $\text{H}_2\text{SO}_4$ , pretreated in 2% HF. The slope increased from 9.5 to 24.5 as  $E_f$  decreased from 1.0 to 0.2 V (Table 5). In the case of the  $\text{Co}_2\text{Si}$  electrode with

the same pretreatment, the slope only increased when  $E_f$  decreased from 1.0 V to 0.5 V (Table 4).

For the  $\text{Co}_2\text{Si}$  electrode, the dependences of  $(-i')^{1/2}/i$  on  $\ln i$  were linear for the mechanically polished electrode or pretreated in 2% HF (Fig. 6a–d). For the  $\text{Co}_2\text{Si}$  electrode pretreated in 2 M KOH solution, when the silicide surface is enriched with cobalt and cobalt oxide may be

**Table 5.** The values of the slopes of the dependences of  $(-di/dt)^{1/2}/i$  on  $\ln i$  for the  $\text{CoSi}_2$  electrode

Pretreatment of electrode surface	Concentration of $\text{H}_2\text{SO}_4$ , mol $\text{L}^{-1}$	$E_p$ , V	Slope of $(-di/dt)^{1/2}/i$ vs. $\ln i$ plot, $(\text{C cm}^{-2})^{-1/2}$	Time interval, s
Mechanical polishing	0.5	1.0	21.7	0.6–40
Treatment in 2% HF	0.5	0.2	24.5	0.5–7.5
			14.3	7.5–42
Treatment in 2% HF	0.5	0.5	10.8	0.4–10
Treatment in 2% HF	0.5	1.0	9.55	1.1–19
Treatment in 2% HF	0.05	1.0	19.1	3.5–12
Treatment in 2 M KOH	0.5	1.0	4.5	1–85
Treatment in 2 M KOH	0.5	0.5	8.0	1–48

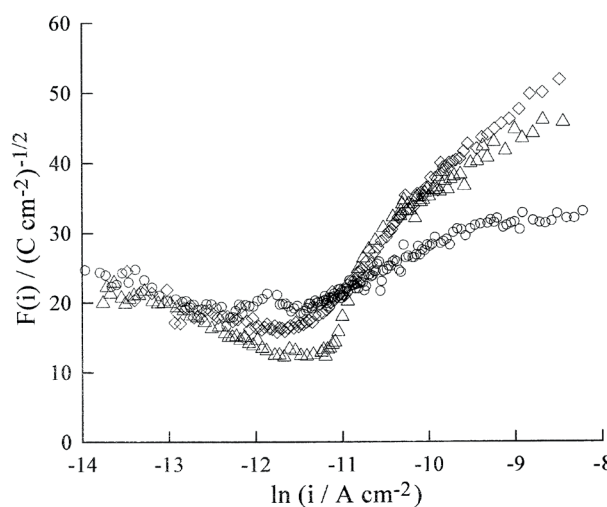
present on the surface, the value of  $(-i')^{1/2}/i$  in a rough approximation does not depend on the current density (Fig. 6e, f). In some cases (Fig. 6g, h), during the growth of the oxide film, there is a transition from a linear change in  $F(i)$  with  $\ln i$  (in accordance with the HFM) to constant  $F(i)$  (in accordance with the PDM). Approximately constant values of  $F(i)$  for the  $\text{Co}_2\text{Si}$  electrodes pretreated in an alkaline solution are 22–24  $(\text{C}/\text{cm}^2)^{-1/2}$  at sufficiently large  $t$  (Fig. 6e–g). To obtain 22  $(\text{C}/\text{cm}^2)^{-1/2}$  from relation (5) derived from the PDM, at  $\alpha_2 = 0.5$  and  $V_m = 11.6 \text{ cm}^3/\text{mol}$  (as for  $\text{CoO}$ ), the electric field strength in the oxide film must be  $2.1 \cdot 10^5 \text{ V}/\text{cm}$ , which can be considered a plausible value for the PDM. In contrast to  $\text{Co}_2\text{Si}$ , for the  $\text{CoSi}_2$  electrode, where the oxide is significantly enriched in silicon dioxide [11], the HFM is also achieved upon pretreatment in 2 M KOH (Fig. 7d).

Thus, with a higher cobalt content on the electrode surface ( $\text{Co}_2\text{Si}$  silicide with higher volume concentration of cobalt, the  $\text{Co}_2\text{Si}$  surface pretreated in a KOH solution), the point defect model is either approximately fulfilled in a wide range of  $t$ , or becomes fulfilled at comparatively high  $t$ . Under the above conditions, the anodic oxide contains higher amounts of cobalt oxide. The main types of point defects in  $\text{CoO}$  are cation vacancies [38]. The  $\text{Co}_3\text{O}_4$  oxide also contains a stoichiometric excess of oxygen [39]. The formation of point defects in  $\text{SiO}_2$  is more complicated compared to  $\text{CoO}$  [40]. These factors contribute to the execution of the PDM for cobalt-rich oxide and do not promote the execution of the PDM for  $\text{SiO}_2$ .

The  $\lg i, \lg t$ -curves with an inflection were observed when using the electrodes pretreated

in 2% HF (Fig. 4, 5). The current density in the  $\lg i, \lg t$ -dependence section after the inflection were higher compared to the continuation of the initial section into the region of large  $t$ . This probably indicates that an additional process is taking place: a) oxidation of cobalt in addition to oxidation of Si resulting in a bilayer structure; b) oxidation of  $\text{Co(II)}$  to a higher oxidation degree (reaction (3)). The higher current densities in 0.05 M  $\text{H}_2\text{SO}_4$  (Fig. 4, 5) can be explained by the fact that with an increase in pH, the equilibrium potential of oxidation reactions (1)–(3) shifts in the negative direction. That is, at a given  $E_p$ , a higher anodic overpotential is generated, which provides an increase in  $i$  at the beginning of passivation.

For  $\text{Co}_2\text{Si}$  pretreated in 2% HF, the dependences  $F(i)$  on  $\ln i$  for the whole studied interval of  $t$  (up to 3000 s) have a complex shape (Fig. 8): at low  $t$


**Fig. 8.** Chronoamperograms for  $\text{Co}_2\text{Si}/0.5 \text{ M H}_2\text{SO}_4$  over a wide time interval, pretreatment in 2% HF. Potential  $E_p$ , V: (○) – 0.2; (◇) – 0.5; (△) – 1.0

(large  $i$ ) there is a linear section, then there is a minimum (corresponds to the inflection on the  $\lg i, \lg t$ -curves), and then  $F(i)$  becomes almost the same constant value for all  $E_r$ . The constant value of  $F(i)$  at large  $t$  could indicate that the point defect model is executed. At high  $t$  (relatively thick oxide films),  $F(i)$  has the same value of  $22-24 \text{ (C/cm}^2\text{)}^{-1/2}$  as after pretreatment in a solution of 2 M KOH. Apparently, when thicker films are formed, the oxide is gradually enriched with cobalt also when the electrode is pretreated in 2% HF or two-layer structures are formed. The structures consist of a  $\text{SiO}_2$  layer and a layer enriched with cobalt oxide under it.

#### 4. Conclusions

The study showed that the kinetics of the anodic oxide film growth on cobalt silicide in sulphuric acid solutions significantly depends on the pretreatment of the electrode surface. This agrees with the literature data indicating that the presence of the native oxide film and surface pretreatment are important factors influencing the formation of the passive films [41, 42].

It was shown that a large number of results are adequately described by the high field model. This is particularly true for the data obtained at short passivation time (up to 30–50 s) without the pretreatment of the  $\text{Co}_2\text{Si}$  electrode in an alkaline solution. When the silicide surface is enriched with metal ( $\text{Co}_2\text{Si}$  pretreated in a 2 M KOH solution) before passivation, the point defect model is executed with sufficiently high values of time.

#### Author contributions

All authors made an equivalent contribution to the preparation of the publication.

#### Conflicts of interest

The authors declare that they have no known competing financial interests or personal relationships that could have influenced the work reported in this paper.

#### References

1. Maurice V., Marcus P. Current developments of nanoscale insight into corrosion protection by passive oxide films. *Current Opinion in Solid State and Materials Science*. 2018;22(4): 156–167. <https://doi.org/10.1016/j.cossms.2018.05.004>

2. Shein A. B. *Electrochemistry of silicides and germanides of transition metal\**. Perm: Perm State Univ. Publ., 2009. 269 p. (In Russ)

3. Schmidt C., Strehblow H.-H. The passivity of Fe/Si alloys in aqueous electrolytes at pH 5 and 9 studied by X-ray photoelectron spectroscopy and ion scattering spectroscopy. *Journal of the Electrochemical Society*. 1998;145(3): 834–840. <https://doi.org/10.1149/1.1838353>

4. Strehblow H.-H., Maurice V., Marcus P. Passivity of metals. In: *Corrosion Mechanisms in Theory and Practice*. P. Marcus (ed.). CRC Press, Taylor & Francis Group; 2012. pp. 235–326.

5. Wolff U., Schneider F., Mummert K., Schultz L. Stability and electrochemical properties of passive layers on Fe-Si alloys. *Corrosion*. 2000;56(12): 1195–1201. <https://doi.org/10.5006/1.3280507>

6. Chen H., Ma Q., Shao X., Ma J., Huang B. X. Corrosion and microstructure of the metal silicide ( $\text{Mo}_{1-x}\text{Nb}_x$ )<sub>5</sub>Si<sub>3</sub>. *Corrosion Science*. 2013;70: 152–160. <https://doi.org/10.1016/j.corsci.2013.01.024>

7. Tang C., Wen F., Chen H., Liu J., Tao G., Xu N., Xue J. Corrosion characteristics of  $\text{Fe}_3\text{Si}$  intermetallic coatings prepared by molten salt infiltration in sulfuric acid solution. *Journal of Alloys and Compounds*. 2019;778: 972–981. <https://doi.org/10.1016/j.jallcom.2018.11.198>

8. Hu L., Hu B., Gui, Y. Study on the melting and corrosion resistance of Fe-Cr-Si dual phase alloy. *IOP Conference Series: Materials Science and Engineering*. 2020;782(2): 022031. <https://doi.org/10.1088/1757-899X/782/2/022031>

9. Zhang Y., Xiao J., Zhang Y., Liu W., Pei W., Zhao A., Zhang W., Zeng, L. The study on corrosion behavior and corrosion resistance of ultralow carbon high silicon iron-based alloy. *Materials Research Express*. 2021;8(2): 026504. <https://doi.org/10.1088/2053-1591/abdc52>

10. Shadrin K. V., Panteleeva V. V., Shein A. B. Passivation of chromium dicilicide in acidic media. *Bulletin of Perm University. Chemistry*. 2021;11(3): 202–211 (In Russ., abstract in Eng.). <https://doi.org/10.17072/2223-1838-2021-3-202-211>

11. Baklanov M. R., Badmaeva I. A., Donaton R. A., Sveshnikova L. L., Storm W., Maex K. Kinetics and mechanism of the etching of  $\text{CoSi}_2$  in HF-based solutions. *Journal of the Electrochemical Society*. 1996;143(10): 3245–3251. <https://doi.org/10.1149/1.1837192>

12. Strehblow H.-H. Passivity of metals. In: *Advances in Electrochemical Science and Engineering*. Vol. 8. R. C. Alkire (ed.). Wiley; 2002. pp. 271–374. <https://doi.org/10.1002/3527600787.ch4>

13. Panteleeva V. V., Shein A. B. Growth of anodic oxide films on iron-triad metal monosilicides in sulfuric acid electrolyte. *Russian Journal of*

- Electrochemistry*. 2014;50(11): 1036–1043. <https://doi.org/10.1134/S102319351411007X>
14. Behazin M., Biesinger M. C., Noël J. J., Wren J. C. Comparative study of film formation on high-purity Co and Stellite-6: Probing the roles of a chromium oxide layer and gamma-radiation. *Corrosion Science*. 2012;63: 40–50. <https://doi.org/10.1016/j.corsci.2012.05.007>
15. Lutton K., Gusieva K., Ott N., Birbilis N., Scully J. R. Understanding multi-element alloy passivation in acidic solutions using operando methods. *Electrochemistry Communications*. 2017;80: 44–47. <https://doi.org/10.1016/j.elecom.2017.05.015>
16. Lutton Cwalina K., Ha H. M., Ott N., Reinke P., Birbilis N., Scully J. R. In operando analysis of passive film growth on Ni-Cr and Ni-Cr-Mo alloys in chloride solutions. *Journal of the Electrochemical Society*. 2019;166(11): C3241–C3253. <https://doi.org/10.1149/2.0261911jes>
17. Wang Z., Di-Franco F., Seyeux A., Zanna S., Maurice V., Marcus P. Passivation-induced physicochemical alterations of the native surface oxide film on 316L austenitic stainless steel. *Journal of the Electrochemical Society*. 2019;166(11): C3376–C3388. <https://doi.org/10.1149/2.0321911jes>
18. Choudhary S., Thomas S., Macdonald D. D., Birbilis N. Growth kinetics of multi-oxide passive film formed upon the multi-principal element alloy AlTiVCr: Effect of transpassive dissolution of V and Cr. *Journal of the Electrochemical Society*. 2021;168: 051506. <https://doi.org/10.1149/1945-7111/ac0018>
19. Burstein G. T. Passivity and localized corrosion. In: *Corrosion. Vol. 1. Metal/Environment Reactions*. L. L. Shreir, R. A. Jarman, G. T. Burstein (eds.). Oxford: Butterworth-Heinemann; 1994. pp. 1:118–1:150. <https://doi.org/10.1016/b978-0-08-052351-4.50013-3>
20. Zhang L., Macdonald D. D., Sikora E., Sikora J. On the kinetics of growth of anodic oxide films. *Journal of the Electrochemical Society*. 1998;145(3): 898–905. <https://doi.org/10.1149/1.1838364>
21. Kichigin V. I., Shein A. B. Effect of anodising on the kinetics of the hydrogen evolution reaction on cobalt silicides in sulphuric acid solution. *Condensed Matter and Interphases*. 2017;19(3): 359–367 (In Russ., abstract in Eng.). <https://doi.org/10.17308/kcmf.2017.19/212>
22. Liu D. Q., Blackwood D. J. Mechanism and dissolution rates of anodic oxide films on silicon. *Electrochimica Acta*. 2013;105: 209–217. <https://doi.org/10.1016/j.electacta.2013.04.024>
23. Thissen P., Seitz O., Chabal Y. J. Wet chemical surface functionalization of oxide-free silicon. *Progress in Surface Science*. 2012;87(9–11): 272–290. <https://doi.org/10.1016/j.progsurf.2012.10.003>
24. Seidel H., Csepregi L., Heuberger A., Baumgärtel H. Anisotropic etching of crystalline silicon in alkaline solutions. I. Orientation dependence and behavior of passivation layers. *Journal of the Electrochemical Society*. 1990;137(11): 3612–3626. <https://doi.org/10.1149/1.2086277>
25. Kichigin V. I., Shein A. B. Anodic behavior of Co<sub>2</sub>Si in potassium hydroxide solutions. *Bulletin of Perm University. Chemistry*. 2011;1(3): 4–14 (In Russ., abstract in Eng.). Available at: [https://www.elibrary.ru/download/elibrary\\_17563295\\_89020211.pdf](https://www.elibrary.ru/download/elibrary_17563295_89020211.pdf)
26. Sukhotin A. M. (ed.). *Handbook of Electrochemistry\**. Leningrad: Khimiya Publ.; 1981. 488 p. (In Russ.).
27. Lohrengel M. M. Thin anodic oxide layers on aluminium and other valve metals: high field regime. *Materials Science and Engineering: R: Reports*. 1993;11(6): 243–294. [https://doi.org/10.1016/0927-796X\(93\)90005-N](https://doi.org/10.1016/0927-796X(93)90005-N)
28. Vanhumbecck J. F., Proost J. Current understanding of Ti anodisation: fundamental, morphological, chemical and mechanical aspects. *Corrosion Reviews*. 2009;27: 117–204. <https://doi.org/10.1515/CORRREV.2009.27.3.117>
29. Macdonald D. D. The point defect model for the passive state. *Journal of the Electrochemical Society*. 1992;139(12): 3434–3449. <https://doi.org/10.1149/1.2069096>
30. Roh B., Macdonald D. D. Passivity of titanium: part II, the defect structure of the anodic oxide film. *Journal of Solid State Electrochemistry*. 2019;23: 1967–1979. <https://doi.org/10.1007/s10008-019-04254-0>
31. Bösing I., La Mantia F., Thöming J. Modeling of electrochemical oxide film growth – a PDM refinement. *Electrochimica Acta*. 2022;406: 139847. <https://doi.org/10.1016/j.electacta.2022.139847>
32. Seyeux A., Maurice V., Marcus P. Oxide film growth kinetics on metals and alloys. I. Physical model. *Journal of the Electrochemical Society*. 2013;160(6): C189–C196. <https://doi.org/10.1149/2.036306jes>
33. Momeni M., Behazin M., Wren J. C. Mass and charge balance (MCB) model simulations of current, oxide growth and dissolution during corrosion of Co-Cr alloy Stellite-6. *Journal of the Electrochemical Society*. 2016;163(3): C94–C105. <https://doi.org/10.1149/2.0721603jes>
34. Lutton K., Scully J. R. Kinetics of oxide growth of passive films on transition metals. *Encyclopedia of Interfacial Chemistry, Surface Science and Electrochemistry*. 2018;284–290. <https://doi.org/10.1016/B978-0-12-409547-2.13576-0>
35. Burstein G. T., Davenport A. J. The current-time relationship during anodic oxide film growth under high electric field. *Journal of the Electrochemical Society*. 1989;136(4): 936–941. <https://doi.org/10.1149/1.2096890>
36. Franssila S. *Introduction to Microfabrication*. John Wiley & Sons; 2010. 518 p. <https://doi.org/10.1002/9781119990413>

37. Nascimento M. L. F., Zanotto E. D. Diffusion processes in vitreous silica revisited. *Physics and Chemistry of Glasses - European Journal of Glass Science and Technology Part B*. 2007;48(4): 201–217. Available at: <https://www.ingentaconnect.com/contentone/sgt/ejgst/2007/00000048/00000004/art00001>

38. Koel G. J., Gellings P. J. The contribution of different types of point defects to diffusion in CoO and NiO during oxidation of the metals. *Oxidation of Metals*. 1972;5: 185–203. <https://doi.org/10.1007/BF00609658>

39. Razina N. F. *Oxide electrodes in aqueous solutions\**. Alma-Ata: Nauka Publ.; 1982. (In Russ.).

40. Deml A. M., Holder A. M., O'Hayre R. P., Musgrave C. B. Intrinsic material properties dictating oxygen vacancy formation energetics in metal oxides. *The Journal of Physical Chemistry Letters*. 2015;6(10): 1948–1953. <https://doi.org/10.1021/acs.jpcclett.5b00710>

41. Vargas R., Carvajal D., Galavis B., Maimone A., Madriz L., Scharifker B. R. High-field growth of semiconducting anodic oxide films on metal surfaces for photocatalytic application. *International Journal of Photoenergy*. 2019: 2571906. <https://doi.org/10.1155/2019/2571906>

42. Ma L., Pascalidou E.-M., Wiame F., Zanna S., Maurice V., Marcus P. Passivation mechanisms and pre-oxidation effects on model surfaces of FeCrNi austenitic stainless steel. *Corrosion Science*. 2020;167: 108483. <https://doi.org/10.1016/j.corsci.2020.108483>

\* Translated by author of the article.

### Information about the authors

Anatoliy B. Shein, Dr. Sci. (Chem.), Full Professor, the Department of Physical Chemistry, Perm State University (Perm, Russian Federation).

<https://orcid.org/0000-0002-2102-0436>  
ashein@psu.ru

Vladimir I. Kichigin, Cand. Sci. (Chem.), Research Fellow at the Department of Physical Chemistry, Perm State University (Perm, Russian Federation).

<https://orcid.org/0000-0002-4668-0756>  
kichigin@psu.ru

Received 27.05.2022; approved after reviewing 04.07.2022; accepted for publication 15.09.2022; published online 25.12.2022.

Translated by Anastasiia Ananeva  
Edited and proofread by Simon Cox





## Original articles

Research article

<https://doi.org/10.17308/kcmf.2022.24/10561>

## Anodic oxide coatings with a hierarchical micronanostructure on sintered titanium powders

N. M. Yakovleva<sup>1</sup>✉, A. M. Shulga<sup>1</sup>, I. V. Lukianchuk<sup>2</sup>, K. V. Stepanova<sup>1</sup>, A. N. Kokatev<sup>1</sup>,  
E. S. Chubieva<sup>1</sup>

<sup>1</sup>Petrozavodsk State University,  
33 Lenina prospekt, Petrozavodsk 185910, Russian Federation

<sup>2</sup>Institute of Chemistry of the Far Eastern Branch of the Russian Academy of Sciences,  
159 100-Letiya Oktyabrya ul., Vladivostok 690022, Russian Federation

### Abstract

TiO<sub>2</sub> nanotubes formed by electrochemical anodising of Ti (titanium foil) are normally X-ray amorphous. To improve their functional properties, they are usually converted into crystalline nanotubes by annealing at  $T \approx 400\text{--}500\text{ }^\circ\text{C}$ . What is more, under certain conditions, oxide films with a hierarchical micronanostructure can be formed on titanium foil by anodising in fluorine-containing electrolytes. Such films contain nanostructured microcones whose atomic structure corresponds to anatase ( $\alpha\text{-TiO}_2$ ). It is interesting to find out whether it is possible to form anodic oxide coatings with a hierarchical micronanostructure on the surface of sintered powders of titanium sponge, which should have much larger specific surfaces and a wider range of applications. This paper is aimed at the study of the process of anodising porous samples of sintered powders of titanium sponge in an aqueous electrolyte (1 M H<sub>2</sub>SO<sub>4</sub> + 0.15 wt % HF).

The object of our study were sintered titanium powders in the form of samples of porous powder materials with a specific area of  $S_{sp} = 1,350\text{ cm}^2/\text{g}$ . Anodising was conducted in a 1 M H<sub>2</sub>SO<sub>4</sub> + 0.15 wt % HF electrolyte at various values of current density ( $j_m$ ). Surface morphology before and after anodising was investigated by scanning electron microscopy and atomic force microscopy. X-ray diffractometry was used to study the phase composition.

The research involved the study of the influence of conditions for the galvanostatic anodising of samples of porous powder materials made from titanium sponge on the growth, morphology, and atomic structure of anodic oxide coatings. For the first time, it was shown that anodising at the values of current density  $j_m = (230\div 1,890)\text{ mA/g}$  leads to the appearance of nanostructured  $\alpha\text{-TiO}_2$  microcones (with base diameters and heights of up to 4  $\mu\text{m}$ ) in an amorphous nanoporous/nanotube oxide matrix (with an effective pore/tube diameter of about 50 nm). Since such coatings have a high specific area and a hierarchical micronanostructure, they are promising for the design of devices for photocatalytic environment purification and production of superhydrophobic surfaces.

**Keywords:** Sintered powders, Porous powder materials, Titanium sponge, Anodic oxide coatings, Structure hierarchy, Microcones, Crystalline, Nanostructured titanium dioxide, Scanning electron microscopy, Atomic force microscopy

**Funding:** The study was carried out within the framework of the R&D Support Programme for Undergraduate and Postgraduate Students of Petrozavodsk State University funded by the Government of the Republic of Karelia (agreement KGRK-21/H2-05 dated of 30.03.2022) and partially by the federal budget funds allocated for the implementation of the state assignment for the Institute of Chemistry of the Far Eastern Branch of the Russian Academy of Sciences (topic No. FWFN (0205) -2022-0001).

**Acknowledgements:** X-ray diffraction and scanning electron microscopy were performed using the equipment of the centres for collective use of the Karelian Research Centre of the Russian Academy of Sciences (Petrozavodsk) and the Institute of Chemistry of the Far Eastern Branch of the Russian Academy of Sciences (Vladivostok), respectively.

✉ Natalia M. Yakovleva, e-mail: [nmyakov@gmail.com](mailto:nmyakov@gmail.com)

© Yakovleva N. M., Shulga A. M., Lukianchuk I. V., Stepanova K. V., Kokatev A. N., Chubieva E. S., 2022



The content is available under Creative Commons Attribution 4.0 License.

**For citation:** Yakovleva N. M., Shulga A. M., Lukianchuk I. V., Stepanova K. V., Kokatev A. N., Chubieva E. S. Anodic oxide coatings with a hierarchical micronanostructure on sintered titanium powders. *Condensed Matter and Interphases*. 2022;24(4): 572–583. <https://doi.org/10.17308/kcmf.2022.24/10561>

**Для цитирования:** Яковлева Н. М., Шульга А. М., Лукиянчук И. В., Степанова К. В., Кокатев А. Н., Чубиева Е. С. Анодно-оксидные покрытия с иерархической микронаноструктурой на спеченных порошках титана. *Конденсированные среды и межфазные границы*. 2022; 24(4): 572–583. <https://doi.org/10.17308/kcmf.2022.24/10561>

## 1. Introduction

Electrochemical anodising allows forming  $\text{TiO}_2$  films directly on titanium substrates. Depending on the process parameters such as electrolyte composition and concentration, voltage/current, and the duration of anodising, anodic oxide coatings (AOCs) of different morphologies and atomic structures can be created.

Anodising Ti in fluorine-containing electrolytes results in the formation of self-organised nanotube or nanoporous AOCs with evenly distributed nanosized structural elements (tubes or pores) [1–7].  $\text{TiO}_2$  nanotubes obtained by electrochemical anodising are normally X-ray amorphous. In many cases, amorphous nanotube AOCs are converted into crystalline AOCs by annealing at  $T \approx 400\text{--}500\text{ }^\circ\text{C}$  to improve their functional properties (catalytic activity, electronic conductivity or mechanical strength), which expands the range of their applications [1,2,6]. Therefore, it is important to form anodic  $\text{TiO}_2$  nanotubes with a crystalline structure without any additional thermal treatment. A number of methods for Ti anodising have been proposed. They allow obtaining  $\text{TiO}_2$  nanotubes at room temperature with a crystalline component in the form of anatase (hereinafter,  $\alpha\text{-TiO}_2$ ) and completely crystalline  $\alpha\text{-TiO}_2$  nanotubes at  $T = 60\text{ }^\circ\text{C}$  [3, 8, 9]. In particular, some authors have reported one-stage synthesis of arrays of  $\alpha\text{-TiO}_2$  crystalline nanotubes by anodising at room temperature by using polyols [10]. Despite certain technological difficulties, researchers have been actively developing the method for converting amorphous  $\text{TiO}_2$  nanotubes into crystalline nanotubes with a  $\alpha\text{-TiO}_2$  structure by water or water vapour treatment [11–13].

Over the past 10 years, a number of works [14–20] have shown that under certain conditions of anodising titanium foil in fluorine-containing aqueous electrolytes, oxide coatings can be formed, whose amorphous matrix has microcone  $\alpha\text{-TiO}_2$  formations. Thus, in 2011, Wang C. et al. [14] reported about a method of anodising Ti foil

(99.6%) in aqueous solutions of  $\text{NH}_4\text{F}$  at room temperature which resulted in the formation of AOCs, on the surface of which there were homogeneously distributed cone-shaped micron formations with a  $\alpha\text{-TiO}_2$  structure. According to the authors, the shape of crystalline formations was flower-like, although it would be more appropriate to call them “microcones” given their geometric shape and dimensional parameters. Each microcone, in its turn, was nanostructured and had a set of layers with a thickness of about 20 nm. It should be noted that similar  $\alpha\text{-TiO}_2$  structures were also found when studying the formation of AOCs on titanium foil in aqueous solutions of acids (sulphuric, orthophosphoric) without adding fluorine [21–25].

Later, it was reported that similar oxide films on Ti were obtained in aqueous solutions of acids ( $\text{H}_3\text{PO}_4$ ,  $\text{H}_2\text{SO}_4$ , and  $\text{C}_2\text{H}_2\text{O}_4$ ) with a HF additive [17–20]. It was found that the critical parameters affecting the appearance of  $\alpha\text{-TiO}_2$  microcones in the amorphous oxide matrix are the value of the applied potential and the concentration of the fluorine-containing additive ( $\text{NH}_4\text{F}$  [14–16] or HF [17–20]). Due to their high surface area, morphological regularity, and a crystalline structure,  $\alpha\text{-TiO}_2$  micronanostructures obtained at room temperature directly on a titanium substrate can be used in various ways. For example, they are a promising material for water photoelectrolysis, solar energy conversion [14], and the manufacture of lithium-ion battery anodes [20, 26, 27]. At present, only the initial assumptions have been made about the mechanism of the formation of anatase microcones when anodising titanium foil in aqueous solutions with fluorine ions. Therefore, this issue needs to be further researched.

Porous powder materials (PPM) obtained by pressure treatment and the sintering of Ti sponge powders are characterised by a set of unique physicochemical properties, including antibacterial effect, accelerated osseointegration with bone tissues, etc. [28, 29]. The formation of nanostructured AOCs on the surface of sintered

powder particles should lead to a noticeable increase in the specific area of the sample and a range of its functional applications. In [7], it was shown for the first time that under certain conditions of anodising samples of titanium sponge PPM samples (hereinafter, TS PPM) in a 1 M  $\text{H}_2\text{SO}_4$  + 0.15 wt% HF aqueous electrolyte, an X-ray amorphous  $\text{TiO}_2$  film with a thickness of about 300 nm was formed on the surface of the sintered powder microparticles. This film was characterised by the presence of evenly distributed open pores/tubes with effective diameters between 30 and 70 nm. What is more, the microinhomogeneous surface of anodised samples both had areas with pores and areas with tubular structures. There is no information on the formation of anodic oxide coatings (AOCs) with hierarchical micronanostructures on the surface of sintered powders of sponge titanium, that is why it is very important to find out whether it is possible to obtain coatings of this type. For this purpose, this paper studies the process of anodising porous materials made from sintered powders of Ti sponge in a 1 M  $\text{H}_2\text{SO}_4$  + 0.15 wt% HF aqueous electrolyte.

## 2. Experimental

In our study, we used sintered titanium powders in the form of samples of porous powder materials (PPM). PPM samples were prepared by pressing sponge powder of technically pure titanium with a fraction of 0.63–1.0 mm at 100–120 MPa followed by vacuum sintering at a temperature of 1,090°C for 70 minutes. As a result, we obtained disc-like samples with a diameter of 20–30 mm, a thickness of 3 mm, and a specific area of  $S_{sp} = 1,350 \text{ cm}^2/\text{g}$  [7,28,30].

The samples were preliminarily degreased in acetone and ethanol in an ultrasonic bath, washed in distilled water, and dried in the air. Anodising was performed in three-electrode electrochemical cells with a tantalum cathode and platinum counter electrode in a 1 M  $\text{H}_2\text{SO}_4$  + 0.15 wt% HF aqueous electrolyte at room temperature in a galvanostatic mode (GSM). To determine the cell current during galvanostatic anodising of sintered powders, it is necessary to know the surface area of the sample, which can be found if the value of the specific surface,  $S_{sp}$ , is known. Thus, to anodise TS PPMs with a

mass of  $m = 1 \text{ g}$  and  $S_{sp} = 1,350 \text{ cm}^2/\text{g}$  at a current density  $j_a = 0.15 \text{ mA}/\text{cm}^2$ , it is necessary to set the value of the cell current at  $I_a \approx 202 \text{ mA}$ . When anodising samples of sintered powders of various sizes (masses) under galvanostatic conditions, it is advisable to compare voltage-time transients in the electrolytic cell,  $U_a(t)$ , obtained at constant current values per unit mass of the sample  $j_m = I_a/m \text{ (mA/g)}$  [31].

In this work, anodising was carried out at the values of  $j_m = 202, 230, 405, \text{ and } 1,890 \text{ mA/g}$ . Normally, the duration of the process was  $t_a = 1 \text{ hour}$ . At  $j_m = 1,890 \text{ mA/g}$ , we studied anodising for  $t_a = 45, 60, \text{ and } 90 \text{ min}$ . During the growth of AOCs, voltage-time transients,  $U_a(t)$ , were recorded using an ERBIY-7115 electronic recorder connected to a computer. The detailed description of the anodising method is presented in the works [7, 31–33].

Scanning electron microscopy (SEM), atomic force microscopy (AFM), and X-ray diffraction were used to study the morphology, elemental composition, and atomic structure of the samples. The surface morphology of the samples before and after anodising was investigated by SEM using high-resolution microscopes *Mira* (Tescan, Czech Republic) and S-55009 (*Hitachi*, Japan). The elemental composition was evaluated by energy dispersive X-ray spectroscopy (EDS) using a *Thermo Scientific* attachment (USA). The data were collected for 5–10 sections, including those of microscopic size (up to  $50 \times 50 \mu\text{m}^2$ ) as well as “dots” of  $50 \times 50 \text{ nm}^2$  and  $10 \times 10 \text{ nm}^2$ . The sections were chosen according to previously obtained SEM images of the surface and their elemental composition was quantitatively analysed.

The AFM studies were conducted in air on a Solver Next (ZAO NT-MDT, Russia) scanning probe microscope in a tapping mode. High-resolution diamond-like carbon tips (*NSG01*) with the length of 125  $\mu\text{m}$ , resonance frequency of 87–230 kHz, and curvature radius of the needle of 10 nm were used. The size of the scan area varied in the range from 1 to 25  $\mu\text{m}^2$ . From 2 to 5 surface sections were scanned. The thickness of the oxide films was assessed by AFM images of the samples [7]. The sequence of processing AFM images is described in [32].

X-ray diffractometry was used to study the phase composition. The samples were studied

using the X-ray technique before and after anodising on a *D8 ADVANCE* (Bruker, Germany) automated diffractometer using  $\text{CuK}\alpha$  radiation in the angular range  $2\theta = (10-90)^\circ$  at  $0.02^\circ$  intervals. The phase composition of AOCs was identified by comparing a set of d-spacings calculated according to the experimental data and the corresponding values for Ti and crystalline modifications of titanium oxides.

### 3. Results and discussion

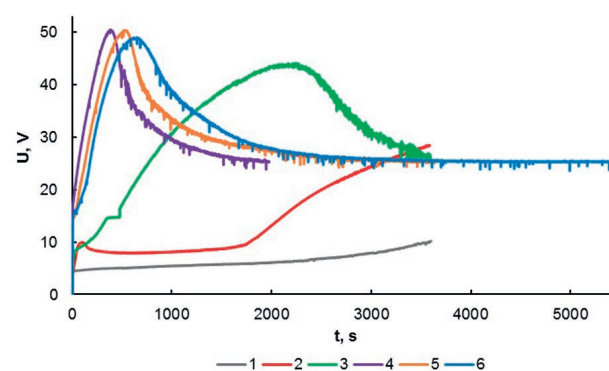
The first stage of the research of galvanostatic anodising of porous samples of sintered powders of Ti sponge in a  $1 \text{ M H}_2\text{SO}_4 + 0.15 \text{ wt\% HF}$  aqueous electrolyte involved the study of the growth kinetics of anodic oxide coatings (AOCs) at constant current values per unit mass of the sample,  $j_m$ , equal to  $j_m = 202, 230, 405,$  and  $1,890 \text{ mA/g}$ . Figure 1 shows the voltage-time transients in the electrolytic cell,  $U_a(t)$ , registered during the growth of AOCs. We can see that  $U_a(t)$  changed noticeably with an increase in the current value.

At values of  $j_m = 202$  and  $230 \text{ mA/g}$ , during the first 30 minutes of the process, kinetic dependencies (Fig. 1, curves 1 and 2) corresponded well to the growth of self-organised porous/tubular AOCs [2, 7, 32] and were characterised by the values of steady-stage voltage between 5 and 9 V. There were successively distinguished sections of  $U_a(t)$  curves that are commonly interpreted as those corresponding to different stages of the formation of self-organised oxide films: the growth of a barrier layer, initiation and self-organisation of pores, and the steady-state growth of the porous/tubular layer. However, further voltage began to grow and reached values of about 20 V ( $j_m = 202 \text{ mA/g}$ ) and 30 V ( $j_m = 230 \text{ mA/g}$ ) at the end of the process ( $t_a = 1 \text{ h}$ ).

The dependencies  $U_a(t)$  (Fig. 1, curves 3-6) recorded at large current values,  $j_m = 405 \text{ mA/g}$  and  $j_m = 1,890 \text{ mA/g}$ , were also close to the typical galvanostatic growth curves of self-organised porous/tubular AOCs. However, the value of steady-stage voltage in such conditions was noticeably higher and close to  $U_a^{\text{st}} \sim (25-27) \text{ V}$ . Also, at  $j_m = 405 \text{ mA/g}$  (Fig. 1, curve 3), 60 minutes of anodising was required for the transition to the stage of steady-state growth, while at  $j_m = 1,890 \text{ mA/g}$ , it took 40 minutes (Fig. 1,

curves 4-6). We can see that at  $j_m = 1,890 \text{ mA/g}$ , the variation of the anodising time between 45 and 90 minutes practically did not cause any changes in  $U_a(t)$ . It should be noted that the presence of numerous voltage peaks at the stage of self-organisation and the steady-state growth of pores was characteristic of  $U_a(t)$  obtained both at  $j_m = 405 \text{ mA/g}$  and  $j_m = 1,890 \text{ mA/g}$  (Fig. 1, curves 3 and 4). Such voltage behaviour can be caused by multiple local breakdowns in the barrier layer [35]. The analysis of the initial sections of the  $U_a(t)$  transients for all of the used values of  $j_m$ , with the exception of  $j_m = 202 \text{ mA/g}$ , showed [31] that in the initial sections, a few seconds after the beginning of anodising, there was a change in the slope of  $U_a(t)$ , which is usually associated with the appearance of the crystalline component  $\alpha\text{-TiO}_2$  in the composition of the amorphous oxide layer [34].

During the next stage, a microscopic study of the surface morphology of the samples before and after anodising was conducted using SEM. According to the data [7], the surface relief of the sample before anodising indicated a sufficiently developed structure characteristic of a titanium sponge [28, 36]. The analysis of the elemental composition of the samples before anodising showed that its main element was Ti ( $C_{\text{Ti}} \approx 90-100 \text{ wt\%}$ ). The presence of C (between 5.5 and 9 wt%) was also established. It was found that some areas had individual defects (micron inclusions whose composition included Si, Ca, Al,



**Fig. 1.** Voltage-time transients,  $U_a(t)$ , recorded during anodising of the samples of porous powder materials made from titanium sponge in a  $1 \text{ M H}_2\text{SO}_4 + 0.15 \text{ wt\% HF}$  solution at different values of current  $j_m$ : 202 mA/g (curve 1,  $t_a = 60 \text{ min}$ ); 230 mA/g (curve 2,  $t_a = 60 \text{ min}$ ); 405 mA/g (curve 3,  $t_a = 60 \text{ min}$ ); 1,890 mA/g (curves 4-6,  $t_a = 45, 60, 90 \text{ min}$ )

and O (up to 20 wt%), which corresponds to the state standard GOST 17746-96 Titanium sponge.

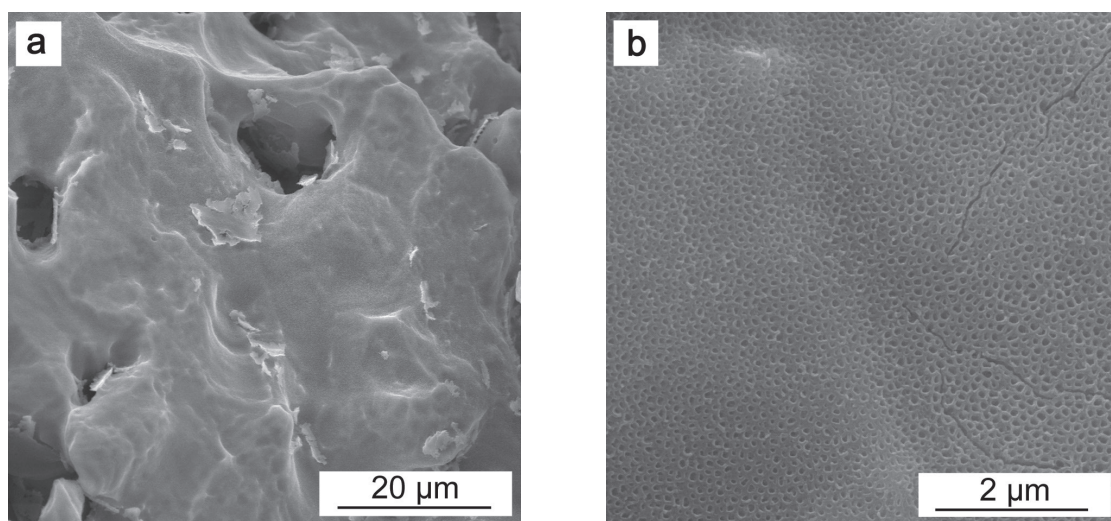
Fig. 2 shows that after anodising at  $j_m = 202$  mA/g, the surfaces of the TS PPM samples had self-organised AOCs with open pores and effective diameters from 40 to 60 nm, which corresponds well to the results [7]. The estimation based on the pore size and the thickness of the oxide layer [7] showed that the surface area of TS PPM samples anodised under such conditions would increase by approximately 10 times.

The study of the morphology of AOCs anodised at  $j_m = 230$  mA/g ( $t_a = 1$  h) mainly revealed regions with a regular-porous relief similar to that shown in Fig. 2. It also revealed separate regions containing a set of rounded formations with a size of 0.2 to 2.0  $\mu\text{m}$  (Fig. 3 a,b) which, according to the results [3,34,35], can be interpreted as crystalline nuclei with a  $\alpha\text{-TiO}_2$  structure (anatase).

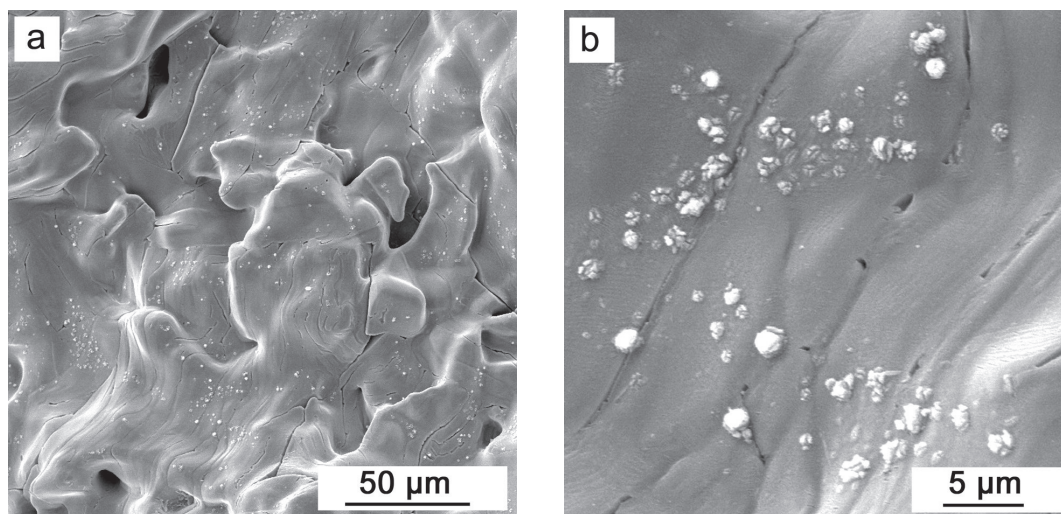
After anodising at  $j_m = 405$  mA/g, unevenly distributed rounded formations of cone-like morphology were observed on the surface of all studied areas of the porous oxide layer (Fig. 4). Their shape was close to conical, their estimated base diameters were between 0.7 and 3.5  $\mu\text{m}$  and their heights were between 0.3 and 3.0  $\mu\text{m}$  (Fig. 4 b, c), which allows calling them microcones (MCC). Each formation, in its turn, was a set of heterogeneous layers with a thickness of about 20–35 nm (Fig. 4c), i.e. they were nanostructured. There were cracks around the cone-like MCCs

and separate depressions, craters (Fig. 4b). It can be assumed that the craters had been filled with MCCs. It means that after anodising for  $t_a = 60$  min at  $j_m = 230$  mA/g, multilayer formations only began to appear on the surface of the porous/tubular oxide film, while at  $j_m = 405$  mA/g, their number and size increased.

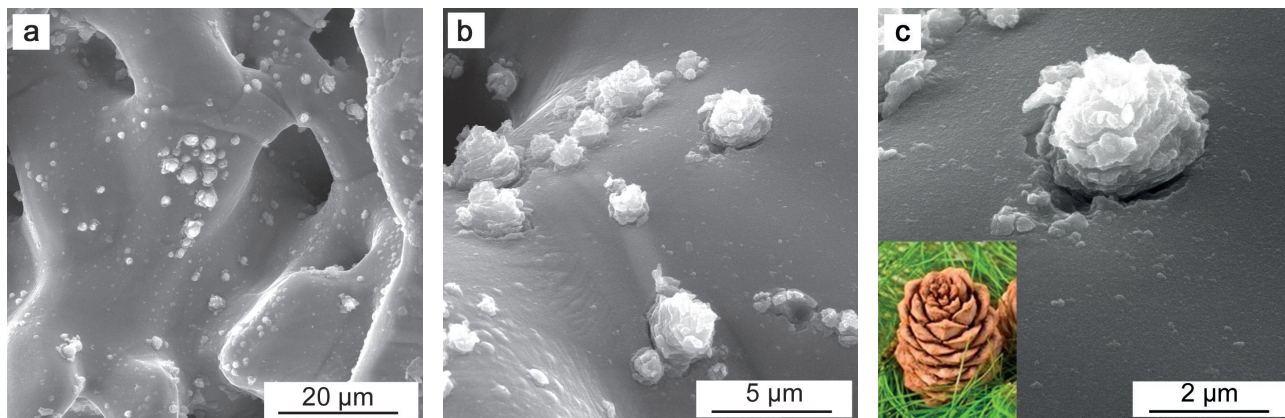
During the final stage, we examined the surface of AOCs obtained at  $j_m = 1,890$  mA/g. Despite bubbling the electrolyte, by the end of the anodising process the temperature near the surface of the sample increased by 15–20°C. Anodising at  $j_m = 1,890$  mA/g for 45 minutes (Fig. 5a) resulted in the uneven distribution of multilayer conical formations of various sizes on the surface of the samples with porous/tubular AOCs. The values of their base diameters varied between 0.8 and 3.0 microns, and their heights varied between 0.8 and 4.0 microns. The thickness of the layers was about 30 nm. As compared to the MCCs formed by anodising at  $j_m = 405$  mA/g (Fig. 4), these MCCs were more elongated and their height in most cases exceeded their base diameter. The analysis of SEM images obtained at larger magnification suggests that the MCC layers were nanoporous, which is consistent with the data in [26]. All studied areas within most MCCs were characterised by cracks around the bases with a width of ~90–150 nm. Cracks also appeared in the areas between MCCs, the number of craters with diameters between 1.0 and 2.5  $\mu\text{m}$



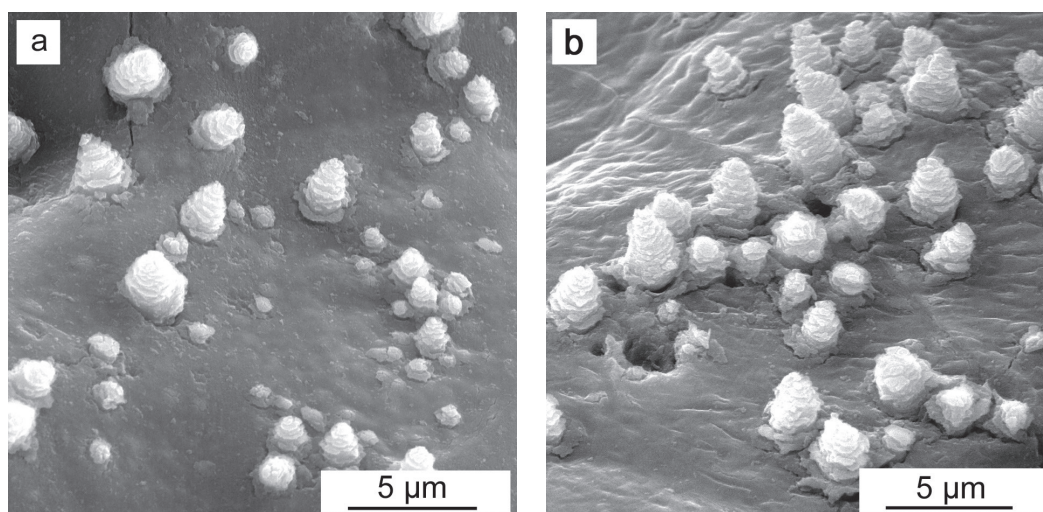
**Fig. 2.** SEM images of the surface of the samples of porous powder materials made from titanium sponge after anodising in a 1 M  $\text{H}_2\text{SO}_4 + 0.15$  wt % HF electrolyte for 1 hour at  $j_m \cong 202$  mA/g. The images were obtained at various magnifications (a, b)



**Fig. 3.** SEM images of sections on the surface of the samples of porous powder materials made from titanium sponge after anodising in a 1 M  $H_2SO_4 + 0.15$  wt % HF electrolyte for 1 hour at  $j_m \cong 230$  mA/g. The images were obtained at various magnifications (a, b)



**Fig. 4.** SEM images of a section on the surface of the samples of porous powder materials made from titanium sponge after anodising in a 1 M  $H_2SO_4 + 0.15$  wt % HF electrolyte for 1 hour at  $j_m \cong 405$  mA/g. The images were obtained at various magnifications (a, b, c)



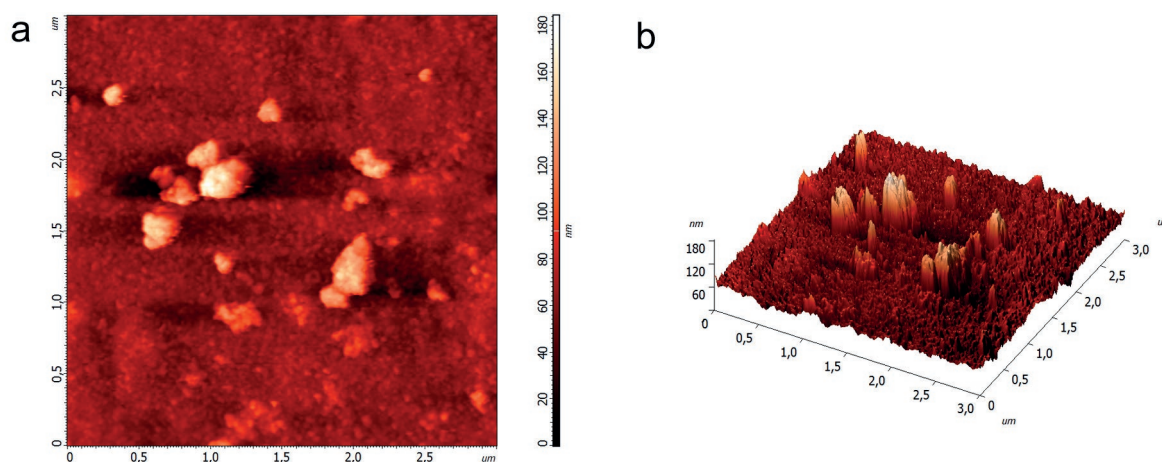
**Fig. 5.** SEM images of the surface of the samples of porous powder materials made from titanium sponge after anodising in a 1 M  $H_2SO_4 + 0.15$  wt % HF electrolyte for 45 (a) and 60 (b) min at  $j_m \cong 1,890$  mA/g

also increased. Increasing the anodising time to  $t_a = 60$  min did not result in any noticeable changes in the appearance of the AOC surface. Multilayer MCCs were unevenly distributed on the surface of the AOCs, the diameters of their bases were in the range from 0.8 to 3.0  $\mu\text{m}$ , their heights were between 1.9 and 4.1  $\mu\text{m}$  (Fig. 5b), and the number of craters and cracks between microcone formations increased. The AFM was used to study in detail the surface relief of the AOC sections between large microcone formations. It can be seen (Fig. 6a, b) that along with surface areas characterised by the presence of regular open pores/tubes ( $d_p \sim 20\text{--}30$  nm), there were unevenly distributed cone-shaped formations with base diameters in the range from 50 to 200 nm and heights below 200 nm. This means that anodising at a current value of  $j_m = 1,890$  mA/g for  $t_a = 60$  min leads to the formation of nanoporous/nanotubular oxide coatings on microparticles of porous powder samples. These coatings have multilayer conical formations whose base diameters and heights vary over a wide range.

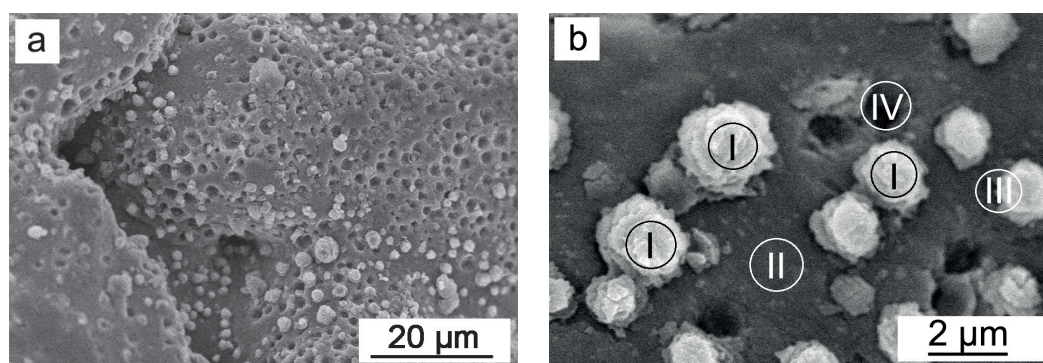
After  $t_a = 90$  min, the studied sections of the AOC surface had multilayer MCCs with base diameters between 0.6 and 3.9  $\mu\text{m}$  and heights between 1.7 and 4.5  $\mu\text{m}$ . The number of craters sharply increased and their estimated diameters were between 0.3 and 3.0  $\mu\text{m}$  (Fig. 7). The elemental composition of AOCs which were formed within  $t_a = 90$  min was studied within different areas: (I) within microcones, (II) between craters/microcones, (III) in the conjugation area of craters and the surface of

the AOC, (IV) at the bottom of craters (Table 1). The obtained data indicate that the MCCs had Ti and O in their composition. The values of weight percent of the elements were  $C_{\text{Ti}} \approx 60$  wt%,  $C_{\text{O}} \approx 40$  wt%, which corresponded well to  $\text{TiO}_2$ . Additionally, an insignificant amount of F (up to 4 wt%) was found in some microcones. The elemental composition of AOCs outside cones and craters also corresponded to  $\text{TiO}_2$ . There were traces of sulphur S (less than 0.2 wt%). The presence of S could be due to the inclusion of  $\text{SO}_4^{2-}$  anions into the porous oxide layer of AOCs during its growth [36]. All studied surface sections were characterised by the presence of 2 to 10 wt% of carbon. It was found that only titanium was present at the bottom of the craters.

Next, an X-ray technique was used to examine the phase composition of the samples before and after anodising at  $j_m = 1,890$  mA/g for 60 and 90 min. In addition to reflections from the titanium substrate, the XRD patterns of the studied samples after anodising had several additional low-intensity lines. Fig. 8 shows a typical XRD pattern of a sample anodised in 1 M  $\text{H}_2\text{SO}_4 + 0.15$  wt % HF solution at a current value of  $j_m = 1,890$  mA/g for  $t_a = 90$  min. Identification of the diffraction lines on the XRD patterns of powder samples is a very challenging task, firstly, due to their low intensity and, secondly, due to the coincident positions of several Bragg reflections. Hence the need for repeated X-ray examination of the samples and strict compliance with the accuracy requirements when aligning the studied object. As a result, we identified isolated



**Fig. 6.** AFM images (2D - a, 3D - b) of the surface of the samples of porous powder material made from titanium sponge after anodising in a 1 M  $\text{H}_2\text{SO}_4 + 0.15$  wt % HF electrolyte for 1 hour at  $j_m \cong 1,890$  mA/g.



**Fig. 7.** SEM images of a section on the surface of the sample of porous powder material made from titanium sponge after anodising in a 1 M  $\text{H}_2\text{SO}_4$  + 0.15 wt % HF electrolyte for 90 min at  $j_m \cong 1,890$  mA/g. The images were obtained at various magnifications (a, b) The results of the EDX analysis of the elemental composition of sections I–IV (b) are presented in Table 1

**Table 1.** The main elemental composition of sections I-IV (Fig. 7B) on the surface of the samples of porous powder materials made from titanium sponge after anodising in a 1 M  $\text{H}_2\text{SO}_4$  + 0.15 wt% HF electrolyte for 90 min at  $j_m$  1,890 mA/g

Element	Mass fraction of the element, C, wt%			
	I	II	III	IV
C	10.0±1.9	5.3±1.3	6.9±1.8	–
O	35.2±3.2	41.4±2.9	33.5±3.3	–
Ti	54.8±1.8	53.2±0.3	59.6±3.5	100.0±1.8

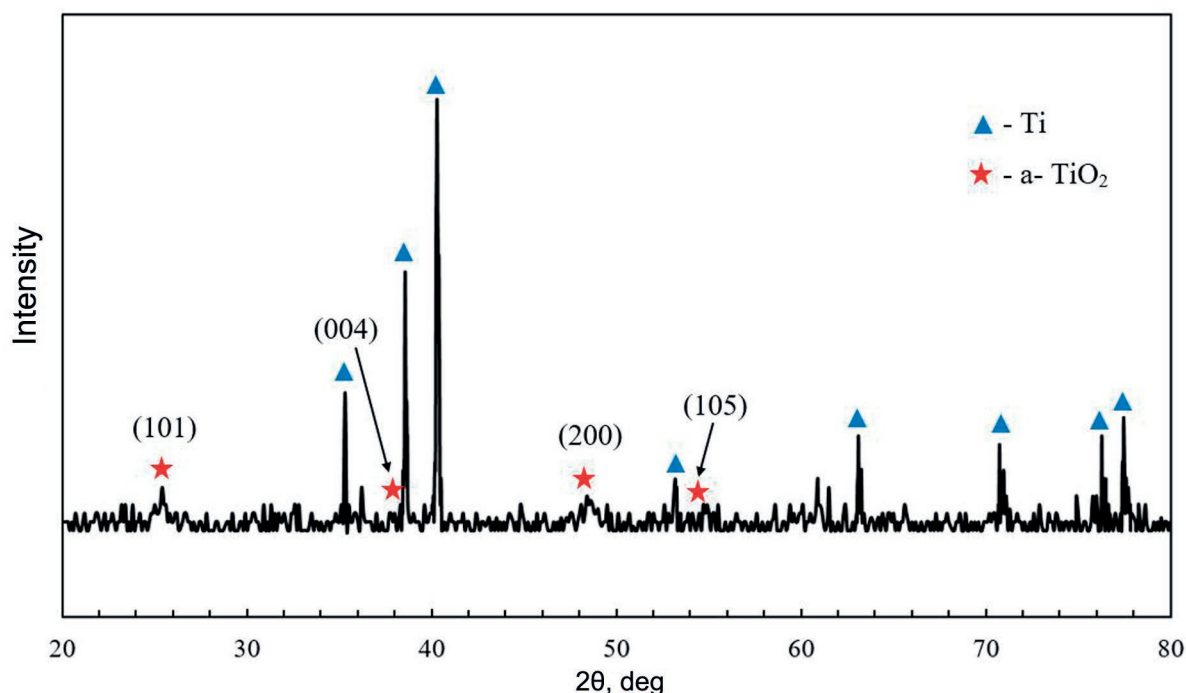
lines corresponding to the Bragg reflections (101) and (200) for  $\alpha$ - $\text{TiO}_2$  with d-spacings:  $d_1 = 0.351$  nm (101),  $d_2 = 0.189$  nm (200). In addition, the asymmetry of the line (002) Ti ( $d = 0.234$  nm) may indicate [17] the presence of a reflection corresponding to the reflection (004) for  $\alpha$ - $\text{TiO}_2$  with  $d_3 = 0.239$  nm. This fact suggests that the phase composition of the microcone formations included in the X-ray amorphous nanoporous/nanotubular titanium oxide matrix corresponded to the crystalline modification of  $\text{TiO}_2$  (anatase). It should also be emphasised that the results of qualitative phase analysis correlate with the data in papers [16-18] devoted to a comprehensive study of the atomic structure of microcone formations in AOCs on titanium foil using X-ray diffraction and X-ray photoelectron spectroscopy.

As has already been noted above, only qualitative models for the formation of such microstructures have been proposed to date. For example, some authors [14] discuss reasons for the formation of anatase microcones during the anodising of compact titanium in aqueous solutions of acids with fluorine ions. They suggest, in accordance with [21–23], that the mechanism of growth of anatase microcrystallites

can be explained by the development of nanosized crystalline nuclei that form in defective sites on the metal/oxide interface under the influence of high local current density. However, they do not describe the effect of fluorine ions. It is believed [22, 23] that the growth of the crystalline component is due, firstly, to local heating, secondly, to compressive stresses that are present on the metal/oxide interface. It was also indicated that one of the reasons for the flower-like shape of the anatase microcones may be due to the reaction of oxygen evolution [38, 39]. When explaining the formation of MCCs by anodising titanium foil in a 1 M  $\text{H}_2\text{SO}_4$  + 0.1 vol.% HF electrolyte, authors [18] presented a model whose determining factor was considered to be the existence of internal compressive stresses leading to the detachment of the oxide film and the appearance of hollow microcone formations. However, the authors did not give any reliable justification for the model.

Taking into account the available information on the growth of anatase microcone formations during anodising of compact titanium [14, 18, 21, 23], it can be assumed that the formation of hierarchical  $\alpha$ - $\text{TiO}_2$  micro-nanostructures





**Fig. 8.** X-ray diffraction (XRD) pattern of the sample of porous powder material made from titanium sponge after anodising in a 1M  $\text{H}_2\text{SO}_4$  + 0.15 wt % HF electrolyte at  $j_m = 1,890$  mA/g,  $t_a = 90$  min

on the surface of TS PPM is also influenced by the heterogeneous relief of the surface of titanium sponge and oxygen-containing inclusions. Moreover, their effect on the process of crystallisations should increase with an increase in the current density of the galvanostatic process, which correlates well with the results of the study of the atomic structure and morphology.

Thus, the study of the growth, morphology, and atomic structure revealed that the proposed treatment conditions for porous materials from sintered powders of Ti sponge allow forming hierarchical micronanostructured anodic oxide coatings characterised by a nanoporous amorphous matrix containing nanostructured anatase microcones.

#### 4. Conclusions

The study of the influence of the conditions of the galvanostatic process on the growth of anodic oxide coatings on the samples of porous powder materials made from titanium sponge in a 1 M  $\text{H}_2\text{SO}_4$  + 0.15 wt% HF electrolyte showed that anodising at a current density of  $j_m \approx 202$  mA/g leads to the formation of an X-ray amorphous layer of  $\text{TiO}_2$  with a thickness of about 250–350 nm and evenly distributed pores/tubes with

effective diameters of  $(50 \pm 20)$  nm. Anodising at large current values of  $j_m$  in the range from 230 to 1,890 mA/g leads to the appearance of nanostructured  $\alpha$ - $\text{TiO}_2$  microcones with base diameters and heights of up to 4–4.5  $\mu\text{m}$ . These microcones are unevenly distributed in the X-ray amorphous oxide matrix. The obtained coatings on the surface of porous materials made from sintered powders of titanium sponge with a high specific area and a hierarchical micro/nanostructure are promising for a whole range of applications, in particular, for the design of devices for photocatalytic environment purification and production of superhydrophobic surfaces, which can be an area for further research.

#### Author contributions

N. M. Yakovleva: scientific supervision of research, concept of research, text writing, final conclusions. A. M. Shulga, K. V. Stepanova, A. N. Kokatev: studying the kinetics of growth and morphology by atomic force microscopy, generalising results, V. Lukianchuk: studying the morphology, elemental composition, atomic structure, scientific editing of the text, E. S. Chubieva: processing microscopic images, preparing figures.

## Conflict of interests

The authors declare that they have no known competing financial interests or personal relationships that could have influenced the work reported in this paper.

## References

- Riboni F., Nguyen N. T., So S., Schmuki P. Aligned metal oxide nanotube arrays: key-aspects of anodic TiO<sub>2</sub> nanotube formation and properties. *Nanoscale Horizons*. 2016;1: 445–466. <https://doi.org/10.1039/C6NH00054A>
- Yakovleva N. M., Kokatev A. N., Chupakhina E. A., Stepanova K. V., Yakovlev A. N., Vasil'ev S. G., Shul'ga A. M. Surface nanostructuring of metals and alloys. Part 2. Nanostructured anodic oxide films on Ti and Ti alloys. *Condensed Matter and Interphases*. 2016;18(1): 6–27. (In Russ., abstract in Eng.). Available at: <https://elibrary.ru/item.asp?id=25946608>
- Lee K., Mazare A., Schmuki P. One-dimensional titanium dioxide nanomaterials: nanotubes. *Chemical Reviews*. 2014;114(1): 9385–9454. <https://doi.org/10.1021/cr500061m>
- Macak J. M., Tsuchiya H., Ghicov A., Yasuda K., Hahn R., Bauer S., Schmuki P. TiO<sub>2</sub> nanotubes: self-organized electrochemical formation, properties and applications. *Current Opinion in Solid State and Materials Science*. 2007;11: 3–18. <https://doi.org/10.1016/j.cossms.2007.08.004>
- Kulkarni M., Mazare A., Gongadze E., Perutkova Š., Kralj-Iglic V., Milošev I., Schmuki P., Iglic A., Mozetic M. Titanium nanostructures for biomedical applications. *Nanotechnology*. 2015;26: 1–18. <https://doi.org/10.1088/0957-4484/26/6/062002>
- Kowalski D., Kim D., Schmuki P. TiO<sub>2</sub> nanotubes, nanochannels and mesosponge: Self-organized formation and applications. *Nano Today*. 2013;8(3): 235–264. <https://doi.org/10.1016/j.nantod.2013.04.010>
- Kokatev A. N., Stepanova K. V., Yakovleva N. M., Tolstik V. E., Shelukhina A. I., Shulga A. M. Self-organization of a bioactive nanostructured oxide layer at the surface of sintered titanium sponge powder subjected to electrochemical anodization. *Technical Physics*. 2018;63(9): 1334–1340. <https://doi.org/10.1134/S1063784218090062>
- Yoriya S., Mor G. K., Sharma S., Grimes C. A. Synthesis of ordered arrays of discrete, partially crystalline titania nanotubes by Ti anodization using diethylene glycol electrolytes. *Journal of Materials Chemistry*. 2008;18(28): 3332–3336. <https://doi.org/10.1039/B802463D>
- Xiao X. F., Ouyang K. G., Liu R. F., Liang J. H. Anatase type titania nanotube arrays direct fabricated by anodization without annealing. *Applied Surface Science*. 2008;255(6): 3659–3663. <https://doi.org/10.1016/j.apsusc.2008.10.014>
- Allam N. K., Grimes C. A. Room temperature one-step polyol synthesis of anatase TiO<sub>2</sub> nanotube arrays: photoelectrochemical properties. *Langmuir*. 2009;25(13): 7234–7240. <https://doi.org/10.1021/la9012747>
- Liao Y., Wang X., Ma Y., Li J., Wen T., Jia L., Zhong Z., Wang L., Zhang D. New mechanistic insight of low temperature crystallization of anodic TiO<sub>2</sub> nanotube array in water. *Crystal Growth & Design*. 2016;16(4): 1786–1791. <https://doi.org/10.1021/acs.cgd.5b01234>
- Lamberti A., Chiodoni A., Shahzad N., Bianco S., Quaglio M., Pirri C. F. Ultrafast room-temperature crystallization of TiO<sub>2</sub> nanotubes exploiting water-vapor treatment. *Scientific Reports*. 2015;5(1): 7808–7013. <https://doi.org/10.1038/srep07808>
- Wang X., Zhang D., Xiang Q., Zhong Z., Liao Y. Review of water-assisted crystallization for TiO<sub>2</sub> nanotubes. *Nano-Micro Letters*. 2018;10(4): 77–105. <https://doi.org/10.1007/s40820-018-0230-4>
- Wang C., Wang M., Xie K., Wu Q., Sun L., Lin Z., Lin C. Room temperature one-step synthesis of microarrays of N-doped flower-like anatase TiO<sub>2</sub> composed of well-defined multilayer nanoflakes by Ti anodization. *Nanotechnology*. 2011;22(30): 305607. <https://doi.org/10.1088/0957-4484/22/30/305607>
- Huang J., Lai Y., Wang L., Li S., Ge M., Zhang K., Fuchs H., Chi L. Controllable wettability and adhesion on bioinspired multifunctional TiO<sub>2</sub> nanostructure surfaces for liquid manipulation. *Journal of Materials Chemistry A*. 2014;2(43): 8531–18538. <https://doi.org/10.1039/C4TA04090B>
- Li S., Li Y., Wang J., Nan Y., Ma B., Liu Z., Gu J. Fabrication of pinecone-like structure superhydrophobic surface on titanium substrate and its self-cleaning property. *Chemical Engineering Journal*. 2016;290: 82–90. <https://doi.org/10.1016/j.cej.2016.01.014>
- Rhee O., Lee G., Choi J. Highly ordered TiO<sub>2</sub> microcones with high rate performance for enhanced lithium-ion storage. *ACS Applied Materials & Interfaces*. 2016;8(23): 14558–14563. <https://doi.org/10.1021/acsami.6b03099>
- Park J., Lee G., Choi J. Key anodization factors for determining the formation of TiO<sub>2</sub> microcones vs nanotubes. *Journal of The Electrochemical Society*. 2017;164(9): D640–D644. <https://doi.org/10.1149/2.1601709jes>
- Park J., Choi J. Formation of well dispersed TiO<sub>2</sub> microcones; the 20% surface occupation. *Applied Surface Science*. 2018;448: 212–218. <https://doi.org/10.1016/j.apsusc.2018.04.033>
- Park J., Kim S., Lee G., Choi J. RGO-coated TiO<sub>2</sub> microcones for high-rate lithium-ion batteries. *ACS*

- Omega*. 2018;3(8): 10205–10210. <https://doi.org/10.1021/acsomega.8b00926>
21. Xing J., Xia Z., Hu J., Zhang Y., Zhong L. Time dependence of growth and crystallization of anodic titanium oxide films in potentiostatic mode. *Corrosion Science*. 2013;75: 212–219. <https://doi.org/10.1016/j.corsci.2013.06.004>
22. Xing J., Li H., Xia Z., Hu J., Zhang Y., Zhong L. Formation and crystallization of anodic oxide films on sputter-deposited titanium in potentiostatic and potential-sweep modes. *Journal of The Electrochemical Society*. 2013;160(10): C503–C510. <https://doi.org/10.1149/2.066310jes>
23. Xing, J.-H. Xia Z.-B., Hu J.-F., Zhang Y.-H., Zhong L. Growth and crystallization of titanium oxide films at different anodization modes. *Journal of The Electrochemical Society*. 2013;160(6): 239–246. <https://doi.org/10.1149/2.070306jes>
24. Palma D. P. da S., Nakazato R. Z., Codaro E. N., Acciari H. A. Morphological and structural variations in anodic films grown on polished and electropolished titanium substrates. *Materials Research*. 2019;22: 1–98. <https://doi.org/10.1590/1980-5373-MR-2019-0362>
25. Zhang L., Duan Y., Gao R., Yang J., Wei K., Tang D., Fu T. The effect of potential on surface characteristic and corrosion resistance of anodic oxide film formed on commercial pure titanium at the potentiodynamic-aging mode. *Materials*. 2019;12(3): 370. <https://doi.org/10.3390/ma12030370>
26. Yoo H., Lee G., Choi J. Binder-free SnO<sub>2</sub>-TiO<sub>2</sub> composite anode with high durability for lithium-ion batteries. *RSC Advances*. 2019;9: 6589–6595. <https://doi.org/10.1039/C8RA10358E>
27. Kim Y.-T., Youk J. H., Choi J. Inverse-direction growth of TiO<sub>2</sub> microcones by subsequent anodization in HClO<sub>4</sub> for increased performance of lithium-ion batteries. *ChemElectroChem*. 2020;7(5): 1057–1285. <https://doi.org/10.1002/celec.202000114>
28. Savich V. V., Bobrovskaya A. I., Taraikovich A. M., Bedenko S. A. Micro- and nanostructures surface foam particles of titanium powder and its influence on properties of porous materials from them. *Nanotechnologies of functional materials (NFM – 2012): proceeding of the international scientific and technical conference, 27–29 June 2012*. St. Petersburg: Polytechnic University Publ.; 2012. p. 523–529. (in Russ., abstract in Eng.)
29. Savich V. V. Methods of porous structure regulation of sintered materials from spongy powders of titanium. *Poroshkovaya metallurgiya*. 2016; 70–76. (in Russ., abstract in Eng.). Available at: <https://elibrary.ru/item.asp?id=37590838>
30. Shelukhina A. I., Stepanova K. V., Kokatev A. N., Tolstik V. E. Surface modification of porous materials made of sponge titanium powder by means of anodic oxidation. *Poroshkovaya metallurgiya*. 2015;38: 180–184. (in Russ., abstract in Eng.)
31. Yakovleva N. M., Shul'ga A. M., Lukiyanchuk I. V., Stepanova K. V., Kokatev A. N. Growth and crystallization of anodic oxide films on sintered titanium powders. In: *Powder metallurgy: Surface Engineering, New Powder Composite materials. Welding. Proc. 12th Int. Sym., 7–9 April 2021, Minsk. In 2 p. Part 2*. Minsk: Belaruskaya nauka Publ.; 2021. p. 421–429. (in Russ., abstract in Eng.)
32. Yakovleva N. M., Shulga A. M., Stepanova K. V., Kokatev A. N., Rudnev V. S., Lukiyanchuk I. V., Kuryavyy V. G. Microcone anodic oxide films on sintered niobium powders. *Condensed Matter and Interphases*. 2020;22(1): 124–134. <https://doi.org/10.17308/kcmf.2020.22/2536>
33. Stepanova K. V., Yakovleva N. M., Kokatev A. N., Pettersson Kh. Nanoporous anodic oxide films on Ti–Al powder alloy. *Proceedings of Petrozavodsk State University. Natural and Engineering Sciences*. 2015;147(2): 81–86. (in Russ., abstract in Eng.). Available at: <https://elibrary.ru/item.asp?id=23306599>
34. Habazaki H., Uozumi M., Konno H., Shimizu K., Skeldon P., Thompson G. E. Crystallization of anodic titania on titanium and its alloys. *Corrosion Science*. 2003;45: 2063–2073. [https://doi.org/10.1016/S0010-938X\(03\)00040-4](https://doi.org/10.1016/S0010-938X(03)00040-4)
35. Habazaki H., Uozumi H., Konno H., Shimizu K., Skeldon P., Thompson G. E., Wood G. C. Breakdown of anodic films on titanium and its suppression by alloying. *Journal of Corrosion Science and Engineering*. 2003;6: 107. Available at: <https://www.jcse.org/viewPaper/ID/206/fajeUDexa2dF4qbiJP7Hh6yvJ8mTNE>
36. Nagesh Ch. R. V. S., Ramachandran C. S., Subramanyam R. B. Methods of titanium sponge production. *Transactions of the Indian Institute of Metals*. 2008;61(5): 341–348. <https://doi.org/10.1007/s12666-008-0065-7>
37. Beranek R., Hildebrand H., Schmuki P. Self-organized porous titanium oxide prepared in H<sub>2</sub>SO<sub>4</sub>/HF electrolytes. *Electrochemical and Solid-State Letters*. 2003;6(3): 12–14. <https://doi.org/10.1149/1.1545192>
38. Mazzarolo A., Curioni M., Vicenzo A., Skeldon P., Thompson G. E. Anodic growth of titanium oxide: Electrochemical behaviour and morphological evolution. *Electrochimica Acta*. 2012;75: 288–295. <https://doi.org/10.1016/j.electacta.2012.04.114>
39. Liu Z. J., Zhong X., Walton J., Thompson G. E. Anodic film growth of titanium oxide using the 3-electrode electrochemical technique: effects of oxygen evolution and morphological characterizations. *Journal of The Electrochemical Society*. 2016;163 (3): E75–E82. <https://doi.org/10.1149/2.0181603jes>

**Information about the authors**

*Natalia M. Yakovleva*, Dr. Sci. (Phys.–Math.), Full Professor, Professor at the Department of Information – Measuring Systems and Physical Electronics, Petrozavodsk State University (Petrozavodsk, Republic of Karelia, Russian Federation).

<https://orcid.org/0000-0003-4294-0183>  
nmyakov@petsu.ru, nmyakov@gmail.com

*Alisa M. Shul'ga*, Engineer, Petrozavodsk State University (Petrozavodsk, Republic of Karelia, Russian Federation).

<https://orcid.org/0000-0002-3844-7110>  
shulga.alisa@gmail.com

*Irina V. Lukiyanchuk*, Cand. Sci. (Chem.), Senior Researcher, Institute of Chemistry, Far-Eastern Branch, Russian Academy of Sciences V(ladivostok, Russian Federation).

<https://orcid.org/0000-0003-1680-4882>  
lukiyanchuk@ich.dvo.ru

*Kristina V. Stepanova*, Cand. Sci. (Tech.), Associate Professor, Petrozavodsk State University, (Petrozavodsk, Republic of Karelia, Russian Federation).

<https://orcid.org/0000-0002-4737-497X>  
lady.cristin4ik@yandex.ru

*Alexander N. Kokatev*, Cand. Sci. (Tech.), Engineer, Petrozavodsk State University (Petrozavodsk, Republic of Karelia, Russian Federation).

<https://orcid.org/0000-0002-9449-1482>  
nelan-oxid@bk.ru

*Elena S. Chubieva*, Engineer, Petrozavodsk State University (Petrozavodsk, Republic of Karelia, Russian Federation).

<https://orcid.org/0000-0001-6782-8089>  
echubieva07@mail.ru

*Received 23.06.2022; approved after reviewing 20.10.2022; accepted for publication 15.11.2022; published online 25.12.2022.*

*Translated by Irina Charychanskaya  
Edited and proofread by Simon Cox*



## Condensed Matter and Interphases

Kondensirovannye Sredy i Mezhfaznye Granitsy  
<https://journals.vsu.ru/kcmf/>

### 90<sup>th</sup> anniversary of the Department of Physical Chemistry of Voronezh State University

The Department of Physical Chemistry as an independent structural subdivision of Voronezh State University (VSU) was founded in 1932. The first head of the Department was Professor N. V. Kultashev, a well-known scientist of the scientific school of the outstanding physical chemist Gustav Tamman at Yuriev University. Since 1924, academic work and extensive scientific research has been carried out at VSU in the field of physical chemistry. These were started under the leadership of N. V. Kultashev. The study of the processes of vacuum evaporation of zinc from alloys with silver and copper for the production of metal membranes concluded with the defence of a Ph.D. thesis by associate professor F. A. Santalov, who was head of the Department from 1938 to 1939. In the period from 1942 to 1954, associate professor S. A. Kretinin was the head of the joint Department of Physical and Colloidal Chemistry.

Since 1939, research into electrochemical corrosion has performed at the Department of Physical Chemistry of Voronezh State University. Assistant A. Ya. Shatalov, under the supervision of Prof. N. V. Kultashev, for the first time performed measurements of the electrode potentials of antimony and other metals. The studies interrupted during the Great Patriotic War were resumed by Associate Professor A. Ya. Shatalov in 1950. The corrosion behaviour of metals in solutions with various acidity was investigated. The defence of his doctoral thesis at the Institute of Physical Chemistry of the Academy of Sciences of the USSR (Moscow) by A. Ya. Shatalov was a notable event that confirmed the productive application of the theory of electrochemical kinetics for the description of corrosion processes on metals in electrolyte solutions. Since 1956, under the guidance of Professor A. Ya. Shatalov, intensive research has been carried out at the

Department of Physical Chemistry relating to the electrochemical corrosion of metals.

In 1979 Professor I. K. Marshakov, became the head of the department and guided systematic studies on anodic dissolution and the selective corrosion of alloys, which he started back in 1958. Professor I. K. Marshakov is one of the founders of a new area in corrosion science, "Electrochemistry and the corrosion of alloys".

A significant contribution to the general theory of alloy dissolution with an analytical description of kinetic regularities was made in the doctoral thesis of A. V. Vvedensky, who was head of the Department from 2000 to 2019. For the first time, a fairly complete and consistent physicochemical model of the anodic dissolution of a homogeneous alloy was presented in the thesis. Professor A. V. Vvedensky continues to actively work at the department and he is the chairman of the dissertation board on physical chemistry, inorganic chemistry, and electrochemistry.

The current head of the Department of Physical Chemistry of VSU is Doctor of Chemical Sciences, Associate Professor O. A. Kozaderov. In his thesis (2016) he established the physicochemical regularities of the formation and development of a nonequilibrium surface layer at the alloy/solution interface under conditions of simultaneous unsteady diffusion processes, phase transformations, and changes in surface morphology.

The main scientific area of the Department of Physical Chemistry of VSU is "Thermodynamics and kinetics of heterogeneous processes in metal and metal-polymer systems with electrochemical, chemical, adsorption and transport stages as a scientific foundation for the creation of new principles of electrocatalytic reaction



The content is available under Creative Commons Attribution 4.0 License.

control, production of highly active electrode materials and the creation of new principles of electrocatalytic reaction control". Fundamental research is carried out within the framework of the state task for universities in the area of scientific research of the Ministry of Science and Higher Education, grant projects of the Russian Science Foundation and the Russian Foundation for Basic Research, the federal scientific and technical programme of development of synchrotron and neutron techniques and research infrastructure and other science support programmes.

The Department has educational and scientific laboratories for electrochemistry and the corrosion of metals and alloys, photoelectrochemistry, the physical chemistry of metal/polymer systems, electrocatalysis, and the electrodeposition of metals and alloys. The workplaces of researchers, teachers, and students are equipped with modern electrochemical stations (IPC-Compact, IPC-Pro L, IPC-Pro MF, P-20X, P-40X, etc.) and computers with specialised software (Comsol Multiphysics, Mathematica, Matlab), which allow them to conduct scientific research at a high level.

Academic cooperation between the Department of Physical Chemistry of Voronezh State University and scientific Russian and foreign organisations is successfully developing. A joint laboratory of Voronezh State University and the A. N. Frumkin Institute of Physical Chemistry and Electrochemistry of the Russian Academy of Sciences "Adjoint processes in Electrochemistry and Metal Corrosion" was created. International projects with the National Chemical Engineering Institute in Paris (France) and the National Institute of Technology in Kurukshetra (India) are supported by national governments. Interactions with real economy enterprises were established and based on requests from these organisations, commercial R&D projects

are carried out. The results of fundamental and applied research are used in solving urgent problems in the field of electrochemical and hydrogen energy, in the synthesis of functional coatings for micro- and nanoelectronics, in the development of effective methods of anti-corrosion protection.

The training of staff for specialised sectors of the economy is carried out at the department within the framework of training courses and practical sessions in physical chemistry and electrochemistry, chemical current sources and electrochemical technologies, quantum chemistry and computer modelling of electrochemical systems, physical chemistry of adsorption processes and thermodynamics of irreversible processes, methods of protection against corrosion. The graduates of the department work at the enterprises of the electronic, energy, and food industries (OAO "Concern SOZVEZDIE", OAO NIIPM, AO NIET, AO VZPP-Mikron, Novovoronezh nuclear power station, GC "EFKO", etc.), in medical organisations, pharmaceutical companies and environmental laboratories (Rospotrebnadzor, AO Binergia, Binnopharm group, OOO DNA-Technologies, etc.), teach at schools and universities, conduct research in scientific organisations (A. N. Frumkin Institute of Physical Chemistry and Electrochemistry and other institutes of the Russian Academy of Sciences).

Today the Department of Physical Chemistry is the core of the dynamically developing and somewhat original Voronezh School of Electrochemists and Corrosionists. Congratulations to the staff of the Department of Physical Chemistry of Voronezh State University on its 90<sup>th</sup> anniversary and wishes for future successes in education and new scientific achievements!

*The Editorial board  
of the journal Condensed Matter and Interphases  
Translated by Valentina Mittova*